

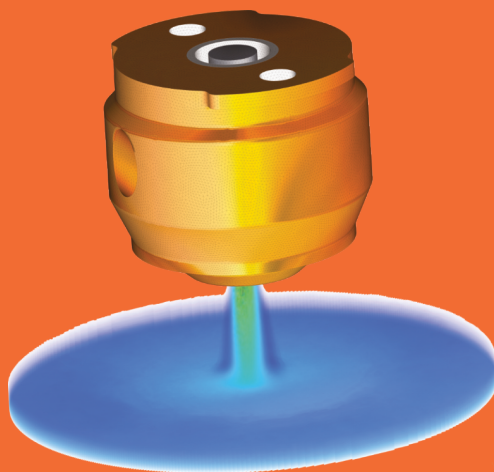
---

# MATHEMATICAL MODELLING OF WELD PHENOMENA

## 13

---

Edited by  
C. Sommitsch  
N. Enzinger  
P. Mayr



# **MATHEMATICAL MODELLING OF WELD PHENOMENA 13**



The delegates of the 13<sup>th</sup> International Seminar 'Numerical Analysis of Weldability' held from 4 - 7 September 2022 at Schloss Seggau near Graz, Austria

# **MATHEMATICAL MODELLING OF WELD PHENOMENA 13**

Selected peer reviewed papers from the  
**13<sup>th</sup> International Seminar**  
**Numerical Analysis of Weldability**  
September 4 - 7, 2022  
Graz - Schloss Seggau - Austria

Edited by

**Christof Sommitsch**

Institute of Materials Science, Joining and Forming  
Graz University of Technology

**Norbert Enzinger**

Institute of Materials Science, Joining and Forming  
Graz University of Technology

**Peter Mayr**

Materials Engineering of Additive Manufacturing  
Technical University of Munich

2023 Verlag der Technischen Universität Graz  
[www.tugraz-verlag.at](http://www.tugraz-verlag.at)

ISSN 2410-0544  
ISBN (print) 978-3-85125-968-1  
ISBN (e-book) 978-3-85125-969-8  
DOI 10.3217/978-3-85125-968-1



This work is licensed under the Creative Commons Attribution 4.0 International (CC BY 4.0) license.

<https://creativecommons.org/licenses/by/4.0/deed.en>

This CC license does not apply to the cover, third party material (attributed to other sources) and content noted otherwise.

Production Secretary, Typeset, Layout

**Isabella Knollseisen**

Institute of Materials Science, Joining and Forming  
Graz University of Technology

Printed & bound  
Koralpendruckerei, Deutschlandsberg, Austria  
[www.koralpendruckerei.at](http://www.koralpendruckerei.at)

# Table of Contents

	<b>Introduction</b>	<b>1</b>
	<b>Obituary Univ.-Prof. i.R. Dipl.-Ing. Dr. mont. Bruno Buchmayr</b>	<b>3</b>
<b>I</b>	<b>Additive Manufacturing</b>	
	<b>High-fidelity numerical modelling of cold spatter formation during laser powder bed fusion of 316-L stainless steel</b>	<b>7</b>
	<i>M. Bayat, J. H. Hattel</i>	
	<b>Comparison between green and infrared laser in laser powder bed fusion of pure copper through high fidelity numerical modelling at meso-scale</b>	<b>21</b>
	<i>W.E. Alphonso, M. Bayat, J. H. Hattel</i>	
	<b>Simulation of microstructure evolution during WAM process</b>	<b>39</b>
	<i>J. Kronsteiner, H. Drexler, S. Hovden, F. Haunreiter, P. O'Toole, A. Molotnikov, M. Easton</i>	
	<b>Numerical prediction of bead formation and build-up toward WAAM process optimization</b>	<b>57</b>
	<i>H. Ben Hamouda, I. O. Felice, J. P. Oliveira, J. Antonissen</i>	
<b>II</b>	<b>Arc Welding, Melt Pool, Solidification</b>	
	<b>Physical mechanisms governing deposition rate in arc welding with a consumable electrode</b>	<b>71</b>
	<i>P. F. Mendez, Z. Yan, V. Núñez Sánchez, S. Chen</i>	
	<b>Numerical study on the formation of a bulging region in partial penetration laser beam welding</b>	<b>101</b>
	<i>A. Artinov, X. Meng, M. Bachmann, M. Rethmeier</i>	
	<b>Modelling of the melt pool behaviour during a pulsed TIG welding operation in a narrow groove</b>	<b>127</b>
	<i>S. Cadiou, A. Baumard, A. Brosse, V. Bruyere</i>	
	<b>A numerical study on the suppression of a detrimental weld pool profile in wire feed laser beam welding by magnetohydrodynamic technique</b>	<b>143</b>
	<i>X. Meng, A. Artinov, M. Bachmann, Ö. Üstündağ, A. Gumenyuk, M. Rethmeier</i>	

	<b>Numerical analysis of the dependency of the weld pool shape on turbulence and thermodynamic activity of solutes in laser beam welding of unalloyed steels</b>	<b>161</b>
	<i>A. Artinov, P. Kising, M. Bachmann, X. Meng, M. Rethmeier</i>	
	<b>FEM study of thermomechanical welding of austenitic stainless steel and experimental validation</b>	<b>189</b>
	<i>P. Wang, B. Szalowski, J. E. Azuke, R. Vallant, M. C. Poletti, N. Enzinger</i>	
<b>III</b>	<b>Artificial Intelligence</b>	
	<b>Study of resistance spot welding via experimental, numerical and advanced analytical methods</b>	<b>205</b>
	<i>H. Gao, R. Zwart, E. vd Aa, T. vd Veldt</i>	
<b>IV</b>	<b>Laser and Electron Beam Welding</b>	
	<b>Establishing an automated heat-source calibration framework</b>	<b>221</b>
	<i>D.K. Rissaki, A.N.Vasileiou, M.C. Smith, O. Muránsky, P.G. Benardos, G.-C. Vosniakos</i>	
	<b>Numerical Analysis of the influence of an auxiliary oscillating magnetic field on suppressing the porosity formation in deep penetration laser beam welding of aluminum alloys</b>	<b>237</b>
	<i>F. Yang, X. Meng, M. Bachmann, A. Artinov, S. N. Putra, M. Rethmeier</i>	
	<b>Simulation of laser assisted double wire deposition welding with two different approaches with eulerian (FVM) and lagrangian (SPH) methods</b>	<b>255</b>
	<i>U. Reisgen, R. Sharma, O. Mokrov, S. Emadmostoufi, J. Kruska, J. Hermsdorf, M. Lammers, T. Bokelmann</i>	
<b>V</b>	<b>Residual Stresses and Distortion</b>	
	<b>Simulation of Residual Stresses During the wire arc additive Manufacturing (WAAM) Process</b>	<b>283</b>
	<i>A. A. Alrumayh, H. F. Nied</i>	
	<b>Numerical analysis of welding process for distortion prediction of pipe structures for aerospace industry</b>	<b>305</b>
	<i>S. Rasche, M. Fischer, J. Hildebrand, J. P. Bergmann</i>	
	<b>Effect of phase- and temperature- dependent strain-hardening slopes on the calculated welding residual stresses in S235 steel</b>	<b>319</b>
	<i>J. Sun, T. Nitschke-Pagel, K. Dilger</i>	

	<b>Validation of Welding Structure Simulations</b>	<b>331</b>
	<i>T. Loose, T. Girresser, J. Goldak</i>	
	<b>Numerical simulation of L-PBF additive manufacturing of medium-manganese steel for automotive crash applications</b>	<b>341</b>
	<i>K. Abburi Venkata, B. Schob, M. Kasprowicz</i>	
	<b>A simulation approach for series production of plasma-based additive manufacturing of Ti-6Al-4V components</b>	<b>361</b>
	<i>M. Bielik, E. Neubauer, M. Kitzmantel, I. Neubauer, E. Kozeschnik</i>	
<b>VI</b>	<b>Microstructural Modelling in Weld Metal and Heat Affected Zone</b>	
	<b>Extraction of process-structure-property linkage using deep learning methods</b>	<b>397</b>
	<i>J. Inoue, S. Noguchi</i>	
	<b>Microstructure evolution subroutine for finite element analysis</b>	<b>407</b>
	<i>Y. V. Shan, B. Viernstein, E. Kozeschnik</i>	
	<b>Stress-strain properties of HSS steel welded joint heterogeneous structure: experimental and numerical evaluation</b>	<b>413</b>
	<i>D. Tomerlin, D. Kozak, N. Gubeljak, M. Magić Kukulj</i>	
<b>VII</b>	<b>Cracking Phenomena and Hydrogen Effects</b>	
	<b>Analysis of Solidification Cracking Considering Mechanical and Metallurgical Factors</b>	<b>431</b>
	<i>S. Maeda, T. Kato, K. Ikushima, M. Shibahara</i>	
	<b>Numerical study of the TEKKEN welding test</b>	<b>449</b>
	<i>A. A. M. Paget, V. Robin, J. Draup, S. Hendili, R. Ufarté, T. Khan, J. Delmas, M. C. Smith</i>	
<b>VIII</b>	<b>Modelling Tools and Computer Programs</b>	
	<b>Assessment of fatigue behaviour of UHSS steel butt-welded joints by means of a fracture mechanics methodology</b>	<b>473</b>
	<i>C. Steimbreyer, N. Gubeljak, T. Vuherer, N. Enzinger, W. Ernst, M. D. Chapetti</i>	
	<b>Efficient numerical analysis of directed energy deposition processes</b>	<b>491</b>
	<i>B. A. M. Elsner, I. Neubauer, L. Raberger</i>	
	<b>Prognosis of seam geometry during laser beam welding</b>	<b>507</b>
	<i>C. Schwarz, M. Puschmann, R. Mauermann</i>	

## **IX Solid State and Friction Stir Welding**

**Numerical analysis of ultrasonic vibration enhanced friction stir welding of dissimilar Al/Mg alloys** 517

*C. L. Yang, C. S. Wu, M. Bachmann, M. Rethmeier*

**A process modelling approach to the development of lap welding procedures** 539

*M. Lewis, S. Smith*

## **X Special Joining Processes**

**Impact of activation in projection welding with capacitor discharge using multiphysics simulation and a process-integrated transition resistance measurement** 551

*J. Koal, M. Baumgarten, J. Zschetzsche, U. Füssel*

**Simulation model for laser hardening of small-diameter holes** 567

*A. Evdokimov, F. Jasiewicz, N. Doynov, R. Ossenbrink, V. Michailov*

**Author Index** 575

## INTRODUCTION

This volume contains 32 selected papers presented at the 13<sup>th</sup> International Seminar ‘Numerical Analysis of Weldability’, held from September 4th to 7th, 2022 at Schloss Seggau near Graz, Austria. As always, this location provided an inspiring environment encouraging friendly and intensive discourse between scientists and engineers. The conference stood up to its reputation as one of the most important forums in the science of welding. The meeting was organized by the Institute of Materials Science, Joining and Forming (IMAT) of Graz University of Technology, and the working group ‘Mathematical Modelling of Weld Phenomena’ of Commission IX of the International Institute of Welding (IIW).

The unique tradition of publishing (all articles refereed, typeset and edited in uniformity; each article is required to be comprehensive in its content) could be maintained also for this edition to serve the welding community as reference literature. The continuity of the previous twelve volumes, Mathematical Modelling of Weld phenomena 1 – 12, has therefore been preserved thanks to the monumental efforts of the Seggau team of IMAT. Special thanks goes to Bettina Schreiner-Föböl, who was in charge of the entire work of coordinating the peer review as well as Isabella Knollseisen for assisting her in the layout creation and editing procedure in a highly ambitious manner. Volume 13 is again published by Verlag der Technischen Universität Graz and all papers have a DOI and are available open access.

The 2022 seminar was attended by 69 delegates coming from 12 countries participating in both, oral sessions and poster presentations in the following sessions:

- I Additive Manufacturing
- II Arc Welding, Melt Pool, Solidification
- III Artificial Intelligence
- IV Laser and Electron Beam Welding
- V Residual Stresses and Distortion
- VI Microstructural Modelling in Weld Metal and Heat Affected Zone
- VII Cracking Phenomena and Hydrogen Effects
- VIII Modelling Tools and Computer Programs
- IX Solid State and Friction Stir Welding
- X Special Joining Processes

The most important observations of this seminar were the fact that modelling approaches in the meantime penetrate many fields of application in welding and recently in additive manufacturing. It helps to solve complex tasks and optimize the welding processes and materials used. By this, it helps to enhance the safety, reliability and economy of welded structures. This was impressively shown by many authors who in addition could verify the calculation results by experimental investigations.

The 2022 IIW Kenneth Easterling Best Paper Award was won by the paper "A numerical study on the suppression of a detrimental weld pool profile in wire feed laser

## Mathematical Modelling of Weld Phenomena 13

beam welding by magnetohydrodynamic technique”, Xiangmeng Meng, Antoni Artinov, Marcel Bachmann, Ömer Üstündağ, Andrey Gumenyuk and Michael Rethmeier. This paper has been valued by an international committee as the best contribution made over the four years proceeding on the advancement of knowledge or practice in respect of mathematical modelling of weld phenomena.

The next International Seminar ‘Numerical Analysis of Weldability’ will take place from September 21st – 24th, 2025 at Schloss Seggau.

Christof Sommitsch, Norbert Enzinger and Peter Mayr  
Graz, July 2023

## OBITUARY: UNIV.-PROF. I.R. DIPL.-ING.

### DR. MONT. BRUNO BUCHMAYR

We say goodbye to a great person, friend, scientist and visionary, who passed away on February 8<sup>th</sup>, 2021, at the age of 66 after a brief and severe illness caused by a Covid 19 infection.

Bruno Buchmayr, born in Leoben in 1954, studied materials science at what was then the Montanistische Hochschule in Leoben and graduated in 1980. During his studies, Bruno Buchmayr already worked as a student assistant at the Institute for Applied Mathematics. After completing his studies, he worked on his dissertation in the field of Materials Science under the guidance of Professor Hellmut Fischmeister, his role model. During that time, I delivered guest lectures from the industry at the Montanuniversität Leoben (University of Leoben). Even as a student, he caught my attention with his outstanding performance. That was the reason why I invited him to join me as an assistant at the Institute for Materials Science and Welding Technology (IWS) when I was appointed to Graz University of Technology in 1982, to assist me in building up the institute. It turned out to be a stroke of luck for my institute, as he worked there for 19 years, achieving remarkable success, until his appointment as a professor of Metal Forming at the Montanuniversität Leoben.

Through his profound expertise developed during his education, his intellect, talent, dedication, and openness to new ideas, he was fully engaged right from the beginning.

Buchmayr was particularly enthusiastic about applying the new insights of mathematical modeling of complex physical and thermodynamic processes using emerging computer applications in the field of Materials Science and Welding Technologies. He aimed to translate these findings into practical applications. He gladly shared his enthusiasm and knowledge with his master and doctoral students at the institute, encouraged and openly supported them. He significantly contributed to the professional success of these young team members, many of whom have made outstanding careers in academia and industry.

His high level of commitment to research and teaching at TU Graz was marked by exceptional developments: In 1988-1989 he received the opportunity for a guest stay at McMaster University in Hamilton, Ontario Canada, as part of an FWF-Erwin Schrödinger scholarship. In 1991, he habilitated in Materials Science and Welding technology at Graz University of Technology. In the same year, he also initiated and led a highly successful Christian Doppler Laboratory for “Computer Modelling of Materials Science and Process Technologies” which ran until 1998.

In 1997 he was appointed as an associate professor and deputy director at the Institute of Materials Science, Welding and Forming. Furthermore, he also played a crucial role in the establishment of competence centers such as the Materials Center Leoben (MCL) at Montanuniversität Leoben and the Virtual Vehicle Research Center (vif) at Graz University of Technology. In both centers, he was appointed a key researcher.

Bruno Buchmayr was one of the pioneers in the field of computer-based modeling of materials and welding technologies in production and in use. His research activities are

documented by many presentations at scientific conferences worldwide and more than 250 publications. The book he wrote "Computers in Materials and Welding Engineering: Application of Mathematical Models" is one of the most widely read works in this field. In 2002 his textbook "Material and Production Technology with Mathcad Modeling and Simulation in Application Examples" was published. The results of his research are characterized by highest scientific quality and additionally show, and this is particularly characteristic for Bruno Buchmayr, a significant potential for implementation in the complex manufacturing environment. The software he developed for thermomechanical rolling, which was implemented at VA-Stahl Linz and VA Draht Donawitz, was decisive for the great success of the Austrian steel industry. His collaboration in the development of cored wire electrodes for Böhler Welding made a lasting contribution to the success of this company.

This list can be continued at will. The so-called WEZ calculator he developed is legendary. It was the world's most complete software program for assisting welding engineers in their difficult questions of mastering the weldability.

On February 1, 2003, Bruno Buchmayr was appointed Professor of Metal Forming at the Montanuniversität Leoben. He continued his scientific focus and successfully linked the areas of simulation, material behavior and design in the field of forming technology. Bruno Buchmayer was always eager to work on future topics. For example, he brought 3D printing for metals to the Montanuniversität Leoben and tried to anchor digitization at the Montanuniversität. He continued to work there in a goal-oriented and successful manner with great sustainability.

His scientific achievements have also been recognized by a large number of awards and honors, such as the Hans-Malzacher-Prize of the EHÖ (ASMET), Prof. Masubuchi-Shinsho Corp. award of the American Welding Society, Franz-Leitner-Prize of the EHÖ (ASMET), ASM European Lecturer, Fellow ASM, Research Award of the Province of Styria 1998.

However, Bruno Buchmayr's commitment went far beyond the scientific activities at the university and he was also a key driving force and important initiator in the public life of the City of Leoben. For his many efforts for the City of Leoben, Bruno Buchmayr was awarded the Golden Medal of Merit of the City of Leoben.

From the list of his achievements alone, it is clear how successful and impressive his work in the fields of materials science, welding technology and production has been. The Austrian research landscape and industry has lost a researcher and scientist who is recognized and respected far beyond its borders.

Bruno Buchmayr was a visionary but always calm, reserved, even modest person who, despite his successes, was very disciplined and professionally extremely demanding and step by step went his own way. He was extremely correct, helpful, profound, religious and for many a very good friend and mentor.

He was always a role model because of his manifold activities. The Austrian Welding Community will always keep an honorable memory of him.

All our deepest sympathy and sincerest condolences go to his wife Gabi and his family.

*Em. Univ.-Prof. Dipl.-Ing. Dr. Horst Cerjak  
Co-founder and honorary chairman of "Numerical Analysis of Weldability"*

# **I Additive Manufacturing**



# HIGH-FIDELITY NUMERICAL MODELLING OF COLD SPATTER FORMATION DURING LASER POWDER BED FUSION OF 316-L STAINLESS STEEL

M. BAYAT<sup>\*,1</sup>, J. H. HATTEL<sup>\*</sup>

*\*Technical University of Denmark (DTU), Building 425, Kgs. 2800 Lyngby, Denmark*

*<sup>1</sup>Corresponding author*

*DOI 10.3217/978-3-85125-968-1-01*

## ABSTRACT

Spatter and denudation are two very well-known phenomena occurring mainly during the laser powder bed fusion process and are defined as ejection and displacement of powder particles, respectively. The main driver of this phenomenon is the formation of a vapor plume jet that is caused by the vaporization of the melt pool which is subjected to the laser beam. In this work, a 3-dimensional transient turbulent computational fluid dynamics model coupled with a discrete element model is developed in the finite volume-based commercial software package Flow-3D AM to simulate the spatter phenomenon. The numerical results show that a localized low-pressure zone forms at the bottom side of the plume jet and this leads to a pseudo-Bernoulli effect that drags nearby powder particles into the area of influence of the vapor plume jet. As a result, the vapor plume acts like a momentum sink and therefore all nearby particles point are dragged towards this region. Furthermore, it is noted that due to the jet's attenuation, powder particles start diverging from the central core region of the vapor plume as they move vertically upwards. It is moreover observed that only particles which are in the very central core region of the plume jet get sufficiently accelerated to depart the computational domain, while the rest of the dragged particles, especially those which undergo an early divergence from the jet axis, get stalled pretty fast as they come in contact with the resting fluid. In the last part of the work, two simulations with two different scanning speeds are carried out, where it is clearly observed that the angle between the departing powder particles and the vertical axis of the plume jet increases with increasing scanning speed.

Keywords: Spatter, Denudation, Discrete Element Method, Computational Fluid Dynamics, L-PBF, Additive Manufacturing

## INTRODUCION

Metal additive manufacturing (MAM) processes are capable of manufacturing very complex metallic components, which are near-to-impossible to make via the current existing conventional processes such as milling and casting. MAM are broadly classified into three primary groups of directed energy deposition (DED), powder bed fusion (PBF) and sheet lamination processes, according to the ASTM standard [1]. Nevertheless, DED

and PBF have received much more attention from both industrial sectors and academia thanks to DED and PBF's high degree of freedom and at the same time their inherent complexity, respectively.

One of the main issues of MAM processes (since we will only focus on DED and PBF, we will use the term MAM to refer to these two processes, henceforth, we will use MAM) is their complexity which is mainly due to the coexistence of a plethora of dependent interactive physical phenomena. These physical phenomena cover a long list ranging from melting, solidification, evaporation, ablation, laser-material interaction, absorption, the Marangoni effect, capillarity and evaporative recoil pressure occurring at meso-scale [2] to micro-scale phenomena such as dendrites' growth and nucleation, epitaxial grain growth and solid state phase transformation [3], [4]. Furthermore, all these physical phenomena occur within a very short timeframe in the order of sub-milliseconds [5] and therefore MAM processes, especially the PBF processes, are highly prone to instabilities. Therefore, any inaccurate selection of input process parameters could potentially lead to defects in the final components and such defects could simply disqualify the sample for the end users.

Over the past few years, advanced numerical simulations have been increasingly used to determine a process window comprising selected input process parameters with two ultimate goals of obtaining a defect-free component and unraveling defect formation mechanisms [6]–[8]. These models could be categorized based on several criteria such as length-scale [9], fidelity level and the involved physics [10] and type of coupling between these physics [11].

One of the two most complicated physical phenomena in PBF (mostly in LPBF) processes are spattering and denudation which are defined as the ejection of powder particles near to the melt pool and then their follow-up unwanted displacement in the vicinity of the scan tracks [12]. Compared to the colossal amount of research contributions that are dedicated to conduction- or transport-based melt pool simulations, there have been perhaps less than a dozen papers on the modelling of spatter and denudation [13]. Masmoudi, Bolot and Coddet. [14] attempted to simulate the vapor plume formation (the main driver of the spatter and denudation phenomena) via adding a mass source term in their model. Bidare et al. [15] made a somewhat more advanced finite element-based 2-dimensional model by taking the thermal aspects of the LPBF process, namely the laser heating effect via a Gaussian heat flux, into consideration and they found the vapour jet's velocity magnitude based on the Knudsen layer's approach. Recently, Bitharas et al. [16] extended this model to 3 dimensions. However, in the same manner as both the two earlier-mentioned works [14], [15], powder particles were not explicitly modelled in these simulations. Li and Tan [17], [18] developed a more advanced model and besides simulating the vapor plume via a continuum-based approach, they modelled particles' motion via the Lagrangian particle tracking method. Nevertheless, they only simulated a limited spatial domain with few powder particles under 2D axisymmetric assumptions.

In this work, we aim to understand the underlying mechanisms behind the spatter phenomenon and its relationship with the denudation of the powder layer via advanced numerical simulation. Therefore, we have developed a coupled finite volume (FVM)-based computational fluid dynamics (CFD) model coupled with the discrete element method (DEM) in the commercial software package Flow-3D, using the AM module. The

CFD model solves coupled partial differential equations of continuity, Reynolds Average Navier-Stokes (RANS), conservation of kinetic energy, conservation of dissipation of kinetic energy and finally, heat transfer. The DEM model solves equations of motions as well as the energy balance equation, based on a lumped thermal body assumption, for every individual powder particle while taking the interaction of powder particles and their collision into account. In the following section, we will go through the modelling details and assumptions for the CFD-DEM model and then we will explain and discuss the results and we will show how different choices of input process parameters can affect the powder dynamics in LPBF.

## NUMERICAL MODEL

In this section, first, we will go through fluid and particles' motion and heat transfer equations and then we will describe the details of the computational domain and the added boundary conditions.

### GOVERNING PHYSICS: FLUID AND PARTICLE MOTION

#### *Fluid flow motion*

The coupled partial differential equations (PDE) of continuity, time-averaged Navier-Stokes, , conservation of kinetic energy and finally, conservation of dissipation of kinetic energy are jointly solved to find the pressure and velocity field vectors in the computational domain belonging to the gas phase. Continuity and the Navier-Stokes equations are given below [19]

$$\frac{\partial u_i^F}{\partial x_i} = 0, \quad (1)$$

$$\rho \left[ \frac{\partial}{\partial t} u_i^F + \frac{\partial}{\partial x_j} (u_j^F u_i^F) \right] = - \frac{\partial p}{\partial x_i} + \rho g_i + \frac{\partial}{\partial x_j} (\sigma_{ij} + \tau_{ij}) + \Phi_i, \quad (2)$$

and  $u_i^F$  (m.s<sup>-1</sup>) is the fluid velocity vector and  $\rho$  (kg.m<sup>-3</sup>) is fluid's density and the two last terms inside the divergent operator,  $\sigma_{ij}$  (Pa) and  $\tau_{ij}$  (Pa) are viscous and turbulent stress tensors and the last term in equation (2) is the source term expressing external volumetric forces. However, in this work it is assumed that the sum of forces exerted on the fluid domain by the moving powder particles is negligible.

$$\sigma_{ij} = \mu_f \left( \frac{\partial u_i^F}{\partial x_j} + \frac{\partial u_j^F}{\partial x_i} \right), \quad (3)$$

$$\tau_{ij} = \mu_{turb} \left( \frac{\partial u_i^F}{\partial x_j} + \frac{\partial u_j^F}{\partial x_i} \right) - \frac{2}{3} \rho k \delta_{ij}, \quad (4)$$

$$\mu_{turb} = \rho C_\mu \frac{k^2}{\epsilon}, \quad (5)$$

where  $\mu_f$  (Pa.s) and  $\mu_{turb}$  (Pa.s) are fluid and turbulent viscosity, respectively [20]–[22].  $k$  ( $\text{m}^2.\text{s}^{-2}$ ) is the turbulent kinetic energy per unit mass for the host fluid, expressed in equations (4) and (5) and  $\varepsilon$  ( $\text{m}^2.\text{s}^{-3}$ ) is the dissipation rate of  $k$  ( $\text{m}^2.\text{s}^{-2}$ ).

$$\rho \left[ \frac{\partial}{\partial t} k + \frac{\partial}{\partial x_j} (u_j^F k) \right] = \frac{\partial}{\partial x_j} \left[ \left( \mu_f + \frac{\mu_{turb}}{\sigma_k} \right) \frac{\partial k}{\partial x_j} \right] + \Pi - \rho \varepsilon \quad (6)$$

$$\rho \left[ \frac{\partial}{\partial t} \varepsilon + \frac{\partial}{\partial x_j} (u_j^F \varepsilon) \right] = \frac{\partial}{\partial x_j} \left[ \left( \mu_f + \frac{\mu_{turb}}{\sigma_\varepsilon} \right) \frac{\partial \varepsilon}{\partial x_j} \right] + \frac{\varepsilon}{k} (C_{\varepsilon 1} \Pi - \rho \varepsilon C_{\varepsilon 2}), \quad (7)$$

$$\Pi = \tau_{ij} \frac{\partial u_i^F}{\partial x_j}. \quad (8)$$

Equations (6) and (7) are transient PDEs of conservation of turbulent kinetic energy and rate of change of turbulent kinetic energy, respectively.

### Particles' motion dynamics

The transient motion of the powder particles is described in the Lagrangian framework and found via solving the following particle force balance equation using DEM [23]

$$m_p \frac{d^2 X_i}{dt^2} = 6\pi\mu_f R_p (u_i^F - U_i^p) + F_i^{collision} + m_p (1 - \frac{\rho_F}{\rho_p}). \quad (9)$$

$R$  (m) and  $m_p$  (kg) are spherical particle's radius and mass, respectively.  $X_i$  (m) and  $U_i$  ( $\text{m}.\text{s}^{-1}$ ) are displacement and velocity vector of particles, in equation (9). The first term on the right hand side of equation (9) is related to viscous drag forces due to the particle-fluid interaction and the second term expresses forces due to particles' collisions, while the last term is related to the combined buoyancy-gravity effect.

$$F_i^{collision} = (\sum k_{eff} X_i^{rel} + \sum \eta_{eff} U_i^{rel}) \quad (10)$$

$k_{eff}$  ( $\text{N}.\text{m}^{-1}$ ) and  $\eta_{eff}$  ( $\text{N}.\text{m}^{-1}.\text{s}^{-1}$ ) are effective spring and damping coefficients and superscript  $(.)^{rel}$  stands for relative motion. And finally and after all the fluid-induced as well as collision forces are calculated, the location of every individual powder particle is determined via

$$\frac{dX_i^p}{dt} = U_i^p \quad (11)$$

### GOVERNING PHYSICS: HEAT TRANSFER

The host fluid and powder particles transfer heat to each other and their temperature gets updated after every increment. Transient PDE of heat transfer in 3 dimensions is solved in the hosting fluid domain to find the temperature field for the chamber gas, whereas transient zero dimension heat balance, derived based on the lumped thermal assumption, is solved for every individual powder particle to find their temperature. Contrary to the one-way coupling between the fluid flow motion and particle dynamics, where fluid-

induced viscous drag forces are added on powder particles, two-way thermal coupling is implemented in this paper, and this takes place via convection heat transfer.

#### *Fluid heat transfer*

The transient temperature field in the fluid domain is determined by solving PDE of heat balance in the host fluid domain

$$\rho c_p \left[ \frac{\partial T}{\partial t} + \frac{\partial}{\partial x_j} (u_j^F T) \right] = \frac{\partial}{\partial x_j} \left( k \frac{\partial T}{\partial x_j} \right) + \frac{\sum h_{p-F} A_{eff} (T_p - T)}{V_c}, \quad (12)$$

where  $c_p$  ( $\text{J.kg}^{-1}.\text{K}^{-1}$ ) and  $k$  ( $\text{W.m}^{-1}.\text{K}^{-1}$ ) are specific heat capacity and thermal conductivity of the fluid in equation (12). The last term in equation (12) is volumetric heat source due to heat transfer from powder particles to the fluid domain within a cell volume  $V_c$  and  $h_{p-F}$  ( $\text{W.m}^{-2}.\text{K}^{-1}$ ) is the convective heat transfer coefficient which is determined by [24]

$$Nu = \frac{2h_{p-F}R}{k} = 2 + 0.6Re^{0.5}Pr^{0.33}. \quad (13)$$

$Re$  (-) and  $Pr$  (-) are Reynolds and Prandtl numbers in equation (13).

#### *Particles heat transfer*

The transient temperature of individual powder particles are found via the following equation [25], [26]

$$m_p c_p^p \frac{dT_p}{dt} = h_{p-F} A_{eff} (T - T_p), \quad (14)$$

and  $c_p^p$  ( $\text{J.kg}^{-1}.\text{K}^{-1}$ ) is the specific heat capacity of powder particles. Moreover, in this work the radiation heat transfer is ignored since it is believed that convection is the main mechanism of heat transfer to the particles due to the very high velocity magnitude of the vapor jet plume.

### COMPUTATIONAL DOMAIN AND BOUNDARY CONDITIONS

Fig. 1 shows a front and a side view of the fluid domain. The impact of the vapor plume is modelled with a moving momentum source with an upward velocity of  $100 \text{ m.s}^{-1}$  which is an average of the previous experimental observations [27], [28]. Furthermore, the momentum source has a fixed temperature of 3000 K, which is close to the boiling temperature of 316-L stainless steel. For such explicit representation of the evaporation plume, it is not possible to involve certain input process parameters such as laser power and the beam size, as the thermal impact from the laser beam is already taken into account by the initial temperature of the jet.

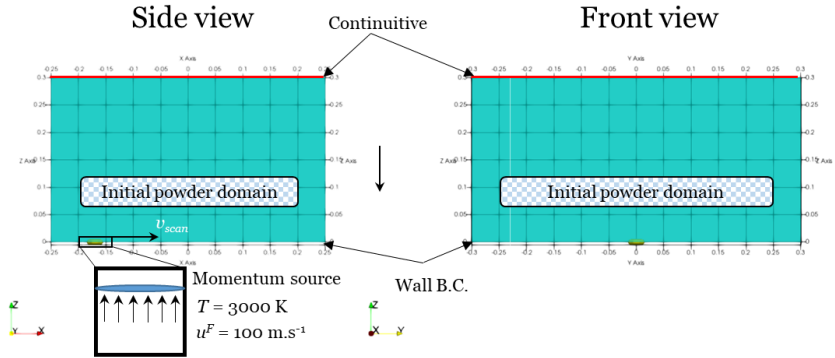


**Fig. 1** Two different views of the computational domain for the fluid domain. The vapor plume is simulated by a moving momentum source with a prescribed temperature of 3000 K.

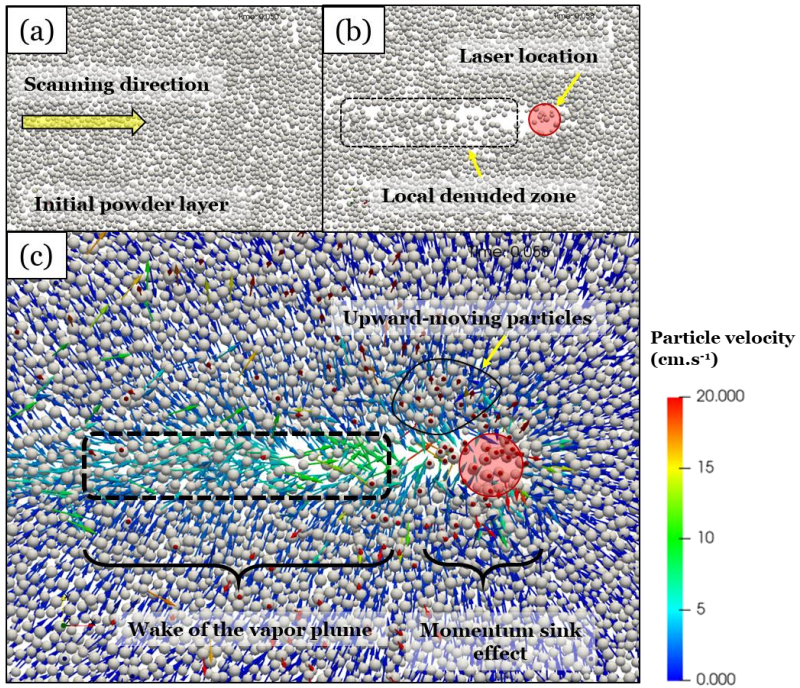
The overall size of the computational domain as also shown in Fig. 1 is 5.00 mm by 6.00 mm by 3.00 mm and the CFD cell size is set to 45  $\mu\text{m}$  and this leads to 989121 cells with an aspect ratio of very close to unity. According to Fig. 1, powder particles are initially set inside the fluid domain at a certain distance from the bottom wall boundary condition. In total 15000 powder particles with four different sizes of 20  $\mu\text{m}$ , 29  $\mu\text{m}$ , 30  $\mu\text{m}$  and 35  $\mu\text{m}$  are set inside the fluid domain. The top boundary condition is set to continuative and this allows both the host fluid and particles to exit the domain. The rest of the boundary conditions are set to symmetry and this is valid as long as the region of interest where high velocity gradients occur, is at a relatively far distance from these boundaries. Details of the employed thermo-physical properties and the implemented process inputs are listed in Table 1.

**Table 1** List of a number of input parameters and thermo-physical properties.

Property	Unit	Value	Property	Unit	Value
$\rho_{air}$	$\text{Kg.m}^{-3}$	1.225	$C_{p,air}$	$\text{J.kg}^{-1}.\text{K}^{-1}$	718
$\rho_{steel}$	$\text{Kg.m}^{-3}$	7900	$C_{p,steel}$	$\text{J.kg}^{-1}.\text{K}^{-1}$	804
$k_{air}$	$\text{W.m}^{-1}.\text{K}^{-1}$	2.346E-02	$\mu_{air}$	$\text{Pa.s}^{-1}$	1.78E-05
$k_{steel}$	$\text{W.m}^{-1}.\text{K}^{-1}$	28	Jet speed	$\text{m.s}^{-1}$	100
$v_{scan}$	$\text{m.s}^{-1}$	0.3, 0.5	Jet diameter	m	2.00E-04

## RESULTS AND DISCUSSION

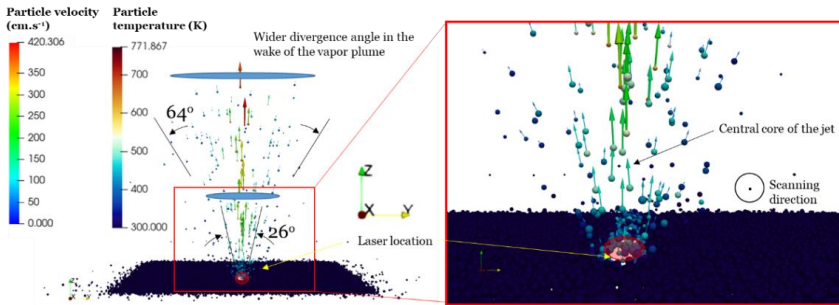
Fig. 2 (a) and (b) show two snapshots from the top view of the powder layer morphology right before the scanning step and at 0.008 seconds during the scanning step, respectively. One can notice in Fig. (b) that the initial local powder layer arrangement is disrupted due to the fluid dynamics impact of the moving vapor plume.



**Fig. 2** (a) and (b) are two snapshots taken at an x-y plane parallel to the powder layer plane before and 0.008 seconds after the start of the scanning process. (c) Shows a magnified view of (b) where detailed powder particles' movement along with their velocity magnitude and directions are shown.

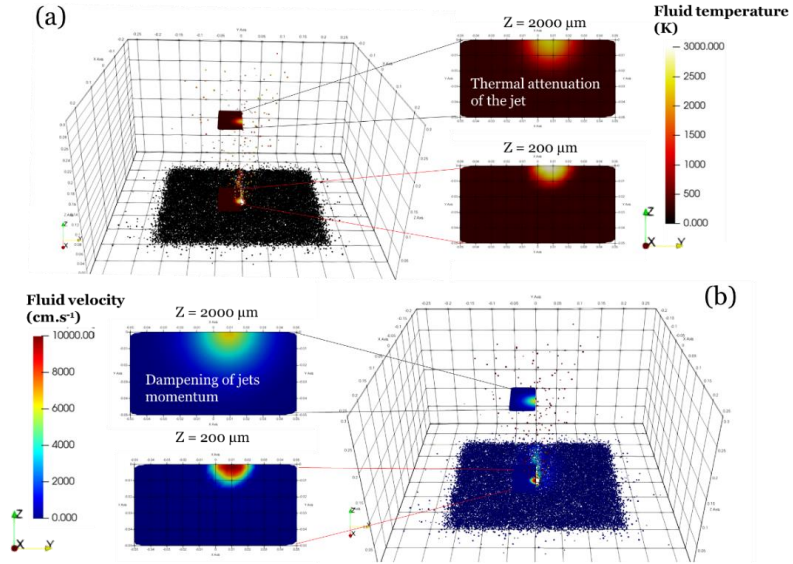
It is furthermore observed in both Fig. 2 (b) that a small region in the immediate wake of the vapor plume and on the powder layer, is striped of powder particles. This is because a noticeable fraction of the powder particles adjacent to the vapor plume's track, is pulled outwards along the z axis and as a result of the viscous drag force imposed by the high-velocity upward plume in those regions, see Fig. 2 (c). One can also clearly see in Fig. 2 (c) that a portion of particles possess vertically-upward velocities and this in essence creates a localized low-pressure region that to some extent and by some simplifying assumptions, is formed due to the Bernoulli effect. This pseudo-Bernoulli effect in turn, acts like a momentum sink in the local areas in the vicinity of the vapor plume. This could be better understood as, according to Fig. 2 (c), all the nearby powder particles are pointing towards this momentum sink area.

Fig. 3 shows the particles' temperature contour as well as their instantaneous trajectories colored with particles' velocity magnitude from the front view.



**Fig. 3** Front view of the ejected powder particles due to the plume movement. Powder particles are colored by their respective temperature while trajectory colors show their magnitude at 0.007 seconds.

Based on Fig. 3 it is noted that although the vapor plume is vertically upwards, powder particles which are impacted by this jet, eject at an angle of approximately 26 degrees right in the zone where the vapor plume is active. At the same time, it is also observed in Fig. 3 that particles' divergence angle increases with an increase in their distance from the plume. This could be attributed to the jet attenuation that typically occurs when a jet is ejected into the nearby resting fluid. To better clarify this growing divergence of the escaping powder particles, contours of the velocity magnitude of the vapor jet and at two vertical locations of  $200\ \mu\text{m}$  and  $2000\ \mu\text{m}$  from the powder bed are shown in Fig. 4 (b). According to this figure, it is noted that due to the impact of the neighboring static fluid on the vapor plume, the jet's maximum velocity magnitude is decreased while at the same time, its area of influence is widened, underlining the jet's momentum attenuation. Therefore, the powder particles that are directly impacted by the vapor plume, obtain dominantly-vertical but diverging velocities and this leads to their divergence from the vertical direction. Interestingly, it is furthermore noted that those particles which are in line with the central core region of the jet, keep their vertical velocity since there is no noticeable radial velocity at this very core region.



**Fig. 4** (a) Temperature contour of powder particles along with contours of vapor plumes temperature at two vertical distances of 200  $\mu\text{m}$  and 2000  $\mu\text{m}$  from the powder bed. (b) 3D velocity magnitude contours of powder particles and 2D velocity contour of the jet at 200  $\mu\text{m}$  and 2000  $\mu\text{m}$  from the powder bed.

The powder particles also transfer heat with the fluid and according to Fig. 3, it is noticed that the maximum powder particles temperature rises to about 772 K. This temperature rise is a result of strong convection between the jet and particles. According to the blow-up part of Fig. 3, only a narrow region of the powder bed undergoes an observable temperature change and this is ascribed to the low thermal conductivity of the powder bed, which is in essence caused by imperfect point contacts with high thermal resistance between particles. Moreover, in the same manner as observed before, the maximum temperature of the plume also declines as the jet moves further inside the nearby resting fluid.

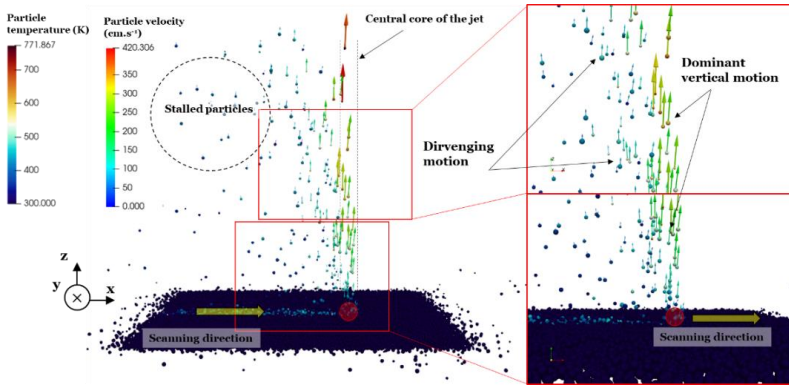


**Fig. 5** Side view of the departing particle - particles are colored with their temperature and particle velocities are colored with particles' velocity magnitude.

Fig. 5 demonstrates a side view of the spattering effect and it is clearly seen in this figure that those particles which move inside the central core of the plume's jet, are accelerated to a maximum velocity of  $4.2 \text{ m.s}^{-1}$  which is primarily vertical. Inside the plume moves along the scanning direction, those particles which were initially inside the core region, gradually lose their velocity due to the damping effect of the drag force of the resting fluid. One can see that at a distance of about 2 mm behind the central core of the jet, powder particles are stalled and undergo the so-called entrainment effect.

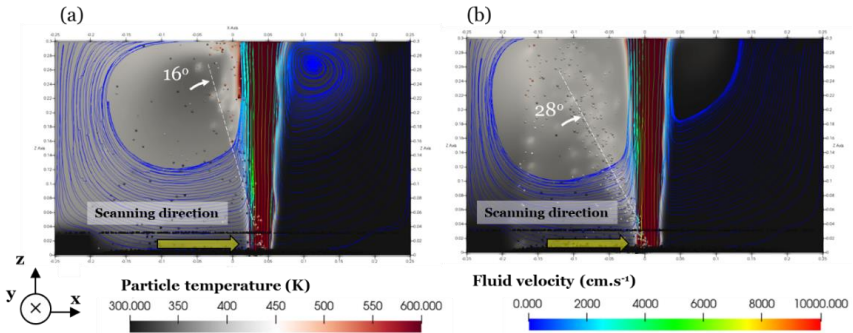


**Fig. 6** Contours of fluid and particles temperature along with fluid's streamlines colored with velocity magnitude at (a)  $300 \text{ mm.s}^{-1}$  and (b)  $500 \text{ mm.s}^{-1}$

Fig. 6 (a) and (b) show contours of fluid and particle temperature from the side view for scanning speed of  $300 \text{ mm.s}^{-1}$  and  $500 \text{ mm.s}^{-1}$ , respectively. The lines in this figure are streamlines that are colored with fluid's velocity magnitude. Based on Fig. 6, it is clearly noted that particles are ejected at an angle from the zone where the plume is formed. This angle is about  $16^\circ$  for a lower scanning speed of  $300 \text{ mm.s}^{-1}$  and  $28^\circ$  for  $500 \text{ mm.s}^{-1}$

scanning speed. The main reason behind this change of ejection angle with respect to the vertical plume jet is, as mentioned earlier, the fact that particles which are inside the central core of the jet, move almost vertically upwards. Therefore, the faster the translational speed of the plume, the shorter will be the vertical thrust of the powder particles. A very similar trend has also been observed in the *in-situ* online monitoring of the L-PBF process of 1.4404 stainless steel in [29] where it is shown that by increasing the scanning velocity of the laser beam, the jet angle deviates further from the perpendicular line normal to the build table. In this scenario, fewer particles will possess high vertical velocities at higher translational speed of the plume. To better understand this effect, one can go to the extreme case and imagine a static plume where the particles will move primarily parallel to the jet direction, thus, there will be no deviation between the jet and the ejected particles.

Furthermore, one can see in Fig. (a) and (b) how high-temperature powder particles that enter the fluid region behind the jet, locally affect the temperature field in the wake of the plume. Moreover, since the interaction time between particles and the jet is shorter at higher scanning speed, particles will have lower temperatures at higher scanning speeds.

### CONCLUSION

In this work, a coupled particle-fluid dynamics numerical simulation of the L-PBF process is developed to study the spatter phenomenon and its resulting denudation. The model is developed in the commercial software package Flow-3D using its AM module and is made of two parts, a CFD model that simulates the heat and fluid flow conditions of the fluid phase, and a DEM model that predicts particles' motion dynamics as well as their thermal conditions. The modelling results demonstrate that the fluid dynamics impact of the high-velocity vapor plume jet creates a localized low-pressure zone near the plume location and this leads to a pseudo-Bernoulli effect that drags nearby powder particles inside the jet plume and then these particles will be lifted upwards due to the very high viscous drag force from the high-speed jet. As a result of this, a local denuded zone will form in the wake of the plume location. Furthermore, it is noted that the linear momentum of the jet starts becoming dampened as the jet comes into contact with neighboring static air. This will then lead to a diverging flow and as a result, powder particles also diverge from the central core of the vapor plume. These particles then quickly lose both their temperature and velocity as they get in contact with the resting static air. Moreover, two cases with scanning speeds of  $300 \text{ mm.s}^{-1}$  and  $500 \text{ mm.s}^{-1}$  were simulated and it is observed that the angle between ejecting powder particles and the vertical plume jet increases from  $16^\circ$  to  $28^\circ$ , mainly because in the latter case, particles have shorter contact with the jet and therefore have lower acceleration compared to the ejecting particles in the case with  $300 \text{ mm.s}^{-1}$ .

### APPENDICES AND ACKNOWLEDGEMENTS

This work has received funding from Independent Research Fund Denmark, DIGI-3D project.

## References

- [1] T. DEBROY et al.: ‘Additive manufacturing of metallic components – Process, structure and properties’, *Prog Mater Sci*, vol. 92, pp. 112-224, 2018, doi: 10.1016/j.pmatsci.2017.10.001.
- [2] M. MARKL and C. KÖRNER: ‘Multiscale Modeling of Powder Bed–Based Additive Manufacturing’, *Annu Rev Mater Res*, vol. 46, no. 1, pp. 93-123, 2016, doi: 10.1146/annurev-matsci-070115-032158.
- [3] A. ZINOVIEV, O. ZINOVIEVA, V. PLOSHIKHIN, V. ROMANOVA and R. BALOKHONOV: ‘Evolution of grain structure during laser additive manufacturing. Simulation by a cellular automata method’, *Mater Des*, vol. 106, pp. 321-329, 2016, doi: 10.1016/j.matdes.2016.05.125.
- [4] Y. ZHANG and J. ZHANG: ‘Modeling of solidification microstructure evolution in laser powder bed fusion fabricated 316L stainless steel using combined computational fluid dynamics and cellular automata’, *Addit Manuf*, vol. 28, no. July 2018, pp. 750-765, 2019, doi: 10.1016/j.addma.2019.06.024.
- [5] A. A. MARTIN et al.: ‘Ultrafast dynamics of laser-metal interactions in additive manufacturing alloys captured by in situ X-ray imaging’, *Mater Today Adv*, vol. 1, p. 100002, 2019, doi: 10.1016/j.mtadv.2019.01.001.
- [6] Y. C. WU et al.: ‘Numerical modeling of melt-pool behavior in selective laser melting with random powder distribution and experimental validation’, *J Mater Process Technol*, vol. 254, no. July 2017, pp. 72-78, 2018, doi: 10.1016/j.jmatprotec.2017.11.032.
- [7] W. GAO, S. ZHAO, Y. WANG, Z. ZHANG, F. LIU and X. LIN: ‘Numerical simulation of thermal field and Fe-based coating doped Ti’, *Int J Heat Mass Transf*, vol. 92, pp. 83-90, 2016, doi: 10.1016/j.ijheatmasstransfer.2015.08.082.
- [8] A. CHARLES, M. BAYAT, A. ELKASEER, L. THUIS, J. H. HATTEL and S. SCHOLZ: ‘Elucidation of dross formation in laser powder bed fusion at down-facing surfaces: Phenomenon-oriented multiphysics simulation and experimental validation’, *Addit Manuf*, vol. 50, 2022, doi: 10.1016/j.addma.2021.102551.
- [9] C. MEIER, R. W. PENNY, Y. ZOU, J. S. GIBBS and A. J. HART: ‘Thermophysical phenomena in metal additive manufacturing by selective laser melting: Fundamentals, modeling, simulation and experimentation’, *ArXiv*, 2017, doi: 10.1615/annualrevheattransfer.2018019042.
- [10] W. KING, A. T. ANDERSON, R. M. FERENCZ, N. E. HODGE, C. KAMATH and S. A. KHAIRALLAH: ‘Overview of modelling and simulation of metal powder bed fusion process at Lawrence Livermore National Laboratory’, *Materials Science and Technology* (United Kingdom), vol. 31, no. 8, pp. 957-968, 2015, doi: 10.1179/1743284714Y.0000000728.
- [11] M. BAYAT, W. DONG, J. THORBORG, A. C. TO and J. H. HATTEL: ‘A review of multi-scale and multi-physics simulations of metal additive manufacturing processes with focus on modeling strategies’, *Addit Manuf*, vol. 47, 2021, doi: 10.1016/j.addma.2021.102278.
- [12] M. J. MATTHEWS, G. GUSS, S. A. KHAIRALLAH, A. M. RUBENCHIK, P. J. DEPOND and W. E. KING: ‘Denudation of metal powder layers in laser powder bed fusion processes’, *Acta Mater*, vol. 114, pp. 33-42, 2016, doi: 10.1016/j.actamat.2016.05.017.

- [13] H. CHEN and W. YAN: ‘Spattering and denudation in laser powder bed fusion process: Multiphase flow modelling’, *Acta Mater*, vol. 196, pp. 154-167, 2020, doi: 10.1016/j.actamat.2020.06.033.
- [14] A. MASMOUDI, R. BOLOT and C. CODDET: ‘Investigation of the laser-powder-atmosphere interaction zone during the selective laser melting process’, *J Mater Process Technol*, vol. 225, pp. 122-132, 2015, doi: 10.1016/j.jmatprotec.2015.05.008.
- [15] P. BIDARE, I. BITHARAS, R. M. WARD, M. M. ATTALLAH and A. J. MOORE: ‘Fluid and particle dynamics in laser powder bed fusion’, *Acta Mater*, vol. 142, pp. 107-120, 2018, doi: 10.1016/j.actamat.2017.09.051.
- [16] I. BITHARAS, A. BURTON, A. J. ROSS and A. J. MOORE: ‘Visualisation and numerical analysis of laser powder bed fusion under cross-flow’, *Addit Manuf*, vol. 37, no. June 2020, p. 101690, 2021, doi: 10.1016/j.addma.2020.101690.
- [17] X. LI and W. TAN: ‘Numerical Modeling of Powder Gas Interaction Relative to Laser Powder Bed Fusion Process’, *Journal of Manufacturing Science and Engineering*, vol. 143, no. May, pp. 1-7, 2021, doi: 10.1115/1.4048443.
- [18] X. LI, C. ZHAO, T. SUN and W. TAN: ‘Revealing transient powder-gas interaction in laser powder bed fusion process through multi-physics modeling and high-speed synchrotron x-ray imaging’, *Addit Manuf*, vol. 35, no. June, p. 101362, 2020, doi: 10.1016/j.addma.2020.101362.
- [19] H. M. DEYLAMI, N. AMANIFARD, S. S. HOSSEININEZHAD and F. DOLATI: ‘Numerical investigation of the wake flow control past a circular cylinder with Electrohydrodynamic actuator’, *European Journal of Mechanics, B/Fluids*, vol. 66, pp. 71-80, 2017, doi: 10.1016/j.euromechflu.2017.06.002.
- [20] O. A. MARZOUK and E. DAVID HUCKABY: ‘Simulation of a swirling gas-particle flow using different k-epsilon models and particle-parcel relationships’, *Engineering Letters*, vol. 18, no. 1, 2010.
- [21] B. AKAY, D. RAGNI, C. S. FERREIRA and G. J. W. VAN BUSSEL: ‘Investigation of the root flow in a Horizontal Axis’, *Wind Energy*, no. August 2016, pp. 1-20, 2013, doi: 10.1002/we.
- [22] A. J. LEW, G. C. BUSCAGLIA and P. M. CARRICA: ‘A Note on the Numerical Treatment of the k-epsilon Turbulence Model’, *Int J Comput Fluid Dyn*, vol. 14, no. 3, pp. 201-209, 2001, doi: 10.1080/10618560108940724.
- [23] A. AGGARWAL et al.: ‘Role of impinging powder particles on melt pool hydrodynamics, thermal behaviour and microstructure in laser-assisted DED process: A particle-scale DEM – CFD – CA approach’, *Int J Heat Mass Transf*, vol. 158, p. 119989, 2020, doi: 10.1016/j.ijheatmasstransfer.2020.119989.
- [24] X. GUAN and Y. F. ZHAO: ‘Numerical modeling of coaxial powder stream in laser-powder-based Directed Energy Deposition process’, *Addit Manuf*, vol. 34, no. April, p. 101226, 2020, doi: 10.1016/j.addma.2020.101226.
- [25] S. Y. WEN, Y. C. SHIN, J. Y. MURTHY and P. E. SOJKA: ‘Modeling of coaxial powder flow for the laser direct deposition process’, *Int J Heat Mass Transf*, vol. 52, no. 25-26, pp. 5867-5877, 2009, doi: 10.1016/j.ijheatmasstransfer.2009.07.018.
- [26] M. BAYAT et al.: ‘On the role of the powder stream on the heat and fluid flow conditions during Directed Energy Deposition of maraging steel – Multiphysics

- modeling and experimental validation', *Addit Manuf*, vol. 43, 2021, doi: 10.1016/j.addma.2021.102021.
- [27] P. BIDARE, I. BITHARAS, R. M. WARD, M. M. ATTALLAH and A. J. MOORE: 'Laser powder bed fusion in high-pressure atmospheres', *International Journal of Advanced Manufacturing Technology*, vol. 99, no. 1-4, pp. 543-555, 2018, doi: 10.1007/s00170-018-2495-7.
- [28] P. BIDARE, I. BITHARAS, R. M. WARD, M. M. ATTALLAH and A. J. MOORE: 'Fluid and particle dynamics in laser powder bed fusion', *Acta Mater*, vol. 142, pp. 107-120, 2018, doi: 10.1016/j.actamat.2017.09.051.
- [29] E. ESCHNER, T. STAUDT and M. SCHMIDT: 'Sensing approach for the in-situ determination of spatter motion within PBF-LB/M', *CIRP Annals*, vol. 71, no. 1, pp. 149-152, Jan. 2022, doi: 10.1016/j.cirp.2022.03.005.

# COMPARISON BETWEEN GREEN AND INFRARED LASER IN LASER POWDER BED FUSION OF PURE COPPER THROUGH HIGH FIDELITY NUMERICAL MODELLING AT MESO-SCALE

W. E. ALPHONSO\*<sup>1</sup>, M. BAYAT\*, J. H. HATTEL\*

*\*Technical University of Denmark (DTU), 2800, Kgs. Lyngby, Denmark*

*<sup>1</sup>Corresponding author*

*DOI 10.3217/978-3-85125-968-1-02*

## ABSTRACT

Laser Powder Bed Fusion (L-PBF) is a Metal Additive Manufacturing (MAM) technology which offers several advantages to industries such as part design freedom, consolidation of assemblies, part customization and low tooling cost over conventional manufacturing processes. Electric coils and thermal management devices are generally manufactured from pure copper due to its high electrical and thermal conductivity properties. Therefore, if L-PBF of pure copper is feasible, geometrically optimized heat sinks and free-form electromagnetic coils can be manufactured. However, producing dense pure copper parts by L-PBF is difficult due to low optical absorptivity to infrared radiation and high thermal conductivity. To produce dense copper parts in a conventional L-PBF system either the power of the infrared laser must be increased above 500W, or a green laser should be used for which copper has a high optical absorptivity. Increasing the infrared laser power can damage the optical components of the laser systems due to back reflections and create instabilities in the process due to thermal-optical phenomenon of the lenses. In this work, a multi-physics meso-scale numerical model based on Finite Volume Method (FVM) is developed in Flow-3D to investigate the physical phenomena interaction which governs the melt pool dynamics and ultimately the part quality. A green laser heat source and an infrared laser heat source are used individually to create single track deposition on pure copper powder bed above a substrate. The effect of the dissimilar optical absorptivity property of laser heat sources on the melt pool dynamics is explored. To validate the numerical model, experiments were conducted wherein single tracks are deposited on a copper powder bed and the simulated melt pool shape and size are compared. As the green laser has a high optical absorptivity, a conduction and keyhole mode melting is possible while for the infrared laser only keyhole mode melting is possible due to low absorptivity. The variation in melting modes with respect to the laser wavelength has an outcome on thermal gradient and cooling rates which ultimately affect the mechanical, electrical, and thermal properties.

Keywords: Pure Copper, Laser Powder Bed Fusion, Finite Volume Method, multi-physics

## INTRODUCTION

MAM technologies provides advantages such as low part weight, high design freedom, part customization and low volume production hence it has gained a lot of attention in the last decade from the aerospace, medical and automotive industries [1]. L-PBF is one of the seven Additive Manufacturing technologies where the working principle is based on spreading a micron-size metal powder on a build plate and using a laser as a heating source to consolidate the powder layer at selected locations according to the sliced CAD geometry. After melting the powder bed, the build plate is lowered by a specific distance and the next layer of powder is coated and melted by the laser. This powder coating and selectively melting steps are repeated in a layer-by-layer fashion which finally leads to a 3D part metal part produced at the end of the process [2]. L-PBF technology also has its disadvantages such as build orientation dependent anisotropy, difficulty in removal of support structures [3] and part defects such as pores, un-melted zones, delamination, warping and residual stresses [4].

L-PBF also many process variables [5] that can affect the final part quality to various degrees and must be optimized to produce a defect-free part, which makes finding the optimal process parameter window for a new material or alloy expensive and time-consuming using a trial-and-error experimental approach. To reduce the experimental cost and increase efficiency of developing a process window for a new material, a fundamental understanding of the thermal-fluid flow phenomena in the melt pool is important. The melt pool is an elementary unit of a 3D printed component, hence any defects formation mechanisms at this scale should be explored. To understand the thermal flow phenomena inside the melt pool experimental in-situ methods such as X-ray imaging, Dynamic X-ray tomography, Schlieren imaging, Optical imaging, Ultrasonic testing, Acoustic Emission Spectroscopy, Optical Emission Spectroscopy, Optical Tomography, Optical Coherence Tomography, Pyrometry and Infrared Imaging are available [6]. However, technologies like X-ray imaging can only be used for single laser track deposition due to their working principle and cannot be implemented in an industrial L-PBF machine. Most of the methods need to be calibrated as they detect a defect signature and not do not observe the actual defect. Hence, physics-based melt pool scale L-PBF numerical methods have been developed to simulate the process so that defect forming mechanisms at different regions of the process window could be identified and new process parameters can be acquired faster for new materials at a relatively low cost. In the meso-scale model, along with the temperature and flow fields, defects such as lack of fusion voids with un-melted powder and gas pores can also be captured [7], [8].

Pure copper produced by L-PBF, however, is a challenge due to copper's intrinsic thermo-electrical properties which make the material appealing for thermal and electrical applications. High thermal conductivity which is desired in cooling devices hinder the L-PBF processing as the deposited thermal energy from the laser is rapidly conducted away from the melt pool and hence less heat is accumulated to melt the material [9]. In addition, the low optical absorptivity of pure copper to infrared laser (1060 nm – 1080 nm) which is commonly used in state-of-the-art L-PBF machines [10] creates an issue as a low effective laser energy is deposited in the powder bed leading to un-melted zones and unstable melt pools. To overcome this challenge, the laser power of the infrared laser in these machines is increased above the standard 400 W. However, by utilizing a high

laser power, the reflected radiation can damage the optics in the laser guiding optical system of the L-PBF machine affecting the lifetime of optical components [9]. To tackle these issues green laser source (515 nm) is used in a new generation of L-PBF as copper and other metals like silver, titanium and steel have a higher optical absorptivity at this wavelength [11].

In this work a numerical meso-scale model of the L-PBF process is developed for pure copper where green and infrared heat sources are used individually to consolidate a single track on a powder bed. To validate the numerical model, experiments under similar conditions were conducted where the solidified melt pools shape and size are used as validation metrics. After validation, the process parameters for the green laser simulation case are altered to change the melting mode from conduction to keyhole thus showcasing the robustness of the model in a different processing mode. Finally, the single-track green laser model is extended to a multiple layer single track model and the numerical results are compared to experiments for validation.

### NUMERICAL MODEL

In this work, an FVM framework is used to develop a Computational Fluid Dynamics (CFD) based high fidelity model which includes physics such as thermal and mass transfer, melting and solidification, evaporation, thermal capillarity, surface tension and ray tracing multiple reflections. A Discrete Element Method (DEM) model is used to generate a powder bed consisting of individual discrete spherical shaped powders whose Particle Size Distribution (PSD) is obtained from the experiments. To reduce the complexity of the model further and increase the computational efficiency some assumptions were made and are listed below:

- The fluid in the melt pool is a Newtonian incompressible fluid.
- The flow in the melt pool is laminar and viscous.
- No gas phase is present above the powder bed and this region is treated as void where no temperature, velocity and pressure field calculated.
- The solidification model is linear, and the temperature interval between the solidus and liquidus temperature is 2° K.
- A Gaussian heat source with multiple reflection ray-tracing algorithm is implemented.
- The powder particles are perfectly spherical.
- Powder spattering is not captured during the melting process.
- The phase change from liquid to vapor is solved explicitly affecting the flow and temperature fields.

Deviation from the set process parameters such as thermal lensing phenomenon [12] in the optical system, the gas crossflow over the powder bed and interaction of the vaporized by-products with the incident laser is not captured by the model and these effects can be captured by using other sub-models. The multiple physics involved in single track L-PBF processing of is shown in Fig. 1.

## FLUID FLOW AND HEAT TRANSFER

The numerical model solves for the temperature and velocity field of the molten metal-induced by the laser heat deposited in the powder layer and substrate. For the fluid flow the Navier Stokes equations of continuity and momentum are solved to obtain the velocity and pressure fields during the laser melting process as shown in Eq. (1) and Eq. (2) respectively [8]

$$\vec{\nabla} \cdot (\vec{V}) = 0 \quad (1)$$

$$\rho \left[ \frac{\partial}{\partial t} (\vec{V}) + \vec{V} \cdot \vec{\nabla} (\vec{V}) \right] = -\vec{\nabla} p + \vec{\nabla} \cdot \left[ \mu \left( \vec{\nabla} \vec{V} + \vec{\nabla} \vec{V}^T - \frac{2}{3} \vec{\nabla} \cdot \vec{V} \right) \right] - \frac{K_c (1-f_l)^2}{C_k + f_l^2} \vec{V} - \rho \vec{g} \beta (T - T_l) \quad (2)$$

Here  $V$  (m/s) is the velocity vector and  $p$  (Pa) is pressure. The second term on the right-hand side of Eq. (2) represents the forces caused by viscous stresses and the third term is the solidification drag force due to the formation of a mushy zone.  $K_c$  (kg/m<sup>3</sup>s) and  $C_k$  (-) are the constants used for solidification drag forces and they are typically in the order of 10<sup>6</sup> and 10<sup>-4</sup>, respectively. The last term in Eq. (2) accounts for the buoyancy effect. In this work the flow is assumed to be incompressible and hence to model the buoyancy force, the Boussinesq approximation has been used where  $\beta$  (1/K) is the thermal expansion coefficient. The fluid flow is coupled with the heat transfer using the energy equation as shown in Eq. (3)

$$\rho \left[ \frac{\partial}{\partial t} (h) + \vec{V} \cdot \vec{\nabla} (h) \right] = \vec{\nabla} \cdot [k_{bulk} (\vec{\nabla} T)] \quad (3)$$

$$h = h_{ref} + C_{p, bulk} (T - T_{ref}) + f_l \Delta H_{sl} \quad (4)$$

$$f_l = \begin{cases} 0 & T < T_s \\ \frac{T - T_s}{T_l - T_s} & T_s \leq T \leq T_l \\ 1 & T > T_l \end{cases} \quad (5)$$

Where  $h$  (kJ/kg) is the specific enthalpy of the metallic phase, and the subscript ‘ref’ stands for the reference state from which the enthalpy is evaluated.  $f_l$  (-) is the liquid fraction function defined in Eq. (5), which for simplicity is approximated by a linear function of temperature in the solidification interval and  $\Delta H_{sl}$  (kJ/kg) in Eq. (4) is the latent heat of fusion. Here the liquid fraction varies linearly between the solidus and liquidus temperatures.

For the material properties such as density, thermal conductivity and specific heat capacity in the solidification interval, the values are calculated by using the liquid  $f_l$  (-) and solid fractions  $f_s$  (-) as shown in Eq. (6), (7) and (8).

$$\rho = f_s \rho_s + f_l \rho_l \quad (6)$$

$$k_{bulk} = f_s k_s + f_l k_l \quad (7)$$

$$C_{p, bulk} = \frac{f_s \rho_s C_{p,s} + f_l \rho_l C_{p,l}}{f_s \rho_s + f_l \rho_l} \quad (8)$$

Where the subscript 's' refers to solid and 'l' refers to liquid.

To track the interface between the void and the metal phases, a Volume of Fluid (VOF) method is used. The free surface is captured using Eq. (9) where the value of the scalar  $F$  (-) varies between zero to one.

$$\frac{\partial}{\partial t}(F) + \vec{\nabla} \cdot (F\vec{V}) = 0 \quad (9)$$

Intermediate values of  $F$  indicate an interface between these two immiscible phases. In this work, the calculation for the gas phase is not included because an assumption is made that the gas flow has an insignificant impact on the melt flow characteristics. Hence, the gas phase is treated as a void with no fluid and thermal properties are assigned to these cells.

#### INTERFACIAL FORCES

One of the driving forces in the melt pool is the thermo-capillary effect also known as Marangoni effect which occurs due to the variation in surface tension of the molten metal with temperature. To account for this phenomenon in the model, a shear stress is defined on the free surface of the melt pool, which causes the molten pool to widen with increasing temperature in the case of a negative surface tension gradient and deepen when the gradient is positive [13]. The change of surface tension with temperature for pure copper is shown in Table 1 and is a linear function. Here the surface tension gradient is active between the liquidus and evaporation temperature, where the metal is in a complete fluid state.

In L-PBF, a micron size laser heat source is used to melt the powder and hence very high temperatures near the boiling point can be achieved leading to localized vaporization where the metal changes its phase from liquid to vapor. This metal vapor phase in turn generates a pressure on the surface of the melt pool, creating a depression zone. This pressure is denoted as recoil pressure and is accounted for in the model as a pressure acting perpendicular to the free surface without implicitly modelling the liquid to vapor phase transition. In summary, the recoil pressure, Marangoni shear force, and surface tension are all acting on the free surface and the force balance at the metal-void interface is expressed by Eq. (10).

$$F_{V/F} = [P_{recoil} + \sigma \cdot \kappa] \vec{n} + [\vec{\nabla} T \cdot \vec{n} (\vec{\nabla} T \cdot \vec{n})] \frac{d\sigma}{dT} \quad (10)$$

The second term on the right-hand side of Eq. (10) is the Marangoni shear stress and  $d\sigma/dT$  ( $\text{kg} \cdot \text{s}^2 \cdot \text{K}^{-1}$ ) represents the dependency of surface tension on temperature and acts tangential to the free surface of the fluid.  $P_{recoil}$  (Pa) is the pressure acting normal to the free surface of the melt pool when temperatures are near the boiling point of the metal and

$\kappa$  ( $\text{m}^{-1}$ ) is the curvature of the free surface of the fluid, whereas ‘ $n$ ’ denotes the normal direction to the interface.

The recoil pressure in the first term Eq. (10) can be expanded and is shown in Eq. (11).

$$P_{recoil}(T) = 0.54P_{atm} e^{\left[ \frac{\Delta H_{lv}}{C_v(\gamma-1)} \left( \frac{1}{T_g T} \right) \right]} \quad (11)$$

Where,  $P_{atm}$  (Pa) is atmospheric ambient pressure,  $\gamma$  is the specific heat ratio,  $\Delta H_{lv}$  (kJ/kg) is the latent heat of vaporization and  $T_g$  is the vaporization temperature.

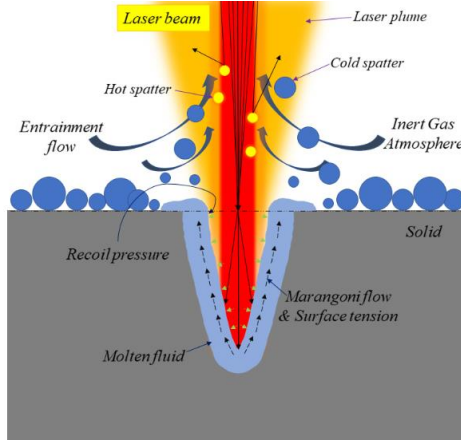


**Fig. 1** Multi-physics phenomena in the laser-material interaction zone.

#### RAY TRACING HEAT SOURCE

The heat source in the model is a laser spot with a predefined diameter that traverses along the powder bed with a particular scanning speed. This laser spot generates an input heat flux into the computational domain and has a Gaussian distribution around the center axis of the laser beam according to Eq. (12).

$$q''_{laser}(x,y) = \frac{2P}{\pi R^2} e^{\left( -\frac{2\left( (x-x_{laser})^2 + (y-y_{laser})^2 \right)}{R^2} \right)} \quad (12)$$

Where  $P$  (J/s),  $R$  (m),  $x_{laser}$  (m) and  $y_{laser}$  (m) are laser power, laser beam spot radius,  $x$  coordinate and  $y$  coordinate of the initial laser position. When the laser is traversing in a straight line in the  $x$ -direction,  $y$  is equal to 0 and  $x$  is equal to  $v \cdot t$ , where  $v$  is laser scanning speed and  $t$  is time. The laser heat flux is discretized from a continuous Gaussian distribution according to the mesh size. The size of the cell determines the discretization

of the laser heat flux as well as the number of rays being generated. The incident rays from the laser undergoes multiple reflections on the melt pool surface and upon every interaction of the ray with the molten metal, the energy of the reflected ray is reduced by a certain amount depending on the optical absorptance value. More details on the ray-tracing algorithm applied in L-PBF can be found in the previous works by the author group [8].

### DOMAIN AND BOUNDARY CONDITIONS

The discrete powder layer for the CFD numerical model is obtained by implementing the DEM where each powder particle is modelled as a sphere and the powder motion is governed by Newton's second law. The DEM modelling is based on a Lagrangian framework where the Hertz-Mindlin contact model is used to capture the collision between particles. In this work, a deposition method is usually denoted as the 'rain-drop' method is used wherein powder particles are dropped from the top of the domain on the bulk/substrate region [14]. The bottom and the side face of the domain are treated as walls and the particles are hence trapped inside the numerical domain. The 'rain-drop' is extremely computationally efficient, as compared to modelling the actual powder deposition process in a L-PBF system where a roller or a spreader is used to deposit thin powder layers. The DEM simulation is halted as soon as the pre-determined powder layer thickness is obtained, and later the powder particles deposited are exported to the CFD model. The particle size distribution (PSD) of the powder used in the DEM model is obtained from size measurements of the copper powder used in the experiments.

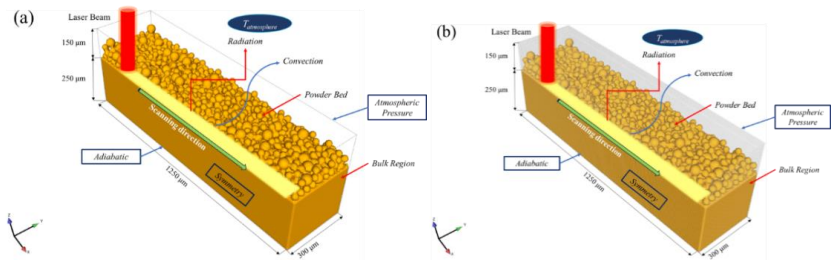


**Fig. 2** Framework for single laser track simulation model including powder bed and substrate (a) computational domain with boundaries (b) discretization of the domain with uniform quad mesh.

The size of the numerical domain is  $1250 \mu\text{m} \times 600 \mu\text{m} \times 400 \mu\text{m}$  for the single-track models. The substrate/bulk region is  $250 \mu\text{m}$  thick and a powder layer thickness of  $100 \mu\text{m}$  is deposited over it as shown in Fig. 2(a). The prescribed laser scanning direction is also shown to be along the x-direction. To reduce computation time, the numerical domain is halved at the laser beam center along the x-z plane and a symmetry boundary

condition is applied. The substrate thickness was increased in simulation cases where the melt pool interacts with the bottom of the domain. The material assigned to the powder bed and substrate is pure copper and the thermo-physical properties used in this work is shown in Table 1. An adiabatic condition is applied at bottom and the side walls of the domain while the top surface is assigned as a pressure outlet. The thermal boundary condition applied on the exposed top surface of the melt pool and is expressed by Eq. (13) and is also shown in Fig. 2.

$$-k \frac{\partial T}{\partial n} = \varepsilon \sigma_{rad} (T_{amb}^4 - T^4) + h_{amb} (T_{amb} - T) - q''_{laser} + q_{vap} \quad (13)$$

where,  $\varepsilon$  (-) and  $\sigma_{rad}$  ( $\text{W}/\text{m}^2/\text{K}^4$ ) represent the emissivity and Stephan-Boltzmann constants respectively,  $h_{amb}$  ( $\text{W}/\text{m}^2/\text{K}$ ) represents convective heat transfer coefficient,  $q''_{laser}$  ( $\text{W}\cdot\text{m}^{-2}$ ) is the laser heat flux and  $q_{vap}$  is the heat loss due to vaporization. The region which is 150  $\mu\text{m}$  in height from the top surface of the bulk region is assigned as a void, so the movement of the free surface interface can be tracked. Fig. 2(b) shows the discretized computational domain with cubic mesh cells which are 5  $\mu\text{m}$  in size. The cell size is selected based on a mesh independency study, wherein an optimized mesh size is obtained that is a compromise between numerical accuracy and computational efficiency.

**Table 1** Thermo-physical properties of pure copper

Parameter	Symbol	Value	Units
Density at Room temperature	$\rho$	8920	$\text{kg}/\text{m}^3$
Viscosity	$\mu$	0.41	$\text{kg}/\text{m}\cdot\text{s}$
Liquidus Temperature	$T_l$	1357	K
Solidus Temperature	$T_s$	1355	K
Boiling Temperature	$T_b$	3220	K
Latent heat of Fusion	$\Delta H_{sl}$	$0.206 \cdot 10^6$	J/kg
Latent heat of Evaporation	$\Delta H_{lv}$	$4.69 \cdot 10^6$	J/kg
Ambient Convective heat transfer	$h_{amb}$	80	$\text{W}/\text{m}^2\text{K}$
Surface tension gradient	$\gamma$	-0.000286	$\text{kg}/\text{s}^2/\text{K}$
Surface tension at liquidus temperature	$\sigma$	0.1304	$\text{kg}/\text{s}^2$
Surface emissivity	$\varepsilon$	0.1	-

It should be noted that pure copper has no solidification interval but to capture the release of latent heat during the melting process, a 2 °K solidification interval is added in the model. It is assumed that the numerical result will be insignificantly affected by using such a narrow solidification interval.

## RESULTS AND DISCUSSION

### GREEN LASER SINGLE TRACK DEPOSITION

For the green laser heat source numerical model two sets of process parameters are selected for validating the numerical accuracy. The first set of process parameters creates

a conduction mode melting during laser scanning due to a low Volumetric Energy Density (VED). VED ( $\text{J}/\text{m}^3$ ) can be defined by the Eq. (14) [15].

$$VED = \frac{P}{v \cdot d \cdot t} \quad (14)$$

where  $P$  is the laser power (W),  $v$  is the scanning speed (mm/s),  $d$  is the laser beam spot size ( $\mu\text{m}$ ) and  $t$  is the powder layer thickness ( $\mu\text{m}$ ). VED condenses all the important process parameters into a single parameter. The second parameter set has a high VED value which causes a keyhole mode melting. The process parameters used in these two cases is shown in Table 2.

**Table 2** Process parameter for single track green L-PBF numerical model

Process Parameter	Low Energy Density	High Energy Density
Power (W)	485	768
Scanning Speed ( $\text{mms}^{-1}$ )	500	500
Beam size ( $\mu\text{m}$ )	150	150
Powder layer thickness ( $\mu\text{m}$ )	100	100
VED ( $\text{J}/\text{mm}^3$ )	65	103

After solving the numerical model, a 2D melt pool contour is extracted at a location along the laser scanning direction where the melt pool has attained a pseudo-steady state i.e., the melt pool size and shape do not vary. The location where the melt pool contour is extracted in each case depends on the value of VED and with a high VED this location is shifted further away from the laser's initial position as it takes longer for the thermo-fluid conditions in the melt pool to stabilize and reach a pseudo-steady state. Therefore, for the high VED case, the melt pool is validated at two locations, 3mm and 7mm away from the start of the single track. The experimental results are taken from the work of [16] where a similar green laser system is utilized when compared to the laser system used to manufacture the single-track thin wall structure investigated in future sections. The PSD of the pure copper powder used for the DEM modelling for the green laser numerical model was also taken from the same work to maintain consistency. The 2D melt pools from the simulation model and experiments are qualitatively compared in Fig. 3 where the model predicts accurately the melt pool shape and size for both melting modes. The measured melt pool dimensions are shown in Table 3 along with the calculated error % which is the difference between the simulation and experimental result. In the numerical result, the melted and non-melted regions is defined as the regions of the metal phase that underwent phase transition from solid to liquid during the laser melting process.

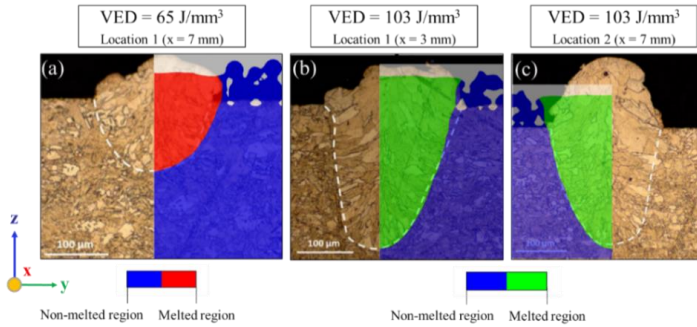


**Fig. 3** 2D melt pool contours from the numerical model compared to experiments [16] for (a)  $VED = 65 \text{ J/mm}^3$  at 7 mm from the beginning of the single track (b)  $VED = 103 \text{ J/mm}^3$  at 3 mm from the beginning of the single track (c)  $VED = 103 \text{ J/mm}^3$  at 7 mm from the beginning of the single track. In the 2D contour, the non-melted region is indicated in blue, and the melted region is indicated by red and green when the VED is  $65 \text{ J/mm}^3$  and  $103 \text{ J/mm}^3$  respectively.

**Table 3** Comparison of melt pool sizes from experimental and numerical results for single track green L-PBF process

Source	Location	VED ( $\text{J/mm}^3$ )	Melt pool width ( $\mu\text{m}$ )	Error in width (%)	Melt Pool depth ( $\mu\text{m}$ )	Error in depth (%)
Experiment	1	65	183		107	
Simulation			200	-9	102	5
Experiment	1	103	238		245	
Simulation			256	-8	237	3
Experiment	2		214		222	
Simulation			256	-20	237	-7

The simulated melt pool matches very well with the experiments and this because the numerical model accounts for all three major physical phenomena occurring in the melt pool during the L-PBF process as explained earlier. The error in the melt pool depth and width can be accounted to the assumptions and simplifications made in the model to successfully compute the melting and solidification process of the powder bed. Melt pool height was not used as a metric to validate the numerical model due to powder spattering and entrainment phenomenon omitted in the model. The 3D temperature contour at time =  $1.8 \mu\text{s}$  for the two process parameters selected is shown in Fig. 4 along with the location where the pseudo-steady 2D melt pool contours were extracted for validation. It should firstly be noted that both selected process parameters can consolidate the powder layer successfully without any defect formation such as un-melted zones and gas pores. A VED of  $65 \text{ J/mm}^3$  creates a shallow U-shaped melt pool with a small melt volume due to less heat energy from laser as shown in Fig. 4(a). At the low VED setting, heat is rapidly dissipated away from the melt pool and hence the dominant heat transfer mechanism is

conduction due to the intrinsic high thermal conductivity of copper. A VED of  $103 \text{ J/mm}^3$  creates a deep and wide melt pool as shown in Fig. 4(b) due to the combining effect of high optical absorptivity to green laser radiation and multiple reflection in the deep vapor depression. The keyhole shaped vapor depression is created due to the rise in local temperature above the boiling point and due to this geometry, multiple laser rays are trapped inside the keyhole due to the multiple reflection (Fresnel absorption) phenomenon, thereby increasing the absolute absorptivity. Hence, a larger melt pool is created and the energy coupling efficiency between the laser and the powder bed is increased. The width of the partially melted powder zone on the edges of the melt pool is small and has constant width when the VED is  $65 \text{ J/mm}^3$  when compared to when the VED is  $103 \text{ J/mm}^3$  thus indicating better stability in the conduction melting mode. Hence, green laser process parameters with VED  $\sim 65 \text{ J/mm}^3$  should be implemented in melting the contours to reduce surface roughness and increase the dimensional tolerance of the part. The process parameters with VED  $\sim 103 \text{ J/mm}^3$  can be implemented in the bulk regions where larger melting zones for each laser scan track is desired to increase the productivity without forming pore defects.

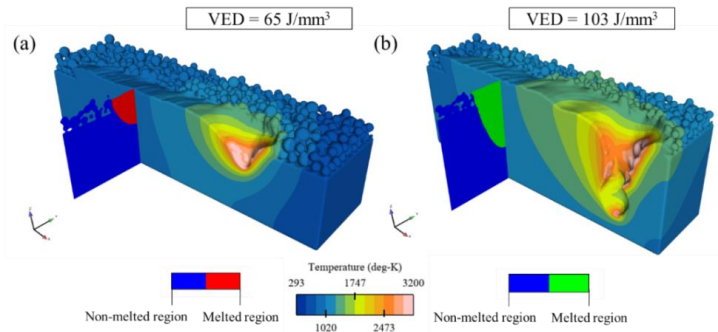


**Fig. 4** 3D temperature contour plots of during single track L-PBF process at time  $1.8 \mu\text{s}$  when (a) VED =  $65 \text{ J/mm}^3$  (b) VED =  $103 \text{ J/mm}^3$  along with 2D melt pool contours at 5 mm from the laser initial position. In the 2D contour, the non-melted region is indicated in blue, and the melted region is indicated by red and green when the VED is  $65 \text{ J/mm}^3$  and  $103 \text{ J/mm}^3$  respectively.

The optical absorptivity for the green laser is 40% and is implemented as an input parameter in the green laser heat source model [17], [18].

#### INFRARED LASER SINGLE TRACK DEPOSITION

Like the green laser model, an infrared laser model is developed for a single-track L-PBF process. However, due to the low optical absorptivity of copper to infrared radiation, the process parameter window for successful melting of the powder bed is narrow. It is difficult to obtain conduction dominant U-shaped melt pools by using an infrared laser

unlike the green laser heat source showed in Fig. 3(a). Therefore, a single parameter set which produces keyhole melting mode was selected for validation and the parameter values are shown in Table 4.

**Table 4** Process parameter for single track infrared L-PBF meso-scale numerical model

Process Parameter	Values
Power (W)	540
Scanning Speed (mm/s )	500
Beam size ( $\mu\text{m}$ )	45
Powder layer thickness ( $\mu\text{m}$ )	100

The calculated VED for the selected process parameters is  $240 \text{ J/mm}^3$ , which is more than twice the value of the energy density implemented in the green laser simulation model. This is due to a selection of a smaller laser beam spot size which is a third used in the green laser model. For validating the model, an experimental result from the work of [19] was chosen where an infrared laser was used for consolidating the powder bed. Like the green laser model, a 2D melt pool contour is taken at a location along the laser scanning direction where the melt pool attains a pseudo-steady state. For the simulation case, a mesh size of  $5 \mu\text{m}$  was used as the size of the computational domain and the powder layer thickness were similar to the single track green laser model. The 2D melt pools contour from the simulation model is compared to the experimental results and is shown in Fig. 5(a). The numerical model predicts the melt pool shape accurately for the selected process parameter. The melt pool dimensions of the simulated and experimental results are shown in Table 5 along with the calculated error %.

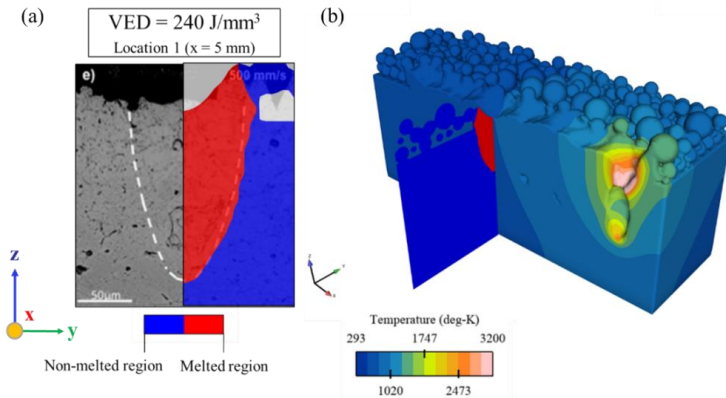


**Fig. 5** (a) 2D melt pool contours from the meso-scale numerical model compared to experiments [19] for  $\text{VED} = 240 \text{ J/mm}^3$  at 5 mm from the beginning of the single track. In the 2D contour, the non-melted region is indicated in blue, and the melted region is indicated by red color. (b) 3D temperature contour plot at time  $1.8 \mu\text{s}$  when  $\text{VED} = 240 \text{ J/mm}^3$  along with 2D melt pool contour at 5 mm from the laser initial position.

**Table 5** Comparison of melt pool dimensions from experimental and numerical results for single track infrared L-PBF process

Source	Melt pool width ( $\mu\text{m}$ )	Error in width (%)	Melt Pool depth ( $\mu\text{m}$ )	Error in depth (%)
Experiments	103		147	
Simulation	124	-21	147	0.4

The error in the melt pool width is four times the mesh size used and therefore it can be accounted to the assumptions made in the numerical model. Along with the other multi-physics phenomena included in the numerical model, recoil pressure and the multiple reflection heat source accurately deposits thermal energy into the powder bed especially when a high VED is implemented, which is shown by less than 1% error in the melt pool depth. At high laser powers, the vapor depression formed on the surface of the melt pool traps the laser radiation increasing the energy coupling efficiency. For an infrared laser, when the laser power is reduced the local temperature in the melt pool is decreased which leads to smaller and shallower melt pool without a keyhole shaped depression zone. Furthermore, the amount of laser ray trapping in the melt pool is reduced resulting in decrease in the energy coupling efficiency and absolute absorptivity. When the absolute absorptivity is the low, the melting mode is conduction dominated which leads to melt pool instability and increase in un-melted zone. There for infrared laser heat sources, successful consolidation of a powder bed can only be achieved in keyhole melting mode. For the validated model, the optical absorptivity of the infrared laser is 12% and is implemented as an input parameter in the multiple reflection ray-tracing model.

The 3D temperature contour for the VED values selected for the single-track L-PBF processing is shown in Fig. 5(b) along with a 2D melt pool contour when the melt pool attains a pseudo-steady state. When implementing a  $\text{VED} = 240 \text{ J/mm}^3$ , a keyhole melting mode is obtained and due to the multiple reflection effect, the energy coupling is increased thus leading to an increase in the melt pool depth and ultimately melt pool volume. The low optical absorptivity of 12% increases the dependence of the energy coupling efficiency solely on the multiple reflection phenomenon which becomes significant at high laser powers due to formation of a keyhole. Processing at such high VED leads to the formation of keyhole induced porosity seen in Fig. 5(b) in the solidified region due to instability in the depression zone. Comparing the melt pool depth of an infrared heat source with a  $\text{VED} = 240 \text{ J/mm}^3$  and a green heat source with a  $\text{VED} = 103 \text{ J/mm}^3$ , it is predicted that the green laser creates a deeper melt pool even with a bigger laser spot size is used.

#### GREEN LASER THIN WALL DEPOSITION

The validated single track green laser model in the previous section is extended to a multi-layer single track L-PBF model. In this model framework, the CFD and DEM solvers are one-way coupled to form a thin wall structure. The framework is similar to the work done in previous work done by the author's group and is explained in [8]. After melting a single track using the CFD solver, the powder bed is allowed to cool to room temperature (300°K). Later the consolidated powder bed is exported in CAD format from

the CFD solver to the DEM model and is assigned as a solid region. In the DEM solver, a powder layer is deposited by the 'rainfall method' over the solidified single track and the remaining un-melted powder regions. The new powder layer along with the solidified single track is imported into the CFD model and a single track is consolidated on the new powder layer. Therefore, in such a way ten single tracks are consolidated one above other along with the un-melted powders powder bed.

To validate the model, a thin wall feature which is made from multiple layers of single-track deposition is printed using a Truprint 1000 green edition L-PBF system. The thin wall feature is scanned using an industrial ZEISS XRadia 520 Versa X-ray CT instrument which was operated at 160 kV with a HE6 filter and a 4X objective. After scanning the thin-wall feature, the generated 1601 2D tomograms were filtered using appropriate denoising algorithms and later reconstructed into a 3D volume which was used for conducting thickness measurements. The process parameters used to print the thin wall on the L-PBF machine is shown in Table 6. The PSD used in the DEM model was obtained from the pure copper powder measurement done using Malvern Panalytical Mastersizer 3000 which is based on laser diffraction principle.

**Table 6** Process parameters used to print thin wall structure

Process Parameters	Values
VED	135 J/mm <sup>3</sup>
Laser type	Continuous wave
Powder layer thickness	30 $\mu$ m
Laser beam spot size	200 $\mu$ m

Instead of scanning the entire thin wall feature, a small portion of the wall is scanned at a higher resolution with a voxel size of 3  $\mu$ m and exposure time of 18 s. The spatial resolution is higher when compared to scan of the entire thin wall which generated a voxel size of 9  $\mu$ m and an exposure time of 4 s was used. With a larger voxel size intricate features such as the micron size copper powders sintered to the side surfaces cannot be accurately resolved. The wall thickness measured from the X ray-CT is compared with the numerical thickness calculated from the 2D temperature contours. Temperatures above 1025°K [20] are assumed to cause powder sintering to the sidewalls after a single laser track is scanned on the powder bed. The numerical thickness is measured after each layer deposition and therefore ten wall thicknesses are measured and the measured location after each layer deposition is shown in Fig. 6. A 2D plane perpendicular to the laser travel direction is located at the center of the laser beam axis during each layer deposition where the temperature field during each layer deposition. The wall thickness is measured after each layer deposition and the thickness is determined based on the width of the temperature iso-line 1025°K which is the sintering temperature of copper powder.

10 thickness measurements along the build direction were obtained from the X-ray CT data and the distance between the measurement location is equidistant as shown in Fig. 7. The thickness measurements from the numerical model and the experiments are shown in Table 7 along with the calculated error %.

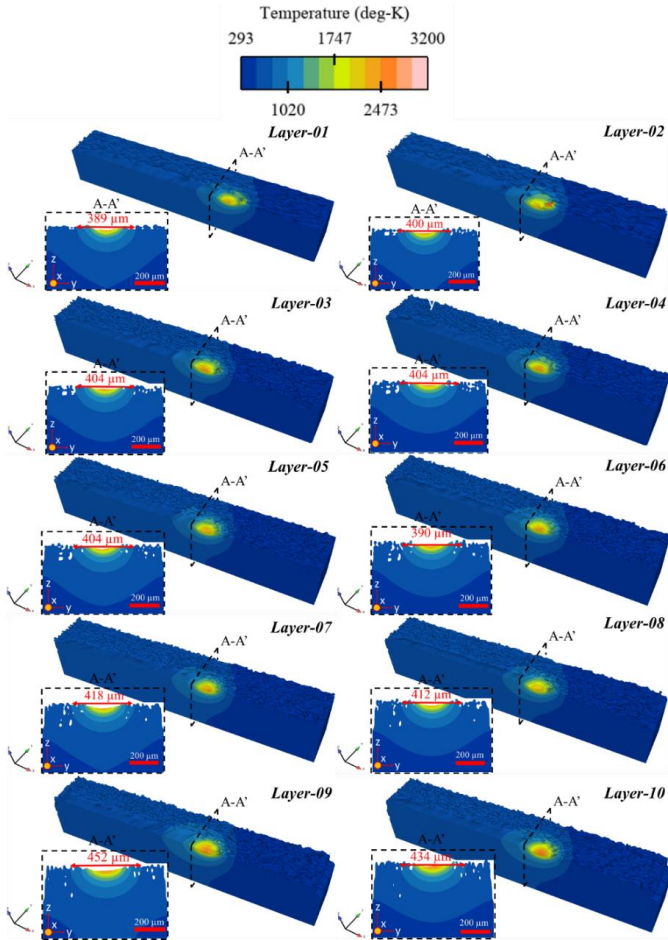


**Fig. 6** 3D temperature contour during the deposition of a single track in each layer at  $t = 3 \mu\text{s}$ . An inset image with each layer deposition depicts a 2D temperature contour on a plane located at the center of the laser and the width of heat affected zone is measured.

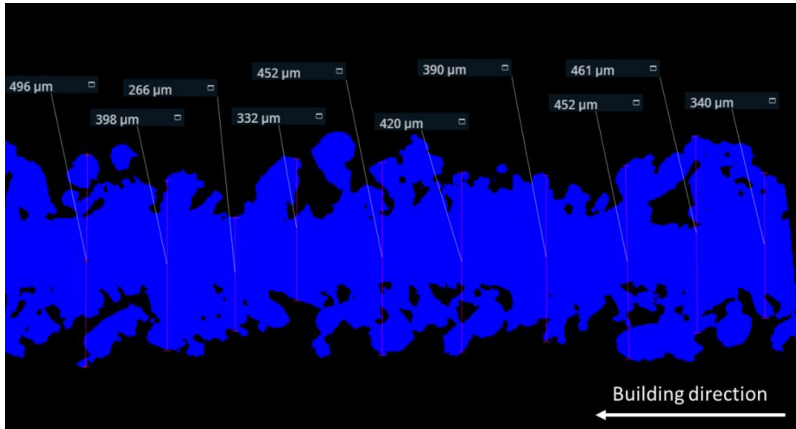


**Fig. 7** Wall thickness measured at a 2D cross-section obtained from X-ray CT at 10 locations equidistant from each other.

**Table 7** Comparison of wall thickness from experimental and numerical results for single track multi-layer green L-PBF process.

Location	Numerical thickness ( $\mu\text{m}$ )	Experimental thickness ( $\mu\text{m}$ )	Error %
1	389	340	-14
2	400	461	13
3	404	452	11
4	404	390	-4
5	404	420	4
6	390	452	14
7	418	332	-26
8	412	226	-82
9	452	398	-13
10	434	496	12
Average	$411 \pm 19$	$397 \pm 76$	-4

From Table 7, the error % in the predicted wall thickness from the numerical meso-scale model has an average value of 4% which is accurate and acceptable. However, at some locations the error % is quite high and this is due to the randomly packed powder bed used in the numerical model. Therefore, it is shown that the meso-scale numerical model can be used to predict the actual thickness of thin-wall structures consisting of single-layer depositions accurately.

## CONCLUSION

In this work a high fidelity meso-scale L-PBF model is developed for pure copper based on FVM method in Flow-3D. Green and infrared laser heat sources were used individually to consolidate the pure copper powder bed deposited over a substrate. The single-track simulation model was validated by comparing the numerical results with experiments where the melt pool shape and size were the quality metrics. The green laser heat source could generate a larger melt pool as compared to the infrared heat source at a lower VED as the absorptivity is higher in the former. In addition, a thin wall structure consisting of single tracks deposited over each other was simulated using a coupled DEM-CFD model and the results were compared with experiments. Wall thickness was used as a quality metric to validate the multi-layer single track model.

Therefore, a green laser is an efficient heat source for processing pure copper in an L-PBF system wherein both conduction mode and keyhole mode melting are possible while with an industrial standard infrared laser only keyhole melting mode is achievable at high laser powers leading to process instabilities.

## APPENDICES AND ACKNOWLEDGEMENTS

This work has received funding from Independent Research Fund Denmark, DIGI-3D project.

## References

- [1] L. JYOTHISH KUMAR, P. M. PANDEY and D. I. WIMPENNY: *3D printing and additive manufacturing technologies*, Springer Singapore, 2018, DOI: 10.1007/978-981-13-0305-0.
- [2] T. DEBROY et al.: 'Additive manufacturing of metallic components – Process, structure and properties', *Progress in Materials Science*, vol. 92, pp. 112-224, 2018, doi: 10.1016/j.pmatsci.2017.10.001.
- [3] C. S. LEFKY, B. ZUCKER, D. WRIGHT, A. R. NASSAR, T. W. SIMPSON and O. J. HILDRETH: 'Dissolvable Supports in Powder Bed Fusion-Printed Stainless Steel', *3D Printing and Additive Manufacturing*, vol. 4, no. 1, pp. 3-11, 2017, doi: 10.1089/3dp.2016.0043.
- [4] J. L. BARTLETT and X. LI: 'An overview of residual stresses in metal powder bed fusion', *Additive Manufacturing*, vol. 27, no. January, pp. 131-149, 2019, doi: 10.1016/j.addma.2019.02.020.
- [5] I. H. AHN: 'Determination of a process window with consideration of effective layer thickness in SLM process', *International Journal of Advanced Manufacturing Technology*, vol. 105, no. 10, pp. 4181-4191, 2019, doi: 10.1007/s00170-019-04402-w.
- [6] R. MCCANN et al.: 'In-situ sensing, process monitoring and machine control in Laser Powder Bed Fusion: A review', *Additive Manufacturing*, vol. 45, no. May, 2021, doi: 10.1016/j.addma.2021.102058.
- [7] M. BAYAT et al.: 'Keyhole-induced porosities in Laser-based Powder Bed Fusion (L-PBF) of Ti6Al4V: High-fidelity modelling and experimental validation', *Additive Manufacturing*, vol. 30, no. August, p. 100835, 2019, doi: 10.1016/j.addma.2019.100835.
- [8] M. BAYAT, S. MOHANTY and J. H. HATTEL: 'Multiphysics modelling of lack-of-fusion voids formation and evolution in IN718 made by multi-track/multi-layer L-PBF', *International*

- Journal of Heat and Mass Transfer*, vol. 139, pp. 95-114, 2019, doi: 10.1016/j.jheatmasstransfer.2019.05.003.
- [9] S. D. JADHAV, L. R. GOOSSENS, Y. KINDS, B. VAN HOOREWEDER and K. VANMEENSEL: 'Laser-based powder bed fusion additive manufacturing of pure copper', *Additive Manufacturing*, vol. 42, no. March, 2021, doi: 10.1016/j.addma.2021.101990.
- [10] S. D. JADHAV, S. DADBAKSH, L. GOOSSENS, J. P. KRUTH, J. VAN HUMBEECK and K. VANMEENSEL: 'Influence of selective laser melting process parameters on texture evolution in pure copper', *Journal of Materials Processing Technology*, vol. 270, no. January, pp. 47-58, 2019, doi: 10.1016/j.jmatprotec.2019.02.022.
- [11] H. SIVA PRASAD, F. BRUECKNER, J. VOLPP and A. F. H. KAPLAN: 'Laser metal deposition of copper on diverse metals using green laser sources', *International Journal of Advanced Manufacturing Technology*, vol. 107, no. 3-4, pp. 1559-1568, 2020, doi: 10.1007/s00170-020-05117-z.
- [12] L. R. GOOSSENS, Y. KINDS, J. P. KRUTH and B. VAN HOOREWEDER: 'On the influence of thermal lensing during selective laser melting', *Solid Freeform Fabrication 2018: Proceedings of the 29th Annual International Solid Freeform Fabrication Symposium - An Additive Manufacturing Conference*, SFF 2018, no. December, pp. 2267-2274, 2020.
- [13] M. BAYAT, V. K. NADIMPALLI, D. B. PEDERSEN and J. H. HATTEL: 'A fundamental investigation of thermo-capillarity in laser powder bed fusion of metals and alloys', *International Journal of Heat and Mass Transfer*, vol. 166, p. 120766, 2021, doi: 10.1016/j.jheatmasstransfer.2020.120766.
- [14] H. CHEN, Q. WEI, Y. ZHANG, F. CHEN, Y. SHI and W. YAN: 'Powder-spreading mechanisms in powder-bed-based additive manufacturing: Experiments and computational modeling', *Acta Materialia*, vol. 179, pp. 158-171, 2019, doi: 10.1016/j.actamat.2019.08.030.
- [15] S. K. NAYAK, S. K. MISHRA, C. P. PAUL, A. N. JINOOP and K. S. BINDRA: 'Effect of energy density on laser powder bed fusion built single tracks and thin wall structures with 100  $\mu\text{m}$  preplaced powder layer thickness', *Optics and Laser Technology*, vol. 125, May 2020, doi: 10.1016/j.optlastec.2019.106016.
- [16] G. NORDET et al.: 'Absorptivity measurements during laser powder bed fusion of pure copper with a 1 kW cw green laser', *Optics & Laser Technology*, vol. 147, no. April 2021, p. 107612, 2022, doi: 10.1016/j.optlastec.2021.107612.
- [17] M. HUMMEL, C. SCHÖLER, A. HÄUSLER, A. GILLNER and R. POPRAWA: 'New approaches on laser micro welding of copper by using a laser beam source with a wavelength of 450 nm', *Journal of Advanced Joining Processes*, vol. 1, no. February, p. 100012, 2020, doi: 10.1016/j.jajp.2020.100012.
- [18] M. HUMMEL, M. KÜLKENS, C. SCHÖLER, W. SCHULZ and A. Gillner, 'In situ X-ray tomography investigations on laser welding of copper with 515 and 1030 nm laser beam sources', *Journal of Manufacturing Processes*, vol. 67, no. April, pp. 170-176, 2021, doi: 10.1016/j.jmapro.2021.04.063.
- [19] L. GARGALIS et al.: 'Determining processing behaviour of pure Cu in laser powder bed fusion using direct micro-calorimetry', *Journal of Materials Processing Technology*, vol. 294, no. March, p. 117130, 2021, doi: 10.1016/j.jmatprotec.2021.117130.
- [20] A. MONDAL, D. AGRAWAL and A. UPADHYAYA: 'Microwave heating of pure copper powder with varying particle size and porosity', *Journal of Microwave Power and Electromagnetic Energy*, vol. 43, no. 1, pp. 4315-43110, 2009, doi: 10.1080/08327823.2008.11688599.

# SIMULATION OF MICROSTRUCTURE EVOLUTION DURING WAM PROCESS

J. KRONSTEINER\*, H. DREXLER\*, S. HOVDEN\*,  
F. HAUNREITER\*, P. O'TOOLE\*\*, A. MOLOTNIKOV\*\*,  
M. EASTON\*\*

\**LKR Light Metals Technologies, Austrian Institute of Technology, Giefinggasse 2, 1210 Vienna, Austria*  
\*\**RMIT Centre for Additive Manufacturing, School of Engineering, Royal Melbourne Institute of Technology, Melbourne,  
VIC 3001, Australia*

DOI 10.3217/978-3-85125-968-1-03

## ABSTRACT

The development of microstructure during Wire-Based Additive Manufacturing (WAM) is of major interest for the Additive Manufacturing (AM) industry. The resulting geometry, mechanical properties, and quality of WAM parts are directly affected by the process conditions. Numerical simulations of WAM processes can predict and optimize the process settings (heat input, thermal conditions, e.g., by pre-heating, ...) and therefore speed-up the trial-and-error phase of the manufacturing process (first time right). The WAM process can be considered as a welding process accompanied by continuous heat-treatment processes (during the build-up of walls the heat source is reheating and even partially remelting existing layers multiple times), the formation of the microstructure mainly depends on the temperature evolution in the part. Two modes of microstructure development are considered: grain nucleation and growth during solidification and growth/recrystallization in the solid phase. To compute grain size considering the interplay of nucleation and growth during solidification, the Interdependence (ID) model is used. Based on the initial grain size distribution, chemical composition, inoculant particles, among other influence factors, the evolution of the microstructure and hot cracking susceptibility during the cooling and reheating cycles of an AM process can be calculated. Both models have been implemented into the Finite Element (FE) solver LS-DYNA®. Depending on the current element temperature either of the two grain morphology models are activated. Here, the evolution of the microstructure including the hot cracking susceptibility during the manufacturing of wall structures is presented. The results obtained from the calculations are compared and validated against our experimental trials. A good agreement between the measured and calculated grain size could be obtained.

Keywords: welding, WAM, microstructure, grain size, solidification

## INTRODUCTION

Additive manufacturing (AM) development activities have increased dramatically during the last few years. There are several reasons for this major interest from industry and academia. Especially in sectors such as aerospace, medical and tooling industries, the following advantages are of interest [1]:

- AM processes have in general superior mechanical properties in comparison to cast counterparts,

- AM enables manufacturing of complex 3D geometries often obtained by topology optimization and integrating structures with recesses and additional functionalities such as cooling channels,
- potential reduction in weight due to optimized material usage and/or expensive light metals such as high-performance aluminum or titanium alloys and therefore reduced CO<sub>2</sub> emissions,
- near net shape manufacturing (depending on the process),
- reduction in scrap material compared to forming and/or machining processes,
- improved properties due to extreme solidification conditions resulting in unique microstructure [2],
- engineering of microstructure during AM processing [2],
- and many more.

Due to the different requirements for different fields of applications, there is a multitude of additive manufacturing methods on the market today. Powder based additive manufacturing methods for metals can maintain very strict geometrical tolerances and therefore high surface quality requirements. However, part size is usually restricted by the AM machine. Most laser-based systems additionally have a maximum build rate in the range of 70-100 cm<sup>3</sup>/h and a limited build volume in the range of 40 x 40 x 40 cm<sup>3</sup> [1,3]. Metal deposition techniques such as laser metal deposition (LMD) and the wire additive manufacturing (WAM) only have very little restrictions on the build size and have the highest build rates of all AM techniques [1]. It is also possible to use graded and hybrid materials by feeding different filler materials simultaneously. However, in terms of geometrical tolerances and surface roughness, these methods are inferior to most powder-based methods. The surface roughness ranges between 10 Ra and 200 Ra but the build rates can be up to 300 cm<sup>3</sup>/h [1].

Whenever large components and a high throughput are favored, WAM is a good choice. This is one of the reasons why WAM is used in this publication. Since wire-based AM processes are in principle welding processes (either using laser, plasma or as in the presented case electric arc) they are thus susceptible to certain defects. Metals which can be processed by WAM need to have good weldability to avoid cracks during solidification.

In addition to titanium and steel, an increasing research activity is visible regarding high-performance aluminum alloys for WAM applications. Due to the key role of 6xxx series alloys for the automobile industry, the implementation of compatible WAM feedstock wire is of major interest [5]. Especially Al-Mg-Si alloys of the 6xxx series, however, show a tendency for hot cracking [4-6]. Hot Cracking is caused by the predominant tensile stresses in the mushy zone due to shrinkage and its interaction with liquid feeding [7]. Liquid feeding has been visualized for steel by Agrawal et al. [8] using in-situ microscopic methods. Since hot cracks originate in the final state of solidification in the semisolid region due to localized applied load, the modelling of the mechanical behavior is of utmost importance [9]. The localized load or even strain or strain rate can occur due to constrained thermal contraction and the density change from liquid to solid [9]. Liquid feeding can compensate for the shrinkage during cooling at low solid fractions. The higher the solid fractions, the more difficult the interdendritic feeding becomes and the higher the chance for hot cracks to occur [9]. Voids can then nucleate

and grow into cracks under a certain applied load [9]. There is also a considerable influence of the alloy composition, especially for aluminum alloys. The interaction between nucleants and solutes was investigated by Easton and StJohn [10, 11]. The Interdependence Theory links grain formation and nucleation selection [12, 13].

In addition to the solidification conditions, WAM processed materials are characterized by the process-intrinsic heat treatment [14]. These heat treatment processes affect solid-state precipitation reactions and thus mechanical properties [15]. In aluminum alloys, this thermal treatment additionally results in grain coarsening reactions [15]. The main focus of this paper is therefore to model the grain coarsening behavior during AM processing on a part-scale using Finite Element (FE) methods.

## MATERIAL MODELLING

To ultimately model the grain size distribution and the susceptibility for hot cracking effects after WAM processing, several numerical methods need to work together. In this work grain formation is calculated by the Interdependence Theory (ID, [12]) while solid-state grain growth is considered using a static recrystallization (ReX) and grain morphology model [16]. The mechanical behavior in the solid state is covered by a dislocation density-based flow stress model [16]. The hot cracking susceptibility is calculated based on the critical strain rate and given by a dimensionless indicator based on the minimal (in plane) strain rate.

Finally, the welding process is covered by a special heat source and element activation technique.

### INTERDEPENDENCE THEORY (ID)

The ID model [12] considers the formation and growth of new grains as depending on the chemical composition of the alloy, the average distance, number and efficiency of activated inoculant particles, the effect of constitutional supercooling regeneration, critical nucleation undercooling on varying inoculant diameters, interface growth velocity and growth restriction factor, among others. The ID links together the nucleation and growth during the initial transient, demonstrating that the nucleation, growth, and activation or inhibition of neighboring heterogenous substrates depends on the growth restriction factor and the growth required to establish constitutional supercooling,  $x_{CS}$ , the diffusion length,  $x_{l_D}$ , and the average distance between potent inoculant particles,  $x_n$ , [12]. For a given inoculated alloy, the grain size can be computed as the sum of these components, by

$$d_g = x_{CS} + x_{l_D} + x_n, \quad (1)$$

These lengths depend on material and process parameters and, as such, link the material response to the process conditions. The terms  $x_{CS}$ ,  $x_{l_D}$ , and  $x_n$  are computed by the following equations,

$$x_{CS} = \frac{D_l z \Delta T_n}{vQ}, \quad (2)$$

$$x_{lD} = \frac{4.6D_l}{v} \left( \frac{c_L - c_0}{c_L(1-k)} \right), \quad (3)$$

$$x_n = \frac{1}{\sqrt[3]{fN_v}}. \quad (4)$$

where  $D_l$  is the liquid diffusion constant,  $\Delta T_n$  is the nucleation temperature computed by Greer's Free Growth model [17],  $v$  is the solidification velocity,  $Q$  is the growth restriction factor [18],  $c_0$  and  $c_L$  are the nominal alloy composition and the maximum liquid composition at the interface,  $k$  is the partition coefficient,  $N_v$  is the volume density of inoculant particles in  $m^{-3}$ , and  $f$  is the relative efficiency of the inoculant. This model has seen broad application to explain nucleation and growth of grains in several alloy systems, including aluminum alloys. To compute the morphology of grains, the grain size is compared to the secondary dendrite arm spacing,  $\lambda_2$ , computed by,

$$\lambda_2 = 5.5[M \cdot t_f]^{-n}, \quad (5)$$

where  $t_f$  is the freezing time, obtained from the process model and assumptions about the mush (see the hot cracking section below),  $n$  is a known material constant between 0.3 and 0.5, and  $M$  is computed from the Gibbs-Thomson coefficient and the value of the growth restriction factors at  $f_s \sim 0$  and  $f_s \sim f_{eutectic}$ , respectively  $Q_{0,j}$  and  $Q_{f,j}$ , by [19],

$$M = \frac{\Gamma}{\sum_{j=1}^n (Q_{0,j} - Q_{f,j})/D_j} \ln \left[ \frac{\sum_{j=1}^n (1 - Q_{f,j}/D_j)}{\sum_{j=1}^n (1 - Q_{0,j}/D_j)} \right] \quad (6)$$

#### HOT CRACKING MODEL

A modified Rappaz-Drezet-Gremaud hot tearing model is used [20] to compute the critical strain rate which is compared to the calculated strain rate in the FE simulation. This model computes the critical strain rate for an alloy solidifying with an equiaxed morphology by considering the ability of the viscous liquid above a growing field of grains to feed the diminishing mush, sufficient to offset solidification shrinkage. This critical strain rate,  $\dot{\epsilon}_{critical}$ , is computed by,

$$\dot{\epsilon}_{critical} = \frac{d_g^2}{180(1+\beta)B\mu L^2} \left( p_m - \frac{4\gamma}{\lambda_2(1-\sqrt[3]{f_{ca}})} \right) - \frac{\nu\beta A}{(1+\beta)BL} \quad (7)$$

where  $\beta$  is the solidification shrinkage,  $\mu$  is the viscosity,  $p_m$  is the metallostatic pressure,  $\gamma$  is the liquid-void surface tension,  $d_g$  is the secondary dendrite arm spacing (or the equiaxed grain size),  $\nu$  is the solid front isotherm velocity and  $L$  is the length of the mushy zone. The term  $f_{ca}$  is the solid fraction where adjacent grains coalesce at the final moments of solidification. The terms, F, A, and B, are computed over the mush length from the temperature at the *coherence* solid fraction,  $T_{co}(f_{co})$ , where strain can be communicated across the mush and the temperature at *coalescence*  $T_{ca}(f_{ca})$ , by

$$A = \Delta T^{-1} \int_{T_{ca}}^{T_{co}} \frac{f_s(T)^2}{(1-f_s(T))^2} dT \quad (8)$$

$$B = \Delta T^{-1} \int_{T_{ca}}^{T_{co}} \frac{(1-f_s(T))^2 F(T)}{(1-f_s(T))^3} dT \quad (9)$$

$$F = \Delta T^{-1} \int_{T_{ca}}^{T_{co}} f_s(T) dT \quad (10)$$

$$\Delta T = T_{co} - T_{ca}. \quad (11)$$

The solid fraction versus temperature curves,  $f_s(T)$ , are computed by Scheil calculation of solidification obtained from JMatPro (Sente Software, UK) [21]. All basic thermophysical properties are obtained from this calculation.

### FLOW STRESS MODEL

As already mentioned in the introduction, hot cracking, but also solid-state grain growth, needs a certain localized load to be promoted. To model the response to mechanical loading, a flow stress model was implemented in the context of FE methods. The so-called mean dislocation density material (MD<sup>2</sup>M) model is based on capturing the localized evolution of mean dislocation density depending on strain, strain rate and temperature. In the case of Additive Manufacturing (AM), the loading originates from the restricted thermal contraction due to the mechanical clamping of the substrate in AM processes. This is also one of the main sources for residual stresses which subsequently influence the hot cracking susceptibility.

The constitutive stress-strain model is commonly written as a sum of an initial yield (threshold) stress,  $\sigma_y$ , and a strain-dependent part,  $\sigma_\rho$ . The latter might be described in a power law form or by using an internal state parameter-based model. In present work we will follow a Kocks-Mecking approach [22,23], which is based on an evolution of the dislocation density  $\rho$ :

$$\sigma = \sigma_y + M \cdot b \cdot G \left( \alpha \sqrt{\rho} + \frac{1}{\delta} \right) \quad (1)$$

The second part in Eq. (1) represents the strain dependent part ( $\sigma_\rho$ ). During deformation, the material substructure with a mean sub-grain size ( $\delta$ ) is formed influencing the third part of Eq. (1) and is inversely proportional to  $\sqrt{\rho}$ . Variables and parameters in Eq. (1) and the following equations are summarized in Table 1. The change in the mean dislocation density by deformation at temperature,  $T$ , with a strain rate,  $\dot{\phi}$ , might be described as a superposition of dislocations production and their annihilation [24-27] as following:

$$\frac{d\rho}{dt} = \frac{M\sqrt{\rho}}{b \cdot A} \dot{\phi} - 2B \frac{d_{ann}}{b} \rho M \dot{\phi} - 2CD \frac{Gb^3}{k_B T} (\rho^2 - \rho_{eq}^2) \quad (2)$$

While the first term corresponds to the increase in dislocation density, the last two terms describe the recovery process by spontaneous annihilation and thermally activated dislocation climb.

The first recovery process happens when two dislocations with antiparallel Burgers vectors come to a critical distance,  $d_{ann}$ , while the second one is thermally activated and controlled by self-diffusion along the dislocations,  $D$ .

Furthermore, equation (2) contains three calibration parameters (A, B, C). A is a material constant depending on the purity, B is associated with the number of activated slip planes and C considers the solute trapping [24]. For simplicity, however, these parameters are normally tuned using the experimental stress–strain curves.

#### GRAIN MORPHOLOGY MODEL

The calculation of the developing microstructure is mainly based on the simulation of grain/subgrain growth and is implemented in the second part of the MD<sup>2</sup>M model. Here, a distinction is made between the grain growth of already existing grains  $\delta^G$  from the melt and recrystallized grains  $\delta^{rex}$ . The growth of existing grains is described by the following expression:

$$\frac{d\delta^G}{dt} = 2 \cdot M_{GB} \cdot \left( \frac{3\cdot\gamma}{\delta^G} + P_D - P_Z \right) \quad (3)$$

In a similar manner, the recrystallized grains  $\delta^{rex}$  can grow according to:

$$\frac{d\delta^{rex}}{dt} = 2 \cdot M_{GB} \cdot (P_D - P_Z) \cdot (1 - X), \quad (4)$$

and the subgrain size  $\delta^S$  evolves due to:

$$\frac{d\delta^S}{dt} = 2 \cdot M_{sub} \cdot (P_D - P_Z) \cdot (1 - X). \quad (5)$$

**Table 1** MD<sup>2</sup>M model variables and physical constants used in Eqs. (1-5).

Description	Variable name	Values	Units
Taylor factor for fcc textures	M	3.06	[-]
Length of the Burgers vector	b	28.6	[nm]
Boltzmann constant	$k_b$	1.381E-23	[J K <sup>-1</sup> ]
Diffusion coefficient in solid state	$D_s$	calculated	[m <sup>2</sup> s <sup>-1</sup> ]
Temperature dependent shear modulus	G(T)	calculated	[Pa]
Grain size	$(\delta_0^G), \delta^G$	calculated	[m]
(Initial) grain size (e. g. from casting)	$d_g$	calculated	[m]
Flow stress (y... yield)	$\sigma, \sigma_y$	calculated	[Pa]
Dislocation density (eq...equilibrium)	$\rho, \rho_{eq}$	calculated	[m <sup>-2</sup> ]
Accumulated dislocation density	$\rho_g$	calculated	[m <sup>-2</sup> ]
Stored energy (in microstructure)	$P_D$	calculated	[Pa]
Mobility of grain and subgrain boundaries	$M_{GB}, M_{sub}$	calculated	[m <sup>2</sup> s kg <sup>-1</sup> ]
Zener pressure (in grains, subgrains)	$P_z, P_{z,sub}$ [16,17]	calculated	[Pa]
Recrystallized fraction	X	calculated	[-]
Critical distance for spontaneous annihilation	$d_{ann}$	calculated	[m]
Subgrain size (eq...equilibrium)	$\delta^S, \delta_{eq}^S$	calculated	[m]
Grain/Subgrain boundary energy	$\gamma, \gamma^S$	calculated	[J m <sup>-2</sup> ]
Alloy specific parameters	$\alpha, A, B, C, K$	calculated	[-]
Plastic strain	$\phi$	calculated	[-]
Local strain rate	$\dot{\phi}$	calculated	[s <sup>-1</sup> ]
Temperature	T	calculated	[K]
Time, time step	$t, dt$	calculated	[s]

## NUMERICAL WELDING MODEL

When all the models are run together in one framework, welding processes of considerable part sizes can be investigated in detail. Firstly, the elements of the current layer were inserted by the SAM (Simulation of Additive Manufacturing, [28]) framework in a quiet state. The welding process was then simulated by the LS-DYNA<sup>®</sup> solver using a Goldak [29] heat source. When the heat source passed over the quiet elements, element activation occurred depending on the element temperature. Similar to the \*MAT\_CWM [30] implementation (CWM ds for Computational Welding Mechanics) in LS-DYNA<sup>®</sup>, a user-defined variant was implemented for the mechanical case. Between start ( $S_{mech}$ ) and end temperature ( $E_{mech}$ ), mechanical properties such as Young's modulus, Poisson ratio, yield stress and thermal expansion coefficient were linearly scaled from "ghost" to realistic values (see Fig. 1 (a)). The main reason for writing a user-defined variant of \*MAT\_CWM was to combine all the above models together (see Fig. 2), which is only possible by applying a user-defined material model. For the activation of the thermal material properties, conventional \*MAT\_THERMAL\_CWM, implemented in LS-DYNA<sup>®</sup>, was used.

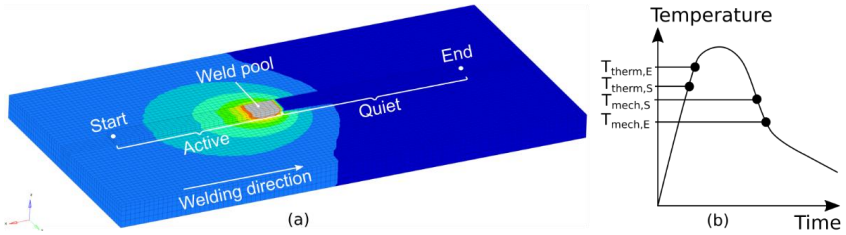


**Fig. 1** Application of the quiet element method for temperature results (a) and diagram showing the thermal and mechanical activation procedure (b)

Here again, thermal properties such as specific heat, thermal conductivity, among others, were linearly scaled between “ghost” and realistic values. Temperature dependent curves were used for the thermal and mechanical properties which were not calculated.

During the mechanical element activation process (between  $T_{mech,S}$  and  $T_{mech,E}$ ), interdependence and hot cracking models were activated. To correctly consider the contraction of the cooling material after solidification in combination with the MD<sup>2</sup>M model, the activation procedure for the user-defined mechanical CWM model was modified.

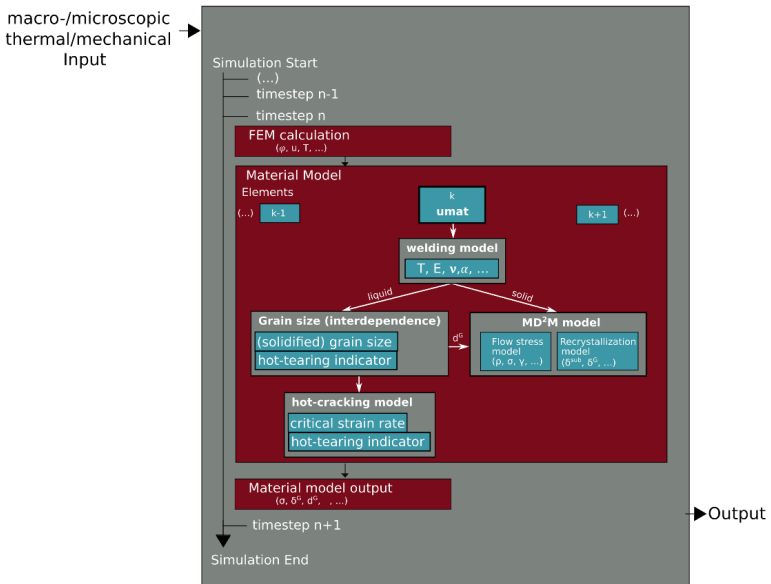


**Fig. 2** Diagram showing the implemented models and the most important variables/parameters

Since the expansion of the material during heating could lead to generation of dislocations even during the “melting” of the material drop,  $T_{mech,S}$  and  $T_{mech,E}$  were defined in such a way that element activation could only happen during the cooling of the molten material (see Fig. 1 (b)) in the mechanical case. The activation of the thermal material properties happened during heating (which is the standard implementation in LS-DYNA®) between  $T_{therm,S}$  and  $T_{therm,E}$ . The contraction of the solidified material led to plastic deformation and thus the production of dislocations due to residual stresses.

Based on the chemical composition, inoculant particles, among other influence factors, the initial microstructure was calculated by the interdependence model during the cooling of the molten material. In areas where the material was already solidified, the grain morphology was further described by the grain growth model which was adapted for AM applications by LKR. When the welding process (including a certain holding time between layers) was finished, the LS-DYNA® simulation was finished too and a new layer (already pre-meshed) was inserted by the SAM framework. After finishing the preparations for the new run, the SAM framework restarted the thermo-mechanical simulation again. This process was repeated until the pre-defined number of layers (48) were produced. The relationship between the models and how they are connected is illustrated in Fig. 2.

### SIMULATION MODEL SETUP

The setup for the simulation model of a simple wall structure was designed in a way to closely resemble the real setup in the workshop (see Fig. 3).

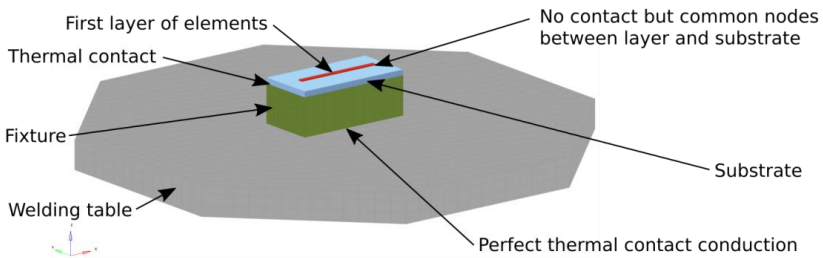


**Fig. 3** Model setup for the WAM simulation of a single wall

Due to the importance of the thermal conditions during WAM processing, the fixture and the welding table were considered as well. In that way, the heat flux into the fixture and the welding table could be taken care of. A combination of convection and radiation was used to set the boundary conditions for the model. Due to the large range of temperatures, the values for convection and radiation were combined into a temperature dependent curve for the convection boundary condition including the effect of radiation [31,32]. This combined approach allows to use °C in the model whereas LS-DYNA® asks

for K when using radiation. The user-defined material models internally convert °C from the model in K.

The heat transfer coefficient (HTC) for the thermal contact between the different parts/materials is hard to define since it depends on temperature, pressure and surface roughness. The HTCs used in this model are based on a correlation of temperature from experiments performed with the same setup and numerical simulations thereof. An HTC of  $1000 \text{ Wm}^{-2}\text{K}^{-1}$  was used for the thermal contact between substrate and fixture, whereas perfect thermal contact conduction was defined between the fixture and the welding table. To achieve a suitable interlayer temperature, two preheating runs were performed by moving the heat source over the substrate without adding material. This is a procedure which is also performed in the experiments and helps to reduce the heat loss into the whole setup.

A mechanical surface to surface contact was used between substrate, fixture, and welding table. The connection between the individual layers was implemented by using common nodes between the elements of the existing and the new layer.

### RESULTS AND DISCUSSION

In the following section we will discuss first the experimental and afterwards the simulation results. The experiments were performed by the project partner RHP-Technology GmbH. The simulation work was performed by LKR using a Linux-based cluster and the commercial LS-DYNA® FEM solver with implemented user-defined material models as described in the section Material Modelling. The build-up process was simulated for 48 layers up to a height of 91.5 mm.

### EXPERIMENTAL RESULTS

By using a plasma metal deposition (PMD) process, RHP produced a wall by welding several layers atop another until a wall was generated (see Fig. 4).

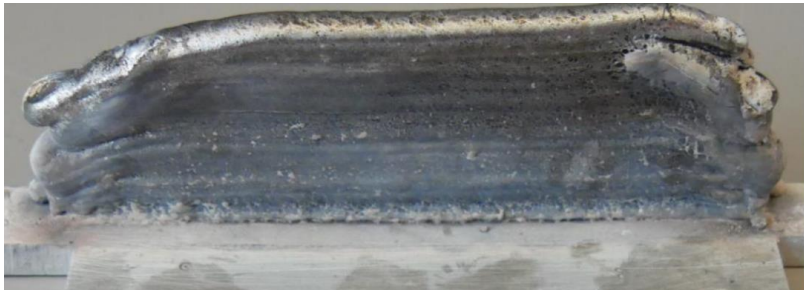


**Fig. 4** Wall samples made from nano-treated 6061NT material

Micrographs of two positions of a section through this wall are given in Fig. 5. A very homogeneous distribution of very fine grains could be found as shown in Fig. 5 (a) and (b).

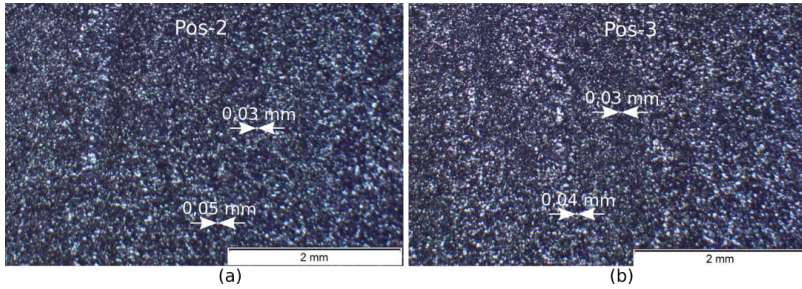


**Fig. 5** Optical Micrographs of pos-2 (a) and pos-3 (b) from Barker etched 6061NT wall samples

The final grain sizes which could be found from the micrographs are in the area of 0.01 to 0.1 mm diameter.

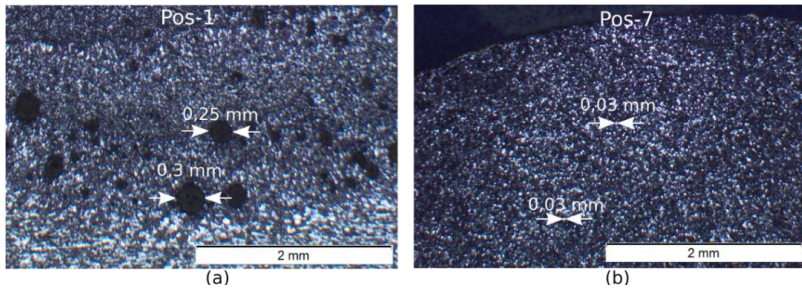


**Fig. 6** Optical Micrograph of bottom (a) and top (b) in Barker etched 6061NT wall samples

Minor voids at the bottom near the interface between substrate and wall are visible in Fig. 6 (a). At the top of the wall (Fig. 6 (b)), the microstructure is still void-free and shows grains of approximately 0.03 mm.

## NUMERICAL RESULTS

Similar to the experimental procedure, the simulation started with two pre-heating runs. Using only the torch (or the Goldak heat source in the simulation), substrate, fixture and welding table were preheated to reduce the heat loss for the first layer and to help get good bonding between the welding material and the substrate (see Fig. 7).

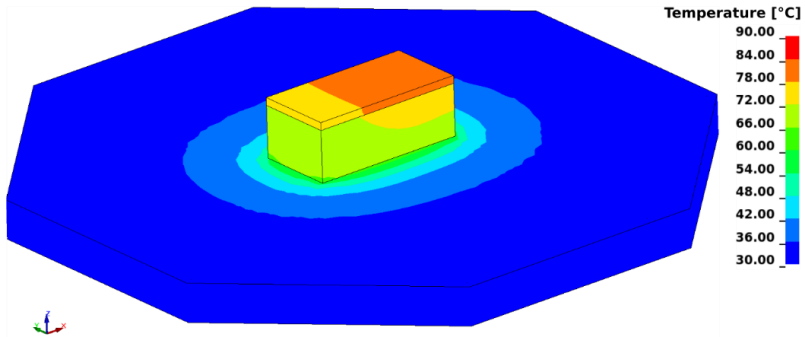


**Fig. 7** Initial temperature distribution of the whole setup after pre-heating

The already pre-activated elements of the substrate were heated during pre-heating to reduce the heat loss during welding. When the first layer was connected to the substrate, the heat loss due to the shared nodes between first layer elements and substrate elements was thus reduced by the pre-heating.

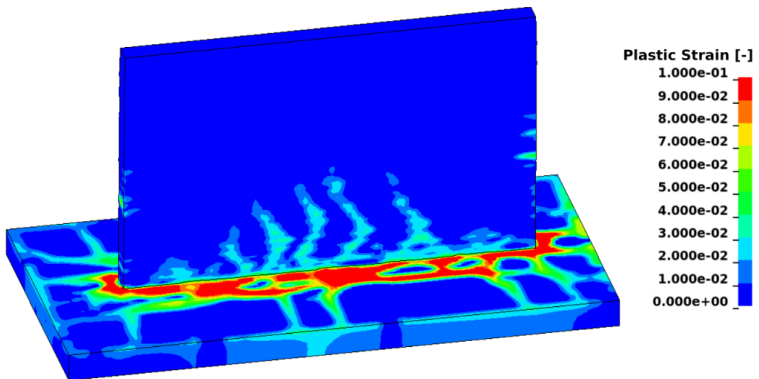


**Fig. 8** Plastic strain distribution after welding of 48 layers including time for cooling

The plastic strain distribution due to the contracting material during cooling is given in Fig. 8 and shows plastic strains near the bottom part of the wall.

The resulting dislocation density distribution due to the plastic strain and temperature is given in Fig. 9. The A, B and C parameters for modelling the stress-strain behavior for the specific alloy was found by curve fitting using the flow curves of 6061NT for several strain rates and temperatures.

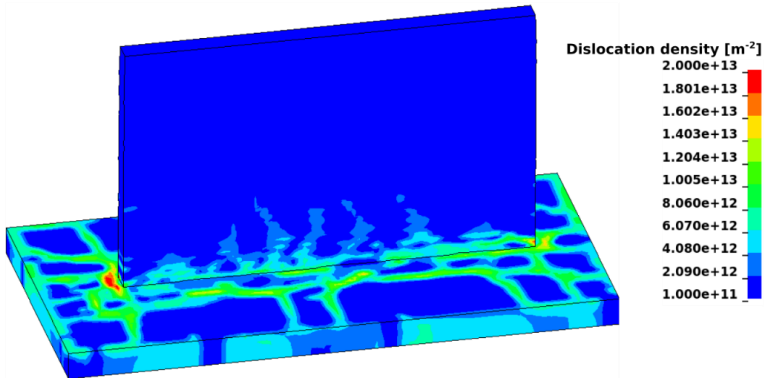


**Fig. 9** Distribution of dislocation density after welding of 48 layers including time for cooling

When the temperature during cooling falls below a critical temperature, the Interdependence model starts calculating the initial grain size coming from the melt. The distribution of initial grain size for 48 layers is illustrated in Fig. 10.

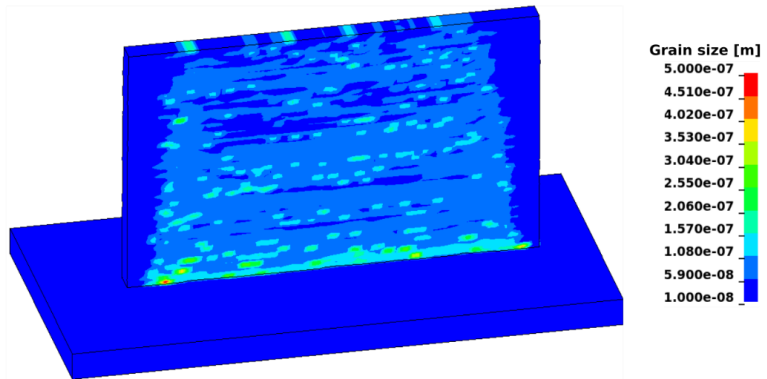


**Fig. 10** Grain size distribution from the interdependence model after welding of 48 layers

When the material is fully solidified, the grain morphology model calculates the grain size evolution during cooling and re-heating. The resulting grain size distribution after welding of 48 layers can be found in Fig. 11. There is a good agreement for the final grain size between experiments and simulations.

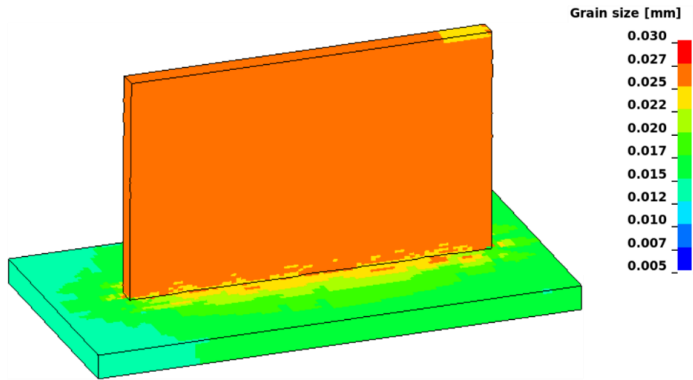


**Fig. 11** Grain size distribution from the grain morphology model after welding of 48 layers

The resulting distribution of residual stresses shows higher values near the wall edges and in general at the bottom and in the base plate (see Fig. 12).

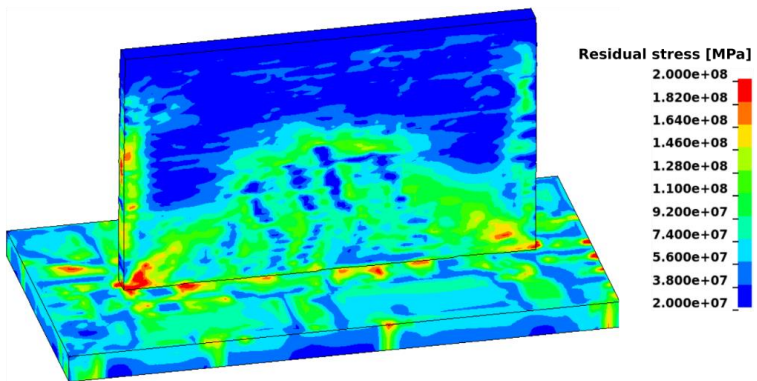


**Fig. 12** Distribution of residual stress in the substrate with the first 48 layers

Finally, the hot cracking model continuously calculates the hot cracking susceptibility. As can be seen in Fig. 13, the probability for hot cracking is especially high near the edges of the walls. With increasing wall height, the critical strain rate grows from the edges in the direction of the center of the wall.

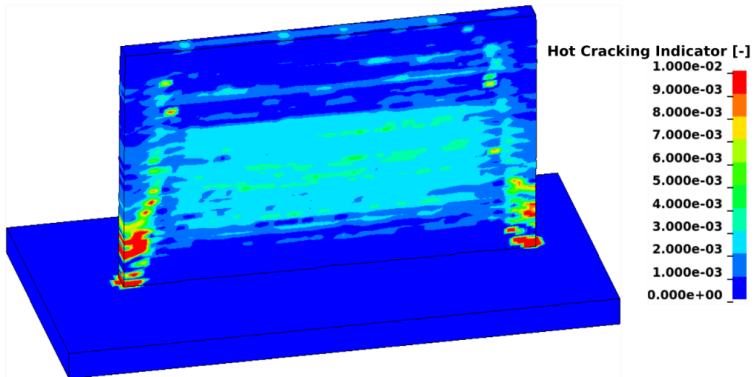


**Fig. 13** Hot Cracking susceptibility for a wall of 91.5 mm height

## CONCLUSION

In the here presented first results from the thermo-mechanical WAM process model, several models could be successfully implemented and coupled to calculate the macro- and microstructure results from the molten material until the failure of the part due to distortion, residual stress and the hot cracking susceptibility. Although further testing and calibration are necessary, reasonable results could already be obtained. Proper validation is also still pending and the application to different geometries and alloys is also a major question. Further tasks are a mesh and timestep sensitivity study in order to reduce the calculation times. With implicit timesteps of 0.25 s for the welding simulation, the fully coupled model takes approximately one 3 hour 15 minutes for a representative layer using 4 nodes on a Linux cluster with 16 cores each.

## APPENDICES AND ACKNOWLEDGEMENTS

The authors would like to thank Austrian Research Promotion Agency (FFG) for sponsoring the research work in the project M4AM (funding scheme: Beyond Europe: 874169), Austrian Federal Ministry for Climate Action, Environment, Energy, Mobility, Innovation and Technology and the Austrian Institute of Technology (AIT) for the technical/financial support in this research work. Special thanks to RHP-Technology GmbH for performing the experimental work during the M4AM project.

## References

- [1] S. GORSSE, C. HUTCHINSON, M. GOUNÉ AND R. BANERJEE: ‘Additive manufacturing of metals: a brief review of the characteristic microstructures and properties of steels’, Ti-6Al-4V and high-entropy alloys, *Science and Technology of Advanced Materials*, Vol.18, No. 1, pp. 584-610, 2017.
- [2] A. PRASAD, L. YUAN, P. LEE, M. PATEL, D. QIU, M. EASTON, D. ST JOHN: ‘Towards understanding grain nucleation under additive manufacturing conditions’, *Acta Materialia*, Vol. 195, pp. 392-403, 2022.
- [3] A. M. KHORASANI, I. GIBSON, J. K. VEETIL, A. H. GHASEMI: ‘A review of technological improvements in laser-based powder bed fusion of metal printers’, *International journal of advanced manufacturing technology*, Vol. 108, No. 1-2, pp. 191-209, 2020, <https://doi.org/10.1007/s00170-020-05361-3>.
- [4] L. SWEET, M. A. EASTON, J. A. TAYLOR, J. F. GRANDFIELD, C. J. DAVIDSON, L. LU, M. J. COUPER AND D. H. STJOHN: ‘Hot Tear Susceptibility of Al-Mg-Si-Fe Alloys with Varying Iron Contents’, *TMA and ASM International*, 2012, <https://doi.org/10.1007/s11661-012-1562-1>.
- [5] T. KLEIN, A. ARNOLDT, R. LAHNSTEINER, M. SCHNALL: ‘Microstructure and mechanical properties of a structurally refined Al–Mg–Si alloy for wire-arc additive manufacturing’, *Materials Science & Engineering A*, Vol. 830, 142318, 2022.
- [6] C. HAGENLOCHER, D. WELLER, R. WEBER, T. GRAF: ‘Reduction of the hot cracking susceptibility of laser beam welds in AlMgSi alloys by increasing the number of grain boundaries’, *Science and Technology of Welding and Joining*, Vol. 24, No. 4, pp. 313-319, 2019.
- [7] N. CONIGLIO, C. E. CROSS: ‘Mechanisms for solidification crack initiation and growth in aluminum welding’, *Int. Mater. Rev.*, Vol. 58, pp. 375-397, 2013, <https://doi.org/10.1179/1743280413Y.0000000020>.
- [8] G. AGARWAL, M. AMIRTHALINGAM, S.C. MOON, R. J. DIPPENAAR, I. M. RICHARDSON, M. J. M. HERMANS: ‘Experimental evidence of liquid feeding during solidification of a steel’, *Scripta Mater.*, Vol. 146, pp. 105-109, 2018, <https://doi.org/10.1016/j.scriptamat.2017.11.003>.
- [9] M. A. EASTON, ET AL.: ‘Observation and Prediction of the Hot Tear Susceptibility of Ternary Al-Si-Mg Alloys’, *The Minerals, Metals & Materials Society and ASM International*, 2012, <https://doi.org/10.1007/s11661-012-1132-6>.
- [10] M. A. EASTON, D. H. STJOHN: ‘A model of grain refinement incorporating alloy constitution and potency of heterogeneous nucleant particles’, *Acta Mater.*, Vol. 49, pp. 1867-1878, 2001, [https://doi.org/10.1016/S1359-6454\(00\)00368-2](https://doi.org/10.1016/S1359-6454(00)00368-2).
- [11] M. A. EASTON, D. H. STJOHN: ‘An analysis of the relationship between grain size, solute content, and the potency and number density of nucleant particles’, *Metall. Mater. Trans. A Phys. Metall. Mater. Sci.*, Vol. 36, pp. 1911-1920, 2005, <https://doi.org/10.1007/s11661-005-0054-y>.
- [12] D. H. STJOHN, M. QIAN, M. A. EASTON, P. CAO: ‘The Interdependence Theory: the relationship between grain formation and nucleant selection’, *Acta Mater.*, Vol. 59, pp. 4907-4921, 2011, <https://doi.org/10.1016/j.actamat.2011.04.035>.
- [13] M. BERMINGHAM, D. STJOHN, M. EASTON, L. YUAN, M. DARGUSCH: ‘Revealing the mechanisms of grain nucleation and formation during additive manufacturing’, *JOM (J. Occup. Med.)*, Vol 72 pp. 1065-1073, 2020, <https://doi.org/10.1007/s11837-020-04019-5>.
- [14] K. OYAMA, S. DIPLAS, M. M’HAMDI, A.E. GUNNAES, A.S. AZAR: ‘Heat source management in wire-arc additive manufacturing process for Al-Mg and Al-Si alloys’, *Addit. Manuf.*, Vol. 26, pp. 180-192, 2019, <https://doi.org/10.1016/j.addma.2019.01.007>.

- [15] T. KLEIN, M. SCHNALL: 'Control of macro-/microstructure and mechanical properties of a wire-arc additive manufactured aluminium alloy', *Int. J. Adv. Manuf. Technol.*, Vol. 108, pp. 235-244, 2020, <https://doi.org/10.1007/s00170-020-05396-6>.
- [16] P. SHERSTNEV, C. MELZER, C. SOMMITSCH: 'Prediction of precipitation kinetics during homogenisation and microstructure evolution during and after hot rolling of AA5083', *Int. J. of Mech. Sci.*, Vol. 54, pp. 12-19, 2012, <https://doi.org/10.1016/j.ijmecsci.2011.09.001>.
- [17] A. L. GREER, A. M. BUNN, A. TRONCHE, P. V. EVANS, D. J. BRISTOW: 'Modelling of inoculation of metallic melts: application to grain refinement of aluminium by Al-Ti-B', *Acta Mater.*, Vol. 48, pp. 2823-2835, 2000.
- [18] I. MAXWELL, A. HELLAWELL: 'A simple model for grain refinement during solidification', *Acta Metall.*, Vol. 23/2, pp. 229-237, 1975.
- [19] M. EASTON, C. DAVIDSON, D. STJOHN: 'Effect of Alloy Composition on the Dendrite Arm Spacing of Multicomponent Aluminum alloys', *Metall. and Mat. Tran. A*, Vol. 41A, pp. 1528-1538, 2010.
- [20] M. RAPPAZ, J.-M. DREZET, M. GREMAUD: 'A new hot-tearing criterion', *Metall. and Mat. Trans. A*, Vol. 30/A, pp. 449-455, 1999.
- [21] N. SAUNDERS, U. K. Z. GUO, X. LI, A. P. MIODOWNNIK, J. -PH. SCHILLÉ: 'Using JMatPro to model materials properties and behavior', *JOM*, Vol. 55, pp. 60-65, 2003, <https://doi.org/10.1007/s11837-003-0013-2>.
- [22] U. F. KOCKS: 'Laws for Work-Hardening and Low-Temperature Creep', *ASME. J. Eng. Mater. Technol.*, Vol. 98(1), pp. 76-85, 1976, <https://doi.org/10.1115/1.3443340>.
- [23] H. MECKING, U. F. KOCKS: 'Kinetics of flow and strain-hardening', *Acta Metallurgica*, Vol. 29, pp. 1865-1875, 1981.
- [24] P. SHERSTNEV, P. LANG, E. KOZESCHNIK: 'Treatment of simultaneous deformation and solid-state precipitation in thermo-kinetic calculations', *ECCOMAS Proceedings*, pp. 5331-5338, 2012.
- [25] E. KABLIMAN, P. SHERSTNEV: 'Integrated Modeling of Strength Evolution in Al-Mg-Si Alloys during Hot Deformation', *Mat. Sci. For.*, Vol. 765, pp. 429-433, 2013.
- [26] E. KABLIMAN, P. SHERSTNEV, J. KRONSTEINER, T. EBNER: 'Physikalisch basierte Simulation des Rekristallisationsverhaltens in einer Al-Cu-Mg-Mn Legierung während der Warmumformung und anschließender Wärmebehandlung', *Tagungsband der 8. Ranshofener Leichtmetalltage*, edited by C. M. Chimani et al., pp. 50-60, 2014.
- [27] J. KREYCA, E. KOZESCHNIK: 'State parameter-based constitutive modelling of stress strain curves in Al-Mg solid solution', *Int. J. Plast.*, Vol. 103, pp. 67-80, 2018.
- [28] S. BROETZ, A. M. HERR: 'Framework for progressive adaptation of FE mesh to simulate generative manufacturing processes', *Manufacturing Letters*, Vol. 24, pp. 52-55, 2020, <https://doi.org/10.1016/j.mfglet.2020.03.005>.
- [29] J. GOLDAK, A. CHAKRAVARTI, M. BIBBY: 'A new finite element model for welding heat sources', *Int. Metal. Trans. B*, Vol. 15, pp. 299-305, 1984.
- [30] P.LINDSTRÖM: 'Improved CWM platform for modelling procedures and their effects on structural behavior', PhD Thesis, Production Technology, University West, 2015.
- [31] F. HAUNREITER: 'Numerisch basierte Schweißleistungsvorhersage für den WAM-Prozess', Master Thesis, University of Applied Sciences FH Technikum Wien, 2021.
- [32] Y. CENGL: 'Introduction to the thermodynamics and heat transfer', *McGraw-Hill Education*, 2008.



# NUMERICAL PREDICTION OF BEAD FORMATION AND BUILD-UP TOWARD WAAM PROCESS OPTIMIZATION

H. BEN HAMOUDA\*, I. O. FELICE\*\*, J. P. OLIVEIRA\*\*\*,\*\*\*,  
J. ANTONISSEN\*

*\*Guaranteed B.V., 9060, Zelzate, Belgium*

*\*\*Department of Mechanical and Industrial Engineering, NOVA School of Science and Technology | FCT NOVA, Campus de Caparica, 2829-516 Caparica, Portugal*

*\*\*\* CENIMAT/13N, Department of Materials Science, NOVA School of Science and Technology, Universidade NOVA de Lisboa, 2829-516 Caparica, Portugal*

DOI 10.3217/978-3-85125-968-1-04

## ABSTRACT

Wire and Arc Additive Manufacturing (WAAM) is a promising solution to produce complex shapes with low buy-to-fly ratio outperforming conventional subtractive manufacturing methods. Generally, this approach relies on robot programs that define the printing path based on a set of pre-defined process parameters. To obtain a net shape WAAM part, the printing path requires controlled bead shape estimation in the preprocessing step. Unlike trial-and-error approach, numerical simulation tries to determine the bead shape by solving coupled physical problems such as fluid dynamics (CFD) and heat transfer. In this work, a numerical tool was deployed to predict single and multiple bead formation given three key process parameters: the wire feed speed, torch travel speed, and voltage. Calculations were performed using ER-90S steel alloy as a printing wire and compared to experimental measurements printed using a MIG/MAG process. As a result, prediction of dimensional features such as the bead height (BH) and width (BW) showed a good agreement with the experiment. Furthermore, the effect of the process parameters was investigated and a parametric study was performed to establish a process guideline that feeds the robot printing strategy.

Keywords: WAAM, MIG/MAG, Bead shape prediction, Process optimization, ER-90S.

## INTRODUCTION

WAAM technology is gaining more and more research focus as a promising manufacturing solution characterized by its flexibility to produce large parts with relatively complex shapes as well as its high deposition rates of 1-10 kg/hr [1]. This technology consists of a Directed Energy Deposition (DED) process that applies an electric arc on the base material surface to melt a feeding wire and generate deposition patterns. To perform accurate and reproducible deposition process, robotic tools are generally relied upon where a Computer Aided Manufacturing (CAM) program defines the deposition trajectory and the corresponding process parameters. This pre-processing step needs to be consistently built-up because a slight deviation between the CAM model

and the part-to-print geometry can alter critically the deposition quality [2] and, thus, increases the risk to worsen its structural integrity. Therefore, ensuring the fidelity of the deposition path to the real geometry during deposition is an essential step to demonstrate a successful robotic WAAM program and a reproducible defect-free printed part. This challenge attracts the main attention of several researchers who proposed multiple methods to control geometrical accuracy, (i) thermal field measurement [3, 4], (ii) process control based on passive-vision sensing [5], and (iii) model predictive control (MPC) [6]. Nevertheless, the experimental methods are labour intensive and require higher process cost, apart from the implementation complexity. To overcome these problems, some researchers relied on predictive analyses tools to control the bead shape.

Among predictive models, artificial intelligence and physics-based solutions attracted several researchers. Xue et al. [7], Hu et al. [8] and Karmuhilan et al. [9] presented predictive models based on Artificial Neural Network (ANN) and genetic algorithms to optimize the initial weights and thresholds of the network linking the welding process parameters and the weld shape and, thus, provide more accurate predictions of the bead shape. Their methods, although giving relatively low prediction errors, require significant effort in building up an extended experimental database, which can be quite costly.

Physics-based models consist generally in solving the thermal problem at the contact between the feeding wire and the substrate. Consequently, the bead shape starts forming progressively during the mixing step and its control is controlled by the thermophysical parameters such as the surface tension and the solidification path. The material deposition at the heated zone is tracked via a coupling with a fluid dynamic model [10]. These models showed generally a strength in tracking the thermophysical parameters evolution during the building process and thus, building complete knowledge of the deposition mechanism. However, some improvement in the coupling method is necessary to reduce the computational cost.

In this work, a physical-based model was utilized to simulate the single bead shape formation considering the material's thermophysical properties. The model couples conventional heat transfer equation with fluid compensation model to assess the thermal field and bead shape formation, respectively. Furthermore, a set of experiences were performed within this work to validate the simulation part. Once validated, the effect of the process parameters on the bead geometry was studied.

### EXPERIMENTAL PROCEDURE

The ER-90S welding wire was utilized as a deposition wire for the Conventional Gas Metal Arc Welding (GMAW) process (also known as MIG/MAG). A structural ASTM A36 hot-rolled plate with dimensions of 10x80x200 mm<sup>3</sup> was considered as the base plate. The general deposition characteristics are given in Table 1.

**Table 1** Deposition process parameters for the ER-90S material

<b>Wire diameter</b>	1 mm
<b>Bead-on-plate length</b>	150 mm
<b>Contact tip to work distance</b>	10 mm
<b>Shielding gas</b>	18% CO <sub>2</sub> + 82% Ar
<b>Shielding gas flow</b>	15 l/min

The experimental procedure to parametrize the welding beads for a Wire and Arc Additive Manufacture (WAAM) process (and then HF-WAAM) and evaluate the weld bead geometry as a function of the wire feed speed (WFS), travel speed (TS), and voltage (U) variables involved the deposition of beads in 15 different combinations, defined by a Box-Behnken Design of Experiments (DOE). As this work aimed to reproduce the geometrical characteristics of the beads, 2 repetitions of the DOE central point were excluded, and then, 13 experiments were analysed and are presented in Table 2. The process used a Pro MIG 3200 power source with a constant voltage dynamic characteristic, which lead to a fixed arc length during deposition, and a Pro MIG 501 control unit. An in-house 3-axis moving table was used to position the plates where the deposition occurred.

**Table 2** Description of the plan of experience

Variables	Experiments												
	1	2	3	4	5	6	7	8	9	10	11	12	13
<b>WFS (m/min)</b>	3	7	3	7	3	7	3	7	5	5	5	5	5
<b>TS (mm/min)</b>	240	240	480	480	360	360	360	360	240	240	480	360	480
<b>U (V)</b>	21	21	21	21	18	18	24	24	18	24	24	21	18

After deposition, the beads were cut in three different positions along the weld bead, always neglecting 30 mm of the extremes to avoid possible negative effects regarding the lack of electrical arc stability. They were grinded, polished, and etched with Nital 2% to evaluate the geometrical aspects, under the output average parameters BW (bead width), BH (bead height), CA (contact angle), and P (penetration), shown in

Fig. 1. Figures of the cross-section were obtained using an Olympus CP21 optical microscope and adjusted using the image software Adobe Photoshop C26. The measurements were performed using the license-free software ImageJ. The deposition rate (DR) and arc energy (AE) were also calculated from the measured data of voltage and current, acquired by an Arduino automation system, and mass before and after deposition obtained with a precision scale.

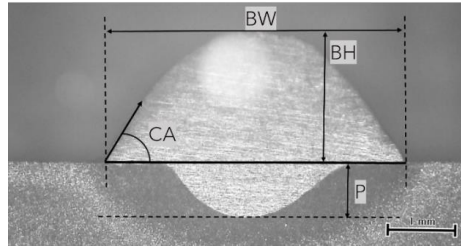


**Fig. 1** Bead macrography with a detailed description of geometrical parameters; BH: bead height, BW: bead width, CA: contact angle and P: penetration depth

### NUMERICAL PROCEDURE

The physical model presented in this work is implemented in a software developed by ISF Aachen for the numerical simulation of the weld seam shape and the temperature, designed originally for GMAW of steel and aluminium [11]. The model description is similar to that shown in reference [12] where some assumptions were made to propose a good cost-accuracy trade-off. The simplified approach is now 2.5D, instead of a full 3D approach in [12], where the weld pool geometry is solved at the cross-section and the third dimension is computed by linear extrusion along the x direction Fig. 2.

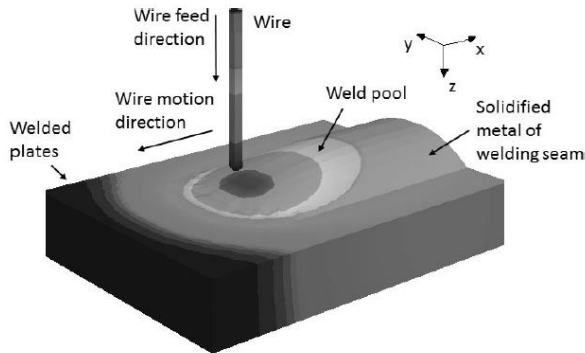


**Fig. 2** Schematic presentation of the single bead printing process (GMAW) [12]

Three main sub-models are included in this tool and the corresponding main factors are given in Table 3.

**Table 3** Present implemented sub-models and their corresponding parameters

Sub-model	Parameters
Heat source	heat conduction in wire, Ohmic heating, contact resistance, anode, cathode and arc column, electromagnetic force
Heat flow	cathode, drop and arc heat sources, T-dependent material properties, Latent heat of fusion, Influence of non-flat surface
Free surface	Arc pressure distribution, gravitation, mass balance, melting isotherm as boundary condition

The different sub-models are interacting as described in Fig. 3. To speed-up the calculations, a weak coupling was applied between the sub-models enabling less iterations to compute the bead geometry and the heat flow. Consequently, some reverse effects such as the influence of the surface deformation on the processes inside the arc are not considered in this tool.

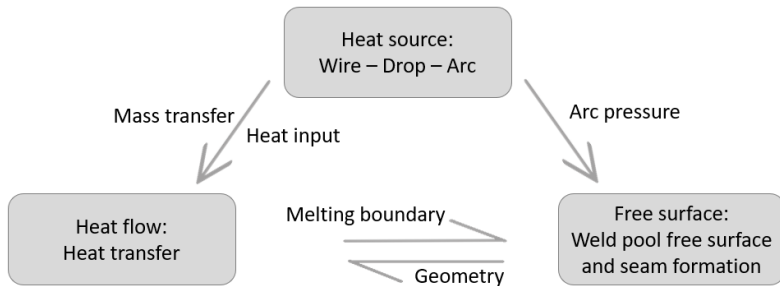


**Fig. 3** Sub-models interaction for the simulation of the bead shape formation [11]

The coupling of the sub-models shown in Fig. 3 is done in an iterative way following this procedure:

- (i) Calculation of arc heat, wire melting, droplets heat and mass
- (ii) Calculation of heat source distribution
- (iii) Calculation of mass source distribution
- (iv) Calculation of heat transfer
- (v) Extraction of liquid area
- (vi) Calculation of weld pool surface deformation
- (vii) Mesh transformation

Within the same iteration, the average weld pool is assessed by solving the arc-droplet-wire part model (i) in the transient where the heat transfer ((ii)..(iv)) and the weld seam ((v)..(vii)) sub-models are solved in a quasi-steady-state.

The heat transfer is assessed via heat conservation equations given for (1) conductive and (2) convective transfers. The two equations are solved using the discrete differences and discrete volume methods, respectively. The sum of the two solutions at the same time

gives the effect of the two process concurrently. The effects of electro-magnetic force, gravitation and surfaces forces are included in the discrete volume equivalent of the momentum conservation algorithm that is defined together with a continuum conservation algorithm to capture the changing in the discrete volume positions.

$$\frac{\partial(\rho h)}{\partial t} = \text{div}(\lambda \text{grad}T) + Q \quad (1)$$

$$\frac{\partial(\rho h)}{\partial t} = \text{div}(h\rho\vec{u}) \quad (2)$$

In Eqn. (1) and (2),  $h$  denotes the enthalpy,  $T$ : temperature;  $\rho$ : density;  $Q$ : arc heat input;  $\lambda$ : thermal conductivity;  $\vec{u}$ : velocity of the convective heat transfer.

The weld pool/seam is computed by solving the Computational Fluid Dynamics (CFD) problem in a quasi-steady state regime using the Lattice-Boltzman approach [13]. The fluid flow compensation method is used for this purpose to compute the droplet mass and velocity at the contact with the arc weld seam considering these effects:

- The flow from cathode area (Fig. 4-(a));
- The effect of the droplet moving in the droplet effect area (Fig. 4-(b));
- The effect of surface forces in the back area of the weld pool.

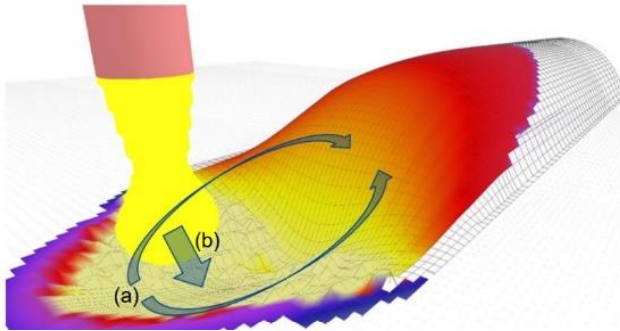


**Fig. 4** Fluid flows in the weld pool derived from (a) cathode areas and (b) droplet impulse

## RESULTS AND DISCUSSION

The bead morphological parameters summarized in Fig. 1 are important input parameters to use in the CAM program. For instance, the bead height (BH) represents the first layer height to be considered in the part slicing step whereas the bead width (BW) parameter is used to define the best overlapping to be applied for an optimal layer build-up [14].

SINGLE BEAD SIMULATION

It is important at this step to notice that the model translates the input process parameters into an equivalent heat source equation known as the double ellipsoid Goldak equation [15]. The shape, given in Fig. 5-(a), shows the seam front and gear ellipsoidal forms that are representing the heat distribution during the building process. An example of the obtained temperature map is given in Fig. 5-(b) confirming the approximation of the double-ellipsoidal heat shape. The different parameters of the Goldak equations are predicted and presented in the appendix (Table 4).

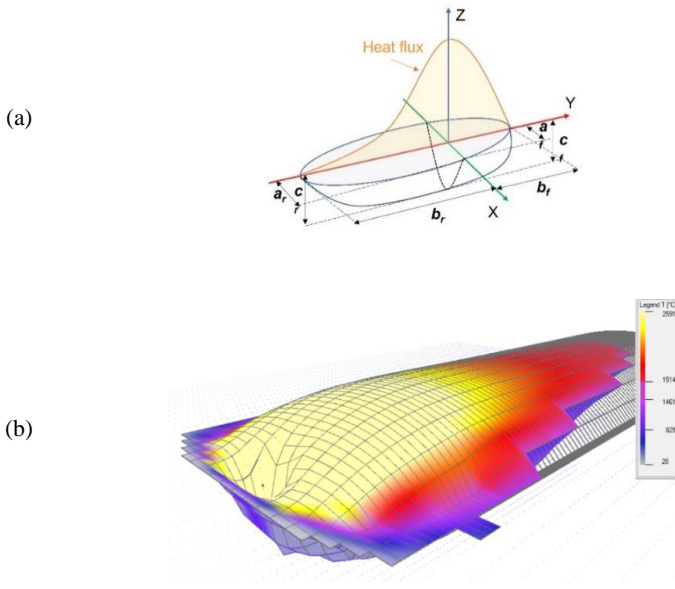


**Fig. 5** (a) double ellipsoid Goldak equation (b) Temperature distribution during the weld seam formation

The obtained results are given in Fig. 6 for three parameters: the bead height (BH), the bead width (BH) and the contact angle (CA). For the bead height, the obtained values are ranging between 1.7mm and 4.1mm depending on the input process parameters which are controlling the heat input. Compared to the experimental measurements, the result showed acceptable prediction errors (average ~17%). For the bead width, results show values varying from 2 to 11 mm. Compared to the experimental results, a higher prediction error was obtained (average ~ 29%). Finally, the contact angle values are comparable to the experimental values within an error range of 21%. The deviations from the experimental results can be explained by the assumptions that were applied to the mathematical model and are more pronounced on the BW and CA parameters. In this

scope, the analyses of the effect of each process parameter on BH and BW mainly could help to explain the origin of these deviations. This task is made in the following section.

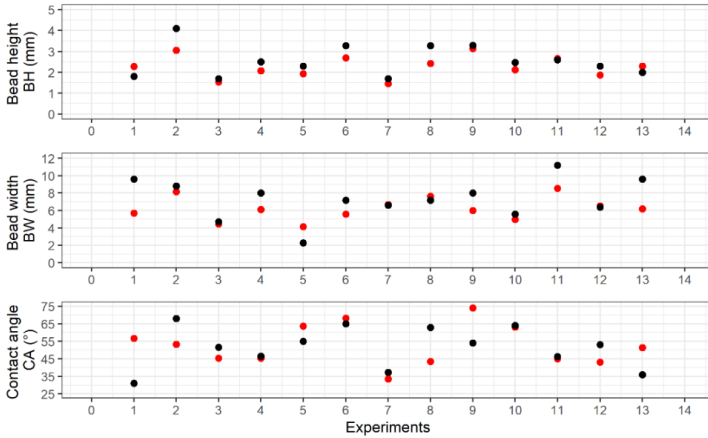


**Fig. 6** Comparison of the predicted (black dots) and experimental (red dots) bead shape parameters

The predicted thermal cycles corresponding to the different experiments are shown in Fig. 7. These profiles were extracted at the centre of the bead for each experiment. Nevertheless, there was no experimental measurement provided to validate this result, work on progress.

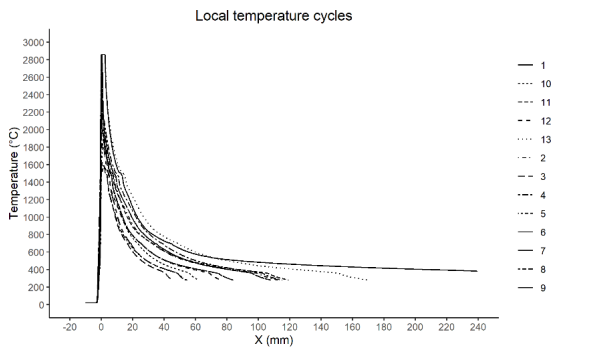


**Fig. 7** Local temperature profiles at the centre of the bead for all the experiments

EFFECT OF THE PROCESS PARAMETERS

The results introduced above consist of a validation step that will be followed by a sensitivity analysis of process parameters (TS, WFS and U) to inspect their influence on the bead shape parameters. Results are given in Fig. 8. These results show a clear non-proportional effect of the torch travel speed versus the bead height and width. This can be explained by the fact that increasing the TS decreases drastically the arc heat input leading to a smaller bead shape. For the other parameters, there is no clear effect on the bead geometry.

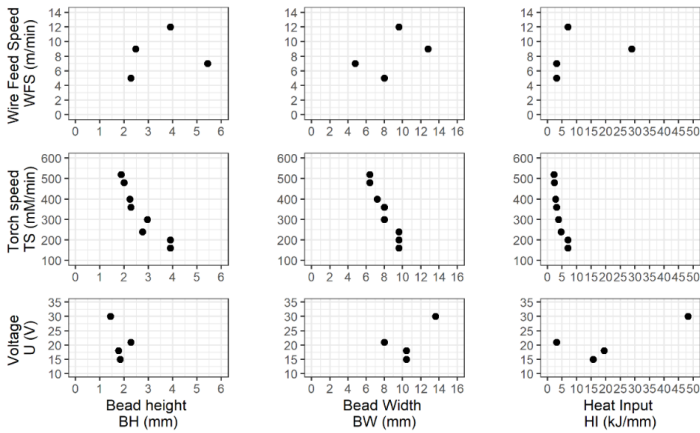


Fig. 8 Effect of WFS, TS and U parameters on BH, BW and HI of the ER-90S material

CONCLUSIONS

Physical modelling helps not only by making fast predictions of the bead geometrical parameters but also by tracking the interaction between the different phenomena coexisting during the printing. In this paper, the focus is made on the bead geometry because of its importance as an input to the robotic WAAM program. The simulated bead height represents the layer thickness whereas the bead width is crucial to define the best overlapping inter-beads. The simulation results for the bead height showed acceptable results in the range of  $\pm 20\%$  compared to the experimental measurements. Furthermore, the parametric study showed the importance of the torch travel speed to control the bead shape via the control of its heat input. Similar investigations of other materials can generate a helpful guideline to control the bead shape and, thus, the printing process with higher quality.

MATHEMATICAL SYMBOLS AND UNITS

- WFS: wire feed speed (m/min)
- TS: travel speed (mm/min)
- U: voltage (V)
- BW: bead width (mm)
- BH: bead height (mm)
- CA: contact angle ( $^{\circ}$ )
- P: penetration (mm)
- DR: deposition rate
- AE: arc energy AE (kJ/mm)
- T: Temperature ( $^{\circ}$ C)
- h: enthalpy ( $J/m^3$ )
- $\rho$ : density ( $kg/m^3$ )
- Q: arc heat input (J/mm)
- $\lambda$ : thermal conductivity ( $W/(m \cdot K)$ )
- $\vec{u}$ : velocity of the convective heat transfer

APPENDICES

**Table 4** Predicted parameters of the Goldak equation

Experience	1	2	3	4	5	6	7	8
<b>Qf(W)</b>	3983	2579.7	998.65	2245.1	1313	2673.2	849.49	2673.2
<b>Qr(W)</b>	2235.9	998.57	646.94	2412.8	520.44	1657.2	874.11	1657.2
<b>af(mm)</b>	0.8	0.8	0.4	0	0	0.4	0	0.4
<b>ar(mm)</b>	15.2	13.2	6.4	14.8	6.4	14	7.6	14
<b>bf(mm)</b>	4.8	3.6	2.36	3.2	2.4	3.2	2.83	3.2
<b>cf(mm)</b>	5.59	1.44	0.32	1.37	0.48	1.36	0.77	1.36
<b>Q(W)</b>	6218.9	3578.3	1645.6	4657.9	1833.5	4330.4	1723.6	4330.4
<b>ff</b>	1.28	1.44	1.21	0.96	1.43	1.23	0.99	1.23
<b>fr</b>	0.72	0.56	0.79	1.04	0.57	0.77	1.01	0.77
<b>br(mm)</b>	4.8	3.6	2.36	3.2	2.4	3.2	2.83	3.2
<b>cr(mm)</b>	5.59	1.44	0.32	1.37	0.48	1.36	0.77	1.36

Experience	9	10	11	12	13
<b>Qf(W)</b>	2143.1	1782.4	1636.5	1615.2	6047.1
<b>Qr(W)</b>	777.62	1064.3	1130.4	1134.8	1851.3
<b>af(mm)</b>	0.8	0	0.4	0	1.2
<b>ar(mm)</b>	9.2	9.6	11.2	8.8	17.6
<b>bf(mm)</b>	3.6	2	5.6	3.2	4.8
<b>cf(mm)</b>	1.27	0.82	1.3	0.52	2.42
<b>Q(W)</b>	2920.7	2846.6	2766.8	2749.9	7898.4
<b>ff</b>	1.47	1.25	1.18	1.17	1.53
<b>fr</b>	0.53	0.75	0.82	0.83	0.47
<b>br(mm)</b>	3.6	2	5.6	3.2	4.8
<b>cr(mm)</b>	1.27	0.82	1.3	0.52	2.42

#### ACKNOWLEDGEMENTS

This activity has received funding from the European Institute of Innovation and Technology (EIT) – Project Smart WAAM: Microstructural Engineering and Integrated Non-Destructive Testing. This body of the European Union receives support from the European Union's Horizon 2020 research and innovation program. IOF and JPO acknowledge the Portuguese Fundação para a Ciência e a Tecnologia (FCT - MCTES) for its financial support via the project UID/EMS/00667/2019 (UNIDEMI). JPO acknowledges the funding of CENIMAT/i3N by national funds through the FCT-Fundação para a Ciência e a Tecnologia, I.P., within the scope of Multiannual Financing of R&D Units, reference UIDB/50025/2020-2023.

#### References

- [1] C. R. CUNNINGHAM, J. M. FLYNN, A. SHOKRANI, V. DHOKIA, S. T. NEWMAN: 'Strategies and processes for high quality wire arc additive manufacturing', Invited review article in *Additive Manufacturing*, 22, 672-686, 2018, <https://doi.org/10.1016/j.addma.2018.06.020>.
- [2] Y. LI, Q. HAN, G. ZHANG, I. HORVÁTH: 'A layers-overlapping strategy for robotic wire and arc additive manufacturing of multi-layer multi-bead components with homogeneous layers', *The International Journal of Advanced Manufacturing Technology*, 96, 3331-3344, 2018, <https://doi.org/10.1007/s00170-018-1786-3>.
- [3] V. L. JORGE, F. R. TEIXEIRA, A. SCOTTI: 'Pyrometrical Interlayer Temperature Measurement in WAAM of Thin Wall: Strategies, Limitations and Functionality', *Metals*, 12, 2022, <https://doi.org/10.3390/met12050765>.

- [4] J. XIONG, Y. ZHANG, Y. PI: 'Control of deposition height in WAAM using visual inspection of previous and current layers', *Journal of Intelligent Manufacturing*, 32, 2209-2217, 2021, <https://doi.org/10.1007/s10845-020-01634-6>.
- [5] Y. HUANG, S. HOU, L. YANG, G. TIAN, Z. YONG, S. LIU: 'Effect of arc dynamic behavior on deposition quality of additive manufactured aluminum alloys', *Journal of Materials Processing Technology*, 295, 117172, 2021, <https://doi.org/10.1016/j.jmatprotec.2021.117172>.
- [6] C. XIA, Z. PAN, S. ZHANG, J. POLDEN, L. WANG, H. LI, Y. XU, S. CHEN: 'Model predictive control of layer width in wire arc additive manufacturing', *Journal of Manufacturing Processes*, 58, 179-186, 2020, <https://doi.org/10.1016/j.jmapro.2020.07.060>.
- [7] Q. XUE, S. MA, Y. LIANG, J. WANG, Y. WANG, F. HE, M. LIU: 'Weld Bead Geometry Prediction of Additive Manufacturing Based on Neural Network', *11<sup>th</sup> International Symposium on Computational Intelligence and Design (ISCID)*, pp. 47-51, 2018 <https://doi.org/10.1109/ISCID.2018.10112>.
- [8] Z. HU, X. QIN, Y. LI, N. MAO: 'Welding parameters prediction for arbitrary layer height in robotic wire and arc additive manufacturing', *Journal of Mechanical Science and Technology*, 34, 1683-1695, 2020, <https://doi.org/10.1007/s12206-020-0331-0>.
- [9] M. KARMUHLAN, A. KUMAR SOOD: 'Intelligent process model for bead geometry prediction in WAAM', *Materials Today*, Proceedings 5, 24005-24013, 2018, <https://doi.org/10.1016/j.matpr.2018.10.193>.
- [10] X. BAI, P. COLEGROVE, J. DING, X. ZHOU, C. DIAO, P. BRIDGEMAN, J. R. HÖNNIGE, H. ZHANG, S. WILLIAMS: 'Numerical analysis of heat transfer and fluid flow in multilayer deposition of PAW-based wire and arc additive manufacturing', *International Journal of Heat and Mass Transfer*, 124, 504-516, 2018, <https://doi.org/10.1016/j.ijheatmasstransfer.2018.03.085>.
- [11] T. LOOSE, O. MOKROV, U. REISGEN: "'SimWeld" and "DynaWeld" - Software tools to set up simulation models for the analysis of welded structures with "LS-Dyna"', *Welding and cutting*, 15, 168-172, 2016.
- [12] O. MOKROV, O. LYSNYI, M. SIMON, U. REISGEN, G. LASCHET, M. APEL: 'Numerical investigation of droplet impact on the welding pool in gas metal arc welding', *Materialwissenschaft und Werkstofftechnik*, 48, 1206-1212, 2017, <https://doi.org/10.1002/mawe.201700147>.
- [13] S. CHEN and G. D. DOOLEN: 'Lattice Boltzmann Method for Fluid Flows', *Annu. Rev. Fluid Mech.*, 30:329-364, 1998.
- [14] Y. LI, Q. HAN, G. ZHANG, I. HORVÁTH: 'A layers-overlapping strategy for robotic wire and arc additive manufacturing of multi-layer multi-bead components with homogeneous layers', *The International Journal of Advanced Manufacturing Technology*, 96, 3331-3344, 2018, <https://doi.org/10.1007/s00170-018-1786-3>.
- [15] J. A. GOLDAK, A. P. CHAKRAVARTI, M. BIBBY: 'A new finite element model for welding heat sources', *Metallurgical Transactions B*, 15, 299-305, 1984.

## **II Arc Welding, Melt Pool, Solidification**



# PHYSICAL MECHANISMS GOVERNING DEPOSITION RATE IN ARC WELDING WITH A CONSUMABLE ELECTRODE

P. F. MENDEZ\*, Z. YAN\*\*, V. NÚÑEZ SÁNCHEZ\*, S. CHEN\*\*

\*Canadian Centre for Welding and Joining, University of Alberta, Canada

\*\*Beijing University of Technology, China

*DOI 10.3217/978-3-85125-968-1-05*

## ABSTRACT

This paper presents a model of deposition rate in gas metal arc welding (GMAW). Some aspects of this model are also helpful to understand related processes such as MCAW, FCAW, SAW, SMAW, EGW, ESW and how-wire additions. Deposition rate is one of the essential factors in calculation of welding costs and times to completion in practical applications. The relationship of deposition rate with current is also determinant of dilution of deposited material (essential concept in overlays) and is a tool of diagnostic of the welding process. For some common materials such as aluminum alloys, the variations in deposition rate with current are not well understood, and common explanations might be misleading. The foundations of the model are mass and energy balances together with the mass and heat transfer mechanisms involved. Heat transfer mechanisms considered include the energy deposited by the fall voltage of the arc against the consumable, Joule heating of the electrode extension, evaporation losses, and heat exchange with the contact tip. The calculation of Joule heating considers the amount and shape of electrical resistivity variation with temperature. The approach presented is in contrast with the common use of company literature for the relationship between current and wire feed speed, or with the use of a second order expression with tabulated constants specific for particular materials and process configurations. The model developed allows to predict the effect of electrode extension and droplet temperature, which are not explicit in current approaches.

Keywords: arc welding, droplet temperature, deposition rate

## INTRODUCTION

Wire-fed processes have the unique property that deposition rate and penetration are coupled, since both are controlled by the same current. The knowledge of the relationship between current and wire feed speed is essential for the determination of welding procedures and is provided in commercial consumable literature.

Commercial literature, however, does not capture the effect of electrode extension and shielding gas. More importantly, when commercial literature is not available, trial and error is the only practical resource left. Much of the commercial literature is now migrating to apps created by the suppliers, yet novel or unusual alloys are not covered in the apps either. The problem of determining procedures using novel consumables is

especially relevant in wire arc additive manufacturing (WAAM), which involves alloys seldom used in welding such as titanium and Inconel.

Attempts to generalize the relationship between current and deposition rate include the use of expressions such as [1]

$$\dot{m} = C_1 I + C_2 I^2 \quad (1)$$

where  $C_1$  and  $C_2$  are empirical constants determined for a given consumable. The problem is again, for new alloys without these empirical constants, there is no guidelines for procedure development. An understanding of the relationship between current and deposition rate will also yield light into droplet temperature, which is one of the main parameters determining fume formation.

Past work has focused on the mass and energy balance during deposition rate, in GMAW early work was done by Lesnewich [1], Halmoy [2], and Waszink [3]. More modern references include [4–6]. In all these cases, knowledge of droplet temperature and vaporization rate are needed, but not available.

This work aims to extend previous efforts by incorporating measured values of droplet temperature and estimating vaporization rates and metal transfer geometries with more detail than any previous research.

## EXPERIMENTS

Droplet temperature was measured using the setup described in [8] illustrated in Fig. 2, and the techniques developed in [9–14]. The values of wire feed speed for steel and pure iron are illustrated in Fig. 1, showing a good match with the tabulated values in [7], but also showing a lower wire feed speed in pure Fe electrode that could not be anticipated.

The values of droplet temperature obtained are illustrated in Fig. 3. the trends obtained are consistent with all previous observations, featuring a “dip” at the point of transition from globular to spray transfer. It is interesting to observe that the droplet temperature in aluminum alloys decreases greatly with the amount of Mg present in the alloy, as first identified in [8]. Similarly, ER80S-G, which contains the high vapor pressure element Mn, displays a lower droplet temperature than the pure iron electrode.

## Mathematical Modelling of Weld Phenomena 13

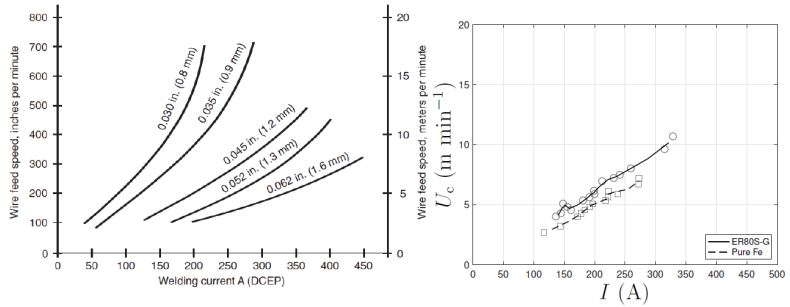


**Fig. 1** Left: Typical representation of current and wire feed speed in solid-steel wire in the commercial literature [7]. Right: Measurements of 1.2 mm wire in experiments performed.

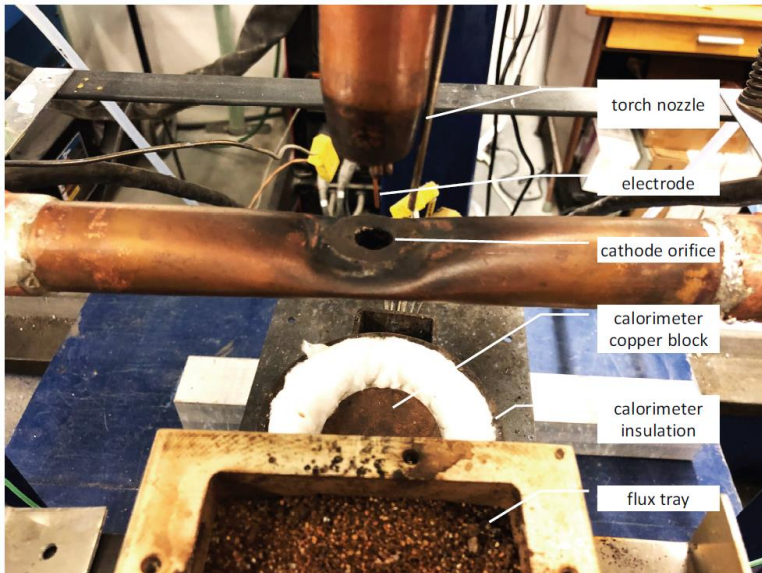


**Fig. 2** Experimental setup for measuring droplet temperature [8]

### Mathematical Modelling of Weld Phenomena 13

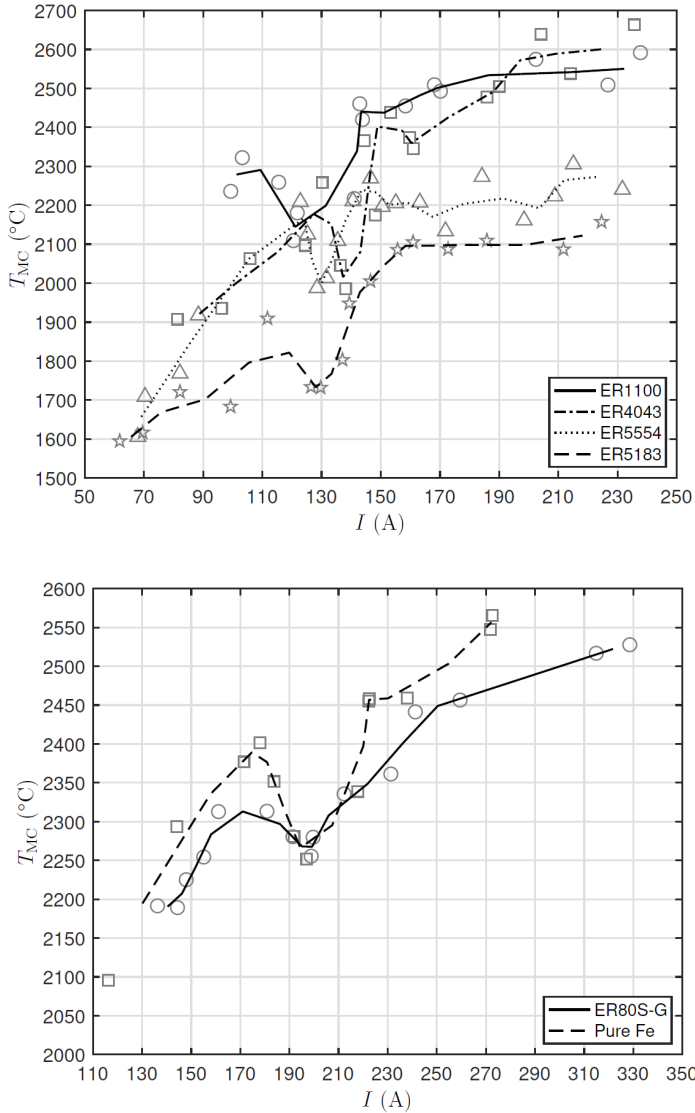


**Fig. 3** Droplet temperature in experiments performed. Markers indicate independent measurements, and trendlines correspond to a moving average of two points.

MASS BALANCE

Consider a melting wire in GMAW with free-flight transfer, as illustrated in Fig. 4. Consider times  $t_1$  and  $t_2$  corresponding to similar stages of two different droplet detachments. The time interval between  $t_1$  and  $t_2$  contains a large number of detachment cycles.

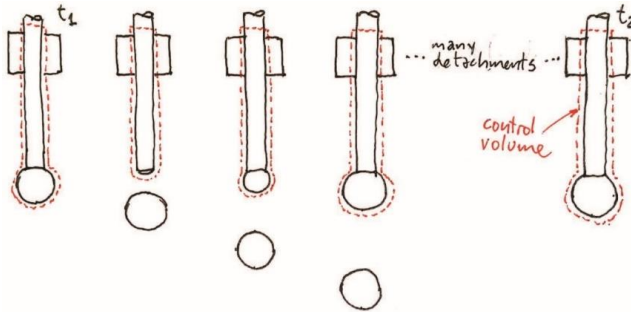


**Fig. 4:** Sequence of droplet detachments in a time interval.

A mass balance between  $t_1$  and  $t_2$  in the control volume indicated in Fig. 4 establishes:

$$\dot{m}_{in} = \dot{m}_{out} \tag{2}$$

where  $m_{in}$  and  $m_{out}$  are the mass that entered and left the control volume between times  $t_1$  and  $t_2$ . The average mass rate between  $t_1$  and  $t_2$  can be calculated as

$$\dot{m} = \frac{m}{t_2 - t_1} \tag{3}$$

resulting in

$$\dot{m}_{in} = \dot{m}_{out} \tag{4}$$

The notation stands for a time average mass rate, it is not an instantaneous value.

MASS ENTERING THE CONTROL VOLUME

The mass rate entering the control volume is given by the wire feed speed and wire cross section. This equation is valid for processes with constant wire feed speed such as standard GMAW or CV-SAW, and variable wire feed speed such as CC-SAW or Fronius MCT GMAW.

$$\dot{m}_{in} = \dot{m}_C = \rho_C A_C U_C \tag{5}$$

where  $\rho_C$  are the density,  $A_C$  cross sectional area, and feeding speed of the wire.

MASS LEAVING THE CONTROL VOLUME

The mass exiting the control volume does it either as molten metal (in the form of droplets and spatter), and metal vapors evaporated from the surface of the droplet:

$$\dot{m}_{out} = \dot{m}_{MC} + \dot{m}_V \quad (6)$$

For the steel experiments performed, the estimated amount of vaporized metal is always below 1% by mass, while for the aluminum experiments, for the Mg-containing alloys it was estimated as reaching up to about 4%.

OVERALL MASS BALANCE

The overall heat balance is obtained by combining equations 4, 5, and 6:

$$\dot{m}_C - \dot{m}_{MC} - \dot{m}_V = 0 \quad (7)$$

ENERGY BALANCE IN GMAW

Similarly as with mass balance, consider the same control volume, and times  $t_1$  and  $t_2$  in Fig. 4 corresponding to similar stages of two different droplet detachments. Because the thermal expansion in the solid or molten metal and the heat generated by viscous dissipation are very small, the conversion between mechanical and thermal energy is negligible in either direction, and the energy balance is in practice a heat balance.

An energy balance in the control volume between  $t_1$  and  $t_2$  establishes:

$$Q_{in} - Q_{out} + Q_{gen} = Q_{st} \quad (8)$$

where  $Q_{in}$  and  $Q_{out}$  are the thermal energies that entered and left the control volume between times  $t_1$  and  $t_2$ .  $Q_{gen}$  is the amount of heat generated inside the control volume, and  $Q_{st}$  is the amount of thermal energy stored inside the control volume during the time interval.

Because at times  $t_1$  and  $t_2$  the control volume contains wire and droplets at the same stage of detachment, the amount of thermal energy contained inside the control volume is the same, so the amount of heat stored between  $t_1$  and  $t_2$  is

$$Q_{st} = 0 \quad (9)$$

An average heat rate between  $t_1$  and  $t_2$  can be calculated as

$$q = \frac{Q}{t_2 - t_1} \quad (10)$$

resulting in the following overall energy balance:

$$q_{in} - q_{out} + q_{gen} = 0 \quad (11)$$

## Mathematical Modelling of Weld Phenomena 13

which also accounts for the absence of heat stored. Similarly as before, the notation stands for a time average heat rate, not an instantaneous value.

### HEAT ENTERING THE CONTROL VOLUME

The heat rate entering the control volume is given by five components: advection by the incoming wire  $q_{adv,in}$ , heat from the arc column towards the electrode  $q_{AC,C}$ , heat conducted from the contact tip to the consumable  $q_{CT,T}$ , heat generated by the electrical resistance at the point of contact with the contact tip  $q_{CT,C}$ , and overall fall voltage  $q_{Cfall}$  on the surface of the electrode. The heat generated by the contact tip contact resistance and the heat generated by the fall voltage are considered to be created at the surface of the electrode:

$$q_{in} = q_{adv,in} + q_{AC,C} + q_{CT,C} + q_{C_{cont}} + q_{C_{fall}} \quad (12)$$

### HEAT LEAVING THE CONTROL VOLUME

The heat rate leaving the control volume is given by two components: advection by the molten metal and by metal vapors  $q_{adv,out}$  and heat lost towards the environment  $q_{C,env}$ :

$$q_{out} = q_{adv,out} + q_{C,env} \quad (13)$$

### HEAT GENERATED INSIDE THE CONTROL VOLUME

The heat rate generated inside the control volume is given by the heat generated by Joule heating in the electrode extension  $q_{EE}$ .

$$q_{gen} = q_{EE} + q_{MC_{joule}} \quad (14)$$

### OVERALL HEAT BALANCE

The overall heat balance is obtained by combining equations 11, 12, and 13:

$$q_{adv,in} + q_{AC,C} + q_{CT,C} - q_{adv,out} - q_{C,env} + q_{EE} + q_{C_{cont}} + q_{C_{fall}} + q_{MC_{joule}} = 0 \quad (15)$$

$$q_{adv,tot} + q_{AC,C} + q_{CT,C} - q_{C,env} + q_{EE} + q_{C_{cont}} + q_{C_{fall}} + q_{MC_{joule}} = 0 \quad (16)$$

where

$$q_{adv,tot} = q_{adv,in} - q_{adv,out} \quad (17)$$

For the steel experiments performed, 80% to 90% of the heat comes was estimated to come from the anode fall voltage, and about 10% from the electrode extension. For the aluminum experiments performed, 90% to 95% came from the anode fall voltage, with

about 1% of the heat coming from the electrode extension. The consumable loses heat to the environment by the mechanisms of convection and radiation, which were determined to be negligible under typical conditions [15].

### METAL TRANSFER GEOMETRY

Metal transfer in free-flight has several different configurations [16, 17]. For the droplet temperature measurements performed, we will consider two representative geometries, illustrated in Fig. 5. This simplification is made acknowledging future work should be able to capture further subtleties, such as the presence of a molten tail in streaming spray transfer.

In the geometry considered,  $d_{MC}$  is the droplet diameter and  $L_{AC,C}$  is the attachment of the arc to the electrode. The size of this attachment is a property of the arc, and there are currently no guidelines on how to predict it. In this work, it will be approximated based on experience as

$$L_{AC,C} = d_C/2 \quad (18)$$

In solid wire processes, the droplet diameter is often estimated from droplet detachment frequency, neglecting the mass lost to evaporation in Eq. 7:

$$d_{MC} = \left( \frac{3}{2} \frac{\rho_C}{\rho_{MC}} \frac{U_C d_C^2}{f_{MC}} \right)^{1/3} \quad (19)$$

The area of attachment of the arc to the droplet, in the case of globular transfer is approximated as

$$A_{AC,C} = \pi L_{AC,C}^2 \quad (20)$$

The detachment frequency in the experiments was measured approximately and only in some experiments. An empirical fit based on welding current was generated.

$$f_{MC} = \begin{cases} C I & \text{for } I \leq I_C \\ A I - B & \text{for } I > I_C \end{cases} \quad (21)$$

where  $I_c$ ,  $A$  and  $B$  are constants determined empirically, and  $C = A B/I_c$ . For the case of a pure Fe consumable, the detachment frequency was not measured, but it is assumed to be the same as in ER80S-G, with  $f_{MC\text{low}} = 50 \text{ s}^{-1}$ ,  $A = 1.565 \text{ s}^{-1}\text{A}^{-1}$ ,  $B = 231.8 \text{ s}^{-1}$ , and  $I_c = 180 \text{ A}$ . The detachment frequency of all aluminum wires was similar, and the same empirical expression is used for all, with  $f_{MC\text{low}} = 25 \text{ s}^{-1}$ ,  $A = 2.688 \text{ s}^{-1}\text{A}^{-1}$ ,  $B = 319.9 \text{ s}^{-1}$ , and  $I_c = 128 \text{ A}$ . The droplet diameters estimated for the experiments performed are between 0.95 and 2 times the wire diameter.

COMPONENTS OF MASS BALANCE

TOTAL MASS EVAPORATED

The total mass evaporated is the sum of vaporization of all components of the alloy:

$$\dot{m}_V = \sum_j \dot{m}_{V_j} \tag{22}$$

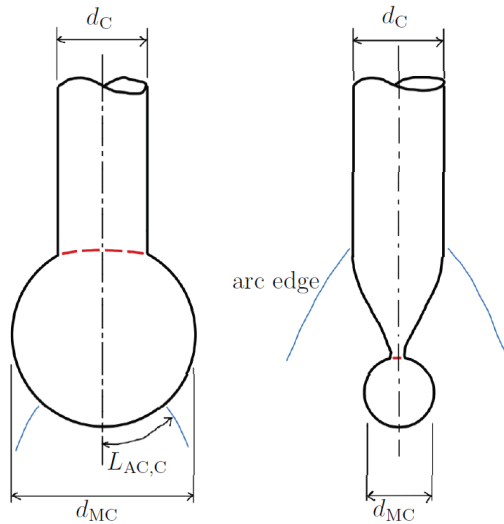


**Fig. 5** Representative configurations for globular (left) and spray transfer (right)

where  $\dot{m}_{V_j}$  is the mass rate of evaporation of each alloying element, e.g. Fe, Mn, etc. in steels, or Al, Mg, etc. in many aluminum alloys. Because of the different vapor pressures of each alloying component, evaporation does not follow the stoichiometry of the melting electrode. For the case of steel wires containing 1.7 wt% Mn, about 55 wt% to 75 wt% of welding fumes are Mn, the rest is Fe, with negligible amounts of other alloying elements. For the case of aluminum, the Mg-containing alloys, Mg can also make up to 75 wt% of their fumes, the rest Al, with negligible amounts of the other alloy components.

EVAPORATION KINETICS

In an alloy, the evaporation of each component is proportional to its mass flux and area of evaporation:

$$\dot{m}_{V_j} = \dot{m}''_{V_j} A_{MC} \quad (23)$$

while the mass flux of each component is proportional to the partial vapor pressure of the component and inversely proportional to the resistance to mass transfer it encounters

$$\dot{m}''_{V_j} = \frac{M_j p_{lg_j}}{R T_{MC_{surf}}} \frac{1}{\mathfrak{R}''_{tot_j}} \quad (24)$$

The partial vapor pressure of the component is proportional to the activity in the alloy [18]

$$p_{lg_j} = a_j p_{lg_{pure_j}} \quad (25)$$

Where  $p_{lg_{pure_j}}$  is the equilibrium vapor pressure of element  $j$  in pure state. In this case, we will approximate the activity  $a_j$  using Raoult's law:

$$a_j = f_{mol_j} \quad (26)$$

The vapor pressure of the component is typically tabulated as:

$$\log p_{lg_{pure_j}} = A + \frac{B}{T_{MC_{surf}}} + C \log T_{MC_{surf}} + D T_{MC_{surf}} 10^{-3} \quad (27)$$

with the values of  $A$ ,  $B$ ,  $C$ ,  $D$  listed in [19], with a special treatment for Si from [20]. The magnitudes  $\dot{m}''_{V_j}$ , which depends on droplet temperature, and  $A_{MC}$  vary as the droplet forms between successive detachments. In the calculations performed,  $T_{MC_{surf}}$  will be assumed to be the average temperature of the droplet just before detachment and  $A_{MC}$  the electrode tip geometry just before detachment.

The total resistance to mass transfer of component  $j$  as having three components: resistance to diffusion through a boundary layer of alloy depletion on the surface of the melt, ( $\mathfrak{R}_{lj}$ ), resistance to evaporation under a partial pressure of vapor  $j$  ( $\mathfrak{R}_{lg_j}$ ), and resistance to diffusion through a boundary layer in the gas phase, outside which the partial pressure of vapor  $j$  is 0.

$$\mathfrak{R}''_{tot_j} = \mathfrak{R}''_{lj} + \mathfrak{R}''_{lg_j} + \mathfrak{R}''_{vj} \quad (28)$$

with

$$\mathfrak{R}''_{lj} = \frac{1}{h_{lj}} \quad (29)$$

$$\mathfrak{R}''_{lg_j} = \sqrt{\frac{2\pi M_j}{RT_{MC_{surf}}}} \quad (30)$$

$$\mathfrak{R}''_{vj} = \frac{1}{h_{vj}} \quad (31)$$

where  $h$  indicates the convection coefficients for mass transfer. The mass transfer resistance of the solvent in the molten consumable (e.g. Fe in steels consumables and Al in aluminum alloys) has a resistance  $\mathfrak{R}''_{lsolvent} = 0$ .

In steels, the dominant resistance to evaporation is the vapor boundary layer, with approximately 95% of total resistance for Fe, and 85% for Mn. The resistance to mass transfer of Mn in the alloy-depleted melt surface is approximately 10%. In aluminum alloys, the vapor boundary layer is dominant for Al (97%) and Mg (80%), the resistance to mass transfer of Mg in the liquid is of the order of 17%. In all cases, the resistance to evaporation at the surface ( $R_{lg}''$ ) is below 10%. This is an important finding indicating the importance of boundary layers in mass losses by evaporation, which are often omitted in the welding literature.

*Diffusion in the melt*

For the melt near the surface, being a free surface, the characteristic velocity of the fluid is not affected by a viscous boundary layer, and mass transfer parameters can be estimated as

$$h_{l_j} = \frac{Sh_{MC_j} D_{MC_j}}{d_{MC}} \quad (32)$$

$$Sh_{MC_j} = 2 + 0.5 Re_{d_{MC}}^{1/2} Sc_{MC_j}^{1/2} \quad (33)$$

$$Re_{d_{MC}} = \frac{U_{MC} d_{MC}}{\nu_{MC}} \quad (34)$$

$$Sc_{MC_j} = \frac{\nu_l}{D_{MC_j}} \quad (35)$$

where  $D_{MC_j}$  is the diffusivity of component  $j$  in the melt,  $U_{MC}$  is the characteristic velocity of molten metal inside the droplet, and  $\nu_{MC}$  is the kinematic viscosity of the molten metal at the bulk temperature of the droplet  $T_{MC}$ . The constant 2 accounts for mass transfer by static diffusion.

The range of  $Sh_{MC}$  spans from orders of  $10^1$  to  $10^3$  in steels and aluminum alloys, indicating that convection dominates over molecular diffusion in the liquid in most cases. The range of  $Sc_{MC}$  spans from orders of  $10^1$  to  $10^5$  in steels and aluminum alloys, indicating that the diffusion occurs in a much narrower range than momentum transport in the liquid.

Diffusivities in the liquid are typically expressed as  $D_{MC_j} = D_{0_j} \exp[-Q_j/(RT)]$  tabulated in [21] for steels, in [22,23] for aluminum, and also in [24,25] for more base alloys. The temperature used for diffusivity and kinematic viscosity is that of the surface of the molten metal,  $T_{MC,surf}$ .

The velocity of melt in globular transfer can be estimated roughly from [3] as shown below, with  $K = 210^{-3} \text{ m s}^{-1} \text{ A}^{-1}$ :

$$U_{MC} = KI \quad (36)$$

*Diffusion in the gas*

For mass transfer in the gas phase, two cases must be considered: evaporation in an inert atmosphere such as GMAW of aluminum alloys using pure Ar shielding, and evaporation in a reactive atmosphere such as GMAW of steel alloys using Ar-O<sub>2</sub> or Ar-CO<sub>2</sub> shielding. In this paper we consider only the first case. In the second case, the reaction reduces the thickness of the boundary layer, resulting in increased evaporation [26,27] and fumes formation [28,29]. The association of carbon with oxygen on the surface of the melt results in an energy source that might be significant, and also on decarburization of the melt.

For the case of diffusion of metal vapors in an inert atmosphere, the convection coefficient for mass transfer can be estimated using the common correlation for convection around spheres [30], also used in [31].

$$h_{Vj} = \frac{Sh_{ACj} D_{ACj}}{d_{MC}} \quad (37)$$

$$Sh_{ACj} = 2 + 0.6 Re_{AC}^{1/2} Sc_{ACj}^{1/3} \quad (38)$$

$$Re_{AC} = \frac{U_{AC} d_{MC}}{\nu_{AC}} \quad (39)$$

$$Sc_{ACj} = \frac{\nu_{ACj}}{D_{ACj}} \quad (40)$$

where  $\nu_{AC}$  is the kinematic viscosity of the plasma and  $D_{ACj}$  is the diffusivity of vapor element  $j$  in the plasma. Both properties are evaluated at a “film temperature” intermediate between the molten surface (of the order of 3000 K for the case of steel and aluminum) and the plasma temperature outside the plasma boundary layer near the surface of the electrode (of the order of 7300 K for the case of Ar, resulting in a “film temperature” of approximately 5000 K). The kinematic viscosity and other thermophysical properties for the plasma are provided, for example in [32]. Typical values of  $Sh_{ACj}$  are around  $10^1$ , indicating convection is dominant. Typical values of  $Re_{AC}$  are of the order of  $10^2$ . Schmidt numbers in the vapor are around 1.5.

The velocity in the arc column  $U_{AC}$  can be estimated as [33]:

$$U_{AC} = \frac{1}{2} \sqrt{\frac{\mu_0 I_{AC,MC}}{\pi \rho_{AC}}} f_{U_{AC}} \quad (41)$$

where  $\mu_0$  is the magnetic permeability of vacuum,  $J_{AC,MC}$  is the current density of the arc attachment with the electrode, and  $\rho_{AC}$  is the density of the plasma at approximately 10000 K, also from [34]. The velocities predicted are of the order of  $200 \text{ ms}^{-1}$ , consistent with typical plasma arc velocities.

The plasma current density can be approximated as

$$J_{AC,MC} = \frac{I}{\pi L_{AC,MC}^2} \quad (42)$$

where  $L_{AC,MC}$  is the radius of arc attachment, which will be approximated as half the consumable diameter; this rough approximation is consistent with the analysis in [3]. The correction factor  $f_{U_{AC}}$  is

$$f_{U_{AC}} = 0.55 \left( \frac{\widehat{Re}_{AC}}{4} \right)^{0.073} \left( \frac{2L_{arc}}{d_c} \right)^{0.0068} \quad (43)$$

Where  $\widehat{Re}_{AC}$  is a nominal Reynolds number calculated using Eq. 41 without the correction factor  $f_{U_{AC}}$ .

Diffusivity in plasmas is very complex [35], and it will be approximated here as diffusion in the gas phase using the Chapman-Enskog theory [36]

$$D_{Ar,j} = \frac{A T^{3/2}}{p \sigma_{Ar,j}^2 \Omega_j M_{Ar,j}^{1/2}} \quad (44)$$

where  $D_{Ar,j}$  is the diffusivity of vapor element  $j$  in Ar in  $\text{cm s}^{-2}$ ,  $A = 2.6610^{-3}$ ,  $p$  is the atmospheric pressure in bar,  $\sigma$  is the effective cross section of atoms in  $\text{\AA}$ ,  $M_{Ar,j}$  is

$$M_{Ar,j} = 2 \left( \frac{1}{M_{Ar}} + \frac{1}{M_j} \right)^{-1} \quad (45)$$

where  $M$  is the molar weight of gases and vapors involved, and  $\Omega_j$  is given by [36]:

$$\Omega_j = \frac{1.06036}{T_j^{*0.15610}} + \frac{0.193}{\exp(0.47633 T_j^*)} + \frac{1.03587}{\exp(1.52996 T_j^*)} + \frac{1.76474}{\exp(3.89411 T_j^*)} \quad (46)$$

where the value of  $T_j^*$  is provided by [27]

$$T_j^* = \frac{k\Gamma_{film}}{\epsilon_{Ar,j}} \quad (47)$$

$$\epsilon_{Ar,j} = \sqrt{\epsilon_{Ar}\epsilon_j} \quad (48)$$

$$\sigma_{Ar,j} = \frac{\sigma_{Ar} + \sigma_j}{2} \quad (49)$$

where  $\varphi$  is the parameter of a Lennard-Jones potential for each component, and it is tabulated. The area from which evaporation happens will be approximated as

$$A_{MC} = \pi d_{MC}^2 f_{A_{MC}} \quad (50)$$

$$f_{A_{MC}} = \exp \left[ - \frac{0.1335}{1 + 2.225 \ln^2(d_{MC}/d_c)} \right] \quad (51)$$

where the correction factor  $f_{A_{MC}}$  is empirical, with the correct properties of becoming one when the droplet is very large in globular transfer, or when the droplet is very small in spray transfer. At the transition from globular to spray, when the droplet has the same diameter as the molten consumable, it has a value of 0.875, which is the intermediate between subtracting the cross sectional area of the consumable (as should be done in globular) and not (as is the case of spray). When the droplet has twice the diameter of the

consumable (chosen as a representative globular transfer situation), this function has the value of 0.9375, corresponding to subtracting the full cross sectional area of the consumable. This approximation does not consider the evolution of surface area as the droplet forms; it only considers the geometry present at detachment, which is an overestimation; conversely, it might underestimate the evaporation area in spray transfer mode in the case there is a long molten tail.

## COMPONENTS OF ENERGY BALANCE

### HEAT BY ADVECTION

Advection is the transport of thermal energy due to the transport of mass. All mass flows involved in the mass balance also represent heat flows according to the following relationship

$$q_{adv} = \dot{m}h \quad (52)$$

where  $q_{adv}$  is the heat transported by advection across the surface of the control volume,  $\dot{m}$  is the mass rate transporting heat across the surface of the control volume, and  $h$  is the enthalpy of the mass crossing the surface of the control volume. Similarly to temperature, enthalpy has an arbitrary reference point which is the same for all enthalpies considered. This equation recognizes that the temperature of the wire is uniform through its cross section. This hypothesis is quite accurate in GMAW except for the region surrounding the point of electrical contact between the wire and the contact tip, which might experience significant local gradients, especially with pulsed current, but this is not a problem because the control volume can be considered to start far upstream from the point of contact, and the exit part of the control volume is also far from the contact point. The hypothesis of uniform temperature might not be accurate in the exit region of the control volume in the case of tubular wires (e.g. MCAW, FCAW), in which the heat generated in the sheath might not propagate to the core of the wire by the time melting is reached.

Considering that the temperature of the wire is uniform across its cross section as it enters the control volume, the heat into the control volume by advection is

$$q_{adv_{in}} = \dot{m}_C h_C \quad (53)$$

where  $h_C$  is the enthalpy of the wire at the temperature it enters the control volume (typically room temperature).

The heat out of the control volume by advection is

$$q_{adv_{out}} = q_{MC} + q_V \quad (54)$$

where  $q_{MC}$  is the energy lost as molten metal in the form of droplets and spatter, and  $q_V$  is the energy lost as metal vapors.

Considering the average temperature of the molten metal exiting the control volume we obtain

$$q_{MC} = \dot{m}_{MC} h_{MC} \quad (55)$$

where  $h_{MC}$  is the average enthalpy of the molten metal, i.e. the average droplet temperature and spatter from the electrode assuming it exits at the same temperature of the droplet. The heat carried out by the metal vapors is

$$q_V = \dot{m}_V h_V \quad (56)$$

where  $h_V$  is the average enthalpy of the metal vapors.

Replacing into Eq. 17 we obtain

$$q_{adv_{out}} = \dot{m}_C h_C - \dot{m}_{MC} h_{MC} - \dot{m}_V h_V \quad (57)$$

Using Eq. 7 we can write

$$q_{adv_{tot}} = -[\dot{m}_C(h_{MC} - h_C) + \dot{m}_V(h_V - h_{MC})] \quad (58)$$

This equation means that the overall effect of advection takes thermal energy away from the control volume, and that the energy exiting has two components: first, the amount of heat used to raise the wire temperature from its starting temperature in solid state to the average temperature of the molten metal at the electrode tip, and the second component is the amount of energy needed to vaporize a (small) fraction of the consumable. This vaporization is the main source of the undesirable welding fumes and black deposits on the base metal when using Al-Mg consumables.

### *Enthalpies associated with melting the wire*

Fig. 6 illustrates the enthalpies associated with metal from the wire, from the moment it leaves the spool to the moment is molten or evaporated.

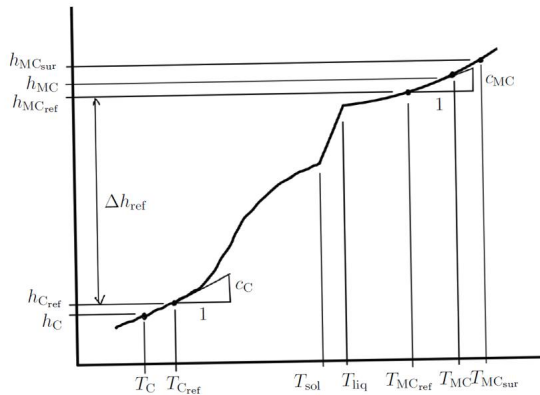


**Fig. 6** Enthalpies associated with melting the wire in GMAW

The wire leaves the spool at temperature  $T_{spool}$ , typically the temperature of the environment, of the order of 20°C in a workshop. The wire enters the control volume with enthalpy  $h_C$ , corresponding to  $T_C$ . Typically, there is no preheating of the wire before it reaches the contact tip; so under normal conditions

$$T_C = T_{spool} \quad (59)$$

where the enthalpy corresponding to  $T_C$  is  $h_C$ . As the wire heats up inside the control volume, enthalpy increases in the form of sensible heat associated with a specific heat, and latent heat associated with transformations such as melting and solid state transformations such as austenization in steel wires. By the time the droplet (or spatter) exits the control volume, the average enthalpy of the molten metal is  $h_{MC}$ , associated with temperature  $T_{MC}$ , which is of the order of 2500°C in steel and 2200°C in aluminum wires [13,14,37,38].

#### *Enthalpies associated with vaporization*

The metal vapors exit the control volume at the same temperature of the surface of the droplet, it is not necessary to reach boiling temperature to evaporate; however, the latent heat of vaporization is still present and must be accounted for. Accounting for the mass rate of the different alloying elements (equation 22), Eq. 56 can be rewritten as

$$q_V = \sum_j \dot{m}_{V_j} h_{V_j} \quad (60)$$

and the average enthalpy of metal vapors can then be calculated as

$$h_V = \frac{\sum_j \dot{m}_{V_j} h_{V_j}}{\dot{m}_V} \quad (61)$$

For each evaporating alloying element, its enthalpy can be calculated as

$$h_{V_j} - h_{MC} = (h_{MC_{sur}} - h_{MC}) + (h_{V_j} - h_{MC_{sur}}) \quad (62)$$

where  $h_{V_j}$  and  $h_{MC_{sur}}$  correspond to the temperature of the surface of the droplet, and their magnitude is the latent heat of vaporization of metal vapor  $j$  at the temperature  $T_{MC_{sur}}$ . Thus:

$$h_{V_j} - h_{MC_{sur}} = h_{lg} \quad (63)$$

where  $h_{lg}$  is tabulated, typically at the boiling temperature at atmospheric pressure. The dependence of latent heat of vaporization with the temperature of vaporization is negligible, and seldom tabulated. Equation 58 can then be rewritten as

$$q_{adv_{tot}} = -\dot{m}_C (h_{MC} - h_C) - \dot{m}_V [h_{lg} + (h_{MC_{sur}} - h_{MC})] \quad (64)$$

Where  $h_{lg}$  is the average enthalpy of vaporization for all metal vapors:

$$h_{lg} \approx \frac{\sum_j \dot{m}_V h_{lgj}}{\dot{m}_V} \quad (65)$$

*Practical expression of enthalpies for calculations*

In welding, metals experience transformations in solid state, melting, and vaporization; for this reason, it is not practical to calculate enthalpies based on tabulated specific and latent heats. We can take advantage of the fact that in welding, metals start in solid state at temperatures typically not far from room temperature, and melt to relatively high temperatures, but in a relatively narrow range. We can select

$$T_{C_{ref}} = 20^\circ C \quad (66)$$

as reference temperature in the solid for all metals. The temperature  $T_{MC_{ref}}$  is the reference temperature for the molten metal. For steel we will use  $2500^\circ C$ , for Aluminum  $2200^\circ C$ . For other alloys we will use a round number close to  $0.9T_{boil}$ , where the temperatures must be in K, and  $T_{boil}$  is the boiling temperature of the base element of the alloy. If more than one element can be considered the solvent (because they have similar amounts in the alloy), we will choose the one with lower boiling temperature.

The reference temperatures correspond with the enthalpies  $h_{rf_{sol}}$  and  $h_{MC_{ref}}$ , with the following enthalpy change:

$$h_{MC_{ref}} - h_{C_{ref}} = \Delta h_{ref} \quad (67)$$

Because the reference temperatures are close to the actual temperatures involved, all latent heats associated with melting and phase transformations are included in  $\Delta h_{ref}$ . The difference between  $\Delta h_{ref}$  and the factor  $(h_{MC} - h_C)$  required in Eq. 64 is due only to sensible heats, which are captured accurately near the reference points by the corresponding specific heats of solid and liquid  $c_C$  and  $c_{MC}$  evaluated at the reference temperatures. This way:

$$h_{MC} - h_C \approx \Delta h_{ref} + c_{MC} (T_{MC} - T_{MC_{ref}}) - c_C (T_C - T_{C_{ref}}) \quad (68)$$

Similarly,  $(h_{MC_{sur}} - h_{MC})$  required in Eq. 64, can be estimated as

$$h_{MC_{sur}} - h_{MC} \approx c_{MC} (T_{MC_{sur}} - T_{MC}) \quad (69)$$

Using the accurate approximations above, the exact calculation of overall heat transferred by advection (equation 58) can be expressed as:

$$q_{adv,tot} \approx -\dot{m}_C [\Delta h_{ref} + c_{MC} (T_{MC} - T_{MC_{ref}}) - c_C (T_C - T_{C_{ref}})] - \dot{m}_V [h_{lg} + c_{MC} (T_{MC_{sur}} - T_{MC})] \quad (70)$$

where the first term on the right of the equation accounts by the energy absorbed by the molten consumable, and the second term accounts for the energy absorbed by vaporization. For then experiments performed in steels, vaporization absorbs less than 1.5% of the total energy, while in aluminum the amount of energy absorbed by the vapors

is about 6% in average, reaching just above 10% in some cases. There is no large difference in the energy absorbed for different alloys.

Experiments show that the temperature of the molten metal in the droplet is fairly uniform [39], such that the temperature of the surface of the droplet where evaporation occurs is not far from the average temperature of the droplet. Because the gradient inside the droplet can be expected to be shallow, the term containing the factor  $(T_{MC_{sur}} - T_{MC})$  is typically negligible.

#### HEAT FROM ARC COLUMN

In the heat exchange between the arc and the electrode, convection dominates over radiation.

$$q_{AC,C} = h_{AC,C} A_{AC,C} (T_{AC_{MC}} - T_{MC_{surf}}) \quad (71)$$

This exchange happens at the area of attachment of the arc to the electrode, which in the case of globular transfer can be estimated using Eq. 20, and for the case of spray transfer will be approximate as the area of the droplet using Eq. 50.

The estimation of convection coefficient is typically based on tabulations of the Nusselt number. In this case, the Nusselt number can be approximated using the heat transfer correlation for a sphere in an external flow [30], similarly as it was done for mass transfer:

$$h_{AC,C} = \frac{k_{AC_{MC}} Nu_{AC,C}}{d_{MC}} \quad (72)$$

$$Nu_{AC,C} = 2 + 0.6 Re_{AC}^{1/2} Pr_{AC}^{1/3} \quad (73)$$

$$Pr_{AC} = \frac{\nu_{AC}}{\alpha_{AC}} \quad (74)$$

For the plasma properties, the temperature considered is the same as for the case of mass diffusion (5000 K for Ar). For the experiments performed,  $h_{AC,C}$  is of the order of  $10^3 \text{ Wm}^{-1}\text{K}^{-1}$ ,  $\nu_{AC,C}$  is between 5 and 8, indicating that advection dominates over conduction, but not by much. the value of Pr at 5000 K is approximately 0.6.

#### HEAT FROM CONTACT TIP TO CONSUMABLE

The consumable touches the contact tip typically at the entrance and at the exit of the contact tip. There is heat exchange through these two points of contact, and also between the inner surface of the contact tip bore and the outer surface of the consumable traversing through the contact tip.

The two points of contact transfer heat differently. The contact at the exit of the contact tip carries the almost all the current, and experiences Joule heating related to the electrical resistance of contact. The contact at the entrance of the contact tip experiences negligible

Joule heating, and its heat exchange is included in the calculation of heat exchange between the surfaces of the contact tip and wire. Thus

$$q_{CT,C} = q_{CT,C_{cont}} + q_{CT,C_{gap}} \quad (75)$$

where  $q_{CT,C}$  is the total heat exchanged between the contact tip and the consumable,  $q_{CT,C_{cont}}$  is the heat exchange by contact at the exit of the contact tip, and  $q_{CT,C_{gap}}$  is the heat exchanged across the gap between the inner surface of the contact tip bore and the outer surface of the electrode. For the experiments performed,  $q_{CT,C}$  is of the order of 30 W,  $q_{CT,C_{cont}}$  is only a fraction of  $q_{CT,C_{gap}}$ , of the order of 15% or less for the case of aluminum alloys, and up to 50% in the case of steels. In aluminum, the flow of  $q_{CT,C_{cont}}$  is estimated to be from the hot contact to the electrode; however, in steels, the consumable at the point of contact can be very hot, and  $q_{CT,C_{cont}}$  flows from the electrode towards the contact tip.

#### *Heat by conduction across the main point of electrical contact*

Both the wire and the contact tip are locally hotter at the main point of electrical contact; however these peak temperatures are different, causing heat to be transferred across the main point of electrical contact. While the peak temperature of the consumable at the electrical contact can be substantially higher than the temperature of the spool, in the absence of intense pulsing, we will assume that the contact tip is at an approximately uniform temperature.

Assuming that the contact tip is hotter than the consumable at the point of electrical contact, the heat transferred across the contact is

$$q_{CT,cont} = \frac{T_{CT} - T_{C_{cont}}}{\mathcal{R}_{CT,C_{cont}}} \quad (76)$$

where  $\mathcal{R}_{CT,C_{cont}}$  is the thermal resistance of contact between consumable and the contact tip,  $T_{CT}$  is the temperature of the contact tip (assumed uniform, typically 350°C [40,41]), and  $T_{C_{cont}}$  is the temperature of the consumable at the point of electrical contact.

To calculate the thermal resistance of contact, we can consider only the dominant component, which is conduction through asperities, neglecting the conduction and radiation through the air in the gaps. In this case, an analogy can be established between the electrical and thermal contact resistances, based on the fact that both contact resistances share the same geometric features at the point of contact. Thus:

$$\mathcal{R}_{CT,C_{cont}} = \frac{k_{CT}^{-1} + k_C^{-1}}{\varrho_{CT} + \varrho_C} R_{CT,C_{cont}} \quad (77)$$

Considering the properties of Table 1, and a representative contact resistance of 1 m $\Omega$  for copper coated consumables and aluminum, Equation 77 indicates a thermal contact resistance at the point of electrical contact of 87 KW<sup>-1</sup> for copper coated consumables, and 76 KW<sup>-1</sup> for aluminum consumables.

The temperature of the consumable at the point of contact can be estimated approximately as

$$T_{C_{cont}} = T_C + \mathcal{R}_{C_{cont}} q_{C_{cont}} \quad (78)$$

where  $q_{C_{cont}}$  is the amount of Joule heating generated on the consumable at the point of contact, calculated in Eq. 84 below.

**Table 1** Thermal and electrical properties of the contact tip and consumables

	$k$ W m <sup>-1</sup> K <sup>-1</sup>		$\rho$ Ω m	
Cu coating	394	†	3 10 <sup>-8</sup>	‡
Steel	41		7 10 <sup>-7</sup>	
Aluminum	229	*	6 10 <sup>-8</sup>	
Contact tip	300	§	3.75 10 <sup>-8</sup>	§

† annealed copper at 200°C [42], ‡ [43],  
\* [44], § Cu Cr Zr tip

The thermal resistance of the consumable at the main point of electrical contact can be estimated using the distributed moving heat source analysis in [45]:

$$\mathcal{R}_{C_{cont}} = 1.13 \frac{1}{k_C} \sqrt{\frac{\alpha_C}{L_{cont}^2 U_C}} \quad (79)$$

where  $\mathcal{R}_{C_{cont}}$  is the thermal resistance of the consumable at the area of contact, based on the maximum temperature of the consumable at the area of contact  $T_{C_{cont}}$ , a square contact, and a uniform distribution of heat flux at the point of contact. The parameter  $U_C$  is wire feed speed,  $L_{cont}$  is the side length of the square that defines the area of contact, and  $k_C$  and  $\alpha_C$  are the thermal conductivity and diffusivity of the consumable at a temperature representative of the area of contact. The thermal resistance of a moving heat source involves the penetration of heat under the surface of the consumable to depths much larger than the thickness of a copper coating, thus the effect of copper coating will be neglected. The value of  $\mathcal{R}_{C_{cont}}$  has little dependence (less than 25%) on the exact shape of the area of contact or the distribution of heat, so the assumption of a square contact or uniform heat flux are not critical for this analysis. For the experiments performed, the value of  $\mathcal{R}_{C_{cont}}$  did not vary much, with an average around 20 KW<sup>-1</sup> for steels, and 12 KW<sup>-1</sup> for aluminum consumables.

The maximum temperature of the consumable at the contact point is important, because if there is localized melting the consumable can weld itself to the contact tip and cause very fast degradation of the contact tip. This problem is especially relevant in the case of pulsed current, where the peak current can be very high (resulting in high  $q_{C_{cont}}$ ), and the wire feed speed is relatively low for that high current (resulting in high  $\mathcal{R}_{C_{cont}}$ ). For the experiments performed,  $T_{C_{cont}}$  was estimated to range between 240°C and 800°C for steels, and 65°C and 400°C in aluminum consumables. A reasonable intermediate choice for temperature at which to evaluate the consumable properties is the average between the maximum temperature at the area of contact and the consumable temperature  $T_{C_{cont,ave}}$  calculated as:

$$T_{C_{cont,inter}} = T_C + 0.5(\hat{T}_{C_{cont}} - T_C) \quad (80)$$

Where  $\hat{T}_{C_{cont}}$  is obtained from Eq. 79 and Eq. 78 using the consumable properties corresponding to  $T_C$ . The size of  $L_{cont}$  depends on the consumable size, the gap with the contact tip, the pressure at the point of contact (related to the cast of the wire), and the amount of wear; a reasonable estimate based on experience is

$$L_{cont} = 0.4d_C \quad (81)$$

The flow of heat  $q_{CT,C_{cont}}$  is quite small for two reasons. First, the thermal resistance at the point of sliding contact is substantially higher than the thermal resistance of the wire. Also, because the temperature difference between the contact tip and the surface of the consumable is small. The small value of  $q_{CT,C_{cont}}$  allows the calculation of  $T_{C_{cont}}$  in Eq. 78 neglecting the heat flux by contact.

### *Heat across the gap between contact tip and consumable*

Outside the main point of electrical contact, the contact tip and the consumable will exchange energy by radiation and conduction across the thin gap between them. Assuming that the contact tip is hotter than the consumable at the point of electrical contact, the heat transferred across the contact is

$$q_{CT,C_{gap}} = \frac{T_{CT}-T_C}{\mathcal{R}_{CT,C_{gap}}} \quad (82)$$

where  $T_C$  is the temperature of the consumable outside the point of electrical contact and  $\mathcal{R}_{CT,C_{gap}}$  is the thermal resistance of the gap between consumable and the contact tip and can be estimated as

$$\mathcal{R}_{CT,C_{gap}} = \frac{1}{\pi^2} \frac{\Delta d_{CT,C}}{d_C L_{CT} k_{gap}} \quad (83)$$

where  $\Delta d_{CT,C}$  is the difference in diameters between the consumable and the bore in the contact tip,  $d_C$  is the diameter of the consumable,  $L_{CT}$  is the length of the contact tip bore, and  $k_{gap}$  is the thermal conductivity of the fluid in the gap between the consumable and the contact tip bore (typically air). A representative value of  $\mathcal{R}_{CT,C_{gap}}$  is  $10 \text{ K W}^{-1}$ . A representative temperature for the consumable is  $20^\circ\text{C}$ , and for the contact tip  $350^\circ\text{C}$  [40,41], resulting in a heat rate  $q_{CT,C_{gap}} \approx 30 \text{ W}$ .

### JOULE HEATING GENERATED AT THE MAIN POINT OF ELECTRICAL CONTACT

The Joule heating generated at the point of electrical contact can be estimated as

$$q_{C_{cont}} = f_{C_{cont}} q_{contJoule} \quad (84)$$

where  $q_{contJoule}$  is the total amount of Joule heating generated at the main point of electrical contact, and  $f_{C_{cont}}$  is the fraction of that heat absorbed by the consumable. This overall heat generated at the point of contact is calculated as

$$q_{cont\_joule} = I^2 R_{cont} \quad (85)$$

where  $I$  is the RMS current, and  $R_{cont}$  is the contact resistance at the point of sliding contact, typically of the order of 1 m $\Omega$ . Assuming that the geometry of electrical conduction through the asperities is symmetrical across the line of contact between the contact tip and then consumable, the fraction of overall Joule heating generated at the contact by the consumable is

$$f_{C_{cont}} = \frac{\rho_{C_{cont,ave}}}{\rho_{C_{cont,ave}} + \rho_{CT}} \quad (86)$$

where  $\rho_{C_{cont,ave}}$  is the electrical resistivity of the consumable surface at the average temperature at the point of contact. For a square contact with a uniform heat distribution, the average surface temperature is [45]:

$$T_{C_{cont,ave}} = T_C + 0.667(T_{C_{cont}} - T_C) \quad (87)$$

Typical values of  $f_{C_{cont}}$  are 0.44 for copper coated wires, 0.88 for non-coated steel wires, and 0.63 for aluminum wires.

#### JOULE HEATING FROM ELECTRODE EXTENSION

The energy generated at the electrode extension by Joule heating ( $q_{EE}$ ) can be calculated as

$$q_{EE} = \frac{\rho_{eff} L I^2}{A_c} \quad (88)$$

where  $\rho_{eff}$  is the effective resistivity of the electrode extension,  $L$  is the length of the electrode extension (time averaged for globular), and  $A_c$  the cross-sectional area of the wire. Following [46], the electrode extension is considered the length of electrode between the exit point of the contact tip and the point of arc attachment illustrated in Fig. 5. The effective resistivity in typical conditions can be calculated with accuracy using the expressions in [15]:

$$\rho_{eff} = \rho_0 M_1 \left[ 2 \frac{\gamma - 1}{b(1-\gamma) + d(1+\gamma)} \right] \quad (89)$$

$$M_1 = \frac{\rho \Delta h_{0,sol} U_C A_c^2}{\rho_0 I^2 L} \quad (90)$$

$$\gamma = \exp(d/M_1) \quad (91)$$

$$d = \sqrt{b^2 - 4a} \quad (92)$$

$$a = -4\Delta\rho_2/\rho_0 \quad (93)$$

$$b = (\Delta\rho_1 + 4\Delta\rho_2)/\rho_0 \quad (94)$$

where  $\rho_0$  is the electrical resistivity at the wire spool temperature (assumed 20°C),  $\Delta\rho_1$  is the variation in resistivity between the spool temperature and solidus,  $\Delta\rho_2$  is the maximum departure from linear in the variation in resistivity, indicated with vertical segments in Fig. 7, using aluminum alloys as examples. The symbol  $\rho$  corresponds to the wire density at room temperature,  $\Delta h_{0,sol}$  is the variation in enthalpy between spool temperature and solidus,  $A_c$  is the cross sectional area of the wire, based on wire diameter  $d_c$ , and  $L$  is the length of electrode extension. The value of  $\rho_{eff}$  varies only slightly with the operating conditions for aluminum, between  $3.0 \cdot 10^{-8} \Omega\text{m}$  and  $3.5 \cdot 10^{-8} \Omega\text{m}$  for all aluminum alloys under all conditions, and varying more widely in ER80S-G, from  $2.6 \cdot 10^7 \Omega\text{m}$  to  $4.5 \cdot 10^7 \Omega\text{m}$ .

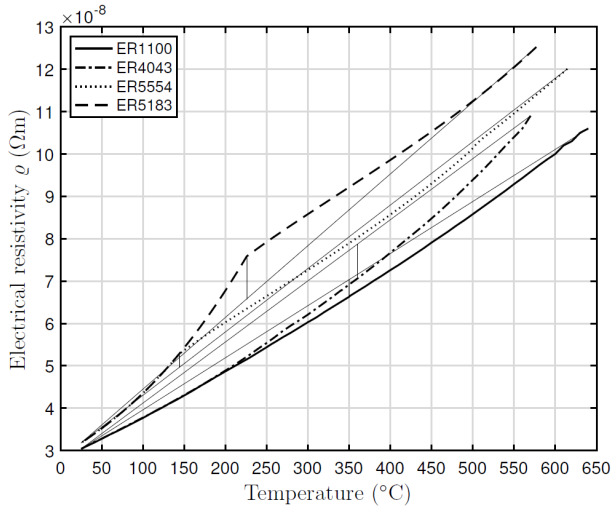


Fig. 7 Electrical resistivity of aluminium alloys tested

#### HEAT FROM OVERALL FALL VOLTAGE

Most of the heat that melts the electrode comes from the overall fall voltage at the electrode often captured as:

$$q_{elec_{over}} = IV_{elec_{over}} \quad (95)$$

Where  $V_{elec_{over}}$  depends only weakly on the welding current. Typically the electrode is positive, making the electrode an anode. In this case, the anode voltage consists of three components

$$V_{elec_{over}} = V_{an_{over}} = V_{an_{fall}} + \phi_{an} + \frac{3}{2} \frac{k_B}{e} T_{ACMC} \quad (96)$$

where  $V_{an_{fall}}$  is typically called the ‘‘anode fall,’’ associated with the non-equilibrium parts of the plasma,  $\phi_{an}$  is the work function of the anode material (the surface of the consumable over the area of arc attachment), and the last term captures the energy deposited by the electrons as they condense on the electrode. The temperature  $T_{ACMC}$  is the temperature of the electrons that deposit on the electrode, of the order of 7300 K for Ar.

The work function is a measure of the energy required to extract an electron from the surface of a solid or liquid cathode. The work function is not a characteristic of a bulk material, but a property of the surface of the material. The work function of crystalline metals often varies by about 10% between different surfaces of the same single crystal, and the work function of molten metal is undistinguishable from that of polycrystalline solid [47]. A reasonable approximation for the effective work function of an alloy ( $\phi_{eff}$ ) can be obtained by using the rule of mixtures:

$$\phi_{eff} = \sum_i f_{mol_i} \phi_i \quad (97)$$

Where  $f_{mol_i}$  is the molar fraction of alloying component  $i$  on the surface, and  $\phi_i$  is its corresponding work function. The effective work function is often undistinguishable from that of the base alloy element. The anode voltage fall is influenced by the size of the arc attachment, the plasma velocity around it, and the presence of metal vapors.

Fig. 8 illustrates the anode fall voltages associated with the experiments performed. The markers correspond to each experiment performed, and the trendlines are two-point moving averages. The lowest horizontal line corresponds to  $\frac{3}{2} \frac{k_B}{e} T_{ACMC}$  in Equation 96 for 7300 K (0.944 V). The multiple closely-packed horizontal lines correspond to  $\phi_{an} + \frac{3}{2} \frac{k_B}{e} T_{ACMC}$ . The small dispersion is due to the different estimated work functions for the different alloy compositions. It can be seen that consumable composition does not change the effective work function far from the value of the solvent. The difference between the trendlines and the highest horizontal lines corresponds to  $V_{an_{fall}}$ , which varies from -1 V to 2 V in the current interpretation of results. The negative value is unlikely, and is discussed in the Discussion section.

#### HEAT GENERATION AT THE MOLTEN CONSUMABLE

The electrode extension ends at the droplet in globular transfer, and at the attachment of the arc in spray transfer (which is approximately coincident with the start of melting). This section beyond the electrode extension will be called the ‘‘molten consumable’’ section. Current flowing through the molten consumable section generates heat that can be calculated as

$$q_{MC_{joule}} = I^2 R_{MC} \quad (98)$$

In globular transfer the resistance can be estimated assuming the path of current inside the current is a truncated cone, from the electrode cross section to the arc attachment. The shape of the droplet changes as it grows, and a time average of this resistance results in

$$R_{MC_{glob}} = \frac{3}{4} \frac{\rho_{MC} d_{MC}}{A_C} \frac{d_C}{2L_{AC,MC}} \quad (99)$$

where the ratio on the right of the equation is typically not far from 1.

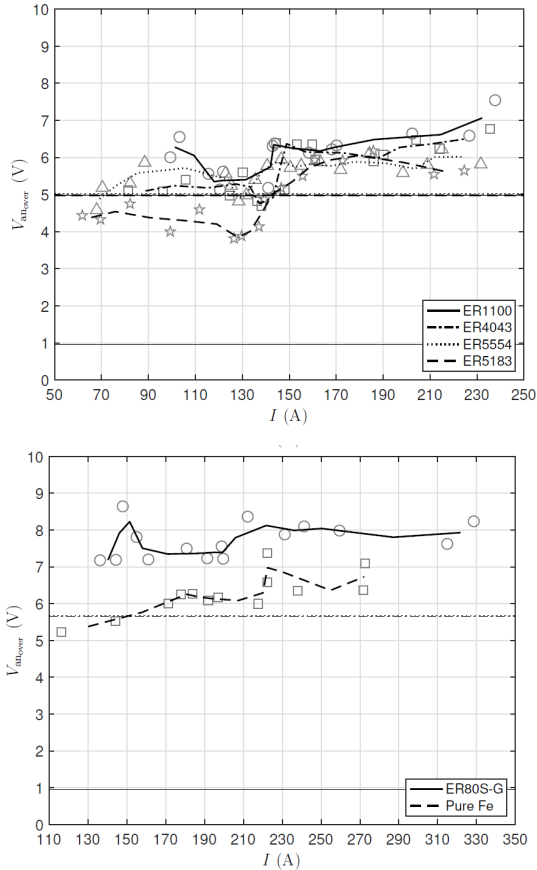


**Fig. 8** Anode fall estimated in experiments performed. Markers indicate independent measurements, and trendlines correspond to a moving average of two points.

In spray transfer, the tapered electrode can be approximated as having a length of the order of the electrode diameter, and a thickness of the neck of the order of half an electrode diameter. Because much current flows through the taper, and the droplet is completely enveloped by the arc, it will be considered that only the taper contributes to Joule heating, resulting in

$$R_{MC_{spray}} = 2 \frac{\rho_c d_c}{A_c} \quad (100)$$

where the resistivity of the consumable corresponds to the melting temperature. Equations 99 and 100 can be blended as an approximation, resulting in

$$R_{MC} = R_{MC_{glob}} + \frac{R_{MC_{spray}} - R_{MC_{glob}}}{1 + \left(\frac{d_{MC}}{d_c}\right)^n} \quad (101)$$

where the value of  $n$  is determined empirically. A reasonable value is  $n = 4.248$ , which results in a 95% approximation to the asymptotic value when the droplet diameter is twice or half that of the consumable. Typical values of  $R_{MC_{glob}}$  are of the order of 1 m $\Omega$  for steels and 0.3 m $\Omega$  for aluminum, and typical values of  $R_{MC_{spray}}$  are approximately a third of those.

## DISCUSSION

This analysis indicates confirms previous findings in [8] that the electrode extension is not influential in aluminum consumables, and that the higher in deposition rate in Mg-containing aluminum alloys are due to their lower droplet temperature, and not their higher resistivity.

This analysis also confirms the hypothesis of [3] in which heat losses by evaporation are small, of the order of 100 W or lower. This small value is still important for an accurate determination of anode fall voltage.

The main source of error in this analysis is associated with the geometry of the electrode tip. A systematic study with high-quality images is necessary to provide an appropriate description of electrode geometry. For droplet detachment frequency measurements, it is recommended to measure the time between a large number of detachments observed in a video capture; for 10 detachments the error would be of the order of 10%, and for 100 detachments, of the order of 1%. The determination of frequency can be accelerated with the use of machine learning, as described in [48].

The negative values of anode fall voltage obtained in Fig. 8 for the globular range are unlikely. One possible source of this surprising result is that evaporation in the globular regime is underestimated. The hypothesis of uniform droplet temperature might need to be reassessed accounting for higher temperatures at the bottom of the droplet, as originally proposed in [49].

The analysis presented can be extended in a straightforward way to other alloys such as stainless steels to estimate the rate of evaporation of Cr. It can also be extended without much difficulty to other wire-based processes such as SAW, FCAW, and MCAW, and

can constitute the basis for an analysis of SMAW. This extension is not without challenges, but the theoretical basis is established.

### CONCLUSIONS

This work presents a complete mass and energy balance of GMAW with solid wire. For the first time, the mass transfer associated with evaporation of a real alloy and its many elements is considered. In contrast with most previous work in which only Langmuir-type evaporation is considered, the resistance to mass transfer in the liquid and gas phases is considered, and it is found that the dominant mechanism in alloy evaporation is diffusion in the gaseous boundary layer. This conclusion is novel and provides explanations to observed phenomena such as the increased fume formation when using reactive gases, which reduce the thickness of the boundary layer.

The value of the anode fall in spray transfer is determined to be of the order of 1 V to 2 V both in steel and aluminum alloys. The estimated value of anode fall voltage in globular transfer varies from -1 V to 2 V. The low and negative values are likely due to the underestimation of evaporation in the globular regime.

This analysis, together with the estimation of anode fall voltage, provides a general way of estimating deposition rate and fume formation rate in any alloy, not just steels and aluminum. This capability is important especially in the field of additive manufacturing, in which new alloys uncommon in welding are explored, and understanding of deposition rate is essential for controlling layer height.

### ACKNOWLEDGEMENTS

The authors would like to acknowledge Prof. Tanaka of Osaka University for the generous gift of a roll of pure iron consumable.

### References

- [1] A. LESNEWICH: 'Control of melting rate and metal transfer in gas-shielded metal-arc welding part i - control of electrode melting rate', *Welding Journal*, pages 343s–353s, 1958.
- [2] E. HALMOY: 'Wire melting rate, droplet temperature, and effective anode melting potential', In: W. Lucas, editor, *Arc Physics and Weld Pool Behaviour*, volume 1, pages 49-57, The Welding Institute, 1979.
- [3] J. H. WASZINK and G. J. P. M. VAN DEN HEUVEL: 'Heat generation and heat flow in the filler metal in GMA welding', *Welding Journal*, pages 269s-282s, 1982.
- [4] G. HUISMANN and H. HOFFMEISTER: 'Sensing metal inert gas process by measuring wire feedrate and current', *Science And Technology Of Welding And Joining*, 4(6):352-356, 1999.
- [5] M. EBERT-SPIEGEL, S.-F. GOECKE and M. RETHMEIER: 'Possibilities for compensating a higher heat input, in particular by the torch offset relative to the top sheet at the fillet weld on a lap joint', *Welding in the World*, 59(3):443-453, 2015.
- [6] YL CHANG and AS BABKIN: 'Calculation of solid wire melting rate in co2 welding', *Welding Journal*, 95(5):163-173, 2016.

- [7] LINCOLN ELECTRIC: *Gas metal arc welding, product and procedure selection*, Report C4.200, Lincoln Electric, 2014.
- [8] Z. YAN, K. S. SCOTT, S. CHEN and P. F. MENDEZ: ‘Deposition rate in gmaw of ER1100 and ER5183 aluminum alloys’, *Welding Journal*, 101:289s-292s, 2022.
- [9] E. SODERSTROM, K. M. SCOTT and P. F. MENDEZ: ‘Calorimetric measurement of droplet temperature in GMAW’, *Welding Journal*, 90(4):77s-84s, 2011.
- [10] K. M. SCOTT: *Heat transfer and calorimetry of tubular ni/wc wires deposited with gmaw*, 2011.
- [11] J. CHAPUIS, K. M. SCOTT, St. D. GUEST, E. SODERSTROM and P. F. MENDEZ: ‘Temperature and Size Measurements of Droplet During Free Flight Gas Metal Arc Welding (Mesures de température et de taille de goutte en vol libre lors d’une opération de soudage MIG-MAG)’, In: *Canadian Welding Association Annual Conference*, 2011.
- [12] J. CHAPUIS, K. M. SCOTT, St. D. GUEST, E. SODERSTROM and P. F. MENDEZ: ‘Droplet calorimetry and high speed videography of free flight metal transfer in gas metal arc welding’, In: *IIW Annual Assembly*, pages Doc.212-1232-12, 2012.
- [13] C. MCINTOSH, J. CHAPUIS and P. F. MENDEZ: ‘Effect of ar-co2 gas blends on droplet temperature in gmaw’, *Welding Journal*, 95(8):273s-279s, 2016.
- [14] C. MCINTOSH and P. F. MENDEZ: ‘Fall voltages in advanced waveform aluminum GMAW’, *Welding Journal*, 96:354s-366s, 2017.
- [15] G. LEHNHOFF and P. F. MENDEZ: ‘Scaling of non-linear effects in heat transfer of a continuously fed melting wire’, *International Journal of Heat and Mass Transfer*, 54:2651-2660, 2011.
- [16] A. SCOTTI, V. PONOMAREV and W. LUCAS: ‘A scientific application oriented classification for metal transfer modes in gma welding’, *Journal of materials processing technology*, 212(6):1406-1413, 2012.
- [17] J. NORRISH: ‘A review of metal transfer classification in arc welding’ (iiv doc. xii-1769-03. bucharest), *Villepinte, France: International Institute of Welding*, 2003.
- [18] A. BLOCK-BOLTEN and T. W. EAGAR: ‘Metal vaporization from weld pools’, *Metallurgical Transactions B*, 15B:461-469, 1984.
- [19] C. B. ALCOCK, V. P. ITKIN and M. K. HERRIGAN: ‘Vapour pressure equations for the metallic elements: 298–2500k’, *Canadian Metallurgical Quarterly*, 23(3):309-313, 1984.
- [20] D. R. LIDE: *CRC handbook of chemistry and physics*, volume 85. CRC press, 88 edition, 2008.
- [21] P. KUBÍČEK and T. PEŘICA: ‘Diffusion in molten metals and melts: application to diffusion in molten iron’, *International metals reviews*, 28(1):131-157, 1983.
- [22] K. UEMURA: ‘The diffusion of various elements into aluminium in molten state (i)’, *Tetsu-to-Hagane*, 25(1):24-29, 1939.
- [23] K. UEMURA: ‘The diffusion of various elements into aluminium in molten state (ii)’, *Tetsu-to-Hagane*, 26(11):813-816, 1940.
- [24] J. B. EDWARDS: *Diffusion in binary liquid-metal systems*, 1968.
- [25] A. K. ROY and R. P. CHHABRA: ‘Prediction of solute diffusion coefficients in liquid metals’, *Metallurgical Transactions A*, 19(2):273-279, 1988.
- [26] E. T. TURKDOGAN, P. GRIEVESON and L. S. DARKEN: ‘The formation of iron oxide fume’, *JOM*, 14(7):521-526, 1962.
- [27] E. T. TURKDOGAN, P. GRIEVESON and L. S. DARKEN: ‘Enhancement of diffusion-limited rates of vaporization of metals’, *The Journal of Physical Chemistry*, 67(8):1647-1654, 1963.
- [28] St. E. FERREE: ‘New generation of cored wires creates less fume and spatter’, *Welding journal*, 74(12):45-49, 1995.

- [29] K. R. CARPENTER, B. J. MONAGHAN and J. NORRISH: 'Influence of shielding gas on fume formation rate for gas metal arc welding of plain carbon steels', In: *Trends in Welding Research*, pages 436-442, 2009.
- [30] T. BERGMAN, A. LAVINNE, F. INCROPERA and D. DEWITT: *Introduction to Heat Transfer*, John Wiley and Sons, New Jersey, United States, sixth edition, 2002.
- [31] C. J. REDDING: 'Fume model for gas metal arc welding', *Welding Journal-New York-*, 81(6):95-S, 2002.
- [32] A. B. MURPHY and C. J. ARUNDELL: 'Transport coefficients of argon, nitrogen, oxygen, argon-nitrogen, and argon-oxygen plasmas', *Plasma Chemistry and Plasma Processing*, 14:451-490, 1994.
- [33] P. F. MENDEZ, M. A. RAMIREZ, G. TRAPAGA and T. W. EAGER: 'Order-of-magnitude scaling of the cathode region in an axisymmetric transferred electric arc', *Metallurgical And Materials Transactions B-Process Metallurgy And Materials Processing Science*, 32(3):547-554, 2001.
- [34] M. A. RAMIREZ: *Mathematical modeling of d. c. electric arc furnace operations*, 2000.
- [35] A. B. MURPHY: 'Calculation and application of combined diffusion coefficients in thermal plasmas', *Scientific reports*, 4(1):1-5, 2014.
- [36] C. R. REID, J. M. PRAUSNITZ and B. E. POLING: *The Properties of Gases and Liquids*. McGraw-Hill, 1987.
- [37] C. MCINTOSH and P. F. MENDEZ: 'Experimental measurements of fall voltages in gas metal arc welding', *Welding Journal*, 96:121s-132s, 2017.
- [38] V. ANDRÉS N. SÁNCHEZ: *Energy balance in gas metal arc welding*, 2021.
- [39] E. SIEWERT, J. SCHEIN and G. FORSTER: 'Determination of enthalpy, temperature, surface tension and geometry of the material transfer in pgmaw for the system argon-iron', *Journal of Physics D: Applied Physics*, 46(22):224008, 2013.
- [40] G. ADAM, T. SIEWERT, T. QUINN and D. VIGLIOTTI: 'Contact tube temperature during gmaw', (80), 2001-12-01 2001.
- [41] D. E. KOLMOGOROV, S. A. SOLODSKY, L. B. GIL and V. I. BERG: 'Effect of various heat sources on heating of contact tip during mig/mag welding', In: *Materials Science Forum*, volume 927, pages 106-111. Trans Tech Publ, 2018.
- [42] C. E. SCHUSTER, M. G. VANGEL, and H. A. SCHAFFT: 'Improved estimation of the resistivity of pure copper and electrical determination of thin copper film dimensions', *Microelectronics Reliability*, 41(2):239-252, 2001.
- [43] J. R. DAVIS: *Concise metals engineering data book*, ASM international, 1997.
- [44] Ø. GRONG: *Metallurgical Modelling of Welding*, Institute of Materials, Cambridge, Great Britain, 1st edition, 1994.
- [45] Y. S. MUZYCHKA and M. M. YOVANOVICH: 'Thermal resistance models for non-circular moving heat sources on a half space', *Journal of Heat Transfer*, 123:624-632, 2001.
- [46] St. EGERLAND: 'A contribution to arc length discussion', *Soldagem & Inspecao*, 20(3):367-380, 2015.
- [47] R. EVANS: 'Surfaces. the surface properties of liquid metals', *Le Journal de Physique Colloques*, 41(C8):C8-775-C8-782, 1980.
- [48] I. GONZÁLEZ PÉREZ, V. MERUANE and P. F. MENDEZ: 'Deep-learning based analysis of metal-transfer images in gmaw process', *Journal of Manufacturing Processes*, 85:9-20, 2023.
- [49] P. F. MENDEZ, N. T. JENKINS and T. W. EAGAR: 'Effect of electrode droplet size on evaporation and fume generation in GMAW', In: *Gas Metal Arc Welding for the 21st Century*, pages 325-332, American Welding Society, 2000.



# NUMERICAL STUDY ON THE FORMATION OF A BULGING REGION IN PARTIAL PENETRATION LASER BEAM WELDING

A. ARTINOV\*, X. MENG\*, M. BACHMANN\*,  
M. RETHMEIER\*\*\*,\*,\*\*,\*

*\*Bundesanstalt für Materialforschung und -prüfung (BAM), Unter den Eichen 87, 12205 Berlin, Germany*

*\*\*Institute of Machine Tools and Factory Management, Technische Universität Berlin, Pascalstraße 8-9, 10587 Berlin, Germany*

*\*\*\*Fraunhofer Institute for Production Systems and Design Technology, Pascalstraße 8-9, 10587 Berlin, Germany*

DOI 10.3217/978-3-85125-968-1-06

## ABSTRACT

A transient three-dimensional thermo-fluid dynamics numerical model was developed to study the formation of a bulging region in partial penetration laser beam welding. The model accounts for the coupling between the fluid flow, the heat transfer, and the keyhole dynamics by considering the effects of multiple reflections and Fresnel absorption of the laser beam in the keyhole, the phase transitions during melting and evaporating, the thermo-capillary convection, the natural convection, and the phase-specific and temperature-dependent material properties up to the evaporation temperature. The validity of the model was backed up by experimentally obtained data, including the drilling time, the weld pool length, the local temperature history outside the weld pool, the process efficiency, and a range of metallographic cross-sections. The model was applied for the cases of partial penetration laser beam welding of 8 mm and 12 mm thick unalloyed steel sheets. The obtained experimental and numerical results reveal that the bulging region forms transiently depending on the penetration depth of the weld, showing a tendency to transition from a slight bulging to a fully developed bulging region between penetration depths of 6 mm and 9 mm, respectively.

Keywords: Laser beam welding, Deep penetration, Bulge formation, Numerical modeling

## INTRODUCTION

In recent years, modern laser systems with high power of up to 100 kW for solid state lasers have been developed, offering a number of technical benefits compared to traditional arc welding techniques, including reduced distortion of the welded components due to locally highly concentrated and precise heat input, high reachable welding speed, a small heat affected zone [4], and enabling single pass welding of sheets with a thickness of up to 50 mm [1–3]. As a result, many new opportunities for applications open up for joining thicker sheets by the laser beam welding technique, e.g., in the manufacturing of high-pressure and vacuum vessels, crane constructions, shipbuilding, and aerospace industry. Nevertheless, as welding speed and sheet thickness increase, new challenges and

issues emerge, such as the formation of non-common defects for specific materials, such as hot-cracking during welding of unalloyed and low-alloyed steels [5–7]. Even though hot-cracking is one of the most researched material phenomena in welding, its nature remains complex [8,9]. However, it is well recognized nowadays that the interplay of three main factors is critical for the welded specimens' susceptibility to cracking, namely the thermal, mechanical, and metallurgical factor [10]. Thereby, the thermal factor defines mainly the amount of solidifying metal, the metallurgical factor determines the temporal and residual strain/stress evolution, and the metallurgical factor governs the local material properties. On the other hand, all three factors and their interactions are greatly influenced by the shape of the weld pool and vice versa, as shown in [11]. Early research on deep penetration electron beam welding proved the importance of this dependency experimentally by introducing a pure Ni wire at different points throughout the thickness of the specimen to visualize the solidification front in the longitudinal section after the welding process. Thereby, a local disturbance of the solidification front was seen in the longitudinal section. This disturbance, nowadays known as the bulging effect, caused a locally delayed solidification, which led to a further increase of the cracking sensitivity [12–15]. To the best of the authors' knowledge, there are just a few published studies on the occurrence of the bulging effect, i.e., the broadening of the weld pool interface during welding with high-power lasers. To overcome the limited experimental accessibility and capture the formation and evolution of the bulging region, state-of-the-art visualization techniques combining quartz glass with high-speed photography and thermal camera recording have been used in more recent research [11,16]. In [17,18] the authors made attempts to measure and quantify the extent of bulging during hybrid laser gas metal arc welding by establishing an angle based on the narrowest and widest cross-sectional dimensions inside the bulging region. Although recent research shows that the bulging effect occurs during laser beam welding of thick steel sheets, the collected data does not allow for a comprehensive study of the weld pool widening, such as the study of its formation mechanisms or its impact on critical factors for defect formation. On the other hand, numerical simulations have provided major insights into the research of complicated processes as computational capacity has improved in the past two decades. The bulging effect can be discovered in various numerical publications, including [19–25], although not being the subject studied therein. In [7,26], its impact on the mechanical factor, i.e., on the temporal strain/stress evolution in the center of the bulging region, has been investigated. The equivalent heat source (EHS) technique, see, e.g., [27], has been used to further enhance this study, [28,29]. The EHS method allows for a precise coupling of the weld pool shape anticipated by a weld pool dynamics simulation and subsequent thermo-mechanical calculations [30,31]. The authors' earlier research [32] provides an overview of the relationship between the bulging effect and the occurrence of hot cracks during complete penetration laser beam welding, taking into account the three main factors. The authors focus on the interplay between the bulge and the increased solidification temperature range caused by segregation of impurities, such as sulfur and phosphorous, leading to their aggregation ahead of the solid-liquid interface. It has already been shown in [33,34], that such a solidification delay reduces the welded components' cracking resistance.

According to the state-of-the-art in the literature, the bulging effect plays a critical role in the formation of defects during complete penetration laser beam welding. However,

most of the numerical works on this subject either ignore the bulging phenomenon completely or focus on its phenomenological reproduction in order to predict its impact on critical factors such as the three main factors determining the specimens' cracking susceptibility. As a result, a more in-depth numerical analysis of this phenomenon is required to comprehend the formation of the bulging during laser beam welding process and select appropriate process parameters. The current research focuses on the formation of the bulge and specifically its relationship to the weld penetration depth. Therefore, an effort is made to develop a three-dimensional transient multiphysics numerical model that considers the most important physical phenomena, including the multiple reflections and Fresnel absorption on the keyhole surface, the vaporization effects, the thermo-capillary, and natural convection, the latent heat of phase transformations, and the temperature-dependent material properties up to the evaporation temperature. Moreover, a large amount of experimental data is collected to verify the model's predictions.

## METHODOLOGY

### MATERIALS

In the welding experiments, two types of unalloyed steel sheets with varying thicknesses were used: 8 mm thick high strength steel sheets for ship structures EH36-N and 12 mm thick structural steel sheets S355J2+N. The EH36-N and S355J2+N sheets had dimensions of 300 mm x 100 mm x 8 mm and 175 mm x 100 mm x 12 mm, respectively. The chemical compositions of the materials used was determined by spectral analysis and are listed in Table 1. Note that the amount of P and S in the steel sheets is very low and therefore the maximum values from the corresponding standard were used in the model.

**Table 1** Measured and standardized chemical composition of the materials used in wt%.

Material	C	Si	Mn	P	S	Cu	Fe
EH36-N	0.260	1.400	0.028	-	-	0.012	bal.
S355J2+N	0.088	0.34	1.38	-	-	0.028	bal.
DIN EN 10025	≤0.2	≤0.55	≤1.6	≤0.025	≤0.035	≤0.55	bal.

### EXPERIMENTS

The technical equipment in the experiments included a Trumpf 16002 disc laser with a 16 kW diode laser illumination, and a Photron FASTCAM SA4 high-speed camera, and thermocouples of type K.

The experimental setup is depicted in Fig. 1, and the process parameters are listed in Table 2. All welds produced in the experiments were bead-on-plate welds. The high-speed camera's frame rate was set to 1000 frames per second, and the diode laser power to 200 W.

The experiments were separated into three steps in total. In the first step, a drilling time estimation for the complete penetration welding on EH36-N sheets was obtained.

Thereby, the optical axis of the high-speed camera lens was aligned perpendicularly to the longitudinal section of the sheet. As a result, the first laser reflection on the top surface can be captured, as well as the moment when the keyhole penetrates the full thickness of the workpiece. In addition, as indicated in Fig. 2 a), thermocouples were placed along the weld centerline. One thermocouple was placed on the top surface of the specimen and used as a trigger. Additionally, three thermocouples were placed on the bottom surface with a distance of around 5 mm to measure the thermal cycle. The moment of complete penetration has been estimated based on the measured time temperature curves. To acquire an accurate averaged value of the drilling period, the experiment was repeated three times.

In the second step of the experiments, the partial penetration welding on the same specimens was performed. Thereby, the weld pool length on the top surface was recorded by the high-speed camera, and the thermal cycles were measured by thermocouples located at different distances from the weld centerline, see Fig. 2 b). The thermocouples utilized in the study were of type K and had a diameter of 0.25 mm.

In the last step, the 12 mm thick S355J2+N sheets were welded. For the sheets welded in the second and third step of the experiment, macro sections were taken from the highlighted locations in Fig. 2 c). Several metallographic cross-sections were obtained using a 2% nital etching. These were subsequently compared to the numerically obtained results.

**Table 2** Processing parameters of the experiments.

Parameters	Value		
Wave length	1030 nm		
Fibre diameter	200 $\mu\text{m}$		
Beam parameter product (BPP)	8 mm mrad		
Focal diameter	500 $\mu\text{m}$		
Focal length	300 mm		
Material	EH36-N		S355J2+N
Penetration	partial	complete	partial
Sheet thickness	8 mm	8 mm	12 mm
Laser power	5 kW	8 kW	8 kW
Focal position	0 mm		
Welding speed	2 m $\text{min}^{-1}$		
Laser torch angle	0°		
Shielding gas nozzle angle	35°		
Shielding gas	Ar, 25 L $\text{min}^{-1}$		

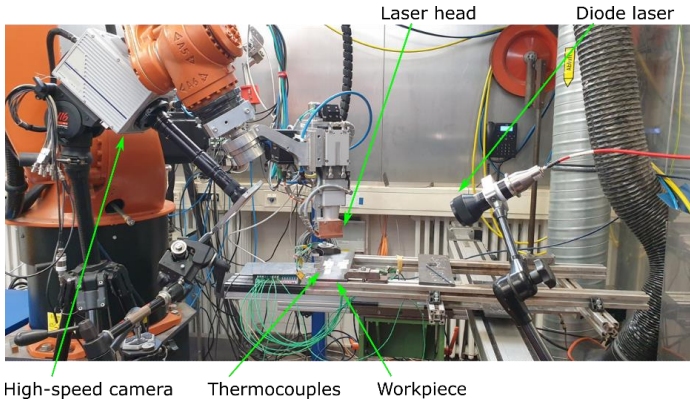


**Fig. 1** Experimental setup

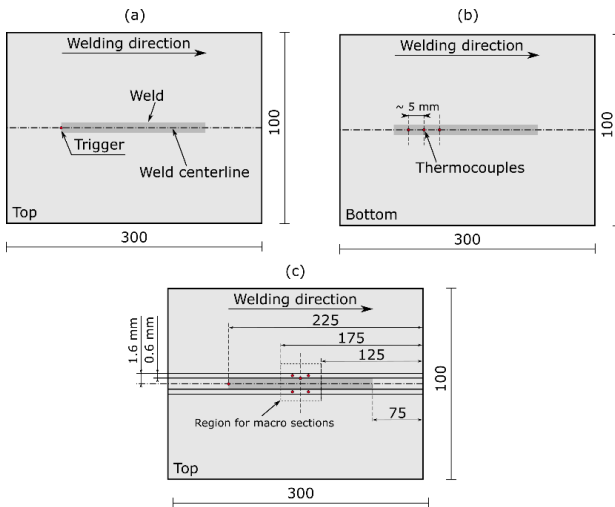


**Fig. 2** Overview of the positions of the thermocouples for the measurement of the: a)-b) laser drilling time and c) time-temperature curves

NUMERICAL MODELING

For the objective of improving the level of understanding regarding the formation of a bulging region, a three-dimensional thermo-fluid dynamics model taking into consideration the free surface tracking by the volume of fluid (VOF) approach has been developed. The numerical framework is based on previous works published in [35–39], with some additional enhancements and modifications.

*Assumptions*

Despite the fact that more complex problems may nowadays be numerically analyzed due to the advances in computing power, substantial simplifications still need to be made in order to get the computational results in a reasonable amount of time. The complex physics behind the laser beam welding process, which includes a variety of strongly coupled, highly nonlinear interactions between the laser radiation, the vapor phase, the molten metal, and the solid material, is another reason for the model's simplifications. The following are the primary assumptions used in the simulation:

- The molten metal is assumed to be Newtonian and incompressible, whereby the flow regime of the liquid metal is considered to be laminar.
- The evaporation of the metal and the vapor flow are not considered in the model. Instead, an empirical model is used to account for the effect of the vapor phase on the surface of the keyhole.
- The impact of the density deviation on the flow due to the temperature difference is modeled using the Boussinesq approximation.

*Governing equations*

In the following, the governing equations that describe the multiphysics model in a fixed Cartesian coordinate system are given. The transient deformation of the solidified weld seam profile and molten pool free surface is modeled using the VOF technique.

- Volume fraction conservation

$$\frac{\partial \alpha_{vol_{steel}}}{\partial t} + \nabla \cdot (\vec{v} \alpha_{vol_{steel}}) = 0, \quad (1)$$

where  $\alpha_{vol_{steel}}$  denotes the volume fraction of the steel phase in a control volume and  $\vec{v} = (u, v, w)$  is the fluid velocity vector. There are three possible conditions for the control volume defined by the volume fraction of the steel, namely a control volume containing only the air phase,  $\alpha_{vol_{steel}} = 0$ , a control volume containing only the steel phase,  $\alpha_{vol_{steel}} = 1$ , and a mixture control volume containing the interface between the steel and the air phases,  $0 < \alpha_{vol_{steel}} < 1$ . Note that the volume fraction conservation equation is solved only for the steel phase; the volume fraction of the air phase is computed based on the following constraint:

$$\sum_{i=1}^2 \alpha_{vol_i} = 1, \quad (2)$$

where the subscript,  $i = 1$ , denotes the steel phase and,  $i = 2$ , the air phase [40]. A piecewise-linear approach is used to reconstruct the steel-air interface, based on the assumption that the interface has a linear slope within each control volume [41]. Volume fraction values between 0.2 and 1 and an empirically determined critical volume fraction gradient value are used to approximate the free surface of the molten pool and the solidified weld.

- Mass conservation

$$\nabla \cdot \vec{v} = 0. \quad (3)$$

- Momentum conservation

Throughout the computational domain, a single momentum equation is solved. The material parameters in each cell are averaged by the volume fraction as a consequence, and the resulting velocity field is shared among the phases. For instance, the density is determined as follows:

$$\rho_{mix} = \alpha_{vol_{steel}} \rho_{steel} + (1 - \alpha_{vol_{steel}}) \rho_{air}, \quad (4)$$

where  $\rho_{mix}$  is the volume-fraction-averaged density;  $\rho_{air}$  and  $\rho_{steel}$  are the densities of the air and steel phases, respectively. This method is used to calculate all remaining properties such as viscosity and thermal conductivity except the thermal expansion coefficient. The momentum equation is given as follows:

$$\rho_{mix} \left( \frac{\partial \vec{v}}{\partial t} + (\vec{v} \cdot \nabla) \vec{v} \right) = -\nabla p + \mu_{mix} \nabla^2 \vec{v} + \rho_{mix} \vec{g} + \vec{S}_m, \quad (5)$$

where  $t$  is the time,  $p$  is the fluid pressure,  $\mu_{mix}$  is the dynamic viscosity,  $\vec{g}$  is the gravitational acceleration vector, and  $\vec{S}_m$  is the momentum source term, which is expressed as follows:

$$\begin{aligned} \vec{S}_m = & -\rho_{steel} \vec{g} \beta_{steel} (T - T_{liq}) + \frac{(1 - \alpha_{liq})^2}{(\alpha_{liq}^3 + \epsilon)} A_{mush} \vec{v} \\ & + \vec{S}_{surf.tension} + \vec{S}_{rec} + \vec{S}_{vapor}, \end{aligned} \quad (6)$$

where  $\beta_{steel}$  is the thermal expansion coefficient,  $T$  is the temperature,  $T_{liq}$  is the liquidus temperature of the unalloyed steel taken as the reference temperature here,  $\alpha_{liq}$  is the liquid volume fraction,  $\epsilon$  is a small number in the order of  $1 \times 10^{-3}$ , used to avoid division by zero, and  $A_{mush}$  is the mushy zone constant.

The thermal buoyancy caused by changes in steel density with temperature is described by the first term on the right-hand side (RHS) of Eq. (6) [42]. The second term on the RHS relates the inverse of the size of the interdendritic structure to the loss of momentum due to solidification in the mushy zone. Thereby, the mushy zone constant  $A_{mush}$  is a measure for the amplitude of the damping, thus it should be very large to allow for a steeper transition of the velocity of the liquid metal to zero as it solidifies, in the current study a value in the order of  $1 \times 10^7 \text{ kg m}^{-3} \text{ s}^{-1}$  was chosen [43,44]. The liquid fraction  $\alpha_{liq}$  is defined as:

$$\alpha_{liq} = \begin{cases} 0 & \text{for } T < T_{sol} \\ \frac{T - T_{sol}}{T_{liq} - T_{sol}} & \text{for } T_{sol} \leq T \leq T_{liq}, \\ 1 & \text{for } T > T_{liq} \end{cases} \quad (7)$$

where  $T_{sol}$  denotes the solidus temperature of the material used. Additionally, the flow in the mushy zone is modeled using the effective viscosity approach. As a result, the coherent solid fraction  $F_c = 0.48$  and the critical solid fraction  $F_{cr} = 0.64$  are used to divide the mushy zone into three subregions. However, each region has a different local viscosity and drag coefficient. The local effective viscosity is expressed as a function of the solid fractions [45]:

$$\mu_{steel} = \mu_0 \left(1 - \frac{F_s}{F_{cr}}\right)^{-1.55}, \quad \text{for } F_s \neq F_{cr}, \quad (8)$$

where  $\mu_0$  is the dynamic viscosity at  $T_{liq}$  and  $F_s$  is the solid fraction. Thereby, a value of 200 Pa s was chosen for the local viscosity in control volumes with a solid fraction higher than the critical solid fraction. The effects of surface tension at the steel-air interface are included in the third term of Eq. (6). Thus, the Marangoni stress resulting from the fluctuation in surface tension is calculated as follows:

$$\tau_{Ma} = \frac{\partial \gamma}{\partial T} \frac{\partial T}{\partial \vec{t}}, \quad (9)$$

where  $\gamma$  is the surface tension and  $\vec{t}$  is the surface unit tangential vector. The surface tension is approximated according to [46]:

$$\begin{aligned} \gamma &= \gamma_0 - \hat{A}(T - T_{liq}) - R_g T \Gamma_s \ln(-1 + K_s a_s) \\ &\text{with } K_s = k_l \exp\left(\frac{-\Delta H_0}{R_g T}\right), \end{aligned} \quad (10)$$

where  $\gamma_0$  is the surface tension of the pure metal (here iron),  $\hat{A}$  is the negative slope of  $\gamma$  as function of the temperature,  $R_g$  is the universal gas constant,  $\Gamma_s$  is the surface excess at saturation,  $a_s$  is the thermodynamic activity,  $k_l$  is a constant related to the entropy of segregation, and  $H_0$  is the standard heat of adsorption. The capillary pressure, which is the differential in pressure along the steel-air interface, is calculated as:

$$p_{ca} = \gamma \kappa, \quad (11)$$

with  $\kappa = \nabla \cdot \vec{\hat{n}}$  defined as the curvature in terms of the divergence of the surface unit normal vector,  $\vec{\hat{n}} = \frac{\vec{n}}{|\vec{n}|}$ ;  $\vec{n} = \nabla \alpha_{vol,steel}$  is the inward surface normal vector defined as the gradient of the volume fraction of the steel phase. The forces acting on the steel-air interface are converted to volume forces using the divergence theorem according to the continuum surface force (CSF) model. Therefore, a transformation term is defined according to [47]:

$$CSF_{momentum} = \frac{\rho_{mix} |\nabla \alpha_{vol,steel}|}{\frac{1}{2}(\rho_{air} + \rho_{steel})}, \quad (12)$$

allowing to compute the volume force:

$$\vec{S}_{surf.tension} = (p_{ca}CSF_{momentum})\vec{n}. \quad (13)$$

One of the main driving forces on the keyhole surface is the evaporation-induced recoil pressure, which is indicated by the fourth term in Eq. (6). According to [48], the recoil pressure is calculated and converted to a volume force as follows:

$$p_{rec} = \frac{AB_0}{\sqrt{A}} \exp\left(-\frac{M_{mol}h_v}{R_gT}\right), \quad \vec{S}_{rec} = (p_{rec}CSF_{momentum})\vec{n}, \quad (14)$$

where  $A$  is a numerical coefficient depending on the ambient pressure and its value is approximately  $0.55\sqrt{K}$  for practical applications;  $B_0$  is a vaporization constant, which in the case of iron equals  $3.9 \times 10^{12} \text{ kg m}^{-1} \text{ s}^{-2}$ ;  $M_{mol}$  is the molar mass, and  $h_v$  is the latent heat of vaporization. The fifth term on the RHS of Eq. (6) includes empirical formulations of the vapor-induced stagnation pressure  $p_{vapor}$  and shear stress  $\tau_{vapor}$ , based on the assumption of a laminar flow regime within the keyhole [49]. According to [19] these can be approximated as given:

$$p_{vapor} = p_0 + \frac{1}{2}\rho_{vapor}|\vec{v}_{\vec{n}}|^2, \quad (15)$$

$$\tau_{vapor} = \frac{1}{8}f\rho_{vapor}|\vec{v}_{\vec{t}}|^2, \quad (16)$$

where  $p_0$  is the vapor or atmospheric pressure,  $\rho_{vapor}$  is the metallic vapor density calculated with the ideal gas equation,  $\vec{v}_{\vec{n}}$  and  $\vec{v}_{\vec{t}}$  are the normal and tangential projections of the vapor velocity vector,  $\vec{V}$ , on the steel-air interface, respectively, and  $f = 64/\text{Re}$ . The metallic vapor velocity vector acts vertically in the thickness direction and its magnitude at the keyhole entrance is assumed to be  $150 \text{ m s}^{-1}$  [50]. Additionally, in the partial penetration case, the vapor velocity is defined as a function of the penetration/keyhole depth,  $h_{depth}$ , increasing linearly from  $0 \text{ m s}^{-1}$  at the keyhole bottom to its maximum value at the keyhole entrance. Note that there are two metallic vapor velocity vectors acting in opposite directions in the complete penetration case. Thereby, one vector increases linearly, starting at two-thirds of the plate thickness, reaching  $150 \text{ m s}^{-1}$  at the keyhole entrance and a second vector increasing in the same manner towards the keyhole exit, reaching  $100 \text{ m s}^{-1}$  at the sheet bottom [51,52]. The projection of the vapor velocity vector onto the surface unit normal vector,  $\vec{n}$ , of the steel-air interface can be obtained as follows:

$$\vec{v}_{\vec{n}} = (\vec{V} \cdot \vec{n})\vec{n}. \quad (17)$$

The following vector equation can then be used to determine the tangential projection of the vapor velocity:

$$\vec{v}_{\vec{t}} = \vec{V} - \vec{v}_{\vec{n}}. \quad (18)$$

Equation 16 is further simplified by substituting the Re number and  $f$  into it:

$$\tau_{vapor} = \frac{8\mu_{T_{max}}|\vec{v}_{\vec{t}}|}{D}, \quad (19)$$

where  $D$  is the averaged diameter of the keyhole and  $\mu_{T_{max}}$  is the dynamic viscosity at the maximum reachable temperature applied in the model. For the calculation of  $D$ , the

keyhole volume,  $V_{key}$ , is approximated as a cylindrical pipe with the length of the keyhole depth,  $h_{depth}$ , giving:

$$D = \sqrt{\frac{4V_{key}}{h_{depth}\pi}}. \quad (20)$$

The dynamic viscosity at  $T_{max}$  is obtained by making use of the kinematic theory of gases:

$$\mu_{T_{max}} = \frac{M_{mol}}{3\sqrt{2}\hat{\sigma}} \sqrt{\frac{8k_b T_{max}}{\pi M_{mol}}}, \quad (21)$$

where  $\hat{\sigma} = \pi d_{mol}^2$  is the collision cross-section of the molecule with the molecular diameter,  $d_{mol}$ , and  $k_b$  is the Boltzmann constant. The dynamic viscosity value for the unalloyed steel used in this study is approximately  $1.62 \times 10^{-4} \text{ kg m}^{-1} \text{ s}^{-1}$  for a superheating temperature of 3400 K [53,54], as shown in Table 1. The corresponding source term can be expressed as:

$$\begin{aligned} \vec{S}_{vapor} &= \vec{S}_{stagnation} + \vec{S}_{shear}, \\ \text{with } \vec{S}_{stagnation} &= (p_{vapor} CSF_{momentum}) \vec{n}, \\ \text{and } \vec{S}_{shear} &= (\tau_{vapor} CSF_{momentum}) \vec{t}. \end{aligned} \quad (22)$$

Here, the shear stress and stagnation pressure are converted to volume forces using the CSF method, in accordance with [55].

- Energy conservation

$$\rho_{mix} \left( \frac{\partial H_{mix}}{\partial t} + (\vec{v} \cdot \nabla) H_{mix} \right) = \nabla \cdot (\lambda_{mix} \nabla T) + S_e, \quad (23)$$

where  $H_{mix}$  is the enthalpy,  $\lambda_{mix}$  is the heat conductivity, and  $S_e$  is the source term. Thereby, the enthalpy of the material is the sum of the sensible enthalpy,  $h_{mix}$ , and the latent heat of fusion of the material used,  $h_f$ :

$$H_{mix} = h_{mix} + h_f, \quad (24)$$

with  $h_{mix}$ :

$$h_{mix} = h_{ref} + \int_{T_{ref}}^T c_{p,mix} dT, \quad (25)$$

where, the subscript, ref, stands for reference and  $c_{p,mix}$  is the specific heat at constant pressure. Furthermore, the latent heat content,  $L$ , in each control volume, is expressed in terms of the latent heat of the material and the liquid fraction:

$$h_f = \alpha_{liq} L, \quad (26)$$

varying between zero in the solid region and  $L$  in the liquid region [43]. The source term can be written as:

$$S_e = S_{laser} + S_{convection} + S_{radiation} + S_{evaporation} + S_{recondensation}. \quad (27)$$

The laser heat flux density is assumed to have a Gaussian-like axisymmetric distribution defined as [19]:

$$q_L(x, y) = \frac{2P_L}{\pi r_{f0}^2} \exp\left(-2 \frac{x^2 + y^2}{r_{f0}^2}\right), \quad (28)$$

where  $P_L$  is the laser power and  $r_{f0}$  is the laser beam radius at the focal plane. A self-consistent ray tracing method described in [19] is used to calculate the three-dimensional energy distribution while taking into account the multiple reflections at the keyhole surface and Fresnel absorption. Thereby, the laser beam is approximated with 755 sub-rays, by discretizing the laser spot in the focal plane by  $31 \times 31$  sub-regions with a length of  $D_{sub} = \frac{2r_{f0}}{31}$ . Thus, the energy density of each sub-ray is location-dependent. The power of each sub-ray is calculated by multiplying the surface area of the sub-region beneath it by the corresponding sub-ray power density:

$$P_{ray}(x, y) = q_L(x, y) \left(\frac{r_{f0}}{31}\right)^2. \quad (29)$$

The initial path of each sub-ray is defined by the diffraction of the laser beam. Therefore, the laser beam radius at any height,  $z$ , along the optical axis is approximated as:

$$r_f(z) = r_{f0} \left(1 + \left(\frac{z - z_0}{z_r}\right)^2\right)^{1/2}. \quad (30)$$

Here  $z_0$  is the position of the focal plane and  $z_r$  is the Rayleigh length. The reflection direction vector,  $\vec{R}_i$ , of the  $i$ -th reflection is calculated by the following vector equation:

$$\vec{R}_i = \vec{R}_{i-1} - 2(\vec{R}_{i-1} \cdot \vec{n})\vec{n}. \quad (31)$$

The direct search method described in [56] is used to select the free surface cell from the center of which the sub-ray is reflected. Furthermore, the absorption rate is calculated using the Fresnel reflection model, as stated in [57]:

$$\hat{\alpha} = 1 - \frac{1}{2} \left( \frac{1 + (1 - \varepsilon \cos \theta_i)^2}{1 + (1 + \varepsilon \cos \theta_i)^2} + \frac{\varepsilon^2 - 2\varepsilon \cos \theta_i + 2 \cos^2 \theta_i}{\varepsilon^2 + 2\varepsilon \cos \theta_i + 2 \cos^2 \theta_i} \right), \quad (32)$$

with  $\varepsilon$  - a material dependent coefficient taken and modified according to [58] and  $\theta_i$  - the incident angle at the  $i$ -th reflection point. The total energy of all sub-ray reflections in the cell is added up, and the laser power absorbed in each cell is determined by dividing the result by the volume of the cell,  $V_{cell}$ :

$$S_{laser}(x, y, z) = \frac{\sum_{j=1}^{755} q_{ray}(x, y)}{V_{cell}}. \quad (33)$$

The convective and radiative heat transfer are taken into account by the second and third terms on the RHS of Eq. (27), defined as:

$$\begin{aligned} q_{convection} &= h_c (T - T_{ref}), \\ q_{radiation} &= \sigma \varepsilon_r (T^4 - T_{ref}^4). \end{aligned} \quad (34)$$

Here  $h_c = 15 \text{ W m}^{-2} \text{ K}^{-1}$  is the heat convection coefficient,  $\sigma$  is the Stefan-Boltzmann constant, and  $\varepsilon_r$  is the emissivity [59]. Note that it is accounted not only for the outward convective and radiative heat fluxes, but as well for the inward heat fluxes due to the high-temperature metal vapor, reaching temperatures of up to 6000 K, known as a

secondary heat effect. For this, the reference temperature,  $T_{ref}$ , was set to 6000 K for the inward heat fluxes, and to 300 K for the computation of the heat loss caused by the outward heat fluxes [60]. In the present study the range of action for the secondary heat effect was adapted according to the geometrical dimensions of preliminary obtained metallographic cross-sections. The evaporation loss source term is calculated according to [61]

$$q_{evaporation} = \rho_{liq} h_v F_e, \quad (35)$$

where  $\rho_{liq}$  is the liquid density and  $F_e$  is the evaporation recession speed. It should be noted that the evaporation loss was only taken into account for control volumes reaching temperatures higher than 2700 K because the formulation of the evaporation model is derived for rapid evaporation and does not account for diffusive evaporation. Due to the numerical adaptation of the critical temperature value of 2700 K, the overall amount of heat loss falls within the experimentally measured range of up to 3%. The recondensation heat flux is described by the last term on the RHS of Eq. (27). From the total amount of evaporation heat loss, estimated with Eq. (35), 18% are considered as local recondensation, and 72% are linearly redistributed along the keyhole, according to [60]. In the case of complete penetration, the amount is redistributed linearly from zero at the keyhole bottom to its maximum value at the keyhole entrance. On the other hand, in the case of partial penetration, the amount of recondensation heat at the keyhole bottom exit is 80% of the amount at the keyhole top exit. It is important to note that the unit for all heat fluxes mentioned above is  $W m^{-2}$ . Therefore, in order to convert the heat fluxes to power densities with the unit of  $W m^{-3}$ , a transformation term is defined that is similar to the one applied in the CSF model:

$$TT_{energy} = \frac{\rho_{mix} c_{p_{mix}} |\nabla \alpha_{vol_{steel}}|}{\frac{1}{2} (\rho_{air} c_{p_{air}} + \rho_{steel} c_{p_{steel}})}. \quad (36)$$

Here  $c_{p_{air}}$  is the specific heat of air; the resulting power densities are given as:

$$S_i = q_i TT_{energy}, \quad (37)$$

where  $i$  stands for convection, radiation, evaporation and recondensation.

### Boundary conditions

The pressure and viscous stress boundary conditions on the steel-air interface are expressed by the following scalar conditions in accordance with the fundamentals of fluid dynamics and assuming that the air phase is inviscid ( $\mu_{air} = 0$ ) and incompressible:

$$p_{air} - p_{steel} + 2\mu_{steel} \frac{\partial \vec{v}_{\vec{n}}}{\partial t} = p_{ca} + p_{rec} + p_{vapor} \quad (38)$$

$$-\mu_{steel} \left( \frac{\partial \vec{v}_{\vec{n}}}{\partial t} + \frac{\partial \vec{v}_{\vec{t}}}{\partial \vec{n}} \right) = \tau_{Ma} + \tau_{vapor}. \quad (39)$$

Note that, as mentioned above, the surface unit normal vector is directed into the steel phase's interior.

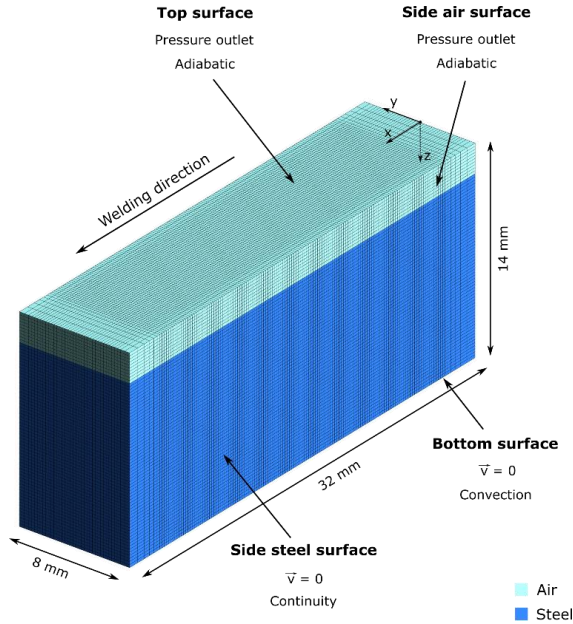


**Fig. 3** Overview of the boundary conditions of the multi-physics model

According to the multiple Fresnel absorption, heat convection, thermal radiation, evaporation, and recondensation, the energy boundary condition on the free surface is given as:

$$-\lambda_{mix} \frac{\partial T}{\partial \vec{n}} = q_L - q_{convection} - q_{radiation} - q_{evaporation} + q_{recondensation}. \quad (40)$$

Convective heat transfer was taken into account at the bottom of the steel-phase domain, where the boundaries of the air-phase domain were configured as pressure outlets. It should be noted that the simulation domain was designed to minimize the computing time. As a result, the actual steel sheets are significantly larger than the computational domain. By applying the continuity boundary condition introduced in [62], an appropriate treatment of the boundaries was ensured. The boundary conditions are shown in Fig. 3.

### *Material properties*

The temperature-dependent material properties utilized in the simulation were implemented up to the maximum temperature of 3400 K specified in the model. Because both materials were unalloyed steels, the same thermo-physical material properties were utilized. The base material was modelled as a ferritic phase, with the properties of the

austenite phase being used for temperatures above the austenitization point. The solid-solid phase transformation was considered by converting it to a specific heat and adding this to the heat capacity curve, see Fig. 4. where the thermophysical material properties are plotted. The value for the steel density was averaged in the temperature range of interest between 1200 K and 2800 K, resulting in  $\rho_{steel} = 7060 \text{ kg m}^{-3}$ .

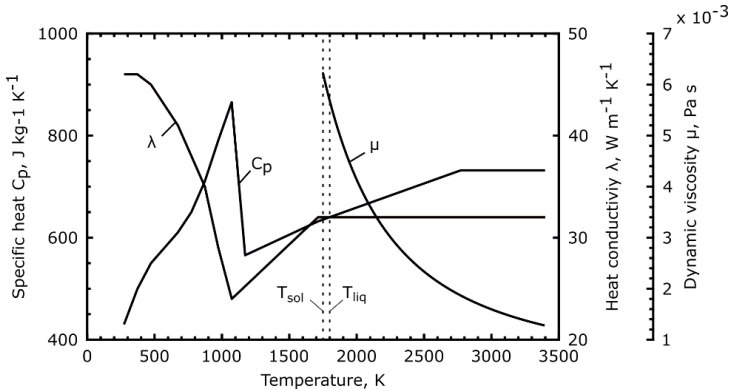


**Fig. 4** Thermo-physical material properties for unalloyed steel utilized in the multi-physics model [46,63,64]

### Numerical setup

The dimensions of the computational domain used in the present study are 32 mm in length, 8 mm in width, and, depending on the thickness of the steel sheets to be welded, 8 mm or 12 mm in thickness, see also Fig. 3. The regions between  $-2.9 \text{ mm} \leq y \leq 2.9 \text{ mm}$  and  $3 \text{ mm} \leq x \leq 29 \text{ mm}$  were finely meshed with a recommended fixed cell size of 0.2 mm according to [65]. The cell size outside these regions are defined by a growth rate of 1.1, resulting in a total amount of 372,960 control volumes for the 12 mm thick steel sheets. To ensure an adequate calculation of the reflection point of the sub-rays, the weld seam start and end locations were chosen within the finely meshed region at  $x = 3.5 \text{ mm}$  and  $x = 28.5 \text{ mm}$ , respectively. Above the steel sheet, an air layer between  $0 \text{ mm} \leq z \leq 2.0 \text{ mm}$  was defined above the steel sheet allowing to track the free steel-air interface by the VOF method. An identical air layer was put beneath the steel sheet for the full penetration calculation. The finite volume software ANSYS Fluent was used to solve all governing equations. The momentum and energy conservation equations were discretized spatially using a second order upwind technique, and the transient terms were discretized using a first order implicit formulation. The PISO approach was utilized for the pressure-velocity coupling, and the Geo-Reconstruct technique was applied to reconstruct the steel-air interface. The computation was carried out on a high-performance computing cluster at the Bundesanstalt für Materialforschung und -prüfung (BAM). In average, 200 hours computing time were needed to simulate 0.6 second real process time.

## RESULTS AND DISCUSSION

### VALIDATION OF THE NUMERICAL RESULTS

To validate the numerical results, several experimental data were measured and analyzed in accordance with the ISO/TS 18166 standard [66]. By comparing the averaged drilling time, the weld pool length, the shape of the fusion zone, and the thermal cycles, the multi-physics model was first validated for the 8 mm thick EH36-N sheets. Following the validation of the model, further results, such as for 12 mm thick sheets, were verified by comparing the fusion line and process efficiency.

#### *Comparison of the averaged drilling time*

The drilling time was measured using a high-speed camera similar to the experimental setup shown in Fig. 1. To determine an average value for the drilling time at 8 mm thick sheets, the experiment was carried out three times. Table 2 lists the parameters of the process. Two frames recorded by the high-speed camera from one of the three measurements are displayed in Fig. 5. As a result, a) denotes the moment of the first reflection on the top surface of the specimen, and b) the moment when complete penetration is achieved. The measurement tolerance was 1 ms because the frame rate was set to 1000 Hz. The drilling time is calculated from the frames and is approximately 197 ms. The second and third measurements took roughly 164 ms and 224 ms, respectively. In addition, based on the thermocouple values, the drilling time was determined, see Fig. 2 a)-b). Around 7 mm ahead of the welding start point, complete penetration was achieved. The drilling time is estimated to be 210 ms. Thereby, the average of all measurements is 198 ms. The numerically obtained drilling curve is shown in Fig. 5. c). As seen, the drilling time is approximately 191 ms, which agrees well with the experimentally obtained values.

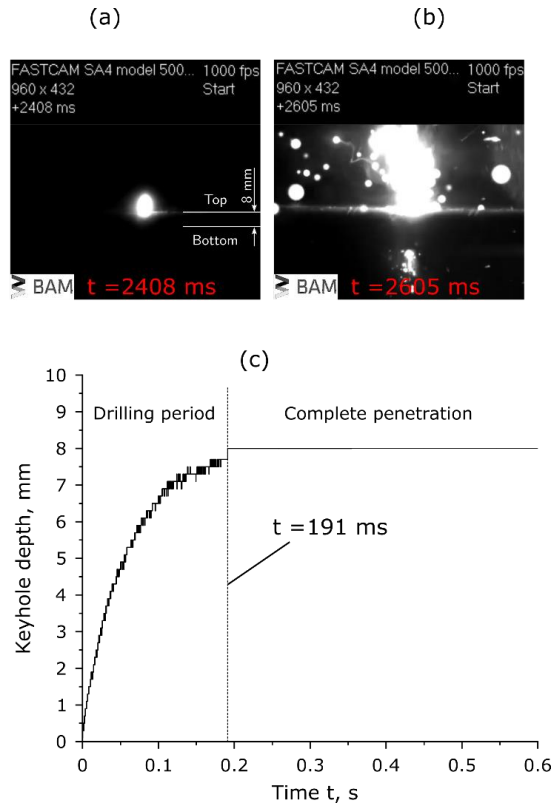


**Fig. 5** Drilling time measured by a high-speed camera: a)-b) experimental, c) numerical drilling time

### *Comparison of the weld pool shape*

The precise prediction of the molten pool and the flow pattern therein was one of the objectives of the numerical model. The solidus isotherm,  $T_{sol}$ , defines the weld pool interface and enables for the extraction of the numerical fusion line from a cross-section as well as the weld pool length on the top surface. Three metallographic cross-sections were taken from the quasi-steady state region of the weld seam, as shown in Fig. 2, to account for the experimental tolerances c). Fig. 6 a)-c) show the shape of the experimental fusion lines for the 8 mm thick sheets. As illustrated in Fig. 6 d), the experimental tolerance is estimated from the overlap of the three fusion lines. In Fig. 6 e), the numerical fusion line is compared to the experimental average, showing good correlation. The multi-physics model was validated for the partial penetration situation of welding 8

mm thick sheets, as stated above. By comparing the fusion line shape and process efficiency, the numerical figures computed for sheets with a thickness of 12 mm were validated as well. The experimentally measured and numerically estimated fusion lines for the 12 mm thick sheets are shown in Fig. 7. As observed, there are rather small differences between the fusion lines, which are attributable to the experiment and model's tolerances. Finally, the weld pool geometry is verified by comparing the measured and simulated weld pool lengths, as shown in Figure 8. The numerical model predicted an 8.2 mm weld pool length, which was slightly shorter than the experimentally measured value of 8.6 mm. It should be noted that the weld pool length varied along the weld seam. Therefore, a tolerance value is defined as a difference below 5%.

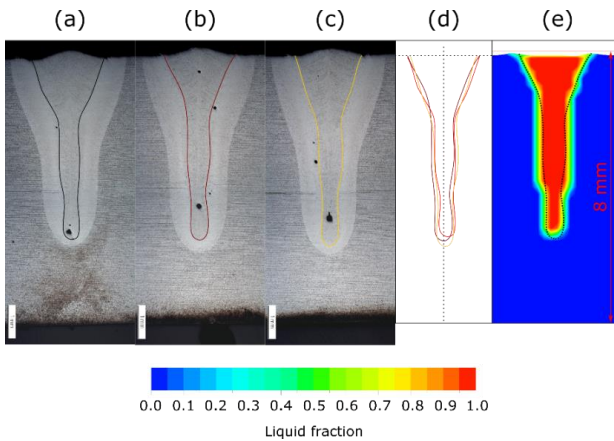


**Fig. 6** a)-c) depict three metallographic cross-sections extracted from the middle of the weld seam of the 8 mm thick sheets. Colored lines are used to highlight the fusion line's shape. In d), the overlap of the three fusion lines defines the experimental tolerance range. The fusion line from b) is compared to the calculated fusion line in e)

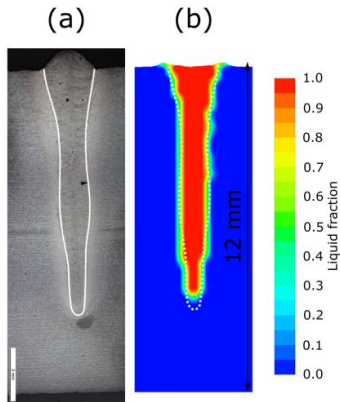


**Fig. 7** a) depicts a metallographic cross-section extracted from the middle of the weld seam for 12 mm thick sheets. A white line highlights the fusion line's contour. b) points out the difference between the experimental and numerical fusion lines

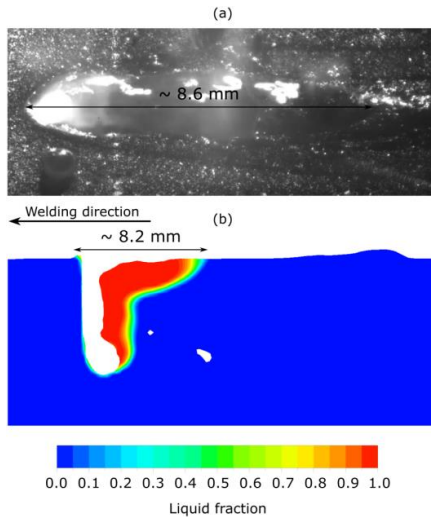


**Fig. 8** a) shows the high-speed camera recorded weld pool length from the middle of the weld seam. b) shows the simulated weld pool length at  $t = 0.33$  s

*Comparison of the thermal cycles and the process efficiency*

The next stage in the validation process is to compare the measured and predicted values for the thermal cycles and process efficiency. The thermal cycles are essential to the welding process because they allow for the prediction of the local microstructure and mechanical characteristics of the component to be joined. The comparison of the measured and calculated time-temperature curves is shown in Fig. 9. Note that a number of time-temperature curves have been obtained experimentally. But for the purposes of comparison, the curve with the highest measured temperature is used. The thermal behavior of the welded sheets is accurately predicted by the numerical model, as shown in Fig. 9. The calculated process efficiency in the model is taken as a validation parameter in addition to the time-temperature curves. The quantity of energy absorbed during the calculations of the complete and partial penetration cases of the 8 mm thick sheets is shown in Fig. 10. The average efficiency in the simulations for both complete and partial penetration was around 79% and 83%, respectively. This agrees well with experimental findings [67] using similar laser powers and processing speeds. It should be noted that the drilling stage of the process was taken into account into the averaged values. The average amount of absorbed energy declines as the process approaches complete penetration at around 200 ms, resulting in a reduced overall averaged amount. The fluctuations of the absorbed heat during partial penetration, on the other hand, are much smaller, caused primarily by fluctuations of the keyhole surface, which have a direct impact on the multiple reflections.

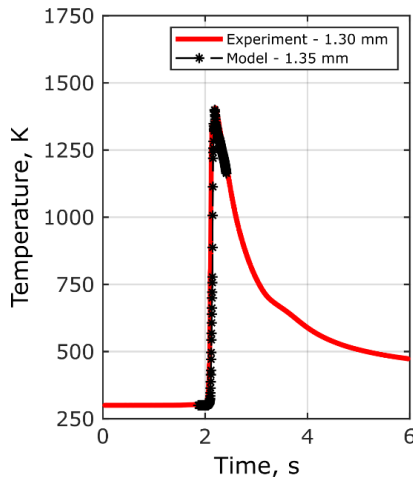


**Fig. 9** Comparison of calculated and measured thermal cycles on the top surface of an 8 mm thick sheet

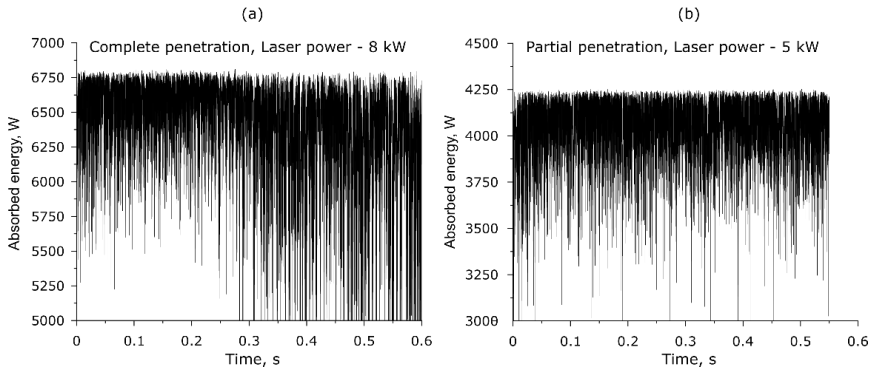


**Fig. 10** Amount of absorbed energy computed with the multi-physics model

#### TRANSITION BEHAVIOR OF THE BULGING EFFECT

The multiphysics model described and validated in the previous sections allowed for the investigation of the fluid flow and thus of the formation of the bulging region. Several experiments and calculations with various sheet thicknesses and welding parameters for the partial penetration case have been carried out in order to estimate the transition from a slight bulge to a fully developed bulging, which can be considered to have a significant impact on the weld seam quality. Based on the numerical results, it was revealed that the flow pattern in the model's longitudinal plane is characterized by two vortices with opposing directions, regardless of the presence of a bulge region. The thermo-capillary driven flow dominates the upper region of the weld pool, creating an elongated weld pool surface. The weld pool length, as shown in Figs. 11 and 12, is strongly dependent on the dynamic behavior of the keyhole due to transient fluctuations and varies along the penetration depth. The vortex in the lower region of the weld pool is rather small, because of the recoil pressure on the keyhole bottom, which is dependent on the amount of absorbed energy and determined by the multiple reflections in the keyhole. The liquid metal in the upper region flows backwards away from the keyhole rear wall, then downwards and forward in the welding direction at about half the length of the weld pool. The molten material at the bottom is pushed backward and redirected upward along the solid-liquid boundary. The two circulations collide and change course toward the rear wall of the keyhole. The interaction of these circulations contributes to the formation of a bulging region. When the recoil pressure-induced circulation in the bottom part of the weld pool, which pushes the liquid metal to the rear part of the weld pool, and the subsurface backflow in the top region, which is a result of mass conservation, collide, a narrowed zone between these is formed. The narrowing of the weld pool geometry leads to a stronger separation of the two main circulations in the top and bottom region of the weld pool, causing an accumulation of molten material in the bottom region. As a result, a bulging effect is formed.

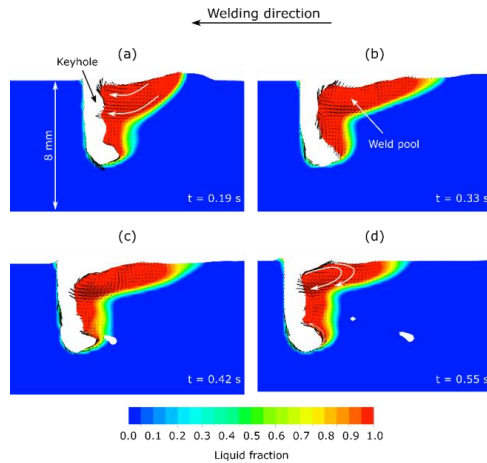


**Fig. 11** Temporal evolution of the calculated weld pool shape in the longitudinal plane during partial penetration welding of 8 mm thick sheets

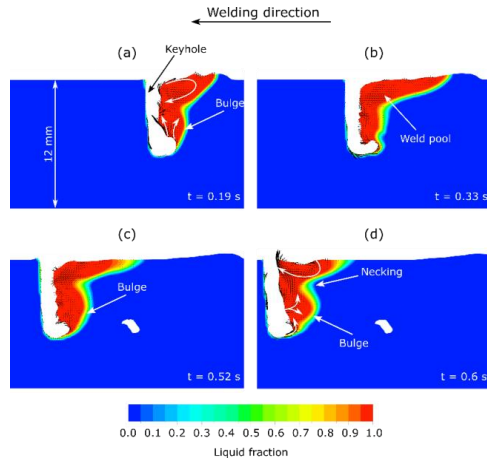


**Fig. 12** Temporal evolution of the calculated weld pool shape in the longitudinal plane during partial penetration welding of 12 mm thick sheets

Even though the flow pattern in the weld pool appears to be independent on the bulging region, a bulging region forms when the size and magnitude of the circulations are large enough. The flow directions in the longitudinal section of both the 8 mm and 12 mm thick steel sheets are very similar, as observed in Figs. 11 and 12. In the case of 8 mm thick sheets, however, the two vortices are not large and strong enough to form a narrowed

region between the top and bottom regions of the weld pool. This statement is as well supported by the experimentally determined depths at which the bulge can be observed in the metallographic cross-sections. According to Figs. 6 and 7, the experimental depths of the center of the bulging region for the 8 mm and 12 mm thick steel sheets are approximately 3.2 mm and 5.2 mm, respectively. As seen in Figs. 11 and 12, these values are in good agreement with the numerically predicted values of 3.8 mm and 4.9 mm. Thereby, the reduced heat input and penetration depth are the cause of the circulations' smaller size and magnitude. The amount of molten material and the penetration depth increase in proportion to the increase in laser power used to weld the 12 mm thick sheets when compared to the case of welding 8 mm sheets. The penetration depth was approximately 5.7 mm and 9.3 mm for the 8 mm and 12 mm sheets, respectively. Thus, as the penetration depth increases, the interaction between the main circulation intensifies, leading to the formation of a necking region between these. The necking forms approximately when the weld pool shape reaches a quasi-steady state, as illustrated in Fig. 12 a). According to numerical observations, both the necking and the bulging are no steady-state phenomena. Although both phenomena are transient, the necking and bulging occur together as if one may be the consequence of the other and vice versa. Moreover, the numerical results show that the bulging occurs at penetration depths above 6 mm and more frequently at penetration depths around 9 mm. Consequently, the region between 6 mm and 9 mm penetration depth can be considered as the transition region from a slight bulge to a fully developed bulge.

### CONCLUSIONS

The mechanism of the so-called bulging effect and its transition behavior, or more precisely its dependence on penetration depth, have been confirmed and studied experimentally as well as numerically in the current work. The following are the main conclusions drawn from the obtained results:

- A three-dimensional transient multi-physics numerical model is established, which automatically accounts for the transition from partial to complete penetration welding and allows for the prediction and study of the formation of a bulging region.
- Several experimental measurements and observations, such as drilling time, weld pool length, thermal cycles, process efficiency, and metallographic cross-sections, show very good agreement with the numerically obtained results.
- A bulging region forms once a necking between the top and bottom regions of the weld pool occurs, separating the two main circulations therein. Moreover, the necking and bulging regions are observed to occur transiently but always simultaneously as if one may be the consequence of the other and vice versa.
- It is found that the bulging effect strongly depends on the penetration depth, with an increasing tendency for a bulging region to form with increasing penetration depth. Moreover, the region between 6 mm and 9 mm penetration depth can be considered as the transition region from a slight bulge to a fully developed bulge.

ACKNOWLEDGEMENTS

This work is funded by the Deutsche Forschungsgemeinschaft (DFG, German Research Foundation) project Nr. 411393804 (BA 5555/5-2), Nr. 416014189 (BA 5555/6-1), and Nr. 466939224 (BA 5555/9-1).

References

- [1] M. BACHMANN, A. GUMENYUK, M. RETHMEIER: 'Welding with high-power lasers: Trends and developments', *Physics Procedia*, 83, pp. 15-25, 2016.
- [2] X. ZHANG, E. ASHIDA, S. TARASAWA, Y. ANMA, M. OKADA, S. KATAYAMA, M. MITZUTANI: 'Welding of thick stainless-steel plates up to 50 mm with high brightness lasers', *Journal of Laser Applications*, 23, 2011.
- [3] A. FRITZSCHE, V. AVILOV, A. GUMENYUK, K. HILGENBERG, M. RETHMEIER, M. HIGH: 'Power laser beam welding of thick-walled ferromagnetic steels with electromagnetic weld pool support', *Phys. Procedia*, 83, pp. 362-372, 2016.
- [4] J.F. READY, D.F. FARSON: 'LIA handbook of laser materials processing' *Laser Institute of America*, Orlando, 2001.
- [5] J. SCHUSTER, S. KEITEL, E. SCHULZE, H. MALY: 'Fachbeiträge-entstehung erstarrungsbedingter risse in Laserstrahlschweißverbindungen an unlegierten und niedriglegierten baustählen', *Schweißen und Schneiden*, 51, pp. 252-257, 1999.
- [6] J. SCHUSTER: 'Heißrisse in Schweißverbindungen: Entstehung, Nachweis und Vermeidung', *DVS-Verlag*, 2004.
- [7] M.O. GEBHARDT, A. GUMENYUK, M. RETHMEIER: 'Numerical analysis of hot cracking in laser hybrid welded tubes', *Advances in Materials Science and Engineering*, 520786, 2004.
- [8] M. RAPPAZ, J. DANTZIG: 'Solidification', *EFPL Press*, first, 2009.
- [9] J. LIPPOLD: 'Welding metallurgy and weldability', *John Wiley & Sons*, 2014.
- [10] C. CROSS: 'On the origin of weld solidification cracking', *Springer*, 3-18, 2005.
- [11] A. ARTINOV N. BAKIR, M. BACHMANN, A. GUMENYUK, M. RETHMEIER: 'Weld pool shape observation in high power laser beam welding' *Procedia CIRP*, 74, pp. 683-686, 2018.
- [12] T. SHIDA, H. OKUMURA, Y. KAWADA: 'Effects of welding parameters and prevention of defects in deep penetration electron beam welding of heavy section steel plates', *Weld. World*, 17, pp. 196-207, 1979.
- [13] S. TSUKAMOTO, H. IRIE, M. INAGAKI: 'Welding defects and molten metal behaviour in electron beam welding', *The fourth international Symposium of the Japan Welding Society*, pp. 115-120, 1982.
- [14] S. TSUKAMOTO, H. IRIE: 'Welding defects and molten metal behaviour in low speed electron beam welding', *Welding in the World*, pp. 130-140, 1985.
- [15] S. TSUKAMOTO, H. IRIE: 'Mechanism of locally delayed solidification in electron beam welding', *Welding international*, 5, pp. 177-183, 1991.
- [16] A. ARTINOV, N. BAKIR, M. BACHMANN, A. GUMENYUK, S.J. NA, M. RETHMEIER: 'On the search for the origin of the bulge effect in high power laser beam welding', *Journal of Laser Applications*, 31, 2019.
- [17] L. BARBETTA, W. WEINGAERTNER, O. SEFFER, R. LAHDO, AND S. KAERLE: 'Influence of molten pool geometry and process parameters on solidification cracks formation in hybrid laser-GMA welding of thick 5L X70 steel plates', in *ABCM International Congress of Manufacturing Engineering (COBEM)*, 8th Brazilian Congress of Manufacturing Engineering, Brazil, pp. 18-22, 2015.
- [18] L.D. BARBETTA, W.L. WEINGAERTNER, O. SEFFER, R. LAHDO, S. KAERLE: 'Influence of molten pool geometry and process parameters on solidification cracks formation in hybrid

- laser-GMA welding of thick 5L X70 steel plates', *ABCM International Congress of Manufacturing Engineering (COBEM)*, 8th Brazilian Congress of Manufacturing Engineering, 2015.
- [19] W.-I. CHO, S.-J. NA, C. THOMY, F. VOLLERTSEN: 'Numerical simulation of molten pool dynamics in high power disk laser welding', *Journal of Materials Processing Technology*, 212, pp. 262-275, 2012.
- [20] M. BACHMANN, V. AVILOV, A. GUMENYUK, M. RETHMEIER: 'Experimental and numerical investigation of an electromagnetic weld pool support system for high power laser beam welding of austenitic stainless steel', *Journal of Materials Processing Technology*, 214 pp. 578-591, 2014.
- [21] M. BACHMANN, V. AVILOV, A. GUMENYUK, M. RETHMEIER: 'Experimental and numerical investigation of an electromagnetic weld pool control for laser beam welding', *Physics Procedia*, 56, pp. 515-524, 2014.
- [22] M. SOHAIL, S.-W. HAN, S.-J. NA, A. GUMENYUK, M. RETHMEIER: 'Numerical investigation of energy input characteristics for high-power fiber laser welding at different positions', *International Journal of Advanced Manufacturing Technology*, 80, pp. 931-946, 2015.
- [23] F. LU, X. LI, Z. LI, X. TANG, H. CUI: 'Formation and influence mechanism of keyhole-induced porosity in deep-penetration laser welding based on 3d transient modeling', *International Journal of Heat and Mass Transfer*, 90 pp. 1143-1152, 2015.
- [24] M. BACHMANN, R. KUNZE, V. AVILOV, M. RETHMEIER: 'Finite element modeling of an alternating current electromagnetic weld pool support in full penetration laser beam welding of thick duplex stainless steel plates', *Journal of Laser Applications*, 28, 2016.
- [25] Z. GAO, P. JIANG, G. MI, L. CAO, W. LIU: 'Investigation on the weld bead profile transformation with the keyhole and molten pool dynamic behavior simulation in high power laser welding', *International Journal of Heat and Mass Transfer*, pp.1304-1313, 2018.
- [26] M.O. GEBHARDT: 'Einfluss von Konstruktion und Schweißparametern auf die Erstarrungsrisse beim Laser-MSG-Hybridschweißen dickwandiger Bauteile experimentelle und numerische Analyse', *Bundesanstalt für Materialforschung und Prüfung (BAM)*, 2014.
- [27] D. RADAJ, H. HÄUSER, S. BRAUN: 'Numerische Simulation von Eigenspannungen und Verzug bei Schweißverbindungen aus AlMgSi-Legierungen', *Konstruktion*, pp. 31-37, 1998.
- [28] A. ARTINOV, M. BACHMANN, M. RETHMEIER: 'Equivalent heat source approach in a 3d transient heat transfer simulation of full-penetration high power laser beam welding of thick metal plates', *International Journal of Heat Mass Transfer*, 122, pp. 1003-1013, 2018.
- [29] N. BAKIR, A. ARTINOV, A. GUMENYUK, M. BACHMANN, M. RETHMEIER: 'Numerical simulation on the origin of solidification cracking in laser welded thick-walled structures', *Metals*, 8, p. 406, 2018.
- [30] A. ARTINOV, V. KARKHIN, N. BAKIR, M. X, M. BACHMANN, A. GUMENYUK, M. RETHMEIER: 'Lam curves approximation for the assessment of the 3-d temperature distribution in keyhole mode welding processes', *Journal of Laser Applications*, 32, 2020.
- [31] A. ARTINOV, V. KARKHIN, P. KHOMICH, M. BACHMANN, M. RETHMEIER: 'Assessment of thermal cycles by combining thermo-fluid dynamics and heat conduction in keyhole mode welding processes', *International Journal of Thermal Sciences*, 145, 2019.
- [32] A. ARTINOV, M. BACHMANN, X. MENG, V. KARKHIN, M. RETHMEIER: 'On the relationship between the bulge effect and the hot cracking formation during deep penetration laser beam welding', *Procedia CIRP*, 94, pp. 5-10, 2020.
- [33] S. KOU: 'Welding Metallurgy', *John Wiley & Sons*, 2003.
- [34] M.E. GLICKSMAN: 'Principles of solidification: An introduction to modern casting and crystal growth concepts', *Springer New York*, 2011.

- [35] X. MENG, M. BACHMANN, A. ARTINOV, M. RETHMEIER: 'Experimental and numerical assessment of weld pool behavior and final microstructure in wire feed laser beam welding with electromagnetic stirring', *Journal of Manufacturing Processes*, 45, pp. 408-418, 2019.
- [36] X. MENG, A. ARTINOV, M. BACHMANN, M. RETHMEIER: 'Numerical and experimental investigation of thermo-fluid flow and element transport in electromagnetic stirring enhanced wire feed laser beam welding', *International Journal of Heat Mass Transfer*, 144, 2019.
- [37] X. MENG, A. ARTINOV, M. BACHMANN, M. RETHMEIER: 'Numerical study of additional element transport in wire feed laser beam welding', *Procedia CIRP*, 94, pp. 722-725, 2020.
- [38] X. MENG, A. ARTINOV, M. BACHMANN, M. RETHMEIER: 'Theoretical study of influence of electromagnetic stirring on transport phenomena in wire feed laser beam welding', *Journal of Laser Applications*, 32 (2), 2020.
- [39] X. MENG, M. BACHMANN, A. ARTINOV, M. RETHMEIER: 'The influence of magnetic field orientation on metal mixing in electromagnetic stirring enhanced wire feed laser beam welding', *Journal of Materials Processing Technology*, 294, 2021.
- [40] C.W. HIRT, B.D. NICHOLS: 'Volume of fluid (VOF) method for the dynamics of free boundaries', *Journal of Computational Physics*, pp. 201-225, 1981.
- [41] D.L. YOUNGS: 'Time-dependent multi-material flow with large fluid distortion', *Numerical Methods for Fluid Dynamics*, 24, pp. 273-285, 1982.
- [42] T.E. FABER: 'Fluid dynamics for physicists', *Cambridge University Press*, 1995.
- [43] V.R. VOLLER, C. PRAKASH: 'A fixed grid numerical modelling methodology for convection-diffusion mushy region phase-change problems', *International journal of heat and mass transfer*, 30, pp. 1709-1719, 1987.
- [44] A.D. BRENT, V.R. VOLLER, K.T.J. REID: 'Enthalpy-porosity technique for modeling convection-diffusion phase change: application to the melting of a pure metal', *Numerical Heat Transfer, Part A Applications*, 13, pp. 297-318, 1988.
- [45] M.H. CHO, Y.C. LIM, D.F. FARSON: 'Simulation of weld pool dynamics in the stationary pulsed gas metal arc welding process and final weld shape', *Welding Journal New-York*, 85, pp. 271-283, 2006.
- [46] P. SAHOO, T. DEBROY, M.J. MCNALLAN: 'Surface tension of binary metal-surface active solute systems under conditions relevant to welding metallurgy', *Metallurgical transactions B*, 19, pp. 483-491, 1988.
- [47] J.U. BRACKBILL, D.B. KOTHE, C. ZEMACH: 'A continuum method for modeling surface tension', *Journal of Computational Physics*, 100, pp. 335-354, 1992.
- [48] V. SEMAK, A. MATSUNAWA: 'The role of recoil pressure in energy balance during laser materials processing', *Journal of Physics D-Applied Physics*, 1997.
- [49] F.M. WHITE: 'Fluid mechanics froth edition', *McGraw-Hill*, New York, 1999.
- [50] E.H. AMARA, A. BENDIB: 'Modelling of vapour flow in deep penetration laser welding', *Journal of Physics D-Applied Physics*, 35, pp. 272-280, 2002.
- [51] D. WU, X. HUA, F. LI, L. HUANG: 'Understanding of spatter formation in fiber laser welding of 5083 aluminum alloy', *International Journal of Heat and Mass Transfer*, pp. 730-740, 2017.
- [52] R. ZHANG, X. TANG, L. XU, F. LU, H. CUI: 'Study of molten pool dynamics and porosity formation mechanism in full penetration fiber laser welding of al-alloy', *International Journal of Heat and Mass Transfer*, 148, 2020.
- [53] W. TAN, N.S. BAILEY, C.S. YUNG: 'Investigation of keyhole plume and molten pool based on a three-dimensional dynamic model with sharp interface formulation', *Journal of Physics D: Applied Physics*, 46, 2013.
- [54] W. TAN, C.S. YUNG: 'Analysis of multi-phase interaction and its effects on keyhole dynamics with a multi-physics numerical model', *Journal of Physics D: Applied Physics*, 47, 2014.
- [55] G.P. SASMAL: 'Numerical modeling of thermocapillary convection with curved and deforming free surfaces', *Previews of Heat and Mass Transfer*, 5(21), pp. 457-458, 1995.

- [56] S.-W. HAN, A. JUNSU, S.J. NA: 'A study on ray tracing method for CFD simulations of laser keyhole welding: progressive search method', *Welding in the World*, 60, pp. 247-258, 2016.
- [57] W. SCHULZ, G. SIMON, H.M. URBASSEK, L. DECKER: 'On laser fusion cutting of metals', *Journal of Physics D-Applied Physics*, 20, pp. 481-488, 1987.
- [58] R. DUCHARME, K. WILLIAMS, P. KAPADIA, J. DOWDEN, B. STEEN, M. GLOWACKI: 'The laser welding of thin metal sheets: an integrated keyhole and weld pool model with supporting experiments', *Journal of physics D: Applied physics*, 27, p. 1619, 1994.
- [59] T.L. BERGMAN, F.P. INCROPERA: 'Fundamentals of heat and mass transfer', *John Wiley & Sons*, 2011.
- [60] S. MUHAMMAD, S. HAN, S.J. NA, A. GUMENYUK, M. RETHMEIER: 'Study on the role of recondensation flux in high power laser welding by computational fluid dynamics simulations', *Journal of Laser Application*, 30, 2018.
- [61] H. KI, P.S. MOHANTY, J. MAZUMDER: 'Modelling of high-density laser-material interaction using fast level set method', *Journal of Physics D: Applied Physics*, 34, pp. 364-372, 2001.
- [62] X. MENG, G. QIN, R. ZONG: 'Thermal behavior and fluid flow during humping formation in high-speed full penetration gas tungsten arc welding', *International Journal of Thermal Science*, 134, pp. 380-391, 2018.
- [63] K.C. MILLS: 'Recommended values of thermophysical properties for selected commercial alloys', *Woodhead Publishing*, 2002.
- [64] Material database, 2009, ESI Group.
- [65] W. I. N. CHO, S.J.: 'Impact, of wavelengths of CO<sub>2</sub>, disk, and green lasers on fusion zone shape in laser welding of steel', *J. Weld. Join*, 38, pp. 235-240, 2020.
- [66] ISO/TS 18166:2016 Numerical welding simulation Execution and documentation.
- [67] Y. KAWAHITO, N. MATSUMOTO, Y. ABE, S. KATAYAMA: 'Relationship of laser absorption to keyhole behavior in high power fiber laser welding of stainless steel and aluminum alloy', *Journal of Materials Processing Technology*, 211, pp. 1563-1568, 2011.

# MODELLING OF THE MELT POOL BEHAVIOUR DURING A PULSED TIG WELDING OPERATION IN A NARROW GROOVE

S. CADIOU\*, A. BAUMARD\*, A. BROSSE\*, V. BRUYERE\*\*

*\*Framatome-DTIM, 2 Rue Professeur Jean Bernard, 69007 Lyon, France*

*\*\*SIMTEC, 5 rue Félix Poulat, 38000 Grenoble, France*

DOI 10.3217/978-3-85125-968-1-07

## ABSTRACT

Arc welding is one of the main processes for assembling metal components in the nuclear industry. To guarantee the quality of the welded assemblies and to predict the characteristics of the weld, it is necessary to master the welding process and have a thorough understanding of the interactions within the melt pool. To this end, the objective of this work is to develop a transient numerical model allowing for the prediction of the behaviour of the melted zone during current pulsation in reasonable computational times. The relevant industrial application in this study is the welding of a narrow groove gap of a stainless steel pipe. The welding process used is pulsed TIG and different synergies are studied. In this work, numerical simulation is used as a predictive analysis tool providing data that complete the experimental ones. Knowing that the predictive aspect of the simulations depends on the modelling choices, it is necessary to consider the main physical phenomena governing the melt pool (thermal transfers, fluid flow, electromagnetism) and to model the mass feeding process using the Arbitrary Lagrangian Eulerian (ALE) method. The development of the magneto-thermohydraulic model with material supply is carried out using the Comsol Multiphysics® software.

Keywords: pulsed TIG welding, groove welding simulation melt pool, magnetohydrodynamics, heat transfer

## INTRODUCTION

Framatome's activities in the nuclear industry require a high level of expertise in assembly processes, including welding processes, to ensure that manufactured components respect industrial standards. This accurate knowledge of assembly processes is historically based on empirical approaches, resulting from experimental feedbacks that have demonstrated their capacity in classifying Framatome as one of the leaders in the mastery of welding techniques. Nevertheless, these experimental approaches are expensive and lead to both a limited understanding of the correlation between the operating parameters and the properties of the welds, and of the origin of the defects generated during welding. To reduce experimental costs and improve the comprehension of welding processes,

Framatome has developed numerical tools. Originally, numerical simulation of welding techniques focused on Thermo-Mechanical-Metallurgical (TMM) studies to predict the distortions and residual stresses of the manufactured assembly. Although the power of computational tools has considerably increased during last decades, assumptions are made to simplify the global physical model and thus reduce computational times. Since 2013, Framatome has been developing predictive tools for numerical simulation. These multiphysics models are based on the process parameters (electric current intensity, arc height, shielding gas flow) to simulate a welding operation. The development of these models enables to study the influence of the process parameters on the physical quantities relevant to TIG (Tungsten Inert Gas) (weld pool, electric arc, detachment of the drop from the filler wire or other), to have a better understanding of the phenomenon involved in welding.

Before developing the different aspects of the model, the physics of arc welding processes is explained in a first section. The numerous physical phenomena involved are described, with particular emphasis on the magnetothermo-hydraulic ones. Then, the results from a simplified model of the pulsed TIG welding process with filler metal in a narrow groove, known as Orbital Narrow Gap GTA (Gas Tungsten Arc) welding, are presented in a second section. The model studied here is considered as simplified because the filler metal is not directly modelled but only included in a source term.

### MATHEMATICAL FORMULATION AND GOVERNING EQUATIONS

The mathematical description made in this section focuses on the modelling of the melt pool. The plasma, the tungsten electrode used for TIG welding and the filler wire integrating the detachment of the drop are not modelled.

The main purpose of this section is to describe the physical phenomena (Fig. 1) in a mathematical form, essential to implement the code defining the numerical model. The calculation code used in this study is the COMSOL Multiphysics® software (version 5.6). As a reminder, the physics explained here is related to electromagnetism, heat transfer and fluid mechanics. The ALE method (Arbitrary Lagrangian Eulerian) is used to describe the free surface.

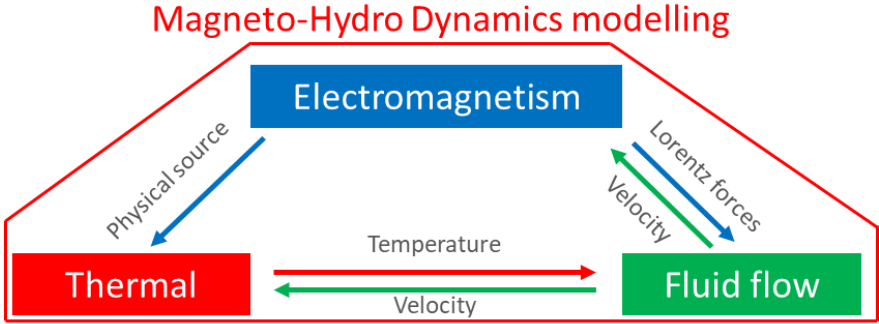


**Fig. 1** Multiphysics couplings in the modelling of arc welding

#### ELECTROMAGNETISM

To determine the electromagnetic forces acting on the flow in the melt pool as well as the Joule effect, the Maxwell equations given below are solved:

$$\text{div} \left( \sigma_e \overrightarrow{\text{grad}}(V) + \sigma_e \frac{\partial \vec{A}}{\partial t} \right) = 0 \quad (1)$$

$$\sigma_e \frac{\partial \vec{A}}{\partial t} + \frac{1}{\mu_0} \overrightarrow{\text{rot}} \left( \overrightarrow{\text{rot}}(\vec{A}) \right) + \sigma_e \overrightarrow{\text{grad}}(V) = \vec{0}$$

where  $\sigma_e$  is the electrical conductivity,  $V$  is the electrical potential,  $\mu_0$  is the magnetic permeability and  $A$  is the magnetic vector potential.

#### THERMAL

The temperature field is calculated using the energy conservation equation:

$$\rho C_p \left( \frac{\partial T}{\partial t} + \vec{v} \cdot \overrightarrow{\text{grad}}(T) \right) = \text{div} \left( \vec{k} \overrightarrow{\text{grad}}(T) \right) + S_v \quad (2)$$

where  $\rho$  is the density,  $C_p$  is the specific heat,  $k$  is the thermal conductivity,  $T$  is the temperature, and  $S_v$  a volumetric heat source term. Here,  $S_v$  is the heating Joule effect (with  $j$  is current density, and  $E$  is electric field):

$$S_v = \vec{j} \cdot \vec{E} \quad (3)$$

## FLUID FLOW

The flows within the melt pool can be calculated from the conservation equations of mass and momentum:

- Conservation of mass:

$$\frac{\partial \rho}{\partial t} + \text{div}(\rho \vec{v}) = 0 \quad (4)$$

where  $\rho$  is the density,  $t$  the time and  $\vec{v}$  the velocity vector.

- Conservation of momentum:

$$\rho \left( \frac{\partial \vec{v}}{\partial t} + \overline{\text{grad}}(\vec{v}) \cdot \vec{v} \right) = \overline{\text{div}} \left[ -P\bar{1} + \mu_f \left( \overline{\text{grad}}(\vec{v}) + {}^t\overline{\text{grad}}(\vec{v}) \right) - \frac{2}{3} \text{div}(\vec{v})\bar{1} \right] + \vec{F}_v \quad (5)$$

where  $P$  is the pressure,  $\bar{1}$  the identity matrix,  $\mu_f$  the dynamic viscosity and  $\vec{F}_v$  the volumetric force detailed below.

In the melt pool, the volumetric forces include the electromagnetic forces, also called Lorentz forces, gravity, the buoyancy effect, also called Boussinesq force and a force of extinction of flow velocities called Darcy, allowing to cancel the velocities in the solid part. More specifically, the Boussinesq force is an upward volumetric force caused by changes in the density of a fluid as a function of variations in its temperature and the effects of gravity. It is related to the phenomenon of natural convection. Most of studies use the Boussinesq approximation. It consists in considering that the density varies linearly with the temperature:

$$\vec{F}_v = \vec{F}_{mag} + \vec{F}_b + \vec{F}_{Darcy} + \vec{F}_{gravity} = \vec{j} \times \vec{B} - \rho_{ref} \beta (T - T_{ref}) \vec{g} - C \frac{(1-f_L)^2}{f_L^2 + b} \vec{v} + \rho \vec{g} \quad (6)$$

where  $\vec{F}_{mag}$  represents the electromagnetic forces,  $\vec{B}$  the magnetic field,  $\vec{j}$  the electric current density,  $\vec{F}_b$  the buoyancy force,  $\vec{F}_{Darcy}$  the Darcy law and  $\vec{F}_{gravity}$  the gravity. The Darcy law enables to stop the fluid flow in the solid region.  $\rho_{ref}$  corresponds to the density at the reference temperature  $T_{ref}$ ,  $\beta$  to the thermal expansion coefficient,  $\vec{g}$  to the acceleration due to gravity,  $C$  and  $b$  are two constants and  $f_L$  is the liquid fraction function. This function is assumed to vary linearly with temperature in the mushy zone as follows:

$$f_L = \begin{cases} 1 & \text{if } T > T_L \\ \frac{T - T_S}{T_L - T_S} & \text{if } T_S \leq T \leq T_L \\ 0 & \text{if } T < T_S \end{cases} \quad (7)$$

where  $T$  is the current temperature,  $T_S$  and  $T_L$  are the solidus and liquidus temperatures of the workpiece.

## INTERFACE EQUATIONS

To model electromagnetism effects, an electric current density is applied using a surfacic Gaussian distribution. The electrical intensity of the process is involved:

$$J_{arc} = d \frac{I_{elec}}{\pi r_0^2} \exp\left(-d \frac{(x-x_0)^2 + (y-y_0)^2}{r_0^2}\right) \quad (8)$$

where  $r_0$  is the arc radius,  $I_{elec}$  the intensity of the electric current,  $x_0$  and  $y_0$  the coordinates of the centre of the welding torch and  $d$  the parameter to be calibrated for the process. In the case of TIG welding with filler metal,  $d$  is generally equal to 3 [1].

To describe thermal effects at the interface, additional energy terms are used to modify the energy balance defined as follows:

$$\vec{q}_{total} \cdot (-\vec{n}) = Q_{arc} + s_{radiation} + s_{convection} \quad (9)$$

where  $\vec{q}_{total}$  is the total heat flux received by  $Q_{arc}$ ,  $s_{radiation}$ , and  $s_{convection}$

The description of these terms is given below:

- The heat input generated by the process is assumed to follow a surfacic Gaussian distribution:

$$Q_{arc} = d \frac{\eta_{elec} U_{elec} I_{elec}}{\pi r_0^2} \exp\left(-d \frac{(x-x_0)^2 + (y-y_0)^2}{r_0^2}\right) \quad (10)$$

where  $U_{elec}$  is the voltage of the electric current and  $\eta_{elec}$  the numerical efficiency applied to the power.

- Radiation losses:

$$s_{radiation} = -\varepsilon \sigma_B (T^4 - T_{amb}^4) \quad (11)$$

where  $\sigma_B$  is the Stefan-Boltzmann constant,  $\varepsilon$  the emissivity,  $T$  the temperature at the surface of the part and  $T_{amb}$  is the ambient temperature.

- Convection losses:

$$s_{convection} = -h_c (T - T_{amb}) \quad (12)$$

where  $h_c$  is a convective exchange coefficient.

## INTERFACE EQUATIONS FOR FLUID FLOW WITH THE FREE INTERFACE (ALE METHOD)

Under the action of the gravitational force, of the arc pressure and of the surface tension acting on the melt pool, the free surface of the molten metal deforms. Even though the amplitude of this deformation is directly related to the welding current and to the arc voltage, it remains relatively low in TIG compared to other welding processes such as MAG, during which the impact of the droplets considerably deforms the free surface [2].

The development of this model is based on the work of Ushio and Wu [3], also taken up by Le Guen [4] and Traidia [2]. It relies on a variational approach which consists in minimizing the total energy of the weld pool and in constraining it to a constant volume, defined by the mass flow rate of filler metal. The energy of the melt pool depends on the variation of the surface energy with the change in the corresponding area (linked to the consideration of the filler metal), on the potential energy due to gravity, and on the work done by arc pressure on the surface. We have designed this approach to predict the deformation of the surface of the weld pool in TIG welding with filler metal using COMSOL Multiphysics® software. The total energy can therefore be expressed according to equation (13).

$$E_{totale} = \iint_S \left( \gamma \left( \sqrt{1 + \phi_{|x}^2 + \phi_{|y}^2} - 1 \right) + \frac{1}{2} \rho g \phi^2 - P_{arc} \phi \right) dx dy \quad (13)$$

where  $S$  is the upper surface of the part,  $\gamma$  the surface tension,  $\rho$  the density of the metal,  $P_{arc}$  the arc pressure,  $\phi$  the space function giving, along the vertical axis  $z$ , the position of the surface of the melt pool with respect to the undistorted reference plane. The indices  $|x$  and  $|y$  correspond to the derivatives of the variables concerned with respect to  $x$  and  $y$ .

The arc pressure is defined by a gaussian distribution of the following form:

$$P_{arc} = dP_{max} \exp \left( -d \frac{(x-x_0)^2 + (y-y_0)^2}{r_0^2} \right) \quad (14)$$

with  $P_{max}$  the maximum pressure of the arc which is defined as follows:

$$P_{max} = \frac{\mu_{0elec} I_{elec}^2}{\pi r_0^2} \quad (15)$$

where, as a reminder,  $r_0$  is the arc radius,  $\mu_{0elec}$  is the magnetic permeability,  $I_{elec}$  is the intensity of the electric current,  $x_0$  and  $y_0$  are the coordinates of the centre of the welding torch, and  $d$  is the parameter to be calibrated for the process, (generally equal to 3 for TIG process application with filler metal [1]).

The Marangoni force, also known as the surface tension gradient force, is also considered. It is defined by the following equation:

$$\vec{F}_{marangoni} = \frac{\partial \gamma}{\partial T} \vec{\nabla}_S T \quad (16)$$

where  $\gamma$  is the surface tension defined according to a Sahoo law [5].

RESULTS AND DISCUSSION

EXPERIMENTAL VALIDATION

The development of the model is based on the TG4 model of the NeT network (Neutron Techniques Standardization for Structural Integrity) [6]. The material used is 316L stainless steel. The geometry of the TG4 groove as well as its dimensions are shown in Fig. . To reduce the duration of the calculation, a local adaptation of the mesh is performed (limiting the number of elements) and only the thermal equations are solved on the totality of the geometry. Consequently, fluid mechanics and electromagnetism are treated in a restricted domain encompassing the melt pool and slightly larger than its size. It is in this domain that the mesh is refined. Moreover, the model being symmetrical with respect to the plane (xz), only half of the geometry is modelled (Fig. 2).

**Table 1** Welding parameters used for TG4 groove [6]

Intensity	Voltage	Travel speed	Wire feed speed	Wire diameter
220 A	10 V	76.2 mm/min	29.67 mm/s	0.9 mm

The welding parameters used to fill the TG4 groove are presented in Table 1 [6] and are used in the numerical model. As the model does not consider the cycles of variation of the wire feed speed, the average value of this wire speed is chosen for the simulation.

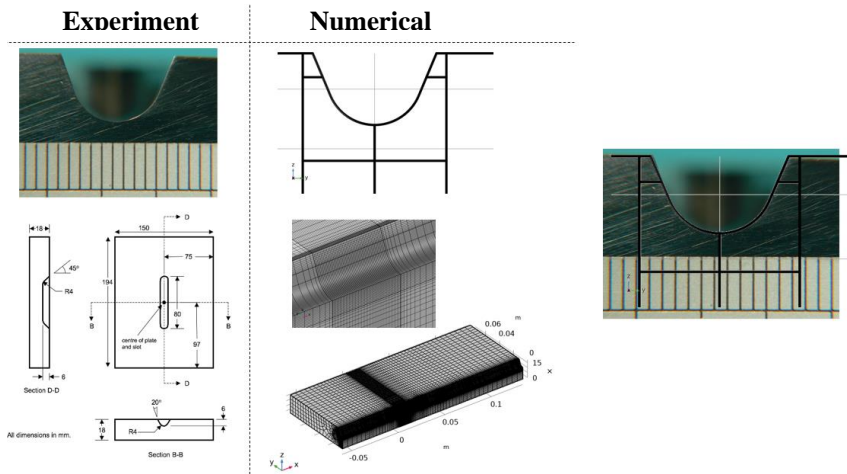


**Fig. 2** Experimental and numerical geometries of the TG4 mock-up groove [6]

The results presented below focus on the behaviour of the melt pool. First, one can observe in Fig. 3 the thermal field as well as the shape of the weld pool, highlighted by the purple curve formed by the Iso-value corresponding to the melting temperature (fixed

at 1700 K). Then in Fig. 4 are represented the velocity field and vectors of the fluid flow within the melt pool.

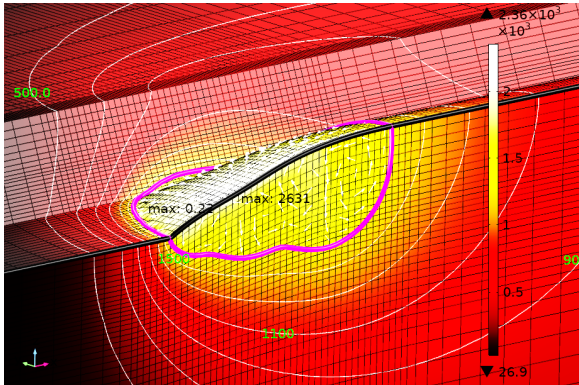


**Fig. 3** Temperature field (in K) in the melt pool of the first bead

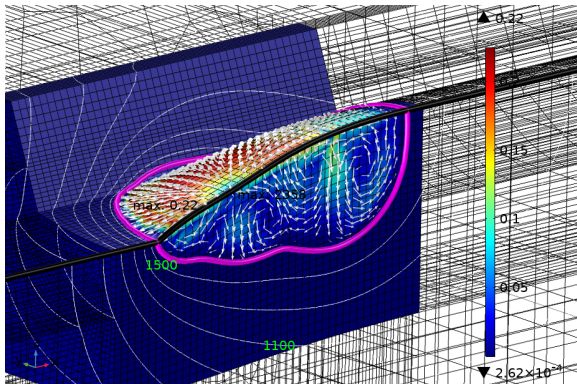


**Fig. 4** Velocity field and vectors (in  $\text{m.s}^{-1}$ ) of the fluid flow in the melt pool of the first bead

To estimate the validity of the model, comparisons between numerical and experimental results are made. More specifically, are compared:

- Macrographs;
- The thermal evolution obtained by thermocouples.

Fig. 5 shows a good agreement between the melted zones obtained experimentally in the case of the TG4 study (surface in the centre of the figure in light grey) and the melted zones generated by numerical simulation (represented by the purple outline).

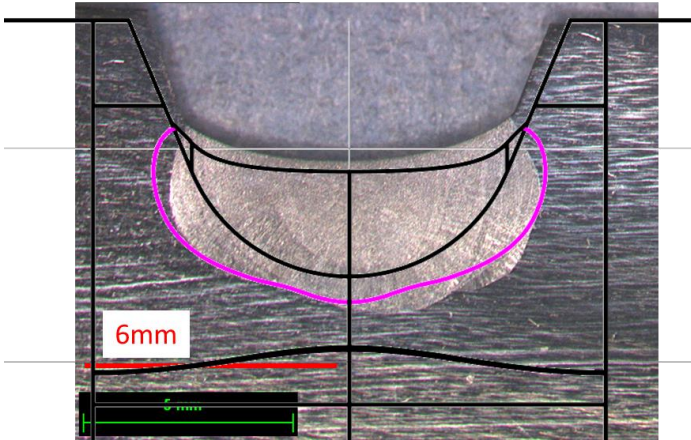


**Fig. 5** Comparison of experimental (light grey) and numerical (purple) melted zones

The next step of validation consists in comparing the thermal numerical field to the experimental one. To that purpose, the temperature values recorded by one of the thermocouples of the TG4 study [6] are used as references. This thermocouple is located at the bottom surface of the groove, aligned with the welding direction and centred on the torch position. The numerical model being stationary, it is necessary before to compare simulation results with the thermocouple data, to transform them to obtain a temporal evolution. To this end, temperatures calculated along the central line located below the groove (shown in blue in Fig. 6) are transformed using the ratio of the position along the welding direction ( $x$ ) and the welding speed:

$$t = \frac{x}{V_s} \quad (17)$$

with  $x$  the position along the welding direction and  $V_s$  the welding speed.

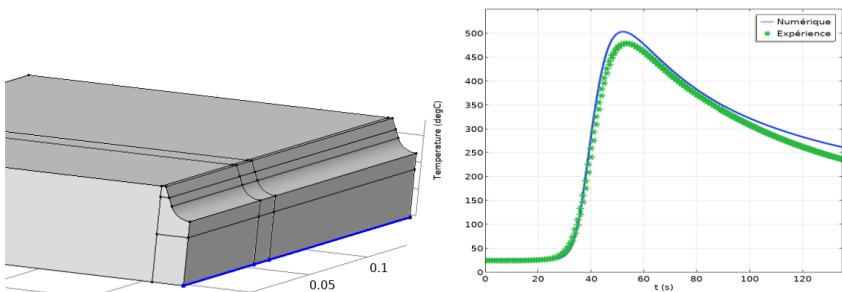


**Fig. 6** Representation of the segment used for the comparison of numerical temperatures and temperature measurements recorded experimentally by the thermocouple

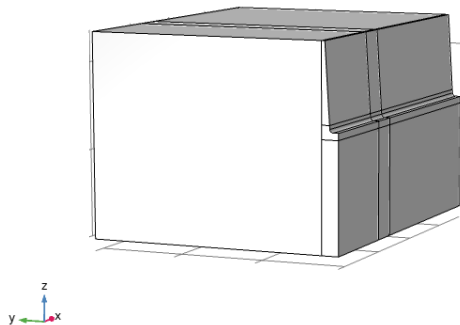
Fig. 6 allows for the comparison of the temperature evolution observed experimentally (via the thermocouple) with the one obtained by simulation. Although the model overestimates the maximum temperature (around  $20^{\circ}\text{C}$ ), we can notice similar trends.

#### PULSED TIG MODEL FOR ORBITAL NARROW

The simulation of the TG4 groove leads to the validation of the model. Indeed, the results indicate its ability to predict the geometry of the bead and the thermal field of the part based on the welding parameters.

To consider the cycles of intensity pulsation, it is then necessary to realize a transient model. A first approach would consist in modelling the formation of the bead from its beginning to its steady state. The main advantage of this model is that the shape of the bead can be simulated from the very first moments of welding. The main disadvantage is that it requires the resolution of fluid mechanics equations over a wide area, which leads to significant calculation times (about a month). This first approach should be avoided when dealing with sensitivity studies on process parameters and therefore is inappropriate in the context of this study.

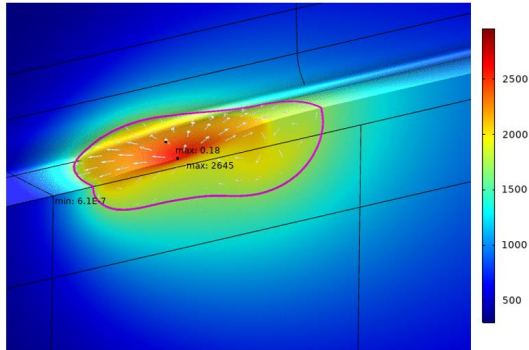
The innovative approach described below enables the integration of the transient aspect of the studied problem, with the advantage of limiting the computational times. It is based on two successive calculations: a stationary calculation identical to the one used in the case of the TG4 model, and a transient magneto-thermohydraulic calculation without filler metal. The first calculation aims at obtaining the established shape of the weld bead from averaged welding parameters, such as the intensity of the electric current. The results obtained at the end of the stationary calculation is then used as initial conditions for the transient calculation. This calculation allows for the simulation of the pulsation cycles of the current intensity and for the study of the consequences of these cycles on the behaviour of the melt pool.



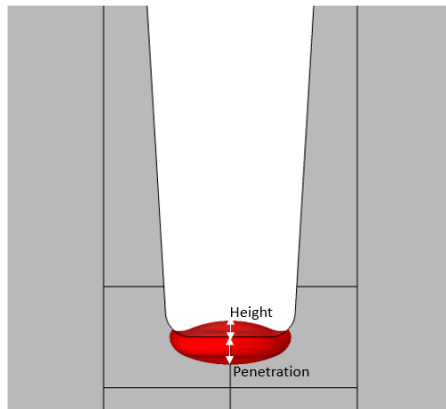
**Fig. 7** Geometry of the narrow gap model with a symmetry of the plane (xz)

Considering the shape of the bead obtained during the transient calculation and assuming a negligible deformation of the weld pool during the pulsation cycles, it was

decided not to model the filler metal. As a note, less than 4 days are needed to simulate 4 seconds of physical time (*i.e.*, real welding time), since the duration of the calculation is around 10 hours for the stationary model and varies from 24 to 72 hours for the transient model. The dimensions of the orbital narrow gap model are confidential. Nevertheless, the geometry of the groove is presented in Fig. 7. The material used is of stainless-steel type. The process parameters used to develop the model are confidential Framatome data.



**Fig. 8** Thermal field (in K) and velocity vectors of the fluid flow within the melt pool. The purple curve corresponds to the melting isovalue (1700 K).



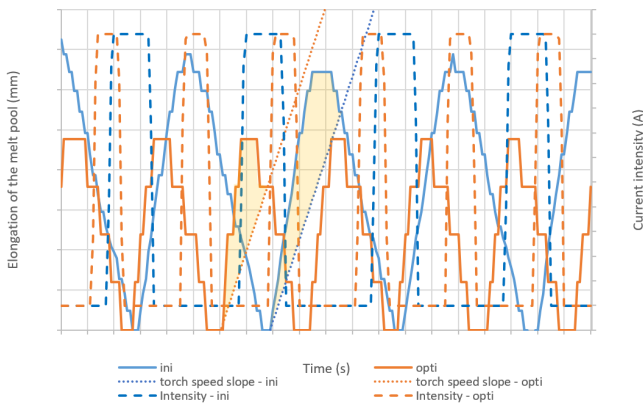
**Fig. 9** Numerical macrograph with the melted zone represented in red (temperature above 1700 K)

Fig. 8 and Fig. 9 summarize the simulation results. Fig. 9 shows the thermal field and the fluid flow velocity vectors within the weld pool. The shape of the melt pool is

represented by the purple curve generated by the fusion isovalue (temperature of 1700 K). Fig. 9, corresponds to the numerical macrograph simulated.

The results from the transient calculation describe the variations in shape of the melt pool during the intensity pulsation cycles. Fig. 10, Fig. 12, Fig. 13 and Fig. 14 show, as a function of intensity, the variations in elongation, width, penetration, and volume of the weld pool respectively. In these figures are plotted:

- Continuous lines: representing the characteristic pool dimensions;
- Dashed lines: depicting the current intensities;
- Dotted lines: corresponding to the slope of the speed of the welding torch (only Fig. 10).



**Fig. 10** Evolution of the elongation of the melt pool during the intensity pulsation cycles using the initial (blue curves) and optimized (orange curves) process parameters

Two different sets of parameters are tested within the framework of this study: an initial one and an “optimized” one that leads to the obtention of a more stable weld pool. During stationary simulations the power is determined by averaging the parameters related to the electric current (intensity and voltage). In the present case, the two sets of parameters, “initial” and “optimized”, give the same average power, which would lead to identical results for a stationary simulation. Therefore, it is important to define a transient model to be able to perform an accurate analysis of the behaviour of the melt pool. In the following, the results of simulations carried out with the initial set of parameters are identified by the blue curves and those related to the optimized set of parameters by the orange curves.

Comparing the curve of the welding torch speed of advance and the elongation of the melt pool (Fig. 10, Fig. 11), one can observe that the pool grows faster than it moves. Indeed, the two areas represented in yellow in the figure located above the dotted lines (slope of the speed of the torch), and under the continuous lines show that the pool grows faster than the torch moves. The weld bead therefore undergoes a remelting during

electric current intensity pulsations. Intensity pulsation cycles also highlight the disadvantage of using stationary calculations.

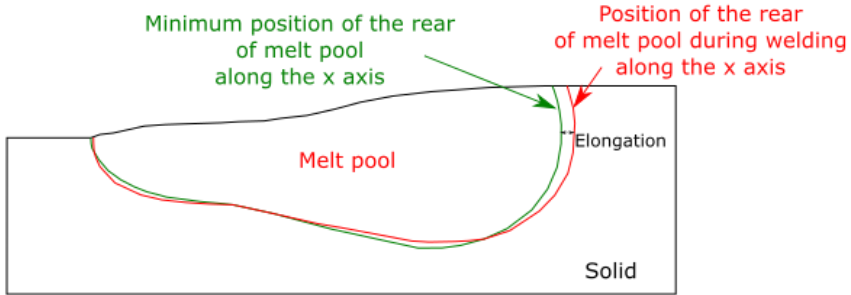


**Fig. 11** Diagram representing the elongation of the melt pool

The results obtained being confidential, only the analysis of the relative deviations,  $\epsilon_{difference}$  is made:

$$\epsilon_{difference} = \frac{variation_{opti} - variation_{ini}}{variation_{ini}} \quad (18)$$

Table 2 summarizes the relative deviations obtained for the various observables, namely the elongation of the melt pool, its width, its penetration, its volume, its maximum temperature and its maximum flow velocity. This table shows that intensity pulsation cycles have a significant impact on the shape of the melt pool. Indeed, the table highlights the fact that the weld pool undergoes less significant variations during a pulsation cycle with the optimized parameters than with the initial parameters, since these variations are reduced by 48% if we focus on the volume of the weld pool. Fig. 12, Fig. 13 and Fig. 14 reinforce the conclusions of Table 2.

**Table 2** Relative deviations of the variations of the different observables

Observables	Relative deviation of the variations between initial and optimized parameters
Elongation of the tail of the weld pool	-28 %
Width	-26 %
Penetration	-3 %
Volume	-48 %
Maximum temperature	-4,56 %
Maximum fluid flow velocity	-5,71 %

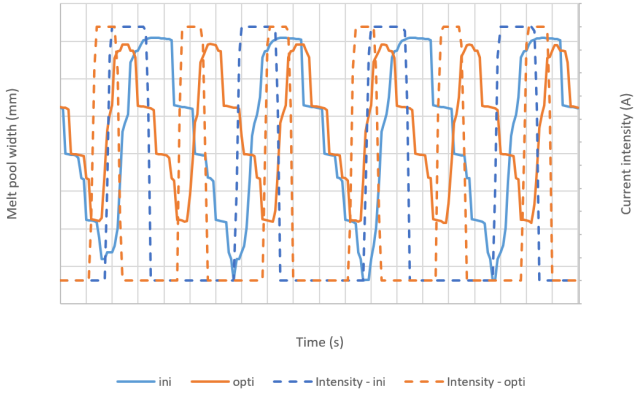


**Fig. 12** Evolution of the width of the melt pool during cycles of intensity pulsation for the initial (blue curves) and optimized (orange curves) parameters

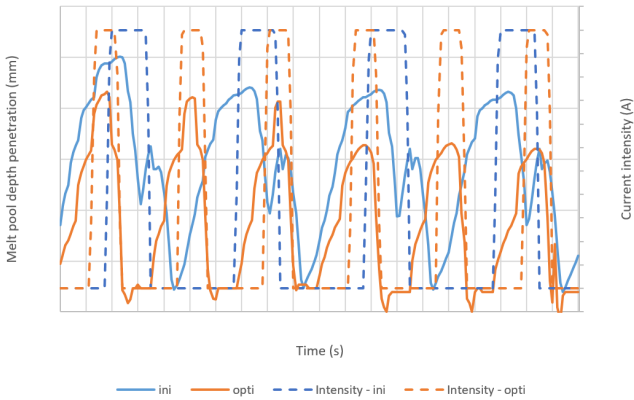


**Fig. 13** Evolution of the melt pool depth penetration during intensity pulsation cycles for initial (blue curves) and optimized (orange curves) parameters

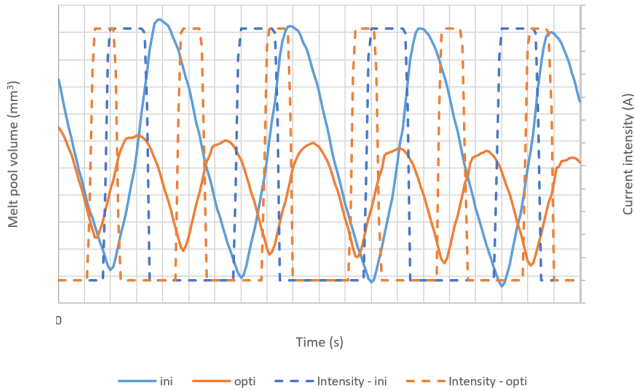


**Fig. 14** Evolution of the melt pool volume during intensity pulsation cycles for initial (blue curves) and optimized (orange curves) parameters

## CONCLUSION

This paper presents some of the work carried out by Framatome in the modelling of the melt pool formed by welding processes aiming at the contribution of the improvement of the control of these processes.

Framatome being interested in the welds used in the nuclear industry, the objective of this study was to develop a model suitable for industrial configurations of the Orbital Narrow Gap GTA Welding type to improve the understanding of the influence of the operating parameters on the behaviour of the weld pool. First step consisted in developing a model consistent with the physics of the weld pool, based on experimental data. A model already used by Framatome was chosen, including a narrow chamfer. After comparing the experimental and numerical temperatures and weld pool shapes, a good agreement was found, allowing for the validation of the defined simulation method for a typical welding configuration.

The methodology was then specially adapted to Orbital Narrow Gap GTA Welding processes, which use a pulsed transfer mode. To this end, in addition to the initial stationary model, a transient magneto-thermohydraulic model considering the cycles of pulsations was developed. Finally, the developed approach offers promising results in reasonable computation times.

## References

- [1] F. HEJRIPOUR, D. T. VALENTINE AND D. K. AIDUN: 'Study of mass transport in cold wire deposition for Wire Arc Additive Manufacturing', *International Journal of Heat and Mass Transfer*, no. 0017-9310 DOI: 10.1016/j.ijheatmasstransfer.2018.04.092, 2018.
- [2] A. TRADIA: *Multiphysics modelling and numerical simulation of GTA weld pools*, PhD Thesis, Ecole Polytechnique, 2011.

- [3] M. USHIO and C. WU: 'Mathematical modeling of three-dimensional heat and fluid flow in a moving gas metal arc weld pool', *Metallurgical and Materials Transactions B-Process Metallurgy and Materials Processing Science*, no. 28:509-516, 1997.
- [4] E. LE GUEN, M. CARIN, R. FABBRO, F. COSTE and P. LE MASSON: '3D heat transfer model of hybrid laser Nd :Yag-MAG welding of S355 steel and experimental validation', *International Journal of Heat and Mass Transfer*, vol. 54, p. 1313-1322, 2011.
- [5] P. SAHOO, T. DEBROY and M. MCNALLAN: 'Surface tension of binary metal-surface active solute systems under conditions relevant to welding metallurgy', *Metall Mater Trans B*, vol. 19, p. 483-491, 1988.
- [6] M. C. SMITH and A. C. SMITH: *2009-09-29\_TG4\_simulation\_protocol*, 2009.
- [7] C. S. WU, P. C. ZHAO and Y. M. ZHANG: 'Numerical simulation of transient', *Welding journal*, 83(12):330s-335s, 2004.

# A NUMERICAL STUDY ON THE SUPPRESSION OF A DETRIMENTAL WELD POOL PROFILE IN WIRE FEED LASER BEAM WELDING BY MAGNETOHYDRODYNAMIC TECHNIQUE

X. MENG\*, A. ARTINOV\*, M. BACHMANN\*, Ö. ÜSTÜNDAĞ\*,  
A. GUMENYUK\*, M. RETHMEIER\*\*.\*.\*.\*.\*.\*

\*BAM Bundesanstalt für Materialforschung und -prüfung, 12205, Unter den Eichen 87, Berlin, Germany

\*\*Technical University Berlin, Institute of Machine Tools and Factory Management, 10587, Pascalstraße 8-9, Berlin, Germany

\*\*\*Fraunhofer Institute for Production Systems and Design Technology, 10587 Pascalstraße 8-9, Berlin, Germany

DOI 10.3217/978-3-85125-968-1-08

## ABSTRACT

The weld quality and the possible defect formation are directly determined by the weld pool shape and the thermo-fluid dynamics therein. In this paper, an untypical weld pool profile, i.e., elongated at its top and bottom but narrowed at the middle, is found experimentally and numerically in the wire feed laser beam welding. The detrimental influence of the weld pool narrowing on the element transport is analyzed and discussed. A magnetohydrodynamic technique is utilized to suppress the narrowing, aiming at a more homogenous element distribution. It is found that a low-temperature region is formed in the middle of the weld pool due to the interaction of the two dominant circulations from the top and bottom regions. The weld pool is significantly narrowed due to the untypical growth of the mushy zone in the low-temperature region, which results in a direct blocking effect on the downward flow and the premature solidification in the middle region. The Lorentz force produced by a transverse oscillating magnetic field shows the potential to change the flow pattern into a single-circulation type and the low-temperature-gradient region is mitigated. Therefore, the downward transfer channel is widened, and its premature solidification is prevented. The numerical results are well validated by experimental measurements of metal/glass observation and X-ray fluorescence element mapping.

Keywords: thermo-fluid flow, element transport, laser beam welding, magnetohydrodynamics, multi-physical modeling

## INTRODUCTION

Laser beam welding (LBW) has attracted more and more academic and industrial attention during the last decades. It shows several superiorities, e.g., precise and highly localized heat input, excellent penetration capacity, low distortion, *etc.* Nonetheless, the utilization of the small laser spot and the resulting high energy density may lead to drawbacks during the practical application of the LBW process. The small laser spot

makes the weld seam sensitive to assembly tolerances of the workpieces. Furthermore, a non-negligible loss of important alloying elements, e.g., Mg or Zn in Al alloy, may occur due to vigorous evaporation [1].

The issues described above can be mitigated or solved by the usage of filler wire, namely, the wire feed laser beam welding (WFLBW). The gap tolerance sensitivity can be significantly reduced by the liquid filler metal. By choosing a filler wire with proper chemical composition, important alloying elements can be supplemented to the weld pool, thus achieving better control over the metallurgical process. However, the weld pool with narrow and deep geometry and high solidification rate causes difficulties in the downward transfer of the filler metal. Often, the filler material accumulates on the upper part of the final weld, undermining the homogeneity of the weld properties [2].

It has been confirmed in numerous studies that during partial penetration LBW the weld pool is typically elongated at the upper region, driven by the recoil pressure and the Marangoni shear stress, compared to the relatively short bottom region [3-6]. Recently, a different type of weld pool shape was observed both experimentally and numerically [7-9]. The weld pool boundary is elongated at the top region and bottom region but significantly narrowed in the middle. Up to now, only a few works have been reported on this untypical weld pool narrowing and its influence on the transport phenomena. It can be easily foreseen that the narrowed region may further deteriorate the downward transport of the filler metal once it is formed during the WFLBW.

Since 2000, magnetohydrodynamic (MHD) technology has shown more and more importance to improve the capacity of the traditional LBW. Different beneficial effects can be produced by choosing a magnetic field with proper position, strength, frequency, and orientation, such as deceleration of the liquid metal in the weld pool [10], electromagnetic support against gravity to eliminate sagging of the weld seam [11], electromagnetic exclusive force to suppress porosity [12], and refinement of the grain structure [13]. The work of Gatzen suggested that during WFLBW of Al alloys, the Si from the filler wire was mixed more uniformly when employing a coaxial alternating magnetic field with a frequency below 25 Hz [14]. In the authors' previous study, a transverse high-frequency magnetic field was imposed from the top side of the workpiece during WFLBW of austenitic steel with filler wire of nickel-based Inconel 625 alloy [15].

As the computational capacity improves, the multi-physical modeling provides great potential to obtain quantitative descriptions of the weld pool behavior under the influence of a magnetic field. A three-dimensional steady-state MHD model with a predefined keyhole profile was developed by Bachmann et al [16-18]. The influences of static and alternating magnetic fields on the weld pool behavior and its prevention of the sagging defect were investigated. The onset of the bulging phenomenon which was characterized by an elongation of the bottom region was reported in the study as well but the impact of the magnetic field on this phenomenon was not further discussed [18]. The enhancement of the material mixing in the weld pool from a low-frequency coaxial magnetic field was explained by Gatzen et al. using an MHD model with a fixed keyhole [19]. The inhomogeneity problem of the element distribution was moderated, but a spatial periodicity of the concentration remained due to the periodic Lorentz force.

Recently, more sophisticated MHD models were developed, in which the free surface tracking algorithm such as volume-of-fluid (VOF) or level-set method was implemented to calculate the transient keyhole shape [20, 21]. Different beneficial effects from the

LBW with a magnetic field, including sagging defect elimination by the electromagnetic support and grain refinement by the thermoelectric current effect, were investigated more deeply. A multi-physical model with the transient keyhole evolution was developed by the authors for the investigation of the electromagnetic stirring enhanced wire feed laser beam welding (EMS-WFLBW) [22-24]. It should be noted that the weld pool in the above studies shows a common shape, i.e., elongated at the upper region and relatively short at the bottom. The problem of inhomogeneous element distribution originates from the steep weld pool shape and the high solidification rate which are inevitable during all deep-penetration LBW processes.

In the present study, a narrowing phenomenon in the middle of the weld pool during WFLBW is found by a real-time metal/glass observation and a multi-physical modeling. An X-ray fluorescence (XRF) element mapping is implemented for the characterization of the material mixing. The formation mechanism of the weld pool narrowing is analyzed and its resulting detrimental effect on the element transport is discussed. By introducing an external oscillating magnetic field, the narrowed region is successfully suppressed, providing a better material mixing in the final weld seam. The influences of the Lorentz force on the transport phenomena in the weld pool and the suppression of the weld pool narrowing are studied as well.

## EXPERIMENTAL SETUP

The base metal was chosen as AISI 304 stainless steel, and the filler wire was NiCr20Mo15 alloy with a diameter of 1.1 mm. A distinct difference in the Ni content existed between the base metal and the filler material (9 % vs. 64 %). The dimensions of the base metal were 200 mm × 60 mm × 10 mm. The laser beam welding was performed with an IPG YLR 20000 laser system. The detailed welding parameters are listed in Table 1.

**Table 1** Welding parameters and laser optical parameters

<b>Welding parameters</b>	<b>Value</b>
Laser power	6.5 kW
Welding speed	1.3 m/min
Wire feeding rate	2.1 m/min
Wire feed angle	33° with respect to the base metal
Shielding gas flow rate	20 L/min
Laser spot diameter at the focal plane	0.56 mm
Wavelength	1070 nm
Focal position	- 3.0 mm

An in-house designed electromagnet was employed to produce sufficient magnetic flux density and frequency [12]. The electromagnet was fixed 2 mm above the base metal. A Hall sensor was used to measure the spatial distribution of the magnetic flux density in cold metal conditions. A metal/glass configuration was applied to observe the real-time weld pool profile in the longitudinal section without filler material [25]. A high-speed camera operating at the frame rate of 3000 Hz was used to capture the weld pool shape from the metal/glass interface. The optical axis of the lens was parallel with the welding plane and perpendicular to the welding direction.

After the welding experiment, the metallurgical specimens were mechanically cut from the weld specimens for transverse and longitudinal observation. The specimens were ground, polished, and etched by a V2A etchant (100 ml H<sub>2</sub>O, 100 ml HNO<sub>3</sub>, and 10 ml HCl). XRF mapping was conducted to measure the Ni content on the longitudinal section to characterize the material mixing.

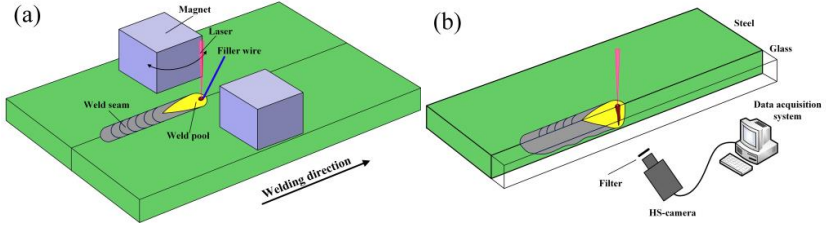


**Fig. 1** Schematic of the experimental setup: (a) EMS-WFLBW, (b) metal/glass observation

## MATHEMATICAL MODELING

A 3D MHD model coupled with the VOF algorithm and element transport equation is developed to calculate the temperature and velocity fields, the keyhole dynamics, the element transport, and the electromagnetic phenomena in both WFLBW and EMS-WFLBW. The flow regime in the weld pool is considered laminar, and the fluid is assumed as Newtonian and incompressible.

### GOVERNING EQUATIONS

The keyhole geometry, as well as the weld pool free surface, is tracked by the VOF method, which is governed by the following equation:

$$\frac{\partial F}{\partial t} + \nabla \cdot (\vec{v}F) = S_F \quad (1)$$

where  $F$  is the volume fraction,  $t$  is the time,  $\vec{v}$  is the velocity vector and  $S_F$  is the source term from the filler metal. The free surface, more precisely the interface between the steel and the Ar gaseous phase, is located within the cells with a volume fraction between 0 and 1.

The transport phenomena can be calculated by solving the conservation equations of mass, momentum, energy, and chemical species, which are defined as follows:

$$\nabla \cdot \vec{v} = \frac{m_w}{\rho} \quad (2)$$

$$\rho \left( \frac{\partial \vec{v}}{\partial t} + (\vec{v} \cdot \nabla) \vec{v} \right) = -\nabla p + \mu \nabla^2 \vec{v} - \mu K \vec{v} + m_w \vec{v}_w + \vec{S}_m \quad (3)$$

$$\rho \left[ \frac{\partial h}{\partial t} + \vec{v} \cdot \nabla h \right] = \nabla \cdot (k \nabla T) + h_w + S_q \quad (4)$$

$$\frac{\partial F_s \rho_s w}{\partial t} + \nabla \cdot (F_s \rho_s \vec{v} w - F_s D \nabla w) = S_{\text{add}} \quad (5)$$

In Eq. (2),  $\rho$  is the density,  $m_w$  is the volumetric mass flow rate from the filler wire. In Eq. (3),  $p$  is the pressure,  $\mu$  is the dynamic viscosity,  $\vec{v}_w$  is the velocity of the molten filler metal,  $K$  is the Carman–Kozeny equation coefficient, which is responsible for the deceleration of the liquid in the mushy zone, and  $\vec{S}_m$  is the momentum source term. In Eq. (4),  $T$  is the temperature,  $k$  is the thermal conductivity,  $h$  is the enthalpy,  $h_w$  is the energy source from the molten filler metal, and  $S_q$  is the additional energy source term. In Eq. (5),  $w$  is the weight percentage,  $F_s$  is the steel volume fraction,  $D$  is the diffusion coefficient of Ni-atoms in iron, and  $S_{\text{add}}$  is the source term from the filler wire.

A magnetic induction equation, rather than the full set of Maxwell equations, is solved for the MHD behavior. This method does not require including the electromagnet in the simulation domain. Instead, the experimentally measured external magnetic field  $\vec{B}_0$  is implemented as input data, as given below:

$$\frac{\partial \vec{b}}{\partial t} + (\vec{v} \cdot \nabla) \vec{b} = \frac{1}{\mu_m \sigma_e} \nabla^2 \vec{b} + \left( (\vec{B}_0 + \vec{b}) \cdot \nabla \right) \vec{v} - (\vec{v} \cdot \nabla) \vec{B}_0 \quad (6)$$

where  $\mu_m$  is the magnetic permeability,  $\sigma_e$  is the electrical conductivity,  $\vec{b}$  is the induced magnetic field from the liquid flow. For simplification, the solidified 304 stainless steel is assumed to keep a perfectly austenitic microstructure, thus  $\mu_m$  is set to 1.

By using  $\vec{B}_0$  and  $\vec{b}$ , the induced Lorentz force which is the driving force from the MHD technique to adjust the weld pool behavior can be calculated as:

$$\vec{j} = \frac{1}{\mu_m} \nabla \times (\vec{B}_0 + \vec{b}) \quad (7)$$

$$\vec{F}_L = \vec{j} \times \vec{B} = \vec{j} \times (\vec{B}_0 + \vec{b}) \quad (8)$$

where  $\vec{j}$  is the current density and  $\vec{F}_L$  is the Lorentz force.

#### PHYSICAL MODELS AND NUMERICAL IMPLEMENTATION

A ray tracing method with a virtual refinement technique is implemented to calculate the multiple reflections of the laser beam and the Fresnel absorption on the keyhole surface. The laser beam was discretized by a sufficient number of sub-rays, and each sub-ray had its location-dependent energy density and initial incidence angle [26]. The laser energy input together with the energy dissipation due to convection, radiation, and evaporation

was employed in the model for the calculation of the temperature field. The recoil pressure as a function of the local temperature [27] was applied to the keyhole surface. The dynamic balance between recoil pressure, hydrostatic pressure, hydrodynamic pressure, and Laplace pressure was calculated to determine the transient keyhole geometry. The thermo-capillary flow driven by the steep temperature gradient on the top surface of the weld pool and the buoyancy based on the Boussinesq approximation were considered as well. Due to the application of the VOF method, all surficial terms should be converted into localized volumetric terms using the continuum surface force method [28]. Therefore, physical mechanisms that contribute to the  $\vec{S}_m$  term included recoil vapor pressure, surface tension, and Marangoni stress. The laser heat flux and the thermal dissipation were also converted and implemented in the  $S_q$  term.

ANSYS Fluent 19.5 was used to solve all transport equations, in which the second order upwind method was utilized for the spatial discretization of the convection-diffusion equations. The PISO algorithm was applied for the pressure-velocity coupling. A simulation with a physical time of 1.5 s was calculated firstly for the reference case of WFLBW. The obtained data were used as the initial condition for the subsequent calculation of MHD cases (1.5 s - 3.0 s). Table 2 lists the multiple simulation cases with different electromagnetic parameters.

Detailed descriptions of the physical models, boundary conditions, numerical considerations, etc. can be found in the authors' previous studies [22-24].

**Table 2** Electromagnetic parameters used in the investigation

Case	Magnetic flux density (mT)	Frequency (kHz)	Angle with respect to transverse direction (deg)	Approach
Ref	-	-	-	Num. & Exp.
1	250	3.6	10	Num. & Exp.
2	250	1.8	10	Num.
3	190	3.6	10	Num.
4	125	3.6	10	Num.

## RESULTS AND DISCUSSION

### MODEL VALIDATION

A comparison of the fusion line shapes between the experimental and numerical results is provided in Fig. 2. The model shows a high accuracy in predicting the weld penetration as well as the weld width. The energy absorption on the keyhole surface and the energy allocation inside the weld pool are influenced by the Lorentz force by changing the keyhole dynamics and the backward flow of the liquid metal [23].

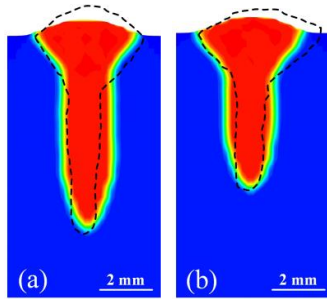


**Fig. 2** Fusion line shapes from the calculations and experiments: (a) reference case, (b) case 1

The calculated Ni distributions along the longitudinal section are compared with the XRF mapping in Fig. 3 for further validation of the model. The final weld from the WFLBW shows a quite inhomogeneous Ni distribution, in which the top Ni-rich zone and the bottom Ni-poor zone are sharply separated by a narrow transition region, as shown in Fig. 3 (a) and (b). The downward transport of the filler metal is significantly enhanced under an oscillating magnetic field (250 mT, 3.6 kHz, 10°), resulting in an improved element dilution, as seen in Fig. 3(c) and (d). The proposed model also provides a successful prediction of this phenomenon. Thus, it can be concluded that the established MHD model can provide an accurate prediction of the element distribution.

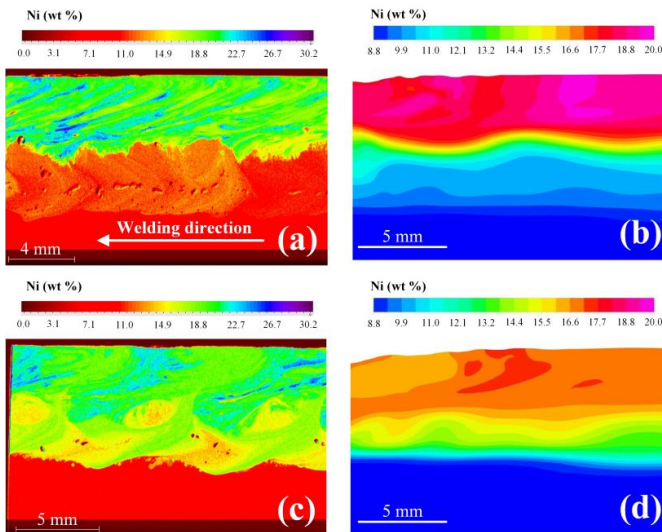


**Fig. 3** Calculated and XRF-measured Ni distribution on the longitudinal section: (a) and (b) from reference case, (c) and (d) from case 1

The transient weld pool profile can be obtained by the metal/glass observation, as shown in Fig. 4. It should be noted that it is only a compromised way by far to experimentally validate the existence of the narrowed region in the WFLBW since the filler wire cannot be introduced in the metal/glass setup. In Fig. 4(a), the laser optical axis is located at the interface between the metal and the glass, thus the symmetrical plane of the weld pool is expected to be observed. The keyhole with high-temperature metal vapor shows the highest brightness in the image. Two strong circulations are formed in the top and bottom regions, respectively, and a noticeable narrowed region in the middle of the weld pool can be identified. The calculated liquid metal flow in Fig. 4 (b) shows a similar pattern compared to the experimental image, and the narrowing phenomenon in the middle region is also reproduced by the model. The solid lines correspond to the solidus and liquidus isotherms. The impact of the absence of the filler wire during the metal/glass observation can hardly be evaluated, making the quantitative comparison between Fig. 4 (a) and (b) challenging. Nevertheless, it can still be confirmed qualitatively that the developed multi-physical model has the capacity to reproduce the narrowing phenomenon in the WFLBW.

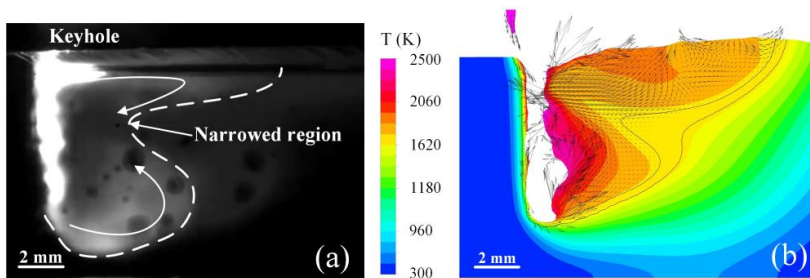


**Fig.4** Comparison of weld pool shapes between (a) metal/glass observation and (b) numerical calculation

#### FORMATION OF THE NARROWING PHENOMENON

As seen in Fig. 4, there are two predominant circulations in the fully developed weld pool. In the upper region, the liquid metal flows backward along the free surface, and then the flow is redirected to flow forward in the longitudinal section. This circulation contributes to the elongated profile of the weld pool and the sufficient material mixing in the upper region. Starting from the bottom of the keyhole, the liquid metal flows backward and upward along with the S/L interface, and subsequently toward the keyhole rear wall, forming the bottom vortex. A confluence of the two circulations is found in the middle region where the untypical narrowing occurs.

According to the available literature, it can be found that either the upper circulation [26, 29] or the lower circulation [30, 31] may dominate the weld pool flow in partial penetration LBW. Both flow patterns will produce a typical weld pool shape, i.e.,

elongated at the top and shortened at the bottom. The flow pattern in Fig. 4(b) which is dominated by two circulations with similar intensities may lead to a unique energy allocation in the weld pool. The free surface of the keyhole receives the laser energy from direct irradiation. For the bulk of liquid metal in the weld pool, the keyhole surface is an equivalent heat source. As the liquid metal flow with higher temperature leaves the vicinity of the keyhole, its enthalpy is gradually transferred into the surrounding liquid metal, which is the dominant energy transfer mechanism from the keyhole to the weld pool. The middle region is where the two circulations end, implying that it receives the least energy from the keyhole.

It should be noted that the liquidus line is significantly narrowed in the middle region, and the solidus boundary, on the contrary, has relatively inapparent narrowing. It results in a mushy zone thickness of up to 3.5 mm between the liquidus and solidus lines. By ignoring the mechanical gouging from the liquid metal, the geometry of the S/L interface is principally determined by the temperature gradient ahead of it [32]. A thermal equilibrium should be built in the S/L region of a weld pool in the quasi-steady state, which means that the energy entering through the liquidus boundary should be equal to the energy leaving the S/L region. The problem can be simplified into a one-dimensional thermal model if the metal flow in the mushy zone is neglected and a linear variation of temperature gradient  $G$  along the solidification direction is assumed:

$$k_1 G_1 \approx k_{\text{mu}} \frac{2(T_L - T_s)}{\delta_{\text{mu}}} \quad (9)$$

where  $k_1$  is the thermal conductivity at the liquidus temperature,  $G_1$  is the temperature gradient at the liquidus line,  $k_{\text{mu}}$  is the averaged thermal conductivity in the mushy zone, and  $\delta_{\text{mu}}$  is the mushy zone thickness. It should be noted that a factor of 2 is used in Eq. (9) for the correction of using the linear term [33].

Fig. 5 shows the temperature gradient along the longitudinal section. It is found that a low-temperature-gradient region forms at the confluent area of the two circulations where the temperature gradient is only  $2 \times 10^4$  K/m -  $3 \times 10^4$  K/m. By substituting the typical values ( $k_1 = 33$  W/m·K,  $k_{\text{mu}} = 31$  W/m·K,  $G_1 = 2.5 \times 10^4$  K/m) into Eq. (9), the mushy zone thickness is calculated as 4.1 mm, which is close to the numerical value of 3.2 mm. The result from the simplified one-dimensional model shows an acceptable agreement with the numerical outcome, implying that the model captures the main physical feature for the formation of the narrowed region. Therefore, it can be inferred that the formation of the low-temperature-gradient region directly leads to the untypical narrowing in the middle region of the weld pool.

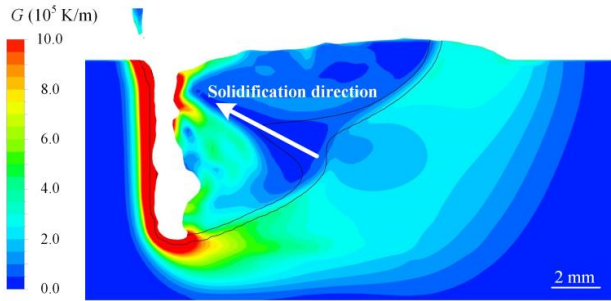


**Fig. 5** Temperature gradient in the longitudinal section in reference case

SUPPRESSION OF NARROWING BY MHD TECHNIQUE

The inhomogeneous element distribution has been recognized as a common problem in WFLBW even if the weld pool has no narrowed region [15, 23, 24]. In the present study, the narrowing phenomenon may lead to further deterioration of the material mixing in the weld pool. A time-averaged  $z$  velocity component within 0.3 s along the thickness direction (Line AB) in the longitudinal section is plotted in Fig. 6. The liquid metal shows a positive component of the  $z$  velocity component in the region near the rear keyhole wall (Line AB). The  $z$  velocity component can reach up to +0.05 m/s in the bottom region, but it decreases dramatically to nearly zero after flowing across the narrowed region. From the viewpoint of mass transfer, the weld pool is segmented by the narrowing region, which is apparently detrimental to material mixing.

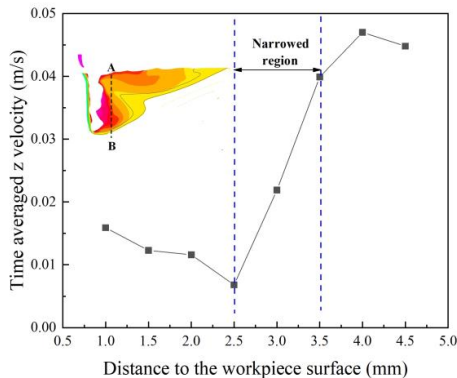


**Fig. 6** Time-averaged  $z$  velocity along the thickness direction in reference case, in which positive value represents upward velocity

Without the narrowing phenomenon, the weld pool shows a typical solidification sequence, i.e., it starts at the region near the fusion line, and the S/L interface moves toward the region near the central line [34-36]. Hereby, the channel for the downward transfer of the filler material remains open during the whole solidification procedure. A premature solidification occurs in the middle region of the transfer channel when the narrowed region is formed. At the position of 3 mm from the center of the keyhole, the middle region has solidified completely, preventing the downward transport of the filler metal.

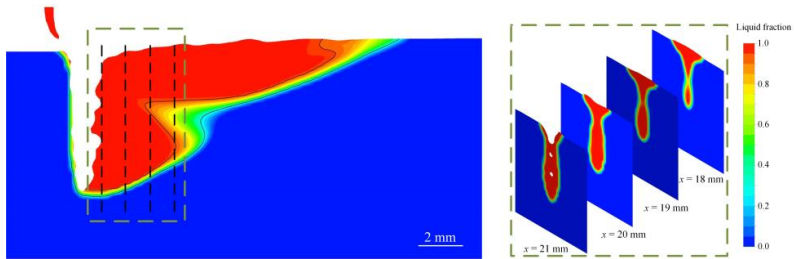


**Fig. 6** Premature solidification caused by the narrowing of the weld pool

The influence of magnetic field under a representative set of welding parameters causing the narrowing phenomenon is focused in this paper. The complex relationship between the welding parameters and magnetic parameters is not further discussed. As seen in Fig. 7, the narrowed region in the middle region of the weld pool is almost eliminated by a magnetic field of 250 mT and 3.6 kHz. More specifically, the thick mushy zone is diminished under the induced Lorentz force, from 3.5 mm to 0.7 mm. Previous studies suggest that a transverse oscillating magnetic field applied from the top side of the workpiece produces a time-averaged downward Lorentz force in the weld pool [16]. This Lorentz force produces a downward stream of liquid metal with a velocity of -0.05 m/s along Line AB. This flow pattern has a positive influence on the downward transport of the filler metal, improving the mixing in the final weld.

On the other hand, the Lorentz force also shows a significant influence on the solidification sequence of the weld pool, see Fig. 8. The premature solidification occurring in the reference case is eliminated, thus the downward transfer channel remains open. It provides an additional benefit to material mixing.

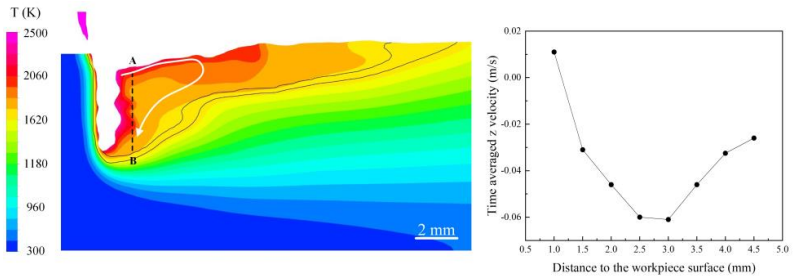


**Fig. 7** Weld pool profile (left) and time-averaged z velocity along the thickness direction (right) in case 1

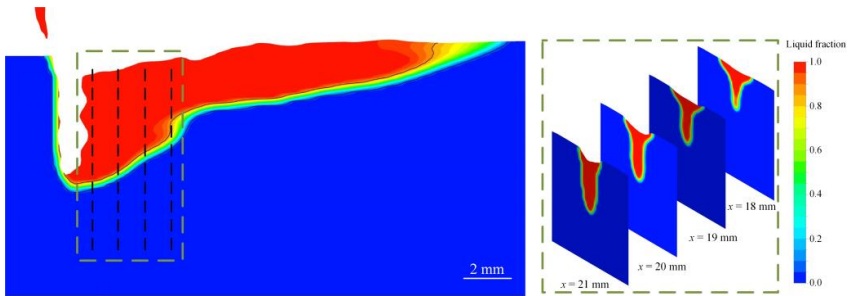


**Fig. 8** Solidification sequence of the weld pool in case 1

The Lorentz force contributes to the suppression of the weld pool narrowing from two aspects: by changing the temperature gradient in front of the liquidus boundary and by the direct mechanical gouging effect. Firstly, the flow regime varies from the two-circulation pattern into a single-circulation pattern, as shown in Fig. 7 by the white arrow. More energy can be transferred from the keyhole region to the middle region, which leads to the variation of temperature gradient in front of the liquidus boundary in Fig. 9. By substituting  $G_1 = 9 \times 10^4 \text{ K/m}$  into Eq. (9), a value of 1.2 mm for  $\delta_{mi}$  is obtained, which is in the right order of magnitude with the numerical results of 0.7 mm. It indicates that the change of the temperature gradient mainly contributes to the elimination of the narrowing. However, it shows a relatively larger error caused by the neglected mechanical gouging effect. The liquid metal flows vertically to the solidification direction, producing a stronger gouging effect on the S/L interface, which results in a thinner mushy zone.

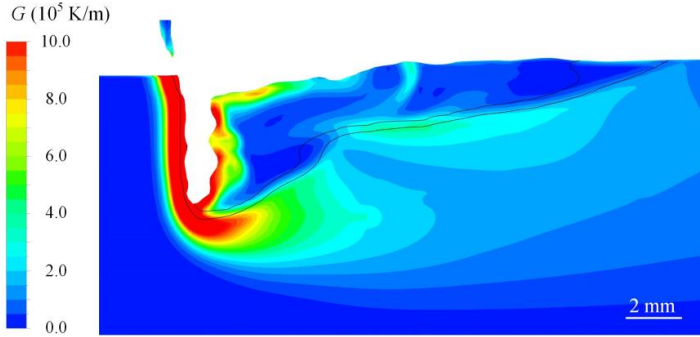


**Fig. 9** Temperature gradient in the longitudinal section in case 1

According to the above analysis, the thickness of the mushy zone in the middle region can be considered as an index to describe the extent of the narrowing. By involving the dimension of the weld pool, a dimensionless mushy zone thickness can be written as

$$\delta_{\text{mu}}^* = \delta_{\text{mu}} / w_{\text{WP}} \quad (10)$$

where  $w_{\text{WP}}$  is the width of the weld pool in the middle region. Higher  $\delta_{\text{mu}}^*$  means more pronounced weld pool narrowing. Different  $\delta_{\text{mu}}^*$  together with the averaged Ni content at the weld bottom under different magnetic flux densities are plotted in Fig. 10. When the magnetic flux density is below 125 mT, the Lorentz force cannot produce apparent suppression on the detrimental narrowing, whereby no improvement of mixing is obtained compared with the reference case. When the magnetic flux density increases from 125 mT to 250 mT, the dimensionless mushy zone thickness decreases dramatically from 0.39 to 0.18. It means that both the direct blocking effect caused by the narrowed region and the premature solidification are inhibited, thus the Ni increment reaches up to 5.7 %.

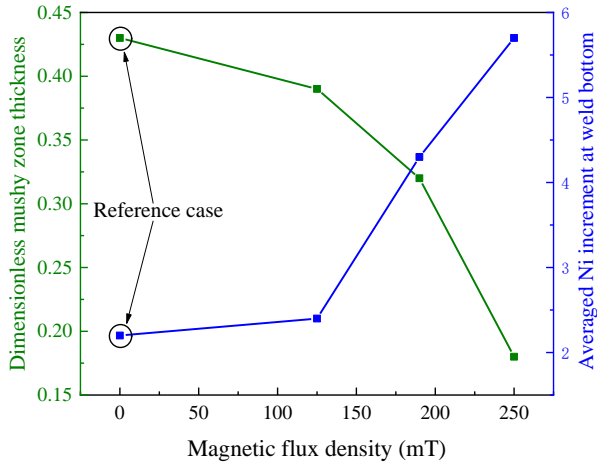


**Fig. 10** Influence of the magnetic flux density on the dimensionless mushy zone thickness and the averaged Ni content

## CONCLUSIONS

In the present study, multi-physical modeling and experiments are utilized to study an untypical narrowing phenomenon in the weld pool during WFLBW. The detrimental effect of the narrowed region on the material mixing is evaluated. An MHD technique is introduced to suppress the narrowing to achieve better material mixing. The main conclusions are drawn below:

- (1) The narrowing may occur when the weld pool flow is dominated by two circulations at the top and bottom regions. A low-temperature-gradient region forms, which leads to the untypical growth of the mushy zone, and correspondingly, the narrowing of the weld pool.
- (2) The narrowing phenomenon produces a direct blocking effect on the mass transport between the top and bottom regions. Premature solidification of the weld pool in the middle region is also caused by the narrowing, and thereby the downward transfer channel is closed completely.
- (3) The narrowing can be suppressed with a transverse oscillating magnetic field. Under the driving of the Lorentz force, the liquid metal flows downward, thus changing the flow pattern from two-circulation to a single-circulation type. The low-temperature-gradient region is mitigated, which significantly thins the mushy zone. The weld pool will not solidify prematurely in the middle region once the narrowed region is fully suppressed.

## ACKNOWLEDGEMENTS

This work is funded by the Deutsche Forschungsgemeinschaft (DFG, German Research Foundation) – project Nr. 416014189 (BA 5555/6-1) and Nr. 411393804 (BA 5555/5-2) .

## References

- [1] A. DILTHEY, A. GOUMENIOUK, V. LOPOTA, G. TURICHIN, E. VALDAITSEVA: ‘Development of a theory for alloying element losses during laser beam welding’, *J. Phys. D-Appl. Phys.*, 34 (1) (2001), 81.
- [2] X. MENG, A. ARTINOV, M. BACHMANN, M. RETHMEIER: ‘Numerical study of additional element transport in wire feed laser beam welding’, *Procedia CIRP*, 94 (2020), 722-725.
- [3] S. KATAYAMA, Y. KAWAHITO, M. MIZUTANI: ‘Elucidation of laser welding phenomena and factors affecting weld penetration and welding defects’, *Phys. Procedia*, (2010) 5, 9-17.
- [4] Y. KAWAHITO, Y.UEMURA, Y. DOI, M. MIZUTANI, K. NISHIMOTO, H. KAWAKAMI, S. KATAYAMA: ‘Elucidation of the effect of welding speed on melt flows in high-brightness and high-power laser welding of stainless steel on basis of three-dimensional X-ray transmission in situ observation’, *Weld. Int.*, 31(3) (2017), 206-213.
- [5] L. HUANG, X. HUA, D. WU, F. LI: ‘Numerical study of keyhole instability and porosity formation mechanism in laser welding of aluminum alloy and steel’, *J. Mater. Process. Technol.*, 252 (2018), 421-431.
- [6] S. PANG, L. CHEN, J. ZHOU, Y. YIN, T. CHEN: ‘A three-dimensional sharp interface model for self-consistent keyhole and weld pool dynamics in deep penetration laser welding’, *J. Phys. D-Appl. Phys.*, 44 (2) (2011) 025301.
- [7] H. WANG, M. NAKANISHI, Y. KAWAHITO: ‘Dynamic balance of heat and mass in high power density laser welding’, *Opt. Express*, 26 (5) (2018), 6392-6399.
- [8] S. MUHAMMAD, S. W. HAN, S. J. NA, A. GUMENYUK, M. RETHMEIER: ‘Numerical investigation of energy input characteristics for high-power fiber laser welding at different positions’, *Int. J. Adv. Manuf. Tech.*, 80 (5) (2015), 931-946.
- [9] Y. FENG, X. GAO, Y. ZHANG, C. PENG, X. GUI, Y. SUN, X. XIAO: ‘Simulation and experiment for dynamics of laser welding keyhole and weld pool at different penetration status’, *Int. J. Adv. Manuf. Tech.*, 112(7) (2021), 2301-2312.
- [10] M. KERN, P. BERGER, H. HUEGEL, ‘Magneto-fluid dynamic control of seam quality in CO2 laser beam welding’, *Weld. J.*, 79 (3) (2000), 72-78.
- [11] V. AVILOV, A. FRITZSCHE, M. BACHMANN, A. GUMENYUK, M. RETHMEIER: ‘Full penetration laser beam welding of thick duplex steel plates with electromagnetic weld pool support’, *J. Laser Appl.*, 28 (2) (2016) 022420.
- [12] A. FRITZSCHE, K. HILGENBERG, F. TEICHMANN, H. PRIES, K. DILGER, M. RETHMEIER: ‘Improved degassing in laser beam welding of aluminum die casting by an electromagnetic field’, *J. Mater. Process. Technol.*, 253 (2018), 51-56.
- [13] R. CHEN, C. WANG, P. JIANG, X. SHAO, Z. ZHAO, Z. GAO, C. YUE: ‘Effect of axial magnetic field in the laser beam welding of stainless steel to aluminum alloy’, *Mater. Des.*, 109 (2019), 146-152.
- [14] M. GATZEN: ‘Influence of low-frequency magnetic fields during laser beam welding of aluminium with filler wire’, *Phys. Procedia*, 39 (2012), 59-66.
- [15] X. MENG, M. BACHMANN, A. ARTINOV, M. RETHMEIER: ‘Experimental and numerical assessment of weld pool behavior and final microstructure in wire feed laser beam welding with electromagnetic stirring’, *J. Manu. Process.*, 45 (2019), 408-418.

- [16] M. BACHMANN, V. AVILOV, A. GUMENYUK, M. RETHMEIER: 'About the influence of a steady magnetic field on weld pool dynamics in partial penetration high power laser beam welding of thick aluminium parts', *Int. J. Heat Mass Transf.*, 60 (2013), 309-321.
- [17] M. BACHMANN, V. AVILOV, A. GUMENYUK, M. RETHMEIER: 'Experimental and numerical investigation of an electromagnetic weld pool support system for high power laser beam welding of austenitic stainless steel', *J. Mater. Process. Technol.*, 214 (2014), 578-591.
- [18] M. BACHMANN, V. AVILOV, A. GUMENYUK, M. RETHMEIER: 'Numerical simulation of full-penetration laser beam welding of thick aluminium plates with inductive support', *J. Phys. D-Appl. Phys.*, 45 (3) (2011) 035201.
- [19] M. GATZEN, Z. TANG, F. VOLLERTSEN: 'Effect of electromagnetic stirring on the element distribution in laser beam welding of aluminium with filler wire', *Phys. Procedia*, 12 (2011) 56-65.
- [20] R. ZHANG, X. TANG, L. XU, F. LU, H. CUI: 'Mechanism study of thermal fluid flow and weld root hump suppression in full penetration laser welding of Al alloy with alternating magnetic field support', *Int. J. Heat Mass Transf.*, 166 (2021) 120759.
- [21] F. X. CHEN, M. LUO, R. HU, R. LI, L. LIANG, S. PANG: 'Thermo-electromagnetic effect on weld microstructure in magnetically assisted laser welding of austenite steel', *J. Manu. Process.*, 41 (2019), 111-118.
- [22] X. MENG, A. ARTINOV, M. BACHMANN, M. RETHMEIER: 'Theoretical study of influence of electromagnetic stirring on transport phenomena in wire feed laser beam welding', *J. Laser Appl.*, 32 (2) (2020) 022026.
- [23] X. MENG, A. ARTINOV, M. BACHMANN, M. RETHMEIER: 'Numerical and experimental investigation of thermo-fluid flow and element transport in electromagnetic stirring enhanced wire feed laser beam welding', *Int. J. Heat Mass Transf.*, 144 (2019) 118663.
- [24] X. MENG, M. BACHMANN, A. ARTINOV, M. RETHMEIER: 'The influence of magnetic field orientation on metal mixing in electromagnetic stirring enhanced wire feed laser beam welding', *J. Mater. Process. Technol.*, 294 (2021) 117135.
- [25] A. ARTINOV, N. BAKIR, M. BACHMANN, A. GUMENYUK, M. RETHMEIER: 'Weld pool shape observation in high power laser beam welding', *Procedia CIRP*, 74 (2018), 683-686.
- [26] W. I. CHO, S. J. NA, C. THOMY, F. VOLLERTSEN: 'Numerical simulation of weld pool dynamics in high power disk laser welding', *J. Mater. Process. Technol.*, 212 (2012), 262-275.
- [27] V. SEMAK, A. MATSUNAWA: 'The role of recoil pressure in energy balance during laser materials processing', *J. Phys. D-Appl. Phys.*, 30 (18) (1997) 2541.
- [28] J. U. BRACKBILL, D. B. KOTHE, C. ZEMACH: 'A continuum method for modeling surface tension', *J. Comput. Phys.*, 100 (2) (1992), 335-354.
- [29] Y. KAWAHITO, K. NAKADA, Y. UEMURA, M. MIZUTANI, K. NISHIMOTO, H. KAWAKAMI, S. KATAYAMA: 'Relationship between melt flows based on three-dimensional X-ray transmission in situ observation and spatter reduction by angle of incidence and defocussing distance in high-power laser welding of stainless steel', *Weld. Int.*, 32 (7) (2018), 485-496.
- [30] D. ZHANG, M. WANG, C. SHU, Y. ZHANG, D. WU, Y. YE: 'Dynamic keyhole behavior and keyhole instability in high power fiber laser welding of stainless steel', *Opt. Laser Technol.*, 114 (2018), 1-9.
- [31] R. LIN, H. P. WANG, F. LU, J. SOLOMON, B. E. CARLSON: 'Numerical study of keyhole dynamics and keyhole-induced porosity formation in remote laser welding of Al alloys', *Int. J. Heat Mass Transf.*, 108 (2017), 244-256.
- [32] M. WU, A. VAKHRUSHEV, G. NUMMER, C. PFEILER, A. KHARICHA, A. LUDWIG: 'Importance of melt flow in solidifying mushy zone', *Open Transp. Phenom. J.*, 2 (2010), 16-23.
- [33] P. F. MENDEZ: 'Characteristic values in the scaling of differential equations in engineering', *J. Appl. Mech.*, 77 (2010) 061017-1.

- [34] W. TAN, Y. C. SHIN: 'Multi-scale modeling of solidification and microstructure development in laser keyhole welding process for austenitic stainless steel', *Comput. Mater. Sci.*, 98 (2015), 446-458.
- [35] W. HUANG, H. WANG, T. RINKER, W. TAN: 'Investigation of metal mixing in laser keyhole welding of dissimilar metals', *Mater. Des.*, 195 (2020) 109056.
- [36] L. J. ZHANG, J. X. ZHANG, A. GUMENYUK, M. RETHMEIER, S. J. NA: 'Numerical simulation of full penetration laser welding of thick steel plate with high power high brightness laser', *J. Mater. Process. Technol.*, 214 (8) (2014), 1710-1720.



# NUMERICAL ANALYSIS OF THE DEPENDENCY OF THE WELD POOL SHAPE ON TURBULENCE AND THERMODYNAMIC ACTIVITY OF SOLUTES IN LASER BEAM WELDING OF UNALLOYED STEELS

A. ARTINOV\*, P. KISING\*, M. BACHMANN\*, X. MENG\*,  
M. RETHMEIER\*\*,\*,\*\*

*\*Bundesanstalt für Materialforschung und -prüfung (BAM), Unter den Eichen 87, 12205 Berlin, Germany*

*\*\*Institute of Machine Tools and Factory Management, Technische Universität Berlin, Pascalstraße 8-9, 10587 Berlin, Germany*

*\*\*\*Fraunhofer Institute for Production Systems and Design Technology, Pascalstraße 8-9, 10587 Berlin, Germany*

DOI 10.3217/978-3-85125-968-1-09

## ABSTRACT

A three-dimensional numerical model was developed to accurately predict the steady-state weld pool shape in full penetration laser beam welding. The model accounts for the coupling between the heat transfer and the fluid dynamics by considering the effects of solid/liquid phase transition, thermo-capillary convection, natural convection, and phase-specific and temperature-dependent material properties up to the evaporation temperature. A fixed right circular cone was utilized as a keyhole geometry to consider the heat absorbed from the laser beam. The model was used to analyze the influence of the thermodynamic activity of solutes and turbulence on the weld pool shape. A mesh sensitivity analysis was performed on a hybrid mesh combining hexahedral and tetrahedral elements. For the case of full penetration laser beam welding of 8 mm thick unalloyed steel sheets, the dependence of the weld pool shape on the surface-active element sulfur was found to be negligible. The analysis of the results showed that a laminar formulation is sufficient for accurately predicting the weld pool shape since the turbulence has a minor impact on the flow dynamics in the weld pool. The validity of the numerical results was backed up by experimental measurements and observations, including weld pool length, local temperature history, and a range of metallographic cross-sections.

Keywords: Weld pool shape, Numerical modeling, Laser beam welding, Thermo-capillary convection, Turbulence

## INTRODUCTION

In recent years, due to the increase in available power outputs of solid-state lasers, modern laser systems allow joining parts in the thickness range of up to 50 mm by single-pass welding [1, 2]. Furthermore, the laser beam welding process brings various advantages, e.g., a narrow heat-affected zone, high efficiency and reproducibility of the welds, high reachable penetration depths and welding speeds, as well as high adaptability of the process. Therefore, the number of applications of the laser beam welding process rises steadily, not only in the workshop but also in the fields [3], e.g., in shipbuilding, by the production of pipelines, high-pressure and vacuum vessels, etc.

Nonetheless, as research results in the past have shown, various defects occur with the increase in welding speed and sheet thickness. These defects include hot cracking [4-7], porosity, laser keyhole instability and collapse [8-9], and other defects.

The formation of these defects is long known to be due to the underlying physical phenomena governing the weld pool dynamics [10]. Studies on laser arc hybrid welding showed that there is a correlation between the weld pool characteristics and the amount of residual porosity in the final weld [11]. The authors examined this correlation under different welding parameters and introduced a characteristic coefficient to predict the amount of residual porosity in the final weld. Multiple studies on the formation of hot cracking showed that there is a strong coherence between the weld pool geometry and the formation of cracks, especially in the so-called bulging region [12-14]. In [15], the relationship between the bulging region and the hot cracking formation in deep penetration laser beam welding was studied, and the authors concluded that the formation of a bulging region in the weld pool directly increases the hot cracking susceptibility.

Due to the importance of the weld pool geometry on the occurring defects and the increase of quality requirements in terms of reproducibility and parameter optimization in modern industry, it is crucial to get further insights into the laser beam welding process. Since extensive experiments and parameter studies are both time-consuming and cost-intensive, it is necessary to develop mathematical models to simulate the laser beam welding process. Nowadays, computational units have the capacity to simulate even very complex physical phenomena. Nevertheless, this has not always been the case, as in the early stages of modeling, researchers did not have the computational power to account for the fluid flow and mass transfer. Moreover, in terms of heat sources, simple point, line, and volumetric heat sources are not sufficient for an accurate description of the energy distributed on the keyhole surface [16-17]. In later stages, when the fluid flow was modeled as well, the accuracy of the results greatly improved. In the beginning, such models were primarily two-dimensional [17-19], until eventually in the 80s the three-dimensional weld pool flow was studied [20]. From there on, with increasing computational power and understanding of the laser beam welding process, the development of thermo-fluid dynamics models, allowing to fully couple the fluid flow and the heat transfer, followed.

In the present time, thermo-fluid dynamics models can be separated into two groups, models that contain a predefined keyhole geometry which is part of the computational domain, aiming to find a balance between simulation time and numerical accuracy, e.g. [21], and dynamic keyhole models that aim to simulate the laser welding process very precisely, e.g. [22-26]. Nevertheless, the development of dynamic models is a very time-

consuming, computer-intensive, and challenging procedure. These models are usually calculated as transient, thus having high runtimes, while only predicting one to two seconds of the actual laser beam welding process. Therefore, simplified models, based on empirical approximations of physical phenomena are highly important for case and parametric studies or more practical applications. In addition, works in the past have shown that models with strong physical simplifications are able to predict the weld pool geometry and fluid flow well even though under short computation times, e.g. [27]. Although many researchers worked with simplified models in the past, there are still various factors that are not sufficiently investigated yet. Turbulence is considered in some works, e.g. [21, 27], but disregarded in most other works. Furthermore, when turbulence is accounted for, primarily the well-known  $k-\varepsilon$  model is utilized, however, there is no validation that this turbulence model is the most suitable to predict the weld pool geometry. The same tendency is observed for the modeling of the thermo-capillary convection, from now on referred to as the Marangoni convection in the present paper. To the best of the authors' knowledge, in most of the published works on the topic the simplified implementation of the Marangoni convection is utilized, i.e., it is considered without accounting for the influence of the surface-active elements, e.g. [21, 27]. Even though these works obtained reasonable results, it is uncertain how the inclusion of surface-active elements influences the weld pool geometry, especially when unalloyed and low-alloyed steels, which typically contain a very low amount of surface-active elements, are studied. In addition, there are few studies on mesh sensitivity showing that the numerically obtained solution is mesh independent, i.e., the solution does not change when reducing the element size.

The present work seeks to investigate the dependency of the weld pool shape on turbulence and thermodynamic activity of solutes in laser beam welding of unalloyed steels and to validate the numerical results by comparing them to experimentally obtained results. Moreover, a mesh sensitivity study is performed to investigate the required minimum element size to account for an adequate numerical accuracy for the case under consideration.

## METHODOLOGY

### MATERIALS

In the welding experiments the unalloyed structural steel EH36-N was utilized. The dimensions of the sheets were 300 mm x 100 mm x 8 mm. The chemical composition was obtained by spectral analysis; the corresponding values in wt.% are listed in Tab. 1. As seen from Table 1, the chemical composition of the material is comparable with this of the structural steel S355 according to the corresponding standard, see DIN EN 10025-2 [28]. Note that the amount of sulfur in the EH36-N steel sheets is very low and therefore the maximum values were taken from the standard and not from the measurement.

**Table 1** Chemical composition of the unalloyed steel EH36-N in wt.%; top: standard DIN EN 10025, bottom: experimental measurements with spectral analysis

C	Si	Mn	Al	Nb	Ni	Cu	Cr	P	S	V	Fe
≤0.2	≤0.55	≤1.6	-	-	-	≤0.55	-	≤0.025	≤0.035	-	bal.

C	Si	Mn	Al	Nb	Ni	Cu	Cr	P	S	V	Fe
0.132	0.260	1.400	0.028	0.036	0.040	0.012	0.040	0.025	0.035	0.006	bal.

## EXPERIMENTS

The processing parameters are summarized in Table 2. Thermocouples of type K with a diameter of 0.25 mm were placed in the middle of the sheet at a lateral distance of around 1 mm from the weld centerline. The positions of the thermocouples on the bottom side were nearly identical to those on the upper side of the workpiece. The exact positions were measured after the welding process with an optical microscope. A schematic showing the starting and ending positions of the laser and the locations of the thermocouples is given in Fig. 1. The complete experimental setup is shown in Fig. 2. Thereby, a diode laser and a high-speed camera were used to illuminate the weld pool on the top surface and measure the weld pool length, respectively.

**Table 2** Processing parameters of the experiments

Parameters	Value	SI-Unit
Laser type	Yb:YAG disc laser	–
Wavelength	1030	nm
Laser power $P_L$	8	kW
Focal diameter	500	μm
Focal length	300	mm
Focal position	0	mm
Laser torch angle	0	deg
Shielding gas	M21	–
Gas flow rate	25	L min <sup>-1</sup>
Welding speed $u_{weld}$	2	m min <sup>-1</sup>

## Mathematical Modelling of Weld Phenomena 13

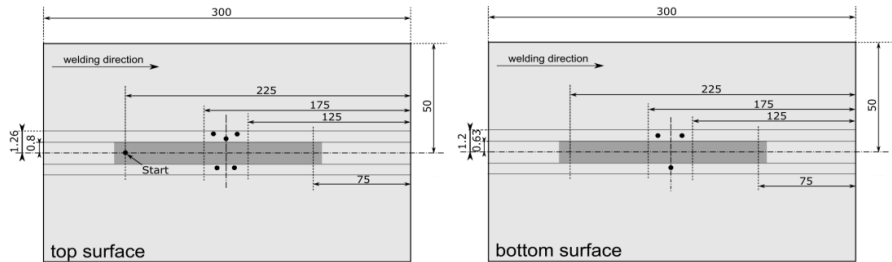


**Fig. 1** Experimental setup of the temperature measurements. The thermocouples are highlighted by the black dots.

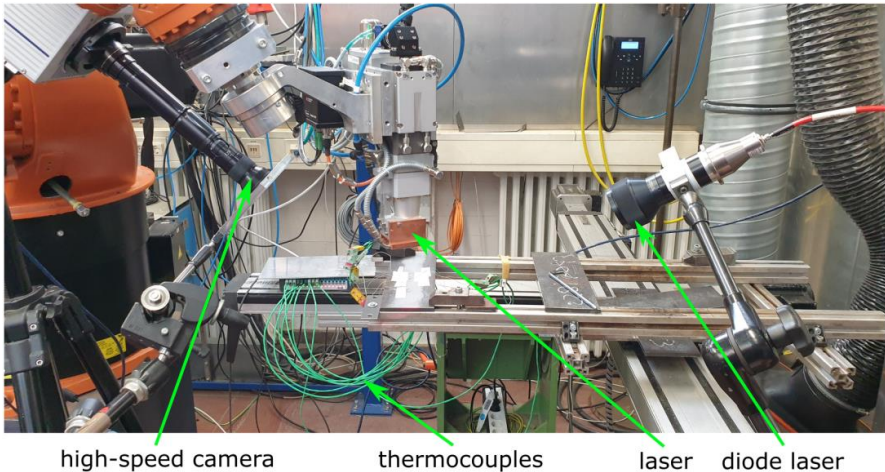


**Fig. 2** Experimental setup

### NUMERICAL MODELING

A three-dimensional numerical model was developed to accurately predict the steady-state weld pool shape in full penetration laser beam welding. The model is based on several previous works with optimizations regarding the prediction of the weld pool shape as well as the weld pool flow. Further information can be obtained from [20, 21, 27].

*Assumptions*

The basic assumptions for thermo-fluid dynamics simulation are according to [21, 27]. These are given as follows:

- Since the process is continuous and the sheets are welded on a linear trajectory, a quasi-steady-state approach was used to mathematically describe the weld pool shape and the local temperature field. Thus, temporal oscillations of the weld pool or the keyhole surfaces were neglected, and the start and the end of the welding process were not modeled.
- The size of the computational domain for the stationary thermo-fluid dynamics simulation was adapted to justify the usage of an adiabatic boundary condition defined on the rear surface, see Fig. 3.
- Fixed geometry of the top and bottom surfaces as well as of the keyhole surface were used, i.e., the recoil pressure was assumed to be perfectly balanced by the surface tension force on the keyhole surface. Furthermore, these surfaces were assumed to be frictionless, and an inclination of the keyhole geometry was not considered due to the comparatively low welding speed used in the experiments, see Tab. 2. The fixed geometry of the keyhole was further exploited as an equivalent heat source (EHS), i.e., the surface temperature of the keyhole was prescribed by the evaporation temperature of the material. This EHS technique assumes that the temperature in the keyhole should be at least equal or higher than the evaporation temperature of the material since part of the material on the keyhole surface vaporizes [29]. Thereby, the keyhole radii can be used as calibration parameter for the EHS. Note, however, that the radii used in the model should lie in the range of the focal spot radius of 250  $\mu\text{m}$ . In the present work the top radius was chosen to be 0.31 mm and the bottom radius was set 0.19 mm.
- In the first simulation stage a laminar formulation was used to predict the weld pool shape. This approach is reasonable, as the areas where high velocities and thus high Reynolds numbers appear are limited to the usually small surface areas that are influenced by the Marangoni convection. In the second simulation stage, three different turbulence models were utilized, including the SST  $k-\omega$  model, the SST  $\gamma$  transition model, and the SST  $\gamma-Re_\theta$  transition model.
- The Boussinesq approximation was used to model the impact of the density deviation, caused by the temperature difference, on the fluid flow in the weld pool [30].
- Solidification was modeled by the enthalpy-porosity approach [31], using the Carman-Kozeny equation for porous media morphology.
- The material properties were taken from the literature and modeled as temperature-dependent up to the evaporation temperature [32–36].
- Heating by the laser induced metal vapor was not considered due to the small differences between the evaporation temperature of the material and the metal vapor temperature as well as the low heat absorption for the wavelength of around 1  $\mu\text{m}$  [37–39].

- Heat losses by radiation were not accounted for due to the high relation of volume versus surface of the steel sheet, e.g. [40].
- The shear stress due to the interaction of evaporating material on the liquid metal was neglected as there is no experimental validation of the velocity distribution along the keyhole surface. Moreover, there is a high discrepancy in the numerically predicted magnitudes of the vapor velocities, e.g. [29, 41-43].
- Since the heat transport at the surface is mainly driven by the Marangoni convection via convective energy transport, the heat exchange with the environment is considered negligible.

### *Governing equations*

The governing equations for the conservation of mass, momentum, and energy are given in the following in the form as these are implemented in the finite volume software ANSYS Fluent which was used for the computations:

- Mass conservation for incompressible flow

$$\nabla \cdot \mathbf{u} = 0, \quad (1)$$

where  $\mathbf{u} = (u, v, w)$  is the fluid velocity vector.

- Momentum conservation

$$\nabla \cdot (\rho \mathbf{u} \mathbf{u}) = -\nabla p + \nabla \cdot (\mu [\nabla \mathbf{u} + \nabla \mathbf{u}^T]) + \rho \mathbf{g} + \mathbf{F}, \quad (2)$$

with source term  $\mathbf{F}$  given as follows:

$$\mathbf{F} = \mathbf{F}_{\text{buo}} + \boldsymbol{\tau}_{\text{Ma}} + \mathbf{C}_{\text{ck}}. \quad (3)$$

The first term on the right-hand side (RHS),  $\mathbf{F}_{\text{buo}}$ , uses the Boussinesq approximation to account for the buoyancy force caused by the deviation of the density with temperature:

$$\mathbf{F}_{\text{buo}} = -\rho \mathbf{g} \beta (T - T_{\text{melt}}). \quad (4)$$

Here  $p$ ,  $\mu$ ,  $\mathbf{g}$  and  $\beta$  are the fluid pressure, the dynamic viscosity, the gravity acceleration vector, and the linear volumetric coefficient of thermal expansion, respectively. The second term on the RHS of Eq. 3 accounts for the Marangoni convection, given as:

$$\boldsymbol{\tau}_{\text{Ma}} = -\frac{\partial \gamma}{\partial T} \nabla_s T, \quad (5)$$

where  $\nabla_s T$  is the temperature gradient on the surface and  $\frac{\partial \gamma}{\partial T}$  is the surface tension gradient with respect to temperature [35] which is expressed as:

$$\frac{d\gamma}{dT} = \frac{\partial \gamma}{\partial T} - R \Gamma_s \ln[1 + k_e \alpha] - \frac{k_e \alpha \Delta H^0 \Gamma_s}{T(1 + k_e \alpha)}. \quad (6)$$

In Eq. 6,  $T$  is the temperature,  $R$  is the universal gas constant,  $\frac{\partial \gamma}{\partial T}$  is the Marangoni coefficient,  $\Gamma_s$  is the interface concentration at the melting temperature,  $k_e$  is a constant related to the entropy of the phase separation and  $\Delta H^0$  is the adsorption heat.

Solidification was modeled with the third term on the RHS of Eq. 3 representing the Carman-Kozeny approach for porous media morphology:

$$C_{ck} = A_{mush} \frac{(1-f_L)^2}{f_L^3 + c_1} (u - u_{weld}). \quad (7)$$

The parameter  $A_{mush}$  is used to adjust the flow damping and is set to  $10^6$  in the model. The parameter  $c_1$  is set to a very small value to avoid division by zero [44]. In addition, solidification is also modeled with the modified viscosity method [45]:

$$\eta_{eff} = \begin{cases} \eta + f & \text{for } T < T_{sol} \\ \eta + f \left( 1 - \frac{T - T_{sol}}{T_{liq} - T_{sol}} \right) & \text{for } T_{sol} \leq T \leq T_{liq}, \\ \eta & \text{for } T > T_{liq} \end{cases} \quad (8)$$

where  $\eta_{eff}$  is the effective viscosity,  $\eta$  the dynamic viscosity,  $T_{sol}$  the solidus temperature,  $T_{liq}$  the liquidus temperature, and  $f$  a constant that is set to 1 in the current study.

- Energy conservation

$$\nabla \cdot (\rho u H) = \nabla \cdot (\lambda \nabla T). \quad (9)$$

Here,  $\lambda$  is the thermal conductivity [46]; the latent heat,  $\Delta H$ , is defined as:

$$\Delta H = f_L H_f, \quad (10)$$

where the function  $f_L$  represents the fraction of the liquid phase and is defined as follows:

$$f_L = \begin{cases} 0 & \text{for } T < T_{sol} \\ \frac{T - T_{sol}}{T_{liq} - T_{sol}} & \text{for } T_{sol} \leq T \leq T_{liq}. \\ 1 & \text{for } T > T_{liq} \end{cases} \quad (11)$$

The iteration between the energy equation (9) and the liquid fraction equation (11) provides the solution for the temperature [46]. In the case of a turbulent flow pattern, the turbulent transport variables are modeled according to the Carman-Kozeny approach:

$$C_{ck,turb} = A_{mush} \frac{(1-f_L)^2}{f_L^3 + c_1} \Phi, \quad (12)$$

where  $\Phi$  represents the turbulent transport variables in each turbulent case ( $k$ ,  $\varepsilon$ ,  $\omega$  etc.) [46].

*Boundary conditions*

The boundary conditions used in the thermo-fluid dynamics model are presented in Fig. 3 and summarized as follows:

- At the inlet of the computational domain, the temperature is set to the room temperature, while the velocity equals the process velocity  $\mathbf{u}_{weld}$ .
- The top, bottom and rear surface, the keyhole surface, and the symmetry plane were set as a free slip condition. Flow components in the normal direction are not present, i.e.,  $u_n = 0$  applies, and there is no existence of a boundary layer formation at these surfaces.
- The fixed keyhole surface was set to the evaporation temperature of the material.

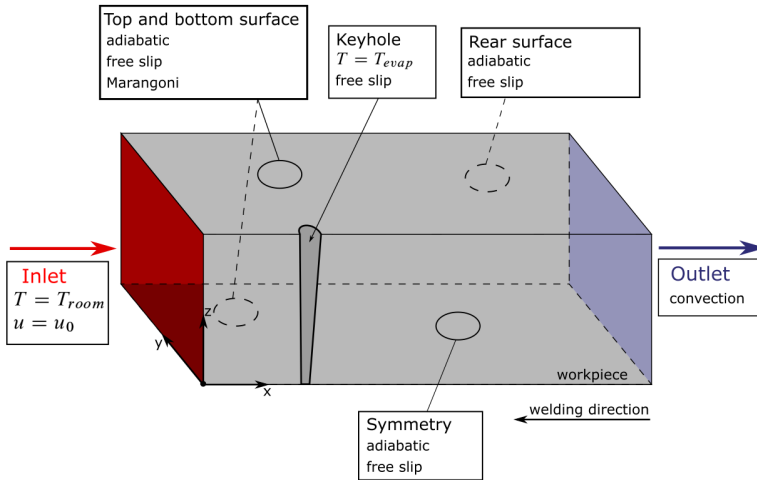


**Fig. 3** Boundary conditions for the CFD-simulation

- Since the temperature-dependent Marangoni convection is the main driving force in the weld pool, it was modeled as shear stress on the top and bottom surfaces of the workpiece, expressed as follows:

$$\eta \frac{\partial u}{\partial z} = \frac{\partial \gamma}{\partial T} \frac{\partial T}{\partial x}, \quad \eta \frac{\partial v}{\partial z} = \frac{\partial \gamma}{\partial T} \frac{\partial T}{\partial y}. \quad (13)$$

- The top, bottom and rear surfaces were modeled as adiabatic:

$$\frac{\partial T}{\partial n} = 0. \quad (14)$$

The discretization of the computational domain is, based on an approach that combines tetrahedral and hexahedral elements in a hybrid mesh shown in Fig. 4. While hexahedral elements usually provide good convergence behavior, tetrahedral elements are good at

filling complex geometries. The advantage of combining both types of elements is to resolve the area around the weld pool by using a very fine mesh, while a coarser mesh may be applied at areas outside of the weld pool. This results in an overall smaller number of elements and thus decreases the simulation time. Furthermore, the use of structured elements leads to an easier comparison between different mesh sizes. The inner, white-bordered block in Fig. 4 is very finely meshed, and the used hexahedral nodes are small enough to resolve the physical phenomena well. The transition area between the white and the dashed black lines, was meshed with tetrahedral elements; these gradually become coarser, being finest at the white border and coarser when reaching the dashed black border. The area outside the dashed black border up to the completely black border represents the coarsest meshed area. Note that on the top and the bottom surface of the inner block a prismatic layer was applied. This was chosen so that the velocity gradients caused by the Marangoni convection can be well resolved, thus supporting convergence of the solution.

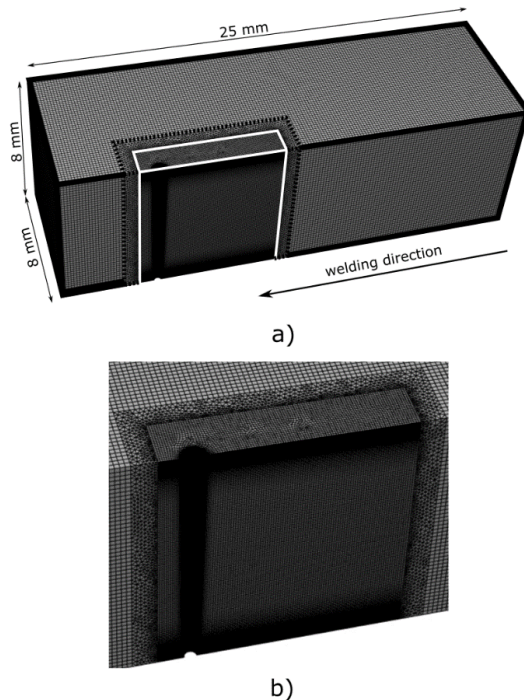


**Fig. 4** a) An overview of the computational domain, b) shows an enlarged view of the mesh in the vicinity of the keyhole

In addition, the influence of the Marangoni convection on the formation of the weld pool was studied. Specifically, the Marangoni convection can be implemented

numerically in two different forms, either by neglecting the surface-active elements or considering these. The Marangoni convection describes the resulting shear stresses, which form on the surface of the molten metal due to the temperature dependence of the surface tension. Since the velocities caused by the Marangoni convection can reach very high values, due to the high temperature gradients, a flow is developed within the weld pool, which can be directly attributed to the Marangoni convection. This flow has a strong impact, both on the shape of the weld pool and the transfer of the heat in the vicinity of the weld pool surface. The surface tension gradient can be represented as a function of the temperature and the chemical activity of surface-active elements as seen in Eq. 6 [47]. It can have both, positive and negative values and has a significant influence on the surface flow; thereby in case of a negative coefficient, the melt flows from areas of higher temperature to areas of lower temperature [10]. The first implementation method would be to neglect the surface-active elements ( $\alpha = 0$ ), thus assuming a constant Marangoni coefficient. The result for a negative constant, which is typical for pure iron, is a flow that is directed away from the hot keyhole surface to the outer edge of the weld pool. However, if the surface-active elements are considered, the flow would instead consist of two opposite-faced vortices [48]. Since the Marangoni convection has a major influence on the formation of the weld pool, a different approach may lead to a significant change in the flow field of the weld pool and thus also on the weld pool geometry.

For the turbulence study, three turbulence models were used to compare the weld pool geometry and the fluid flow therein; these include the SST  $k-\omega$  model, the  $\gamma$  transition model, and the  $\gamma-Re_\theta$  transition model. An advantage of the transition models is that these can consider both, a laminar and a turbulent flow pattern, in different regions of the weld pool, simultaneously. It is reasonable to apply these models, since the weld pool flow is unlikely to be either completely laminar or turbulent [49]. Because of the vortices that are present when using the variable surface tension gradient, an adverse pressure gradient develops in the region where these collide. Therefore, it is reasonable to assume that the  $k-\varepsilon$  turbulence model is not the best choice, as it is known to lead to difficulties when an adverse pressure gradient is present [50]. On the other hand, the SST  $k-\omega$  model represents a good alternative. The turbulence parameters for the different models are the standard values set by Fluent according to empirical measurements and available literature.

### *Material properties*

The material properties are defined as a function of temperature up to the maximum temperature of 3100 K and are shown in Fig. 5, Fig. 6, and Table 3. The value for the steel density was averaged over the interval of interest, between 1200 K and 2800 K, resulting in  $\rho_{steel} = 7060 \text{ kg m}^{-3}$ .

**Table 3** Material properties of the unalloyed steel EH36-N

Material property		Value	SI-Unit
Melting temperature	$T_{melt}$	1750	K
Solidus temperature	$T_{sol}$	1710	K
Liquidus temperature	$T_{liq}$	1790	K
Latent Heat	$H_i$	247000	J kg <sup>-1</sup>
Thermal expansion	$\beta$	$1.5 \cdot 10^{-5}$	K <sup>-1</sup>
Marangoni coefficient	$\frac{\partial \gamma}{\partial T}$	$-4.3 \cdot 10^{-4}$	N m <sup>-1</sup> K <sup>-1</sup>
Surface excess at saturation	$\Gamma_s$	$1.3 \cdot 10^{-5}$	mol m <sup>-2</sup>
Universal gas constant	$R$	$8.314 \cdot 10^{-3}$	J mol <sup>-1</sup> K <sup>-1</sup>
Constant related to the entropy of segregation	$k_e$	$3.18 \cdot 10^{-3}$	-
Standard heat of adsorption	$\Delta H^0$	$-1.66 \cdot 10^5$	J mol <sup>-1</sup>
Thermodynamic activity	$\alpha$	0.035	-

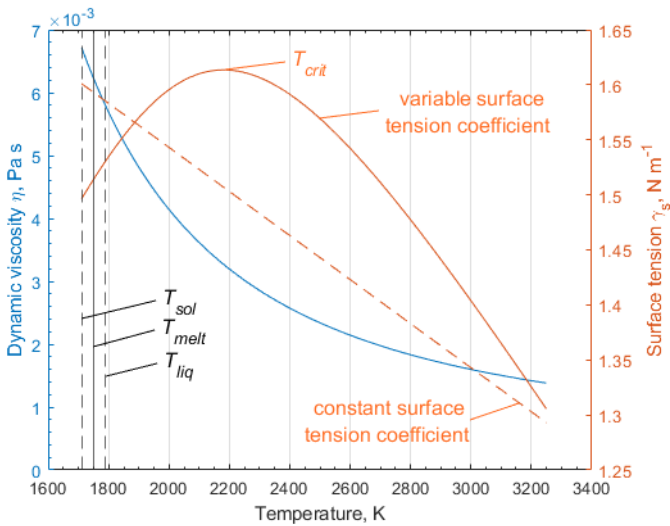


**Fig. 5** Thermophysical properties of the unalloyed steel EH36-N

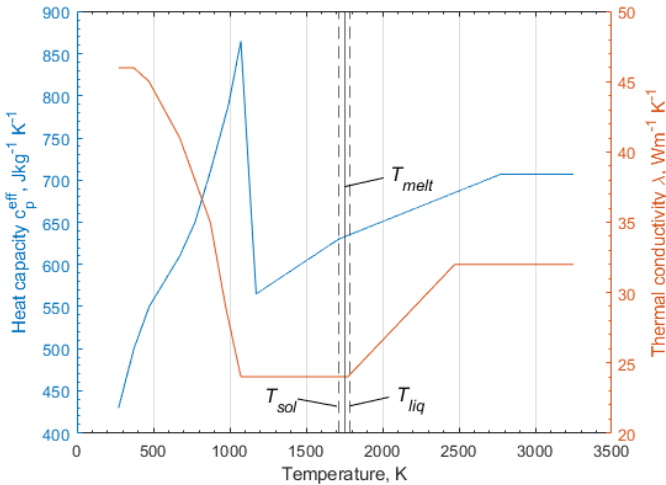


**Fig. 6** Thermophysical properties of the unalloyed steel EH36-N

### *Numerical setup*

The modeling framework presented in this work was executed with the finite volume software ANSYS Fluent. For the performed simulations the stationary, pressure-dependent, coupled PISO solver was used. It solves a coupled system of equations consisting of the conservation of momentum and the pressure-based conversation of mass. Calculation of the gradients was performed with the GREEN-GAUSS Node-Based scheme; this approach is more precise compared to the alternative schemes, the Least Squares Cell-Based scheme, and the GREEN-GAUSS Cell-Based scheme, while being heavier in computation work [46]. For the interpolation of the pressure the PRESTO! (PREssure STaggering Option) scheme was used as it led to a good convergence behavior in the simulations. The interpolation for the conservation of momentum was performed with First-Order Upwind scheme; for the energy equation the Second-Order Upwind scheme was used. The difference between the two interpolation types is that the Second-Order Upwind scheme is more precise, but usually leads to a worse convergence behavior, see [46]. In the simulations including a turbulent model, the additional transport parameters were as well interpolated using the First-Order Upwind scheme.

## RESULTS

## MESH SENSITIVITY STUDY

To account for a mesh-independent solution, a mesh sensitivity study with four different meshes was conducted. Note that only the element size in the inner, white highlighted block in Fig. 4, was changed, since the weld pool is located in this area. Furthermore, all numerically determined weld pool geometries were calculated with a laminar formulation of the flow pattern in the weld pool. The usage of tetrahedral elements in the transition layer also leads to a change in the number of elements in the transition area, since it is directly linked to the elements of the inner block. The specified mesh size of the inner block and the total number of elements for each mesh are summarized in Table 4. An overview of the computed weld pools for the different meshes is shown in Fig. 7. It can be seen that the size of the weld pool computed with mesh 1 is underestimated on the top and bottom sides of the workpiece compared to the solutions obtained with the finer meshes 3 and 4. Compared to mesh 2, the length of the weld pool on the top surface resembles that of mesh 3 and 4, while the length on the bottom surface deviates. The numerical results were considered to be mesh independent for mesh 3, as the weld pool geometry did not change when the finest mesh, mesh 4, was used, see Fig. 8. Therefore, mesh 3 was chosen to be utilized in the present studies, representing the best compromise between numerical accuracy and computational intensity.

**Table 4** Meshes and corresponding mesh sizes used for the mesh sensitivity study

Mesh name	Element size in the inner block	Total number of elements	Runtime
Mesh 1	$1 \cdot 10^{-4}$ m	$0.94 \cdot 10^6$	20 min
Mesh 2	$8 \cdot 10^{-5}$ m	$1.20 \cdot 10^6$	34 min
Mesh 3	$7 \cdot 10^{-5}$ m	$1.42 \cdot 10^6$	52 min
Mesh 4	$5 \cdot 10^{-5}$ m	$2.41 \cdot 10^6$	91 min

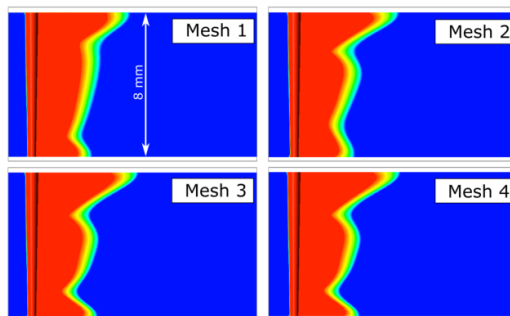


**Fig. 7** Numerically determined weld pool geometries in the symmetry plane of the model

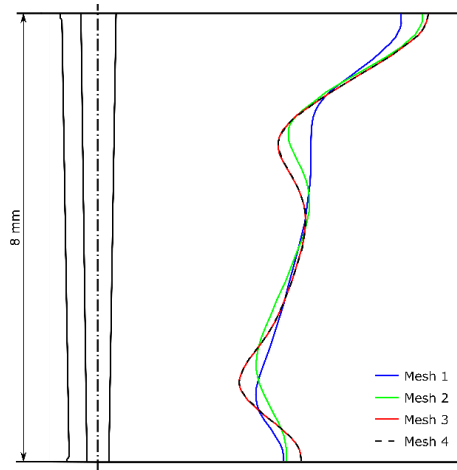


**Fig. 8** Comparison of the contours of the weld pools by using the melting isotherms at  $T_{melt} = 1750$  K

## EXPERIMENTS

Several cross-sections along the weld seam were obtained to account for the experimental tolerances and to validate the numerically obtained results according to the ISO/TS 18166 standard [51]. Two cross sections, namely the widest and narrowest, were compared to the numerically obtained cross-section. A metallographic specimen is shown in Fig. 9 a), where the fusion line is highlighted in white; in Fig. 9 b) a comparison of all fusion lines was performed; the modeled fusion line is highlighted in black. This was obtained by a projection of the weld pool using the melt temperature  $T_{melt}$ . The numerically obtained fusion line agrees well with the two experimentally determined fusion lines. Note that due to the conical approximation of the keyhole geometry in the model, there is a linear decrease in width of the modeled fusion line along the thickness of the steel sheet.

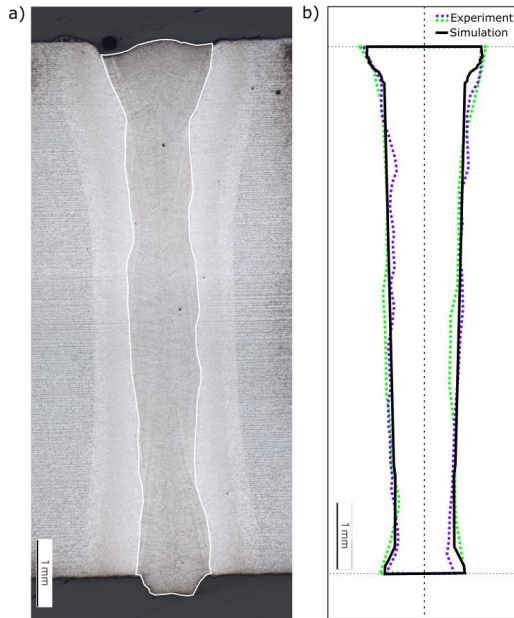


**Fig. 9** a) shows an exemplary metallographic cross section from the experiment, b) shows the comparison of the experimentally obtained and numerically predicted fusion lines

In addition, the experimentally determined weld pool length is compared with the modeled weld pool length. In Fig. 10 a) the weld pool on the top surface was recorded by a high-speed camera. As seen in Fig. 10 a), the length of the weld pool has been estimated to approx. 6.3 mm. The experimentally determined weld pool length has been compared with the weld pool length in the model, defined by the fusion isotherm at  $T_{melt} = 1750$  K on the symmetry plane, see Fig. 10 b). As seen, the numerical value of 6.2 mm corresponds very well to the measured one in the experiment.

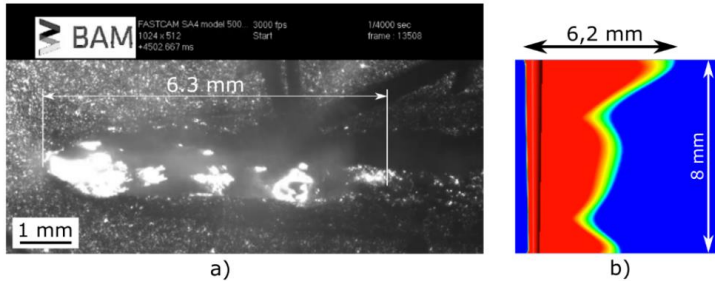


**Fig. 10** a) shows the weld pool on the top surface of the steel sheet, recorded by a high speed-camera, b) shows the numerically predicted weld pool for the laminar case

Fig. 11 shows the experimental and numerical time-temperature curves for different distances from the weld centerline. The curves were aligned so that the maximum temperature values measured in the experiment and predicted in the simulation lie on top of each other. As seen from the comparison, the peak temperatures in the experiment as well as in the model are in close agreement. Hence, it can be concluded that the numerical model represents the thermal behavior of the welded steel sheets accurately.

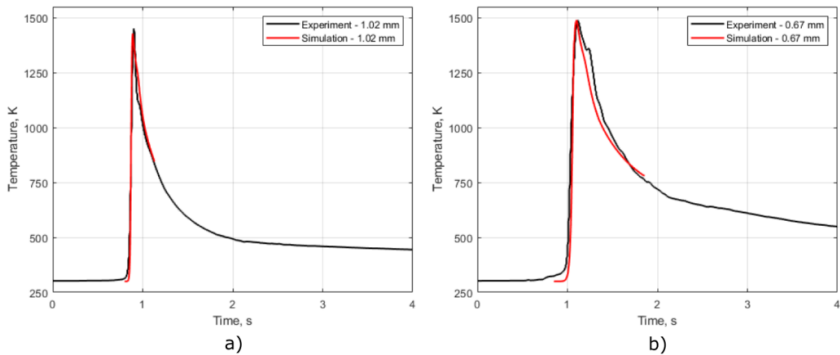


**Fig. 11** Comparison of the numerically and experimentally obtained temperature curves a) on the top side of the sheet, b) on the bottom side of the sheet

#### IMPACT OF THE SURFACE-ACTIVE ELEMENTS ON THE WELD POOL GEOMETRY

The Marangoni convection plays a crucial role on the weld pool geometry and the heat transfer near the surface, usually this is considered as independent of the surface-activity. In the current study, two implementations were considered, neglecting, and considering the surface-active element sulfur. To compare both implementations and derive the best practices concerning their usage, the weld pool geometry was compared in Fig. 12. Note

that when neglecting the surface-active elements, the surface-tension gradient  $\gamma'$ , was set to  $-0.00043 \text{ N m}^{-1} \text{ K}$ .

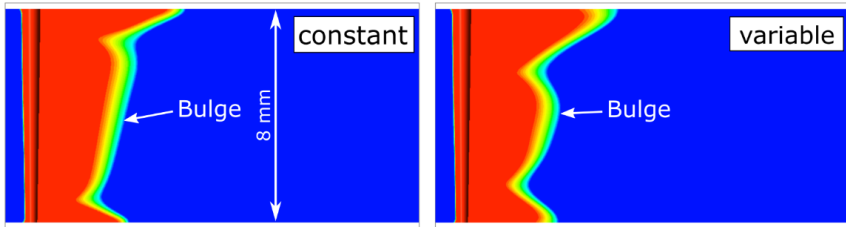


**Fig. 12** Comparison of the calculated weld pool geometries in the symmetry plane for the different implementations of the Marangoni convection

It can be seen that the bulge for the variable surface tension gradient is more pronounced because the weld pool is more constricted in the top and bottom part; this can be explained by looking at the strong differences in the fluid flow, seen in Fig. 13. There the black lines highlight the melting isotherms. In the case of a constant surface tension gradient the backflow to the keyhole from the inner weld pool region is located much closer to the top surface.

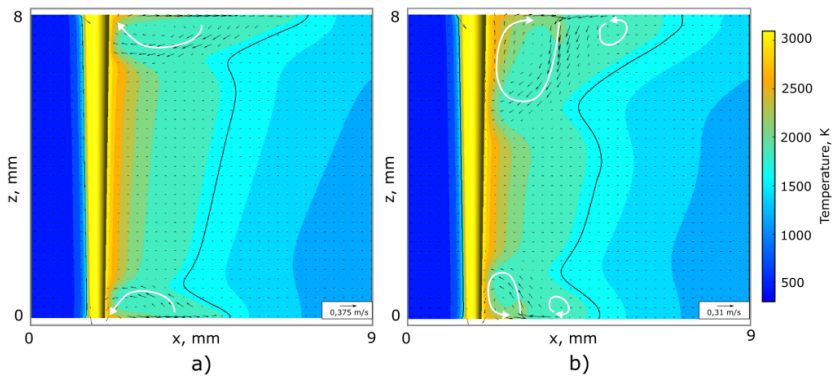


**Fig. 13** Comparison of the weld pool flow in the symmetry plane for the different implementations of the Marangoni convection a) constant surface-tension gradient, b) variable surface-tension gradient

This phenomenon can be explained by examining the velocity fields on the top surface shown in Fig. 14. Due to the Marangoni stresses acting in both directions, opposite to the welding direction in the high-temperature region near the keyhole, and in the welding direction near the outer edge of the weld pool, two opposite-faced vortices are formed, which are the cause for the deep backflow.

In Fig. 15 the numerically obtained fusion lines for both approaches are compared to the experimentally obtained fusion lines, showing only minor deviations. In Fig. 16, on the other hand, the melting isotherms for the variable and constant surface tension are compared. These show strong differences in the upper weld pool region and smaller deviations in the lower weld pool region. Based on the results it can be concluded that sulfur amounts of about 350 ppm may lead to visible changes of the shape of the weld pool. However, the total size and especially the length on the top and bottom surfaces remain unchanged.

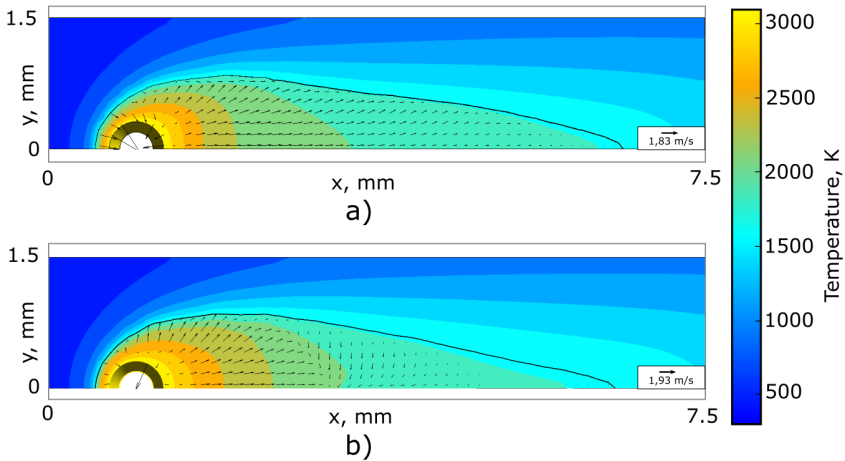


**Fig. 14** Comparison of the weld pool flow on the top surface for the different implementations of the Marangoni convection a) constant surface-tension gradient, b) variable surface-tension gradient

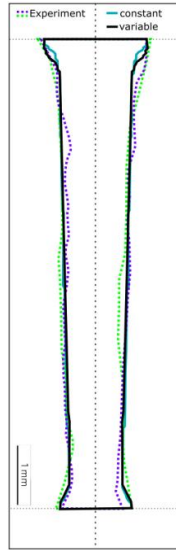


**Fig. 15** Comparison of the numerically predicted fusion lines for the constant and variable surface-tension gradient to the experimentally obtained fusion lines

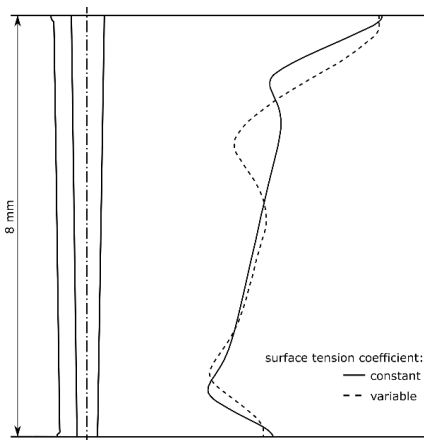


**Fig. 16** Comparison of the contours of the calculated weld pool geometries by using the melting isotherms at  $T_{melt} = 1750$  K

TURBULENCE STUDY

To study the influence of a turbulent flow pattern on the weld pool geometry and the fluid flow therein, the results obtained with the three different turbulence models were compared with the results from the laminar model. The corresponding velocity fields to the three studied turbulent formulations and the laminar formulation are shown in Fig. 17; the black lines highlight again the melting isotherms. It is shown that the fusion isotherms at  $T_{melt}$  have little to no deviations from each other. However, the velocity fields show minor differences where the maximum velocity for the SST  $k-\omega$  model is smaller compared to the rest.

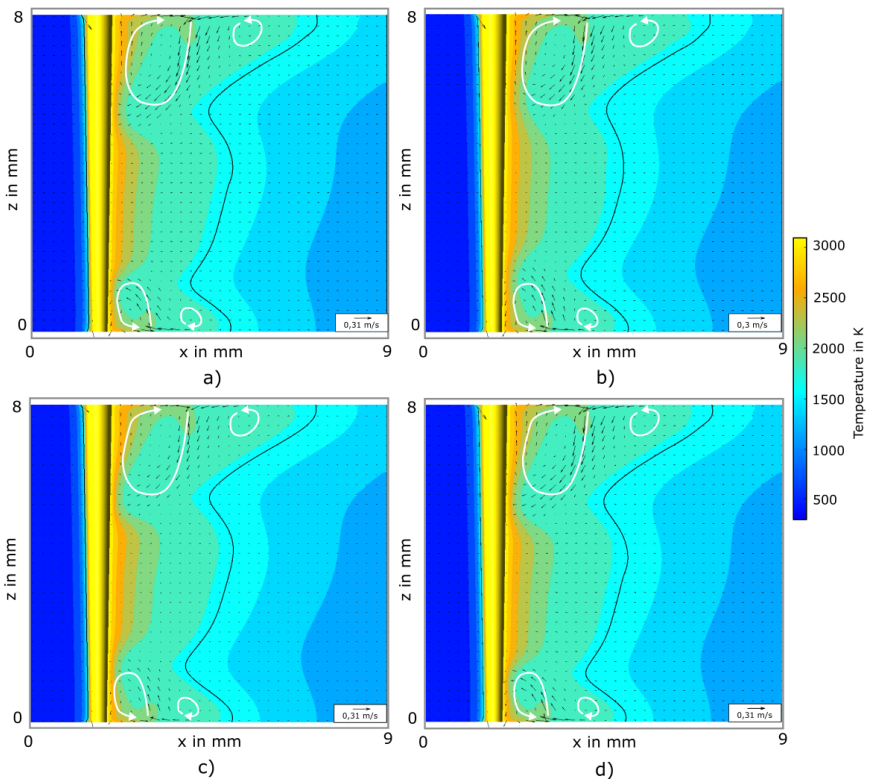


**Fig. 17** Calculated velocity fields in the symmetry plane with the different formulations a) laminar formulation, b) SST  $k-\omega$  model, c)  $\gamma$  transition model, and d)  $\gamma-Re_{\theta}$  transition model

This observation is confirmed by looking at Fig. 18, which depicts the averaged velocity components within the weld pool, in the x- and y-directions, as well as the average absolute velocity, over the height of the weld pool. The SST  $\gamma-Re_{\theta}$  transition model shows the biggest difference on the upper and lower side of the weld pool compared to the other models, where only small deviations are found. Even though these velocity deviations exist, these seemingly do not affect the weld pool geometry strong enough and barely make up for a small change in the fluid flow and thus in the weld pool shape as well.

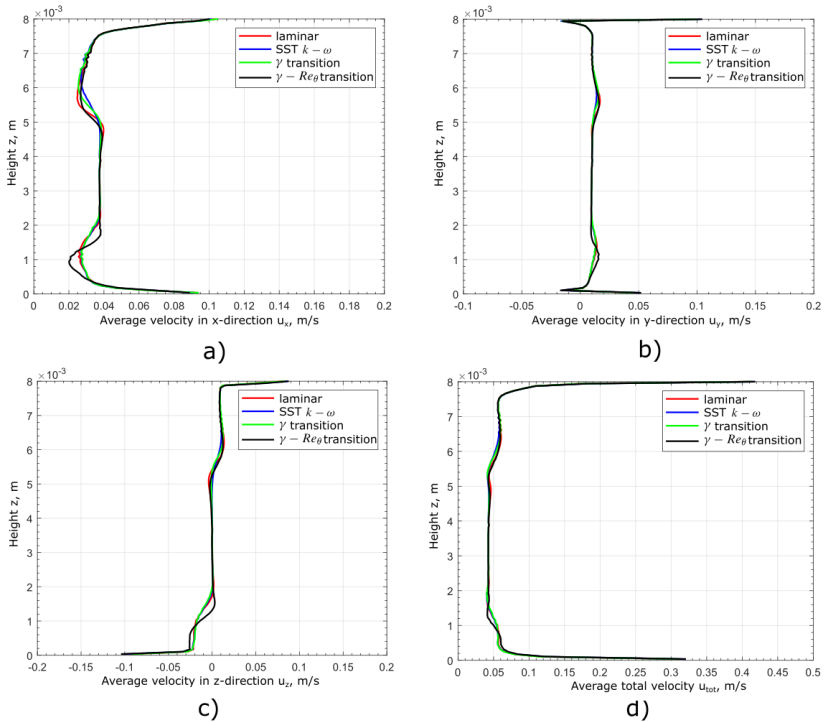


**Fig. 18** Computed averaged velocity components in the weld pool with the four studied formulations in a) x-direction, b) y-direction, c) z-direction, and d) the computed averaged total velocity

The numerically predicted fusion lines with the different turbulence models and the laminar model are shown in Fig. 19. It can be concluded that the studied turbulence models resulted in very similar fusion lines. Nonetheless, the fusion line predicted with the laminar formulation slightly differs from the fusion lines obtained with the turbulent models.

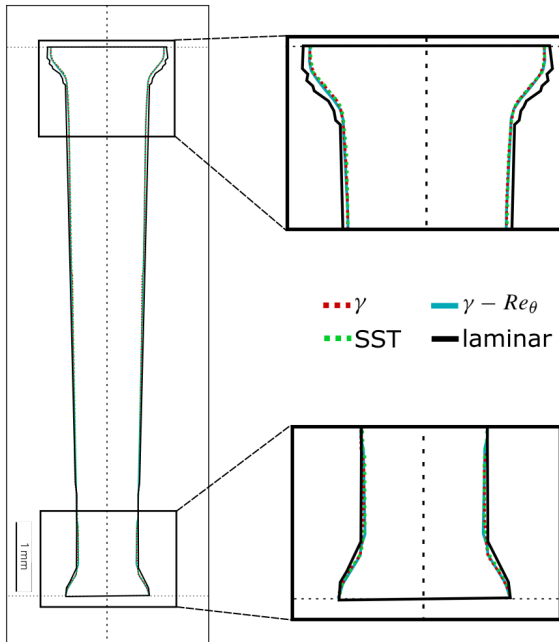


**Fig. 19** Comparison of the fusion lines obtained by the laminar formulation and turbulence models

## CONCLUSIONS

The present work aimed at extending an existing numerical model to accurately predict the steady-state weld pool shape in complete penetration laser beam welding. To validate the numerical results, experiments were carried out. The measured results were used to validate the laminar formulation of the model by comparing the weld pool length, the fusion lines, and the time-temperature curves. In addition, to assure numerical accuracy, a mesh sensitivity study was performed using a specially designed hybrid mesh. To study the influence of the Marangoni convection on the weld pool geometry, the influence of the surface-active elements was either considered or neglected in the model. Furthermore, a turbulence study was performed to investigate the influence of a turbulent flow pattern on the weld pool geometry and the corresponding velocity fields. The following conclusions were drawn from the obtained numerical and experimental results:

- The experimentally determined fusion lines, time temperature curves and weld pool lengths were used to validate the model and agreed well with the numerically predicted results.

- The mesh sensitivity analysis showed that a minimum element size of  $7 \cdot 10^{-5}$  m was necessary to obtain mesh-independent results for the studies performed in the present work.
- The study of the influence of the Marangoni convection on the weld pool geometry showed that sulfur amounts of about 350 ppm may lead to visible changes in the fluid dynamics. As a result, the weld pool shape changes slightly in the regions below and above the top and bottom surface. Nonetheless, no change in the dimensions of the remaining regions, e.g., in the weld pool length on the top and bottom surfaces, was observed.
- According to the turbulence study, the weld pool geometry for the laminar and turbulent formulations practically did not change, however there are minor deviations in the developed fluid flow in the weld pool.
- Based on the obtained results, it can be concluded that the consideration of the surface-active elements and the accounting for turbulence has barely a practical influence on the weld pool geometry when the unalloyed structural steel EH36-N is utilized. Therefore, their consideration is not needed when the main objective of the model is to predict the weld pool geometry.

#### ACKNOWLEDGEMENTS

This work is funded by the Deutsche Forschungsgemeinschaft (DFG, German Research Foundation) project Nr. 411393804 (BA 5555/5-2), Nr. 416014189 (BA 5555/6-1), and Nr. 466939224 (BA 5555/9-1).

#### References

- [1] M. BACHMANN, A. GUMENYUK, M. RETHMEIER: 'Welding with high-power lasers: trends and developments', *Phys. Proc.*, 83 15-25, 2016.
- [2] X. ZHANG, E. ASHIDA, S. TARASAWA, Y. ANMA, M. OKADA, S. KATAYAMA, M. MITZUTANI: 'Welding of thick stainless steel plates up to 50 mm with high brightness lasers', *J. Laser Appl.*, 23 (2) 022002, 2011.
- [3] J. F. READY, D. F. FARSON (EDS.): 'LIA Handbook of Laser Materials Processing', *Laser Institute of America*, Orlando, 2001.
- [4] J. SCHUSTER, S. KEITEL, E. SCHULZE, H. MALY: 'Fachbeiträge-Entstehung erstarrungsbedingter Risse in Laserstrahlschweißverbindungen an unlegierten und niedriglegierten Baustählen', *Schweißen und Schneiden*, No. 51, pp. 252-257, 1999.
- [5] J. SCHUSTER: 'Heißrisse in Schweißverbindungen: Entstehung, Nachweis und Vermeidung', *DVS-Verlag*; 2004.
- [6] M. O. GEBHARDT, A. GUMENYUK, M. RETHMEIER: 'Numerical analysis of hot cracking in laser hybrid welded tubes', *Advances in Materials Science and Engineering*, 520786, 2013.
- [7] A. ARTINOV, N. BAKIR, M. BACHMANN, A. GUMENYUK M. RETHMEIER: 'Weld pool shape observation in high power laser beam welding', *Physics Procedia*, 2018.
- [8] A. B. D. GINGELL AND T. G. GOOCH: 'Review of factors influencing porosity in aluminium arc welds', *TWI members report*, Ref: 7322.01/97/954.3, 1997.
- [9] B. F. DIXON AND J. C. RITTER: 'Solidification cracking in high strength steels welded by electron beam and laser beam processes', *Today and Tomorrow in Science and Technology of*

*Welding and Joining, Proceedings 7<sup>th</sup> International JWS Symposium*, Kobe, Japan, November 2001.

- [10] T. SHIDA, H. OKUMURA, Y. KAWADA: 'Effects of welding parameters and prevention of defects in deep penetration electron beam welding of heavy section steel plates', *Welding in the World*, pp. 196-207, 1979.
- [11] C. ZHANG, M. GAO, D. WANG, J. YIN, X. ZENG: 'Relationship between pool characteristic and weld porosity in laser arc hybrid welding of AA6082 aluminum alloy', *Journal of Materials Processing Technology*, Volume 240, 2017.
- [12] S. TSUKAMOTO, H. IRIE, M. INAGAKI: 'Welding Defects and Molten Metal Behaviour in Electron Beam Welding', *The fourth international Symposium of the Japan Welding Society*, pp. 115-120, 1982.
- [13] S. TSUKAMOTO, H. IRIE: 'Welding defects and molten metal behaviour in low speed electron beam welding', *Welding in the World*, 23, pp. 130-140, 1985.
- [14] S. TSUKAMOTO, H. IRIE: 'Mechanism of locally delayed solidification in electron beam welding', *Welding international*, pp. 177-183, 1991.
- [15] A. ARTINOV, M. BACHMANN, X. MENG, V. KARKHIN, M. RETHMEIER: 'On the relationship between the bulge effect and the hot cracking formation during deep penetration laser beam welding', *Procedia CIRP*, Volume 94, 2020.
- [16] D. T. SWIFT-HOOK, A. E. F. GICK: 'Penetration welding with lasers', *Welding journal* 52, Nr. 11, pp. 492-499, 1973.
- [17] K. N. LANKALAPALLI, J. F. TU, M. GARTNER: 'A model for estimating penetration depth of laser welding processes', *Journal of Physics D: Applied Physics*, 29. Jg., Nr. 7, p. 1831, 1996.
- [18] C. CHAN, J. MAZUMDER, M. M. CHEN: 'A two-dimensional transient model for convection in laser melted pool', *Metallurgical Transactions A*, 15. Jg., Nr. 12, pp. 2175-2184, 1984.
- [19] Y. F. HSU, B. RUBINSKY: 'Two-dimensional heat transfer study on the keyhole plasma arc welding process', *International Journal of Heat and Mass Transfer*, 31. Jg., Nr. 7, pp. 1409-1421, 1988.
- [20] M. BECK: 'Modellierung des Lasertiefschweißens', *Teubner*, 1996.
- [21] A. ARTINOV, M. BACHMANN, M. RETHMEIER: 'Equivalent heat source approach in a 3D transient heat transfer simulation of full-penetration high power laser beam welding of thick metal plates', *International Journal of Heat and Mass Transfer*, 122. Jg., pp. 1003-1013, 2018.
- [22] M. GEIGER, K. H. LEITZ, H. KOCH, A. OTTO: 'A 3D transient model of keyhole and melt pool dynamics in laser beam welding applied to the joining of zinc coated sheets', *Production Engineering*, 3. Jg., Nr. 2, pp. 127-136, 2009.
- [23] D. W. CHO, W. I. CHO, S. J. NA: 'Modeling and simulation of arc: Laser and hybrid welding process', *Journal of Manufacturing Processes*, 16. Jg., Nr. 1, pp. 26-55, 2014.
- [24] X. MENG, M. BACHMANN, A. ARTINOV, M. RETHMEIER: 'Experimental and numerical assessment of weld pool behavior and final microstructure in wire feed laser beam welding with electromagnetic stirring', *Journal of Manufacturing Processes*, 45. Jg., pp. 408-418, 2019.
- [25] A. ARTINOV, X. MENG, M. BACHMANN, M. RETHMEIER: 'Study on the transition behavior of the bulging effect during deep penetration laser beam welding', *International Journal of Heat and Mass Transfer*, 184. Jg., p. 122171, 2022.
- [26] S. PANG, L. CHENG, J. ZHOU, Y. YIN, T. CHEN: 'A three-dimensional sharp interface model for self-consistent keyhole and weld pool dynamics in deep penetration laser welding', *Journal of Physics D: Applied Physics*, 44. Jg., Nr. 2, p. 025301, 2010.
- [27] M. BACHMANN: *Numerische Modellierung einer elektromagnetischen Schmelzbadkontrolle beim Laserstrahlschweißen von nicht-ferromagnetischen Werkstoffen*, thesis, Bundesanstalt für Materialforschung und-prüfung (BAM), 2014.

- [28] DIN EN 10025-2:2019-10: 'Part 2: Technical delivery conditions for non-alloy structural steels'.
- [29] W. TAN, N. S. BAILEY, C. S. YUNG: 'Investigation of keyhole plume and molten pool based on a three-dimensional dynamic model with sharp interface formulation', *Journal of Physics D: Applied Physics*, 46(5) 055501, 2013.
- [30] T.E. FABER: 'Fluid Dynamics for Physicists', *Cambridge University Press*, 1995.
- [31] A. D. BRENT, V. R. VOLLER, K. T. J. REID: 'Enthalpy-porosity technique for modelling convection-diffusion phase change: application to the melting of a pure metal', *Numerical Heat Transf., Part A Applications*, pp. 297-318, 1988.
- [32] ESI GROUP: Material Database, 2009.
- [33] F. RICHTER: 'Physikalische Eigenschaften von Stählen und ihre Temperaturabhängigkeit', *Stahleisen-Sonderbericht*, Heft 10, 1983.
- [34] J. HILDEBRAND: *Numerische Schweißsimulation-Bestimmung von Temperatur, Gefüge und Eigenspannung an Schweißverbindungen aus Stahl- und Glaswerkstoffen*, thesis, Bauhaus-Universität Weimar, 2008.
- [35] P. SAHOO, T. DEBROY, M. J. MCNALLAN: 'Surface tension of binary metal-surface active solute systems under conditions relevant to welding metallurgy', *Metall. Mater. Trans.*, pp. 483-491, 1988.
- [36] K.C. MILLS: 'Recommended Values of Thermophysical Properties for Selected Commercial Alloys', *Woodhead Publishing*, 2002.
- [37] H. HÜGEL, F. DAUSINGER: 'Fundamentals of Laser Induced Processes', *Landolt-Börnstein VIII/1C*, 2004.
- [38] P. SHCHEGLOV, S. A. USPENSKIY, A. GUMENYUK, V. N. PETROVSKIY, M. RETHMEIER, V. M. YERMACHENKO: 'Plume attenuation of laser radiation during high power fiber laser welding', *Laser Phys. Lett.*, pp. 475-480, 2011.
- [39] P. SHCHEGLOV, A. GUMENYUK, I. B. GORNUSHKIN, M. RETHMEIER, V. N. PETROVSKIY: 'Vapor-plasma plume investigation during high-power fiber laser welding', *Laser Phys.*, p. 016001, 2013.
- [40] J. GOLDAK, A. CHAKRAVARTI, M. BIBBY: 'A new finite element model for welding heat sources', *Metallurgical transactions B*, pp. 299-305, 1984.
- [41] M. COURTOIS, M. CARIN, P. LE MASSON, S. GAIED: 'A two-dimensional axially-symmetric model of keyhole and melt pool dynamics during spot laser welding', *Metallurgical Research & Technology*, 110(2), pp. 165-173, 2013.
- [42] S. PANG, X. CHEN, X. SHAO, S. GONG, J. XIAO: 'Dynamics of vapor plume in transient keyhole during laser welding of stainless steel: Local evaporation, plume swing and gas entrapment into porosity', *Optics and Lasers in Engineering*, Volume 82, pp. 28-40, 2016.
- [43] X. CHEN, S. PANG, X. SHAO, C. WANG, X. ZHANG, P. JIANG & J. XIAO: 'Sub-microsecond vapor plume dynamics under different keyhole penetration regimes in deep penetration laser welding', *Journal of Physics D: Applied Physics*, 50(20), 2017.
- [44] V. R. VOLLER, C. PRAKASH: 'A fixed grid numerical modelling methodology for convection-diffusion mushy region phase-change problems', *International journal of heat and mass transfer*, pp. 1709-1719, 1987.
- [45] V. BRUYERE, C. TOUVREY, P. NAMY: 'A phase field approach to model laser power control in spot laser welding', *Proceedings of the 2014 Comsol Conference*, Cambridge, 2014.
- [46] ANSYS FLUENT: 'ANSYS fluent theory guide', *ANSYS Inc.*, USA, 2021.
- [47] K. C. MILLS, E. D. HONDROS, M. MCLEAN: 'Marangoni effects in welding', *Philosophical Transactions of the Royal Society of London. Series A: Mathematical, Physical and Engineering Sciences*, Nr. 1739, pp. 911-925, 1998.
- [48] A. FEY, S. ULRICH, S. JAHN, P. SCHAAF: 'Numerical analysis of temperature distribution during laser deep welding of duplex stainless steel using a two-beam method', *Welding in the World*, Nr. 4, pp. 623-632, 2020.

- [49] R. T. C. CHOO, J. SZEKELY: 'The possible role of turbulence in GTA weld pool behavior', *Welding Journal-New York*, p. 25, 1994.
- [50] W. RODI, G. SCHEUERER: 'Scrutinizing the k- $\epsilon$  turbulence model under adverse pressure gradient conditions', *J. Fluids Eng.*, pp. 174-179, 1986.
- [51] ISO/TS 18166:2016 'Numerical welding simulation Execution and documentation'.



# FEM STUDY OF THERMOMECHANICAL WELDING OF AUSTENITIC STAINLESS STEEL AND EXPERIMENTAL VALIDATION

P. WANG\*, B. SZALOWSKI\*, J. E. AZUKE\*\*, R. VALLANT\*,  
M. C. POLETTI\*, N. ENZINGER\*

*\*Institute of Materials Science, Joining and Forming, Graz University of Technology, Kopernikusgasse 24/I, 8010 Graz, Austria*

*\*\*Faculty of Engineering at the Mondragon University, Goiru Kalea, 2, 20500 Arrasate, Gipuzkoa, Spain*

DOI 10.3217/978-3-85125-968-1-10

## ABSTRACT

A coarse-grained microstructure is usually formed in the fusion zone (FZ) and heat-affected zone (HAZ) of TIG welds. The coarse grains usually degrade the service performance and difficult the inspection of welds. Since the austenitic stainless steels do not transform in solid-state, hammering applied on the hot already solidified weld during cooling can be used to promote grain refinement. In this study, large local plastic deformation on the solidified TIG welds of AISI 304L austenitic stainless steel was applied by frequent hammering (at 35 Hz) at a distance of 20 mm behind the welding heat source. The microstructure of welds with and without hammering are characterized using light optical microscopy. Additionally, the temperature, effective strain, and effective strain rate distributions were calculated using the finite element modelling, simulating the integrated arc welding and frequently plastic deformation via the SFTC Deform®-3D. The microstructures were significantly refined in FZ due to mechanical vibration of the solidifying phase and dynamic recrystallization of the solid phase due to large local strains and strain rates. The grains in the HAZ remain coarse because of the negligible plastic deformation. The fusion line can be simulated accurately, and larger temperature heterogeneity was observed in the hammered welds. Therefore, the coupled thermomechanical simulation revealed the correlation of microstructure refinement in the weld and the thermomechanical welding process.

Keywords: Austenitic stainless steel; Thermomechanical welding; Mechanical vibration; Grain refinement; FEM simulation

## INTRODUCTION

Fusion welding, as one of the most essential joining methods, is usually used for manufacturing austenitic stainless steels (ASS), for example the Tungsten Insert Gas (TIG) welding for AISI 304L [1, 2]. Although its simplicity of execution, TIG welding usually involves a large localized heat input, and the weld region experiences complex thermal cycles due to localized heating and cooling steps. Generally, these result in large residual stress and heterogeneous microstructures, as well as coarse-grains in the fusion zone (FZ) and heat-affected zone (HAZ) of the welds [3]. Grain size has a significant impact on material properties [2, 4]. Refining the weld microstructure can improve

mechanical properties such as tensile strength, hardness, and toughness [4, 5]. Grain refinement methods include various heat treatment processes occurring after phase transformation or twinning [1, 6], the application of mechanical and/or electromagnetic vibrations during welding or additive manufacturing [7-9], and the thermomechanical processing, for example involving severe plastic deformation [10]. Due to the absence of phase transformation in the ASS during the cooling stage when performing the fusion welding, grain refinement of weld microstructures can be achieved by utilizing vibration on the weld pool and plastic deformation on the solidifying weld. The finite element method (FEM) is the predictive tool to investigate coupled or uncoupled thermal and mechanical analysis of welding processes: temperature field, plastic deformation and heat source modelling [11, 12].

In this paper, the authors developed a 3D FE model of the proposed thermomechanical welding process, which can accurately predict the coupled thermomechanical fields (i.e., distributions of the effective strain, effective strain rate, and temperature), and also their corresponding evolution histories within both FZ and HAZ during the whole welding process.

### RESEARCH METHOD

#### EXPERIMENTAL SETUP

The setup of the thermomechanical welding (TMW) system is presented in Fig. 1 (a) with a pneumatic hammer. The properties of the pneumatic hammer are the average free stroke of 13 mm and a cycling frequency of 35 Hz at a constant air pressure of 6 bar [13, 14]. The hammer is made of 42CrMo4 steel with a hardness of 550 HV 10. The rectangular tip is with dimensions of 15 × 2 mm. Fig. 1 (b) shows the deformed surface after the hammering. Fig. 1 (c) shows a simple 2D diagram of the TMW system with four parameters, i.e.,  $a_1$  to  $a_4$ , determining the positions of the hammer and torch with a needle. The distances of the hammer and torch needle to the substrate are denoted by  $a_1$  and  $a_2$ , respectively.  $a_3$  is the offset between the hammer and the torch needle and determines the distance of starting the hammering after the TIG welding.  $a_4$  is the tilt angle of the torch or torch needle, influencing on both, the power density and the final geometry of the fusion zone. The torch combined with the needle was held at a fixed height. The pneumatic hammer moves in a vertical direction. The substrate was moved unidirectionally at a specific speed, depending on the welding speed.

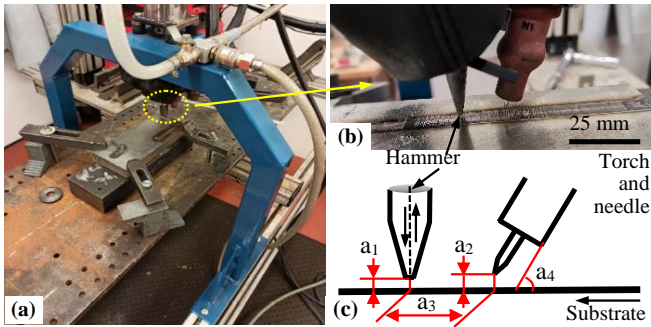


**Fig. 1** (a) setup of the thermomechanical welding (TMW) system with a pneumatic hammer, (b) the magnified photo of the hammer and torch marked by the dashed ellipse in (a), and (c) a 2D schematic diagram of the TMW system with  $a_1$  to  $a_4$  showing the positions of hammer and torch

The cycling load of the hammer was measured by a load cell [13]. The temperature field adjacent to the TIG weld seam was determined by five individual K-type thermocouples aligned perpendicularly to the central line, and their positions (T1 to T5) are as shown in Fig. 2.

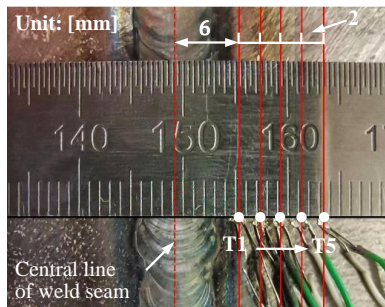


**Fig. 2** Positions of the five K-type thermocouples T1 to T5 arranged away from the central line of the TIG bead plate weld seam

FE MODEL DESCRIPTION

*Heat Source Model*

The Goldak's double-ellipsoid heat source model was used to determine the distribution of the temperatures within the workpiece. The schematic illustration of Goldak's double ellipsoidal heat source model [15] is shown in Fig. 3. The parameters  $a_f$  and  $a_r$  are the lengths of front and rear semi-axes, and  $b$  and  $c$  are the width and depth of the heat source, respectively.

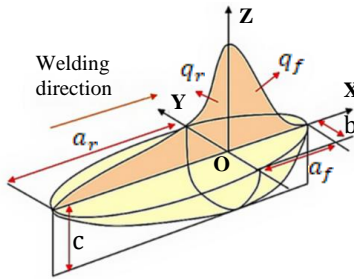


**Fig. 3** Schematic diagram of the Goldak's double ellipsoidal heat source model [16]

The Goldak's double-ellipsoid heat source model can be described by two power densities, i.e.,  $q_f$  in Eq. 1 and  $q_r$  in Eq. 2, belonging to the frontal and rear ellipsoids, respectively. The calibration of both Eq. 1 and Eq. 2 consists in adjusting the three parameters  $k$ ,  $l$ , and  $m$ . In this way, the modified and calibrated double ellipsoidal heat source can be used for the TIG welding simulation via the Deform<sup>®</sup>-3D software. The parameters  $f_f$  and  $f_r$  are the factors for distributing the energy input power  $Q$  to the front and rear ellipsoids of heat source, where its sum equals two (Eq. 3). Considering the FZ geometry and the continuity of the volumetric heat source, the factor  $f_f$  is calculated according to Eq. 4 [17, 18]. The size of the fusion zone is determined by  $a_f$ ,  $a_r$ ,  $b$  and  $c$ . These four parameters are measured on the basis of carried out experiments and are taken from the cross-section metallography of the weld seam. The heat source properties are shown in Table 1.

$$q_f(x, y, z) = \frac{6\sqrt{3}Qf_f}{\pi\sqrt{\pi a_r bc}} \exp\left[-\left(\frac{kx^2}{a_f^2} + \frac{ly^2}{b^2} + \frac{mz^2}{c^2}\right)\right] \quad (1)$$

$$q_r(x, y, z) = \frac{6\sqrt{3}Qf_r}{\pi\sqrt{\pi a_r bc}} \exp\left[-\left(\frac{kx^2}{a_r^2} + \frac{ly^2}{b^2} + \frac{mz^2}{c^2}\right)\right] \quad (2)$$

$$f_f + f_r = 2 \tag{3}$$

$$f_f = 2 / (1 + a_f / a_r) \tag{4}$$

where  $q_f(x, y, z)$  – thermal flow density of the frontal ellipsoid [ $W \cdot mm^{-3}$ ];  $q_r(x, y, z)$  – thermal flow density of the rear ellipsoid [ $W \cdot mm^{-3}$ ];  $a_f, a_r, b, c$  – parameters for describing the dimension of the volume of heat input [mm];  $x, y, z$  – point’s coordinates [mm];  $f_f, f_r$  – constants influencing energy distribution [-];  $k, l, m$  – parameters used for modifying and calibrating the heat source [-];  $Q$  – the overall heat source power [W].

**Table 1** Parameters of the Goldak’s double ellipsoidal heat source

$a_f$ [mm]	$a_r$ [mm]	$b$ [mm]	$c$ [mm]	$\eta$ [-]	$Q$ [W]	$f_f$ [-]	$f_r$ [-]	$k$ [-]	$l$ [-]	$m$ [-]
3.49	2.08	3.26	1.20	0.88	1540	0.75	1.25	3	1.44	3.5

The overall heat source power  $Q$  is calculated as a product of both, the voltage and the current (Eq. 5). This result also needs to be multiplied by the heat transfer efficiency  $\eta$  from the heat source to the material. For the TIG welding method, the  $\eta$  does not change so much, and according to standards, it has values between 0.86 and 0.88 [19]. The value of  $\eta$  is set to 0.88.

$$Q = \eta UI \tag{5}$$

where,  $Q$  – heat source power [W];  $U$  – welding voltage [V];  $I$  – welding current [A];  $\eta$  – the efficiency of heat transfer [-].

### Mesh and Dimensions

The commercial FE software SFTC Deform<sup>®</sup>-3D (version 12.0) is used for the thermomechanical welding simulations. The geometric size of the FEM model is shown in Fig. 4. The chosen dimensions for the substrate were  $100 \times 50 \times 30$  mm with a total of 8000 tetrahedral elements with a prior size ratio of 2. Small tetrahedral elements were additionally set using the function of “Mesh windows” in the region affected by the TMW, as shown in Fig. 4. The size ratio to outside elements is 0.05. Additionally, the SFTC Deform<sup>®</sup>-3D has the function of automatically remeshing controlled by given remeshing criteria and weighting factors. The hammer was set as the rigid top die. A total of 500 steps with a step size of 0.1s/step were used for the FEM simulation.

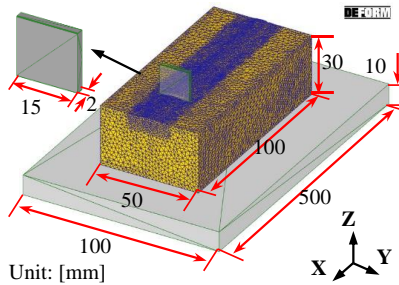


**Fig. 4** Three-dimensional finite element mesh for the viscoplastic substrate and the rigid hammer in the thermomechanical welding system using the Deform@-3D model

#### *Validation of the FE Model*

Experimental validation was performed to prove the accuracy of the numerical simulation by the following aspects. The measured temperature curves of the five selected points (T1 ~ T5 seen in Fig. 2) adjacent to the weld seam were compared with the corresponding simulated values.

#### EXPERIMENTAL PROCEDURE

The TIG bead on plate welding and the TMW were both conducted on the identical substrate, i.e., an as-received hot-rolled AISI 304L plate with the dimensions of  $100 \times 50 \times 30$  mm. The composition of the investigated material is listed in Table 2. In addition, the heat capacity, the thermal conductivity coefficient, and the shear modulus can be found in Appendix 1, obtained from the software JMatPro<sup>®</sup>-7.0. Their thermophysical properties were formally incorporated into the FE model (section 0) to optimize the material property.

**Table 2** Chemical composition of the AISI 304L austenitic stainless steel (wt %)

Element	Cr	Mn	Ni	Si	C	N	P	S	Fe
Wt. %	18.055	1.773	8.010	0.374	0.018	0.071	0.036	0.001	Balance

The welding current and voltage were kept constant: 125 A and 14 V, respectively. The welding torch was fixed on a frame, and the relative moving speed of the plate was 2 mm/s. The offset between the hammer and torch was 20 mm. A constant air pressure ( $P_{\text{air}}$  [bar]) of 6 bar was used for the pneumatic hammer. The shield gas used was 100% Argon, with a flow rate of 12 l/s. All TMW parameters were listed in Table 3.

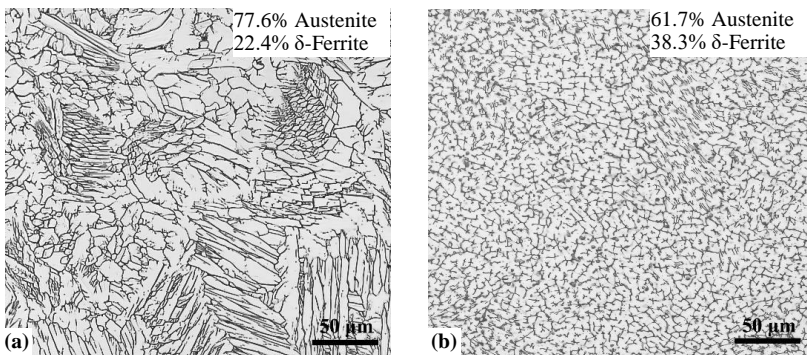
**Table 3** Parameters of the thermomechanical welding

$V$ [mm/s]	$I$ [A]	$U$ [V]	$P_{air}$ [bar]	$V_{Ar}$ [l/s]	$a_1$ [mm]	$a_2$ [mm]	$a_3$ [mm]	$a_4$ [°]
2	125	14	6	0.2	3	4	20	80

Standard metallographic techniques were used for cutting, grinding and polishing the samples at the cross-section of welds for microstructure analysis. The samples were electrolytically etched with a solution containing 60 vol% of nitric acid and 40 vol% distilled water [20, 21]. The microstructure was captured using a light optical microscope (Zeiss Observer.Z1m with an Axio-Cam-MRC5 camera). The contents of both phases were calculated via the ImageJ analyzer [21]. The movement of the hammer was controlled by adopting the “Mechanical press” type. The substrate and bottom die were both pushed to the +X direction at a constant speed of 2 mm/s.

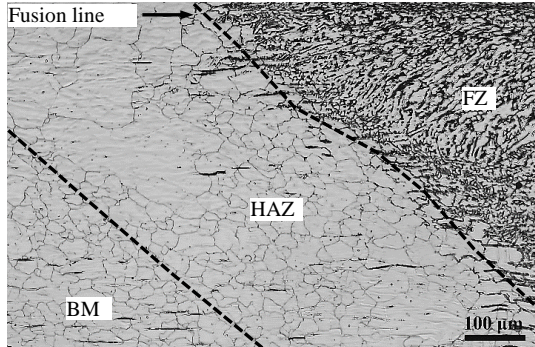
### RESULTS AND DISCUSSION

Fig. 5 (a) and (b) comparatively display the microstructures of the fusion zone in the single TIG weld and TMW weld, respectively. Coarse dendrites were observed in the TIG weld, and while fine solidified microstructure was obtained with the contribution of frequent hammering, as shown in Fig. 5 (b). The frequent plastic deformation and mechanical vibration [9, 23] were introduced to the weld during solidification, which resulted in the distinct solidification and grain growth modes. Apart from the large differences in the grain microstructure, the phase contents are different. Assuming that the black lines and dots in Fig. 5 are  $\delta$ -ferrite and the rest is  $\gamma$ -austenite. The content of the vermicular  $\delta$ -ferrite [24] in the TMW weld is 38.3 vol% , relatively higher than that in the TIG weld (22.4 vol%) and significantly higher than that in the initial condition ( $\sim 3$  vol% measured previously [25]).



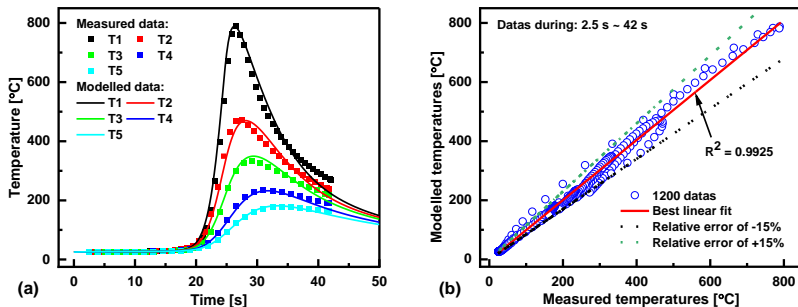
**Fig. 5** LOM observations of the fusion zone in the TIG welding sample (a) and thermomechanical welding (i.e., TMW) sample (b) obtained at welding conditions of the current 125 A, speed 2 mm/s, and a 20 mm offset between the TIG torch and hammer for the TMW

In addition, the microstructure of the HAZ for the TMW weld can be seen in Fig. 6. It shows that the grains in the HAZ is relatively larger than that of base material (BM) as a consequence of grain coarsening due to the large thermal effect [22].



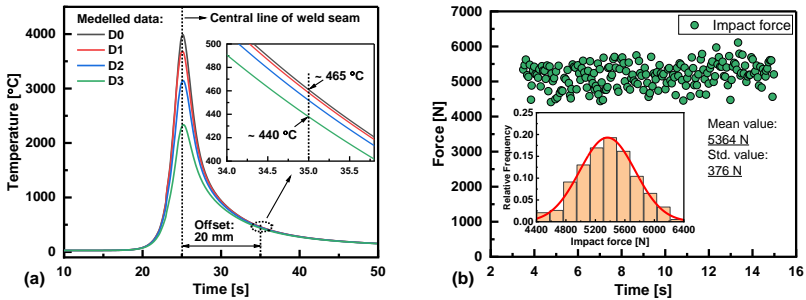
**Fig. 6** LOM observation of the heat-affected zone at the cross-section of the thermomechanical welding (i.e., TMW) weld of AISI 304L austenitic stainless steel

Fig. 7 (a) shows the plots of simulated and measured temperature evolutions of the selected five points (i.e., T1 to T5, as shown in Fig. 2). The simulated data were obtained using the point tracking technique through the post-processing of Deform<sup>®</sup>.3D. It can be seen that a good fitness of these temperatures was obtained, which is identified by a higher determination coefficient ( $R^2 = 0.9925$ ), evaluated from Fig. 7 (b) [26]. The optimized double ellipsoid heat source model with the adjusted model parameters  $k$ ,  $l$ ,  $m$ , and  $\eta$  in Eqs. (1 to 4), as well as the used temperature dependent materials properties can closely reproduce the real temperature fields.



**Fig. 7** Comparison of the simulated and measured temperature evolutions of points T1 to T5 from Fig. 2 using the point tracking technique (a), and the corresponding correlation evaluation of both data (b)

The temperature evolution at the FZ can be plotted at several specific points (D0 to D4) as shown in Fig. 8 (a). The point D0 is in the central line of the weld seam (i.e., the dash line as shown in Fig. 2), where the torch needle passed through. Points D1, D2, and D3 are located in the FZ, aligned perpendicularly to the welding trajectory and with 1 mm, 2 mm, and 3 mm distances away from the point D0, respectively. Due to the welding speed of 2 mm/s and the offset of 20 mm, the calculated time after the solidification and when the hammer hits the FZ is 10 s (between dashed lines) as shown in Fig. 8 (a). The temperatures of these four points are within the range of 440 °C ~ 465 °C, i.e., this should be the approximate temperature where the frequent hammering occurs after the TIG welding conditions of current 125A and speed 2 mm/s. Fig. 8 (b) shows that the average hammering force is 5364 N measured by the load cell when the interspace of the hammer top tip to the substrate is 3 mm, i.e., the parameter  $a_1$  as shown in Fig. 1 (c) equals to 3 mm.



**Fig. 8** Temperature evolution of four specific points in the TIG weld seam (D0 to D4) at welding conditions of current 125A and speed 2mms-1 (a), and (b) the evolution of maximum impact forces of frequent hammering measured by the load cell [13, 14]. D0 is located in the central line of the weld seam, and D1 ~ D3 is aligned with an interspace of 1 mm perpendicularly to the central line.

Fig. 9 shows the distribution maps of simulated effective strain, temperature, and effective strain rate on a slice, i.e., the cross-section of weld, and the corresponding histograms. The position of slice is where starting the hammering. It can be seen that the plastic deformation occurs generally in a small region, as indicated in Fig. 9 (a) and (c). Fig. 9 (b) displays the current temperatures that fit the temperature range as discussed in Fig. 8. In addition, the histograms of the effective strain, temperature, and effective strain rate are shown in Fig. 9 (d), (e) and (f), respectively. Such three histograms can be used for improving the processing parameters (for example, modifying hammer offsets to increase/decrease temperatures for starting deformation). In addition, the evolutions of the simulated temperature, effective strain, and effective strain rate of specific points in the TMW weld (i.e., FZ and HAZ) can be used to develop microstructure evolution models of the AISI 304L by incorporating the recrystallization models (SRX and DDRX) and grain coarsening.

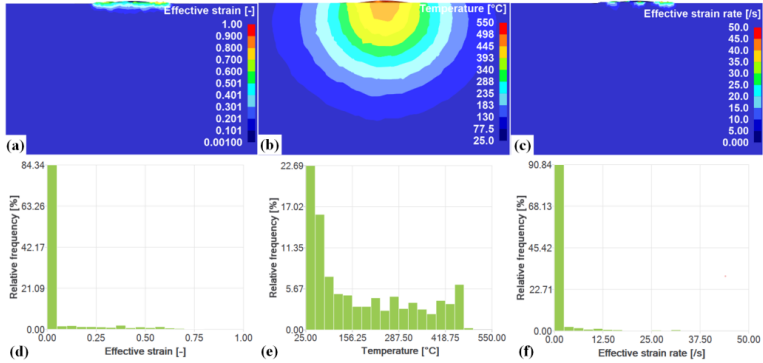


**Fig. 9** Distributions of the effective strain (a), temperature (b), and effective strain rate (c) in a slice of the cross-section of AISI 304L thermomechanical weld at TIG welding conditions of current 125 A, voltage 14V, speed 2 mm/s, and a 20 mm offset between the TIG torch and hammer, and (d), (e) and (f) are the corresponding histograms of (a), (b) and (c), respectively

### SUMMARY AND CONCLUSIONS

The TIG welding and thermomechanical welding (i.e., TMW) were both conducted on the samples of AISI 304L. TMW is composed of TIG welding and subsequent hammering. The plastic deformation was carried out on the cooling TIG weld using frequent hammering with a 20 mm offset between the TIG torch and hammer. The microstructures were compared to analyze the effect of frequent hammering on the microstructure evolution. With the aid of the finite element model, both fields and evolutions of temperature, effective strain, and effective strain rate on the TMW welds were modelled and experimentally validated. Several conclusions are summarized as follows,

- a. The solidified microstructure of the fusion zone is relatively fine in the TMW weld than that in the TIG weld at conditions of welding current 125 A and welding speed 2 mm/s. The contribution of frequent hammering can promote the refinement of the fusion zone microstructure.
- b. The finite element (FE) numerical results show that the simulated temperature field has a good agreement with the test measurements. The fields of simulated effective strain, effective strain rate, and temperature reveal the conditions of the deformation for the frequent hammering.
- c. During the TMW process, the evolutions of temperature, effective strain, and effective strain rate can be obtained from the FEM simulation for selected points. These can be used in future steps for optimizing the TMW process and modelling the related microstructure evolution.

## ACKNOWLEDGMENT

The authors carried out this work under the project of FWF Project in Austria-Thermomechanical welding (No. 16732).

## APPENDIX I

Fig. A-1 shows the evolution curves of several simulated thermo-physical properties of the as-received AISI 304L, i.e., the thermal conductivity  $k$  [W/(m·K)], the shear modulus  $G$  [GPa], and the specific heat coefficient  $C_p$  [J/(g·K)] with respect to temperature  $T$  [°C]. These data were simulated by the JMatPro®- v. 7.0 calculated with the compositions as listed in Table 2, which were used to adjust the temperature-dependent material properties in the Deform®-3D FEM model.

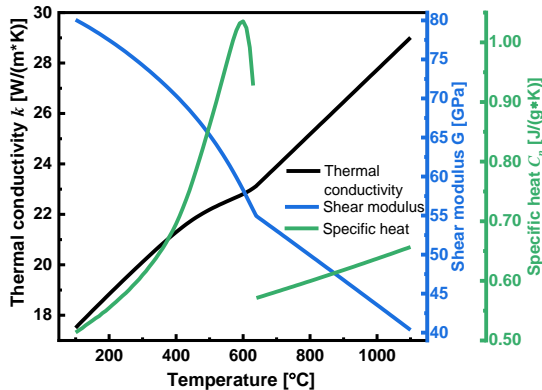


**Fig. A-1** The simulated material properties of thermal conductivity, heat capacity, and shear modulus of the as-received AISI 304L by JMatPro®- v. 7.0

## References

- [1] F. SADEGHI ET AL.: 'Role of the annealing twin boundary on the athermal  $\alpha'$ -martensite formation in a 304 austenitic stainless steel', *Materialia*, 20, 2021.
- [2] L.C. LI ET AL.: 'Effect of welding heat input on grain size and microstructure of 316L stainless steel welded Joint', *Applied Mechanics and Materials*, Trans Tech Publ., 2013.
- [3] P. VASANTHARAJA ET AL.: 'Assessment of Residual Stresses and Distortion in Stainless Steel Weld Joints', *Materials and Manufacturing Processes*, 27(12), p. 1376-1381, 2012.
- [4] J. MORRIS JR.: 'The influence of grain size on the mechanical properties of steel', 2001.
- [5] P. WANG ET AL.: 'Effect of grain ultra-refinement on microstructure, tensile property, and corrosion behavior of low alloy steel', *Materials Characterization*, 179, p. 111385, 2021.

- [6] D. PODDAR, A. CHAKRABORTY and RAVI KUMAR B.: ‘Annealing twin evolution in the grain-growth stagnant austenitic stainless steel microstructure’, *Materials Characterization*, 155, p. 109791, 2019.
- [7] T. WEN ET AL.: ‘Influence of high frequency vibration on microstructure and mechanical properties of TIG welding joints of AZ31 magnesium alloy’, *Transactions of Nonferrous Metals Society of China*, 25(2), p. 397-404, 2015.
- [8] M. SABZI and S.M. DEZFULI: ‘Drastic improvement in mechanical properties and weldability of 316L stainless steel weld joints by using electromagnetic vibration during GTAW process’, *Journal of Manufacturing Processes*, 33, p. 74-85, 2018.
- [9] C. MA ET AL.: ‘Investigation of In Situ Vibration During Wire and Arc Additive Manufacturing’, *3d Printing and Additive Manufacturing*, 2021.
- [10] S.M. AL-QAWABAH and A.I. ZAID: ‘Different methods for grain refinement of materials’, *International Journal Of Scientific & Engineering Research*, Volume 7, Issue 7, p. 8, 2016.
- [11] A.K. MONDAL ET AL.: ‘Development of avocado shape heat source model for finite element based heat transfer analysis of high-velocity arc welding process’, *International Journal of Thermal Sciences*, 166, p. 107005, 2021.
- [12] J.J. XU ET AL.: ‘Temperature and residual stress simulations of the NeT single-bead-on-plate specimen using SYSWELD’, *International Journal of Pressure Vessels and Piping*, 99-100, p. 51-60, 2012.
- [13] J.E. AZKUE: *In-situ analysis of thermomechanical welding process*, bachelor thesis Mondragon University Faculty of Engineering, Spain, 2022.
- [14] B. SZALOWSKI ET AL.: ‘Effect of local deformation during TIG welding of austenitic stainless steel on the microstructure and hardness’, in *ESSC & Duplex 2022*, Verona, Italy, 2022.
- [15] J. GOLDAK, A. CHAKRAVARTI and M. BIBBY: ‘A new finite element model for welding heat sources’, *Metallurgical Transactions B*, 15(2), p. 299-305, 1984.
- [16] Z. SAMAD, N.H.M. NOR and E.R.I. FAUZI: ‘Thermo-Mechanical Simulation of Temperature Distribution and Prediction of Heat-Affected Zone Size in MIG Welding Process on Aluminium Alloy EN AW 6082-T6’, *IOP Conference Series: Materials Science and Engineering*, 530, 2019.
- [17] G. FU ET AL.: ‘Parameter determination of double-ellipsoidal heat source model and its application in the multi-pass welding process’, *Ships and Offshore Structures*, 10(2), p. 204-217, 2015.
- [18] A. LUNDBÄCK: *Finite element modelling and simulation of welding of aerospace components*, thesis, Luleå tekniska universitet, 2003.
- [19] J. DUPONT and A. MARDER: ‘Thermal efficiency of arc welding processes’, *Welding Journal-Including Welding Research Supplement*, 74(12), p. 406s, 1995.
- [20] B. SZALOWSKI: *Effect of Thermomechanical Welding on the Austenitic Stainless Steel*, master thesis, Institute of Materials Science, Joining and Forming, Graz University of Technology, 2022.
- [21] A. BAGHDADCHI, V.A. HOSSEINI and L. KARLSSON: ‘Identification and quantification of martensite in ferritic-austenitic stainless steels and welds’, *Journal of Materials Research and Technology-Jmr&T*, 15, p. 3610-3621, 2021.
- [22] T. SAKAI ET AL.: ‘Dynamic and post-dynamic recrystallization under hot, cold and severe plastic deformation conditions’, *Progress in Materials Science*, 60, p. 130-207, 2014.
- [23] H.H. ZARGARI ET AL.: ‘Metallurgical Characterization of Penetration Shape Change in Workpiece Vibration-Assisted Tandem-Pulsed Gas Metal Arc Welding’, *Materials*, 13(14), 2020.
- [24] S.A. DAVID: ‘Ferrite Morphology and Variations in Ferrite Content in Austenitic Stainless-Steel Welds’, *Welding Journal*, 60(4), p. S63-S71, 1981.

- [25] M.F. SIDDIQUI: *Recrystallization and Grain Growth Behavior of Austenitic Stainless Steel 304L*, master thesis, IMAT-Institute of Materials Science, Joining and Forming, Graz University of Technology, 2021.
- [26] D. SAMANTARAY, S. MANDAL and A.K. BHADURI: 'A critical comparison of various data processing methods in simple uni-axial compression testing', *Materials & Design*, 32(5), p. 2797-2802, 2011.



# **III Artificial Intelligence**



# STUDY OF RESISTANCE SPOT WELDING VIA EXPERIMENTAL, NUMERICAL AND ADVANCED ANALYTICAL METHODS

H. GAO, R. ZWART, E. VD AA, T. VD VELDT

*Tata Steel in the Netherlands*

*DOI 10.3217/978-3-85125-968-1-11*

## ABSTRACT

In this work, finite element welding models are firstly validated with experimental measurements. Cases with different weld time, weld current and squeeze force are subsequently simulated in order to create a new database. Multiple linear regression, decision tree and random forest methods are used to train the analytical models. The trained analytical models are used to predict new experiments with reasonably good accuracy. In addition, weights for the input variables are explicitly ranked and discussed, which provides valuable information for optimizing the welding process. The main conclusions are summarized as follows,

- The approaches proposed in this work to combine the experiments, numerical models and analytical models are proven to be reliable and can be extended to other materials and processes.
- Increase in weld time or weld current, or decrease in squeeze force will increase the nugget size. With the studied material, multiple linear regression model provides two equations to calculate the nugget diameter and height with respect to weld time, weld current and squeeze force. Decision tree has a slightly better accuracy than multiple linear regression. Random forest provides the best predictions.
- Weld current has a dominating weight (more than 0.85) to determine the final nugget size. Squeeze force has a weight of 0.12 for determining the nugget height.

Key words: Resistance spot welding, Finite element model, Advanced analytics, AHSS

## INTRODUCTION

Advanced high strength steels (AHSS) are increasingly used by the automotive manufacturers to reduce weight of a vehicle. A 10% reduction in vehicle weight can save fuel by 3% to 7% [1]. It has been reported that more than 4000 welds are made on a body in white car frame [2]. Resistance spot welding is the mostly applied method due to low cost, high degree of automation and small workload. The strength of a weld is strongly dependent on the weld nugget size. Therefore, it is of great importance to understand the relationship between the weld nugget size and welding parameters.

Finite element modelling is a widely used method to predict thermal and mechanical material responses during welding [3]. However, a virtual heat flux with a certain distribution has to be defined for simulation of either a laser welding or arc welding process [4-5], which always leads to a discussion on its reliability. Simulation of resistance spot welding can be fully based on the physics of Joule heating, where heat generation is calculated from the contact resistance at the sheet interface [6]. Therefore, combination of experimental and numerical approaches becomes an effective way to gain a better insight of temperature and strain/stress evolution during resistance spot welding and optimize welding parameters on demand. However, for a physical-based model with complex structure and processing conditions, calculation time for a numerical model can be very expensive. In addition, weights of input variables cannot be explicitly studied from simulation. Any changes in material properties, sample dimension and welding parameters will lead to a re-run of the model.

With development of modern high-speed computers, modeling based on big data has become a powerful approach to control and optimize different process parameters. Advanced analytical model has proven to an effective tool for resolving complex problems related to multiple factors [7]. Therefore, combination of experimental, numerical and advanced analytical methods to study resistance spot welding is explored in this work. An advanced high strength steel DP800-GI with a thickness of 1.2 mm was selected for resistance spot welding experiments. Finite element welding models are firstly constructed and validated with experimental measurements. A new database with different squeeze force, weld time and weld current are subsequently simulated. Multiple linear regression, decision tree and random forest methods are used to train the analytical models. The trained analytical models are used to predict new experiments with reasonably good accuracy. In addition, weights for the input variables are explicitly ranked and discussed, which provides valuable information for optimizing the welding process.

## MATERIALS AND METHODS

### MATERIAL AND WELDING EXPERIMENT

A dual phase (DP) steel with a thickness of 1.2 mm was selected for the experimental approaches in this study. This steel was received in a cold-rolled and galvanized condition with a coating weight of 50 gm<sup>-2</sup>. The testing coupons were prepared with a dimension of 45 mm x 45 mm. The chemical compositions of the studied material with Fe balanced are listed in Table 1.

**Table 1** Chemical composition of studied material with Fe balanced (wt%)

C	Si	Mn	Al
0.15	0.096	2.063	0.647

Resistance spot welds were produced on a 1000 MHz MFDC spot welding machine, using a constant current regulation. ISO5821 F1-16-20-6 CuCr1Zr electrodes were tip-

dressed before use. The welding specification was according to the VDEh SEP1220-2 standard [8], as shown in Table 2. The welding current range was determined by producing two welds per current setting, starting from a welding current of 3.0 kA with an increment step of 0.2 kA. The minimum current was found when the weld spot diameter is greater than  $4\sqrt{t}$  ( $t$  refers to sample thickness). When splash occurs between the sheets in two subsequent welds at identical welding current settings, the welding current was decreased in steps of 0.1 kA. The maximum current was determined until three consecutive welds were made without splash.

**Table 2** Welding specification according to SEP1220-2

Force (kN)	Squeeze time (ms)	Weld time (ms)	Hold time (ms)
4	400	320	200

NUMERICAL MODEL

SORPAS@2D welding is used in this work for modelling approaches. Temperature dependent material properties of DP800, such as thermal conductivity, specific heat capacity, density, thermal expansion coefficient, Young’s modulus, flow stress curves, were obtained from the SORPAS materials database. For welding simulation, a 1000Hz DC arbitrary projection/spot welding machine was selected from the SORPAS machine database and ISO5821 F1-16-20-6 CuCr1Zr electrodes with a geometry matching the experimental configuration were defined. Zinc surface coating was selected with a thickness of 50 g/m<sup>2</sup>. The model set-up for resistance spot welding is shown in Fig. 1. The numerical welding simulation in this work follows the ISO/TS 18166 guidelines [9].

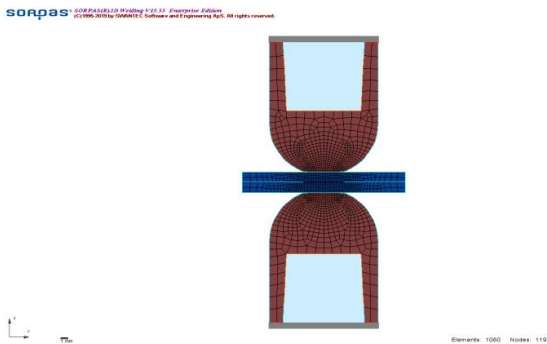


**Fig. 1** Model set-up and mesh arrangement

ADVANCED ANALYTICAL MODEL

Advanced analytics employs predictive modeling, statistical methods, machine learning and process automation techniques beyond the capacities of traditional business intelligence (BI) tools to analyze data or business information. Three advanced analytical models were used in this study, i.e., multiple linear regression, decision tree and random forest. The scripts were compiled using Python language. Packages of SCIPY, PANDAS and NUMPY were imported.

Multiple linear regression (MLR) is a method used to model the linear relationship between a dependent variable and two or more independent variables. The MLR equation can be expressed as follows,

$$y = b_0 + b_1x_1 + b_2x_2 + \dots + b_px_p \quad (1)$$

where  $y$  is the predicted or expected value of the dependent variable,  $x_1$  through  $x_p$  are  $p$  distinct independent or predictor variables,  $b_0$  is the value of  $y$  when all the independent variables ( $x_1$  through  $x_p$ ) are equal to zero, and  $b_1$  through  $b_p$  are the estimated regression coefficients. Each regression coefficient represents the change in  $y$  relative to a one-unit change in the respective independent variable. MLR is based on ordinary-least-squares (OLS), the model is fit such that the sum-of-squares of differences of observed and predicted values is minimized.

Decision tree builds regression or classification models in the form of a tree structure. It breaks down a dataset into smaller and smaller subsets while at the same time an associated decision tree is incrementally developed. The final result is a tree with decision nodes and leaf nodes. A decision node has two or more branches, each representing values for the attribute tested. Leaf node represents a decision on the numerical target. The topmost decision node in a tree which corresponds to the best predictor called root node. A node will be split if this split induces a decrease of the impurity greater than or equal to this value. The weighted impurity decrease equation is the following,

$$N_t / N * (impurity - N_{t_R} / N_t * right\_impurity - N_{t_L} / N_t * left\_impurity) \quad (2)$$

where  $N$  is the total number of samples,  $N_t$  is the number of samples at the current node,  $N_{t_L}$  is the number of samples in the left child, and  $N_{t_R}$  is the number of samples in the right child. The advantages of decision trees are simple to understand and interpret and capable of handle both categorical and numerical data. However, a small change in the training data can result in a large change in the tree and consequently the final predictions.

Random forest is a model made up of many decision trees. Rather than just simply averaging the prediction of trees, this model uses two key concepts: random sampling of training data points when building trees and random subsets of features considered when splitting nodes.

RESULTS AND DISCUSSION

VALIDITY OF MATERIAL PROPERTIES AND NUMERICAL MODEL

The SORPAS material database provides properties of universal steel grades (e.g., Mild steels, Dual phase steels, TRIP steels). DP800 was chosen in this work. In order to check the validity of the input material properties, chemical composition of the studied material from Table 1 was imported into JMatPro® to calculate the temperature dependent material properties, and then compared with those from the SORPAS materials database, as shown in Fig. 2. Reasonable agreements have been achieved for both the thermal conductivity and electrical resistivity. As temperature increases, the thermal conductivity from SORPAS database firstly increases to 35.4 W/ m K, and then decreases to 26.1 W/m K, and increases again at high temperatures up to 36.1 W/m K. The calculated thermal conductivity from JMatPro has a slightly overestimation in the temperature range from 300 to 1000 °C. For the electrical resistivity, it increases at elevated temperature. A very good agreement has been achieved between SORPAS and JMatPro. Thermal conductivity and electrical resistivity are the two most important properties for an electrical-thermal analysis, which determines the heat generation at the interfaces and the final weld nugget shape.

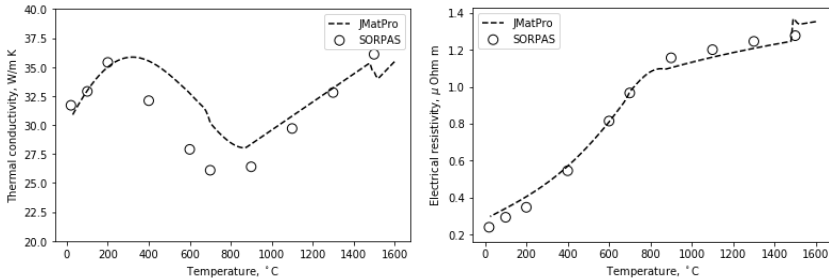


**Fig. 2** Comparison of thermal conductivity (left) and electrical resistivity (right) from SORPAS and JMatPro

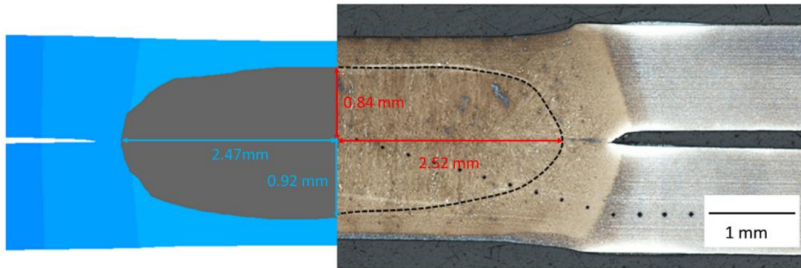


**Fig. 3** Weld nugget size from numerical prediction and experiment measurement with welding current of 6 kA

The weld nugget size was used for validation of the numerical model. The welded sample was cut into cross-section and etched to visualize the weld fusion area. A comparison of the weld nuggets size with a welding current of 6 kA is shown in Fig. 3. A good agreement of the weld nugget shape between the experimental measurement and numerical prediction has been achieved.

#### ADVANCED ANALYTICS

After validation of the numerical model, in total 64 testing conditions were simulated considering different combinations of weld current (7-10 kA), squeeze force (3.5-5 kN) and weld time (280-400 ms). Hold time does not affect the nugget size and it is therefore not investigated. The simulated nugget diameter and height are listed in Table 3. It needs to be addressed that the “Height” exported from SORPAS output is half of the real nugget height. With the same force and time, diameter and height increase when current is increased. With the same force and current, diameter and height increase when time is increased. Increase either in time or current will increase the total heat input, and thus enlarge the nugget size. With the same time and current, diameter and height decrease when force is increased. Increase in force will increase the contact area and decrease the contact resistance at sheets interface. The total heat input is as a result decreased, and thus reduce the nugget size.

## Mathematical Modelling of Weld Phenomena 13

**Table 3** Simulated weld nugget diameter and height with different combinations of squeeze force, weld time and weld current

Sample	Force (kN)	Time (ms)	Current (kA)	Diameter (mm)	Height (mm)
1	3.5	280	7	4.4237	0.70182
2	3.5	280	8	5.5245	0.89669
3	3.5	280	9	6.1294	0.94104
4	3.5	280	10	6.553	0.98001
5	4	280	7	4.1062	0.64227
6	4	280	8	5.2759	0.86884
7	4	280	9	6.0805	0.92618
8	4	280	10	6.5191	0.96463
9	4.5	280	7	3.9487	0.61293
10	4.5	280	8	5.1783	0.82468
11	4.5	280	9	6.06	0.91139
12	4.5	280	10	6.5057	0.95405
13	5	280	7	3.8082	0.55913
14	5	280	8	5.0542	0.77551
15	5	280	9	5.8206	0.89114
16	5	280	10	6.475	0.92805
17	3.5	320	7	4.6984	0.79285
18	3.5	320	8	5.6941	0.90322
19	3.5	320	9	6.2977	0.94355
20	3.5	320	10	6.7896	0.97874
21	4	320	7	4.5206	0.71044
22	4	320	8	5.6094	0.88946
23	4	320	9	6.202	0.92883
24	4	320	10	6.7442	0.96341
25	4.5	320	7	4.4326	0.68644
26	4.5	320	8	5.558	0.85753
27	4.5	320	9	6.1441	0.91349
28	4.5	320	10	6.7214	0.9525
29	5	320	7	4.0425	0.60017
30	5	320	8	5.3025	0.80125
31	5	320	9	6.1551	0.92083
32	5	320	10	6.6625	0.92901
33	3.5	360	7	5.0532	0.80764
34	3.5	360	8	5.8877	0.90686
35	3.5	360	9	6.3962	0.94257
36	3.5	360	10	6.9645	0.9772

## Mathematical Modelling of Weld Phenomena 13

37	4	360	7	4.8429	0.73625
38	4	360	8	5.8274	0.88872
39	4	360	9	6.3159	0.92887
40	4	360	10	6.9162	0.96132
41	4.5	360	7	4.6282	0.69027
42	4.5	360	8	5.7638	0.85777
43	4.5	360	9	6.3221	0.91415
44	4.5	360	10	6.8847	0.94867
45	5	360	7	4.3306	0.61704
46	5	360	8	5.5532	0.80036
47	5	360	9	6.2265	0.89761
48	5	360	10	6.746	0.92515
49	3.5	400	7	5.2071	0.8065
50	3.5	400	8	6.068	0.90581
51	3.5	400	9	6.587	0.94096
52	3.5	400	10	7.0357	0.96976
53	4	400	7	5.0281	0.73714
54	4	400	8	5.9915	0.88744
55	4	400	9	6.543	0.92703
56	4	400	10	7.0007	0.95227
57	4.5	400	7	4.883	0.69821
58	4.5	400	8	5.9304	0.8567
59	4.5	400	9	6.4763	0.91282
60	4.5	400	10	6.9718	0.93797
61	5	400	7	4.5363	0.63719
62	5	400	8	5.654	0.79939
63	5	400	9	6.3993	0.89579
64	5	400	10	6.9479	0.92291

The created database is divided into two sets, 70 % of which was used for training the model, and 30 % was kept for validation. Weld nugget diameter and height are defined as target functions. Three advanced analytical models were used, *i.e.*, multiple linear regression, decision tree and random forest. The associated results are shown in Fig. 4. A dashed line is plotted in every figure for reference. A shorter distance of the dots to the dashed line indicates a better fit of the predictions. R square ( $R^2$ ) and root mean square error (RMSE) of the models are shown in Table 4. For nugget diameter prediction, the  $R^2$  of the multiple linear regression model is 0.951 with a RMSE of 0.193 mm. Decision tree model shows a better prediction between 5.5 mm and 6.5 mm. The  $R^2$  and RMSE are 0.973 and 0.141 mm respectively. Random forest model improves the prediction by random sampling the training points and random subset of features when splitting the nodes. The  $R^2$  of random forest reaches 0.979 with a RMSE of 0.126 mm. For nugget

height prediction, the  $R^2$  of multiple linear regression model only achieves 0.803, while decision tree and random forest have a better accuracy of 0.93 and 0.966, respectively.

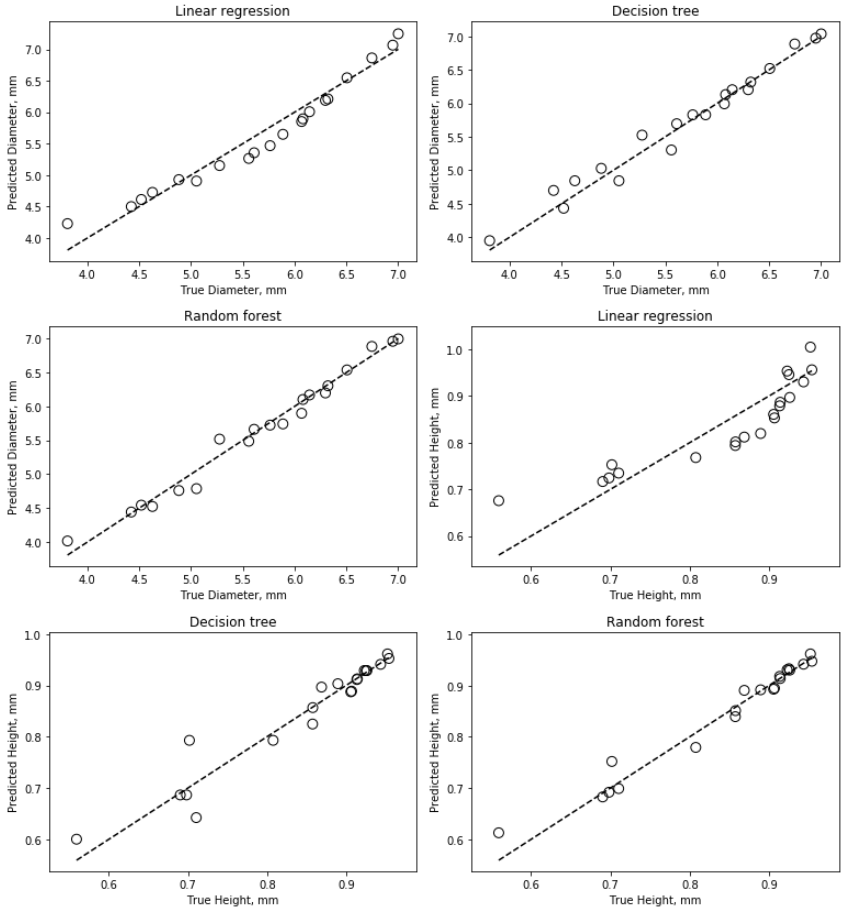


**Fig. 4** Results of multi-linear regression, decision tree and random forest models

**Table 4** Results from different advanced analytical models.

	Linear regression	Decision tree	Random forest	Linear regression	Decision tree	Random forest
	Diameter			Height		
<b>R<sup>2</sup></b>	0.951	0.973	0.979	0.803	0.930	0.966
<b>RMSE</b>	0.193	0.141	0.126	0.048	0.028	0.019

**Table 5** Weighting factors of decision tree and random forest models.

	Decision tree	Random forest	Decision tree	Random forest
	Diameter		Height	
<b>Force</b>	0.036	0.030	0.129	0.123
<b>Time</b>	0.065	0.062	0.021	0.020
<b>Current</b>	0.899	0.908	0.850	0.857

From the multiple linear regression model, three coefficients and one intercept of the input variables can be obtained. Therefore, a multi-linear equation can be generated to predict the weld nugget diameter and height based on force, time and current,

$$Diameter = -0.181 * force + 0.005 * time + 0.743 * current - 1.488 \quad (3)$$

$$Height = -0.051 * force + 0.0002 * time + 0.085 * current + 0.284 \quad (4)$$

Table 5 shows the weights of force, time and current related to nugget size. From the decision tree model, weld current is the dominating variable (more than 0.899) to determine the nugget diameter. Random forest model shows a slightly higher weight (0.908) than that of the decision tree. Weld time is ranked the second and squeeze force has the least influence on the nugget diameter. For prediction of nugget height, weld current has still the dominating weight of 0.85. However, squeeze force is ranked the second in the order of 0.12. Weld time has the least influence on the nugget height.

Besides ranking the weights of input variables, another advantage of using a tree-like model is to trace the split at every node. The ‘sklearn.tree’ package was used to export the data for node split. Fig. 5 shows the tree layout using ‘Graphviz’. As ‘current’ has the most weight in determining the nugget size, it was picked as the root node. The threshold is 8.5 kA with 44 samples. The target value is 5.851 mm. 24 samples were found with ‘current’ greater than the first threshold. As there are many branches generated in the subsequent judgements, only the bottommost branch is chosen here for discussion. The second judgement is ‘current’ less than 9.5 kA, which returns 12 samples with ‘truth’ and 12 samples with ‘false’. The third judgement is ‘time’ less than 300 ms, which returns 7 samples with ‘truth’ and 5 samples with ‘false’. The fourth judgement is ‘time’ less than 380 ms, which returns 3 samples with ‘truth’ and 4 samples with ‘false’. The fifth judgement is ‘force less than 4 kN, which determines the weld diameter of 7.036 mm with ‘truth’ and 6.972 mm with ‘false’. The similar interpretations can be applied to other branches.

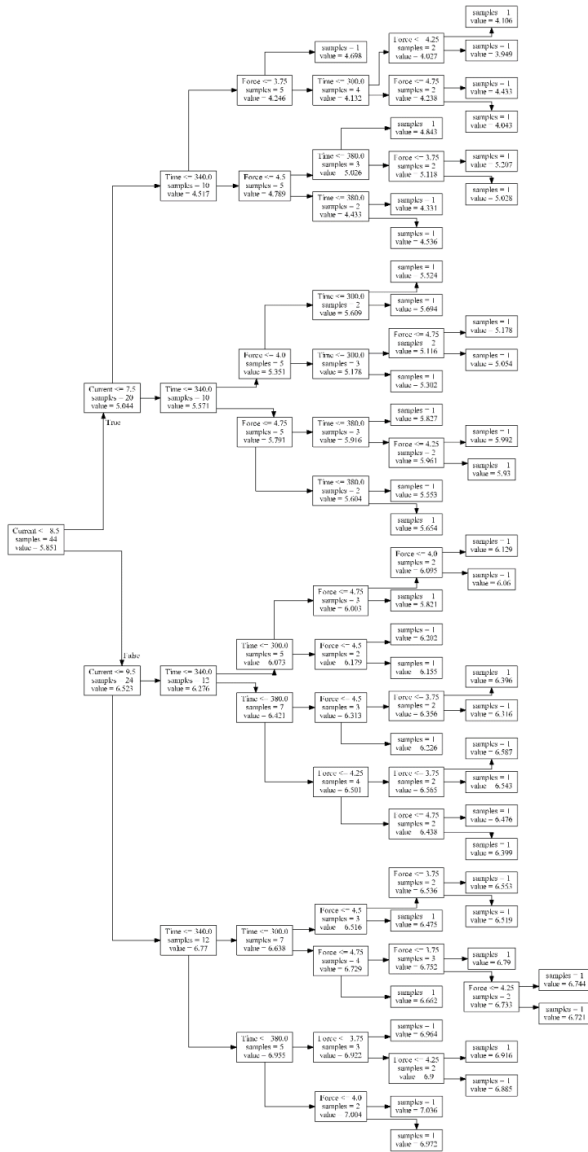


Fig. 5 Node split with respect to squeeze force, weld time and current

## CONCLUDING REMARKS

In this work, finite element welding models are firstly validated with experimental measurements. Cases with different weld time, weld current and squeeze force are subsequently simulated in order to create a new database. Multiple linear regression, decision tree and random forest methods are used to train the analytical models. The trained analytical models are used to predict new experiments with reasonably good accuracy. In addition, weights for the input variables are explicitly ranked and discussed, which provides valuable information for optimizing the welding process. The main conclusions are summarized as follows,

- The approaches proposed in this work to combine the experiments, numerical models and analytical models are proven to be reliable and can be extended to other materials and processes.
- Increase in weld time or weld current, or decrease in squeeze force will increase the nugget size. With the studied material, multiple linear regression model provides two equations to calculate the nugget diameter and height with respect to weld time, weld current and squeeze force. Decision tree has a slightly better accuracy than multiple linear regression. Random forest provides the best predictions.
- Weld current has a dominating weight (more than 0.85) to determine the final nugget size. Squeeze force has a weight of 0.12 for determining the nugget height.

## References

- [1] W.J. JOOST: 'Reducing Vehicle Weight and Improving U.S. Energy Efficiency Using Integrated Computational Materials Engineering', *JOM* 64, 2012, pp. 1032-1038.
- [2] M.P. MALI, K. INAMDAR: 'Effect of Spot Weld Position Variation on Quality of Automobile Sheet Metal Parts', *International Journal of Applied Research in Mechanical Engineering*, 2013, pp. 170-174.
- [3] K. HEMMESI, M. FARAJIAN: 'Numerical Welding Simulation as a Basis for Structural Integrity Assessment of Structures: Microstructure and Residual Stresses', 2018, Article 74466.
- [4] G. AGARWAL, A. KUMAR, I.M. RICHARDSON, M.J.M. HERMANS: 'Evaluation of solidification cracking susceptibility during laser welding in advanced high strength automotive steels', *Materials & Design*, Vol. 183, 2019, Article 108104.
- [5] H. GAO, R.K. DUTTA, R.M. HUIZENGA, M. AMIRTHALINGAM, M.J.M. HERMANS, T. BUSLAPS, I.M. RICHARDSON: 'Pass-by-pass stress evolution in multipass welds', *Science and Technology of Welding and Joining*, Vol. 19, 2014, pp. 256-264.
- [6] A. KUMAR, S. PANDA, G.K. GHOSH, R.K. PATEL: 'Numerical simulation of weld nugget in resistance spot welding process', *Materials Today: Proceedings*, Vol. 27, Part 3, 2020, pp. 2958-2963.
- [7] W. GUAN, Y. ZHAO, Y. LIU, S. KANG, D. WANG, L. CUI: 'Force data-driven machine learning for defects in friction stir welding', *Scripta Materialia*, Vol. 217, 2022, Article 114765.

- [8] *Stahl-Eisen-Prüfblätter Des Stahlinstituts VDEh*: ‘Testing and Documentation Guideline for the Joinability of Steel Sheet Part 2: Resistance Spot Welding’, 2008.
- [9] ISO/TS 18166:2016 Numerical welding simulation - Execution and documentation.



# **IV Laser and Electron Beam Welding**



# ESTABLISHING AN AUTOMATED HEAT-SOURCE CALIBRATION FRAMEWORK

D. K. RISSAKI\*, A. N. VASILEIOU\*, M. C. SMITH\*,  
O. MURÁNSKY\*\*, P. G. BENARDOS\*\*\*,  
G.-C. VOSNIAKOS\*\*\*

*\*The University of Manchester, Department of Mechanical, Aerospace and Civil Engineering, Sackville Street, Manchester M139PL, UK*

*\*\*ANSTO, Institute of Materials Engineering, New Illawarra Road, Lucas Heights, NSW, Australia*

*\*\*\*National Technical University of Athens, School of Mechanical Engineering, Manufacturing Technology Laboratory, GR-15773 Athens, Greece*

DOI 10.3217/978-3-85125-968-1-12

## ABSTRACT

Heat source model calibration is a critical step in the process of developing a weld model. This typically involves running a thermal analysis for various sets of welding input parameters (efficiency, heat source radii, etc), and comparing the simulation results against experimental data, including thermocouple traces and fusion zone boundaries. This trial-and-error approach takes time and requires user judgement. This work aims towards establishing an automation and optimisation framework for heat-source calibration. Exhaustive search, exploration of solution space, and identification of suitable metrics are implemented and applied for the automated heat source calibration of a previously validated arc welding benchmark.

Keywords: heat source calibration, automation, optimisation

## INTRODUCTION

The heat source calibration procedure is a required step to perform finite element welding simulations. The aim of heat source calibration is the identification of realistic heat source parameters for a given welding procedure [1-3]. The heat source parameters include the heat efficiency, the type and size of heat source distribution and its vertical position. The heat source calibration is usually a computationally intensive procedure of trial-and-error, which requires user judgement because of the presence of multiple good solutions and lack of strict guidance for how to handle them. The automation and optimisation of heat source calibration would accelerate the process and would ensure that an optimal solution is found.

Numerous research papers have been focused on the automation and optimisation of heat source calibration, and applied optimisation algorithms to determine the appropriate combination of heat source distribution parameters and heat efficiency simultaneously [4-7] or just the heat source distribution parameters with fixed efficiency [8]. However, the heat efficiency can be determined prior to the heat source geometric parameters by using

experimental data from far-field thermocouples, that is thermocouples far from the weld centre line [9]. The separate determination of heat efficiency and heat source parameters would simplify the optimisation procedure, as the combinations of parameters that need to be examined to find the best solution vector would be significantly reduced. Moreover, the correct efficiency could be safely determined, rather than its correct value being lost in the potentially multiple good solutions of this multi-variable optimisation problem.

This paper aims to establish a framework for implementing this two-step optimisation process for heat source calibration, with the first step being the fixation of heat efficiency and the second the determination of heat source parameters. More specifically, using as case study the NeT project Task Group 4 (TG4) specimen [10-11], an exhaustive search was performed to evaluate the solution space and different metrics were assessed to identify the best strategy for implementing an automated optimised heat source calibration.

### NET-TG4 SPECIMENS

The specimens that were used as a case study in this research are from NeT Task Group 4 (TG4) [10-11]. They are AISI 316L(N) austenitic stainless steel plates with a 3-pass TIG weld in a slot. The filler metal was of type AISI 316L, the travel speed was 76.2 mm/min and no weaving was used. With the same welding parameters, many identical mock-ups were fabricated by this Task Group. In the current research, the experimental thermocouple data used were from specimens named 2-1A and 3-1B, and the experimental fusion boundary was taken from the macrograph of the specimen named 1-2B (Fig. 1). Only the 1<sup>st</sup> pass was studied.

The experimental thermocouple data were obtained from 12 locations on each specimen, as shown in Fig. 2. The thermocouples at the start and stop ends were not included in the analysis of this research, to minimise the influence of starting and stopping effects and concentrate on quasi-steady-state conditions at the bead mid-length. Thus, only the mid-length thermocouples were used, that is TC2, TC5, TC10, TC11, TC12 on the front (welded) face and TC7, TC8, TC9 on the back face. The temperature increases (maximum temperature minus initial temperature) of these thermocouples were examined, to identify which ones can be considered far-field (adequately far from heat source to not be very influenced by the local heat source characteristics). The lowest temperature increases were experienced by TC5, TC7, TC8, TC12, as can be seen in Table 1. Thus, these thermocouples will be characterised as far-field. The rest of the thermocouples used in this study, that is TC2, TC9, TC10, TC11, experienced high temperature increases and will be characterised as near-field. The temperature increases were in accordance with the distance of thermocouples from the heat source. More specifically, the nearer the thermocouple position to the heat source the higher the temperature increase experienced. The nominal positions of thermocouples can be seen in Table 1. The actual positions measured after completion of welding were slightly different from nominal, and the estimated actual positions of thermocouples were used in the simulations of this study, as it can be seen in Table 1.

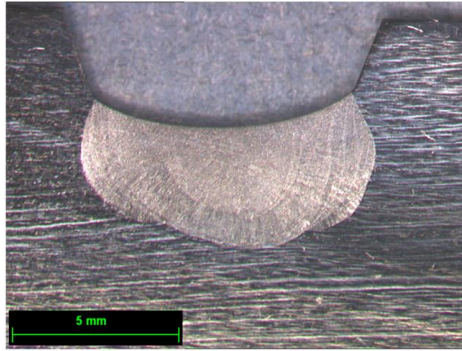


**Fig. 1** Macrograph of 1-2B specimen that was used in this study as representative fusion boundary of NeT-TG4 benchmark [10]

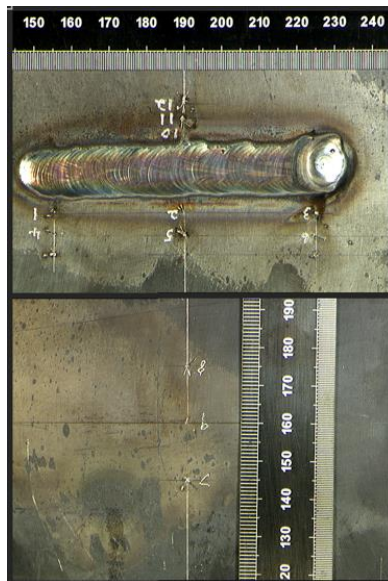


**Fig. 2** Positioning of thermocouples on 3-1B mock-up [12]

**Table 1** Experimental temperature increases  $\Delta T$  (maximum - initial temperature) for thermocouples of specimens 2-1A and 3-1B and thermocouple nominal and estimated actual positions.

thermocouple	$\Delta T_{exp}$	$\Delta T_{exp}$	x	y	x	x	y	y
	2-1A	3-1B	nominal	nominal	actual	actual	actual	actual
					2-1A	3-1B	2-1A	3-1B
TC2	386.0	490.6	+13	0	12.4	12	0	0
TC5	246.3	265.7	+18	0	17.5	18.1	0	0
TC7	267.8	284.3	+15	18	14.3	15.1	18	18
TC8	284.9	255.7	-15	18	15.1	15.1	18	18
TC9	453.8	456.9	0	18	0.1	0.4	18	18
TC10	533.6	622.9	-9	0	8.9	8.6	0	0
TC11	350.5	371.6	-13	0	12.8	13.5	0	0
TC12	228.0	217.9	-18	0	18	17.1	0	0

EXHAUSTIVE SEARCH FOR HEAT EFFICIENCY

3-D steady-state analysis was performed with the FEAT-WMT heat source fitting tool [13]. The temperature dependent material properties and other weld modelling details can be found in [14-15], and were the same for all simulations of this study. The type of heat source used was ellipsoid, described by the Eq. (1):

$$q = \frac{Q}{Va} \exp - \left\{ \left( \frac{x}{rl} \right)^2 + \left( \frac{y}{rv} \right)^2 + \left( \frac{z}{ra} \right)^2 \right\} \tag{1}$$

where q is the power per unit volume, Q is the total power deposited, (x,y,z) is the geometric center of the distribution, and r<sub>l</sub>, r<sub>v</sub>, r<sub>a</sub> are the radii of distribution in the lateral, vertical and axial directions respectively. The quantity Va is adjusted by the FEAT-WMT program automatically, so that the total power input is Q.

The three heat source distribution radii were first fixed to 1.0 mm size each, and many simulations run with different values of heat efficiency (from 10% to 100%). It was expected that the simulation temperature increase in far-field thermocouple points would not be much influenced by the arbitrary initial choice of heat source geometrical parameters. Therefore, it was expected that the heat efficiency could be quickly and accurately determined by comparing the temperature increases at these far-field points with the experimental ones, until an efficiency is found in which these two temperature increases are as close as possible. The metric used for comparison of the far-field temperature curves was the root mean square error (RMSE) of thermocouple increases, Eq. (2):

$$RMSE = \sqrt{\left\{ \sum_{i=1}^{i=n} \frac{1}{n} \{ (\Delta T_{TCi,sim} - \Delta T_{TCi,exp}) / \Delta T_{TCi,exp} \}^2 \right\}} \tag{2}$$

where n is the number of far-field thermocouples (n = 4 for this study) and ‘i’ is the thermocouple numbering.  $\Delta T$  denotes the temperature increase (maximum - initial temperature), and ‘sim’ refers to the simulation temperature increase, while ‘exp’ to the experimental one.

Both 2-1A and 3-1B specimens were found to have only one efficiency that minimises the RMSE. For the 2-1A specimen the efficiency that minimised the RMSE was 74% and for the 3-1B specimen it was 73%. Because of this slight disagreement, the average of the two RMSE was calculated and found that it was minimised at 74% efficiency, as it can be seen in Fig. 3. A similar triangular shape of graph was observed for the RMSE-efficiency graph of specimen 2-1A, of specimen 3-1B and in all other RMSE-efficiency graphs plotted in this study. Another method of using both specimens to determine the efficiency would be to use thermocouples from both specimens to calculate a single RMSE. One thing that should be considered in that case would be that the thermocouples used in each of the specimens should be equal in number, so that the specimen with more thermocouples does not dominate in the RMSE calculation. Both methods seem reasonable; however, they could lead to slightly different results.

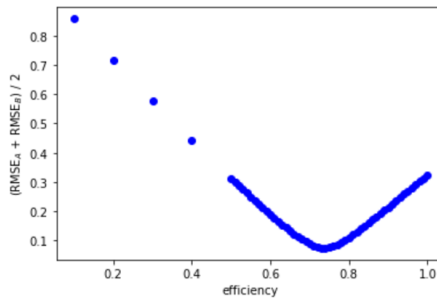


**Fig. 3** Average RMSE of mock-ups 2-1A and 3-1B of far-field thermocouples for various values of heat efficiency

## EXHAUSTIVE SEARCH FOR HEAT SOURCE RADII

After the initial fixation of efficiency to 74% based on experimental and simulation far-field thermocouple comparison, the solution space for best choice of heat source radii was examined. Based on previous experience within NeT-TG4, the interval of exploration that would possibly contain the optimal heat source radii solution was judged to be within the 1.0-3.0 mm interval for each of the three radii ( $r_a$ ,  $r_l$ ,  $r_v$ ). Many simulations were run, with altogether having all possible combinations of heat source radii within the specified interval and with step of 0.1 mm. The efficiency was kept fixed for all these simulations at 74%.

A metric was developed to compare the experimental and simulation fusion boundary shapes automatically. Two mean square errors (MSE)<sup>1</sup> between the two fusion boundary shapes were calculated, one in respect to x axis (measuring the vertical distance of the two curves) and one in respect to y axis (measuring the horizontal distance of the two curves). The final metric for automatic fusion boundary comparison was the average value of the horizontal MSE and vertical MSE. This metric was proved capable of comparing any two curves of fusion boundaries, regardless of their different shapes and scales; the shapes of the whole profiles of the two curves were compared and the melted area was indirectly compared as well. Fig. 4 illustrates an example of fusion boundary comparison with this metric. The code to implement this metric, as well as the rest of the code of this study, can be found at [16].

The steps to implement this fusion boundary comparison metric were the following:

1. The simulation and experimental fusion boundary profiles should be at the same scale and aligned on the vertical axis. Also, in axisymmetric weld simulations, the simulation fusion boundary should be mirrored at the vertical axis to acquire both left and right profiles.
2. To calculate the horizontal fusion boundary MSE, the right halves of simulation and experimental fusion boundaries were isolated, and their axes flipped (the x axis of the graphs to be used as y axis and vice versa), so for the profiles to form functions.
3. Cubic interpolation was performed to the exact same points of horizontal axis for both simulation and experimental half profiles.
4. The mean square error between the interpolated points (their mean squared vertical distance) was calculated.
5. The steps 2-4 were repeated for the left halves of simulation and experimental fusion boundaries. Then the right horizontal and left horizontal MSEs were averaged to find the total horizontal MSE.
6. To calculate the vertical fusion boundary MSE, the x and y axes remained as they were (no flipping), but only the bottom profile was kept, so that it formed a function.
7. Then, the steps 3, 4 were implemented.
8. Finally, the horizontal and vertical MSEs were averaged to form the total fusion boundary MSE.

---

<sup>1</sup> mean square error is the average squared difference between some estimated ( $\hat{Y}_i$ ) and actual ( $Y_i$ ) values, given by the formula  $MSE = \frac{1}{n} \sum_{i=0}^n (\hat{Y}_i - Y_i)^2$ .

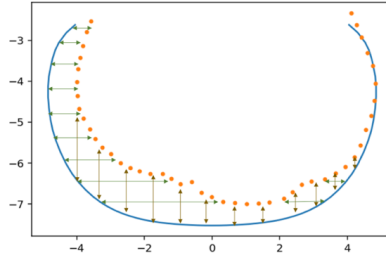


**Fig. 4** Visual representation of fusion boundary comparison of simulation solution (effic. = 74%,  $r_a=1.0$ ,  $r_l=1.5$ ,  $r_v=2.5$ ) and experimental fusion boundary. The vertical MSE of this comparison is 0.89, the horizontal MSE is 1.34, and thus the total (averaged) MSE is 1.12.

Many different simulation fusion boundaries were generated from the exhaustive search of heat source radii solutions, and some trends were observed. By increasing only one radius each time and keeping the rest at small values, it was noticed that the increase of vertical radius  $r_v$  increased the depth of simulation fusion boundary, the increase of lateral radius  $r_l$  increased its width, and the increase of axial radius  $r_a$  reduced the melted area a little.

The fusion boundary comparison metric was found to be influenced by all three heat source distribution radii, as it can be seen in Fig. 5. The solution that minimised this metric was ( $r_a=2.9$ ,  $r_l=2.2$ ,  $r_v=1.5$ ).

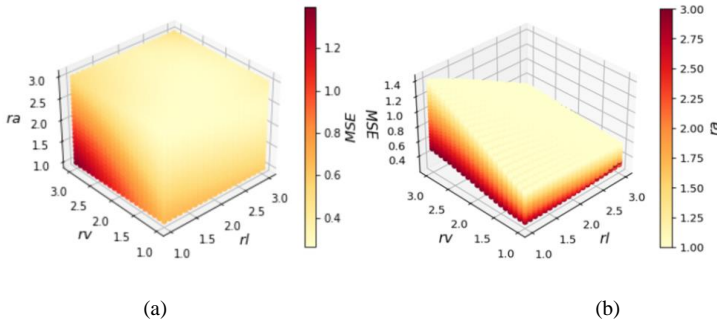


**Fig. 5** Fusion boundary MSE of the exhaustive search of radii interval 1.0-3.0 and efficiency fixed to 74%. In subfigure (a) the MSE is represented by the colour map in a three-axes space of radii values, while in subfigure (b) the MSE is represented by the vertical axis. The minimum MSE value is at ( $r_a=2.9$ ,  $r_l=2.2$ ,  $r_v=1.5$ ).

The thermocouple RMSEs, far-field and near-field, were also examined. For far-field thermocouples the RMSE described by Eq. 2 was used, and the RMSEs of the two specimens 2-1A and 3-1B were averaged. For near-field thermocouples however, a weighted RMSE was used, described by the Eq. 3. Weighted means that, each thermocouple term in the RMSE expression was divided by the total number of

thermocouples that were located in the same side with this thermocouple term (left side, right side, or middle). The reason for this was that the number of near-field thermocouples on the left side of the weld was different to the number of near-field thermocouples on the right side. Since the experimental fusion boundary has not always symmetry about the vertical axis, the thermocouples on the left side of the weld might have different opinion on the heat source parameters than the thermocouples on the right. If a non-weighted RMSE was used, then the opinion of the side with more thermocouples would dominate, and we would not want such bias.

$$RMSE_{weighted} = \sqrt{\left\{ \left[ \frac{(\Delta T_{TC2, sim} - \Delta T_{TC2, exp})}{\Delta T_{TC2, exp}} \right]^2 + \left[ \frac{(\Delta T_{TC10, sim} - \Delta T_{TC10, exp})}{\Delta T_{TC10, exp}} \right]^2 + \frac{(\Delta T_{TC11, sim} - \Delta T_{TC11, exp})}{\Delta T_{TC11, exp}} \right\} / 2 + \left[ \frac{(\Delta T_{TC9, sim} - \Delta T_{TC9, exp})}{\Delta T_{TC9, exp}} \right]^2 / 3} \quad (3)$$

The weighted RMSE of each specimen 2-1A and 3-1B was calculated and then they were averaged across the two specimens. In the following text, when referring to RMSE of far-field or near-field thermocouples we will mean that Eq. 2 and Eq. 3 were used respectively, and also that the calculated RMSEs were averaged across the two specimens.

The far-field thermocouples showed very low variation of RMSE value with different combinations of heat source radii, as it can be seen in Fig. 6, and they appeared to be mainly influenced by lateral radius ( $r_l$ ). The near-field thermocouples also showed to have small influence by the heat source radii, as can be seen in Fig. 7, and were found to be influenced more by the vertical and lateral radii ( $r_l$  and  $r_v$ ) rather than the axial ( $r_a$ ). It should be pointed out however, that these observations were true for the specific interval of solution space that was examined (1.0 - 3.0), and cannot be safely generalised for other intervals or welding cases.

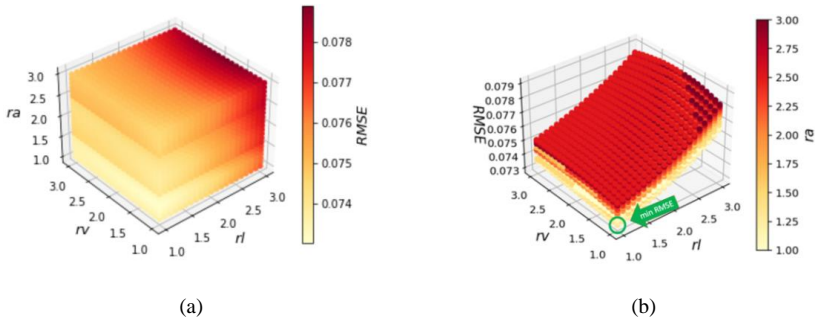


**Fig. 6** RMSE of far-field thermocouples (averaged across specimens 2-1A and 3-1B) of the exhaustive search of radii interval 1.0-3.0 and efficiency fixed to 74%. In subfigure (a), the RMSE is represented by the colour map in a three-axes space of radii values. In subfigure (b), the RMSE is represented by the vertical axis and its minimum value ( $r_a=1.3$ ,  $r_l=1.0$ ,  $r_v=1.0$ ) is pointed out by the arrow.

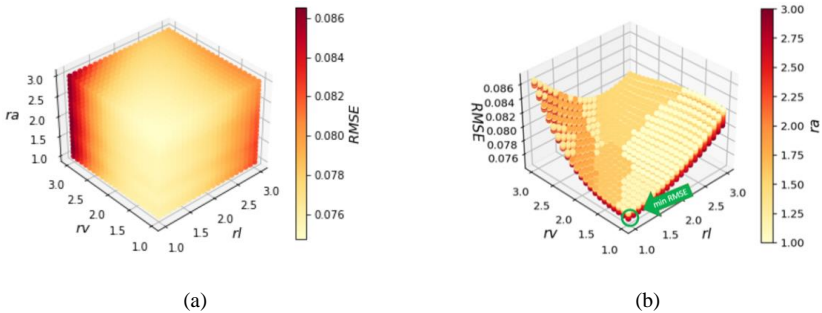


**Fig. 7** Weighted RMSE of near-field thermocouples (averaged across specimens 2-1A and 3-1B) of the exhaustive search of radii interval 1.0-3.0 and efficiency fixed to 74%. In subfigure (a), the RMSE is represented by the colour map in a three-axes space of radii values. In subfigure (b), the RMSE is represented by the vertical axis and its minimum value ( $r_a=3.0$ ,  $r_r=1.0$ ,  $r_v=1.0$ ) is pointed out by the arrow.

It is of interest that both far-field and near-field show preference towards the ( $r_a=1.0$ ,  $r_r=1.0$ ,  $r_v=1.0$ ) corner of solution space. Specifically, the optimal solution according to the RMSE of far-field thermocouples was ( $r_a=1.3$ ,  $r_r=1.0$ ,  $r_v=1.0$ ) and according to the weighted RMSE of near-field thermocouples it was ( $r_a=3.0$ ,  $r_r=1.0$ ,  $r_v=1.0$ ). At this point, let's remind to the reader that, this exhaustive search of heat source radii was conducted with 74% efficiency which was found by arbitrarily fixing the heat source radii to the ( $r_a=1.0$ ,  $r_r=1.0$ ,  $r_v=1.0$ ) vector. So, shall we trust the thermocouples' opinion or shall we first investigate if they are influenced by the arbitrary choice of heat source radii that was used for determining the efficiency? To answer this question, the same procedure was followed, but now by fixing the efficiency with heat source radii vector ( $r_a=3.0$ ,  $r_r=3.0$ ,  $r_v=3.0$ ).

The results showed that we were right to think that the thermocouples' opinions were biased by the choice of radii initialisation vector. After fixing the heat source radii to ( $r_a=3.0$ ,  $r_r=3.0$ ,  $r_v=3.0$ ), the optimal efficiency was found with the same method as before, that is, by minimising the RMSE, but now the optimal efficiency was found to be 72% (instead of 74% that was found previously with fixing the radii to ( $r_a=1.0$ ,  $r_r=1.0$ ,  $r_v=1.0$ )). Then, the exhaustive search of heat source radii solutions was again performed in the 1.0-3.0 interval for each radius, but with 0.5 step now (less data points than before) to reduce the computational cost. It was found that both far-field thermocouples showed a preference towards the new choice of radii ( $r_a=3.0$ ,  $r_r=3.0$ ,  $r_v=3.0$ ). Specifically, the best solution for far-field thermocouples was ( $r_a=3.0$ ,  $r_r=1.0$ ,  $r_v=3.0$ ) and for near-field thermocouples ( $r_a=3.0$ ,  $r_r=1.5$ ,  $r_v=1.5$ ). On the other hand, the fusion boundary metric again appeared not to be influenced by the arbitrary choice of radii, and gave best solution of ( $r_a=3.0$ ,  $r_r=1.5$ ,  $r_v=1.5$ ), which is closed to the previous solution of ( $r_a=2.9$ ,  $r_r=2.2$ ,  $r_v=1.5$ ).

After these observations, it was judged that the best metric for radii determination out of the three metrics, namely RMSE of far-field thermocouples, weighted RMSE of near-field thermocouples, and fusion boundary comparison, was the fusion boundary one. This is because it was the least biased by the initial heat source radii selection of heat

efficiency determination. The thermocouple metrics or any other metric that is a combination of fusion boundary and thermocouple metrics, might shift the radii solution to areas biased by the initial choice of radii to fix the efficiency.

### HEAT SOURCE CALIBRATION

The aim of heat source calibration is to find the optimal values of heat efficiency, heat source radii, and sometimes other parameters as well, such as the vertical position of the heat source. By optimal values we mean that, we want the values that would result in a finite element thermal solution as close to the experimental one as possible.

In this research, the heat efficiency and heat source radii ( $r_a$ ,  $r_l$ ,  $r_v$ ) were calibrated for NeT-TG4 specimen. Initially, the heat source radii values were fixed to an arbitrary number ( $r_a=1.0$ ,  $r_l=1.0$ ,  $r_v=1.0$ ) and the optimal efficiency was found (74%). Then, with efficiency fixed, the optimal heat source parameters were determined based on the fusion boundary comparison metric that was developed in this study. The optimal heat source radii found at this stage were ( $r_a=2.9$ ,  $r_l=2.2$ ,  $r_v=1.5$ ). The far-field and near-field thermocouple metrics were not used for heat source radii determination, as they were found to be significantly influenced by the initial heat source radii vector chosen to determine the efficiency. However, it was found that, the fusion boundary metric was slightly influenced by the initial choice of heat source radii as well, since the heat efficiency was slightly different depending on this choice. It was then clear that an iterative process is necessary in order to find the optimal combination of efficiency and heat source radii, until the efficiency value does not change any more. This procedure was followed for the NeT-TG4 specimen and is schematically illustrated in Fig. 8.

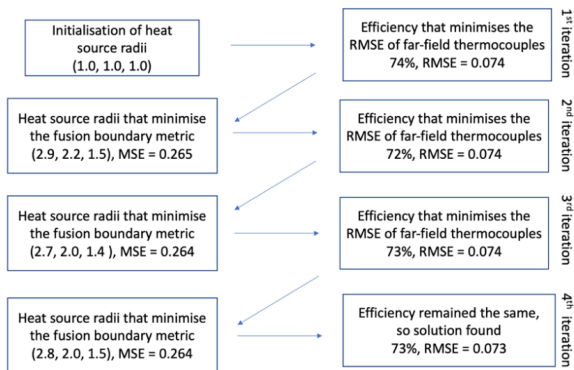


**Fig. 8** Heat source calibration iterative process for exploration interval of 2<sup>nd</sup> iteration 1.0-3.0 for each heat source radius

The interval of exploration for efficiency was 10-100% in all iterations (although very low values wouldn't be realistic). For the 2<sup>nd</sup> iteration (the numbering of iterations is

described in Fig. 8), the interval of exploration for heat source radii was 1.0-3.0 for each radius. In consequent iterations however, the interval of exploration for heat source radii was reduced, to avoid unnecessary computational cost, and it was selected to include the interval of 10 best solutions (according to fusion boundary metric) of the previous iteration. Also, areas outside this exploration interval were explored, in cases where the solution was close to the boundaries of interval of the previous iteration. Following that method, the exploration interval for heat source radii was ( $r_a=2.7-3.3$ ,  $r_l=1.8-2.6$ ,  $r_v=1.3-1.7$ ) for the 3<sup>rd</sup> iteration and ( $r_a=2.5-2.8$ ,  $r_l=1.8-2.0$ ,  $r_v=1.3-1.6$ ) for the 4<sup>th</sup>, with step 0.1. At some iterations the interval of exploration might have been tighter than ideally, but this was to reduce the computational cost of the exhaustive search. The fusion boundary shapes for each solution of each iteration were very similar, and they matched the experimental fusion boundary very well.

The final solution, which was heat efficiency 73% and heat source radii  $r_a=2.8$ ,  $r_l=2.0$ ,  $r_v=1.5$ , is illustrated in Fig. 9, along with the experimental fusion boundary. The vertical MSE of the two curves was 0.16, the horizontal MSE was 0.37, and their average (total MSE) was 0.26. This MSE value should be considered very low, due to the asymmetry of the experimental fusion boundary about the vertical axis, and also due to the fluctuations of its profile, whilst the simulation fusion boundary profile was symmetrical and smoother.

As for the thermocouple metrics for the final solution (effic.=73%,  $r_a=2.8$ ,  $r_l=2.0$ ,  $r_v=1.5$ ), the RMSE of far-field thermocouples was found to be 0.073 and the near-field thermocouple weighted RMSE was 0.075. Fig. 10 shows that the simulation temperature increases (maximum - initial temperature) versus the experimental temperature increases of thermocouples of the two specimens. As it can be seen, the near-field thermocouples for specimen 3-1B were a bit underpredicted, whilst for specimen 2-1A were a bit overpredicted.

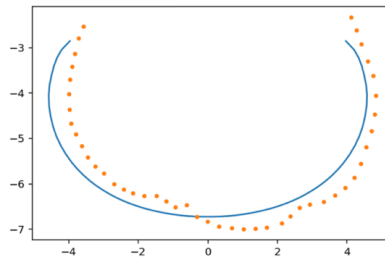


**Fig. 9** Final solution of iterative process of radii exploration interval of 2<sup>nd</sup> iteration 1.0-3.0, that is, efficiency 73% and heat source radii ( $r_a=2.8$ ,  $r_l=2.0$ ,  $r_v=1.5$ )

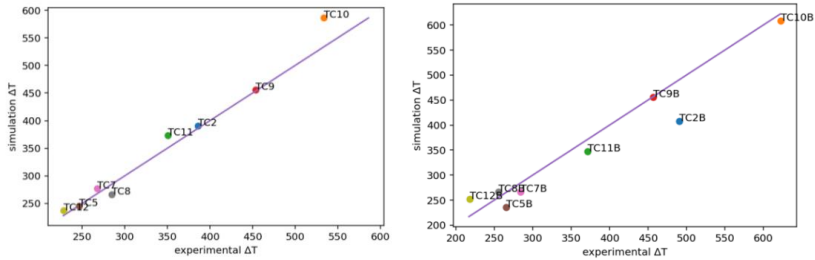


**Fig. 10** Thermocouples’ experimental versus simulation temperature increases of final solution (effic.=73%,  $r_a=2.8$ ,  $r_l=2.0$ ,  $r_v=1.5$ ) for specimens 2-1A (left) and 3-1B (right)

### MULTIPLE GOOD SOLUTIONS

The examination of solution space of the iterative process of fixing the efficiency first and then the heat source radii based on the fusion boundary comparison led to a single area of solution space of best solution. This means that, the problem appeared to have one optimal solution and not many different optimal solutions. Furthermore, the solution space seemed smooth, meaning that, the thermocouple and fusion boundary metrics changed almost continuously with the solution space. However, let’s remind the reader that, the interval of radii exploration that we started with (1.0-3.0) was rather small and based on previous experience from the NeT-TG4 project. What would happen if we started with another solution space interval? Could we have many different solutions that appear optimal? To answer these questions, the exhaustive search of solution space was repeated, but now with radii exploration interval 0.1-2.0, with step 0.1. The initialisation of heat source radii vector was again ( $r_a=1.0$ ,  $r_l=1.0$ ,  $r_v=1.0$ ) and hence the initial efficiency was fixed to 74%.

The results showed that the fusion boundary comparison metric gave now a completely different optimal solution of 2<sup>nd</sup> iteration ( $r_a=2.0$ ,  $r_l=0.8$ ,  $r_v=0.1$ ) compared to the solution of 2<sup>nd</sup> iteration of previous exploration ( $r_a=2.9$ ,  $r_l=2.2$ ,  $r_v=1.5$ ). The heat efficiency of 2<sup>nd</sup> iteration was now found 74% (same as 1<sup>st</sup> iteration), and so the algorithm stopped, giving final solution ( $r_a=2.0$ ,  $r_l=0.8$ ,  $r_v=0.1$ ), as described in Fig. 11. Because the axial radius of the solution was in the upper boundary of exploration interval ( $r_a = 2.0$ ), if we wanted to be more detailed, the algorithm should had restarted with an expanded exploration interval towards the upper boundary region of  $r_a$ , to ensure that the optimal solution would be found for this region of good solutions. Nevertheless, the solution (effic.=74%,  $r_a=2.0$ ,  $r_l=0.8$ ,  $r_v=0.1$ ) had a decent total MSE of 0.35 (average of horizontal and vertical MSEs), but a bit larger than the total MSE of 0.26 of final solution (effic.=73%,  $r_a=2.8$ ,  $r_l=2.0$ ,  $r_v=1.5$ ) of the previous exploration, and its fusion boundary is illustrated in Fig. 12.

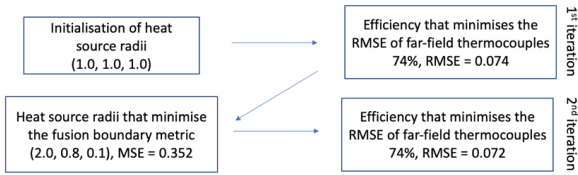


**Fig. 11** Heat source calibration iterative process for exploration interval of 2<sup>nd</sup> iteration 0.1-2.0 for each heat source radius

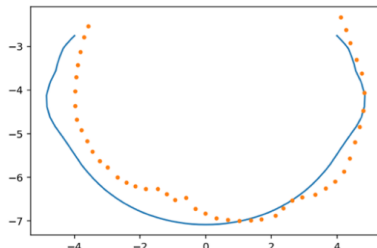


**Fig. 12** Final solution of iterative process of radii exploration interval of 2<sup>nd</sup> iteration 0.1-2.0, that is, efficiency 74% and heat source radii ( $r_a=2.0$ ,  $r_l=0.8$ ,  $r_v=0.1$ )

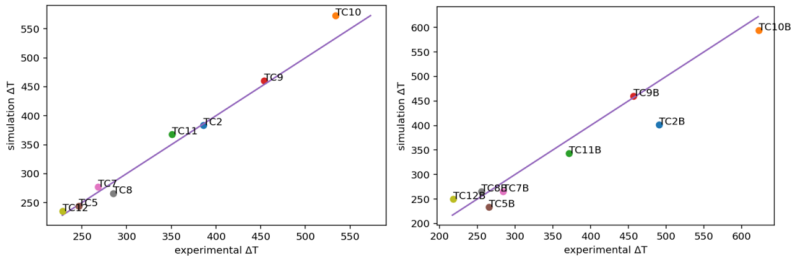


**Fig. 13** Thermocouples’ experimental versus simulation temperature increases of final solution (effic.=74%,  $r_a=2.0$ ,  $r_l=0.8$ ,  $r_v=0.1$ ) for specimens 2-1A (left) and 3-1B (right)

Regarding the thermocouple metrics, they were found to be very similar across both solutions. For solution (effic.=74%,  $r_a=2.0$ ,  $r_l=0.8$ ,  $r_v=0.1$ ) the far-field thermocouple RMSE was 0.072 and the weighted RMSE value of near-field thermocouples was 0.075, which were almost the same with the previous solution (effic.=73%,  $r_a=2.8$ ,  $r_l=2.0$ ,  $r_v=1.5$ ). Fig. 13 illustrates the simulation temperature increases of this solution and shows that they were very similar with the temperature increases of the previous solution.

According to these observations, in an adequately large interval of exploration, multiple different regions of good solutions might appear. The fusion boundary metric for

the multiple good solutions might be similar. The thermocouple metrics across these solutions might be similar too. In this study, two different good solution regions were identified for NeT-TG4, which were (effic.=73%,  $r_a=2.8$ ,  $r_l=2.0$ ,  $r_v=1.5$ ) and (effic.=74%,  $r_a=2.0$ ,  $r_l=0.8$ ,  $r_v=0.1$ ) (and probably other good solution regions exist for this specimen as well, outside the intervals examined in this study). However, the fusion boundary metric was better for the former solution rather than the latter, and thus it would be justified to choose the (effic.=73%,  $r_a=2.8$ ,  $r_l=2.0$ ,  $r_v=1.5$ ) as the best option.

## CONCLUSIONS

The conclusions of this research were the following:

1. The automatic fusion boundary metric that was developed in this study was able to compare all fusion boundary shapes and sizes and was easy to implement, by averaging the MSE of differences of the experimental and simulation fusion boundary curves both in horizontal and in vertical axis. This metric could be used as target value for fusion boundary comparisons in structural integrity assessment guidelines. When deciding the target value for this metric, the experimental fusion boundary asymmetry by the vertical axis should be taken into consideration and also the fluctuations of its profile, as with their increase the value of the metric would increase too.
2. The determination of efficiency before the heat source radii accelerated the heat source calibration process, by reducing the exploration space. The proposed guidelines for automated heat source calibration of heat efficiency and heat source radii can be summarised as follows:
  - a. Firstly, an arbitrary vector for the heat source radii is selected, preferably realistic in size, that is, some mm smaller than the width of the macrograph.
  - b. Then, the heat efficiency is determined by minimising the RMSE value of far-field thermocouples, as these thermocouples can approximately estimate the heat efficiency regardless the choice of initialising heat source radii vector.
  - c. An interval of exploration of possible heat source radii solutions is then selected. The efficiency is kept fixed to the value that was previously determined, and the heat source radii vector that minimises the fusion boundary metric is selected. The thermocouple metrics (far-field and near-field) are not used at this stage to find the heat source radii, since their preferences could be biased towards the initialising heat source radii vector.
  - d. The heat efficiency is then recalculated, and an iterative process begins between heat source radii and efficiency calculation, until the efficiency does not change any more. In every iteration, for computational efficiency, the interval of exploration can be narrowed down to regions around the interval of radii value of 'n' best solutions of the previous iteration.
3. Depending on the interval of exploration, very different heat source radii solutions, that give almost equally good results, can be found. In contrast to the heat source radii solutions, by following the method of firstly fixing the

efficiency with far-field thermocouples, the solutions for efficiency can deviate only a little.

4. Appropriate optimisation algorithms could be selected to accelerate the automated heat source calibration workflow. The heat efficiency was found to have only one value which minimises the RMSE of far-field thermocouples. Therefore, the exhaustive search could be easily substituted with any optimisation algorithm that searches for one minimum and does not require the function's derivative (e.g., golden-section search). The optimisation of heat source radii is a more complex problem. The fusion boundary metric appears to have a continuous value in the solution space. However, multiple different good solutions seem to exist (many local minima). Therefore, a gradient based optimisation algorithm that does not require the function's derivatives and also that can handle many local minima could be used.

### FUTURE WORK

In this study automated heat source calibration was performed with exhaustive search. However, this requires computational time (for this research the computational time was about 5 days). Instead of exhaustive search, optimisation algorithms could be used to find the minima to further accelerate the heat source calibration (particularly useful if large solution space intervals need to be explored) and to ensure that the optimal solution is found. So, future work will be focused on implementation of appropriate optimisation algorithms. Also, future work will include the application of the optimised heat source calibration workflow to new specimens and welding processes so to assess its general applicability.

### ACKNOWLEDGMENTS

The authors are grateful and wish to acknowledge the NeT European Network for the provision of data and the protocols. The authors would also like to acknowledge the computational shared facility of the University of Manchester, in which the simulations for this study were run. M. C. Smith, A.N. Vasileiou and D.K. Rissaki are supported by the SINDRI - Synergistic utilisation of Informatics and Data centric Integrity engineering, EPSRC Prosperity Partnership (Grant number: EP/V038079/1) and University of Manchester's Dalton Nuclear Institute.

### References

- [1] AKRIVOS V., MURANSKY O., DEPRADEUX L., SMITH M.C., VASILEIOU A., DEACONU V., ET AL: 'On the Accurate Prediction of Residual Stress in a Three-Pass Slot Nickel-Base Repair Weld by Numerical Simulations', *Journal of Manufacturing and Materials Processing*, 2022, 6(3):61.
- [2] VASILEIOU A.N., SMITH M.C., BALAKRISHNAN J., FRANCIS J.A., HAMELIN C.J.: 'The impact of transformation plasticity on the electron beam welding of thick-section ferritic steel components', *Nuclear engineering and design*, 2017, 323:309-16.

- [3] BELOUAH S., BOREL D., DELMAS J., HENDILI S., ROBIN V.: ‘Open-source Numerical Simulation Softwares and Skill-Modules for Welding Simulation’.
- [4] BELITZKI A., MARDER C., HUISSEL A., ZAEH M.F.: ‘Automated heat source calibration for the numerical simulation of laser beam welded components’, *Production Engineering*, 2016, 10(2):129-36.
- [5] FARIAS R., TEIXEIRA P., VILARINHO L.: ‘An efficient computational approach for heat source optimization in numerical simulations of arc welding processes’, *Journal of Constructional Steel Research*, 2021, 176:106382.
- [6] SHIRAIWA T., ENOKI M., GOTO S., HIRAIDE T.: ‘Data Assimilation in the Welding Process for Analysis of Weld Toe Geometry and Heat Source Model’, *ISIJ International*, 2020, ISIJINT-2019-720.
- [7] PYO C., KIM J., KIM J.: ‘Estimation of heat source model’s parameters for GMAW with non-linear global optimization - part I: Application of multi-Island genetic algorithm’, *Metals*, 2020, 10(7):885.
- [8] GU Y., LI Y., YONG Y., XU F., SU L.: ‘Determination of parameters of double-ellipsoidal heat source model based on optimization method’, *Welding in the World*, 2019, 63(2):365-76.
- [9] SMITH M., SMITH A., WIMPORY R., OHMS C.: ‘A review of the NeT Task Group 1 residual stress measurement and analysis round robin on a single weld bead-on-plate specimen’, *International Journal of Pressure Vessels and Piping*, 2014, 120:93-140.
- [10] SMITH M.C., SMITH A.C.: ‘Advances in weld residual stress prediction: A review of the NeT TG4 simulation round robin part 1, thermal analyses’, *International Journal of Pressure Vessels and Piping*, 2018, 164:109-29.
- [11] SMITH M.C., SMITH A.C., OHMS C., WIMPORY R.C.: ‘The NeT Task Group 4 residual stress measurement and analysis round robin on a three-pass slot-welded plate specimen’, *International Journal of Pressure Vessels and Piping*, 2018, 164:3-21.
- [12] SMITH M., SMITH A.: *NeT Task Group 4: Three-Pass Slot Weld Specimen in Austenitic Stainless Steel*, Issue 1, Appendix F: As-installed thermocouple positions and their impact on measured temperatures, 29/9/2009.
- [13] Featplus Limited, Feat-Wmt: *Weld-Modelling Tool User Guide*, 2019.
- [14] MURANSKY O., BENDEICH P.J., SMITH M.C., KIRSTEIN O., EDWARDS L., HOLDEN T.M., editors: ‘Analysis of Residual Stresses in Three-Pass Slot Weld (NeT-TG4): Finite Element Modelling and Neutron Diffraction’, *Pressure Vessels and Piping Conference*, 2010.
- [15] MURÁNSKY O., SMITH M.C., BENDEICH P.J., HOLDEN T., LUZIN V., MARTINS R., ET AL: ‘Comprehensive numerical analysis of a three-pass bead-in-slot weld and its critical validation using neutron and synchrotron diffraction residual stress measurements’, *International Journal of Solids and Structures*, 2012, 49(9):1045-62.
- [16] [https://github.com/dimitrarissaki/establishing\\_an\\_automated\\_heat\\_source\\_calibration\\_framework.git](https://github.com/dimitrarissaki/establishing_an_automated_heat_source_calibration_framework.git)

# NUMERICAL ANALYSIS OF THE INFLUENCE OF AN AUXILIARY OSCILLATING MAGNETIC FIELD ON SUPPRESSING THE POROSITY FORMATION IN DEEP PENETRATION LASER BEAM WELDING OF ALUMINUM ALLOYS

F. YANG\*, X. MENG\*, M. BACHMANN\*, A. ARTINOV\*,  
S. N. PUTRA\*, M. RETHMEIER\*\*.\*.\*\*\*

\*Bundesanstalt für Materialforschung und prüfung (BAM), Unter den Eichen 87, 12205 Berlin, Germany

\*\*Institute of Machine Tools and Factory Management, Technische Universität Berlin, Pascalstraße 8-9, 10587 Berlin, Germany \*\*\*Fraunhofer Institute for Production Systems and Design Technology, Pascalstraße 8-9, 10587 Berlin, Germany

DOI 10.3217/978-3-85125-968-1-13

## ABSTRACT

The contactless magnetohydrodynamic technology has been considered as a potential and promising method to improve the weld qualities of deep penetration laser beam welding. In this paper, numerical investigations are conducted to study the influence of the auxiliary oscillating magnetic field on the porosity suppression in laser beam welding of 5754 aluminum alloy. To obtain a deeper insight into the suppression mechanism, a three-dimensional transient multi-physical model is developed to calculate the heat transfer, fluid flow, keyhole dynamic, and magnetohydrodynamics. A ray tracing algorithm is employed to calculate the laser energy distribution on the keyhole wall. A time-averaged downward Lorentz force is produced by an oscillating magnetic field. This force acts in the molten pool, leading to a dominant downward flow motion in the longitudinal section, which blocks the bubble migration from the keyhole tip to the rear part of the molten pool. Therefore, the possibility for the bubbles to be captured by the solidification front is reduced. The electromagnetic expulsive force provides an additional upward escaping speed for the bubbles of 1 m/s ~ 5 m/s in the lower and middle region of the molten pool. The simulation results are in a good agreement with experimental measurements. Based on the results obtained in this study, a better understanding of the underlying physics in laser beam welding enhanced by an auxiliary oscillating magnetic field can be provided and thus the welding process can be further optimized reducing the porosity formation.

Keywords: Deep penetration laser beam welding; Oscillating magnetic field; Numerical simulation; Porosity; Molten pool behaviour.

## INTRODUCTION

Deep penetration laser beam welding (LBW) has been developed as a promising technology with numerous applications in joining thick plates above 5 mm [1]. Compared

to traditional arc welding, deep penetration LBW shows more advantages including large aspect ratio, high welding speed, narrow heat affected zone, and low weld distortion [2]. Based on the above-mentioned advantages, wide applications of this technology have been achieved in joining thick plates of aluminum alloy.

However, porosities are commonly observed in the LBW joints of aluminum alloys, which result in deterioration of the welded joints' quality and reliability [3,4]. The porosities in LBW joints can be classified as the so-called metallurgical and process porosity [5]. The metallurgical porosity is not the main emphasis of this study which is caused by the elements with low boiling-point from base metal and moisture in the atmosphere or shielding gas. Process porosity induced by keyhole instability with a size larger than 100  $\mu\text{m}$  has been drawing more and more attention. The formation of the process porosity can be mainly ascribed to the keyhole collapse, dynamic melt flow behind the keyhole, and high solidification rate [6-9]. Furthermore, researchers have investigated many suppression methods of process porosity during deep penetration LBW. For example, the methods of using different shielding gases [9], changing the angle of incident laser beam [10], conducting welding under vacuum [11], applying hybrid welding [12], and performing welding coupled with oscillating laser beam [13] have been investigated in detail.

Recently, contactless magnetohydrodynamic (MHD) technology has been recognized as a potential way to improve the deep penetration LBW, which can control the flow pattern of melting liquid by the induced Lorentz force from external magnetic fields. The welding quality can be improved based on multiple effects of braking, supporting, and stirring achieved by different Lorentz force application methods performed with multiple types of magnetic fields (steady magnetic field or oscillating magnetic field) and magnetic field directions [14-16]. Moreover, researchers found that external magnetic fields can suppress process porosity significantly. Huang et al. [17] reported that the porosity defect is eliminated obviously by using an auxiliary steady magnetic field during laser beam welding of steel. The reasons limiting porosity formation by the steady magnetic field are mainly related to the increased stability of the keyhole, the larger bubble escape speed, and the lower solidification rate of the weld pool. Fritzsche et al. [18] applied a transverse oscillating magnetic field in a partial penetration LBW of aluminum. Significant porosity suppression of more than 70% and better surface stabilization were achieved.

Although the effect of the external magnetic fields on the porosity suppression have been verified by experiments, a deeper insight into the relationships between magnetic fields, keyhole dynamics, and process porosity is harder to obtain because of the non-transparent molten metal and the small diameter of the keyhole. Moreover, the fluid flow behaviour in the molten pool is highly nonlinear, which makes the quantitative experimental analysis difficult. Therefore, multi-physical modeling is a powerful tool to investigate the physical interaction mechanisms between keyhole dynamics, process porosity, and MHD behaviour. Recently, a few researchers have developed three dimensional multi-physical models to investigate the formation of porosity, in which the Volume of Fluid method (VOF) was applied to capture the free surface of the keyhole [6, 8]. Furthermore, some numerical models were established with consideration of external magnetic field. Zhang et al. [19] built a three-dimensional transient numerical model to investigate the influence mechanism of an alternating magnetic field on the weld root hump suppression in full penetration laser welding of aluminum. Meng et al. [20]

investigated the highly transient keyhole dynamics under a magnetic field by using multi-physical modeling. The correlation between the porosity mitigation and molten pool dynamics effected by magnetic field was elucidated in detail. Liu et al. [21] studied the influence of the magnetic field orientation on suppressing porosity by establishing a numerical model coupled with MHD. They found the keyhole stability was well improved when the magnetic fields were horizontally parallel and perpendicular to the welding direction.

However, further quantitative analysis of the interaction mechanisms between keyhole dynamics, process porosity, and MHD behaviour during deep penetration LBW is still lacking. In the present study, a 3D transient multi-physical numerical model, coupled with the VOF algorithm and a MHD model, has been developed to investigate this interaction mechanism. The weld pool behaviour is analysed under the influence of the Lorentz force and the corresponding suppression mechanism of the magnetic field on process porosity during deep penetration LBW is discussed.

## EXPERIMENTAL PROCEDURE

The experiments of butt welding were conducted by an IPG YLR 20000 laser welding system. The welding parameters used in the experiments are listed in Table 1. The 5754 aluminum alloy was used as base metal with dimensions of  $200 \text{ mm} \times 50 \text{ mm} \times 10 \text{ mm}$ . The laser beam was inclined in a forward direction with an angle of  $10^\circ$ . Pure Ar was used as shielding gas with a flow rate of 20 l/min, which was placed in the backward direction with an angle of  $15^\circ$ . A high-speed camera was used to capture the temporal evolution of the molten pool from a side view with a frequency of 1000 frames/s. The molten pool depth, width, and length extracted from the experimental results are used for the verification of the numerically obtained results. The experimental platform is shown in Fig. 1 (a).

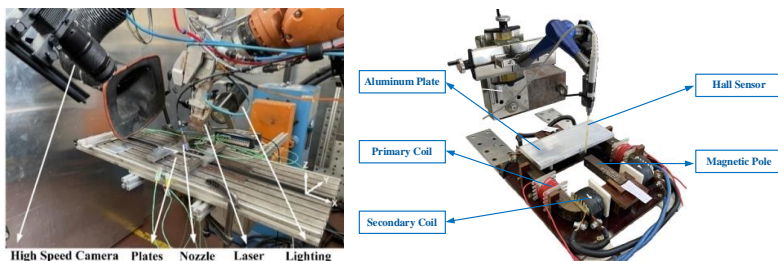


**Fig. 1** Experimental setup: (a) laser beam welding platform; (b) Measurement platform of magnetic fields distribution in the cold material

The oscillating magnetic field are produced by an in-house developed alternating current (AC) electromagnet. The dimension of the cross-section of the magnetic pole is  $20 \text{ mm} \times 20 \text{ mm}$  and the distance between the two magnetic poles is 15 mm. In order to simplify the model, the generation of the external magnetic field is not considered in this model. Therefore, the magnetic field was measured by a Hall sensor in a cold condition

before the laser was turned on and it was applied directly in this model, the measurement platform is shown in Fig.1 (b). The peak magnetic flux density produced by this oscillating magnetic system is 220 mT and the frequency is 1830 Hz, which is used in this numerical model. Fig. 2 shows the spatial distribution of magnetic flux density.

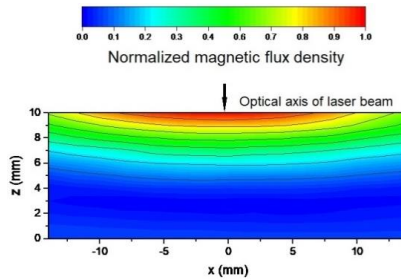


**Fig. 2** Normalized magnetic flux density (Frequency: 1830 Hz, Peak magnetic flux density: 220 mT)

The joints were cut perpendicular to the weld seam by mechanical cutting and subsequently the cross-section of samples was polished and etched by 2.5 ml HNO<sub>3</sub> + 1.5 ml HCl + 1 ml HF + 95 ml H<sub>2</sub>O. The fusion line shape in the cross-section was observed by an optical microscope.

**Table 1** Welding parameters in experiments and simulation

Parameters	Value
Laser power	5 kW
Laser spot diameter at focal plane	520 $\mu$ m
Wavelength	1070 nm
Focal length	350 mm
Focal position	0 mm
Welding speed	2 m/min

## MATHEMATICAL MODELING

A three-dimensional transient multi-physical model accounting for the VOF method and MHD has been developed to calculate the heat transfer, fluid flow, and the keyhole dynamics. Some simplifications are applied to reduce the computing costs because of the highly complex and multi-physical coupled fluid flow behavior in the molten pool. The assumptions are as follows:

- The flow regime of the liquid metal flow is laminar. The liquid metal is considered as Newtonian and incompressible. The buoyance term follows the Boussinesq approximation.

- The metal vapor in the keyhole is weakly ionized, thereby the gaseous phase in the model is considered electrically non-conductive.
- The effect of shielding gas is neglected in the simulation.
- The thermoelectric effect and the Joule heating are not taken into consideration.

#### GOVERNING EQUATIONS

Based on the assumptions, the governing equation in a fixed Cartesian coordinates system can be mathematically described as following:

- VOF equation

$$\rho \frac{\partial \phi}{\partial t} + \nabla \cdot (\vec{v} \phi) = 0, \quad (1)$$

where  $\phi$  is the volume fraction of aluminum,  $t$  is the time and  $\vec{v} = (v_x, v_y, v_z)$  is the fluid velocity vector.

- Mass conservation

$$\nabla \cdot \vec{v} = 0. \quad (2)$$

- Energy conservation

$$\rho \left[ \frac{\partial h}{\partial t} + (\vec{v} \cdot \nabla) h \right] = \nabla \cdot (k \nabla T) + S_q, \quad (3)$$

where  $h$  is the enthalpy,  $k$  is the thermal conductivity, and  $S_q$  is the energy source term. All surface energies are converted to volumetric energies by the continuum surface force method because of the application of the VOF method [22]. This additional source terms consider the laser heat flux density, the convective and radiative heat transfer, the evaporation loss, and the recondensation.

- Navier-stokes equation

$$\rho \left( \frac{\partial \vec{v}}{\partial t} + (\vec{v} \cdot \nabla) \vec{v} \right) = -\nabla p + \mu \nabla^2 \vec{v} + \rho \vec{g} - \beta \rho (T - T_L) \vec{g} - \mu K \vec{v} + \vec{S}_m, \quad (4)$$

where  $\rho$  is the density,  $p$  is the hydrodynamic pressure,  $\mu$  is the viscosity,  $\vec{g}$  is the gravitational acceleration vector,  $T$  is the temperature,  $T_L$  is the liquidus temperature,  $K$  is the Carman-Kozeny equation [23]. The effects of surface tension along the aluminum-air interface, the recoil pressure induced by evaporation, the stagnation pressure and shear stress on the keyhole surface are as well converted into volumetric forces and implemented into the additional momentum source  $\vec{S}_m$ .

- Magnetic induction equation

The magnetic induction equation can be written as following according to Ohm's law and Maxwell's equation:

$$\frac{\partial \vec{b}}{\partial t} + (\vec{v} \cdot \nabla) \vec{b} = \frac{1}{\mu_m \sigma_e} \nabla^2 \vec{b} + \left( (\vec{B}_0 + \vec{b}) \cdot \nabla \right) \vec{v} - (\vec{v} \cdot \nabla) \cdot \vec{B}_0, \quad (5)$$

where  $\vec{b}$  is the magnetic field induced by the liquid flow,  $\vec{B}_0$  is an external magnetic field measured by a Hall sensor,  $\mu_m$  is the magnetic permeability, and  $\sigma_e$  is the electrical conductivity. The induced current density  $\vec{j}$  and Lorentz force  $\vec{F}_L$  are written as the following:

$$\vec{j} = \frac{1}{\mu_m} \nabla \times (\vec{B}_0 + \vec{b}), \quad (6)$$

$$\vec{F}_L = \vec{j} \times (\vec{B}_0 + \vec{b}), \quad (7)$$

The Lorentz force is then introduced as part of the momentum source term.

### PHYSICAL MODELS

The laser beam profile is assumed to have a Gaussian-like axisymmetric distribution, which can be expressed as follows:

$$q_L = \frac{2P_L}{\pi r_z^2} \cdot \exp\left(-2 \frac{x^2 + y^2}{r_z^2}\right), \quad (8)$$

$$r_z = r_f \left[ 1 + \left( \frac{z - z_f}{z_r} \right)^2 \right]^{\frac{1}{2}}, \quad (9)$$

where  $q_L$  denotes the heat density function,  $P_L$  is the laser power,  $r_z$  is the radius of the laser beam at  $z$  distance away from the focal plane,  $x$  and  $y$  are the coordinates,  $z_f$  is the position of the focal plane,  $r_f$  is the laser beam radius at the focal plane.

In this model, a ray tracing algorithm developed by Cho et al. is applied to calculate the ray reflections [24]. For this purpose, the laser beam energy is discretized into several energy bundles. Meanwhile, finer secondary virtual cells on the keyhole wall are used to improve the accuracy of the ray tracing algorithm. Note that this virtual approach comes without significant increase of the calculating time [20, 25, 26]. The Fresnel absorption happened during every reflection can be calculated by the following equation:

$$\alpha = 1 - \frac{1}{2} \left( \frac{1 + (1 - \varepsilon \cos \varphi)^2}{1 + (1 + \varepsilon \cos \varphi)^2} + \frac{\varepsilon^2 - 2\varepsilon \cos \varphi + 2\cos^2 \varphi}{\varepsilon^2 + 2\varepsilon \cos \varphi + 2\cos^2 \varphi} \right), \quad (10)$$

where  $\varphi$  is the angle between the incident ray and the surface normal,  $\varepsilon$  is a coefficient determined by the laser type and the material properties, which is set as 0.087 in this model [27].

The recoil pressure due to evaporation is described as follows [28]:

$$P_r = 0.54 P_0 \exp\left(l_v M \frac{T - T_b}{RT_b}\right), \quad (11)$$

where  $P_r$  is the recoil pressure,  $P_0$  is the atmospheric pressure,  $l_v$  is the latent heat of vaporization,  $M$  is the atomic mass,  $T_b$  is the boiling temperature, and  $R$  is the universal gas constant.

The normal capillary pressure  $P_{ca}$  and the tangential Marangoni stress  $\tau_{ma}$  can be written as:

$$P_{ca} = \gamma\kappa, \quad (12)$$

$$\tau_{ma} = \frac{\partial\gamma}{\partial T} \frac{\partial T}{\partial \vec{s}}, \quad (13)$$

where  $\gamma$  is the surface tension of aluminum [8],  $\kappa$  and  $\vec{s}$  are the curvature and the tangential vector of keyhole surface, respectively.

In addition, the influence of thermal (secondary heating  $q_{plume}$  and recondensation  $q_{recond}$ ) and momentum from high-speed metal vapor (stagnation pressure  $P_{sta}$  and shear stress  $\tau_{vap}$ ) on the keyhole are also considered in this model [24,29].

#### BOUNDARY CONDITION

The energy balance on the keyhole wall can be described as:

$$-k \frac{\partial T}{\partial \vec{n}} = q_L - h_c(T - T_0) - \sigma \varepsilon_r(T^4 - T_0^4) - \rho v_{evp} \Delta L_v + q_{plume} + q_{recond}, \quad (14)$$

where  $\vec{n}$  is the normal vector of the free surface,  $h_c$  is the coefficient of the convective heat transfer,  $T_0$  is the ambient temperature,  $\sigma$  is the Stefan-Boltzmann constant,  $v_{evp}$  is the recession speed of the free surface.

The force balance on the keyhole wall can be written as:

$$-p + 2\mu \frac{\partial v_n}{\partial \vec{n}} = p_r + p_{sta} + p_{ca} \quad (15)$$

$$-\mu \frac{\partial v_t}{\partial \vec{n}} = \tau_{ma} + \tau_{vap} \quad (16)$$

where  $v_n$  is the normal velocity and  $v_t$  is the tangential velocity. Eq. (15) describes the force balance in normal direction and the force balance in tangential direction can be expressed by Eq. (16).

Another energy and electromagnetic boundary conditions are shown in Table 2. The continuum boundary condition is applied on the side face of the geometry model to allow for realistic and accurate description of the thermal and electromagnetic conduction in a semi-infinite domain.

**Table 2** Energy and electromagnetic boundary conditions

	Energy	Electromagnetic
Top	$\partial T / \partial \vec{n} = 0$	$\vec{j} = 0$
Side aluminum surface	Continuum boundary [30]	Continuum boundary [30]
Side gas surface	$\partial T / \partial \vec{n} = 0$	$\vec{j} = 0$
Bottom	$-k \partial T / \partial \vec{n} = -h_c(T - T_0) - \sigma \varepsilon_r(T^4 - T_0^4)$	$\vec{j} = 0$

The initial conditions are:

$$T|_{t=0} = 300 \text{ K}, \vec{v}|_{t=0} = 0, \vec{b}|_{t=0} = 0 \quad (17)$$

#### NUMERICAL SETUP

Fig. 3 shows the schematic of the computational domain. The dimensions of the geometric model are 20 mm × 8 mm × 12 mm, the gas phase layer with 2 mm thickness is built above the workpiece. A uniform hexahedral cell size of 0.2 mm was used to discretize the computational domain.

All transport equations are solved with the commercial software ANSYS FLUENT. The discretization of the momentum and energy conservation equations was done by a second order upwind algorithm. The velocity-pressure coupling is achieved by the Pressure Implicit with Splitting of Operators (PISO) method. The aluminum-air interface is reconstructed by the Geo-Reconstruct method. The simulation was calculated by a high-performance computing cluster in the Bundesanstalt für Materialforschung und prüfung (BAM) with 80 CPU cores and 768 GB RAM. About 96 h computational time were consumed to simulate 0.45 s physical welding time.

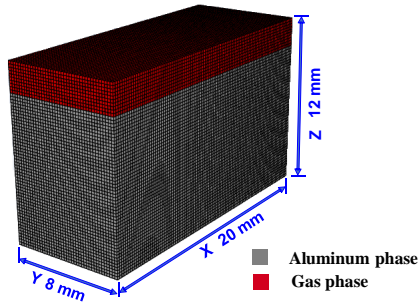


Fig. 3 Schematic of computational domain

## RESULTS AND DISCUSSION

### EXPERIMENT RESULTS AND VALIDATION

Severe porosity defects can be identified from the longitudinal section of the LBW joints of 5754 aluminum alloy, see Fig.4. The porosity shown in the dashed rectangle (I, II) is typical keyhole-induced process pores, whose shape can be either spherical or irregular and the size of these porosities are usually larger than that of metallurgical porosity. According to the research of Fritzsche et al. [18] and Bachmann et al. [31], a

significant reduction of porosity can be achieved by the application of magnetic fields. Therefore, the objectives of the present study focus on the analysis of the suppression mechanism of magnetic fields on keyhole induced process porosity by using the numerical results.



**Fig. 4** Longitudinal section of LBWed joints of 5754 aluminum alloy

A series comparison between the experimental and calculated results were conducted. The molten pool on the top surface is typical teardrop shape, which is similar as the numerical result, see Fig. 5. In Fig.6, the dashed line is the profile of the final weld. Table 3 lists the errors between the experimental and the simulated results. From Fig.5, Fig.6 and Table 3, the profile of the calculated fusion zone shows good agreement with the experimental results. The errors between the experimental results and the calculated results are lower than 10%. The above comparison validates the numerical model which can thus be used in the following analysis.



**Fig. 5** Comparison between experimental and calculated molten pool length without magnetic fields: (a) experiment results; (b) calculated results (the red region in the simulation result represents the calculated weld region)

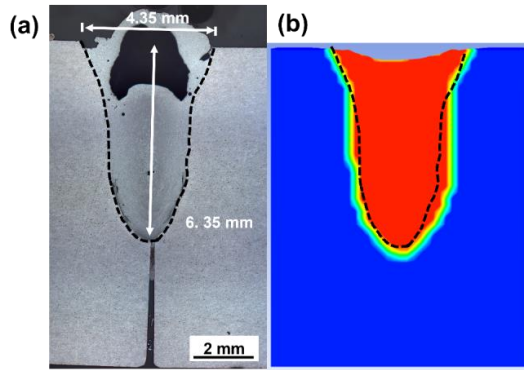


**Fig. 6** Comparison between experimental and calculated fusion zones without magnetic fields: (a) experiment results; (b) calculated results (the red region in the simulation result represents the calculated weld region)

**Table 3** Deviations between experimental and calculated results without magnetic fields

	Width of molten pool	Length of molten pool	Depth of molten pool
Experiment	4.35 mm	8.52 mm	6.35 mm
Simulation	4.69 mm	7.70 mm	6.75 mm
Errors	8%	10%	6%

#### ELECTROMAGNETIC BEHAVIOUR

The eddy currents are induced by an oscillating magnetic field in the workpiece, as shown in Fig.7. For a better visualization of the eddy current distribution, the magnitude is normalized by the maximal value. Two predominant circulating currents are found in the longitudinal section. This can be attributed to the fact that the value of the electric conductivity decreases with increasing temperature and the gaseous phase in the keyhole is also assumed as non-conductive. Thus, the keyhole with high temperature and the gaseous phase in the inner keyhole can be regarded as an electric barrier. The eddy current flow can be either clockwise or anti-clockwise, which is determined by the temporal variation of the magnetic flux density. The maximum value of the induced eddy current is  $2.5 \times 10^7$  A/m<sup>2</sup>. This flow pattern of the induced current is similar with the research results of Meng et al. [32]. and Bachmann et al. [33], but the magnitude is much higher due to the high electrical conductivity of aluminum.

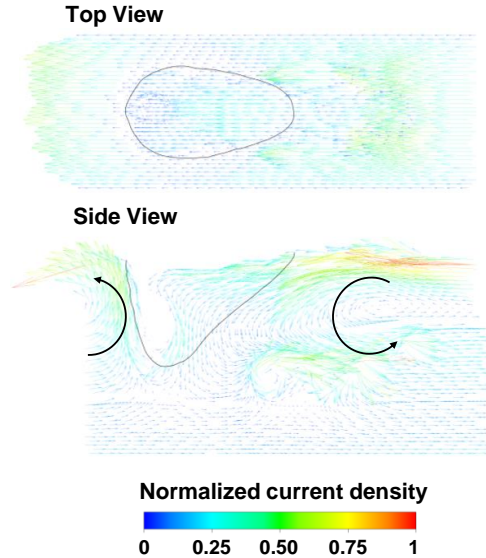


**Fig. 7** Vector field of the induced eddy current

The Lorentz force is produced by the oscillating magnetic fields and its self-induced electric current. Intuitively, it shows periodic expansive and compressive effects like the oscillation of the magnetic field. The Lorentz force is the strongest on the top surface of the workpiece due to the maximum magnetic flux density occurred on the top position (see Fig. 2). Because of the skin effect, the induced Lorentz force will reduce sharply along the vertical direction. The Lorentz force in vertical direction at point A is extracted and shown in Fig. 8. The periodical upward and downward Lorentz force oscillates with a frequency of 3660 Hz which is double as high compared to the frequency of the magnetic field. According to Fig. 8, the maximum upward Lorentz force at point A is reached within the range of  $1 \sim 3 \times 10^5 \text{ N/m}^3$ .

After  $\frac{1}{4}$  period of the oscillating magnetic field, the maximum downward Lorentz force can be produced with the value of  $2.5 \sim 4.5 \times 10^5 \text{ N/m}^3$ . From a time-average viewpoint, the downward Lorentz force can be produced in the molten pool by the oscillating magnetic fields. For the keyhole, the expansive and compressive Lorentz force can as well be produced on the keyhole wall. Meng et al. [20] indicated that the Lorentz force formed on the opening of the keyhole has a significant effect on the laser absorption.

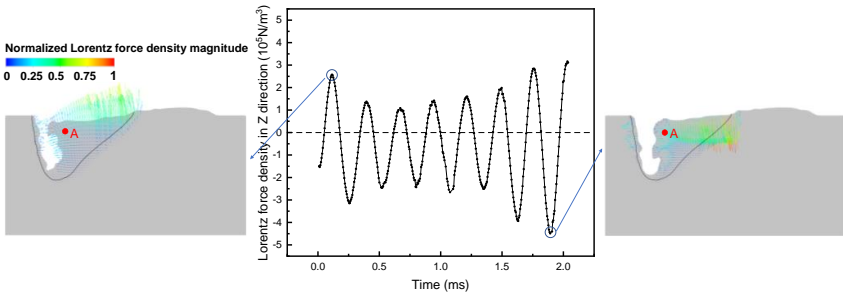


**Fig. 8** Distribution of Lorentz force density in molten pool

#### MOLTEN POOL BEHAVIOUR AND KEYHOLE DYNAMICS

Fig. 9 shows the comparison of the calculated temperature and velocity fields between the LBW and LBW assisted with an external magnetic field after the quasi-steady state is reached. It is considered that the fluid flow pattern in the molten pool has a remarkable effect on the porosity formation. There are two main flow circulations, see Fig. 9, in the well-developed molten pool without a magnetic field. The predominant flow routine of the molten metal in the longitudinal section is marked with white arrows. These two typical flow circulations were as well confirmed by the numerical and experimental research results from Liu et al. [21] and Kawahito et al. [34]. The upper circulation contributes to the formation of the elongated molten pool profile. It should be noted that the thin layer of the liquid metal on the keyhole front wall shows a fast downward flow under the recoil pressure. This downward flow is redirected at the liquid/solid boundary to form the second circulation at the bottom. The existence of the bottom circulation is not stable. It can disappear during the calculation sometimes and be rebuilt by the downward liquid metal from the keyhole wall. It has been found that the bottom circulation plays a crucial role in the formation and migration of the bubbles [6]. The formation of the bubbles can be mainly attributed to the collapse of the keyhole tip. The bottom circulation tends to push the formed bubbles to the solidification front, which increases the possibility of the capture of the bubbles [6,8].

The application of an external magnetic field has a significant impact on the fluid flow pattern in the molten pool. The backward flow at the top region is enhanced by the Lorentz force, and thus both the length and the width of the molten pool is increased. The reason that the keyhole depth decreases after applying the magnetic fields is that the induced Lorentz force changes the energy distribution by affecting the diameter of the keyhole opening and the protrusions' position in keyhole wall [21]. By comparing Fig. 9 (b) and (d), it shows that an apparent downward flow is formed in the longitudinal section due to the time-averaged downward Lorentz force, which brings a suppression on the occurrence of the bottom circulation. This transformation of the flow mode is helpful for suppressing the formation of porosities. The bubble migration routine from the keyhole tip to the rear part of the molten pool is blocked by the enhanced downward fluid flow.

Thus, the possibility of the moving bubble captured by the solidification front can be reduced. The bubble formed in the keyhole tip has more opportunity to re-merge to the keyhole or move upward. Therefore, the process porosity can be suppressed.

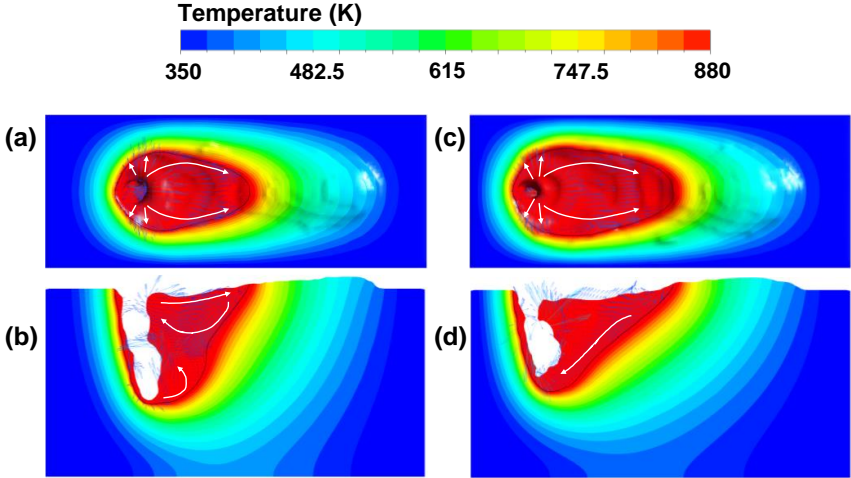


**Fig. 9** Calculated temperature and velocity fields ( $t = 0.357$  s): (a) top surface of the molten pool without magnetic field; (b) x-z central surface without magnetic field; (c) top surface of molten pool with magnetic field; (d) x-z central surface with magnetic field

The pressure difference that exists around non-conducting porosities can cause the electromagnetic expulsive forces due to the generation of the Lorentz force. If the liquid metal movement is ignored, the liquid flow will be deemed as Stokes flow. The additional escaping speed provided by the electromagnetic expulsive force can be described as:

$$\frac{3}{4} \frac{\pi d_B^3}{6} F_L = 3\pi \mu d_B v_{esc} \quad [20]$$

The accelerating process of the bubble is ignored, the constant escaping speed contributed by electromagnetic expulsive force can be calculated from this equation when the forces on the bubble are balanced. The term on the left-hand side is the electromagnetic expulsive force proposed by Leenov-Kolin's theory from Takahashi et al. [35]. The term on the right-hand side represents the total drag force on the bubble. Here  $d_B$  is the pore diameter (here an average pore diameter of 1.15 mm is chosen according to Fig. 4),  $F_L$  is the Lorentz force density,  $v_{esc}$  is the upward escaping velocity contributed by the electromagnetic expulsive force. The electromagnetic expulsive force induced by the Lorentz force can provide the bubble an additional escaping velocity in most areas of the molten pool, see Fig. 10. The additional escaping speed is higher on the top region of molten pool because of the maximum Lorentz force there. This larger additional escaping speed in the top region has no higher significance for the bubble escaping. However, the induced electromagnetic expulsive force still provides an additional upward escaping

speed within the range of 1 m/s ~ 5 m/s in the lower and middle part of the molten pool, which is a crucial factor for bubble escaping and suppressing porosity. Thus, the bubbles have more opportunity to escape from the molten pool because of the application of the external oscillating magnetic field. From Fig.4, two typical diameters of pores (Pore I and II) are extracted. Pore I is a single larger pore whose equivalent diameter is 1.92 mm. According to Eq. (20), the larger bubble with diameter of 1.92 mm has an additional upward escaping speed with 3 m/s ~ 13 m/s under the vertical component of Lorentz force of  $1.5 \times 10^4 \text{ N/m}^3 \sim 6 \times 10^4 \text{ N/m}^3$  in the lower and middle part of the molten pool. However, the smaller bubble (Pore II) with diameter 0.38 mm just be given an additional upward escaping speed within the range of 0.1 m/s ~ 0.5 m/s in the lower and middle region of the molten pool. It means that especially the larger bubbles have more possibilities to escape from molten pool.

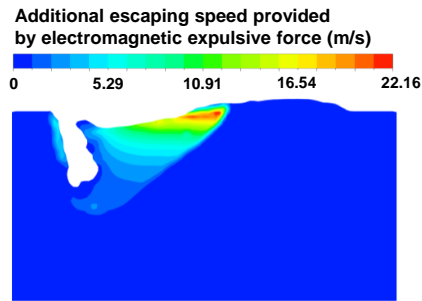


**Fig. 10** Additional escaping speed provided by external magnetic expulsive force

A statistical analysis on the keyhole collapse position is conducted, which is given in Fig. 11. 83% of the keyhole collapse happens at the position between 0 mm ~ 1 mm above the keyhole bottom when a magnetic field is applied. The collapse possibility of 78% occurs at the position between 0 mm ~ 1 mm when the LBW conducted without magnetic fields. Moreover, the collapse occurred randomly at the upper and middle part of the keyhole. This distribution result disagrees with the standard normal distribution of keyhole collapse position during the LBW of titanium alloy reported by Pang et al. [36]. It also disobeys log-normal distribution occurred during the LBW process of 304L steel studied by Meng et al. [20]. This phenomenon may be associate to the lower viscosity and surface tension coefficient of molten aluminum alloy compared to steel and titanium alloys. The lower viscosity and surface tension coefficient make the keyhole dynamic behavior changes more significantly and the keyhole collapse occurs more frequently, which may exhibit entirely different dynamic behavior compared to titanium and steel. Therefore, the keyhole dynamic behavior of aluminum alloy LBW with auxiliary magnetic fields requires further investigation.

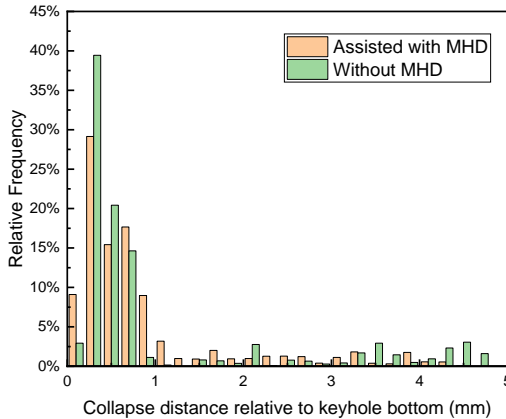


Fig. 11 Probability histogram of the collapse distance relative to keyhole bottom

## CONCLUSION

- (1) A 3D transient multi-physical LBW model coupled with an external oscillating magnetic field is developed to investigate the relationship between the magnetic fields, keyhole dynamics and process porosity.
- (2) The application of external magnetic fields has a strong influence on the molten pool profile and fluid flow pattern. An apparent downward flow is formed in the longitudinal section under the effect of the Lorentz force.
- (3) The enhanced downward fluid flow blocks the bubble migration routine from the keyhole tip to the rear part of the molten pool. The possibility of the bubbles captured by the solidification front reduces notably. The electromagnetic expulsive force induced by Lorentz force can provide the bubble with  $1 \text{ m/s} \sim 5 \text{ m/s}$  additional upward escaping speed in the lower and middle regions of the molten pool.

## ACKNOWLEDGEMENT

This work is funded by China Scholarship Council (Nr. 202008080270) and the Deutsche Forschungsgemeinschaft (DFG, German Research Foundation) project Nr. 411393804 (BA 5555/5-2), Nr. 416014189 (BA 5555/6-1), and Nr. 466939224 (BA 5555/9-1).

## References

- [1] M. BACHMANN, A. GUMENYUK, M. RETHMEIER: 'Welding with high-power lasers: Trends and developments', *Phys Procedia*, 83, 15-25, 2016.
- [2] JF. READY, DF. FARSON, T. FEELEY: *LIA Hand Book of Laser Materials Processing*, 2001.

- [3] H. ZHAO, DR. WHITE, T. DEBROY: 'Current issues and problems in laser welding of automotive aluminum alloys', *International Materials Reviews*, 44(6), 238-266, 1999.
- [4] S. KATAYAMA, CD. LUNDIN: 'Laser welding of aluminum alloy 5456', *Welding International*, 6(6), 425-435, 1992.
- [5] A. MATSUNAWA, JD. KIM, S. KATAYAMA: 'Porosity formation in laser welding-Mechanisms and suppression methods', *International Congress on Applications of Lasers & Electro-Optics*, 1997(1), G73-G82, 1997.
- [6] L. HUANG, X. HUA, D. WU, F. LI: 'Numerical study of keyhole instability and porosity formation mechanism in laser welding of aluminum alloy and steel', *Journal of Materials Processing Technology*, 252, 421-431, 2018.
- [7] R. ZHANG, X. TANG, L. XU, F. LU, H. CUI: 'Study of molten pool dynamics and porosity formation mechanism in full penetration fiber laser welding of Al-alloy', *International Journal of Heat Mass Transfer*, 148, 119089, 2020.
- [8] R. LIN, H. WANG, F. LU, J. SOLOMON, BE. CARLSON: 'Numerical study of keyhole dynamics and keyhole-induced porosity formation in remote laser welding of Al alloys', *International Journal of Heat and Mass Transfer*, 108, 244-256, 2017.
- [9] A. MATSUNAWA, M. MIZUTANI, S. KATAYAMA: 'Porosity formation mechanism and its prevention in laser welding', *Welding International*, 17(6), 431-437, 2003.
- [10] N. SETO, S. KATAYAMA, A. MATSUNAWA: 'Porosity formation mechanism and reduction method in CO<sub>2</sub> laser welding of stainless steel', *Welding International*, 16(6), 451-460, 2002.
- [11] M. JIANG, X. CHEN, Y. CHEN, W. TAO: 'Increasing keyhole stability of fiber laser welding under reduced ambient pressure', *Journal of Materials Processing Technology*, 268: 213-222, 2019.
- [12] M. CHEN, J. XU, L. XIN, Z. ZHAO, F. WU, S. MA, Y. ZHANG: 'Effect of keyhole characteristics on porosity formation during pulsed laser-GTA hybrid welding of AZ31B magnesium alloy', *Optics and Lasers in Engineering*, 93, 139-145, 2017.
- [13] W. KE, X. BU, JP. OLIVEIRA, W. XU, Z. WANG, Z. ZENG: 'Modeling and numerical study of keyhole-induced porosity formation in laser beam oscillating welding of 5A06 aluminum alloy', *Optics & Laser Technology*, 133, 106540, 2021.
- [14] M. BACHMANN, V. AVILOV, A. GUMENYUK: 'Numerical assessment and experimental verification of the influence of the Hartmann effect in laser beam welding processes by steady magnetic fields', *International Journal of Thermal Sciences*, 101, 24-34, 2016.
- [15] VV. AVILOV, A. GUMENYUK, M. LAMMERS, M. RETHMEIER: 'PA position full penetration high power laser beam welding of up to 30 mm thick AlMg3 plates using electromagnetic weld pool support', *Science and Technology of Welding and Joining*, 17(2), 128-133, 2012.
- [16] M. GATZEN, Z. TANG, F. VOLLERTSEN, M. MIZUTANI, S. KATAYAMA: 'X-ray investigation of melt flow behavior under magnetic stirring regime in laser beam welding of aluminum', *Journal of Laser Applications*, 23(3), 032002, 2011.
- [17] L. HUANG, P. LIU, S. ZHU, X. HUA, S. DONG: 'Experimental research on formation mechanism of porosity in magnetic field assisted laser welding of steel', *Journal of Manufacturing Processes*, 50, 596-602, 2020.
- [18] A. FRITZSCHE, K. HILGENBERG, F. TEICHMANN, H. PRIES, K. DILGER, M. RETHMEIER: 'Improved degassing in laser beam welding of aluminum die casting by an electromagnetic field', *Journal of Materials Processing Technology*, 253, 51-56, 2018.
- [19] R. ZHANG, X. TANG, L. XU, F. LU, H. CUI: 'Mechanism study of thermal fluid flow and weld root hump suppression in full penetration laser welding of Al alloy with alternating magnetic field support', *International Journal of Heat and Mass Transfer*, 166, 120759, 2021.
- [20] X. MENG, M. BACHMANN, A. ARTINOV, M. RETHMEIER: 'A study of the magnetohydrodynamic effect on keyhole dynamics and defect mitigation in laser beam welding', *Journal of Materials Processing Technology*, 307, 117636, 2022.

- [21] F. LIU, H. WANG, X. MENG, C. TAN, B. CHEN, X. SONG: 'Effect of magnetic field orientation on suppressing porosity in steady-magnetic-field-assisted aluminum alloy deep-penetration laser welding', *Journal of Materials Processing Technology*, 304, 117569, 2022.
- [22] J. BRACKBILL, D. KOTHE, C. ZEMACH: 'A continuum method for modeling surface tension', *Journal of Computational Physics*, 100(2): 335-354, 1992.
- [23] V.R. VOLLER, C. PRAKASH: 'A fixed grid numerical modeling methodology for convection-diffusion mushy region phase change problem', *International Journal of Heat and Mass Transfer*, 30, 1709-1719, 1987.
- [24] WI. CHO, SJ. NA, C. THOMY, F. VOLLERTSEN: 'Numerical simulation of molten pool dynamics in high power disk laser welding', *Journal of Materials Processing Technology*, 212(1), 262-275, 2012.
- [25] SW. HAN, J. AHN, SJ. NA: 'A study on ray tracing method for CFD simulations of laser keyhole welding: progressive search method', *Welding in the World*, 60(2), 247-258, 2016.
- [26] X. MENG, A. ARTINOV, M. BACHMANN, Ö. ÜSTÜNDAĞ, A. GUMENYUK, M. RETHMEIER: 'The detrimental molten pool narrowing phenomenon in wire feed laser beam welding and its suppression by magnetohydrodynamic technique', *International Journal of Heat and Mass Transfer*, 193: 122913, 2022.
- [27] R. DUCHARME, K. WILLIAMS, P. KAPADIA, J. DOWDEN, B. STEEN, M. GLOWACKI: 'The laser welding of thin metal sheets: an integrated keyhole and weld pool model with supporting experiments', *Journal of Physics D: Applied Physics*, 27(8): 1619, 1994.
- [28] M. ALLMEN, A. BLATTER: 'Laser-Beam interactions with materials (second ed.)', *Springer*, New York, 1995.
- [29] S. MUHAMMAD, S. HAN, S. NA, A. GUMENYUK, M. RETHMEIER: 'Study on the role of recondensation flux in high power laser welding by computational fluid dynamics simulations', *Journal of Laser Applications*, 30(1), 012013, 2018.
- [30] X. MENG, G. QIN, R. ZONG: 'Thermal behavior and fluid flow during humping formation in high-speed full penetration gas tungsten arc welding', *International Journal of Thermal Sciences*, 134, 380-391, 2018.
- [31] M. BACHMANN, V. AVILOV, A. GUMENYUK, M. RETHMEIER: 'Experimental and numerical investigation of an electromagnetic weld pool control for laser beam welding', *Physics Procedia*, 56, 515-524, 2014.
- [32] X. MENG, M. BACHMANN, A. ARTINOV, M. RETHMEIER: 'The influence of magnetic field orientation on metal mixing in electromagnetic stirring enhanced wire feed laser beam welding', *Journal of Materials Processing Technology*, 294, 117135, 2021.
- [33] M. BACHMANN, R. KUNZE, V. AVILOV, M. RETHMEIER: 'Finite element modeling of an alternating current electromagnetic weld pool support in full penetration laser beam welding of thick duplex stainless steel plates', *Journal of Laser Application*, 28(2): 022404, 2016.
- [34] Y. KAWAHITO, Y. UEMURA, Y. DOI, M. MIZUTANI, K. NISHIMOTO, H. KAWAKAMI, M. TANAKA, H. FUJI, K. NAKATA, S. KATAYAMA: 'Elucidation of the effect of welding speed on melt flows in high-brightness and high-power laser welding of stainless steel on basis of three dimensional X-ray transmission in situ observation', *Welding International*, 31(3):206-213, 2017.
- [35] K. TAKAHASHI, S. TANIGUCHI: 'Electromagnetic separation of nonmetallic inclusion from liquid metal by imposition of high frequency magnetic field', *ISIJ international*, 43(6): 820-827, 2003.
- [36] S. PANG, W. CHEN, W. WANG: 'A Quantitative Model of Keyhole Instability Induced Porosity in Laser Welding of Titanium Alloy', *Metallurgical and Materials Transactions A*, 45(6): 2808-2818, 2014.



# SIMULATION OF LASER ASSISTED DOUBLE WIRE DEPOSITION WELDING WITH TWO DIFFERENT APPROACHES WITH EULERIAN (FVM) AND LAGRANGIAN (SPH) METHODS

U. REISGEN\*, R. SHARMA\*, O. MOKROV\*,  
S. EMADMOSTOUFI\*, J. KRUSKA\*, J. HERMSDORF\*\*,  
M. LAMMERS\*\*, T. BOKELMANN\*\*

*\*Welding and Joining Institute RWTH Aachen University, Pontstr. 49, 52062 Aachen, North Rhine Westphalia, Germany*

*\*\*Laser Zentrum Hannover (LZH) e.V., Hollerithallee 8, 30419 Hannover, Lower Saxony, Germany*

DOI 10.3217/978-3-85125-968-1-14

## ABSTRACT

Laser-assisted double-wire deposition welding is a welding process developed at LZH to increase the deposition rate with the minimum degree of dilution of the surfacing layer. The use of the laser beam serves to locally heat up the molten pool and substrate surface and, thanks to a smaller wetting angle, leads to improved bond to the substrate, which causes a wider and deeper weld pool. The aim of this paper is to investigate the basics of this process using numerical methods. The free surface of the deposition layer, the mass flow of the melting wires in the weld pool, as well as interphase mass exchange (e. g. evaporation), laser absorption and interphase heat balance were calculated. Two different simulation methods Eulerian finite volume method (FVM) and Lagrangian smooth particle hydrodynamics (SPH) were used to build the model. This paper deals with the model construction as well as the precision and computational effort of these methods. The results of both methods agree with each other. Conclusions were drawn about the advantages and limitations of both methods

Keywords: Laser-assisted double-wire deposition welding, simulation method, FVM, SPH, Eulerian, Lagrangian

## INTRODUCTION

Laser assisted double wire welding with non-transferred arc (LDNA) is a process developed by Laser Zentrum Hannover (LZH) for metal deposition and surfacing. In this process, the arc is ignited between two continuously fed wire electrodes. The wire electrodes melt and the droplets fall onto the substrate surface. This process offers not only a low degree of dilution, but also a high deposition rate.

The droplets, depending on the size, temperature and velocity and their falling trajectory, can affect the weld pool hydrodynamics. Heat and volume of dripped metal

adds heat into the weld pool. Size, velocity and direction of the molten droplets lead to additional momentum into the welding pool.

To improve the connection of the cladding layer, a laser beam oscillates transversely to the welding direction. This oscillation leads to an improved wetting angle on the sides with local heating of the weld pool, especially at the edges, and avoids the undercut formation (Fig. 1).

Because of the local heating of the laser beam, the melt evaporates partially on the surface of the melt pool. In addition, this heating affects the local temperature of the melt pool surface and thus the surface tension, which in turn causes additional convection due to the Marangoni effect. The absorption of the laser beam depends on the angle of the incident beam and the temperature of the free weld pool surface. The physical phenomena are shown in the Fig. 2.

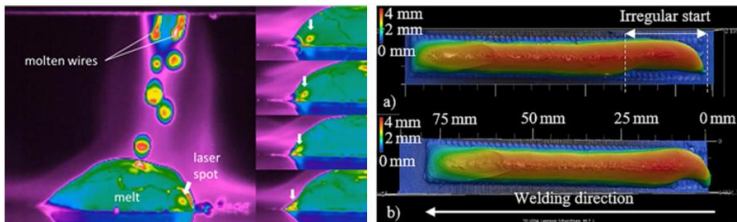


**Fig. 1** Left, falling droplets and local heating by laser during the LDNA process, captured transversely to weld direction by thermal camera, colours represent different temperatures. Right, the solidified weld seam topology with laser scanning microscopy (LSM), the colours illustrate the height of deposited layer

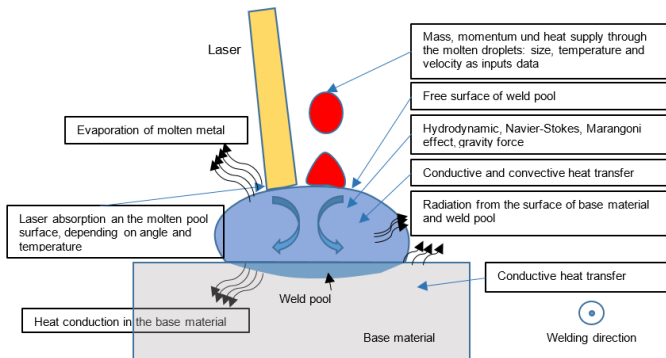


**Fig. 2** Schematic cross section, explanation of all to be simulated phenomena of the process

For the simulative investigation of the LDNA process two different models based on differing approaches are developed. The first one, finite volume method (FVM), as an Eulerian method, implemented in ANSYS CFX® is compared with the Lagrangian method Smoothed Particle Hydrodynamics (SPH).

The SPH is a mesh-free Lagrangian method, which in recent years has received growing attention for the investigation of fluid dynamics problems. SPH is particularly well suited for the modelling of free surfaces, since those are handled implicitly by the discretization technique, which makes it an appealing method for the investigation of welding simulations. In this work the open source SPH frameworks SPLisHSPlasH [1] is used. The framework has an extended library to allow heat transfer, physical surface phenomena, viscous fluid behaviour and simplified solidification calculations. It has previously been used for the simulation of manufacturing processes, especially the problem of fluid mass and heat transfer in [2, 3]. It allows the development of a simulation model of the LDNA process.

Furthermore, the aim is that the algorithms developed for this work will be integrated into the main SPLisHSPlasH framework.

## STATE OF ART

In order to experimentally investigate the process, number of experimental tests, which have been described earlier in [4–8], were carried out. The physical phenomena that occur in this process have not been determined in a simulation so far. This investigation is the computer-aided description of this process. However, there are various simulative tests for other similar welding processes. Often equivalent heat sources are used for thermal modelling of deposition welding, for example, Amal et al. [9] used equivalent heat source to calculate the residual stresses in "Wire arc additive manufacturing" using commercial software Simufact. Zheng et al. [10] built up numerical model for regulation of heat input and Nikam et al. [11] tried the thermal analysis of multilayer metallic deposition during plasma arc based additive manufacturing. Chai et al. [12] implemented the laser powder interaction in a thermal analysis with cellular automaton in laser cladding process. Although their results show good geometric agreement with the real process, they cannot precisely determine the temperatures in cross-sections. Han et al. [13] investigated on hybrid laser and submerged arc cladding, and simulated the resulting residual stresses. Zhang et al. [14] considered the hydrodynamic and microstructure evolution in laser cladding process using a coupled model of FEM and cellular automaton.

Song et al. [15] investigated on the internal molten flow convection on evolution of the solidification. They also believe that the Marangoni effect has a magnificent influence on the cladding layer.

Eulerian methods are very common for the simulation of arc welding processes and have been used since the advent of computational welding simulation. A common difficulty in these methods is the calculation of free surface flows. There are several numerical approaches which are commonly used for the description of these free surface flows. They can be divided into two main groups [16]. The first group includes the so-called Front Capturing Methods (FCM) in which a fixed Eulerian computational mesh is employed and a free surface is "expanded" along the volume of a certain layer. The thickness of this layer corresponds to several lengths of a computational cell. The most popular FCM are Volume of Fluid (VOF) [17, 18] and Level Set (LS) [19] methods. There also exists a number of other approaches where the free surface is considered as a sharp interface between two media, e.g., [20–22]. There the Arbitrary–Lagrangian–

Eulerian method (ALE) is used, which allows the deformation of the mesh, but it does not allow to solve problems with significant topological changes, like flow-splitting. However, most common arc welding processes involve a melting, detachment and an impingement of a filler material into a weld pool. Both the approaches, the VOF/LS and the ALE are only limited satisfactory to accurately capture the process. Due to its strengths in modelling free surfaces as well as considering discontinuities and large topological changes and deformations, the SPH method became an interesting approach for modelling arc welding processes. However, a very little is known yet about the quantitative performance for the calculation of conductive/convective heat transfer compared to the established Eulerian methods, in the context of arc welding processes.

#### SMOOTHED PARTICLE HYDRODYNAMICS FOR WELDING PROCESS SIMULATION

The smoothed particle hydrodynamics (SPH) method was originally proposed by Lucy [23] and Gingold and Monaghan [24] in the field of Astrophysics. Since then it has been adopted for many different applications, including the simulation of weld pool dynamics. The mesh-free nature of SPH enables the simulation of large deformations, free surface motion and coupling of many physical processes, which makes it an attractive method for many real-world problems.

Das and Cleary [25] use SPH in three-dimensional arc welding simulations in order to study temperature distributions, flow patterns and plastic strain in the filler material and residual thermal stresses in the work piece. Ito et al. [26] perform full simulations of tungsten inert gas (TIG) welding using the SPH method and show results for different material properties due to different sulphur contents and evaluate the flow patterns and the shape of the weld pool.

Trautmann et al. [27] similarly perform weld pool simulations using SPH for a TIG welding process. They consider buoyancy, viscosity and surface tension as flow driving forces and the arc pressure, shear and all relevant thermal effects were parameterized using experimental studies. The penetration profiles of three different welding currents were compared to experimental results and decent agreement was shown. A hybrid approach is investigated by Komen et al. [28], who use an Eulerian grid and Lagrangian particles in conjunction, in order to simulate gas metal arc welding (GMAW). Molten metal is simulated by means of SPH, while the arc plasma and gas are simulated on a grid. The methods are then weakly coupled and executed iteratively.

Komen et al. [29] also simulate the GMAW process under consideration of droplet formation and compare the weld pool shapes against experimental results. In order to visualize results more easily, they use an ensemble averaging in order to transfer particle data onto a regular grid. These types of simulations are difficult to validate, as they describe very complex systems with many interacting components, and this is evident with Trautmann et al. [27] being one of the few works which attempts to validate their results using experimental data. In this paper, we choose to compare our proposed SPH method against Eulerian simulations, as a proof of concept which shows that SPH is able to obtain very good agreement in the resulting weld pool shapes, as well as temperature and velocity distributions. Similar comparative studies were conducted by Jeske et al. [2, 3]. In [2] excellent results of the SPH method when compared against the Eulerian VOF

method for the simulation of droplet impacts in thermal spraying were obtained. In [3] the Eulerian and SPH methods were compared regarding the simulation of flows arising under the action of the Lorentz force with variable distributions of electric current density during tungsten electrode welding. A remarkable agreement between the melt pool shapes, which are highly dependent upon these forces, is shown. This allows to justify the usage of SPH to obtain physically meaningful results, especially for cases that pose more difficulty for Eulerian methods, for instance when considering free surfaces. The studies carried out confirm the qualitative accuracy of the proposed method as well as the SPH method in general for such applications.

### MODEL

#### GENERAL MODEL ASSUMPTIONS

Both variants of the model are based on the following general assumptions:

- Molten metal is a Newtonian, incompressible, laminar fluid
- The Arc is not transferred to the molten metal in the LDNA process, therefore, the electromagnetic forces and arc are not modelled. The focus lies on the droplet behaviour during falling, without consideration of formation of the droplets in the arc.
- Droplet behaviour (spatial velocity, temperature, size) has been measured using a thermal camera.
- Gravity and its influences on the falling droplets and on natural convection in gas phase as well as in molten metal is considered.
- The solidification is modelled using the enthalpy porosity method.
- For the evaporation, mass loss is excluded. (Euler's method can account for mass loss, but the SPH method needs further development for this goal)

Some differences at a glance:

- In Euler's method, the molten metal is in interaction with surrounding gas phase. In SPH, the gas phase was excluded.
- The scattering of the laser beam in Euler's method is isotropic, but was not taken into account in SPH.
- The Marangoni effect as a result of the temperature dependent surface tension was taken into account in Euler's method but not in the SPH because of the constant surface tension with corresponding SPH development status.
- The hydrodynamics in the melt pool was taken into account in both models, but in Euler's method it is a result of the droplet momentum and the density variation with temperature, but in SPH the density is considered constant, therefore the hydrodynamics are only affected via droplet momentum.

The enthalpy-porosity approach [30, 31] is used in both the SPH and FVM simulations. This method aims to precisely model the flow during the solidification by introducing an

additional deceleration in the Navier-Stokes equation for material between the solidus and liquidus temperature. Because of that it is sometimes referred to as a momentum loss or momentum sink.

The symbols used in the mathematical model are listed in the Table 1.

**Table 1** Symbols used in the mathematical model chapter

Symbol	Definition	Symbol	Definition
$\vec{v}$	Velocity vector in momentum equation	$I_0$	Energy of incident radiation on the surface
$p$	Pressure	$I(z)$	Energy of transmitted radiation in depth z
$\eta$	Dynamic viscosity	$l$	Path length of transmission
$\lambda$	Lame constant	$\dot{M}_w$	Wire mass rate
$\vec{f}$	Gravity	$\dot{M}_d$	Droplet mass rate
$S_s$	mass source of shielding gas	$v_w$	Wire feeding speed
$S_m$	mass source of molten metal	$A_w$	Wire cross section area
$T$	Temperature	$R_w$	Radius of wire
$k$	Heat conductivity	$R_d$	Radius of droplet
$C_p$	Specific heat capacity	$V_d$	Volume of droplet
$\rho$	Density	$v_{d1}$	Frequency of inflow of drops 1
$v$	Velocity	$v_{d2}$	Frequency of inflow of drops 2
$q_{vol}$	Volume heat source in energy equation	$s_{d1}$	Switch function I/O of droplet 1
$q_{rad}$	Volume heat source via Radiation	$s_{d2}$	Switch function I/O of droplet 2
$T_0$	Ambient temperature	$\theta$	Step function
$q_b$	Volume heat source for laser beam	$\rho_m$	Density of molten metal
$P$	Laser beam power	$f_{d1}$	Normalisation factor of mass for droplet 1
$\mu$	Attenuation coefficient	$f_{d2}$	Normalisation factor of mass for droplet 2
$\mu_a$	Absorption coefficient	$\dot{m}_{d1}$	Mass flux of droplet 1
$\mu_s$	Scattering coefficient	$(\dot{m}_{d1})'$	Mass flux of droplet 1 with irregularity
$a(T)$	Temperature dependent absorption fraction	$\dot{m}_{d2}$	Mass flux of droplet 2
$Tr$	Transmittance	$(\dot{m}_{d2})'$	Mass flux of droplet 2 with irregularity
$d_d$	Droplet distance	$c_{p,m}$	Specific Heat capacity of molten metal
$(d_d)'$	Droplet distance with irregularity	$T_b$	Boiling temperature
$v_x$	Drop velocity in longitudinal direction (x)	$L_b$	Latent Heat of evaporation
$v_y$	Drop velocity in transverse direction (y)	$\dot{m}_e$	Mass flux of evaporated metal
$v_z$	Droplet speed in height direction (z)	$\delta t$	Time increment
$v_{xz}$	Diagonal drop speed in xz plane	$\mathcal{N}$	SPH neighbourhood relation
$v_{xyz}$	Diagonal droplet speed	$\mathcal{N}_x$	Set of neighbours at location x

## Mathematical Modelling of Weld Phenomena 13

$\alpha$	Droplet angel over longitudinal direction	$V_i$	Volume of particle $i$
$\dot{q}_e$	Heat flux of evaporation	$A_i$	Arbitrary quantity $A$ of particle $i$
$\beta$	Droplet angel over transversal direction	$W(x; h)$	SPH smoothing kernel
$v_p$	Droplet parallelity frequency	$h$	Smoothing radius
$M_x$	longitudinal momentum loss	$\chi$	Coverage angle
$M_y$	Transversal momentum loss	$\varphi$	Laser angle to altitudinal direction
$M_z$	altitudinal momentum loss	$C(x)$	SPH color field
$C$	Morphological constant	$\kappa$	curvature
$s_m$	Activation switch for Momentum Loss	$\gamma$	Surface tension coefficient
$u_x$	fluid velocity in longitudinal direction (x)	$T_i$	Temperature of particle $i$
$u_y$	fluid velocity in transverse direction (y)	$\dot{q}$	Heat flux in Lagrangian approach
$u_z$	fluid velocity in height direction (z)	$r_i$	Heat source radius
$v_w$	Welding speed	$r$	Distance from centre of Gaussian
$\phi_m$	Volume of fluid of molten metal	$\epsilon$	Emissivity
$T_m$	Temperature of molten metal	$\sigma$	Stefan Boltzmann constant
$T_s$	Solidus temperature	$h$	Heat transfer coefficient
$T_l$	Liquidus temperature	$r_p$	Particle radius
$w_e$	Mass Fraction of evaporated metal	$n$	Surface normal

### EULERIAN APPROACH

#### GEOMETRY AND BOUNDARY CONDITIONS IN EULERIAN APPROACH

The model contains two domains, the substrate (the lower one) which consists of the base material and the cladding layer (the upper one), see Fig. 3. The cladding layer consists of the incoming molten metal, the shielding gas and the metal vapour in a varying combination. The base material, as fluid (see 4.2), flows through the substrate domain with the welding velocity in moving coordinate system. The melt adheres to the contact surface between the cladding layer and the substrate. The top and lateral sides of the upper domain are described as open with a relative pressure of 0 [Pa] and a black body temperature of 300 [K]. The upper surface has the unity volume fraction of gas mixture with the shielding gas mass fraction to be 1 and the beam source of the laser as the Monte Carlo method of boundary condition. This is a ANSYS CFX implemented method of "ray tracing" in which material is irradiated with a certain number (here 10000) energetic rays and depending on the angle of incidence and the radiation properties of material (absorption and scattering) these are absorbed or scattered.

Except for the contact surface with the coating layer, the other surfaces in the substrate are defined as frictionless (slip wall), which loss the heat with convection (heat transfer coefficient) and radiation (Stefan Boltzmann's law).

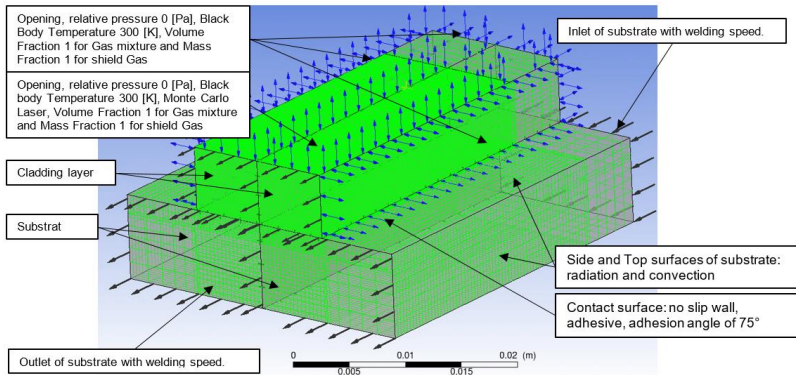


**Fig. 3** Domain geometry, meshing and boundary conditions

Droplets drop diagonally from right side to molten pool (Fig. 6 & Fig. 7), so the hydrodynamics and solidification front would not be symmetrical. Therefore, we could not use symmetrical geometry and meshing, and the problem should be solved in the whole domain.

#### MATHEMATICAL MODEL

In this paper, the authors used FVM in multiphysics multiphase model with inhomogeneous heat and mass transfer with consideration of hydrodynamics and convection in the molten pool, Marangoni effect, radiation from the molten pool and solidified cladding layer to ambient and secondary heat gained via scattered laser beam.

Although the Euler approach is suitable for implementing some phenomena like evaporation of molten metal due to oscillating of laser beam, heat gain and loss via shielding gas flow in and out of arc area and heat radiation of the arc on the molten pool, these were not taken into account in the model, because the main aim of this article is to compare the FVM Eulerian and the SPH Lagrangian method.

In order to be able to simulate both physical states of material (solid and liquid) in a moving coordinate system, both physical states of metal are described as fluid. This type of implementation is typical for ANSYS CFX. In addition, during and after solidification, the increasing viscosity and enthalpy porosity result in damping the flows, so that the solidified fluid is numerically still a fluid, but behaves like a solid.

The cladding domain consists of molten metal and gas (mixture of shielding gas and metal vapour). These phases should be separated from each other via the free surface task. The Volume of Fluid (VOF) method is used to calculate the free surface of the molten metal. The volume fraction of the melt in each cell is described as follows:

- $VOF = 1$ , there is only molten metal in the element
- $VOF = 0$ , there is only gas (mixture of shielding gas and metal vapour) in the element

- $0 < VOF < 1$ , melt fills only a part of an element, thus it forms the free surface of molten pool.

There should be some cells between VOF 0 and 1 (Fig. 4). This requires very fine meshing wherever the melt pool surface is formed during the process. This results in a very high computational effort in this method. The surface tension plays an important role and the Marangoni effect is also taken into account due to the temperature-dependent description of the surface tension.

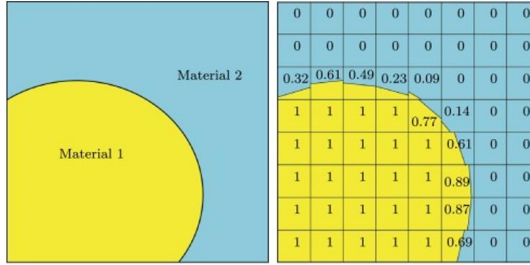


**Fig. 4** The schematic volume of the fraction to model the free surface between two media [32]

The mass flux of the inflowing droplets into the domain results from the mass conservation of the melted wires. The frequency of the mass supply of the droplets into the domain is described on the basis of the measured droplet size and sphere shape via thermal camera. Therefore, droplets are modelled also spherical, and defined in the model with Gaussian mass distribution for numerical reasons.

Navier-Stokes equation for incompressible molten metal

$$\rho \frac{D\vec{v}}{Dt} = \rho \left( \frac{\partial \vec{v}}{\partial t} + (\vec{v} \cdot \nabla) \vec{v} \right) = -\nabla p + \mu \Delta \vec{v} + (\lambda + \mu) \nabla (\nabla \cdot \vec{v}) + \vec{f} \quad (1)$$

Mass balance equation (continuity):

$$\frac{D\rho}{Dt} = \frac{\partial \rho}{\partial t} + \nabla \rho = S_s + S_m \quad (2)$$

Energy equation:

$$C_p \rho \frac{\partial T}{\partial t} = \nabla (\lambda \nabla T) - \nabla (\rho C_p v T) + q_{vol} \quad (3)$$

$$q_{vol} = q_h + q_{rad} + q_b \quad (4)$$

$$q_{rad} = \varepsilon \sigma (T^4 - T_0^4) \delta \quad (5)$$

$$q_h = h(T - T_0) \delta \quad (6)$$

$$\delta = \sqrt{(\nabla \phi_m)^2} \quad (7)$$

$$q_b = \frac{\mu P}{\pi R_b^2} \quad (8)$$

As the materials (substrate and cladding layer) are not transparent, the laser beam does not get transmitted through the medium. Therefore, attenuation coefficient results from the sum of absorption and scattering.

$$\mu = \mu_a + \mu_s \quad (9)$$

$$\mu = -\frac{1}{l} \ln(Tr) \quad (10)$$

$$Tr = \frac{I(z)}{I_0} = \text{assumed as } e^{-4} \text{ in path length } 1 \text{ [mm]} \quad (11)$$

$$\mu_a = a(T)\mu \quad (12)$$

$$\mu_s = (1 - a(T))\mu \quad (13)$$

As already mentioned, the Monte Carlo method can take into account the angle of incidence and the absorption and scattering properties of the medium. One can add a temperature dependency to the Monte Carlo method by using the temperature-dependent absorption fraction.

Mass source:

$$\dot{M}_w = \dot{M}_d \quad (14)$$

$$v_w A_w = \dot{n}_{d1} V_d \quad (15)$$

$$\begin{cases} v_{d1} = \frac{v_{w1} A_{w1}}{V_d} \\ v_{d2} = \frac{v_{w2} A_{w2}}{V_d} \end{cases} \quad A_w = \pi R_w^2, \quad V_d = \frac{4}{3} \pi R_d^3 \quad (16)$$

In order to develop drop-like mass flow, the mass source is time-modulated. The general on/off function can be written as follows:

$$s_d = \Theta \left( 0.5 \operatorname{Sin} \left( 2\pi v_{d1} \left( t + \frac{\xi}{2\pi v_{d1}} \right) \right) + 0.5 - |\operatorname{sin}(\xi)| \right) \quad (17)$$

Here  $\xi=64^\circ$  was assumed

$$s_{d1} = \Theta \left( 0.5 \operatorname{Sin} \left( 2\pi v_{d1} \left( t + \frac{\arcsin(0.9)}{2\pi v_{d1}} \right) \right) - 0.4 \right) \quad (18)$$

$$s_{d2} = \Theta \left( 0.5 \operatorname{Sin} \left( 2\pi v_{d2} \left( t + \frac{\arcsin(0.9)}{2\pi v_{d2}} \right) \right) - 0.4 \right) \quad (19)$$

The on/off switch function within the laser period ( $T=0.05$  [s]) can be seen in the Fig. 5.

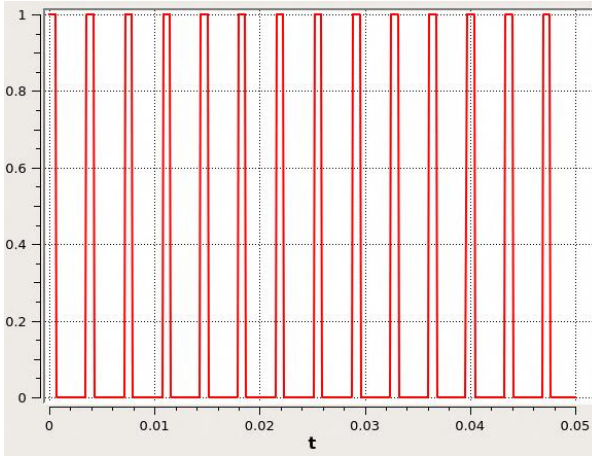


**Fig. 5** Switch function of first wire droplets in mass flux function

The above function turns on the mass flow source of the drops only a fraction of the time. To ensure the mass conservation of the melted wires, the function shall be normalized and the integration in one second gives 1: Therefore, the mass rate function is settled with the following factor:

$$f_{d1} = \left( \int_0^1 s_{d1} dt \right)^{-1} = 5.605 \quad (20)$$

$$f_{d2} = \left( \int_0^1 s_{d2} dt \right)^{-1} = 5.218 \quad (21)$$

The mass flux is found as follows:

$\dot{m}_d = \text{Normalising factor} \times \text{time switch} \times \text{droplet mass} \times \text{number of droplets} \times \text{mass distribution}$

$$\dot{m}_{d1} = 8\sqrt{3} f_{d1} s_{d1} \rho_m v_{d1} \exp\left(\frac{-3}{R_d^2}((x - x_{01})^2 + (y - y_0)^2 + (z - z_0)^2)\right) \quad (22)$$

$$\dot{m}_{d2} = 8\sqrt{3} f_{d2} s_{d2} \rho_m v_{d2} \exp\left(\frac{-3}{R_d^2}((x - x_{02})^2 + (y - y_0)^2 + (z - z_0)^2)\right) \quad (23)$$

$$x_{02} = x_{01} + d_d \quad (24)$$

At the beginning of the process, when the arc is ignited, the process can be unstable and the droplets are twice as large in diameter. Therefore the droplets have eight times the volume. In order to map this time in the simulation, we can change the mass flux and droplet distances for a so-called irregularity time,  $t_i$  as follows:

$$(\dot{m}_{d1})' = \dot{m}_{d1}(1 + 7\theta(t_i - t)) \quad (25)$$

$$(\dot{m}_{d2})' = \dot{m}_{d2}(1 + 7\theta(t_i - t)) \quad (26)$$

$$(d_d)' = d_d + 0.5\theta(t_i - t) \quad (27)$$

The measurement of the drop velocity ( $v_{xz}$ ) is carried out by recording a high-speed camera (Fig. 6) and analyzing the frame rate and the distance covered by the drops. The angles of the droplet trajectory across the transverse ( $\beta$ ) and longitudinal ( $\alpha$ ) directions are measured using two mounted cameras (Fig. 7). The projection of the droplet velocity in the longitudinal and vertical and transvers directions is calculated using the analysis of the recordings of the two mentioned mounted camera as follows:

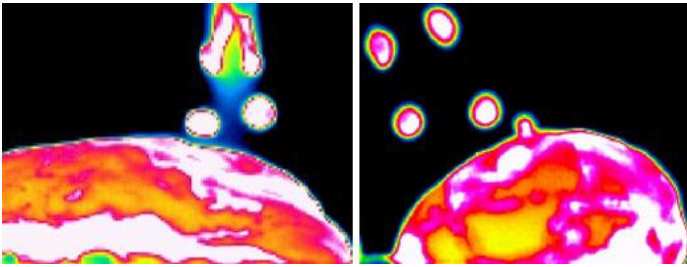


**Fig. 6** Droplet size and trajectories, left: over longitudinal direction (camera transverse) and right: over transversal direction, (camera in welding direction)

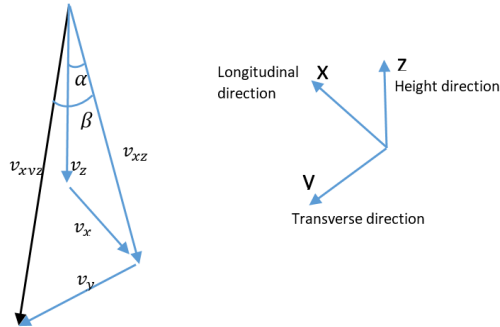


**Fig. 7** Velocity vectors in longitudinal, transversal and altitudinal directions

$$v_{xz} = v_{xyZ} \cos(\beta) \quad (28)$$

$$v_y = v_{xyZ} \sin(\beta) = v_{xz} \tan(\beta) \quad (29)$$

$$v_z = -v_{xz} \cos(\alpha) \quad (30)$$

Since the drops have opposite directions about the longitudinal axis, then:

$$v_{x1} = -v_{xz} \sin(\alpha) \quad (31)$$

$$v_{x2} = v_{xz} \sin(\alpha) \quad (32)$$

The angle of the drops of the respective wires to the height axis (longitudinal velocity) varies constantly, so that the drops diverge (opposite direction) or converge and have parallel trajectories in the course of the process.

Therefore, the angle  $\alpha$  is sinusoidal and time-dependent as follows, in which  $v_p$  describes the frequency of how often the drops diverge or converge.

$$\alpha = 5 \sin\left(2\pi v_p \left(t - \frac{1}{4v_p}\right)\right) + 5 \quad (33)$$

After solidification, the velocity vectors should only show the welding speed of the sheet metal. In order to dampen the velocity vectors in the solidified layer, the enthalpy porosity method is used as follows:

$$M_x = -C s_m (u_x - v_w) \quad (34)$$

$$M_y = -C s_m (u_y) \quad (35)$$

$$M_z = -C s_m (u_z) \quad (36)$$

In which  $s_s$  is the switch to activate momentum loss function for temperatures below the melting point and volume fractions above 0.5:

$$s_m = \theta(\phi_m - 0.5)\theta(T_s - T_m) \quad (37)$$

For the representation of evaporation, the mass and heat balance of evaporation should be implemented as mass and heat source. Mass fraction of the vaporized metal from temperatures above the boiling point results from the ratio of the absorbed enthalpy to the latent heat:

$$w_e = c_{p,m}(T_m - T_b)\theta(T_m - T_b)/L_b \quad (38)$$

The evaporation mass flux results from the mass fraction of the vaporized metal and the available molten metal mass per volume in the cell (product of density and volume of fraction) divided by time:

$$\dot{m}_e = w_b \phi_m \rho_m / \delta t \quad (39)$$

The evaporation is calculated from the evaporation mass flux and the latent heat of evaporation:

$$\dot{q}_e = \dot{m}_e L_b \quad (40)$$

## SMOOTHED PARTICLE HYDRODYNAMICS

The smoothed particle hydrodynamics method was adapted to the problem of fluid dynamics by Müller et al. [33]. It is a mesh-free method, i.e. it does not require connectivity information between discretization points. The absence of explicit connectivity information through a mesh lifts one of the major limitations of mesh-based methods, namely the limitation of possible movement of the discretization points. In contrast to mesh-based methods, mesh-free methods allow for free movement of the discretization points. This, in turn enables movement of the discretization points according to the velocity field, i.e. enabling a Lagrangian treatment of the underlying fluid.

SPH is one of the most widely adopted Lagrangian methods, where physical quantities are discretized onto a set of freely mobile discretization points. Each of these points carries the physical quantities associated with it as it moves according to the velocity field. The points are often thought of and visualized as particles by associating a certain spatial extent with each discretization point, hence the name smoothed particle hydrodynamics. In lieu of a mesh for connectivity information and since interactions between “close” points are necessary for a physically accurate simulation, SPH makes use of a neighbourhood relation  $\mathcal{N}$ . Complete pairwise interactions between all particles in a simulation is computationally infeasible, therefore SPH typically utilizes an efficient search structure to determine neighbourhoods such as the one presented in [34], as well as limiting the sizes of these neighbourhoods.

In SPH an arbitrary quantity  $A(\vec{x})$ , that was discretized onto particles can thus be computed by interpolating the local neighbourhood  $\mathcal{N}_{\vec{x}}$  of the sample point  $\vec{x}$ :

$$A(\vec{x}) = \sum_{j \in \mathcal{N}_{\vec{x}}} V_j A_j W(\vec{x} - \vec{x}_j; h) \quad (41)$$

This kernel function is used as a weighing scheme for particles depending on their spatial relation to the sample point. Generally particles that are further away from the sampling point, have a lower contribution to the quantity  $A(\vec{x})$ , than nearer particles. This weighing results in a smoothed field  $A(\vec{x})$ , hence the name smoothed particle hydrodynamics. A well-known function that could be used as a kernel would be the Gaussian function. However, it has one disadvantage, namely that it has infinite support, which means all particles in the simulation would add small contributions to any interpolation. As noted before the number of contributing particles should always be large enough for good interpolations, but as small as possible such that the interpolation is efficiently computable. Therefore, the most frequently used kernel functions have a finite support and are scaled according to the smoothing length parameter  $h$ , such that only a small number of particles, namely those for which  $|\vec{x} - \vec{x}_j| < h$ , need to be considered for the interpolation. In this paper the cubic spline kernel [35] is used.

It is important to note that the SPLisHSPlasH library itself is an ongoing research project in active development. As such there are many physical phenomena that are not yet taken into account, either due to lack of existing implementations within SPLisHSPlasH, or a lack of well-founded methods for their modelling in SPH in general. As such simpler compensation models were developed and applied for the LDNA SPH simulation. Despite these, often rather crude compensation models, we were able to show

remarkable results for the SPH simulation of the LDNA process including very good agreement with the simulation in ANSYS CFX.

Since SPH has been adapted to the problem of fluid dynamics, a large number of methods have been proposed for various phenomena, typically associated with fluid dynamic simulations, e.g. pressure, viscosity and surface tension solvers. Beyond that however, there are several important physical phenomena that arise in welding simulations, which are not part of the typical SPH repertoire. This includes thermal effects, such as heat in- and outputs, thermal conduction and a solidification/melting model, electromagnetic effects, such as Lorentz forces for droplet detachment and melt pool flows.

Nonetheless, they are crucial and some treatment of these phenomena is necessary to obtain accurate welding simulations.

### BOUNDARY CONDITIONS IN SPH AND MOVING DOMAIN OF MASS AND HEAT FLUX

In contrast to Eulerian approaches, where the need to discretize and solve the entire domain generally places quite significant restrictions on the potential, the domain in SPH is theoretically and practically unbounded (Fig. 8 & Fig. 9). This is due to the fact, that equations are only solved at particle locations, i.e. only where material exists. As a consequence, large but sparse and potentially even unbounded domains are very feasible. On the other hand, many boundary conditions that are easily formulated in an Eulerian frame are more complicated to realize in a Lagrangian one, most importantly here are mass in- and outlets. As such mimicking the welding movement by a mass inlet and outlet parametrized by the welding speed, as it was done in the FVM simulation, is not a very natural formulation for the SPH simulation.

Rather in SPH it is much more appropriate and easier to keep the substrate fixed, and moving the wire mass source according to the welding speed instead. The relative movement between substrate and wire mass source remains the same, however the absolute frame of reference differs between the simulations.

Furthermore, this means that many other effects are defined relatively to the mass source, such as droplet acceleration and the position of the laser. In the moment this movement is a uniform horizontal movement for both wires along the weld direction as specified by the welding speed.

As already stated the SPH interactions are only calculated between particles, therefore SPH boundary conditions are free-slip by default, unless additional effects, that change boundary behaviour, are specified. As this was the condition for FVM there was no reason to change it in the SPH simulation.

Since SPH currently forbids movement of any particles below the melting temperature, gravity does not affect the solid material.

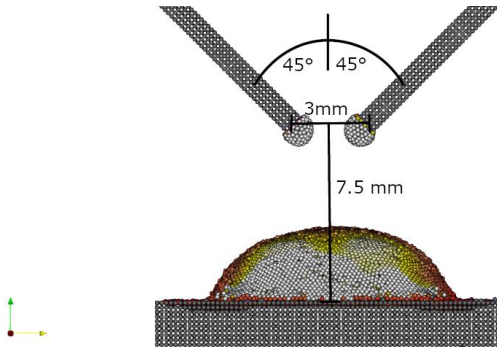


**Fig. 8** Front view of simulation geometry with schematic arrangement annotations

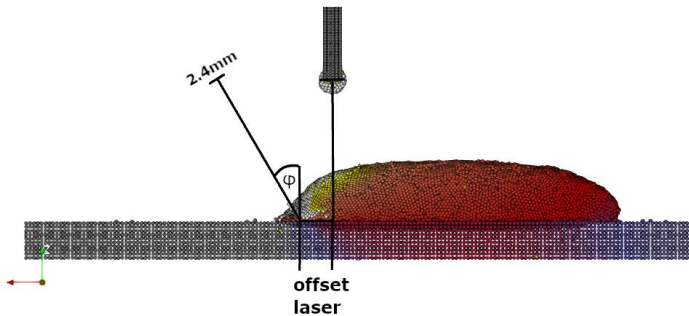


**Fig. 9** Side view of simulation geometry.  $\phi$  and laser offset are variable parameters

Molten material with a temperature of  $T$  (In this case 2100 K, according to experimental measurements) drops on the surface, which constitutes mass and energy addition into the cladding layer. Secondly, the laser/heat-source constitutes another energy input into the substrate and cladding layer. Lastly convection between material and air, as well as thermal radiation at the material surface constitute an energy loss of the system.

#### DENSITY

Arguably the biggest limitation of the framework for the purpose of welding simulations is the lack of variable density. Currently, a material can have a single density, independent of its temperature. However, since density is closely related to the pressure solver of SPH, the implementation of the temperature dependant density is under development in the current solver. In the current state of the simulation framework, either mass or volume will deviate from observed values. Whether mass or volume are

determined accurately and whether over- or underestimates of the other are made is up to the user, depending on the values and compensation models used. Treating mass correctly was deemed to be of higher priority, such that accuracy regarding energy models is retained. As such the entire material is assumed to have a density of molten steel ( $6793.7 \text{ kg/m}^3$ ) and the push speed of the welding wire is adjusted upwards by a factor around  $7948.9 / 6793.7 \approx 1.17$ , such that mass gain of the simulation is correct. This results in correct mass and volume for molten regions, but an overestimation of volume by roughly 15 % for the solidified welding seam. Even if the consideration of the density change is algorithmically possible, this assumption is often used for the simulation of the flows in the melt pool, since the correct consideration of the density change causes massive additional calculation work.

### WIRE MASS SOURCES AND MOVEMENT

As stated previously that the wire mass sources are the moving reference points. Since the domain in SPH is not restricted, it is also entirely feasible to initialize the entire mass that will be introduced over the course of the simulation at the initial time step. Over the course of the simulation this material is pushed over the wire mass source with the wire feed speed. This treatment allows the use of the easier and generally more robust particle-particle surface tension and viscosity formulas instead of particle-boundary formulas, since there is always a layer of solid particles to interact with above the layer currently passing the mass source point.

Mass is pushed past the mass source point as specified by the direction parameter and feed speed parameters. Currently the wires are arranged in a  $45^\circ$  angle from the height axis (see, with two different, but constant over time, feed speeds for the first and second wire, determined from the mass fluxes  $\dot{m}_{d1}$  and  $\dot{m}_{d2}$ , quantitatively same as realized in the FVM approach.

### DROPLET DETACHMENT PROCESS

The simulation framework does not contain any models relating to electricity and its effects. This means that electromagnetic effects are not taken into account, specifically those relating to the electric arc. To facilitate droplet detachment without a physical treatment of the electromagnetic forces, droplet particles are periodically accelerated to a sufficient velocity for regular, uniform droplet detachment as observed in experiments. The detachment frequency was chosen at 100 Hz according to experimental data. Secondly, the energy gain in the wires by current running through them is also not modelled. Instead particles close to the tip of the wire have their temperature simply set to 2100 K, which conforms roughly to temperature observations of the droplet at 170 A. Through these two mechanisms orderly droplet formation and detachment are achieved.

DETERMINATION OF SURFACES

A prerequisite for the application of various boundary conditions is a determination of surfaces, mainly which particles belong to a surface, and are thus subject to these boundary conditions. While SPH is very well suited for the simulation of free moving of the particles, the actual extraction of these is a widely known problem, for which numerous differing approaches have been proposed. A very robust approach, that strikes the balance between high quality results and computational efficiency, is the so-called coverage technique [36]. First for all particles, the local coverage vector at a point  $\vec{x}$  can be calculated as

$$\vec{n} = \sum_{j \in N_{\vec{x}}} (\vec{x} - \vec{x}_j) \tag{42}$$

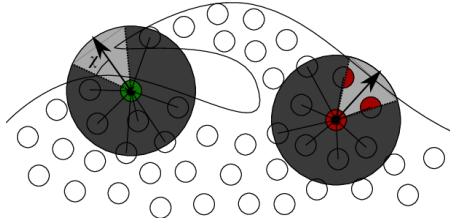


**Fig. 10** Classification of surface particles using the coating method. The green particle (left) is classified as surface particle and the red particle (right) is classified as internal (not surface particle). [3]

In fully occupied regions this vector will be close to zero as all conditions are cancelled. This vector will be significantly different from 0 only in partially unoccupied regions and will be directed towards the region of the local lowest particle density. Thus, it acts as a geometric estimate of the normal vector for the local neighbourhood. The cone defined by the particle location, this local coverage vector and the angle  $\chi$  can then be checked for the presence of particles. If no particles are detected within the cone, the particle is classified as a surface particle. (Fig. 10). The angle  $\chi$  remains a parameter of the method, in experiments it was found that  $\chi = 30^\circ$  leads to excellent classification results, so this value was used in all simulations.

SURFACE TENSION

To model the surface tension of the fluid, the method from [33] was used. There the surface normals are estimated using the gradient  $\vec{n} = \nabla C$  of the so-called color field, defined as

$$C(x) = \sum_{j \in N_{\vec{x}}} V_j W(\vec{x} - \vec{x}_j; h) \tag{43}$$

The color field is a simple SPH interpolation without the discretized quantity in the equation, meaning that quantity is implicitly 1 for all particles.

The resulting field is 1 in fully occupied regions, 0 in empty regions and between 0 and 1 in partially occupied regions. The gradient of this field, always pointing in the direction of maximum color gain, can be treated as a stand-in for the surface normal.

From the normals it is possible to estimate the curvature as

$$\kappa = \frac{-\nabla^2 c}{|\vec{n}|} \quad (44)$$

Given a surface tension coefficient  $\gamma$ , the force arising due to surface tension can then be calculated as

$$f_S = \gamma \kappa \vec{n} \quad (45)$$

Note that the used surface tension force in the actual version of simulation solver is not dependent upon temperature. This limits the model somewhat for the use in welding simulations, where temperature gradients, and associated surface tension gradients occur.

#### VISCOSITY & COHESION

To model the viscosity, the model presented by Weiler et al. [37], with the adaption of temperature-dependency, was used. Additionally cohesion and XSPH [38] models were integrated into viscosity model. The cohesion force acts in a similar way to the surface tension, but differs in the algorithmic formulation. Through cohesion all particles add an accelerating contribution to their neighbourhood based on the velocity difference between particles. In fully dense regions the cohesive force should equalize to 0. The XSPH method is used to alleviate noise in the particle velocities, which can be introduced by a multitude of sources, e.g. by unfavourable neighbourhoods. To avoid unwanted effects from noisy velocities, they are slightly smoothed over the neighbourhood. Note that XSPH does not add or remove momentum, it simply redistributes it over the neighbourhoods.

Both of these models were found to lead to more stable results, especially for droplets in flight, which are subject to much higher velocities than the rest of the material.

#### RADIATION & CONVECTION

Models for radiative and convective heat transfer are implemented. Losses through thermal radiation for a surface particle  $i$ , as determined by the coverage approach, are implemented in the same way as by the Eulerian approach with the equation [6], but each particle will be addressed in the SPH-method as

$$\dot{q} = \varepsilon \sigma (T^4 - T_0^4) \quad (46)$$

A heat flux between the environment and the material for a surface particle  $i$ , again as determined by the coverage approach is implemented as

$$\dot{q} = h(T - T_0) \quad (47)$$

To apply these heat fluxes an estimation of the exposed surface area is needed. Unfortunately, there is no model implemented within SPlisHSPlasH at the moment that can determine the exposed area of a surface particle. Such a model would require careful design, testing and an evaluation of its correctness, and would thus likely constitute a scientific contribution on its own. Therefore, both convection and radiation currently use a constant estimate of  $A = (2r_p)^2$ , i.e. a squared particle diameter, for the exposed surface area per particle. This estimate is accurate for flat regions, but an overestimate for concave regions and an underestimate for convex regions. Here we argue that the use of this estimation is appropriate, since the error introduced by it, is negligible, and other parameters such as the coefficients  $\epsilon$  and  $h$ , which were not subject to careful adjustment, have a far more significant impact on the final result.

#### LASER EFFECT

In the SPH simulation the laser is defined using a projective 2D approach. First a projection plane, from which the effect originates, is defined by an extent and a normal direction, defining the direction in which the effect is applied. For all these particle positions, multiple conditions are checked, namely are they within the dimension of the plane, i.e. can be reached from the plane by following the normal, are they in the correct direction from the plane, are their normals and the heat source normal oriented opposite, and finally are they a surface particles as determined by the coverage method [36] described above. In this manner it is possible to calculate all particles that should be effected by the heat source through local conditions, without differentiating between cladding layer and substrate particles.

Lastly the strength of the heat source influence can be defined as any two dimensional function, that exists in the plane defined at the start. After having identified all relevant particles, it is possible to project them into this plane, to calculate the point from which a ray following the normal would have originated, and evaluate the function there.

In this work the function that gives the energy distribution is an isotropic two dimensional Gaussian with the radius  $r_l$ . The energy flux for a particle  $i$ , whose projected point has a distance of  $r$  to the center of the Gaussian is therefore computed as

$$\dot{q}_i = \frac{3P}{\pi r_l^2} \exp\left(\frac{-3r^2}{r_l^2}\right) \quad (48)$$

Currently, there is no variable absorption of the power based on the angle of incidence, however there is a general absorption scaling factor, currently set to 50 %.

The laser is defined in terms of a source and target point. The beam originates from the source point and is targeted toward the target point. Initially the target point is located on the substrate surface with a parametrized laser offset (see Fig. 9). The source point is located 300 mm away according to the angle  $\varphi$ , in accordance with the arrangement of the real process. These two points are defined relative to the wire mass source, so they move at the welding speed. Additionally, the target point oscillates sinusoidal with a frequency of 10 Hz and an amplitude of 6.6 mm along the y-axis during the simulation.

## RESULTS AND DISCUSSION

The simulations in both approaches were performed on a single node on the RWTH CLAIX-18 cluster made up of two Intel Xeon Platinum 8160 “SkyLake” Processors (2.1 GHz, 24 cores each).

The LDNA simulation with FVM model used a mesh with 690K elements, 722K nodes. The smallest size of elements is 0.15 [mm] in the free surface area. Numerically, the model becomes more stable over time and the convergence of liquid and gas improves. The Root Mean Square (RMS) for convergence of fluid medium fluctuates around  $1e-4$  and around  $1e-6$  for the shielding gas.

In the FVM approach, 0.5 [s] of the process were simulated in 84h, 18m or 4046 core-hours. The wall time was not used only for calculation. This time results from 8.5% variable updates and 0.7% for writing 2500 output data and 90.8% for miscellaneous including calculation.

The SPH model consisted of 607K particles with a radius of 0.1 [mm], which were simulated for 4 [s] of LDNA process. The SPH simulation for the first second of the process took 09h, 21m on the specified hardware, simulating the entire process took 30h, 20m.

In both cases (Fig. 11), FVM (left) and SPH (right), the falling droplets into the weld pool can be seen.

The surface in the FVM is defined as Volume of fluid of 0.5. With very fine meshing, the boundaries of the VOF 0.5 and 0.9 can be close. However, in this case the need for a very fine mesh greatly increases the computation effort.

Both approaches can be used for simulating the LDNA process and show good qualitative agreement, both between SPH and FVM methods and between simulation and Experiment. For the quantitative agreement, the other parameters, including in particular surface tension and density as well as angle-dependent absorption coefficients in SPH, still have to be calibrated. The deformation of the melt surface due to the droplet momentum can be represented very well in the Euler approach. The current version's SPH approach needs to be further developed for surface effects.

For more complex droplet detachment topologies, the SPH method is better suited than the FVM. Since SPH natively ensures mass conservation and due to its mesh-free formulation, simulation of next passes in multilayer deposition welding would not lead to a significant additional computational effort.

The evaporation process is an important part of the LDNA process in reality. As such quantitative agreement between a simulation and reality would require a model in this regard. The sub-model of evaporation can be described as a combination of mass, heat loss and momentum gain. The phenomenon of heat, mass and momentum change through evaporation can be implemented very well in the Euler approach. For SPH, the decrease in heat and increase in momentum during evaporation can be taken into account, but there is currently no such model in the SPLisHSPlasH framework. The development of an evaporation model dealing with heat, mass and momentum change for SPLisHSPlasH is a further aim.

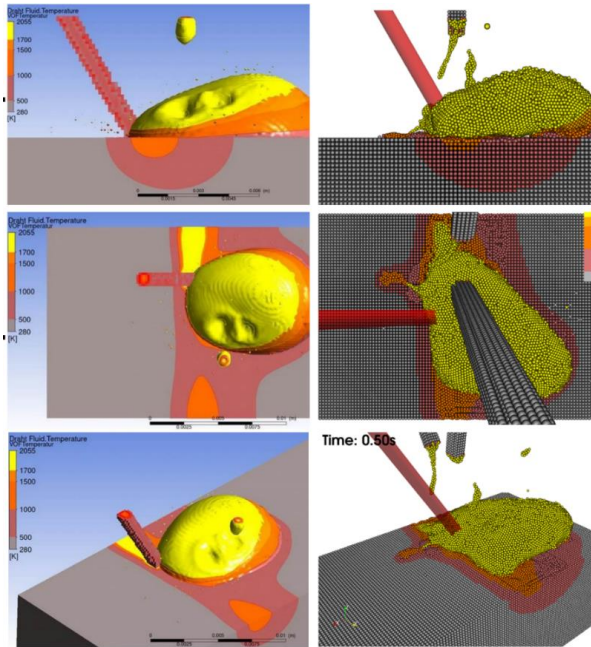


**Fig. 11** The simulation results for the FVM (left) and SPH (right) methods

## CONCLUSION

Both approaches offer the possibility to simulate the LDNA process. We can note a qualitative agreement, both between SPH and FVM method and between simulations and experiments. The computational resources needed for the FVM method is larger than that for the SPH method by about a factor of 17. The FVM method provides a more accurate representation of the process with physical phenomena such as evaporation, as well as surface formation and modification by the local forces present. The FVM method should be used for higher accuracies or for a fine description of surface phenomena.

The SPH method offers significantly faster simulation times for processes where flow is the dominant phenomenon, while still producing results with close agreement to FVM. It is especially suited for processes with discontinued flows. As the SPH formulation explicitly only discretizes the fluid and solid metal, the environment and its various effects are neglected.

If neglecting the effect of the protective atmosphere is acceptable for a simulation case, the simulation results for such processes could be available in a significantly shorter time and with comparable agreement.

## ACKNOWLEDGMENT

The investigations have been carried out within the research project DFG 423140171. The authors would like to express their special gratitude to the German Research Foundation (DFG).

The authors gratefully acknowledge the computing time granted by the NHR4CES Resource allocation Board and provided on the supercomputer CLAIX at RWTH Aachen University as part of the NHR4CES infrastructure. The calculations for this research were conducted with computing resources under the project 20019.

## References

- [1] BENDER, J.: *SPlisHSPlasH*, <https://github.com/InteractiveComputerGraphics/SPlisHSPlasH>, 2022.
- [2] S.R. JESKE, J. BENDER, K. BOBZIN, H. HEINEMANN, K. JASUTYN, M. SIMON, O. MOKROV, R. SHARMA, U. REISGEN: 'Application and benchmark of SPH for modeling the impact in thermal spraying', *Comp. Part. Mech.*, 2022, <https://doi.org/10.1007/s40571-022-00459-9>.
- [3] S.R. JESKE, M.S. SIMON, O. SEMENOV, J. KRUSKA, O. MOKROV, R. SHARMA, U. REISGEN, J. BENDER: 'Quantitative evaluation of SPH in TIG spot welding', *Comp. Part. Mech.*, 2022, <https://doi.org/10.1007/s40571-022-00465-x>.
- [4] A. BARROI, J. AMELIA, J. HERMSDORF, S. KAIERLE, V. WESLING: 'Influence of the Laser and its Scan Width in the LDNA Surfacing Process', *Physics Procedia*, 2014, <https://doi.org/10.1016/j.phpro.2014.08.164>.
- [5] A. BARROI, J. HERMSDORF, U. PRANK, S. KAIERLE: 'A Novel Approach for High Deposition Rate Cladding with Minimal Dilution with an Arc – Laser Process Combination', *Physics Procedia*, 2013, <https://doi.org/10.1016/j.phpro.2013.03.076>.
- [6] A. BARROI, F. ZIMMERMANN, J. HERMSDORF, S. KAIERLE, V. WESLING, L. OVERMEYER: 'Evaluation of the laser assisted double wire with nontransferred arc surfacing process for cladding', *Journal of Laser Applications*, 2016, <https://doi.org/10.2351/1.4944001>.
- [7] T. BOKELMANN, M. LAMMERS, J. HERMSDORF, S. EMADMOSTOUFI, O. MOKROV, R. SHARMA, U. REISGEN, S. KAIERLE: 'Experimental setup for determination of absorption coefficient of laser radiation in molten metals as a function of temperature and angle', In: *Proceedings of Lasers in Manufacturing Conference (WLT-LiM)*, 2021, Online Conference, 21-24 June 2021.
- [8] T. BOKELMANN, M. TEGTMEIER, M. LAMMERS, J. HERMSDORF, S. KAIERLE, S. EMADMOSTOUFI, O. MOKROV, R. SHARMA, U. REISGEN: 'Influence of the laser beam parameters in the laser assisted double wire welding with nontransferred arc process on the seam geometry of generatively manufactured structures', *Journal of Laser Applications*, 2021, <https://doi.org/10.2351/7.0000521>.
- [9] M.S. AMAL, C.T. JUSTUS PANICKER, V. SENTHILKUMAR: 'Simulation of wire arc additive manufacturing to find out the optimal path planning strategy', *Materials Today: Proceedings*, 2022, <https://doi.org/10.1016/j.matpr.2022.06.338>.
- [10] Y. ZHENG, Z. YU, J. XIE, J. CHEN, C. YU, J. XU, H. LU: 'A numerical model-based deposition strategy for heat input regulation during plasma arc-based additive manufacturing', *Additive Manufacturing*, 2022, <https://doi.org/10.1016/j.addma.2022.102986>.
- [11] S.H. NIKAM, N.K. JAIN: 'Three-dimensional thermal analysis of multi-layer metallic deposition by micro-plasma transferred arc process using finite element simulation', *Journal of Materials Processing Technology*, 2017, <https://doi.org/10.1016/j.jmatprotec.2017.05.043>.

- [12] Q. CHAI, C. FANG, J. HU, Y. XING, D. HUANG: 'Cellular automaton model for the simulation of laser cladding profile of metal alloys', *Materials & Design*, 2020, <https://doi.org/10.1016/j.matdes.2020.109033>.
- [13] X. HAN, C. LI, X. CHEN, S. JIA: 'Numerical simulation and experimental study on the composite process of submerged arc cladding and laser cladding', *Surface and Coatings Technology*, 2022, <https://doi.org/10.1016/j.surfcoat.2022.128432>.
- [14] L. WANG, D. ZHANG, C. CHEN, H. FU, X. SUN: 'Multi-physics field coupling and microstructure numerical simulation of laser cladding for engine crankshaft based on CA-FE method and experimental study', *Surface and Coatings Technology*, 2022, <https://doi.org/10.1016/j.surfcoat.2022.128396>.
- [15] B. SONG, T. YU, X. JIANG, W. XI, X. LIN: 'The relationship between convection mechanism and solidification structure of the iron-based molten pool in metal laser direct deposition', *International Journal of Mechanical Sciences*, 2020, <https://doi.org/10.1016/j.ijmecsci.2019.105207>.
- [16] A.P. SEMYONOV: 'Methods of mathematical modelling of the processes of electrode metal droplet formation and transfer in consumable electrode welding', *Paton Weld J* 10, 2-10, 2014.
- [17] J. HAIDAR, J.J. LOWKE: 'Predictions of metal droplet formation in arc welding', *J. Phys. D: Appl. Phys*, 1996, <https://doi.org/10.1088/0022-3727/29/12/003>.
- [18] M. HERTEL, U. FÜSSEL, M. SCHNICK: 'Numerical simulation of the plasma-MIG process-interactions of the arcs, droplet detachment and weld pool formation', *Weld World*, 2014, <https://doi.org/10.1007/s40194-013-0095-6>.
- [19] S. CADIOU, M. COURTOIS, M. CARIN, W. BERCKMANS, P. LE MASSON: '3D heat transfer, fluid flow and electromagnetic model for cold metal transfer wire arc additive manufacturing (Cmt-Waam)', *Additive Manufacturing*, 2020, <https://doi.org/10.1016/j.addma.2020.101541>.
- [20] M. MEDALE, S. RABIER, C. XHAARD: 'A Thermo-Hydraulic Numerical Model for High Energy Welding Processes', *Revue Européenne des Eléments Finis*, 2004, <https://doi.org/10.3166/reef.13.207-229>.
- [21] M. MEDALE, C. TOUVREY, R. FABBRO: 'An axi-symmetric thermo-hydraulic model to better understand spot laser welding', *European Journal of Computational Mechanics*, 2008, <https://doi.org/10.3166/remn.17.795-806>.
- [22] M.C. NGUYEN, M. MEDALE, O. ASSERIN, S. GOUNAND, P. GILLES: 'Sensitivity to welding positions and parameters in GTA welding with a 3D multiphysics numerical model', *Numerical Heat Transfer, Part A: Applications*, 2017, <https://doi.org/10.1080/10407782.2016.1264747>.
- [23] L.B. LUCY: 'A numerical approach to the testing of the fission hypothesis', *The Astronomical Journal*, 1977, <https://doi.org/10.1086/112164>.
- [24] R.A. GINGOLD, J.J. MONAGHAN: 'Smoothed particle hydrodynamics: theory and application to non-spherical stars', *Monthly notices of the royal astronomical society*, 1977, <https://doi.org/10.1093/mnras/181.3.375>.
- [25] R. DAS, P.W. CLEARY: 'Three-dimensional modelling of coupled flow dynamics, heat transfer and residual stress generation in arc welding processes using the mesh-free SPH method', *Journal of Computational Science*, 2016, <https://doi.org/10.1016/j.jocs.2016.03.006>.
- [26] I. MASUMI, N. YU, I. SEIICHIRO, F. YU, S. MASAYA: 'Numerical Simulation of Joining Process in a TIG Welding System Using Incompressible SPH Method', *Quarterly Journal of the Japan Welding Society*, 2015, <https://doi.org/10.2207/qjws.33.34s>.
- [27] M. TRAUTMANN, M. HERTEL, U. FÜSSEL: 'Numerical simulation of weld pool dynamics using a SPH approach', *Weld World*, 2018, <https://doi.org/10.1007/s40194-018-0615-5>.
- [28] H. KOMEN, M. TANAKA, H. TERASAKI: 'Three-Dimensional Simulation of Gas Metal Arc Welding Process Using Particle-Grid Hybrid Method', *Quarterly Journal of the Japan Welding Society*, 2020, <https://doi.org/10.2207/qjws.38.25s>.

- [29] H. KOMEN, M. SHIGETA, M. TANAKA: ‘Numerical simulation of molten metal droplet transfer and weld pool convection during gas metal arc welding using incompressible smoothed particle hydrodynamics method’, *International Journal of Heat and Mass Transfer*, 2018, <https://doi.org/10.1016/j.ijheatmasstransfer.2018.01.059>.
- [30] A. D. BRENT, V. R. VOLLER, K. J. REID: ‘Enthalpy-porosity technique for modeling convection-diffusion phase change: application to the melting of a pure metal’, *Numerical Heat Transfer*, 1988, <https://doi.org/10.1080/10407788808913615>.
- [31] V.R. VOLLER, A.D. BRENT, C. PRAKASH: ‘Modelling the mushy region in a binary alloy’, *Applied Mathematical Modelling*, 1990, [https://doi.org/10.1016/0307-904x\(90\)90084-i](https://doi.org/10.1016/0307-904x(90)90084-i).
- [32] A. PATHAK, M. RAESSI: ‘A three-dimensional volume-of-fluid method for reconstructing and advecting three-material interfaces forming contact lines’, *Journal of Computational Physics*, 2016, <https://doi.org/10.1016/j.jcp.2015.11.062>.
- [33] M. MÜLLER, D. CHARYPAR, M. GROSS: ‘Particle-Based Fluid Simulation for Interactive Applications’, 2003.
- [34] M. IHMSEN, N. AKINCI, M. BECKER, M. TESCHNER: ‘A Parallel SPH Implementation on Multi-Core CPUs’, *Computer Graphics Forum*, 2011, <https://doi.org/10.1111/j.1467-8659.2010.01832.x>.
- [35] J.J. MONAGHAN: ‘Smoothed Particle Hydrodynamics’, *Annu. Rev. Astron. Astrophys.*, 1992, <https://doi.org/10.1146/annurev.aa.30.090192.002551>.
- [36] A. BARECASCO, H. TERRISSA, C.F. NAA: ‘Simple free-surface detection in two and three-dimensional SPH solver’, <http://arxiv.org/pdf/1309.4290v1>, 2013.
- [37] M. WEILER, D. KOSCHIER, M. BRAND, J. BENDER: ‘A Physically Consistent Implicit Viscosity Solver for SPH Fluids’, *Computer Graphics Forum*, 2018, <https://doi.org/10.1111/cgf.13349>.
- [38] H. SCHECHTER, R. BRIDSON: ‘Ghost SPH for animating water’, *ACM Trans. Graph.*, 2012, <https://doi.org/10.1145/2185520.2185557>.



# **V Residual Stresses and Distortion**



# SIMULATION OF RESIDUAL STRESSES DURING THE WIRE ARC ADDITIVE MANUFACTURING (WAAM) PROCESS

A. A. ALRUMAYH\*, H. F. NIED\*\*

*\*Department of Mechanical Engineering, College of Engineering, Qassim University, Unaizah,, Saudi Arabia*

*\*\*Mechanical Engineering and Mechanics, Lehigh University, Bethlehem, PA 18015, USA*

DOI 10.3217/978-3-85125-968-1-15

## ABSTRACT

This study examines the residual stresses and distortion that can occur during the Wire Arc Additive Manufacturing (WAAM) process. Of particular interest is the evolution of the residual stresses due to the repetitive heating and cooling associated with the moving arc heat source and deposition of hot metal during the layer-by-layer metal deposition process. The presented results show how the fundamental welding process parameters, thermomechanical material properties, and clamping/fixture conditions affect the post-processing residual stresses. For thin-walled structures, these residual stresses can result in significant warpage and/or premature cracking. This computational study is primarily based on the application of finite element models generated using the SYSWELD finite element software to simulate the coupled heat transfer and mechanical behavior during the layer-by-layer "printing" of a thin, 3-D rectangular plate. Of particular interest are the residual stress comparisons between an austenitic stainless steel, AISI 316L, and a low-carbon steel alloy, S355J2G3. The differences in residual stresses are closely related to the differences in the volumetric strains associated with the metallurgical phase changes between these two different steel alloys.

Keywords: Additive Manufacturing, WAAM, residual stresses, deformation, phase changes, isotropic hardness, heat treatment, size effects

## INTRODUCTION

WAAM (Wire Arc Additive Manufacturing), is an effective Additive Manufacturing (AM) process that provides an economical technology path for fabricating large mechanical components [1-3]. The ability to build large load-bearing parts, in some cases up to a few meters in size [2], with significant geometric complexity [3], is particularly attractive for structural applications (Fig. 1). The two most frequently employed deposition techniques used in conventional WAAM processes are: Gas Metal-Arc Welding (GMAW) and Gas Tungsten-Arc Welding (GTAW). The energy efficiency of the electric arc can be as much as 90% in these welding processes.



**Fig. 1** Sample WAAM structural components fabricated at Lehigh University's Additive Manufacturing Life Analysis Lab. Courtesy of Dr. C. Haden

Of particular significance for the fabrication of large metal parts is WAAM's capacity for high deposition rates, generally lower system and material costs, and a lower likelihood of oxide contamination [4-5]. For example, WAAM can attain deposition rates of 3–7.8 kg/h, whereas powder bed based systems usually only have deposition rates of 0.12–0.6 kg/h [6]. Typical metal alloys used in WAAM include: titanium and its alloys, steel, aluminum, and nickel alloys. It is well-known that wire fed AM systems generally provide relatively low resolution when compared with most powder-based deposition processes. Not only are the feed wire diameters considerably larger than the fine powder sizes available for powdered metals, but arc welding also introduces a larger melt pool size and relatively high post-weld distortion. The typical reported "precision" attained using WAAM is on the order of  $\pm 0.2$  mm vs  $\pm 0.04$  mm for powder-based systems. Thus, WAAM is generally not recommended for "printing" intricate parts with small length scale features [7-8].

WAAM processes can introduce very large residual stresses [9], which if not relieved can lead to undesirable distortion, especially in thin-walled parts. Since WAAM is based on well-understood direct fusion welding processes, conventional welding process parameters can be effectively utilized and controlled with little trial and error. The most important welding parameters are the arc voltage, arc current, shielding gas, nozzle-base distance, travel speed, wire feed speed, and wire diameter. These process parameters are known to most strongly influence the weld bead geometry, distortion, and resulting residual stresses [3]. The main issues encountered in WAAM are the same as those associated with all fusion welding processes, i.e., potential lack of fusion, porosity, vaporization, undesirable mechanical properties in the heat affected zone, grain structure, surface finish, deformation and distortions, high residual stresses, and cracking [10].

Fortunately, some of these issues are the result of reversible thermal effects and can be mediated by post-weld heat treatment. The quality of the weld bead profile is a common controllable issue and is caused by three main factors: layer thickness deviation, undercutting, and unsymmetrical weld beads [11-12]. WAAM welding residual stresses can result in distortions and/or cracking in the finished work piece.

During the AM deposition process, the sequentially deposited metal layers are repeatedly heated from the heat of other successively deposited bead layers. This introduces a complex thermal cycle for each layer [13]. Since WAAM is a high heat input process, the heat affected zone can be large and may lead to undesirable metallurgical changes that can contribute to localized cracking. If the thermal gradients are large enough, and the workpiece is highly constrained, the residual stresses can be quite high. Generally, the internal stresses are relieved to some degree when the work piece is unclamped, but this can result in undesirable warpage. Finally, it has been observed that the largest residual stress component is usually coincident with the direction of the deposition path [12].

As shown in Fig. 2, even a relatively simple build of a rectangular plate using WAAM can develop slight dimensional deviations that can propagate upwards through the build layers. Thus, minor defects in the build process tend to be amplified during the deposition of subsequent layers [6]. In addition, it has been observed that the last few layers in the AM deposition process exhibit higher hardness, because these layers experience fewer reheating cycles [14].

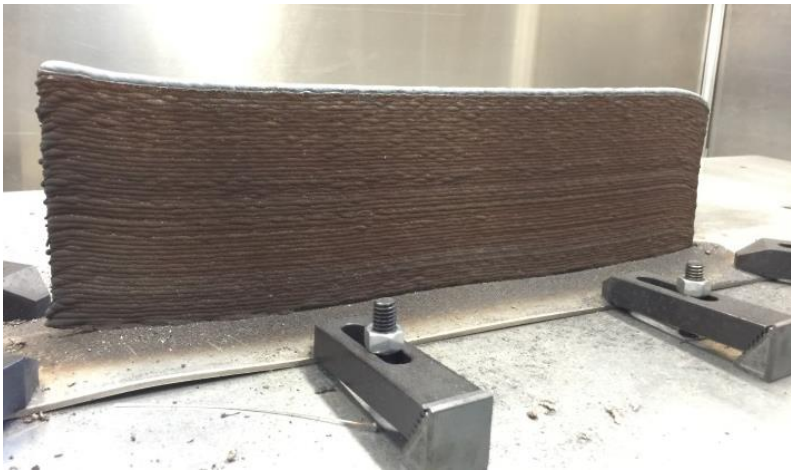


**Fig. 2** WAAM build of a rectangular plate, in the clamped configuration, depicting the layer-by-layer macroscopic structure formation. Note the local lifting in the base plate, due to residual stresses. Lehigh University's Additive Manufacturing Life Analysis Lab. Courtesy of Dr. C. Haden

Various techniques have been explored to improve and control the build geometry, the residual stresses and metallurgical properties during WAAM processing. Some of the techniques that have been investigated for improving WAAM residual stresses and minimizing welding distortion include: preheating the substrate prior to deposition, selective secondary heating, spatial and temporal optimization of the weld path, and high-pressure rolling [14-22]. Because of the large number of controllable welding parameters, it is not particularly effective to rely solely on an experimental approach to optimize the quality of WAAM builds. It is recognized that computational simulations can greatly assist in the development of improved build processes based on well-established welding physics.

Because of the highly nonlinear thermomechanical behavior associated with welding deposition processes, FEA (finite element analysis) codes are the preferred computational tools for simulating transient heat transfer and residual stress evolution during welding. For welding process simulations, most general purpose, commercially available, software packages are usually adequate, but may be cumbersome to use for modeling specific welding processes. In this study, the authors used ESI's specialized FEA welding simulation software, SYSWELD [23], which provides built in tools that greatly simplify the input of welding process parameters that can be adequately characterized using a predefined moving heat source [24-26]. SYSWELD can also be used to obtain the phase proportions, hardness, distortions, residual stresses, and plastic strains distributions associated with post-weld heat treatment [27]. In order to systematically understand and improve WAAM process, it is desirable to accurately simulate multipass welding in detail using a variety of weld deposition paths and welding parameters. However, it's unlikely that a brute force modeling/simulation approach will be very effective for modeling complex AM builds, since the computational requirements needed to sequentially model the deposition of every single build layer in a complex build is well beyond current computational capabilities. Currently, it is feasible to perform computational simulations of multipass welding for a few hundred weld passes. However, the information obtained from "local" detail models can ultimately be used to develop more efficient global simulation models, where the local models form the basis, or building blocks, for global models that incorporate local temperatures, stresses and strains into the global model.

## MODELLING DETAILS

The problem of interest in this study is the layer-by-layer WAAM build of a flat metal plate, as shown in Figs. 2 and 3. A number of these plates were fabricated at Lehigh University in a separate study to measure fatigue crack growth rates in stainless steel WAAM specimens cut from the plates shown [28]. During the fabrication of these plate specimens, it was noted that the residual stresses that were introduced during the build process were of sufficient magnitude to noticeably bend the 5 mm thick base plate, as shown in Fig. 3, upon release of the clamping fixtures.



**Fig. 3** WAAM fabricated 304 stainless steel plate. Note the bending of the solid base plate after release from the clamping fixtures. Lehigh University’s Additive Manufacturing Life Analysis Lab [28]

The computational simulations presented in this paper examine the differences in the evolution of the residual stress, displacements, hardness, and phase changes for two specific alloys: 1) 316L austenitic stainless steel, and 2) S355J2G3 low-carbon steel. The reason these specific steel alloys were selected, is because they exhibit markedly different phase change behaviors and their temperature dependent material properties have been accurately characterized and incorporated into the SYSWELD material property database. It is believed that these two steel alloys effectively demonstrate the fundamental difference in residual stress evolution between two broad classes of carbon steels and austenitic stainless steels of interest for many WAAM applications. Table 1 provides the chemical composition of the two alloys.

**Table 1** Chemical composition of the steel alloys used in WAAM simulations

Element %	C	Cr	Mn	Mo	Ni	P	S	Si
AISI 316L	0.03	17	2	2.5	12	0.045	0.03	0.75
S355J2G3	0.18	-	1.6	-	-	0.035	0.035	0.55

The melting points are 1400°C for 316L, and 1500°C for S355J2G3. Fig. 4 depicts the Young’s modulus for these alloys as a function of temperature.

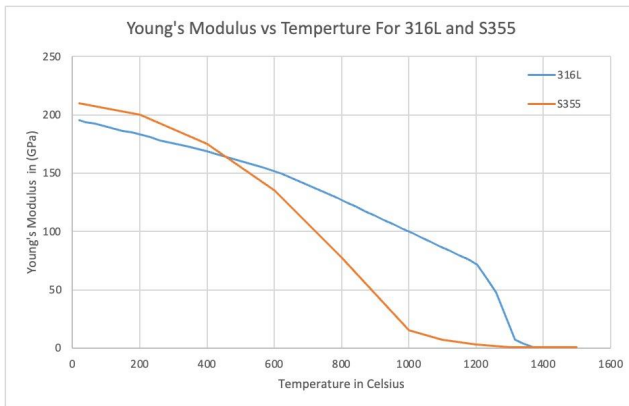


**Fig. 4** Young’s Modulus vs Temperature For 316L and S355

The other critical mechanical property that has a strong influence on the residual stress state is the temperature dependent yield strength depicted in Fig. 5. This figure shows the yield strength for 316L in one phase and for all six phases of the low-carbon steel S355J2G3. As can be seen in the figure, there is little difference between the nominal yield strengths above 800°C, while above 1300°C, the yield strengths (and stiffness) for both alloys are essentially zero for all material phases. Therefore, above 1300°C, any inaccuracies in the local moving heat source model will have little influence on the stress state. However, as post-weld cooling occurs, it is expected that there will be significant differences in the residual stresses between these two alloys as a function of temperature.

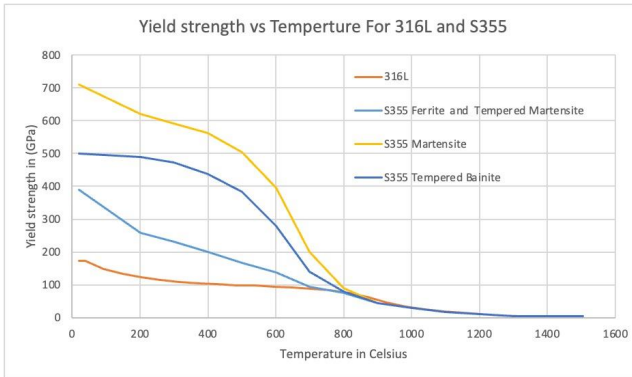


**Fig. 5** Yield strength vs Temperature for 316L and S355J2G3

Table 2 gives the basic welding parameters used to compare AM builds for both of the steel alloys described above. Since the thermomechanical properties are different for these alloys, 316 L required a power input of 1015 W to form a satisfactory weld pool size, and 1265 W was used for the low-carbon steel S355J2G3 in order to obtain equivalent weld pool dimensions.

**Table 2** WAAM simulation processes parameters in SYSWELD

WAAM parameters	316L	S355J2G3
Input power (Watts)	1015	1265
Substrate and Wire Material	Stainless-steel 316L	Low carbon steel S355J2G3
Welding speed (mm/s)		2.5
Number of layers		38
Layer length (mm)		700
Layer Height (mm)		2.4
Layer Thickness (mm)		8
Substrate Dimension (mm)		5 X 100 X 855

The simulated WAAM builds were patterned after the process variables and dimensions used in [28], to fabricate the plate shown in Fig. 3. A standard double

ellipsoid moving heat source was used to model the arc welding process. The path of the metal deposition was a unidirectional path, where the individual deposition sequences started at the leftmost end of the plate and ended at the rightmost end for each build layer. With the welding speed set at 2.5 mm per second, each layer took 280 seconds to complete. There was no time delay between the completion of one build layer and the start of the next.

Since the welding simulations in this study did not attempt to model the fluid mechanics, electromagnetic, and surface tension effects in the weld pool, it was necessary to “define” a priori the shape and dimensions of the weld pool and deposited metal geometry based on experimental measurements. For this study, cut sections were taken from samples generated in [28] to determine the shape of the individual weld bead layers. Printed plates were vertically cross-sectioned, ground, polished, and etched to clearly visualize the borders between each individual printed layer. Fig. 6 shows the actual printed cross section and the representative finite element mesh used in the numerical simulations. It is believed that the simplified cross-sectional geometry used for the numerical simulations, reasonably represents the printed cross section geometry in some average sense.

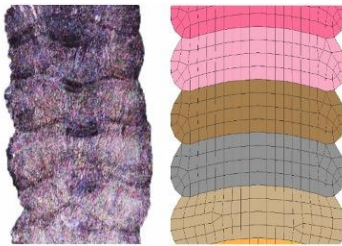


**Fig. 6** Comparison between the experimentally generated layer cross-sections (left) and the finite element mesh used for the numerical models (right)

The  $\frac{1}{2}$  symmetry model shown in Fig. 7, was used to reduce computation times and to clearly visualize differences between the internal temperatures and stresses on the symmetry plane and the external surface. During the welding simulations, clamped boundary conditions, which prevented vertical ( $z$ ) displacements, were specified on the corners and the mid-side of the substrate. The clamped areas are shown as red rectangular regions on the substrate surface in Fig. 7. After the workpiece cooled, the clamped boundary conditions were removed to obtain the final residual stresses and displaced configuration.

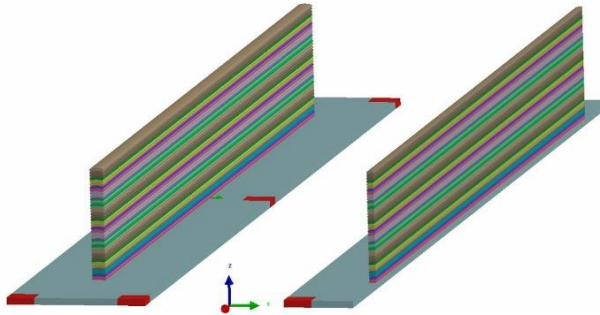


**Fig. 7** Full 3-D model (left), symmetry model (right)

## SIMULATION RESULTS

### HEAT TRANSFER AND TEMPERATURES

In multipass welding, where layers of hot metal are deposited on top of previously deposited cooler metal, the dominant heat transfer mechanism is conduction through the metal layers. Some heat is lost through surface convection and radiant heat transfer, but these losses are relatively small during the actual welding process. In the development of the WAAM models, care was taken to ensure that temperatures in each newly deposited layer attained the designated melt temperature. Typically, 3 nodes in a newly deposited layer (shown in Fig. 8) were monitored during the welding simulations to ensure that melt temperatures were achieved in each deposited layer. The moving arc weld heat source was also defined in such a manner that sufficiently high temperatures were reached on the boundaries between adjacent layers to allow for interlayer fusion. This meant that the defined heat source's ellipsoidal boundary had to penetrate to a sufficient depth into a previously deposited layer.

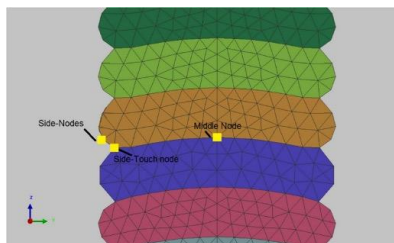


**Fig. 8** Locations where temperatures were monitored to ensure bulk melting in each new layer

Fig. 9 shows the temperature history profiles, during the deposition of each layer at the nodes depicted in Fig. 8, for selected layers in the 316L stainless steel model. In general, the temperature history profile for each new layer is very similar to the temperatures observed in previous layers. As the build progresses, and subsequent layers are deposited, a new, lower temperature peak is observed in each of the previously deposited layers due to conduction effects. As the moving heat source increments upwards following the deposition of each new layer, the temperature peak gets smaller and smaller in the lower, previously deposited layers. In Fig. 9 it can be seen that for each layer, the melting point temperature of 1400°C is exceeded twice at the center node on the lower weld interfaces. This is because it is the closet node to the moving heat source when the next layer is deposited. It's interesting to note that evidence of this secondary melting effect can be seen by the small dark regions depicted in the weld bead cross-sections shown in the left image in Fig. 6. Similar temperature history profiles are obtained for the low-carbon steel material model, S355J2G3, shown in Fig. 10. Because of the higher power input and higher melting point for the low-carbon steel, the temperatures at the monitored nodes initially exceed 1500° during the layer's deposition. But otherwise, the heat transfer behavior, i.e., repeated rapid heating and cooling is identical to the 316L behavior.

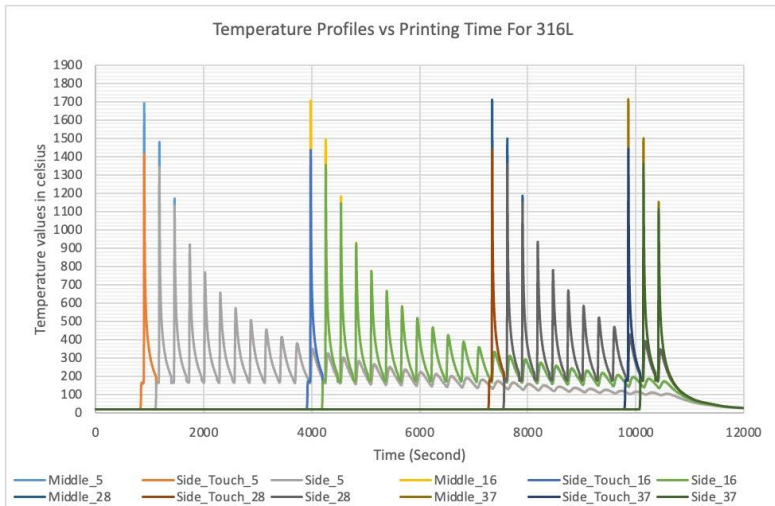


**Fig. 9** Temperature history at specific points shown in Fig. 8 for layers 5, 16, 28, and 37 for 316L stainless steel

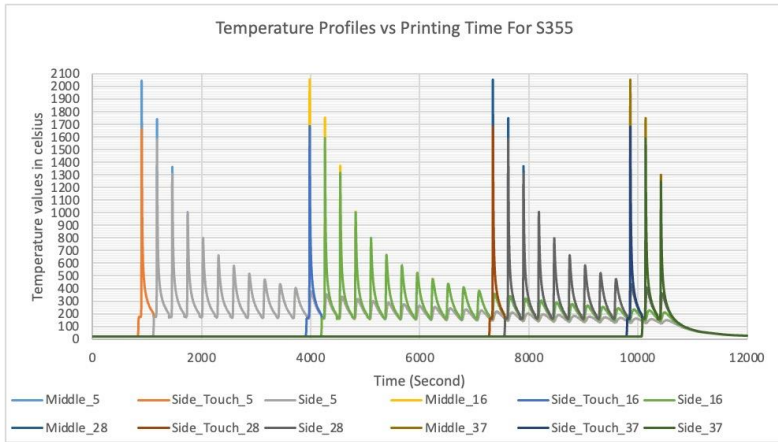


**Fig. 10** Temperature history at specific points shown in Fig. 8 for layers 5, 16, 28, and 37 for S355J2G3 low-carbon steel

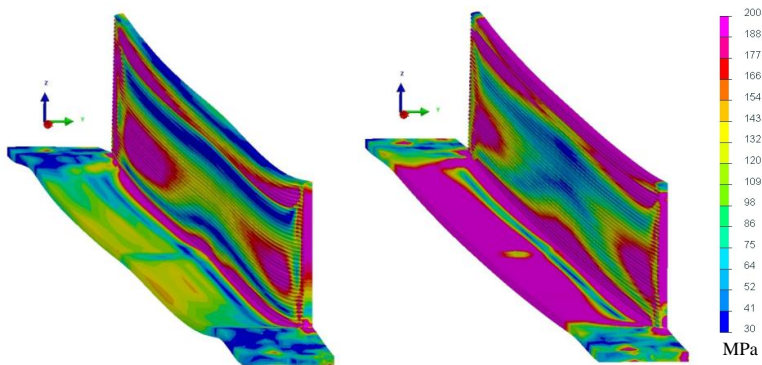
### RESIDUAL STRESSES

The stresses computed during welding simulations rely on the transient temperature histories to calculate the thermal stresses, plastic strains and phase changes. Within any given deposited layer, the stresses become negligible close to the alloy’s melt temperature and then begin to increase in magnitude during cooling, resulting in the final residual stress state. Since stress equilibrium must be maintained, regions of high tension are typically balanced with adjacent compressive zones. The longitudinal residual stress, i.e., the stress component coaxial with the direction of weld metal deposition, will be designated as ( $\sigma_{xx}$ ), the maximum principal stress ( $\sigma_1$ ), and the von Mises stress ( $\sigma_v$ ). A quick comparison of the maximum and minimum residual stress magnitudes obtained from 316L builds and low-carbon steel S355J2G3 builds is given in Table 3. These maximum stresses provide some sense of the residual stress magnitudes involved in a WAAM build of a flat plate, but also include local stress concentration effects at reentrant corners. The low-carbon steel has considerably higher magnitude residual stresses. It is interesting to compare the von Mises stress values in the table with the uniaxial room temperature yield stress given in Fig. 5. Not only have both of these alloys yielded in the most highly stressed regions, but also significant strain hardening has occurred to attain some of the high von Mises stress levels given in Table 3.

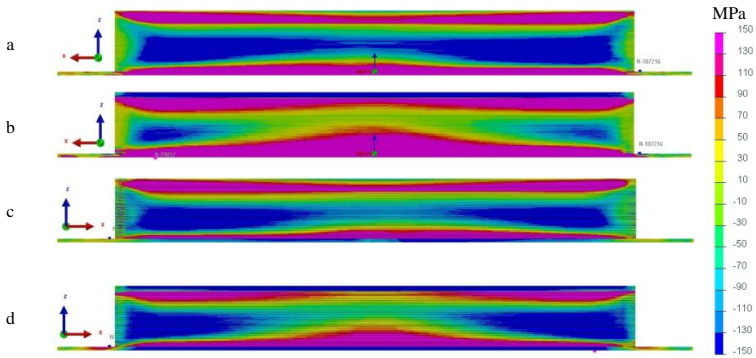
**Table 3** maximum residual stresses for both material models in terms of  $\sigma_{xx}$ ,  $\sigma_1$ ,  $\sigma_v$ .

Material	Residual stress	Maximum (MPa)	Minimum (MPa)	Range
316L	$\sigma_{xx}$	361	-291	652
	$\sigma_1$	463	-83	551
	$\sigma_v$	389	1.3	387.3
S355J2G3	$\sigma_{xx}$	593	-545	1138
	$\sigma_1$	593	-208	801
	$\sigma_v$	591	1.6	589.4

Fig. 11 contains contour plots of the von Mises residual stresses for both 316L and S355J2G3, using the same reference scale. These 1/2 symmetry images show the von Mises stresses viewed from the direction of the outermost, air exposed, surface of the plate, in the deformed configuration (exaggerated), after release of the clamp restraints. Though the residual stress magnitudes are different, there are great similarities in the stress contours. It is also recognized that the residual stresses in the base plates are considerably larger for the S355J2G3 material model. It is also noted that close to the top surface of the vertical plate there are significant differences in the residual stress state in the last few layers in comparison with layers lower down in the build. Fig. 12 a, b shows the  $\sigma_{xx}$  residual stress contours for 316L and S355, on the internal symmetry planes in the respective AM plates after removal of the clamp restraints. In contrast, Fig. 12 c, d shows the longitudinal stress component from a point of view looking at the opposite surface, i.e., the outermost air exposed surface of the plate. The stress contour plots in Fig. 12 very clearly show the fundamental nature of the residual stress state in the central portion of the WAAM built plates, with high tension along the base, compression in the plate interior mid-level, and then tension close to the top surface. Interestingly, both materials exhibit compressive longitudinal stresses on the topmost surface of the plate.

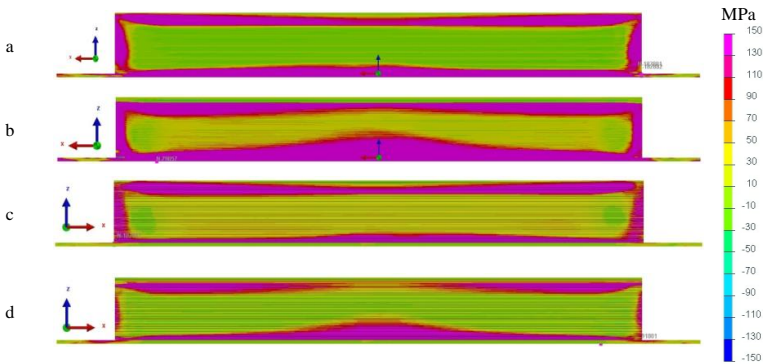


**Fig.11** Von Mises residual stress  $\sigma_v$  contour plots: a) 316L stainless steel, b) S355J2G3 low-carbon steel



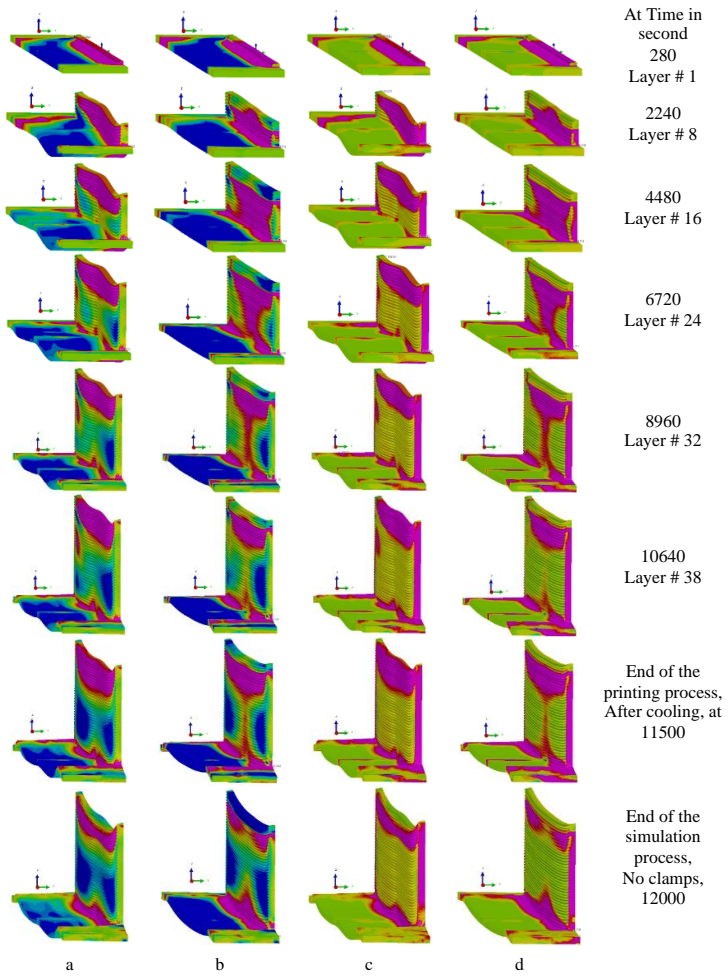
**Fig. 12** Longitudinal residual stress  $\sigma_{xx}$ : a) 316L internal symmetry cross section, b) S355 internal symmetry cross section, c) 316L external surface face, d) S355 external surface face

Fig. 13 shows the maximum principal stress contours,  $\sigma_1$ , after unclamping, from the same perspectives used in Fig. 12. The close relationship between the maximum principal stresses and the longitudinal stresses in the central portion of the plates, indicates that the longitudinal stress,  $\sigma_{xx}$ , is the dominant residual stress component in the interior of the plate. Close to the ends of the plate, where  $\sigma_{xx}$  must be zero, the vertical,  $\sigma_{zz}$ , stress component becomes the dominant residual stress, thus forming the “picture frame” residual stress field depicted by the maximum principal stress contours shown in Fig. 13.



**Fig. 13** Maximum principle residual stress  $\sigma_1$ : a) 316L internal symmetry cross section, b) S355 internal symmetry cross section, c) 316L external surface face, d) S355 external surface face

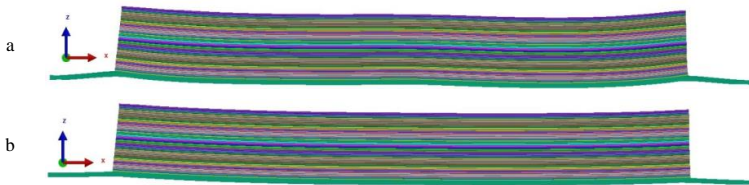
Figs. 11, 12, and 13 depict the final residual stress state after a complex sequence of processing events, where thin hot metal layers are deposited in conjunction with a moving arc weld heat source. Heat transfer effects and clamping restraints play an important role in the evolution of the residual stresses, which after final cooling are obtained following elastic release of the clamping boundary conditions. To better understand how the final residual stresses are obtained, it is instructive to follow the stress evolution as a function of time. Fig. 14 depicts the evolution of the longitudinal stresses,  $\sigma_{xx}$ , and the maximum principal stresses,  $\sigma_1$ , as a function of time during WAAM deposition, workpiece cooling, and final release of clamping restraints. The sequence of images in Fig. 14 show stress contour plots on the exaggerated deformed configuration at times: 280, 2240, 4480, 6720, 8960, 10640, 11500, and 12000 seconds. The first six time intervals correspond to the completion of the deposition of layers 1, 8, 16, 24, 32, and 38. Cooling then starts at 10,640 s, and continues after release of the clamps after 11,500 s. After a small amount of additional cooling (Figs. 9-10), the final residual stresses are shown at 12,000 s. The side-by-side images in Fig. 14 show snapshots of the  $\sigma_{xx}$  and  $\sigma_1$  stresses for both steel alloy models. One observation is that as the number of printed layers increases, the size of the tensile residual stress zone  $\sigma_{xx}$  (Fig. 14 *a, b*), associated with the layers of the most recently deposited metal, moves upwards and maintains an essentially constant vertical dimension. The zone of longitudinal tension is “balanced” by a wide vertical zone of longitudinal compression that continuously increases as the build height increases and the bulk of the metal in the central core region of the plate cools. Thus, in a simplified sense, the residual stress state progresses as a finite width “tension zone” that moves upwards following the vertical motion of the moving heat source as the metal cools. The bulk of the metal in the cooler midsection of the plate is subjected to compressive  $\sigma_{xx}$  stresses, which continuously increases in extent as the AM build continues to cool. Another interesting observation from Fig. 14, is that there always is a difference in the local residual stress state in the last few uppermost layers of deposited metal between 316L and S355J2G3. It is believed that these differences are directly related to the volumetric strains associated with the phase transformations that occur during rapid cooling in the low-carbon steel alloy, S355J2G3.



**Fig. 14** Residual stress evolution as a function of time: a)  $\sigma_{xx}$  316L, b)  $\sigma_{xx}$  S355, c)  $\sigma_1$  316L, d)  $\sigma_1$  S355

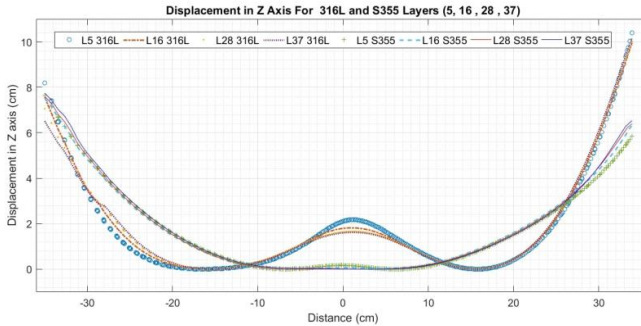
WARPAGE AND DEFORMATION

Fig. 15 shows the vertical displacement ( $z$ -direction), for both material models. In general, during a single weld pass, a newly deposited metal layer tends to contract in the longitudinal direction as it cools, resulting in upwards bending of the substrate plate. This overall behavior is exhibited by both material models depicted in Fig. 15 and is consistent with the observed bending deformation shown in the baseplate in the photograph in Fig. 3. The clamping boundary conditions, thickness of the substrate and localized plastic deformation can also affect the final amount of vertical displacement. For example, an increase in thickness of the base substrate will decrease the displacements, but will also increase the magnitude of the  $\sigma_{xx}$  residual stresses.



**Fig. 15** Deformed (warped) configuration after release from clamp restraints: a) 316L b) S355

Fig. 16 shows the final  $z$ -displacements, after clamping has been released, for selected layers (5, 16, 28, and 37) as viewed from the vertical symmetry plane. It is immediately noticeable that the 316L material model results in upwards displacements both at the extreme ends of the deposited layers and also on the vertical center line. In contrast, the S355J2G3 material model gives smoothly increasing displacements from the plate's center line out to the edges of the printed plate. The differences in post-weld warping appears to be due to the lower yield stress in 316L and localized plastic deformation that occurs in the base plate while the plate is tightly clamped during the WAAM process. In the 316L model, the greatest  $z$ -displacement occurs at the starting point of deposition (righthand side of plot in Fig. 16) with a value of 10.39 mm for layer 5. At the symmetry line, the  $z$ -displacement is 2.2 mm for this layer, and the  $z$ -displacement at the end of the line build is 8.2 mm. As can be seen, the  $z$ -displacements in succeeding layers were essentially identical. For the S355J2G3 low-carbon steel material model, the greatest  $z$ -displacement value was smaller, 7.73 mm, occurring at the end of the deposition path (lefthand side of Fig. 16), while at the start position on the righthand side of Fig. 16, a  $z$ -displacement of 6.53 mm was calculated. The displacement difference between the two ends in each layer were almost 2.2 mm for the 316L build and 1.2 mm for the S355J2G3 material model.



**Fig. 16** Comparison of vertical (z-displacements) for 4 discrete layers (5, 16, 28, 37) for 316L and S355

#### PHASE TRANSFORMATIONS

The primary reason why S355J2G3 low-carbon steel was chosen for direct WAAM comparisons with the austenitic stainless steel, 316L, was to examine the role that phase transformations play in the development of the final residual stresses and material properties. In contrast to austenitic stainless steels, it is well known that low-carbon steels exhibit a variety of phase transformations during heating and cooling. In the SYSWELD simulations, continuous cooling transformation (CCT) diagrams are used to estimate the phase transformation percentages during the rapid cooling associated with welding. Fig. 17 shows the final SYSWELD predicted phase percentages, in the interior of the plate, i.e., on the large vertical plane of symmetry. As shown in this figure, the bulk of the S355J2G3 printed plate is ferrite (Fig. 17a), which is not surprising, since the bulk of the metal is subjected to repeated heating cycles over an extended period of time. A small percentage of martensite is obtained in the final build layers on the top of the plate (Fig. 17 b). The last four layers of the build also contain a significant percentage of tempered bainite (Fig. 17c), these layers are exposed to low cycle heating for shorter periods of time. As shown in Fig. 17d, a low percentage (~15%) of tempered martensite is also predicted near the end regions of the printed plate. This is due to the different heat transfer conditions and cooling rates that occur near the edges of the plate as compared with the central bulk of the plate.

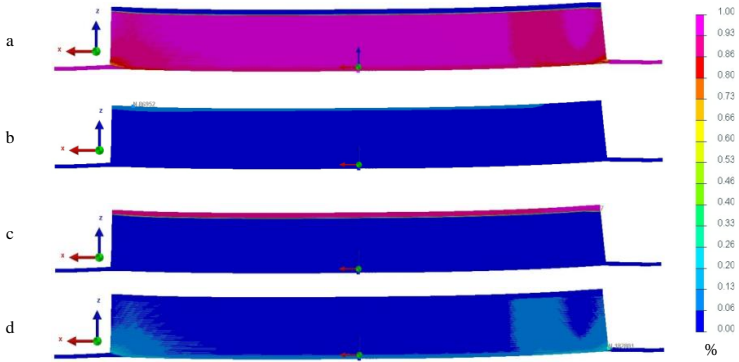


**Fig. 17** Post-processing phase percentages and distributions for S355J2G3: a) Ferrite, b) Martensite, c) Tempered Bainite, d) Tempered Martensite

#### HARDNESS VARIATIONS

Fig. 18 a, b shows the computed hardness results that were obtained from both material models. For the 316L model, it can be seen that for the bulk of the plate, the hardness values are between 150 to 370 (MPa), while in the S355J2G3 printed plate, the predicted range of hardness values is between 370 to 540 (MPa). The last four deposited layers in the S355J2G3 material model predict high hardness values close to the top surface of the plate. This occurs because of the tempered bainite phase transformation as shown in Fig. 17c.

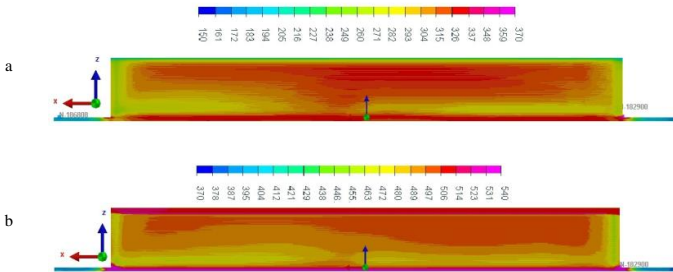


**Fig. 18** Predicted hardness variations for: a) 316L b) S355J2G3

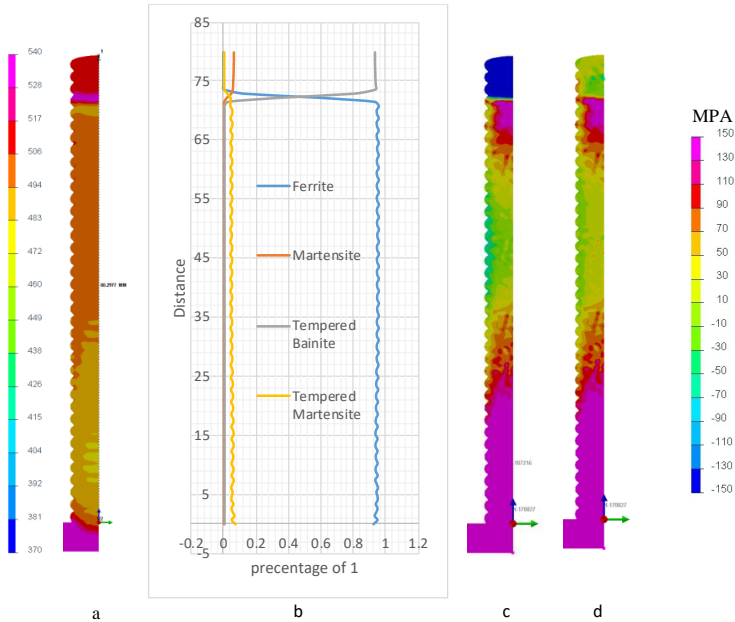


**Figure 19** Comparisons in the cross-section plane of the  $\frac{1}{2}$ -symmetry model for S355J2G3: a) hardness (MPa), b) microstructural phase percentages, c)  $\sigma_{xx}$  stress component, and d)  $\sigma_1$  maximum principal stress

Fig. 19 (a, b) shows the relationship between the predicted hardness values and the corresponding phase transformation percentages in the  $\frac{1}{2}$  symmetry cross-section that is perpendicular to the direction of material deposition in the WAAM S355J2G3 low-carbon steel printed plate. In Fig 19a it can be clearly seen how the hardness varies from the bottom to the top of the printed plate and also varies through the thickness of the plate. For example, in the central portion of the plate, the hardness on the exterior surface is higher than on the interior plane of symmetry. The hardness differences through the plate thickness can be attributed to the through thickness thermal gradient, which is directly related to the convective cooling conditions on the plate surface. In Fig. 19 (c, d) are the corresponding contour plots for the residual stress components  $\sigma_{xx}$ , and the maximum principal stress  $\sigma_1$ , on the same  $\frac{1}{2}$  symmetry cross-section for the S355J2G3 plate. The hardness distribution corresponds to the ratios of the different microstructural phases and the phase transformation percentages, e.g., regions with high percentages of ferrite have relatively low hardness, while regions of the printed plate with high percentages of tempered bainite, have the highest hardness values.

The phase transformations, which introduce differential volumetric strains, also affect the local residual stresses. For example, the  $\sigma_{xx}$  stress component throughout most of the printed plate varies smoothly from tension to relatively low compression. However, where the tempered bainite phase transformation has occurred, e.g., near the top of the

plate, there is a sudden jump to the highly compressive residual stress shown in Fig. 19c. Because of the transformation from ferrite to tempered bainite, the microstructural hardness also attains its highest value at this same location. For the 316L material model, there are no phase transformations, and the entire printed plate is austenite. Thus, the residual stresses for 316L are determined solely by the temperature dependent thermomechanical properties of the alloy and generally result in residual stresses that can be evaluated as thermal stresses.

### CONCLUSIONS

Two material models were used to simulate the WAAM deposition process using the commercially available finite element software, SYSWELD. The WAAM simulation models were based on two very different types of steel alloys: austenitic stainless steel grade 316L and low-carbon steel S355J2G3. Using a simple, thin plate geometry as an example WAAM printed structure, it was shown that there are a great number of similarities during the evolution of residual stresses and distortion for both of these alloys. For example, even though the heat transfer and metal deposition details are quite complex during WAAM processing, it appears that the resulting residual stress state can be adequately characterized in terms of the maximum principal stresses, in the form of a moving rectangular region of relatively low compression, completely encircled by a rectangular “frame” of high tensile residual stress, as depicted graphically in Fig. 13.

As expected, the S355J2G3 low-carbon steel material model resulted in significantly higher residual stress magnitudes than the austenitic stainless steel 316L. However, WAAM simulations for the 316L showed greater welding distortions. This is perhaps not too surprising, since stainless steels generally have relatively high coefficients of thermal expansion and low thermal diffusivity when compared with low-carbon steels. Actual residual stresses and distortions associated with WAAM processing also depend on a relatively large number of controllable parameters, e.g., deposition velocity, heat source energy density, preheating, clamping restraints, deposition path, etc. In this study it has been demonstrated that it is possible to realistically simulate many important physical aspects of the WAAM deposition process using conventional arc welding numerical models. What is not clear is how to best develop numerical simulations for far more complex WAAM geometric builds that might involve many orders of magnitude more weld passes. It is likely that the most effective modeling approach for evaluating much larger WAAM builds in the future will be based on the results obtained from detailed thermomechanical submodels of the sort explored in this study to create much larger global models that do not explicitly model the details associated with every individual weld pass.

### References

- [1] O. YILMAZ, A.A. UGLA: ‘Development of a cold wire-feed additive layer manufacturing system using shaped metal deposition method’, *J. Mech. Sci. Technol.*, 31, pp. 1611-1620, 2017, doi:10.1007/s12206-017-0308-9.

- [2] F. MONTEVECCHI, G. VENTURINI, A. SCIPPA, G. CAMPATELLI: 'Finite Element Modelling of Wire-arc-additive-manufacturing Process', *Procedia CIRP*, 55, pp. 109-114, 2016, doi:10.1016/j.procir.2016.08.024.
- [3] VENTURINI, F. MONTEVECCHI, A. SCIPPA, G. CAMPATELLI: 'Optimization of WAAM Deposition Patterns for T-crossing Features', *Procedia CIRP*, 55, 95-100, 2016, doi:10.1016/j.procir.2016.08.043.
- [4] D. DING, Z. PAN, D. CUIURI, H. LI: 'Wire-feed additive manufacturing of metal components: technologies, developments and future interests', *Int. J. Adv. Manuf. Technol*, 81, pp. 465-481, 2015. doi:10.1007/s00170-015-7077-3.
- [5] C. SHEN, Z. PAN, D. CUIURI, J. ROBERTS, H. LI: 'Fabrication of Fe-FeAl Functionally Graded Material Using the Wire-Arc Additive Manufacturing Process', *Metall. Mater. Trans. B*, 47, pp. 763-772, 2016, doi:10.1007/s11663-015-0509-5.
- [6] D. DING, Z. PAN, C. DOMINIC, H. LI: 'Process Planning Strategy for Wire and Arc Additive Manufacturing', in *Robotic Welding, Intelligence and Automation, RWIA 2014, Advances in Intelligent Systems and Computing*, Vol. 363, Springer, Cham., pp. 437-450, 2015, doi.org/10.1007/978-3-319-18997-0\_37.
- [7] J. RUAN, T.E. SPARKS, Z. FAN, J.K. STROBLE, A. PANACKAL: 'A Review of Layer Based Manufacturing Processes for Metals', *Proceedings of the 17th Annual Solid Freeform Fabrication Symposium (2006, Austin, TX)*, pp. 233-245, 2006, doi.org/10.26153/tsw/7133.
- [8] Z. PAN, D. DING, B. WU, D. CUIURI: 'Arc Welding Processes for Additive Manufacturing: A Review', *Transactions on intelligent welding manufacturing*, pp. 3-24, 2018, doi:10.1007/978-981-10-5355-9.
- [9] H. GENG, J. XIONG, D. HUANG, X. LIN, J. LI: 'A prediction model of layer geometrical size in wire and arc additive manufacture using response surface methodology', *Int. J. Adv. Manuf. Technol*, 93, pp. 175-186, 2017, doi:10.1007/s00170-015-8147-2.
- [10] B.A. SZOST, S. TERZI, F. MARTINA, D. BOISSELIER, A. PRYTULIAK, T. PIRLING, M. HOFMANN, D.J. JARVIS: 'A comparative study of additive manufacturing techniques: Residual stress and microstructural analysis of CLAD and WAAM printed Ti-6Al-4V components', *Mater. Des*, 89, pp. 559-567, 2016, doi:10.1016/j.matdes.2015.09.115.
- [11] A. BUSACHI, J. ERKOYUNCU, P. COLEGROVE, F. MARTINA, J. DING: 'Designing a WAAM based manufacturing system for defence applications', *Procedia CIRP*, 37, pp. 48-53, 2015, doi:10.1016/j.procir.2015.08.085.
- [12] S.W. WILLIAMS, F. MARTINA, A.C. ADDISON, J. DING, G. PARDAL, P. COLEGROVE: 'Wire + Arc Additive Manufacturing', *Mater. Sci. Technol*, 32, pp. 641-647, 2016, doi:10.1179/1743284715Y.0000000073.
- [13] J.Y. BAI, C.L. YANG, S.B. LIN, B.L. DONG, C.L. FAN: 'Mechanical properties of 2219-Al components produced by additive manufacturing with TIG', *Int. J. Adv. Manuf. Technol*, 86, pp. 479-485, 2016, doi:10.1007/s00170-015-8168-x.
- [14] S. SURYAKUMAR, K.P. KARUNAKARAN, U. CHANDRASEKHAR, M.A. SOMASHEKARA: 'A study of the mechanical properties of objects built through weld-deposition', *Proc. Inst. Mech. Eng., Part B: J. Eng. Manuf.*, 227(8), pp. 1138-1147, 2013, doi:10.1177/0954405413482122.
- [15] C. V. HADEN, G. ZENG, F.M. CARTER, C. RUHL, B.A. KRICK, D.G. HARLOW: 'Wire and arc additive manufactured steel: Tensile and wear properties', *Addit. Manuf.*, 16, pp. 115-123, 2017, doi:10.1016/j.addma.2017.05.010.
- [16] N.W. KLINGBEIL, J.L. BEUTH, R.K. CHIN, C.H. AMON: 'Residual stress-induced warping in direct metal solid freeform fabrication', *Int. J. Mech. Sci.*, 44, pp. 57-77, 2002, doi:10.1016/S0020-7403(01)00084-4.
- [17] E.R. DENLINGER, J.C. HEIGEL, P. MICHALERIS, T.A. PALMER: 'Effect of inter-layer dwell time on distortion and residual stress in additive manufacturing of titanium and nickel alloys', *J. Mater. Process. Technol.*, 215, pp. 123-131, 2015, doi:10.1016/j.jmatprotec.2014.07.030.

- [18] X. BAI, H. ZHANG, G. WANG: 'Modeling of the moving induction heating used as secondary heat source in weld-based additive manufacturing', *Int. J. Adv. Manuf. Technol.*, 77 pp. 717-727, 2015, doi:10.1007/s00170-014-6475-2.
- [19] P.A. COLEGROVE, H.E. COULES, J. FAIRMAN, F. MARTINA, T. KASHOUB, H. MAMASH, L.D. COZZOLINO: 'Microstructure and residual stress improvement in wire and arc additively manufactured parts through high-pressure rolling', *J. Mater. Process. Technol.*, 213, pp. 1782-1791, 2013, doi:10.1016/j.jmatprotec.2013.04.012.
- [20] A.H. NICKEL, D.M. BARNETT, F.B. PRINZ: 'Thermal stresses and deposition patterns in layered manufacturing', *Mater. Sci. Eng. A.*, 317, pp. 59-64, 2001, doi:10.1016/S0921-5093(01)01179-0.
- [21] H. ZHAO, G. ZHANG, Z. YIN, L. WU: 'A 3D dynamic analysis of thermal behavior during single-pass multi-layer weld-based rapid prototyping', *J. Mater. Process. Technol.*, 211(3), pp. 488-495, 2011, doi:10.1016/j.jmatprotec.2010.11.002.
- [22] H. ZHAO, G. ZHANG, Z. YIN, L. WU: 'Three-dimensional finite element analysis of thermal stress in single-pass multi-layer weld-based rapid prototyping', *J. Mater. Process. Technol.*, 212, pp. 276-285, 2012, doi:10.1016/j.jmatprotec.2011.09.012.
- [23] SYSWELD 2021.0 – Documentation Package, ESI North America, Farmington Hills, MI.
- [24] W. WORLD, L.E. SOUDAGE, D. LE, T. GUWAHATI, T. BOMBAY: 'Efficient estimation of volumetric heat source in fusion welding process simulation', in *Fusion Welding Process Simulation*, 56, pp. 88-97, 2013, doi:10.1007/BF03321399.
- [25] M.P. MUGHAL, H. FAWAD, R.A. MUFTI: 'Three-dimensional finite-element modelling of deformation in weld-based rapid prototyping', *Proc. Inst. Mech. Eng., Part C: J. Mech. Eng. Sci.*, 220(6), pp. 875-885, 2006, doi:10.1243/09544062JMES164.
- [26] DING, P. COLEGROVE, J. MEHNEN, S. GANGULY, P.M.S. ALMEIDA, F. WANG, S. WILLIAMS: 'Thermo-mechanical analysis of Wire and Arc Additive Layer Manufacturing process on large multi-layer parts', *Comput. Mater. Sci.*, 50, pp. 3315-3322, 2011, doi:10.1016/j.commatsci.2011.06.023.
- [27] T. KIK, M. SLOVACEK, J. MORAVEC, M. VANEK: 'Numerical Simulations of Heat Treatment Processes', *Appl. Mech. Mater, Trans Tech Publications*, Vol. 809-810, pp. 799-804, 2015, doi:10.4028/www.scientific.net/AMM.809-810.799.
- [28] J.V. GORDON, C.V. HADEN, H.F. NIED, R.P. VINCI, D.G. HARLOW: 'Fatigue crack growth anisotropy, texture and residual stress in austenitic steel made by wire and arc additive manufacturing', *Mater. Sci. Eng. A.*, 724, pp. 431-438, 2018, doi:10.1016/j.msea.2018.03.075.



# NUMERICAL ANALYSIS OF WELDING PROCESS FOR DISTORTION PREDICTION OF PIPE STRUCTURES FOR AEROSPACE INDUSTRY

S. RASCHE\*, M. FISCHER\*\*, J. HILDEBRAND\*,  
J. P. BERGMANN\*

*\*Technische Universität Ilmenau, 98693 Ilmenau, Germany*

*\*\*PFW Aerospace GmbH, 67346 Speyer, Germany*

*DOI 10.3217/978-3-85125-968-1-16*

## ABSTRACT

The preferred joining process for lightweight titanium alloyed pipe structures used in aerospace industry is Tungsten Inert Gas welding. The further development and automation of the currently time-consuming and cost-intensive manual production of titanium bleed-air tubes is addressed in the collaborative research project ASciE. The Production Technology Group at Technische Universität Ilmenau works together with PFW Aerospace GmbH to develop finite element simulation models for the distortion prediction of thin-walled welded pipe structures. In this project the influence of varying welding process parameters and heat source models as well as different clamping conditions and thermal boundary conditions on the welded geometry will be studied numerically. The real geometry of the circumferential welded components is measured by means of an optical 3D measurement system, which is well suited for the evaluation of spatial distortions of structures with high resolution. Therefore, the prediction quality of the numerical model can be validated. This conference contribution presents an example of a butt welded pipe component, the results of 3D measurement and the results of finite element analyses. The challenges that arise for a realistic prediction of the welding distortion of the thin-walled pipe component will be discussed.

Keywords: Welding process simulation, TIG welding, distortion prediction, optical 3D scan, thin-walled titanium alloyed pipe structures

## INTRODUCTION

Lightweight structures made of titanium alloys are essential in aircraft construction due to the outstanding properties (low density, high strength, corrosion resistant) of this material. The preferred joining process of the titanium alloy components is Tungsten Inert Gas (TIG) welding. The further development and automation of the currently time-consuming and cost-intensive manual production of titanium bleed-air tubes is addressed in the new research project ASciE (20W1903B), which is funded by German Federal Ministry for Economic Affairs and Climate Action in the framework of Luftfahrtforschungsprogramm

des Bundes (LuFo). The Production Technology Group at Technische Universität Ilmenau works together with PFW Aerospace GmbH to develop finite element simulation models for the distortion prediction of thin-walled welded pipe structures.

High quality demands must be met in the production of the weld seams. The wall thickness of the investigated components ranges between 0.4 mm and 1.6 mm and the tube diameter is about one hundred times the wall thickness. The weld seams are designed as butt joints with an I-seam and technical zero gap. The width of the melting zone is five to ten times the wall thickness. Therefore, it should be obvious that the distortion of the tubes to be welded have to be within a very small range. To capture the actual geometry of the welded components they are measured by means of an optical 3D measurement system (GOM ATOS). By comparing the surfaces of the 3D scanned component and the CAD model, the real spatial deformation can be determined, which can be compared with the predicted deformation from a numerical simulation. This enables the validation of the prediction quality of the numerical model. In this project the influence of varying welding process parameters and heat source models as well as different clamping conditions and thermal boundary conditions will be studied numerically.

This conference contribution shows an example of 3D measurement and finite element simulation of the welding process of a real titanium alloy component and the challenges that arise for numerical analysis.

### DESCRIPTION OF THE COMPONENT AND THE WELDING PROCESS

Fig. 1 shows a photo of the TIG welded titanium alloy component manufactured by PFW Aerospace GmbH with two circumferential seams. The geometry is axially symmetric. The diameter of the tube between the two flanges is 50.8 mm. The wall thickness on both sides of each weld seam is 0.4 mm. The photo shows the measured width of the fusion zone, which varies between 4.0 mm and 4.5 mm, which is more than ten times of the wall thickness. The correct relative positioning of tube and flange is guaranteed by the help of mechanical calibration and mounting tools, which are the experienced know-how of PFW Aerospace GmbH. A multi-part welding insert is mounted before welding and guarantees that the tube diameters of the butt weld are aligned carefully. It has the function of a clamping tool, which fixes the position of the parts to be joined and additionally provides the shielding gas flow at the weld root inside the pipe.

Circumferential TIG welding is performed with argon shielding gas flow on the inside and outside of the pipe. The pipe rotates with horizontal axis of rotation while the welding torch is hold in flat welding position. The filler material is added continuously to the weld bead with a wire feed rate of 70 mm/min. The welding speed is 120 mm/min.

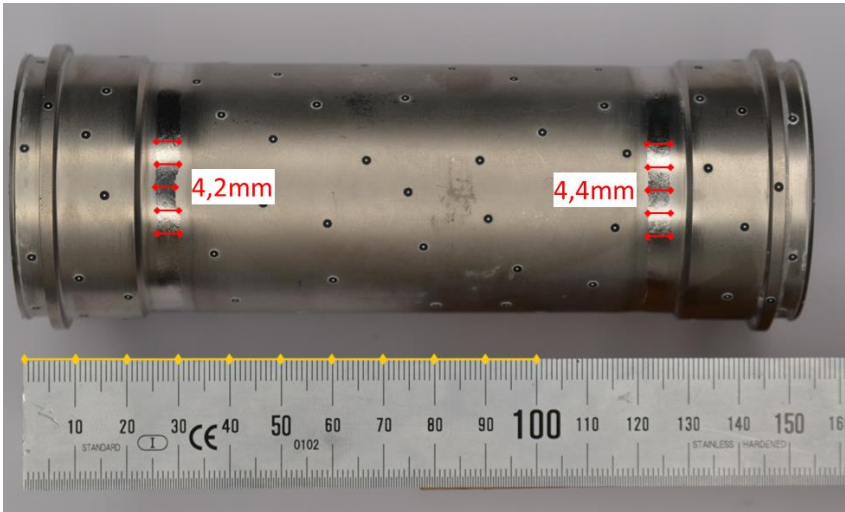


**Fig. 1** Example of a TIG welded titanium alloy component for aerospace industry from PFW Aerospace GmbH. The wall thickness of the pipe component with a diameter of 50.8 mm is only 0.4 mm. The surface is covered with marker points necessary for the 3D scan.

### OPTICAL SCAN OF GEOMETRY

The real geometry of the welded components is measured by means of an optical 3D measurement system, which is well suited for the evaluation of spatial distortions of the structures with high resolution. The industrial metrology 3D scanner GOM ATOS Core 45 (GOM GmbH, Braunschweig, Germany) with a resolution of 0.02 mm was used in our case. A white scanning spray was applied before scanning with the fringe projection technique. The precise fringe patterns are projected onto the surface of the object and are captured by two cameras based on the stereo camera principle. GOM's projection technology works with narrow-band blue light, which means that interfering ambient light can be filtered out during image acquisition.

Small measuring points (0.4 mm) were glued onto the component surface as can be seen in Fig. 1. The measurement points are needed to compute a triangulated surface mesh from a large number of acquired images taken from different spatial directions. The initially computed mesh has 26 million facets. For further processing the file size was reduced to 1.5 million facets using a coarsening and normalization algorithm. The triangulated surface mesh was compared to the CAD model using GOM Inspect software. Fig. 2 shows the calculated deviation of the actual geometry as color-coded plot. Deviation is defined as the shortest distance in the normal direction of the nominal surface of the CAD geometry. A positive deviation means that the actual surface is outside the volume of the CAD model, a negative deviation means that the actual surface is inside the

volume. Fig. 3 shows another enlarged view of the measured deviations. The circular holes are cut-outs at the positions of the marker points.

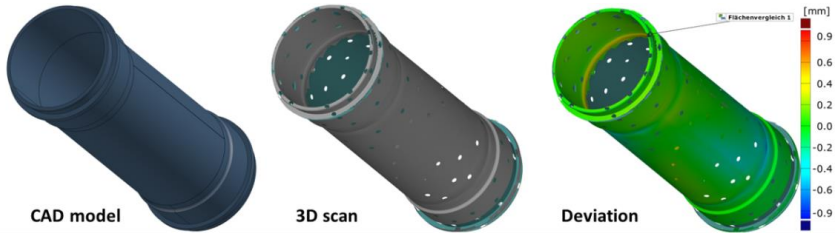


**Fig. 2** Deviation between CAD model and 3D scan of the surface of the welded component

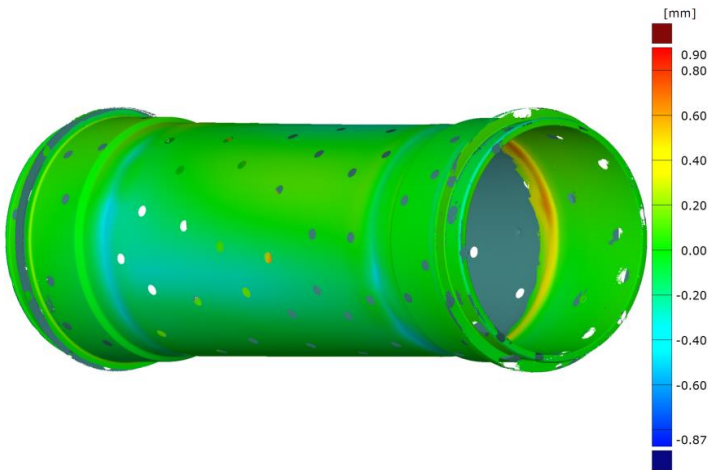


**Fig. 3** Deviation between CAD model and 3D scan of the surface of the welded component

The deviation plots show, that distortions are mainly found in circumferential direction of the two welded seams. The root of both welds has a convex shape with a positive deviation of 0.4 mm to 0.8 mm (yellow to red). The top of the welds have a slightly concave shape with negative deviations up to 0.4 mm (cyan). The other regions in green colour coincide with the CAD surface.

## FINITE ELEMENT MODELING

A finite element model of the welding process has been developed using Simufact Welding 2020. The CAD geometry is imported from STEP files. The material model of

TiAl6V4 with temperature dependent properties is taken from the Simufact Material 2020 database. Transient thermal simulations were performed to calibrate the heat source model before models for the coupled thermo-mechanical simulation were developed. In this paper, only the model for welding simulation of the first of two welds is presented.

### GEOMETRY AND MESH

The individual parts of the component were imported as STEP files. Simplified geometries of the welding insert and the welding bead were designed and imported as STEP file too. Fig. 4 shows a cross section trough the geometry. The volume of the deposited welding filler material was calculated on the basis of the welding instruction and is  $77 \text{ mm}^3$ .

The deformable parts were meshed with hexahedral solid elements using the Simufact Welding mesher. The overall number of volume elements is 129256. Four element layers of 0.1 mm thickness are used near the weld seam, see Fig. 5. The element edge length in axial and tangential direction is 0.4 mm.

The welding insert, which has the function of a clamping tool, is modelled with rigid surface elements. An interference fit of 0.05 mm is assumed to model the clamping force in an initial simulation step. That means, the inner radius of the pipe will be expanded by 0.025 mm due to the oversize of the welding insert in the contact region.

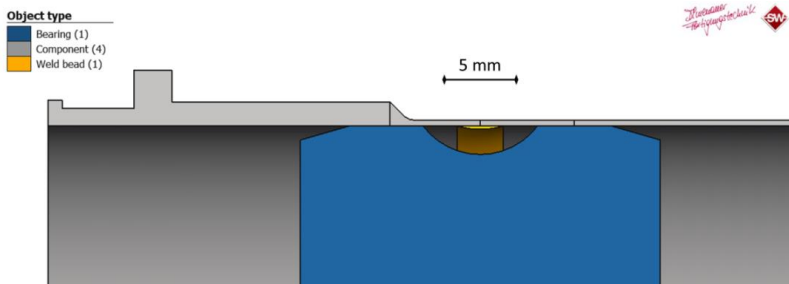


**Fig. 4** Cross section through the axisymmetric geometry of the finite element model

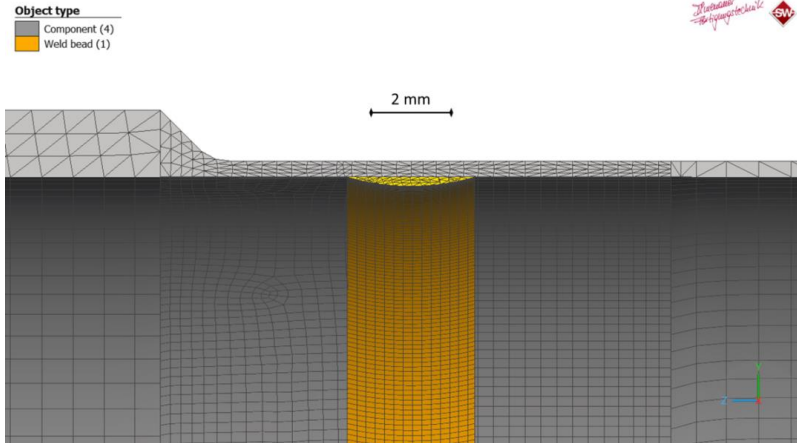


**Fig. 5** Cross section through the mesh of the finite element model near the weld seam

#### MATERIAL MODEL

The material model of TiAl6V4 is taken from the Simufact Material 2020 database. The physical, thermal and mechanical material properties are defined as function of temperature between 20 °C and 1600 °C. Above the last point in the material tables, the material properties are set as constant values. Constants used in the material model are Poisson’s ratio, melting enthalpy, solidus temperature and melting temperature, see Table 1. Temperature dependent material properties are defined for thermal conductivity, specific heat capacity, Young’s modulus, density, thermal expansion coefficient and yield stress. Their values at room temperature are given in Table 2. The temperature dependent flow curves are shown in the diagram in Fig. 6.

**Table 1** Material constants of TiAl6V4 used in the model

Poisson’s ratio	Solidus temperature (°C)	Melting temperature (°C)	Melting enthalpy (J/kg)
0,26	1550	1600	419000

**Table 2** Material parameters of TiAl6V4 at room temperature

Thermal conductivity (W/(m·K))	Specific heat capacity (J/(g·K))	Young's modulus (MPa)	Density (kg/m <sup>3</sup> )	Thermal expansion coefficient (1/K)	Initial yield stress (MPa)
6,0	0,54	115600	4482	8.85·10 <sup>-6</sup>	1170

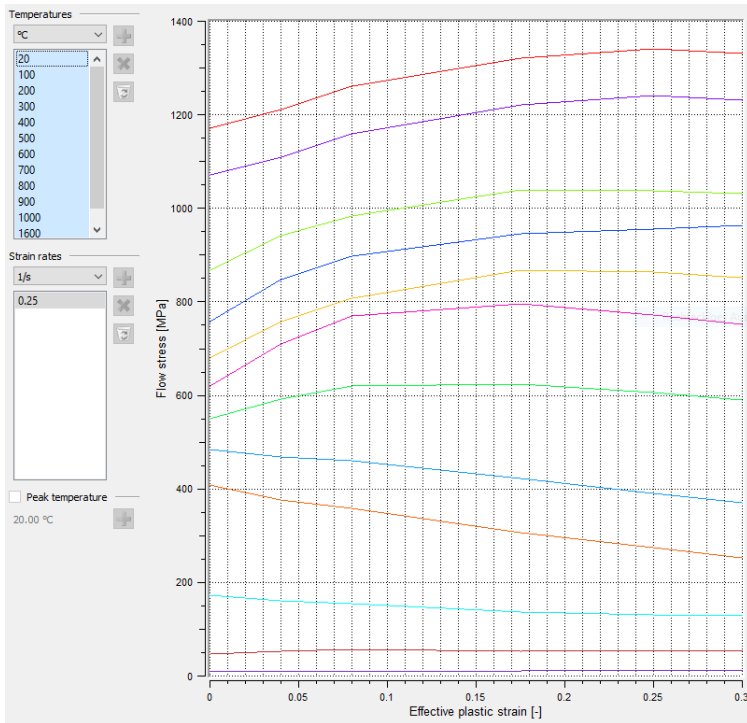


**Fig. 6** Flow curves from 20 °C to 1600 °C for TiAl6V4 from Simufact Material database

### PROCESS PARAMETERS

The welding process parameters were taken from the welding instructions, see Table 3. The efficiency parameter was calibrated together with the heat source model until the simulated width of the fusion zone matches the measured width with an accuracy tolerance of  $\pm 2\%$ .

**Table 3** Welding process parameters used for 0.4 mm wall thickness

Current (A)	Voltage (V)	Welding speed (mm/s)	Energy per length (J/cm)	Efficiency
22	8	2	880	0.8

HEAT SOURCE MODEL

The heat input  $Q$  is modelled with a volumetric heat source. The double ellipsoid heat source model by Goldak [2] is used as the conventional standard heat source model for arc welding simulations. The spatial distributions of the heat flux density in the front and rear quadrants,  $q_f$  and  $q_r$ , respectively, are defined as

$$q_f(x, y, z) = \frac{6\sqrt{3}f_f Q}{a_f b d \pi \sqrt{\pi}} \exp\left(-3\left(\frac{x^2}{a_f^2} + \frac{y^2}{b^2} + \frac{z^2}{d^2}\right)\right) \tag{1}$$

and

$$q_r(x, y, z) = \frac{6\sqrt{3}f_r Q}{a_r b d \pi \sqrt{\pi}} \exp\left(-3\left(\frac{x^2}{a_r^2} + \frac{y^2}{b^2} + \frac{z^2}{d^2}\right)\right) \tag{2}$$

with a moving local coordinate system  $(x,y,z)$  in the center of the ellipsoid. Five parameters have to be set in Simufact Welding, the half width  $b$ , the depth  $d$ , the front length  $a_f$ , the rear length  $a_r$  and the Gaussian parameter  $M$ , which defines the width of the Gaussian bell curve and is set to 3 by default. The fractions  $f_f$  and  $f_r$  of the heat deposited in the front and rear quadrants must satisfy the condition  $f_f + f_r = 2$  to maintain the total power.

The four geometric parameters represent the size of the weld pool and have to be calibrated. The parameters used in the model are given in Table 4, they were calibrated until the simulated width of the fusion zone matches the measured width with an accuracy tolerance of  $\pm 2\%$ .

**Table 4** Calibrated parameters of the double ellipsoid volume heat source model

Front length $a_f$ (mm)	Rear length $a_r$ (mm)	Half width $b$ (mm)	Depth $d$ (mm)	Gaussian parameter $M$	Heat front fraction $f_f$
1.2	4.0	2.0	1.2	3	0.4615

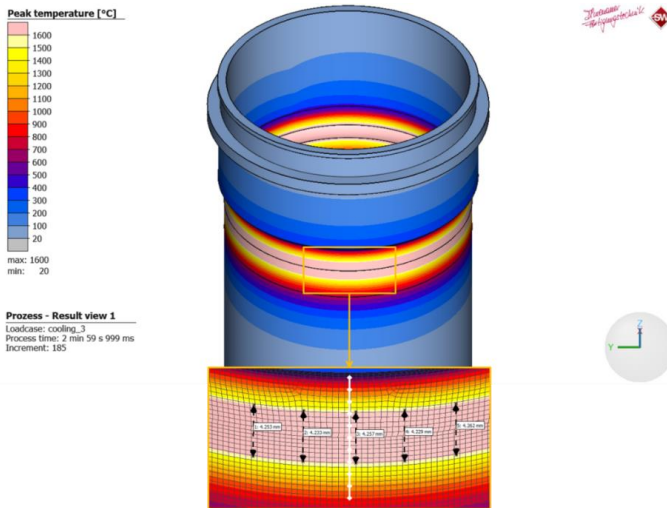
RESULTS AND DISCUSSION

THERMAL SIMULATION

The calibration of the heat source model and the thermal efficiency was performed with a transient thermal model. The following thermal boundary condition settings were used:

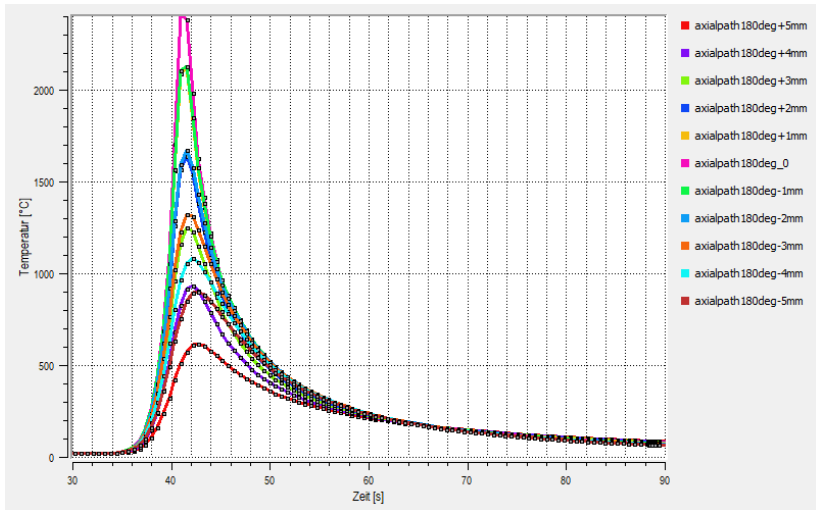
- Initial and ambient temperature: 20 °C
- Convective heat transfer coefficient: 20 W/(m<sup>2</sup>·K)
- Contact heat transfer coefficient: 1000 W/(m<sup>2</sup>·K)
- Emission coefficient: 0.6

Fig. 7 shows the simulated width of the weld seam in a plot of peak temperature at a distance of 180° from start of welding. The width varies between 4.2 mm and 4.3 mm with a mean value of 4.25 mm. The simulated width agrees with the median value of the measured width, which varies between 4.0 mm and 4.5 mm.



**Fig. 7** Peak temperature plot with measurement of the simulated weld seam width after calibration of the heat source. A 10 mm long evaluation path transverse to the weld seam was drawn into the enlarged image detail.

The corresponding plot of temperature-time history is shown in Fig. 8 for eleven equidistant points (distance 1 mm) along a path transverse to the weld seam. Due to the increase in cross section in the flange, the temperature profile is not exactly symmetric with respect to the weld seam.



**Fig. 8** Computed surface temperatures of points along a path perpendicular to the weld seam

### THERMOMECHANICAL SIMULATION

The calculation of deformations and stresses has been performed with a coupled thermo-mechanical finite element analysis using the previously calibrated heat source. The deformations and stresses are influenced not only by the thermal expansion, but also by the clamping forces. Clamping by the welding insert is activated before welding starts and deactivated after cooling. Touching contact is defined between the component and the welding insert with a friction coefficient value of 0.2. Glued contact is defined between different meshes of the same part. Touching contact with glue on peak temperature is defined at the welding seam.

The predicted deformation normal to the surface can be seen in Fig. 9. The upper image shows the deformation of the circumferential weld after 180° have been welded, the lower image shows the deformation at the end of the simulation, when the component has cooled down and the clamping is deactivated. Obviously, the weld seam bulges outwards in this simulation, while the deformation is directed inwards in the 3D scan of the real component. Variations in the heat source and welding process parameters did not fundamentally alter the results. Due to the curvature of the pipe, the heated zone will always bulge outwards when thermal expansion is simulated without additional surface forces.

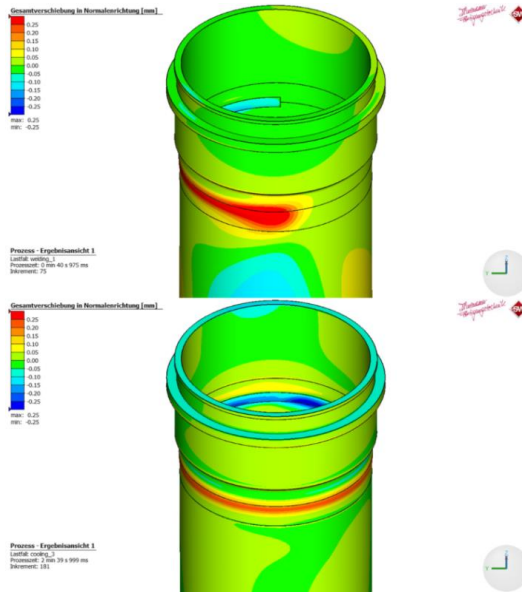


**Fig. 9** Predicted deformation normal to the surface 180 ° after start of welding (upper picture) and at the end of the simulation (lower picture)

The reason for this incorrect prediction is that compressive forces on the surface of the molten pool are not considered. The formation of the melt pool surface is influenced by gravity, surface tension, arc pressure, evaporation pressure and drop impact pressure [4]. It is known from literature [5], that several welding process parameters influence the arc stagnation pressure significantly. For example, argon shielding gas used for TIG welding increases the arc pressure significantly in comparison with helium [6]. In many cases, these forces can be neglected, if the fusion zone is stabilized by the stiffness of the surrounding material. But in our case, the fusion zone goes through the entire wall thickness and the fusion zone width is at least ten times of the wall thickness. An enhanced model approach, which models this influence in a simplified way, is presented in the next section.

#### ENHANCED THERMOMECHANICAL SIMULATION

The measured deformation from the 3D scan and the predicted deformation from the previous model indicate that there is a not negligible compressive force on the weld pool surface that moves with the electric arc and that is directed inward. Considering, that the welding arc acts as a source of force over the molten pool, the arc stagnation pressure is an important variable for the formation of the weld bead geometry and the final quality of the weld seam [5]. From experimental studies of the influence of process gases in TIG

welding [6] is known, that the arc stagnation pressure over radius has the shape of a Gaussian bell curve. We had neither a suitable modelling tool in Simufact Welding 2020 nor the necessary data to model this force directly. Instead, we propose a simple indirect approach to apply a pressure distribution in the desired direction to the weld.

A kinematic constraint is added to the weld zone of the model. A rigid ring shell is inserted to the model with a tight gap to the surface of the pipe. When the deformed pipe surface gets in contact to the shell, a pressure distribution is created, which constrains the further outward expansion. In a first approximation, this model approach can describe the effect of the forces on the surface of the molten zone. The shape and gap distance of such a numerical shaping tool has to be calibrated, of course.

Fig. 10 shows the predicted deformation with a kinematic constrained weld bead formation. An initial contact gap of 0.05 mm is modelled. When the radial displacement of the heat affected zone exceeds 0.05 mm in the previous model, it is constrained in this new model and a surface pressure distribution evolves in the heat affected zone. At the end of the simulation, when the component has cooled down and the clamping is deactivated, the weld seam curves inwards in the same manner as in the 3D scan of the welded geometry.

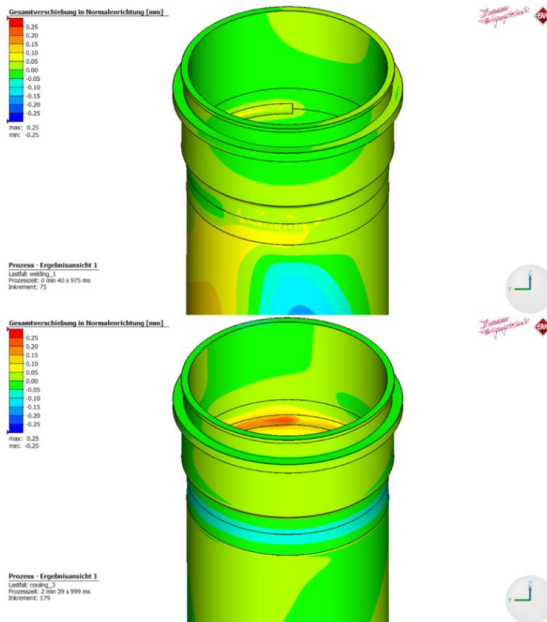


**Fig. 10** Predicted deformation normal to the surface 180 ° after start of welding (upper picture) and at the end of the simulation (lower picture). Simulation results with enhanced model applying a kinematic constraint to the weld zone.

## SUMMARY AND CONCLUSIONS

High quality demands in aircraft industry must be met in the production of the weld seams of lightweight structures. In the same way, numerical models must have a high predictive accuracy if the simulation results are to be used in the design of manufacturing processes. A finite element model for the distortion prediction of a thin-walled TIG-welded titanium alloy pipe component was developed with the purpose of achieving a reliable prediction of the process-induced deformations during welding. The weld seams that were examined are designed as butt joints with an I-seam. The width of the melting zone is ten times the wall thickness.

To capture the actual geometry of the welded components, they were measured by means of an optical 3D measurement system. By comparing the surfaces of the 3D scanned component and the CAD model, it is possible to determine the real spatial deformation, which was compared with the predicted deformation from the finite element analysis. The thermal simulation using a calibrated Goldak heat source provided very accurate results for the size of the fusion zone. The predicted deformations from the thermo-mechanical simulation with the first model unexpectedly gave results that differed significantly from the measured deformations. The simulated weld seam has bulged outwards, while it is slightly curved inwards in reality. The cause was identified in the unconsidered compressive forces on the weld pool exerted by the arc welding process. The thermomechanical model was therefore enhanced with a kinematic constraint approach, which is suited to model these compressive forces indirectly. When material expands radially outward as a result of thermal expansion, an inward directed pressure distribution is generated in the area of the weld zone. By the help of this simple model extension the prediction of the deformations has been substantially improved. With the enhanced model the weld seam curves inwards in the same manner as in the 3D scan of the welded geometry.

From an engineering point of view the presented simplified model approach for considering compressive forces on the weld pool in the finite element analysis leads to satisfying results. However, prior knowledge of the weld bead geometry is necessary, which we obtained from the 3D scan. From a scientific point of view, there is a need for a more physical approach. Like the Goldak heat source for heat input a moving source of distributed mechanical forces acting on the weld pool leading to correct shape of the weld bead surface should be implemented in welding simulation software.

Future work in the research project will focus on the numerical investigation of the influence of modified welding process parameters and mechanical clamping conditions on the distortion of welded pipe structures.

## ACKNOWLEDGEMENTS

The presented research within the collaborative project ASciE (20W1903B) is funded by German Federal Ministry for Economic Affairs and Climate Action in the framework of Luftfahrtforschungsprogramm des Bundes (LuFo). The financial support is gratefully acknowledged.

References

- [1] E. DOEGE, H. MEYER-NOLKEMPER, I. SAEED: *Fließkurven-Atlas metallischer Werkstoffe*, Carl Hanser Verlag, München Wien, 1986.
- [2] J. GOLDAK, A. CHAKRAVARTI, M. BIBBY: 'A New Finite Element Model for Welding Heat Sources', *Metallurgical Transactions B*, Vol. 15, No. 2, pp. 299-305, 1984.
- [3] J. A. GOLDAK, M. AKHLAGI: *Computational Welding mechanics*, Springer, 2005.
- [4] D. RADAJ: *Schweißprozesssimulation: Grundlagen und Anwendungen*, DVS-Verlag, Düsseldorf, 1999.
- [5] G. DE SIMAS ASQUEL, A. P. S. BITTENCOURT, T. V. DA CUNHA: 'Effect of welding variables on GTAW arc stagnation pressure', *Welding in the World*, Vol. 64, pp. 1149-1160, 2020.
- [6] J. ZÄHR, U. FÜSSEL, M. HERTEL, M. LOHSE, M. SENDE, M. SCHNICK: 'Numerical and experimental studies of the influence of process gases in TIG welding', *Welding in the World*, Vol. 56, pp. 85-92, 2012.

# EFFECT OF PHASE- AND TEMPERATURE-DEPENDENT STRAIN-HARDENING SLOPES ON THE CALCULATED WELDING RESIDUAL STRESSES IN S235 STEEL

J. SUN\*, T. NITSCHKE-PAGEL\*, K. DILGER\*

*\*Technische Universität Braunschweig, 38106 Braunschweig, Germany*

10.3217/978-3-85125-968-1-17

## ABSTRACT

The purpose of this work is to systematically clarify the impact of phase- and temperature-dependent strain-hardening slopes on the calculated welding residual stresses in the commonly used structural steel S235. Both experimental methods and numerical simulation have been utilized for investigation. The results reveal that the temperature-dependent strain-hardening slopes of the generated phases (austenite and bainite here) have nearly no influence on the simulated welding residual stresses. The calculated magnitude of longitudinal residual stress in the base metal near the weld area is highly sensitive to the applied strain-hardening slopes of the initial microstructure (ferrite here), while that of transverse residual stress is not. Meanwhile, comparing to the strain-hardening slope of the initial microstructure at elevated temperatures, that at room temperature plays a critical role in the simulated longitudinal residual stress. In this study, the guidance on how to economically and reliably determine the temperature- and phase-dependent strain-hardening slopes of a given steel in numerical welding simulation is provided.

Keywords: Strain-hardening slopes; Structural steel S235; Numerical simulation; Welding residual stresses.

## INTRODUCTION

Arc welding has been widely used to join steels in manufacturing industries because of its low-cost equipment and portability [1]. Nevertheless, the extremely inhomogeneous temperature field is formed during arc welding due to the highly localized arc energy input. The shrinkage of the heated zone is strongly hindered by the surrounding cold area [2]. As a consequence, residual stresses are unavoidably generated in the weldments [3, 4]. It is well known that the tensile residual stress might reduce the fatigue strength [5]. Therefore, it is of critical significance to accurately predict the magnitude and distribution of residual stresses for the assessment of structural integrity of welded components.

With the enhancement of computing technology and computational welding mechanics (CWM), numerical simulation using the finite element method (FEM) becomes a reliable,

economical, and efficient alternative to obtain the magnitude and distribution of welding residual stresses [4, 6]. In comparison to the experimental methods often requiring a considerable amount of cost, time, and effort, numerical simulation has been drawn increasing attention from manufacturing industries.

During arc welding, the steel near the molten area experiences a plastic compression-tension yielding [3]. Based on the measured stress-strain curves of the widely used steels, it can be found that the commonly applied steels in practice usually show the obvious strain-hardening phenomenon [7-8]. Therefore, it is necessary to carefully consider strain-hardening phenomenon in numerical welding simulation. If the strain hardening effect is taken into account in numerical welding simulation, three very important aspects should be carefully considered: strain-hardening model, strain-hardening recovery, and strain-hardening slope [9]. Until now, great effort has been made to clarify which strain-hardening model is the best for a given steel in numerical welding simulation and to study the mechanism of strain-hardening recovery [9-10]. However, there is less literature to illustrate the effect of strain-hardening slope on the calculated welding residual stresses. It is well known that the strain-hardening slope might be not only temperature but also phase dependent. How to economically and reliably determine the temperature- and phase-dependent strain-hardening slopes of a given steel in numerical welding simulation is currently unclear.

As fundamental research, the numerical sensitivity analyses based on Sysweld software have been conducted to illuminate how the strain-hardening slopes are economically and reasonably determined for the accurate prediction of residual stresses in S235 steel weldments. Meanwhile, the mechanical tensile tests were performed to measure the stress-strain curves at different temperatures. The welding experiments were carried out to measure the temperature results and residual stresses for validation.

## EXPERIMENTAL PROCEDURE

The base metal (BM) is the structural steel S235JR. The measured stress-strain curves of the given steel S235JR at various temperatures are shown in Fig. 1. The tungsten inert gas (TIG) arc welding was applied to produce the single-pass weldment without the addition of a filler wire. The designed size of the weld plate is  $200 \times 150 \times 10$  mm as seen in Fig. 2. The applied welding current is 200 A, welding voltage is 12.5 V, and welding speed is 10 cm/min.

Before welding, thermocouples were arranged on the top surface of the weld specimen for measuring the temperature history. After welding, the X-ray diffraction method was applied to measure the welding residual stresses. The macrograph at the transverse mid-cross section were measured by using the optical microscope.

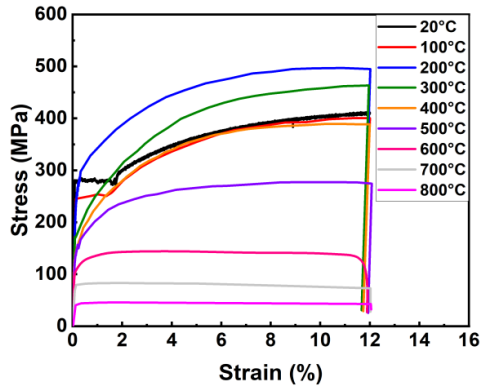


Fig. 1 Measured stress-strain curves at different temperatures of base plate

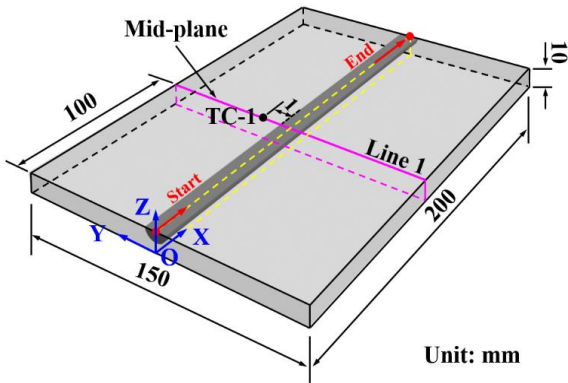
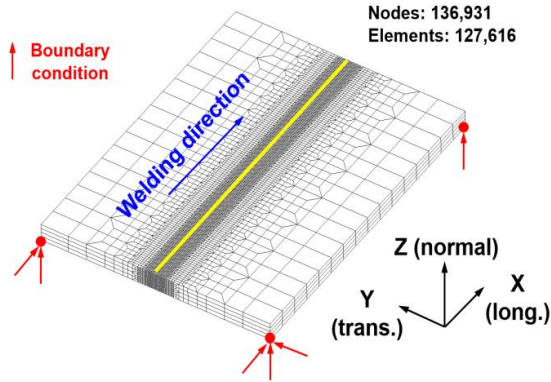


Fig. 2 Designed geometry of the weld specimen

### FINITE ELEMENT ANALYSIS

The created FE mesh model can be seen in Fig. 3. The size of the FE model is completely the same as that of the experimental weld sample (see Fig. 2). The finer meshes were designed in and near the weld, while the coarser meshes were applied in the area away from the weld. In the present work, the subsequently coupled thermo-metallurgical-mechanical FEM was applied for numerical welding simulation here.



**Fig. 3** Created finite element model

#### THERMAL ANALYSIS

Goldak's double ellipsoidal heat source was used to simulate the arc energy input here [11]. The used thermal properties of the given structural steel S235JR can be seen in [10]. The fusion zone (FZ) was assumed to be the area with peak temperature higher than 1500 °C, while the temperature range of the heat-affected zone (HAZ) was between 750 and 1500 °C [10]. The heat transfer caused by the thermal conduction was calculated based on Fourier rule. The heat loss induced by heat convection ( $q_c$ ) and radiation ( $q_r$ ) was considered according to Newton's law and Stefan-Boltzmann law, respectively.

#### METALLURGICAL ANALYSIS

In the present study, the austenization start (Ac1) and end (Ac3) temperature were set as 730 and 860 °C, respectively [10]. The applied continuous-cooling-transformation (CCT) diagram for the given steel S235JR here as seen in Fig. 4 refers to that of S235 steel provided by Loose [12]. In the current work, the diffusive phase transformation from austenite to ferrite/pearlite/bainite was calculated according to the Leblond kinematic rule. The displacive phase transformation from austenite to martensite was simulated based on the Koistinen-Marburger (KM) relationship model. Furthermore, the linear mixture rule was utilized to determine the material properties of the phase mixture [10].

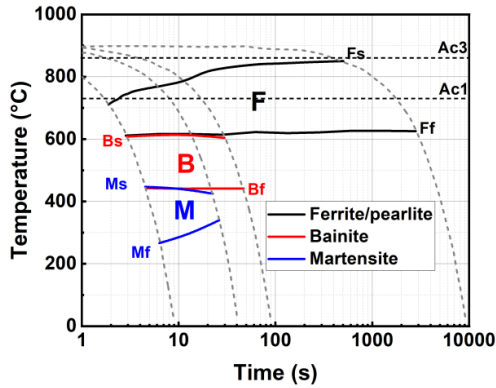
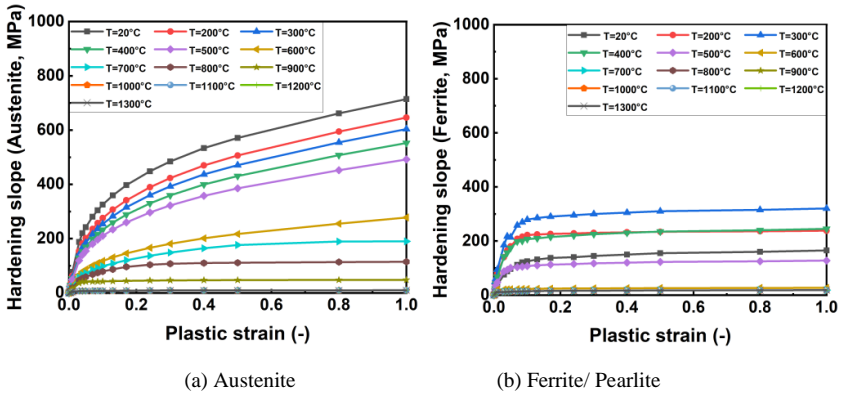


Fig. 4 Continuous-cooling-transformation diagram of S235 steel (refer to [12])

MECHANICAL ANALYSIS

The utilized mechanical properties of the given steel S235JR steel here can be found in [10]. The strain-hardening slopes of austenite, bainite, and martensite were taken from that in S235J2G3 steel included in the Simufact.welding material database, while that of ferrite were obtained from the experimental results as seen in Fig. 5 [10]. Note that the material properties of ferrite and pearlite in steels are usually assumed to be the same.



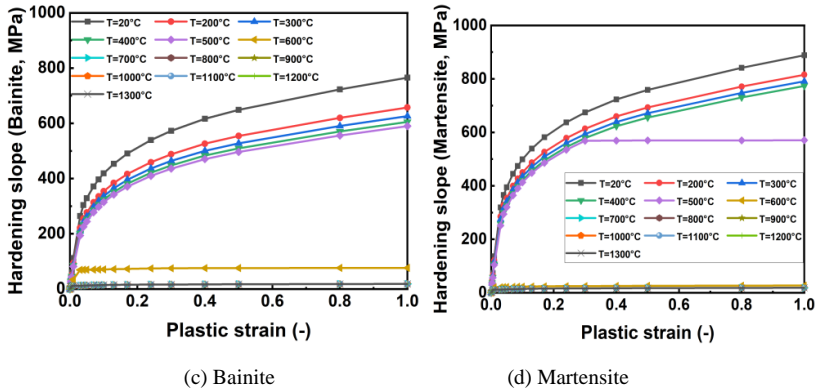


Fig. 5 Strain-hardening slopes of S235 steel

SIMULATION CASES

In this study, the cases in Table 1 were elaborately designed and performed using Sysweld software for studying the effect of strain-hardening slope on welding residual stresses. The isotropic hardening model was employed and the annealing temperature was set as 860 °C (Ac3) for all the cases in Table 1 [10]. Note that all these cases are the same except the employed strain-hardening slopes. Here, cases A-1 and B-1 are identical and considered to be the standard case. The “Fig.5 (No change)” in Table 1 means the strain-hardening slopes are equal to that in Fig.5.

Table 1 Simulation cases

Cases		Strain-hardening slope
Group A	Case A-1	Fig. 5 (No change)
	Case A-2	Austenite: 5 times
	Case A-3	Bainite: 5 times
	Case A-4	Ferrite: 5 times
Group B	Case B-1	Fig. 5 (No change)
	Case B-2	All temperatures: Ferrite: 5 times
	Case B-3	All temperatures except $T_{RT}$ : Ferrite: 5 times
	Case B-4	Only $T_{RT}$ : Ferrite: 5 times

In Group A, the effect of the phase-dependent strain-hardening slopes on the calculated welding residual stresses was systematically investigated. The strain-hardening slopes of only one of the phases in each case were changed, while the rest were kept as the same as that in the standard case. For example, just all the temperature-dependent strain-hardening slopes of ferrite simultaneously were highly increased 5 times in Case A-4. Since almost no martensite is generated in the weldment after welding based on the measured thermal results as seen later, the variation in the strain-hardening slopes of martensite was not

investigated here. In Group B, the impact of the temperature-dependent strain-hardening slopes of S235 steel base metal (ferrite) on the calculated welding residual stresses was systematically studied. Here, the strain-hardening slope of ferrite at different temperatures was changed. For instance, the strain-hardening slopes of ferrite at all temperatures were increased 5 times in Case B-2, while that only at room temperature  $T_{RT}$  were increased 5 times in Case B-4.

## RESULTS AND DISCUSSION

### WELDING TEMPERATURE FIELD

Since the subsequently coupled FEM was employed in numerical simulation and only the strain-hardening model as well as slope in the mechanical analysis were changed here, it can be expected that the calculated welding temperature fields in all these cases in Table 1 are nearly the same. For this reason, the calculated welding temperature field in Case A-1 is taken as an example for comparison with the experimental results.

Fig. 6 compares the calculated and measured weld dimension in the transverse mid-cross section. From this figure, it can be found that the calculated sizes of FZ and HAZ match the experimental results very well. Fig. 7 shows the predicted and measured thermal cycles at the TC-1 location (see Fig. 2). In Fig. 7, the simulated cooling rate  $\Delta t_{8/5}$  time is in good agreement with the experimental data. According to the above comparisons, it can be concluded that the current thermal analysis is reliable and can provide the reasonable welding temperature field.

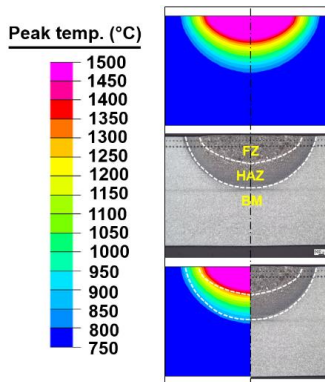


**Fig. 6** Peak temperature distribution

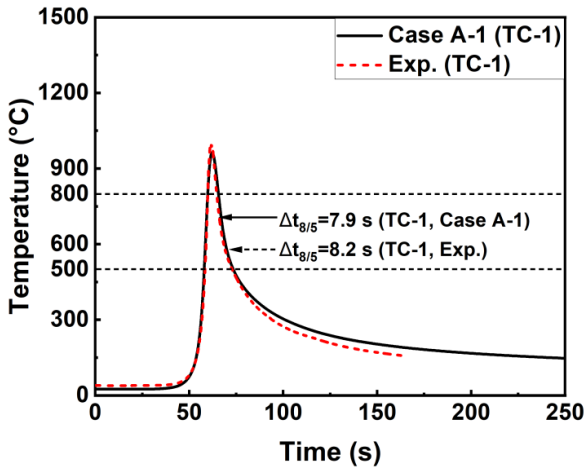
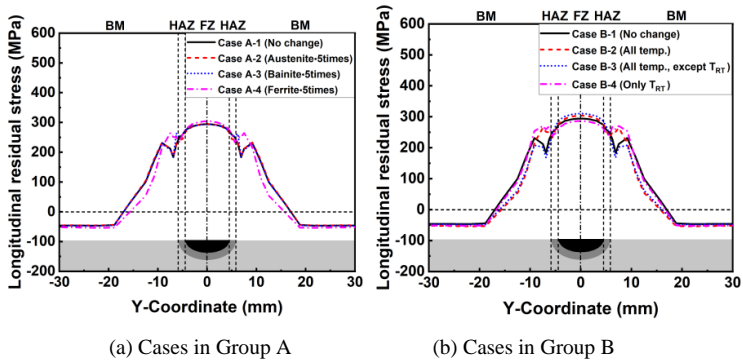


Fig.7 Thermal cycles at TC-1 location

WELDING RESIDUAL STRESSES

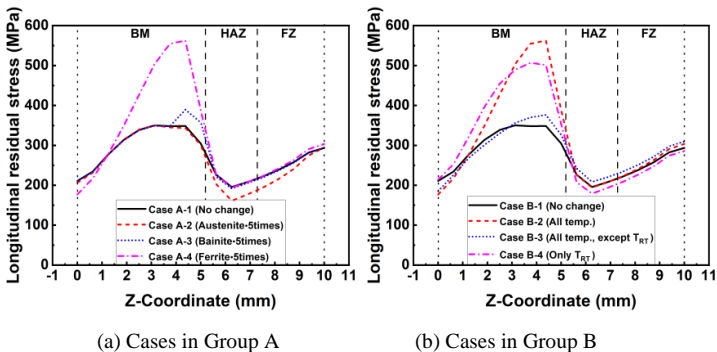
*Longitudinal residual stress*

Fig. 8 depicts the longitudinal residual stress distribution along line 1 simulated by the cases in groups A and B. In Fig. 8a, the calculated results along line 1 in case A-1, A-2, and A-3 are nearly the same. Nevertheless, the predictions in Case A-4 are different from that in the other three cases mainly in the base metal near the weld area. This is due to that solid-state phase transformation (SSPT) mainly occurs in the weld area, which nearly eliminates the strain-hardening effect [9]. In Fig. 8b, the predictions in Case B-1 and Case B-3 are nearly the same. That in Case B-2 and Case B-4 are almost identical. Nevertheless, the calculated results in Case B-1 is quite different from that in Case B-2 mainly in the base metal near the weld area.



**Fig. 8** Predicted longitudinal residual stress distribution along line 1 in cases of groups A and B

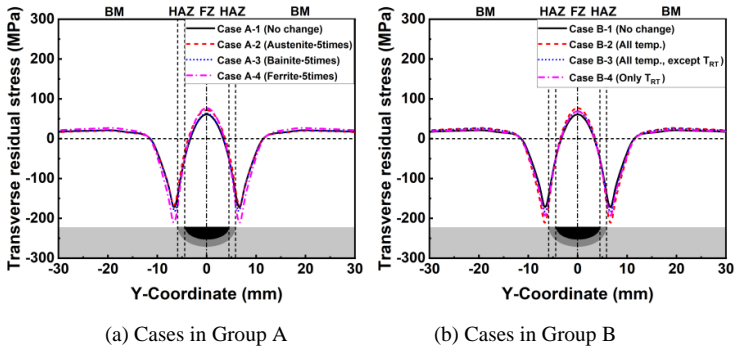
Fig. 9 shows the longitudinal residual stress distributions along line 2 calculated by the cases in groups A and B. From Fig. 9a, it can be seen that the calculated results in the weld area in these cases are nearly the same, while that in the base metal near the weld area in Case A-4 are much higher than that in the other three cases. In Fig. 9, the predictions in the base metal very close to the weld area in Case A-3 is a little higher than that in Case A-1 or Case A-2. Furthermore, the calculated results in the weld area in Case A-2 are slightly different from that in the other three cases. This is because the austenite exists before SSPT but then fades away after SSPT, while the bainite arises and remains after SSPT. Meanwhile, partial SSPT occurs at the border area of HAZ. It should be noted that these slight differences are induced by the high increase in the strain-hardening slopes of austenite and bainite fivefold here. In Fig. 9b, the predictions in Case B-1 and Case B-3 are very close, which is different from that in Case B-2 and Case B-4. The calculated results in Case B-4 is quite similar to that in Case B-2 overall.



**Fig. 9** Predicted longitudinal residual stress distribution along line 2 in cases of groups A and B

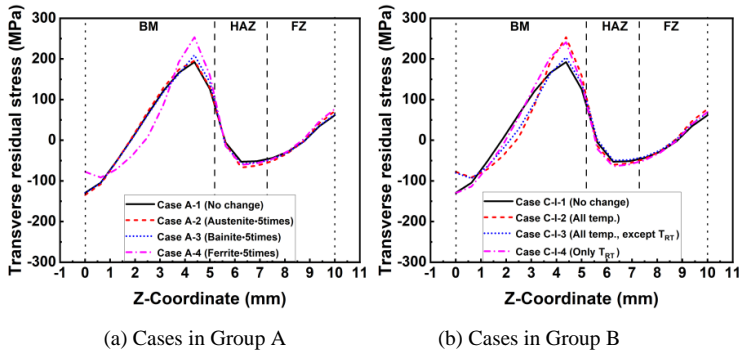
*Transverse residual stress*

Fig. 10 presents the simulated transverse residual stress distribution along line 1 in cases of groups A and B. From Fig. 10, one can see that the calculations are nearly the same except a certain difference in base metal very close to the weld area.



**Fig. 10** Predicted transverse residual stress distribution along line 1 in cases of groups A and B

Fig. 11 depicts the transverse residual stress distribution along line 2 simulated by the cases in groups A and B. From Fig. 11a, one can see that the calculations in Case A-1, Case A-2, and Case A-3 are nearly the same, which are different from that in Case A-4 mainly in the base metal near the weld area. However, it should be mentioned that the difference in the calculated magnitude of transverse residual stress in the base metal near the weld area between Case B-4 and Case B-1 (or Case B-2, Case B-3) is rather low. Furthermore, this small deviation is obtained by highly increasing the strain-hardening slopes of ferrite fivefold here. In Fig. 11b, the predictions in Case B-1 and Case B-3 are nearly the same. That in Case B-2 and Case B-4 are similar. Nevertheless, the calculated results in Case B-1 is slightly different from that in Case B-2 mainly in the base metal near the weld area.



**Fig. 11** Predicted transverse residual stress distribution along line 2 in cases of groups A and B

## CONCLUSIONS

- (1) The variations in the strain-hardening slopes of the generated phases (austenite and bainite here) have nearly no effect on the calculated welding residual stresses.
- (2) The calculated magnitude of longitudinal residual stress in the base metal near the weld area is highly sensitive to the applied strain-hardening slopes of the initial microstructure (ferrite here), while that of transverse residual stress is nearly not.
- (3) In comparison to the strain-hardening slopes of the parent microstructure at elevated temperatures, that at room temperature plays a critical role in the predicted longitudinal residual stresses.
- (4) Guidance on how to economically and reliably determine the phase- and temperature-dependent strain-hardening slopes of a given steel in numerical welding simulation is provided.

## APPENDICES AND ACKNOWLEDGEMENTS

The authors are grateful for the financial support provided by the German Research Foundation “Deutsche Forschungsgemeinschaft (DFG)” through the projects NI 508/14-2 and SU 1411/1-1 for the present research.

## References

- [1] J. GRANJON: *Fundamentals of welding metallurgy*, Cambridge, 2002.
- [2] TH. NITSCHKE-PAGEL and H. WOHLFAHRT: ‘Residual stresses in welded joints – sources and consequences’, *Master. Sci. Forum* Vol. 404, pp. 215-226, 2002.
- [3] D. RADAJ: *Heat effects of welding on temperature field, residual stress and distortion*, Berlin-Heidelberg, 1992.

- [4] Y. UEDA, H. MURAKAWA and N. MA: *Welding deformation and residual stress prevention*, Berlin-Heidelberg, 2012.
- [5] TH. NITSCHKE-PAGEL and J. HENSEL: 'An enhancement of the current design concepts for the improved consideration of residual stresses in fatigue-loaded welds', *Welding in the world*, Vol. 65, pp. 643-651, 2021.
- [6] L. LINDGREN: *COMPUTATIONAL WELDING MECHANICS*, CAMBRIDGE, 2007.
- [7] Nickel Institution: *The Nickel Advantage – Nickel in stainless steel – Eurometaux*, 2008.
- [8] M. FARAJAN: 'Welding residual stress behavior under mechanical loading'. *Welding in the world*, Vol. 57, pp. 157-169, 2013.
- [9] J. SUN, J. HENSEL, J. KLASSEN, TH. NITSCHKE-PAGEL and K. DILGER: 'Solid-state phase transformation and strain hardening on the residual stresses in S355 steel weldments', *Journal of material processing technology*, Vol. 265, pp. 173-184, 2019.
- [10] J. SUN, TH. NITSCHKE-PAGEL, K. DILGER: 'Influence of strain-hardening models and slopes on the predicted residual stresses in structural steel S235 weldments', *Journal of materials research and technology*, Vol. 19, pp. 4044-4062, 2022.
- [11] J. GOLDAK: *Computational welding mechanics*, Springer, 2005.
- [12] T. LOOSE: *Einfluß des transienten Schweißvorganges auf Verzug Eigenspannungen und Stabilitätsverhalten axial gedrückter Kreiszyinderschalen aus Stahl*, thesis, Karlsruhe: Universität Fridericiana zu Karlsruhe, 2007.

# VALIDATION OF WELDING STRUCTURE SIMULATIONS

T. LOOSE\*, T. GIRRESSER\*\*, J. GOLDAK\*\*\*

*\*Dr. Loose GmbH, 75045 Walzbachtal, Germany, Orcid Id: 0000-0002-1756-0392*

*\*\*Technologie-Institut für Metall & Engineering GmbH (TIME), 57537 Wissen / Sieg, Germany*

*\*\*\*Goldak Technologies Inc., KIV 7C2 Ottawa, Canada*

DOI 10.3217/978-3-85125-968-1-18

## ABSTRACT

The Welding structure simulation is a numerical method that predicts distortions, residual stresses and microstructure in welded structures. It enables design engineers to optimize the design and the manufacturing process for the strength and usability of the assembly. To trust the simulation software, it should be validated to demonstrate that the predictions provide a best fit with the reality.

We want to prove, that our numerical model of simulation matches the physical behavior of the reality. We must ensure that the virtual experiment matches the physical experiment and that we compare the same sensor and virtual data:

- Same time
- Same location
- Same state

Previously, the comparison between the virtual and physical experiment was limited to the final result: final distortion, final residual stress and final residual strain. Now also the transient state during the process shall be considered: transient measurement of temperature field, strain field or deformation.

This validates not only the final results but also the computational algorithm that leads to these results. This paper presents transient results of validation experiments with the scope on deformation. The experiment, welding of an orthotropic plate, was chosen in accordance with a published experiment from Murakawa [1]. Because the process is transient, it is important that the transient data be compared.

## INTRODUCTION

The weld structure simulation as a special application of the finite element method considers the effects from welding on the entire component. The input variable is the heat input from the welding heat source. This is applied in the form of a so-called equivalent heat source. This means that any fusion welding process can be modelled, regardless of how the fusion heat is generated. Of course, all boundary conditions must be considered in the model. This includes the clamping device, heat dissipation through clamping or cooling jaws and tacking.

Results from the weld structure simulation include the geometry change due to welding, weld distortion, residual stresses and plastic strains, and if the microstructure transformation calculation is included, the microstructure state after welding and the resulting changing yield strength.

The most precise method is the transient method. The transient method provides results over time and is chosen as the simulation method for the virtual experiment.

Since the transient method involves a large computational overhead in terms of time, simplifying methods have been developed in the past. These include the metatransient method [2] or the shrinkage force method. In the metatransient method, a seam section is heated simultaneously instead of a migrating heat source. In the shrinkage force method, substitute expansions are applied in the seam area. Both methods are intended to provide accurate final results, but the results over time may differ from reality.

The specimen for the Experiment is shown in Fig. 1.



**Fig. 1** Test specimen - TIME stiffened plate

### EXPERIMENTAL SETUP

For this purpose, an orthotropic plate 1200 mm x 600 mm x 6 mm made of low alloyed steel grade S235JR was chosen. On the plate, two longitudinal stiffeners 1000 mm x 100 mm x 6 mm and 3 transverse stiffeners 400 mm x 100 mm x 6 mm were welded. The stiffeners are fixed with a total of 17 tack welds (Fig. 2).

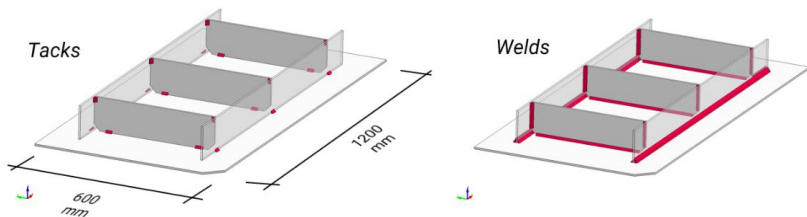


**Fig. 2** Dimension, tack welds and welds of test specimen

The slab is supported in a statically determinate manner and supported at three corners. The fourth corner remains free. This is the corner where the greatest distortion occurs during welding. The corner opposite the free corner on the long side is chamfered so that the corners of the plate can be clearly assigned (Fig. 3). While the tack welds are being

welded, the plate is supported at the center transverse stiffener on each outer side with a jack (fig 3, “A” and “B”). Without support, the plate deflects under its own weight to such an extent that an excessive gap is created between the plate and the stiffener. After tack welding, the support is removed. This leads to a lowering of the plate at the unsupported corner. In the simulation, the removal of the support is mapped realistically.

Since only rigid body modes are constrained by the permanent supports, the experimental setup allows significant deformation during welding. This is intended to provide a meaningful comparison between the calculated and the experimental results.

During welding, the movements normal to the plate are measured at five points with cable wire sensors. The position of the cable wire sensors is shown in Fig. 3 too. At the same locations, the vertical distortion is evaluated from the simulation.

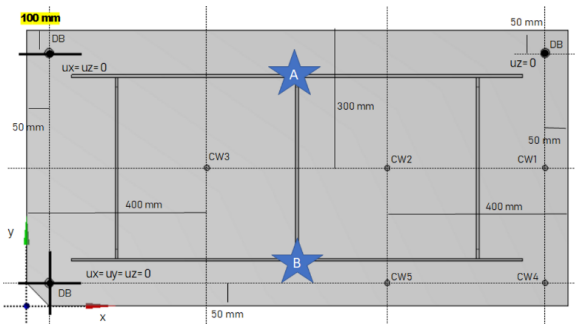


**Fig. 3** The points with permanent support that constrain rigid body motion are labelled DB, the temporary supports are labelled A and B and the wire sensors are labelled CW1 to CW5

The weld sequence is documented in Fig. 4. The longitudinal seams are first welded on the outside as a two-layer seam with 3 weld beads. All other 17 seams are executed as single-layer fillet welds.

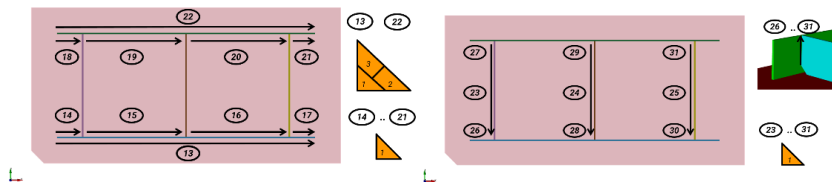


**Fig. 4** Weld sequence

There are two groups of welds, fillet weld in horizontal position PB and vertical fillet weld in ascending position PG.

Process parameter for the horizontal welds, position PB:

- Wire Diameter: 1,2 mm
- Wire feed speed: 8 m/min

- Travel speed: 45 cm/min
- U:  $23.5 \pm 2$  V, I:  $258 \pm 10$  A
- Weave bead with
  - amplitude: 1 mm
  - frequency: 2.78 Hz

Process parameter for the vertical welds, position PF:

- Wire Diameter: 1,2 mm
- Wire feed speed: 2 m/min
- Vertical travel speed: 4.9 cm/min
- U: 14.9 V, I: 96 A
- Triangle weave bead with
  - Weave speed: 50 cm/min
  - Weave amplitude: 5.5 mm
  - Weave frequency: 2 Hz

### DATA SYNCHRONISATION

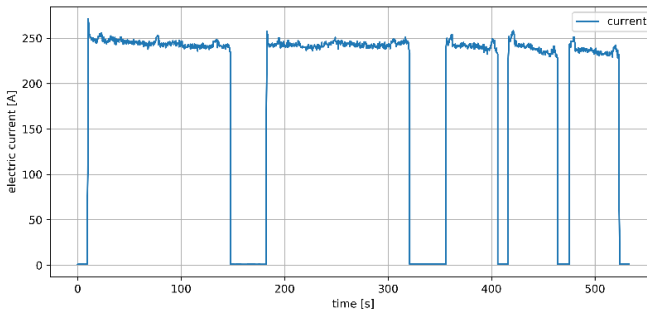


**Fig. 5** Electrical current during welding

The challenge is to synchronize the measured data from experiment with the simulated data. For this purpose, the welding times are recorded redundantly several times:

- Time determination with stopwatch and manual logging
- Video recording
- Recording with infrared camera (FLIR)
- Measurement of current (Fig. 5) and voltage during welding
- Recording with infrared camera (FLIR)
- Measurement of current and voltage

From the redundant recording, the start and end times of the individual welding beads can be determined very precisely and entered them into the process plan for the simulation.

NUMERICAL MODEL AND SIMULATION

The plate is represented by solid element model with hexahedron and pentahedron elements. The general mesh size is 5 mm, the mesh size in filler area 1 mm lateral. 2 element layers are chosen in plate thickness direction (Fig. 6). The single parts are meshed independently with non-coincident mesh and joined to each other by contact formulation.

$$q_i = Qf_i \frac{3}{2\pi a_i b c} \quad \text{with } i := \{f, r\} \tag{1}$$

$$q = q_f \quad \text{if } u \geq 0 \quad \text{and} \quad 1 > \left(\frac{u}{a_f}\right)^2 + \left(\frac{v}{b}\right)^2 + \left(\frac{w}{c}\right)^2 \quad \text{else} \tag{2}$$

$$q = q_r \quad \text{if } u < 0 \quad \text{and} \quad 1 > \left(\frac{u}{a_r}\right)^2 + \left(\frac{v}{b}\right)^2 + \left(\frac{w}{c}\right)^2 \quad \text{else} \quad q = 0 \tag{3}$$

The double-ellipsoidal heat source is used. In contrast to Goldak's assumption [3], a constant distributed heat source density is assumed over the ellipsoid [2] according to Eqn. (1) to (3). In Eqn. (1) to (3)  $q$  denotes the energy density per unit time,  $Q$  denotes the energy per unit time,  $a$ ,  $b$  and  $c$  denote the radii of the ellipsoid and  $u$ ,  $v$ ,  $w$  denote the local heat source coordinates, with respect to indices  $f$  as front and  $r$  as rear. A single-phase material model is applied which considers the transformation strain and temperature dependent material parameters. For the mechanical material part, LS-DYNA material model \*MAT\_270 is used and \*MAT\_T07 for the thermal material model, respectively.

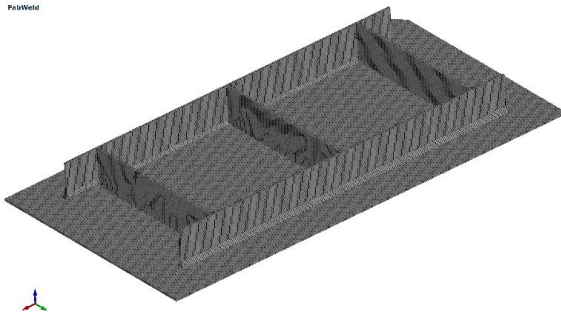
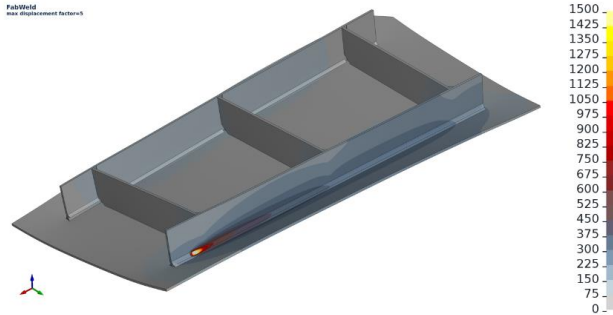


Fig. 6 Simulation - model mesh

FabWeld is used for the model setup and the LS-DYNA code for the calculation. In Fig. 7 the calculated temperature field on 5-times magnified deformed structure is displayed.



**Fig. 7** Temperature displayed on 5-times magnified deformed structure

## RESULTS

Fig. 8 to Fig. 12 show the result of the validation test for the five cable wire sensors. The graph compares the vertical deformations measured with cable wire transducers with the calculated vertical deformations. It can be seen on the graph that the deformation jump caused by removing the center bearings after tack welding is accurately represented by the simulation. The vertical distortion during the entire welding process is also calculated correctly. This proves that the applied calculation method of the weld structure simulation can accurately reproduce the deformation behavior during the entire welding process. This finding is new, since previously only final results, i.e., the condition after welding and cooling, were used for validation. In order to fully use weld structure simulation to analyze welding, the simulation results must also be accurate throughout the process. For example, this comes into play when the gap formations during welding are to be investigated to check the clamping or tacking concept.

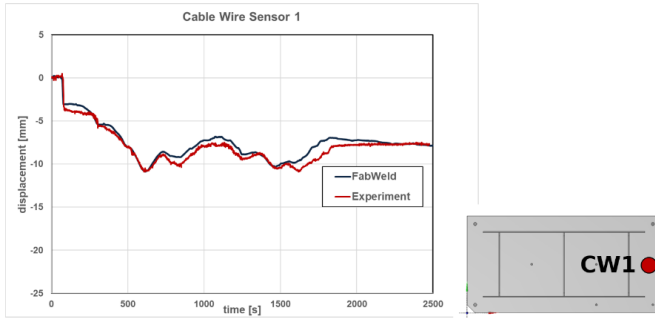


Fig. 8 Result cable wire sensor 1

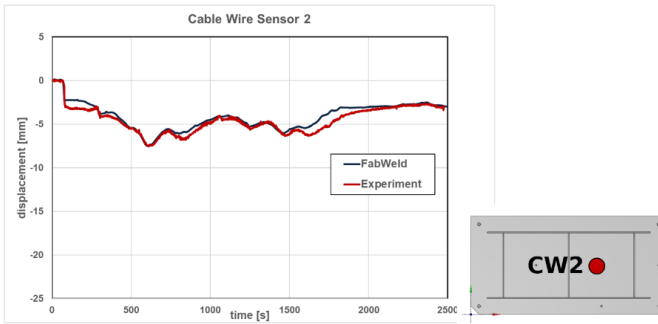


Fig. 9 Result cable wire sensor 2

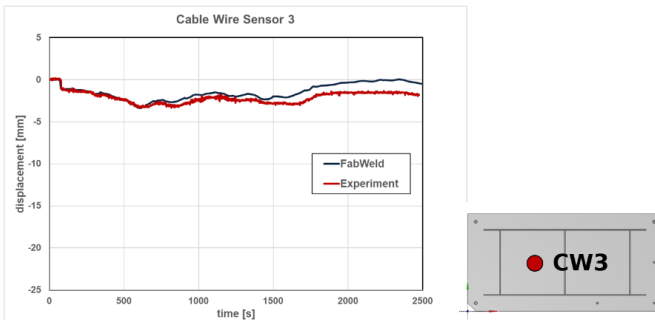


Fig. 10 Result cable wire sensor 3

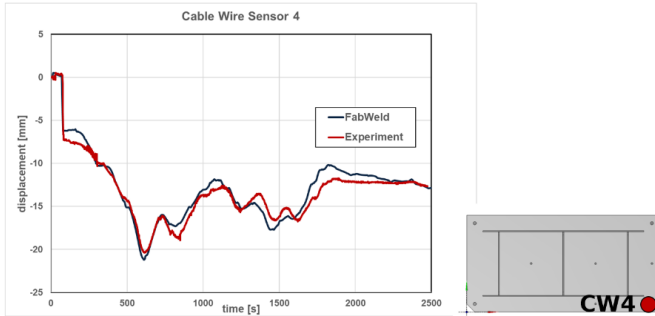


Fig. 11 Result cable wire sensor 4

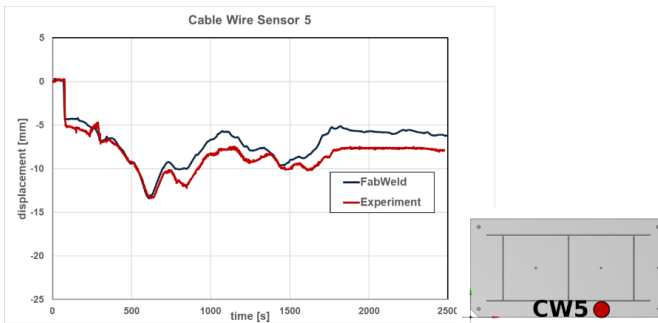


Fig. 12 Result cable wire sensor 5

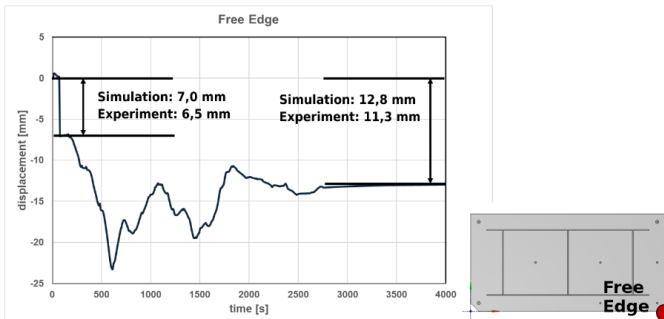
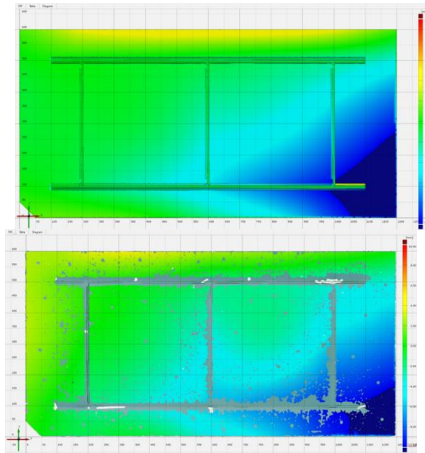


Fig. 13 Vertical deformation on free edge

Fig. 13 shows the vertical deformation on the free edge. The calculation results are confirmed by discrete measured values from the physical experiment. Firstly, the vertical

jump when removing the temporary jacks after tack welding, and secondly by the total distortion after complete cooling. In addition, the warped structure after complete cooling is also calculated correctly. This is shown by the comparison of the surface deviation in Fig. 14.



**Fig. 14** Surface deviation. Left simulation, right experiment

## SUMMARY AND CONCLUSION

An orthotropic plate made of low alloyed steel grade S235JR with gas metal arc fillet welds is chosen for validation experiment to demonstrate the calculation quality of the welding structure simulation. The model is set up according to the state of the art.

It could be shown, if one

- predicts the material behavior correctly,
- predicts the driving physical effects,
- predicts the right boundary conditions,
- predicts the process correctly,
- compares synchronized data - same location - same time,

one obtains agreement between virtual simulation and real experiment.

This study shows that weld structure simulation can be used for accurate distortion prediction. This makes it possible to understand the distortion behavior and to perform efficient distortion management.

References

- [1] J. WANG, M. SHIBAHARA, X. ZHANG, H. MURAKAWA: 'Analysis of Twisting Distortion of Thin Plate Stiffened Structure Caused by Welding', *Journal of Materials Processing Tech.*, 2012, Vol. 212, Issue 8, pp 1075-1715.
- [2] T. LOOSE and J. ROHBRECHT: 'Equivalent energy method for welding structure analysis', *Welding and Cutting*, Vol. 17, No. 3, 2018.
- [3] J. GOLDAK, A. CHAKRAAVARTI, M. BIBBY: 'A new finite element model for welding heat sources', *Metallurgical Transactions B*, pp. 299-305, 1984.

# NUMERICAL SIMULATION OF L-PBF ADDITIVE MANUFACTURING OF MEDIUM- MANGANESE STEEL FOR AUTOMOTIVE CRASH APPLICATIONS

K. ABBURI VENKATA\*, B. SCHOB\*\*, M. KASPROWICZ\*\*\*

*\*Simufact Engineering part of Hexagon, 21079 Hamburg, Germany*

*\*\*Technische Universität Chemnitz, 09107 Chemnitz, Germany*

*\*\*\*Wadim Plast Sp. z o. o., 05-816 Reguły, Poland*

DOI 10.3217/978-3-85125-968-1-19

## ABSTRACT

Advanced High Strength Steels (AHSS) such as dual-phase steels are favoured for conventional crash box applications due to the excellent combination of strength and ductility. Generation three AHSS steels such as medium-Manganese Transformation Induced Plasticity (TRIP) steels are a possible alternative to fabricate prototype crash-boxes with equivalent properties of a conventional crash-box due to the TRIP effects. Laser Power Bed Fusion (L-PBF) can produce prototype crash boxes without the requirement of costly dies as in conventional manufacturing. This allows significant benefit in lead times and cost efficiency in manufacturing prototype crash boxes. A reliable numerical simulation tool can predict the L-PBF build process accurately while considering the thermo-metallurgical and mechanical behaviour of the material under multiple thermal cycles and aid the prototype design phase. In the current paper, an improved methodology for the simulation of L-PBF build process using finite element (FE) framework is presented. The proposed methodology provides better spatial resolution of the build process and considers the effects of phase transformation in the medium-Manganese TRIP steel during multiple thermal cycles thereby increasing the accuracy of numerical predictions. The model is set-up and analysed using commercial software Simufact Welding 2022 based on FE solver Marc 2021.2. A comparison of the simulation results with that of experimental analysis on a simple cantilever and a representative double-hat profile crash geometry indicates a very good agreement proving the suitability of the current approach for accurate simulation of L-PBF process whilst maintaining reasonable computational efficiency.

Keywords: L-PBF, additive Manufacturing, medium-Manganese TRIP steel, crash box, numerical simulation

## INTRODUCTION

Deep-drawn parts are normally used in crash applications for body-in-white (BIW) vehicle structures [1, 2]. Automotive crash box is one of the most important parts for crash energy absorption and is equipped at the front end of a car [3]. The crash boxes connect the bumper cross member to the longitudinal beam and converts the dynamic

energy to deformation energy in case of frontal crashes. Manufacturing of these parts in conventional ways, even in prototyping phase, requires expensive tooling such as forming dies making the whole process time consuming and costly and therefore forms a serious bottleneck in the vehicle development process.

The need for improved fuel economy and reduced CO<sub>2</sub> emissions in automotive industry has led to significant developments in lightweight materials with higher strength [4]. The conventional materials such as low carbon steels and cast steels are replaced with Advanced High Strength Steels (AHSS) such as dual steels, Transformation-Induced Plasticity (TRIP) steels due to their superior stiffness, strength, crash energy absorption capacity and low production costs in large quantities [5, 6]. In addition, the better formability of AHSS steels provides greater flexibility to optimise the component geometry.

Even with the flexibility in design and advanced materials, there are still significant lead times and costs incurred in conventional deep-drawing approaches owing to the expensive tooling and dies. Any design modification even in prototyping phase requires new tooling which can quickly escalate the costs and manufacturing lead times in the development process. On the other hand, Additive Manufacturing (AM) specifically, Selective Laser Melting (SLM) or Laser-Powder Bed Fusion (L-PBF) offer enormous design freedom while lowering the manufacturing times significantly [4].

The suitability of the L-PBF process to crash applications requires not only printing of the parts but also achieving the desired stiffness and crash performance of components produced by the AM process. The materials currently available for AM were not specifically developed for automotive industry which is further true for crash applications. Furthermore, the quality of materials produced by L-PBF process usually is unsuitable for crash applications. Therefore, appropriate post-processing is required to achieve the desired equivalent crash behaviour to that of conventional crash bodies.

With these considerations, a novel medium manganese TRIP steel is considered that was specifically developed for automotive applications using L-PBF process with minor modifications in the composition [7, 8]. In order to understand the overall influence of manufacturing history on the final crash performance of the component, a simulation model of the whole manufacturing process chain is indispensable.

In the present paper a simulation framework is presented for the numerical analysis of L-PBF process and post-processing of the novel medium manganese TRIP steel developed for crash applications. The simulation approach incorporates the multi-cycle Solid-State Phase Transformation (SSPT) experienced by this material during the build as well as the phase reversion during post-build heat treatment (HT). The results are validated with experimental investigations on a simple cantilever and a representative crash geometry (double hat profile) for the entire process chain.

EXPERIMENTAL INVESTIGATION

For the purpose of this research an experimental medium manganese steel was investigated, whose chemical composition is provided in Table 1. The details of the development of the steel and the material properties are already published elsewhere [8].

**Table 1** Chemical composition of the experimental medium manganese steel

Element	Fe	Mn	Si	Al	P	C	S	O	N	H
(%)	balance	7.5– 8.5	0.4– 0.5	1.7– 2.0	0– 0.05	0.08– 0.15	0– 0.05	0– 0.05	0– 0.03	0– 0.005

Two specimen geometries were fabricated to validate the simulation framework developed for the whole process chain. The first geometry is a simple cantilever specimen and the second is a complex representative geometry of the crash box namely double hat profile. The two specimens are shown in Fig. 1. The specimen dimensions are  $72\text{mm} \times 12\text{mm} \times 15\text{mm}$  and  $118\text{mm} \times 79\text{mm} \times 200\text{mm}$  for the cantilever and double hat geometries respectively. The nominal thickness of the double hat profile is 2 mm.

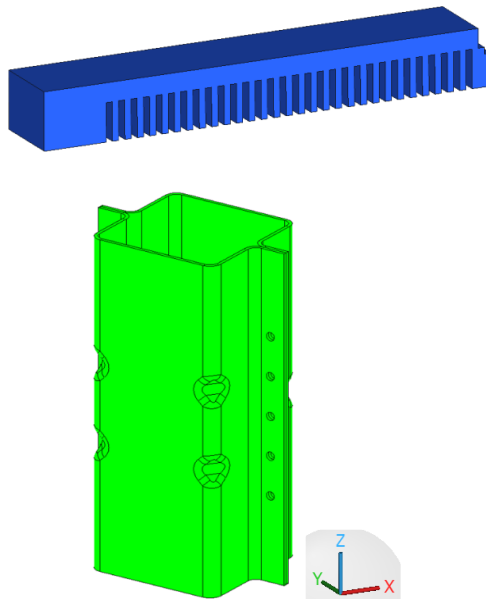


**Fig. 1** Cantilever specimen (top) and double hat geometry (bottom)

The process parameters and heat treatment conditions for both geometries are provided in Table 2 and Table 3 respectively. The deflection of the cantilever geometry was measured in as built and HT conditions as +0.69mm and -0.25mm respectively, by using

a cutting plane at a height of 2.6mm from the base of the cantilever. Three-dimensional (3D) surface scan was performed on the double hat profile in build and HT conditions which were then used to validate the predictions from the simulations.

**Table 2** SLM process parameters for double-hat geometry

Geometry	Laser power (W)	Laser speed (m/s)	Hatch distance (mm)	Layer thickness (mm)	Laser spot diameter (mm)
Cantilever	250	1.0	0.08	0.03	0.1
Double hat	265	1.0	0.09	0.03	0.1

**Table 3** HT parameters for cantilever and double hat geometry

Geometry	Hold Temperature (C)	Hold time (h)
Cantilever	670	1.0
Double hat	670	6.0

Post-build global HT (heat treatment) is applied to the cantilever and double-hat geometry such that the content of austenite is significantly increased and the yield strength of the material is reduced to acceptable levels (~ 650 - 675 MPa) as that of conventional crash-box material. Careful investigation was undertaken to determine the right HT hold temperature and hold time such that the material has desired crash properties subsequently. It was determined that HT at 670 °C for 6 h on the double hat geometry resulted in best material properties with an austenite content of ~ 40% through experimental investigation. On the cantilever specimen, HT at 670 °C was applied for 1 h to achieve similar levels of austenite in the component after HT.

## NUMERICAL INVESTIGATION

### L-PBF BUILD

To ensure better accuracy of the L-PBF process and capture the transient thermal behaviour effectively, without entirely sacrificing computational efficiency, a different scheme of layer deposition than conventional approach is utilised. The details of the implementation and the approach were published in Ref. [8]. Based on the equivalent heat flux method, the power required for heating the entire track is calculated, keeping the heating time and the velocity of the robot the same as in the actual L-PBF process. To increase the accuracy of the predictions in the baseplate, a mesh refinement is used in the baseplate closer to the double-hat and the regions away from the part are meshed with coarser elements. First order hexahedral elements with an approximate size of 1 mm are used for meshing both the geometries. In order to facilitate the creation of structured mesh, the holes in the geometry are ignored as these can be later created via a machining simulation.

The model is set-up in commercial welding software Simufact Welding 2022 (based on Finite Element (FE) solver Marc 2021.2) using the dedicated DED (Directed Energy Deposition) module. Considering that the thermal behaviour of the molten material is the major contributor to the subsequent stress/strain and phase generation in L-PBF process, which is similar to that of DED fundamentally, the analysis was modelled using DED

module for ease of modelling and usage of certain in-built features. The mesh of the cantilever and double hat geometry along with the baseplates are shown in Fig. 2 and Fig. 3 respectively. The baseplate is considered as the same material as that of components and maintained at a temperature of 125 °C during the build process. To avoid rigid body movement, some nodes on the bottom surface of the baseplate are fixed. Temperature dependent thermal, mechanical properties and stress/strain curves generated using JMatPro were employed for the thermo-mechanical simulation of the SLM process. Element activation and deactivation is used to mimic the deposition of powder layers sequentially.

Furthermore, in L-PBF process, the build part is surrounded by powder that acts as a heat insulation and therefore, the heat loss to the surroundings is significantly different than that of a DED process. The simulation has been modified to take this into account by allowing only the top surface of the current layer to contribute to the heat losses. Since the available top surface for heat loss changes dynamically with every new track, this surface is recalculated after every subsequent new track is laid. In order to achieve this constant time stepping scheme was used for the heating process to recalculate the available surface for convection/radiation during L-PBF build.

The heat loss from the top surface is calculated using a convective heat transfer coefficient of 250 W/m<sup>2</sup>K and a radiation emissivity of 0.9. The contact heat transfer coefficient between the part and the baseplate is also modelled using a contact heat transfer coefficient of 1000 W/m<sup>2</sup>K. The entire cantilever and double-hat profile are considered as single parts with no contact considerations between one layer to another and therefore no contact heat transfer is modelled between individual layers of the specimens.

### MULTI-CYCLE SSPT

During the build process the previously deposited layers will be subjected to multiple thermal cycles, leading to multiple phase transformation or even partial phase transformation during heating from martensite to austenite. Similarly, during cooling down, there can be several cases where the handling of retained austenite requires different approaches. To support the simulation of phase transformation of the material during multiple cycles and accurately predict the phases and the volume change effects, a new methodology is suggested where partial transformation during heating and handling of retained austenite for various cool down scenarios are proposed.

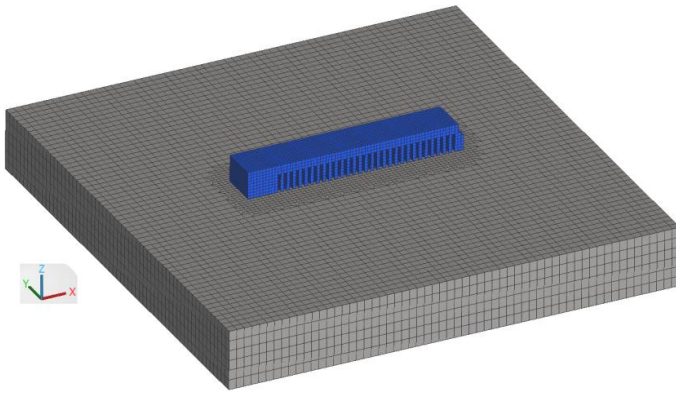


**Fig. 2** FE mesh of the cantilever specimen with baseplate highlighting mesh refinement on baseplate

**Object type**

- Component (1)
- Weld bead (1)

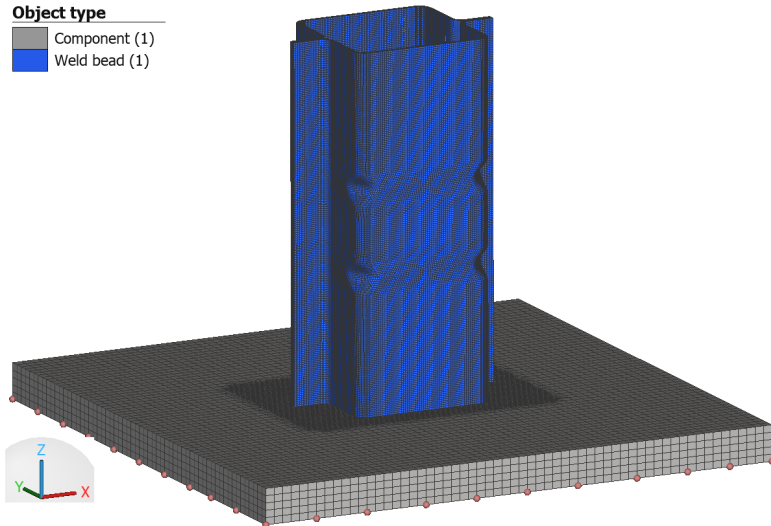


**Fig. 3** FE mesh of the double hat geometry with baseplate highlighting mesh refinement on baseplate

This also handles the volume change effects during transformation. The phase change during heating is based on linear austenitisation rule and the martensite formation during cooling uses Koistinen-Marburger (KM) relation [9].

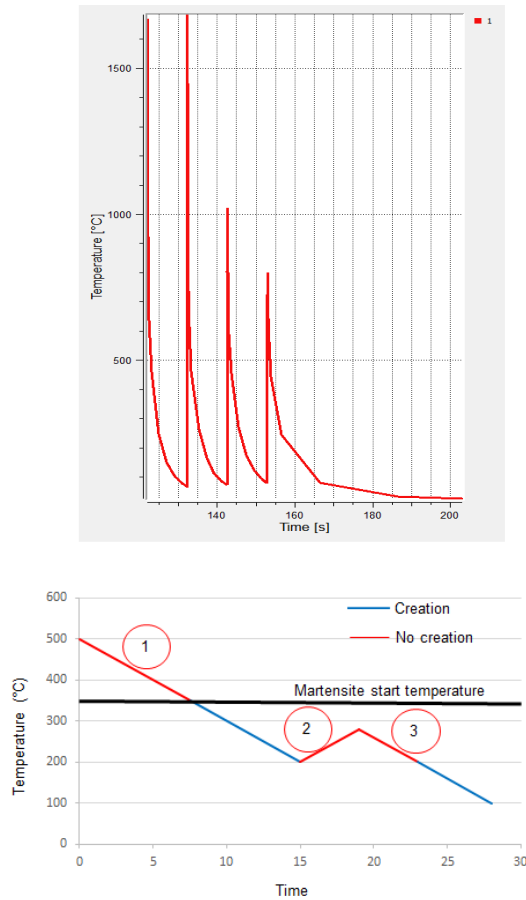


**Fig. 4** Predicted multi-cycle thermal history (top) and phase evolution (bottom) during L-PBF build of medium manganese experimental TRIP steel

A schematic of the various cases for creation and non-creation of martensite during cool down is presented in Fig. 4 (bottom). The figure depicts only the cool down cases and the logic of martensite phase formation during multiple thermal cycles. The region shown as 1 indicates the cooling down of material but above martensite start temperature, whereas regions 2 and 3 indicate situations where the temperature of the material point during subsequent thermal cycles, does not go beyond martensite start temperature but is definitely more than the temperature state from previous cycle's cooling stage. In these situations, there will not be any martensite creation. The regions marked blue are those where martensite calculation is undertaken. In order to transform retained austenite to martensite, without reheating above AC1 (no fresh austenite), additional thermal or

mechanical energy should be available than the previous cooling state. This is due to increased stability of retained austenite due to increased amount of carbon, which also reduces the  $M_s$  (martensite start temperature) significantly. So further transformation is only achieved by cooling down below the previous cooling temperature. Since region 3 is above this, it is considered that the thermal energy available here is not enough to convert the retained austenite to martensite. Any TRIP effects present during the build process are ignored due to lack of any appropriate material data or evidence for such an effect during the build process.

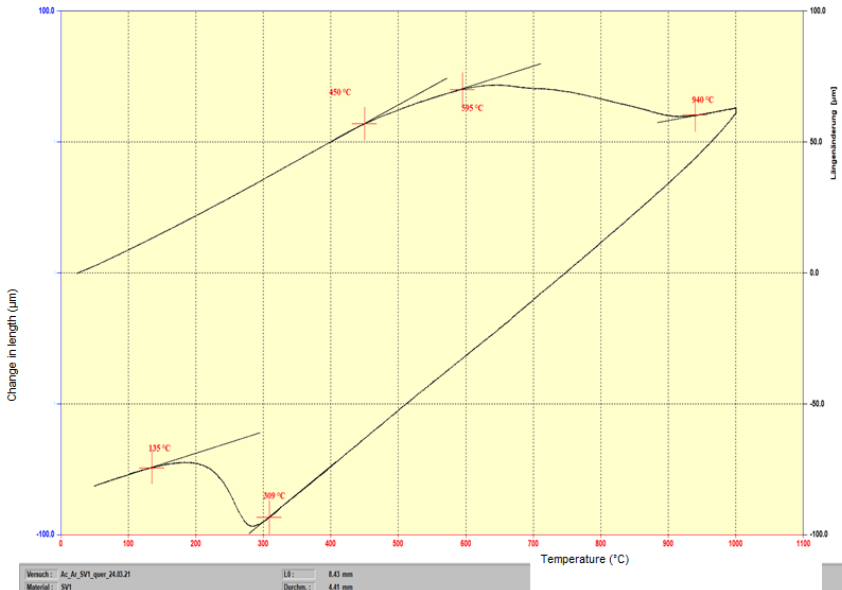


**Fig. 5.** Experimental dilatometry data for the proposed TRIP steel

The volume change associated with martensitic transformation has a significant influence on the stress/strain behaviour during welding process and this has been accounted using KM equation and the dilatational change measured through experiments as shown in Fig. 5. The tests were conducted with a heating rate of 30 K/s and a cooling rate of 100 K/s. Using the same dilatometry data, the temperatures AC1 (austenite start temperature), AC3 (austenite finish temperature),  $M_f$  (martensite finish temperature) and  $M_s$  (martensite start temperature) were identified. Linear austenitisation rule was applied between AC1 and AC3 to calculate the percentage of austenite formation as a function of temperature.

### HT SIMULATION AND BASEPLATE REMOVAL

Post-build HT was simulated using the HT module in Simufact Welding 2022 as part of process-chain modelling, in order to achieve the required microstructure and material properties for crash applications. During HT, history from build process was considered as initial state and the residual stresses/strains, local hardening and phase distribution were predicted for the cantilever and double hat geometries. This allowed for the relaxation and redistribution of residual stresses/strains from the build process during HT due to reduced yield strength at higher temperatures. In addition, the martensite and austenite phases were also predicted using KM equation, after HT, resulting in further modification of the material properties. The KM parameters were calibrated such that the martensite and reverted austenite phase fractions were ~60% and 40% respectively after HT. Creep was not considered during HT simulation due to lack of appropriate material data.

After HT, the baseplate was removed through machining which was also simulated as part of process-chain modelling. The resulting residual stresses/strains from the HT simulation were provided as initial state to the cutting simulation which was also modelled using Simufact Welding 2022. Since there was no thermal behaviour during cutting, elastic-plastic material behaviour was assumed during the cutting process. The baseplate was removed using “DEACTIVATE” elements option which simulated the removal of material and relaxation of internal stresses/strains due to the deformation of the part. The phase behaviour was also not considered as the material phases are not expected to alter during the cutting operation.

### MAPPING OF RESULTS FOR CRASH SIMULATION

The purpose of the process-chain simulation and analyses was so that the actual material state prior to crash simulation, arising from the manufacturing history, is accurately captured. Consequently, the aim of the research is to analyse the material state through predictions throughout the process-chain and finally apply this as initial state to the crash simulations. The build, HT and subsequent baseplate removal simulations were all analysed using 3D hexahedral elements whereas crash simulation requires a shell mesh. So, it was essential to map results such as stresses and local hardening after baseplate removal simulation, to a shell mesh. This was achieved using a third-party mapping software MpCCI mapper developed by Fraunhofer SCAI [10]. The kinematic result quantities such as residual stresses/strains were mapped from the hexahedral mesh to the shell mesh. This was achieved through aligning the positions of both meshes in a coordinate system.

RESULTS AND DISCUSSION

BUILD PROCESS

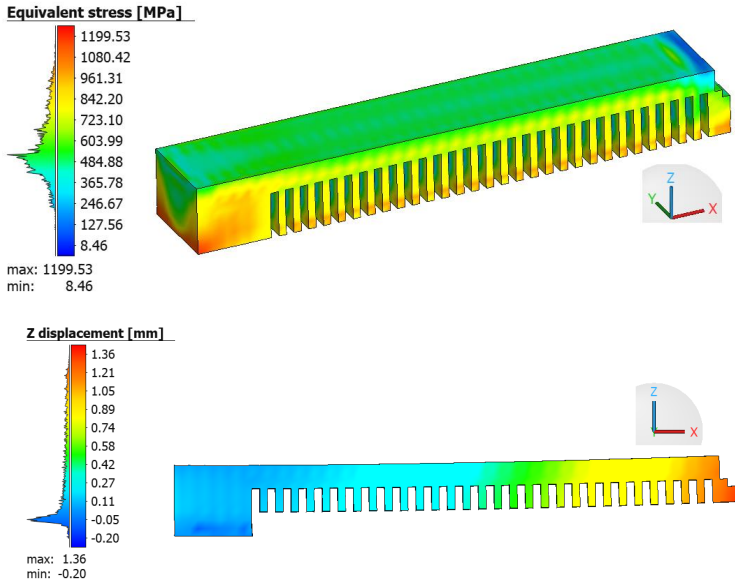


**Fig. 6** Predicted equivalent stress in cantilever geometry after build (top) and displacement of the cantilever after cutting in build state



**Fig. 7** Printed cantilever for experimental investigation and validation of simulation

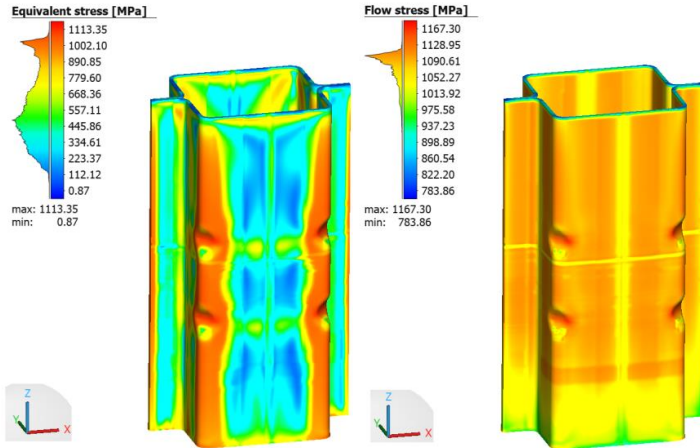


**Fig. 8** Predicted equivalent stress (left) and flow stress in the double-hat specimen (right)

Based on the simulation methodology presented in above sections in addition to the material phase transformation modelling, the thermal history in the double-hat profile is predicted which was used to predict the phase evolution, stresses and deformation in the part. Fig. 6 shows the equivalent stress distribution predicted in the cantilever (top) and the deflection of the cantilever after cutting from the baseplate is shown below. It is to be noted that in both cases the cantilever is attached fully and partially to the baseplate respectively, although it is not displayed. The positive deflection of the cantilever is +1.36 mm which is larger than the measured deflection (see EXPERIMENTAL INVESTIGATION). However, this discrepancy can be attributed to the presence of another cantilever built on the same baseplate as evident from Fig. 7, which can alter the thermal behaviour during the build process. Nevertheless, the deflection direction matches between the predictions and measurements.

Fig. 8 shows the equivalent stress distribution predicted in the double hat specimen on the left side and the flow stress/hardening on the right. Results indicate that AM process introduces considerable residual stresses and hardening in the part due to repetitive thermal cycles. The distribution of martensite phase and total deformation is presented in Fig. 9. It can be seen from the phase distribution that the martensite phase is not the same across various regions in the layer. The same is observed in the temperature predictions in the part as depicted in Fig. 10 (left) where the temperature predictions are different between layers and also within a certain layer. The analysis has been terminated when the temperature at every integration point reached below 50 °C to save computational time.

The image on the right side in Fig. 10 shows the track-based deposition of the layer profile from left to right. It is interesting to note that the temperature in the previously deposited layer is different across various tracks in the same layer, owing to the differences in the deposition and cooling times/sequence within the layer. This shows that with the proposed methodology greater resolution is achieved within a layer. These differences in the cooling times/sequence led to differences in the predicted martensite

fractions within a layer. Since the stresses are calculated as a weighted sum of the individual phase fractions, the hardening and the flow stress values are also different within a layer, thereby providing greater spatial resolution and improved accuracy in the overall performance of simulation.

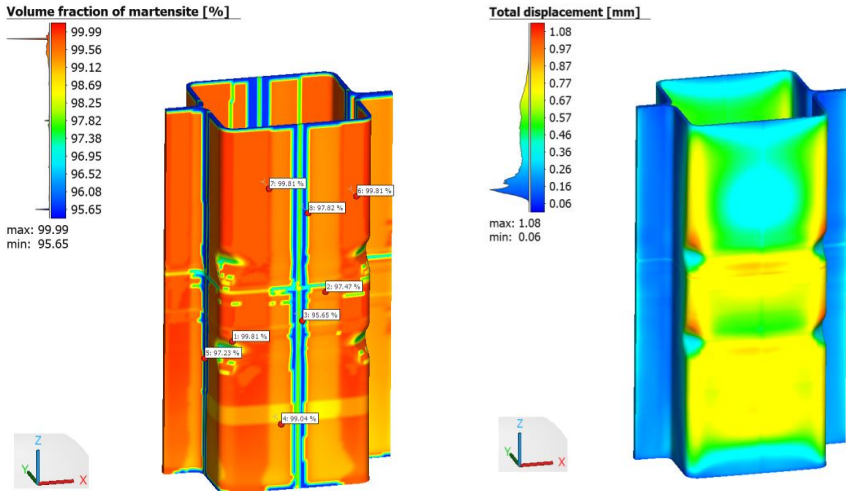


**Fig. 9** Martensite volume fraction as a function of component dimensions (left) and total displacement (right) in the double-hat specimen due to L-PBF build

#### HT AND BASEPLATE REMOVAL

The residual stresses (top) and deformation (below) in the cantilever specimen subsequent to HT and partial cutting of the baseplate are shown in Fig. 11. It is interesting to note that the deformation profile indicates a downward deflection with a magnitude of -0.64 mm after HT. This agrees qualitatively well with experimental results where the deflection of the cantilever was negative after HT. Fig. 12 shows the predicted martensite phase in the cantilever specimen after HT process.

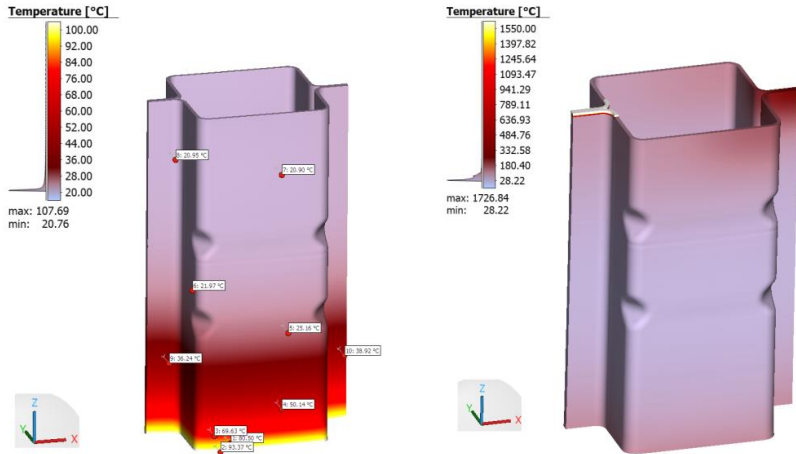


**Fig. 10** Predicted temperature distribution in the double-hat specimen (left); track based element activation (right)

The predicted martensite phase (left) and total deformation (right) in the double hat specimen after global HT process are displayed in Fig. 13. It is seen that after HT, the overall martensite fraction drops to 60% as opposed to ~99% from the build simulation. Fig. 14 shows the equivalent stress in the specimen after HT (left) and removal of baseplate (right) respectively. It is visible that the residual stresses are reduced significantly due to HT compared to that of the build simulation, which are further relaxed with the removal of baseplate. This clearly demonstrates that the process-chain simulation has captured the real material behaviour satisfactorily.

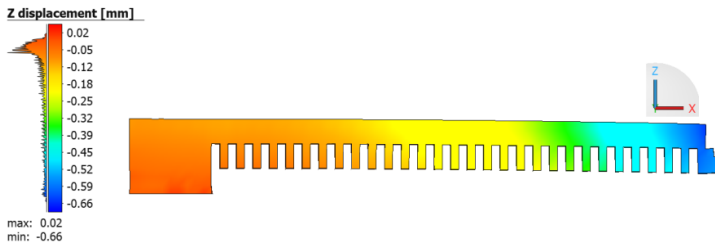
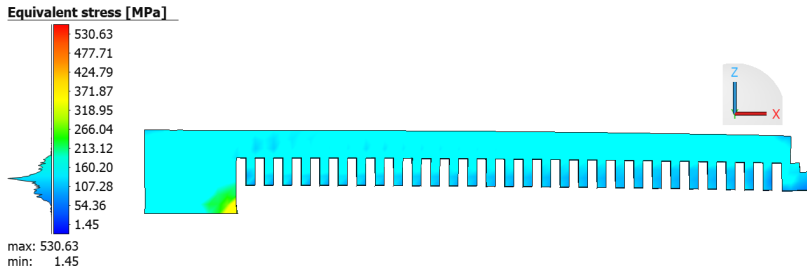


**Fig. 11** Predicted residual stresses (top) and deflection (below) in the cantilever specimen after HT and removal of baseplate

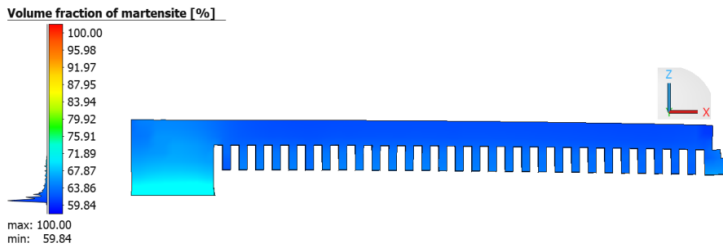


**Fig. 12** Predicted martensite phase in the cantilever specimen after HT

#### VALIDATION OF SIMULATION PREDICTIONS

To validate the build simulation and the predicted behaviour of the cantilever and double hat profile, comparison of predictions with experimental measurements was performed. For the cantilever profile, the measured deflection of the cantilever in build and HT conditions, due to partial cutting of the baseplate was compared with that from predictions. A good agreement was observed in the deflection profiles qualitatively with measurements.

The experimentally measured 3D surface scan of the double hat specimen is compared against that of predicted profile/surface of the geometry after build simulation using GOM Inspect 2018 tool. The comparison of the scanned profile of the geometry with that of predicted scanned profile is displayed in Fig. 15. The measurements were made on the specimen with the baseplate still attached, after the build. It is observed that the predictions match closely with experiments especially closer to the baseplate. As the build height increases, there is a variation of  $\sim 1.2$  mm between the measured and predicted profiles. This can be explained due to the discrepancies between the predicted and actual thermal profile inside the build chamber as the build height increases. Another reason to which this difference can be ascribed to is the assumed material properties in the simulation. Since these were extracted using JMatPro rather than actual material characterisation, this can lead to some variation in the results.

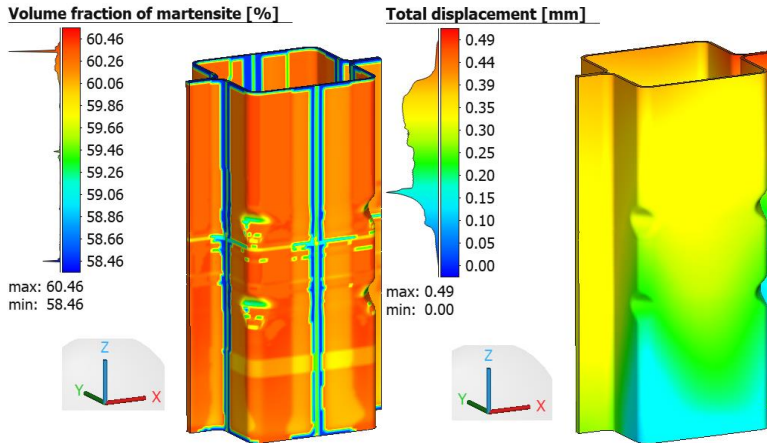


**Fig. 13** Predicted martensite phase (left) and total deformation (right) in the double hat specimen after HT and removal of baseplate

The predicted stress relaxation due to HT and removal of baseplate of the double hat profile is also validated with experimental measurement as shown in Fig. 16. The measured surface of the double hat specimen after HT and removal of baseplate is compared against measured surface. It is observed that the simulation predictions match very well with those from experiments validating the process chain simulation.

#### MAPPING OF RESULTS

The mapped values of the stresses and strains onto the shell mesh are shown in Fig. 17 top and bottom respectively. Comparing Fig. 14 (right) and 17 (below), it can be agreed upon that the results from the hexahedral mesh were mapped accurately onto the shell mesh. This shell mesh with the mapped stresses and hardening will be used subsequently in

crash simulation. In this manner the entire manufacturing and process history of the crash specimen is considered in crash simulation for greater accuracy.

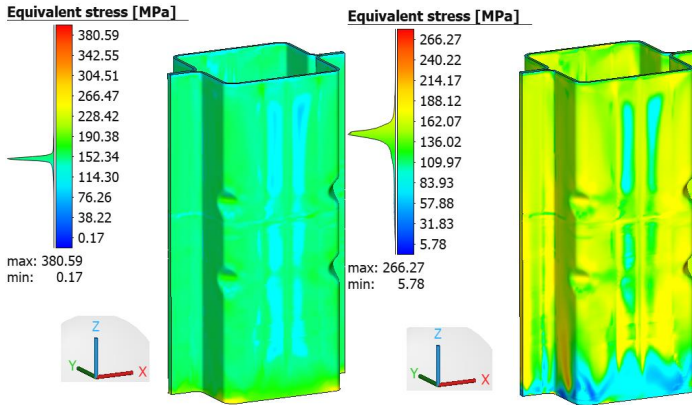


**Fig. 14** Predicted residual stresses in the double hat specimen after HT (left) and removal of baseplate (right)

## CONCLUSIONS

The paper presented a framework for the process-chain simulation for manufacturing prototype components for crash applications using L-PBF. The build process, HT and baseplate removal are simulated to predict the final material state for crash applications. Advanced material behaviour such as multi-cycle phase transformation and phase change during build and HT processes are captured in the simulation. The process-chain is tested on two different geometries namely cantilever and double hat profile to study the suitability of the simulation framework for L-PBF manufacturing of crash components. Based on the work presented the following conclusions can be drawn.

1. Simulation of L-PBF with increased spatial and temporal resolution increases the accuracy of the predictions.
2. It is essential to capture the multi-cycle phase transformation of the material during L-PBF build for accuracy and reliability in predictions.
3. Validation of the simulation framework on simple geometries such as cantilever can improve confidence in the predictions.
4. The simulation framework developed enables the consideration of manufacturing history and appropriate material state in a valid manner for high fidelity applications such as crash using L-PBF process.

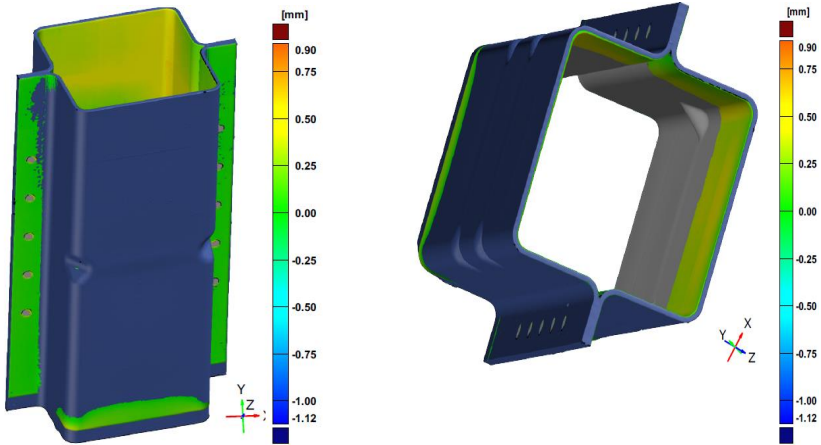


**Fig. 15** Comparison of predicted and measured surface profile of double-hat geometry after build

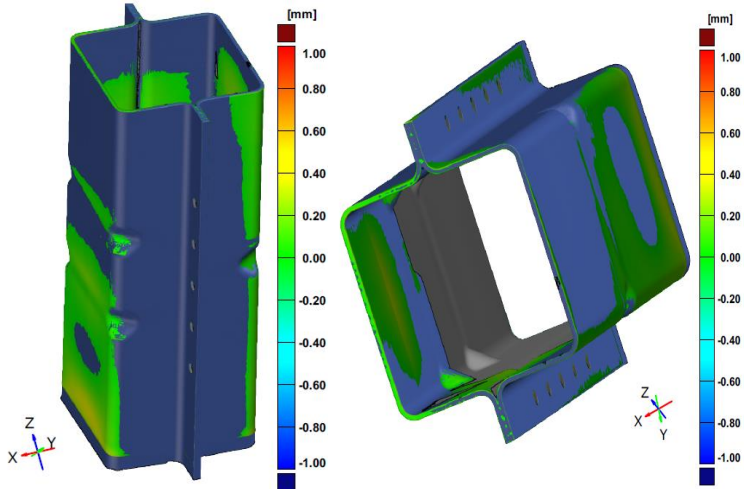


**Fig. 16** Comparison of predicted and measured surface profile of double-hat geometry after HT and removal of baseplate

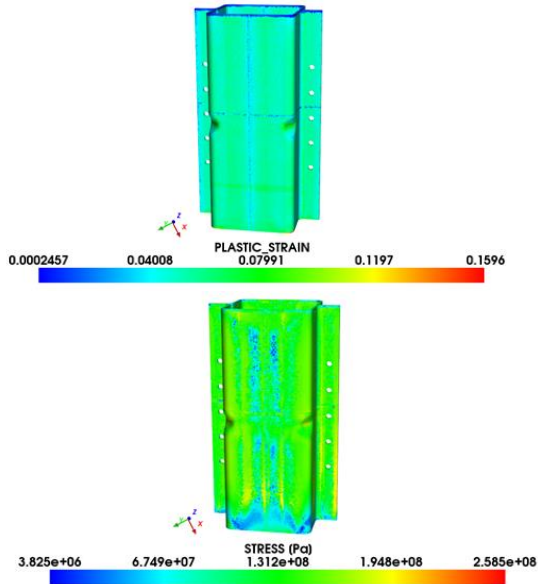


**Fig. 17** Mapped equivalent plastic strain (top) and stress (below) on double hat shell mesh with holes

### ACKNOWLEDGEMENTS

This work was performed within the project “Additive Manufacturing Technologies for Crash loaded structural Components (AM-Crash)” and supported by the Federal Ministry of Education and Research (BMBF) and by the Polish National Centre for Research and Development (NCBR) under international programme M-ERA.NET 2 Cofund Financial support is gratefully acknowledged. The authors are grateful for all the support, experimental and validation data from project partners.

### References

- [1] C.D. HORVATH: ‘Advanced steels for lightweight automotive structures, Materials, Design and Manufacturing for Lightweight Vehicles’, *Woodhead Publishing*, 2010, Pages 35-78, ISBN 9781845694630, <https://doi.org/10.1533/9781845697822.1.35>.
- [2] A. DEB: ‘Chapter 11 - Crashworthiness design issues for lightweight vehicles, Materials, Design and Manufacturing for Lightweight Vehicles’ (Second Edition), *Woodhead Publishing*, 2021, Pages 433-470, ISBN 9780128187128, <https://doi.org/10.1016/B978-0-12-818712-8.00011-2>.

- [3] N.S. YUSOF, S. SAPUAN, M.T.H. SULTAN, M. JAWAID, M. MALEQUE: ‘Design and materials development of automotive crash box: a review’, *Ciência & Tecnologia dos Materiais*, 29, 2017, 129-144. [10.1016/j.ctmat.2017.09.003](https://doi.org/10.1016/j.ctmat.2017.09.003).
- [4] A. BORRELLI, G. D’ERRICO, C. BORRELLI, R. CITARELLA: ‘Assessment of Crash Performance of an Automotive Component Made through Additive Manufacturing’, *Applied Sciences*, 10(24), 9106, 2020, <https://doi.org/10.3390/app10249106>.
- [5] J. GALAN, L. SAMEK, P. VERLEYSEN, K. VERBEKEN, Y. HOUBAERT: ‘Advanced high strength steels for automotive industry’, *Revista de Metalurgia*, 48(2), 18-131, 2012, doi: 10.3989/revmetal.115.
- [6] R. KUZIAK, R. KAWALLA, S. WAENGLER: ‘Advanced high strength steels for automotive industry’, *Archives of Civil and Mechanical Engineering*, 8(2), 2008, DOI: 10.1016/S1644-9665(12)601.
- [7] M. HOFEMANN et al.: ‘Ein niedriglegierter Stahlwerkstoff für die Laseradditive Fertigung Prozesskette und Eigenschaften’, In: Lachmayer R., Rettschlag K., Kaieler S. (eds) *Konstruktion für die Additive Fertigung 2019*, Springer Vieweg, Berlin, Heidelberg, 2020, [https://doi.org/10.1007/978-3-662-61149-4\\_3](https://doi.org/10.1007/978-3-662-61149-4_3).
- [8] K. ABBURI VENKATA et al.: ‘Accurate numerical prediction of thermo-mechanical behaviour and phase fractions in SLM components of advanced high strength steels for automotive applications’, *Technologies for Lightweight Structures* 5(1), 2021, pp. 41-50, Special issue: 5th International MERGE Technologies Conference (IMTC), 1<sup>st</sup>-2nd December 2021, Chemnitz.
- [9] D. KOISTINEN, R. MARBURGER: ‘A General Equation Prescribing the Extent of the Austenite-Martensite Transformation in Pure Iron-Carbon Alloys and Plain Carbon Steels’, *Acta Metallurgica*, 7, 59-60, 1959, [https://doi.org/10.1016/0001-6160\(59\)90170-1](https://doi.org/10.1016/0001-6160(59)90170-1).
- [10] <https://www.scai.fraunhofer.de/en/cross-sectional-topics/software-and-services-for-the-automobile-industry/mpcci-mapper-in-practice.html>.



# A SIMULATION APPROACH FOR SERIES PRODUCTION OF PLASMA-BASED ADDITIVE MANUFACTURING OF Ti-6Al-4V COMPONENTS

M. BIELIK\*, E. NEUBAUER\*, M. KITZMANTEL\*,  
I. NEUBAUER\*\*, E. KOZESCHNIK\*\*\*

*\*RHP-Technology GmbH, 2444 Seibersdorf, Austria*

*\*\*Simufact engineering GmbH, 21079 Hamburg, Germany*

*\*\*\*TU Wien, 1060 Vienna, Austria*

*DOI 10.3217/978-3-85125-968-1-20*

## ABSTRACT

Plasma Metal Deposition (PMD®) is a variant of a directed energy deposition (DED) process that uses an arc welding process to additively manufacture metal components. This process is characterised by relatively high deposition rates, low restrictions regarding the build space, low investment, and operating costs, and is, therefore, predestined for the series production of large structural parts. Additionally, advances in machine development, path planning, and the use of structural welding simulations are bringing these additive manufacturing (AM) technologies into the focus of modern production strategies. To ensure the quality of additively manufactured components in an exactly reproducible manner is, however, a challenge. This requires the complete reproducibility of the manufacturing process and the materials used. This paper investigates the Plasma Metal Deposition manufacturing process of a small batch of Ti-6Al-4V components. Numerical approaches for predicting temperature fields, distortions and residual stresses are examined using the Finite Element (FE) software Simufact Welding 8.0. The focus of the investigations is on the numerical analysis of the influence of the manufacturing process on the mechanical behaviour for multi-layer components. As an outstanding example, the manufacturing of an aerospace bracket is presented.

Keywords: Additive Manufacturing, Direct Energy Deposition, Plasma Metal Deposition, Space, Aerospace, Ti-6Al-4V, Simufact Welding

## INTRODUCTION

Additive manufacturing (AM) is a group of manufacturing technologies that build physical three-dimensional objects by successive addition of material. AM has shown substantial growth in recent years and it is assumed that the technology and the industry are reaching increasing market maturity. Therefore, a growing number of companies are using AM for customised products and series production [1]. Wire Arc Additive Manufacturing (WAAM) is an emerging technology that has become a very promising

alternative to high-value large metal components in various industries. The technology combines arc welding with wire feeding and is able to benefit from design freedom, buy-to-fly ratios as low as 1.8, potentially no constraints in size, and low cycle times [2], [3]. WAAM is a manufacturing technology similar to multi-pass welding, which can be used to build components such as flanges, brackets, rocket components, or printing directly on fabricated components, such as, a WAAM-printed fuselage with stiffening structures. Components are built layer-by-layer depositing the melted material along predefined welding paths creating the 3D printed structure. One of the limitations of the WAAM process, however, is the formation of distortions caused by the build-up of residual stress as a result of the large thermal gradients induced during the repeated melting and solidification of the material. Deformation and residual stresses of WAAM components (unclamped condition after the deposition process) have been studied extensively in [4]–[7] for titanium and steel structures. Residual stress is affecting several failure mechanisms including fracture and fatigue properties, stress corrosion cracking and distortion [8]. Thus, in order to optimise the WAAM process prior to the deposition and reduce residual stresses and distortion, a thermo-mechanical finite element (FE) model is set-up. By means of the simulation model, the temperature field, distortions, and residual stresses are predicted and analysed. The temperature field and its gradients have been determined by using Goldak’s double ellipsoid heat source model [9]. For the verification of the FE models, measurements have been performed on the deposited components with regard to temperature field distributions and weld deformations. The acquired simulation results are used for the production of a near-net-shape aerospace bracket.

## METHODOLOGY

### MATERIALS AND SET-UP

Deposition experiments are performed on Ti-6Al-4V baseplates with dimensions of 200x50x10 mm. Cold Ti-6Al-4V wire with a diameter of 1.2 mm is fed by an automatic wire feeder. High purity argon (99.99 %) is used as shielding and plasma gas. Thin-walled samples (so called demonstrators) are manufactured by depositing a single row of successive weld beads along the centreline of plates. Both, baseplates and welding wire with chemical composition listed in Table 1 are commercially sourced conforming to ASTM B265 and AWS A5.16-07, respectively.

**Table 1** Chemical composition of Ti-6Al-4V wire and base plates (wt.%)

	Ti	Al	V	Fe	C	N	H	O
Wire	Bal.	6.24	4.16	0.15	0.015	0.008	0.003	0.13
Base plates	Bal.	6.12	4.07	0.178	0.019	0.011	0.002	0.012

The equipment used for the welding process is shown in Fig. 1 (a) and consists of a complete WAAM system at RHP-Technology utilising plasma metal deposition. The AM process is enclosed in an airtight welding chamber filled with high purity argon with a

low moisture content, thus utilising a protective gas atmosphere and giving adequate shielding. In the case of oxygen sensitive materials, such as titanium, the encapsulated system allows manufacturing in a controlled environment, and potentially can reduce oxygen levels to less than 100 ppm. Two blind holes of 6 mm diameter are machined along the centreline of the base plates. These holes are used to additionally position the plates inside the working space and reference to the tool coordinate system (Fig. 1 (b)).

(a)



(b)

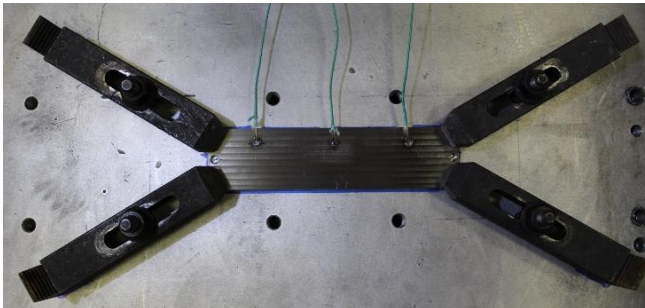


**Fig. 1** (a) Model of the welding chamber; (b) Experimental set-up inside the PMD system

The baseplates are fixed to the backing plate of the WAAM system using four clamps placed at specified positions to ensure identical clamping conditions for all demonstrators. The studs are tightened crosswise with a torque of 80 Nm. Prior to the AM process, the baseplates are degreased and cleaned with acetone to eliminate surface contamination. Deposition is initiated below a residual oxygen content of less than 100 ppm  $O_2$  measured

with a residual oxygen analyser OXY 3 by ORBITEC, which has a measuring range from 5ppm to 21 % O<sub>2</sub>. A single track wide bidirectional deposition strategy is adopted, i.e., the starting point of the next layer is where the previous layer finished. Cold wire is fed by an automatic wire feeder transversal to the welding direction to avoid rotation of the torch. Although in-house research at RHP-Technology has shown that a feed mode, in which the wire is fed ahead of the arc yields more consistent weld beads, the transversal position is a good compromise for the bidirectional welding strategy. Further automation of the custom-made machine would be required to rotate the torch according to the direction of deposition. The deposition strategy is shown in Fig. 2, where the orange lines represent the movement of the torch. A standard reference coordinate system of the single wall is defined, in which  $x$  is parallel to the travel direction of the torch,  $y$  is the transverse direction, and  $z$  is parallel to the building direction of the wall. When the torch comes to the end of the weld bead, the arc is extinguished, the torch increases its height in  $z$  direction and remains in this park position for a defined cooling time. After the dwell time has elapsed, the torch moves in negative  $z$  direction towards the end position of the previous layer and starts to deposit a new layer in the reverse direction. Thereby, the distance between the torch and the deposited layers is kept constant at 10 mm. This process is repeated until a desired number of layers is deposited.

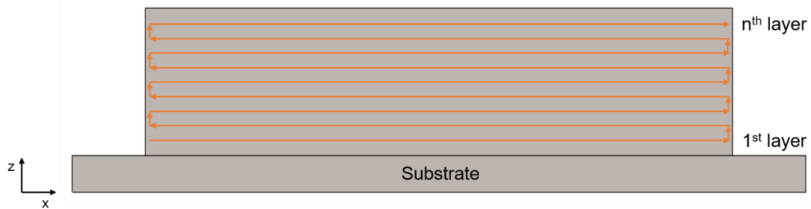


**Fig. 2** Bidirectional building strategy

The bidirectional strategy aims to mitigate the inconsistency in wall height as reported by Martina et al. [2]. Using a unidirectional welding strategy, i.e., starting each layer at the same point, will cause a hump in the beginning and a depression towards the end of a wall. The same authors [2] attribute the depression at the end to a build-up of heat caused by the lack of heat sink in front of the torch and the hump in the beginning may be caused by thermal effects associated with the deposition on the cold base material.

Ten thin-walled demonstrators are manufactured to investigate post-process distortion and weld induced residual stresses, which are generated by the high thermal input of the PMD process. Demonstrators D1 and D2 are fabricated to test and adjust the welding parameters and are excluded from further analysis. Before deposition, all baseplates are preheated with two single passes of the arc without feeding wire to avoid the first single track to become too narrow and prevent separation of the wall from the baseplate. All demonstrators from D3 to D10 are deposited employing the same set of parameters, which are listed in Table 2.

**Table 2** Deposition parameters

Description	Symbol	Preheating	Deposition	Unit
Wire diameter	$d$	-	1.2	[mm]
Welding current	$I$	130	140	[A]
Voltage	$U$	25	25	[V]
Travel speed	$v_{TS}$	300	200	[mm/min]
Feed rate	$f$	-	0.9	[kg/h]
Wire feed speed	$v_{WFS}$	-	2910	[mm/min]
Cooling time	$t_{cool}$	1	30	[s]
Total dwell time	$t_{dwell}$	9	38	[s]
Number of layers	$N$	2	32	[-]
Pilot gas		1.5	1.5	[l/min]
Shielding gas		5	5	[l/min]

## IN SITU TEMPERATURE MEASUREMENT

In situ measurements of the temperature are made at three selected locations on top of the baseplates using 0.81 mm diameter type-K thermocouples provided by OMEGA, as shown in Fig. 3 (a). The thermocouples have a glass fibre isolation and an accuracy of  $\pm 2.2$  °C or  $\pm 0.75$  % in a temperature range from 0 to 1250 °C. The thermocouples are welded on the top surface of the baseplates to ensure a proper thermal contact and are covered with steel sleeves to shield them from the plasma (Fig. 3 (b)). Test runs have shown that a current can be induced through electro-magnetic effects of the plasma leading to noise in the data. In addition, the steel sleeves prevent the thermocouples from being exposed to the direct heat of the plasma which can lead to a detachment of the joints. The goal is to place the thermocouples as close as possible to the deposited wall, but still gain significant data. A PCE-T 390 multichannel digital thermometer is used to read and store the thermocouple signals. Temperature is recorded with a sampling frequency of 1 Hz.

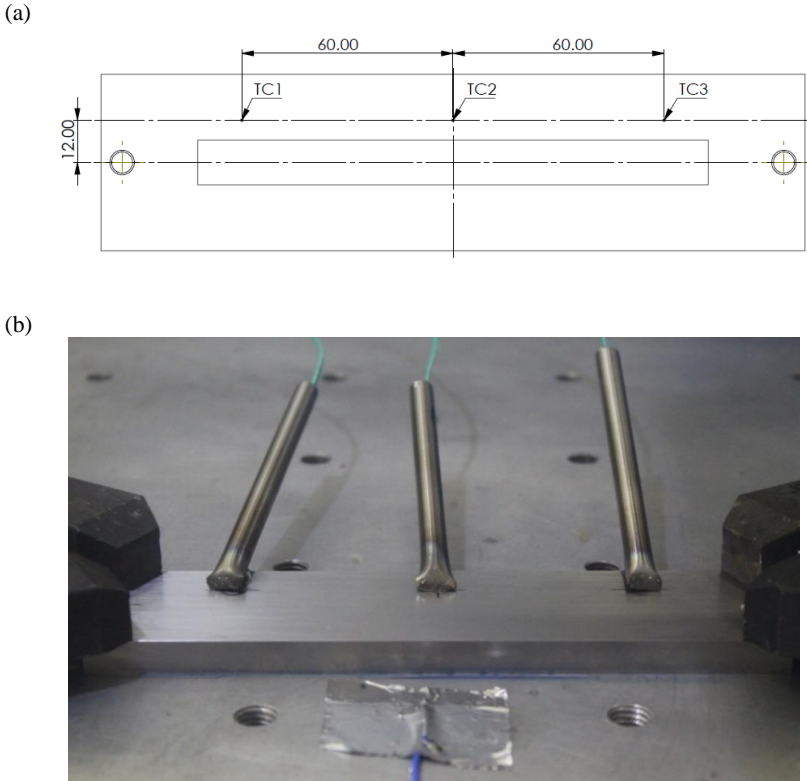


**Fig. 3** (a) Schematic view of the thermocouple locations on the top surface of the baseplate; (b) Steel pipes protecting the thermocouples from the plasma

Additional PCE TF-500 type K thermocouples are installed to capture the temperature of the backing plate, the clamps and the ambient inside the welding chamber. The thermocouple data are processed in MATLAB R2016a to determine temperature profiles of the plasma metal deposition process. The temperature history is further used to validate the numerical model in Simufact Welding 8.0.

#### POST-PROCESS DISTORTION MEASUREMENTS

Distortion is defined as the changes in the dimensions and the shape of a workpiece. Dimensional and shape changes can occur individually, but are usually superimposed. To obtain distortions imposed by the PMD process, the pre- and post-process profiles of the baseplates are scanned utilising a coordinate measuring machine (CMM). Measurements with a HEXAGON m&h IRP40.02 infrared touch probe system with a 1 mm ruby stylus

are performed along the top and bottom surfaces of the baseplates. The measurement grid on the top surface consists of 40 points, whereas the measurement grid on the bottom surface consists of 45 points, respectively. The locations at both surfaces are identified in Fig. 4.

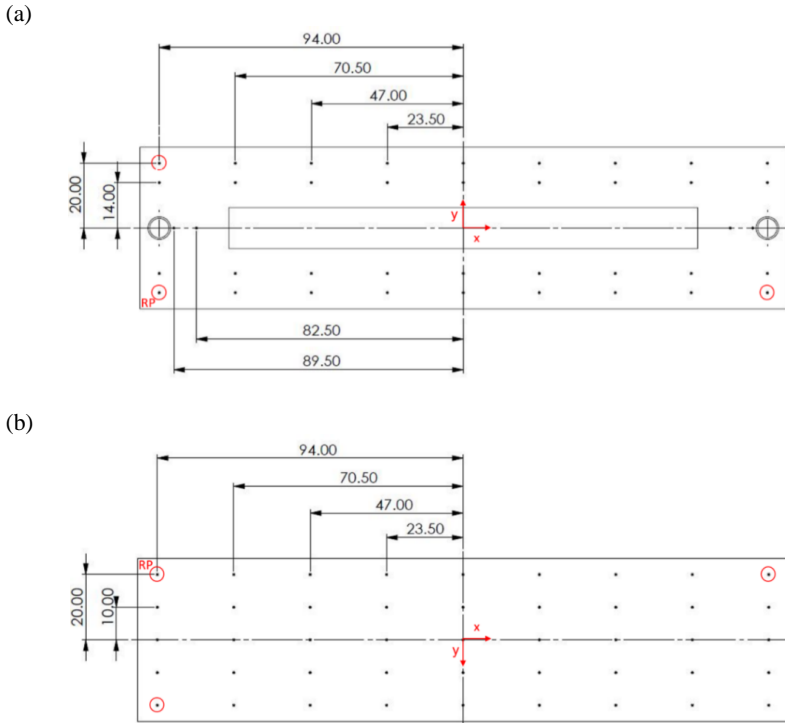


**Fig. 4** Schematic view of CMM points on the (a) top surface, and (b) bottom surface of the baseplate

The bottom surface is scanned with a 9x5 measurement grid, with a grid spacing of 23.5 mm in x and 10 mm in y direction. A different strategy is adopted for the top surface, since the single bead wall and the two blind holes do not allow a constant grid spacing. Hence, a measurement grid of 40 points in total is defined for the top surface. A reference plane with the points marked in red is constructed for each surface to align the coordinate frames of both surfaces. Rigid body translation and rotation is applied to make these planes parallel to the xy-plane. Additionally, a reference point (RP) is defined as centre of rotation. The results from the discrete data points are then used to calculate the changes in plate profile and out-of-plane distortion by subtracting the pre-process from the post-process measurements. For reasons of symmetry, sampling lines along the

longitudinal direction with symmetric  $y$ -values are merged to one single line and their mean values and standard deviations are calculated. This results in effective sampling lines for  $y=0$  mm,  $y=14$  mm and  $y=20$  mm for the top surface and  $y=0$  mm,  $y=10$  mm,  $y=20$  mm for the bottom surface, respectively. The experimentally determined distortion is used to evaluate the simulation results obtained by Simufact Welding 8.0. Since the building strategy causes a symmetry break along the transverse direction, this analysis method is not applicable for the transverse direction.

#### SIMULATION SET-UP

The process simulation of the PMD process to predict the temperature distribution in the component as well as the resulting distortion and residual stresses is set-up within Simufact Welding 8.0. Simufact Welding software covers different welding processes and encompasses the modelling of elastic-plastic behaviour of materials and structural welding simulation. The current release, Simufact Welding 2021, already includes a direct energy deposition tool [10]. The thermal analysis of the WAAM process involves the solution of a heat transfer problem with a moving heat source. Since 1984, the most widely used model in computational welding mechanics has been the power density distribution function with net weld power and weld pool shape, size and position as a function of time introduced by Goldak et al. [9] for the simulation of welding processes. Within the arc welding module, Simufact Welding 8.0 employs the Goldak double ellipsoid as standard heat source (Fig. 5). The moving double ellipsoid model can describe a wide variety of welding techniques, including gas metal arc welding, gas tungsten arc welding, shielded metal arc welding and submerged arc welding [11].

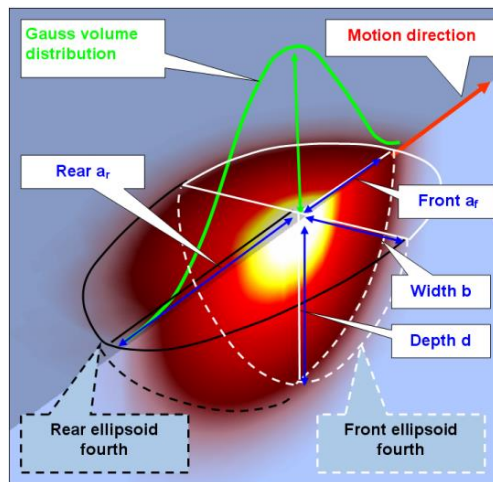


Fig. 5 Illustration of Goldak's double ellipsoid heat source model [11]

Inputs for Goldak’s double ellipsoid heat source model include the calibration of six parameters  $a_f$ ,  $a_r$ ,  $b$ ,  $d$ ,  $M$  and  $\eta$  to calibrate the heat source model [11]. The heat source parameters have been determined in a previous study and are listed in Table 3.

**Table 3** Goldak double ellipsoid heat source parameters

Run	$a_f$ [mm]	$a_r$ [mm]	$b$ [mm]	$d$ [mm]	$M$ [-]	$f_r$ [-]
Preheating	2.85	5.70	2.85	1.4	0	0.66
Deposition	6.72	13.44	6.72	4.41	0	0.66

The cooling behaviour and arc efficiency are determined by inverse simulation. From this, an arc efficiency of 0.4, an emissivity of 0.7, a convective heat transfer coefficient of 8 W/(m<sup>2</sup>·K) and a contact heat transfer coefficient of 10 W/(m<sup>2</sup>·K) are obtained. The parameters for the thermal boundary conditions are assumed to be independent of the temperature. A summary of the welding parameters used for the simulation is presented in Table 4.

**Table 4** Welding parameters

Run	$I$ [A]	$U$ [V]	$v_{TS}$ [mm/min]	$\eta$ [-]	$E_1$ [J/mm]
Preheating	130	25	300	0.4	260
Deposition	140	25	200	0.4	420

### MATERIAL DEPOSITION MODELLING

Plasma metal deposition can be related to a multi-layer welding process, in which the filler material is melted and deposited layer-by-layer. The deposition of the melted material along the welding path has to be implemented in the physics based finite element framework of the additive manufacturing process. Depending on the finite element activation/deactivation technique, the filler material can be simulated in two ways: the quiet element method or the inactive element method [12], [13]. The quiet element method is based on the initial existence of all elements in the model, i.e., all elements of the mesh defining the baseplate and successive layers to be deposited are included in the initial computational model. These elements are made passive (quiet) by multiplying material properties by scaling factors which do not affect the rest of the model. As material is deposited, the real thermo-physical properties are re-established based on the location of the energy source switching the elements to active. In this study, the quiet element method is used. The second approach removes elements representing material to be deposited from the computational analysis up to their activation. According to the metal deposition along the welding path, elements are switched to active and assembled into the model. Thus, only the mesh representing the base material and already deposited layers are computed and assembled into the global matrix. Michaleris [14] developed a hybrid quiet/inactive element method accelerating computer run times. Hereby, elements corresponding to material deposition are initially inactive and elements of the current deposited layer are switched to quiet. Based on the location of the energy source, quiet

elements are switched to active as material is deposited. This approach is implemented in Simufact Welding 2021.

Within Simufact Welding, the welding process is designed based upon manufacturing data: welding process, energy input, welding speed, filler material, welding metallurgy, clamping concept, components and the finite element mesh have to be defined. All components have been designed in SolidWorks 2018 and meshed in Abaqus CAE 6.14. Symmetry properties are exploited by modelling only one half of the calibration setup. This significantly reduces calculation time. To determine the cross-section profiles of the fabricated Ti-6Al-4V walls, demonstrator 3 is exemplarily cut in two halves using WEDM. The cut surface of one half is then scanned with an Alicona Infinite Focus optical 3D measurement system. The 3D point cloud obtained is analysed and edited in MATLAB 2016a. From the three-dimensional data points, a two-dimensional projection of the cut surface is computed. Points defining the boundary of the surface are determined and exported to SolidWorks 2018. Within the CAD software, the imported points are connected using spline interpolation to reconstruct the cross section of demonstrator 3. The 2D surface scan of the cross section and the reconstructed cross section are shown in Fig. 6.

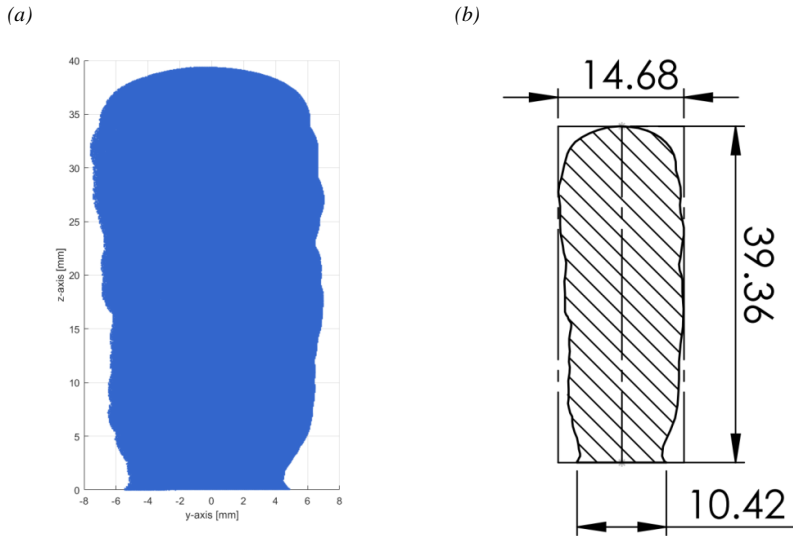


**Fig. 6** (a) Point cloud derived in MATLAB; (b) Derived CAD model within SolidWorks

In this study, each welding seam is considered as rectangular cross section. This approach reduces model complexity and enables engineers to set up simulations faster. For components with more complex geometries, the implementation of detailed weld beads increases the modelling effort. Moreover, the exact geometry of the weld beads is not always known. Some numerical studies considered each welding seam as rectangular cross section yielding good results [4], [15]. To determine the rectangular cross-section

profiles, area and height of the wall are divided by the total number of deposited layers. The dimensions used for the determination of the rectangular layer geometry are summarised in Table 5.

**Table 5** Cross-sectional dimensions of demonstrator 3

Total area [mm <sup>2</sup> ]	Total wall height [mm]	Number of layers [-]
498.15	39.36	32

From Table 5, the cross-sectional area and layer height for each deposited layer are determined as 15.6 mm<sup>2</sup> and 1.2 mm, respectively. The wall width of each layer is the result of the cross-sectional area divided by the layer height yielding 12.7 mm. An overview of the layer geometry is presented in Table 6.

**Table 6** Layer dimensions

CSA [mm <sup>2</sup> ]	Layer height [mm]	Wall width [mm]
15.6	1.2	12.7

With these parameters, the 3D model of the deposited wall is reconstructed in a layer-wise fashion. A model view of the plasma metal deposition process is shown in Fig. 7.

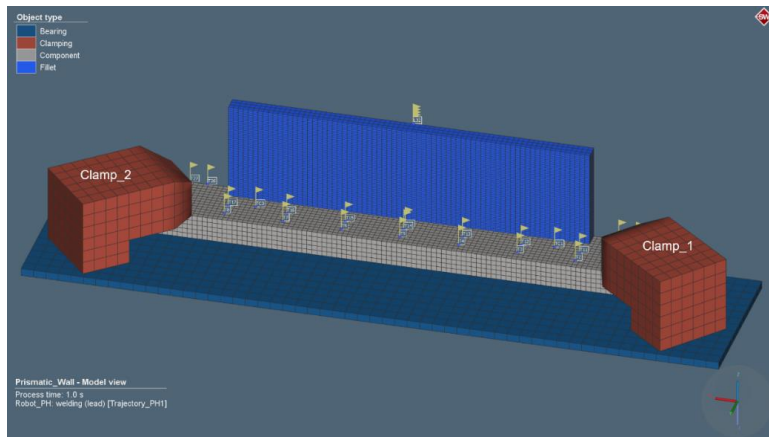


**Fig. 7** Half-symmetry model of the PMD process

The backing plate is modelled as a bearing. This type of boundary condition enables separation and sliding of components in contact with the bearing and prevents nodes of components in contact with the bearing from movement into the bearing. The clamping concept of the deposition experiments is implemented in the simulation using simplified models of the clamps. In Simufact Welding, clamps work as springs applying a force opposite to a movement normal to the surface depending on the size of the displacements.

Additionally, clamps are pressing components against each other. The clamping movement is controlled via a stiffness and a force. The stiffness is estimated 3,837 N/mm and the clamping force 67,6 N as outlined in the “Appendices”. The estimation of these parameters has been performed in Abaqus CAE6.14 using the finite element approach. For the plasma metal deposition model, linear hexahedral elements with eight integration points are used for the thermo-mechanical simulation. The baseplate and the layers are meshed with a global element size of 2 mm, the backing plate and the clamps with a global element size of 5 mm. Each layer is additionally seeded with two elements over the layer height. The overall mesh consists of a total number of 21,820 elements and total number of 39,406 nodes. To trace result values at certain positions in the model, particles are defined at coordinates corresponding to the measurement grid used for the distortion measurements and to the thermocouple locations. In addition, particles are placed along the geometric centreline of the wall ranging from the bottom of the baseplate to the top layer. The results of the tracking points are used to compare the numerical data with the experiments.

Within the robot menu in Simufact Welding, different timings of the welding process can be adjusted. This enables a close to reality integration of sequences of the welding process from the G-code directly into the simulation. The exact timings for preheating and layer deposition are shown in Fig. 8.

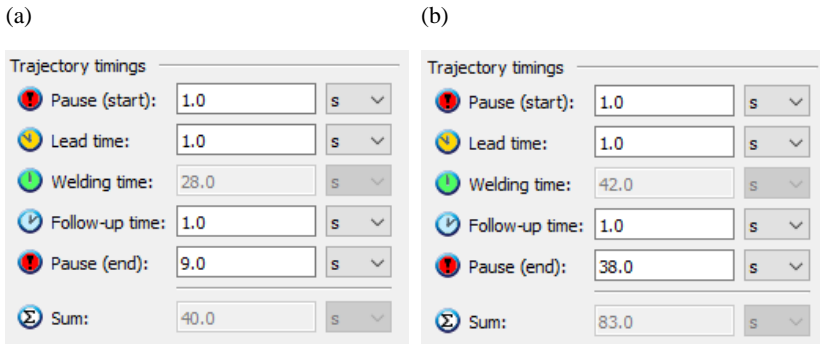


**Fig. 8** Trajectory timings: (a) Preheating; (b) Deposition

The pause time in the beginning considers a delay time to purge locally with argon (no energy input), while the lead time considers a delay with an active heat source to melt the material at the start point. Within the lead time, the feed of the wire is initiated. During the first two sequences, there is no movement of the heat source. The welding time is automatically calculated by Simufact Welding as the quotient of trajectory length and welding speed. At the end of the trajectory, the movement stops, but the heat source is still active. This time period is called follow-up time. The cooling time between layers for preheating and printing is set to 1 s and 30 s, respectively, which yield, together with the travel movements of the gantry to the park position, a total dwell time of 9 s and 38 s between subsequent layers (no energy input).

Based on the experimental trials, the time frame for depositing the walls and cooling down to room temperature is known. As a result, the total simulation time is set to 4,000 s. To investigate the behaviour of the wall upon clamp release, the model is computed using three different strategies for unclamping. Fig. 9 schematically shows the individual clamp release times.

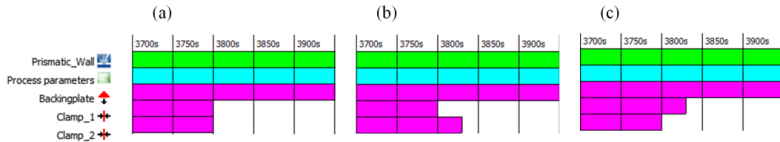


**Fig. 9** Process control centre indicating clamp release times: (a) Simultaneous unclamping; (b) Clamp 1 followed by clamp 2; (c) Clamp 2 followed by clamp 1

The delay time for non-simultaneous release of clamp 1 and clamp 2 and vice versa is set to 30 s. This time interval approximately corresponds to manual release of the clamps after the deposition process.

AEROSPACE BRACKET MODEL

Finally, a common connecting element or fastening element in the aerospace industry is analysed. Aircraft brackets are essentially supported structures that are used to attach two different components while supporting one over the other. Redesigning brackets for AM can result in significant reduction of material costs, reduced mechanical post processing, weight savings and can decrease fuel consumption of airplanes. The 3D model of the to-built geometry and the part after machining are schematically shown in Fig. 10.

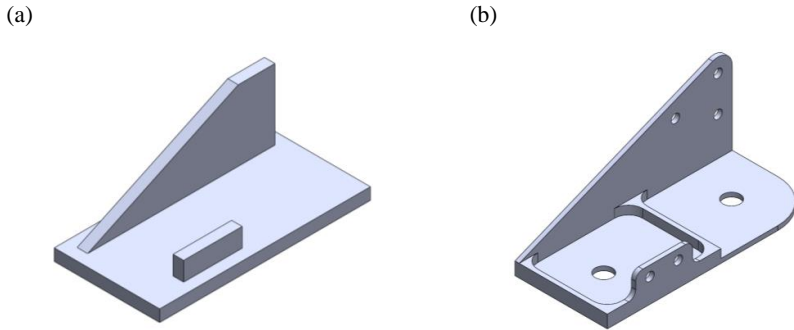


**Fig. 10** 3D model of the bracket in the (a) as-built condition and (b) after final machining

Fig. 10 (a) shows that the to-be-built geometry is oversized in order to incorporate the final geometry and to take into account the material loss due to mechanical postprocessing. From this CAD file, the building strategy for the PMD process is derived. The part consists of two single walls deposited on a rectangular Ti-6Al-4V baseplate. The walls are built up layer by layer until a pre-defined height is reached. The goal is to determine the optimal building strategy by using numerical simulations to minimise distortion and reduce residual stresses. Two building strategies are investigated: firstly, the small wall is deposited followed by the subsequent deposition of the inclined wall and, secondly, a layer of the small wall is followed by a layer of the inclined wall. Both strategies are based on bidirectional layer deposition. The baseplate is fixed to the backing plate of the welding chamber with two clamps. Prior to deposition, the cold baseplate is preheated with the arc to improve bonding of the first layers to the baseplate. A model view of the bracket is shown in Fig. 11. The set-up allows no exploitation of symmetry properties.

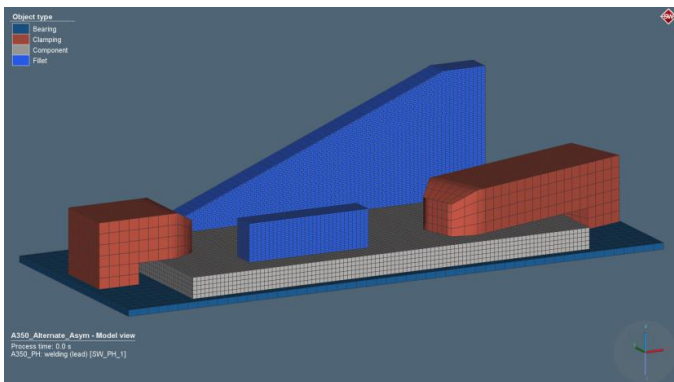


**Fig. 11** Model view of the airplane bracket

Linear hexahedral elements with eight integration points are used for the thermo-mechanical simulation. The baseplate and the walls are meshed with a global element size of 2 mm, the backing plate and the clamps with a global element size of 5 mm. Each layer is additionally seeded with two elements over the layer height. The overall mesh consists of a total number of 61,612 elements and total number of 96,450 nodes. The deposition parameters for the fabrication of the bracket correspond to the parameters utilised for the additive manufacturing of the single wall structures listed in Table 4. The dwell time between layers is estimated with 6 s, which corresponds to the time needed for the gantry to travel from the end position of the current layer to the start position of the subsequent layer. The total simulation time is set to 3,600 s. Clamps are released simultaneously after 3,540 s. Accordingly, the results achieved are used to elaborate an optimal building strategy for the process to demonstrate the practicability of numerical simulations on an industrial scale.

## RESULTS

### Ti-6Al-4V SINGLE WALL STRUCTURES

A series of eight single wall structures is fabricated using a plasma-based direct energy deposition process. As material of interest, an  $\alpha/\beta$  titanium alloy (Ti-6Al-4V) is investigated. Multi-layer walls are deposited along the centreline of the baseplate with reversed welding directions for each layer. Each wall consists of 32 layers. Average wall height and average maximum wall width have been measured at the centre of the deposited walls and are  $37.5 \pm 1.0$  mm and  $13.3 \pm 0.5$  mm, respectively. The average mass of the single wall structures is  $300 \pm 11$  g. The total layer height divided by the number of layers yields an average layer height of  $1.2 \pm 0.1$  mm. An example of a Ti-6Al-4V wall built by plasma metal deposition is shown in Fig. 12.

(a)



(b)

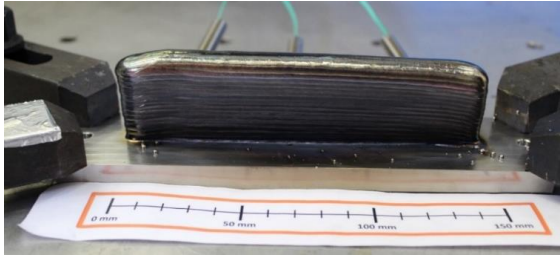


**Fig. 12** Ti-6Al-4V single wall structure produced with plasma metal deposition

All demonstrators have a silver colour which is a sign of proper shielding against atmospheric contamination. The surface discoloration of Ti-6Al-4V can be used to visually assess the degree of oxidation. With increasing oxidation, the surface colour changes from metallic silver, light straw through dark straw, light blue, dark blue, to grey and powdery [16]. Further visual assessment reveals an increase in wall width along the build height. This observation is also confirmed by measurements of the layer height and wall width during deposition. The layer height and the maximum wall width (considering the surface waviness of the weld) are measured with a calliper after the 10<sup>th</sup>, 20<sup>th</sup> and 32<sup>nd</sup> layer at the centre of the wall. Since manual recording of measurement data inside the welding chamber is quite laborious and, in order not to interrupt the continuity of the process, measurements are only conducted at a few points. The layer height and wall width along the build height can be seen in Fig. 13.

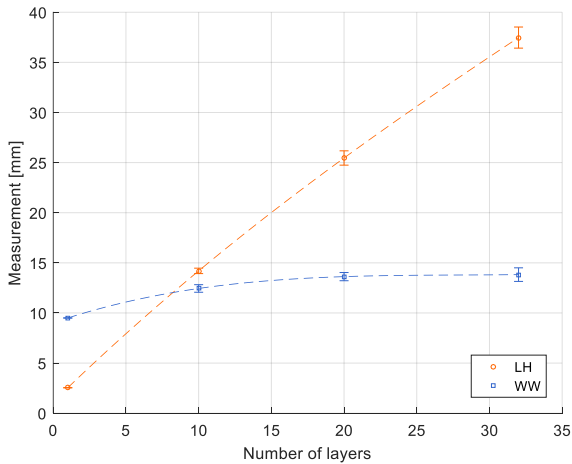


**Fig. 13** Layer height and wall width measured during deposition

Fig. 13 shows that the layer height increases nearly linearly with increasing wall height. The width of the cross section, on the contrary, experiences a steady increase from the first layer, reaching a steady deposition width at higher layers. This geometry-related phenomenon can be explained by the balance of heat input and dissipation. In the first few layers, the thermal effect of the baseplate leads to a reduction in wall width (WW) and an increase in layer height (LH). This effect has been observed by Martina et al. [2], [7] and described by Wu et al. [16]. The thermal history of WAAM components is governed by a balance between conduction, convection, and radiation. As reported by Wu et al. [16], the cold baseplate acts as a heat sink in the first layers, leading to faster cooling rates and, thus, narrower beads. Convection and radiation become more significant with the component being built up layer by layer. With an increasing wall height, the conductive thermal resistance to the baseplate, which heats up during the deposition process, is increased. Despite titanium being a poor thermal conductor, convection and radiation are less effective than conduction. The molten pool dissipates heat at slower rates and, therefore, wider beads can be observed with increasing wall height until the heat dissipation and heat input reach a balance resulting in steady wall widths. For a more precise evaluation, additional measurement data are required. The results shown, however, reflect the balance of energy input and dissipation as a geometrical boundary condition well and give insight into the development of the cross sections of deposited walls at constant deposition parameters. To achieve consistent geometrical dimensions, i.e., WW and LH, throughout the whole AM process, the building strategy must be adopted accordingly. For the sake of simplicity, all layers have been built with the same set of parameters and consistent building strategy. Single wall model

### *Thermal*

The numerical model for the plasma metal deposition of the single wall structures employs the double ellipsoid heat sources for preheating and depositing obtained from the calibration procedure. The parameters for the thermal boundary conditions are maintained except for the contact heat transfer coefficient. The baseplate is now in contact with the aluminium backing plate. The contact heat loss through the backing plate is determined by running a series of numerical trials and tuning the values such that the predicted temperature profiles match the experimental results. A value of  $100 \text{ W}/(\text{m}^2\cdot\text{K})$  gives the best match with the experiments. Fig. 14 presents the experimentally measured and numerically obtained temperature profiles during deposition and cooling.

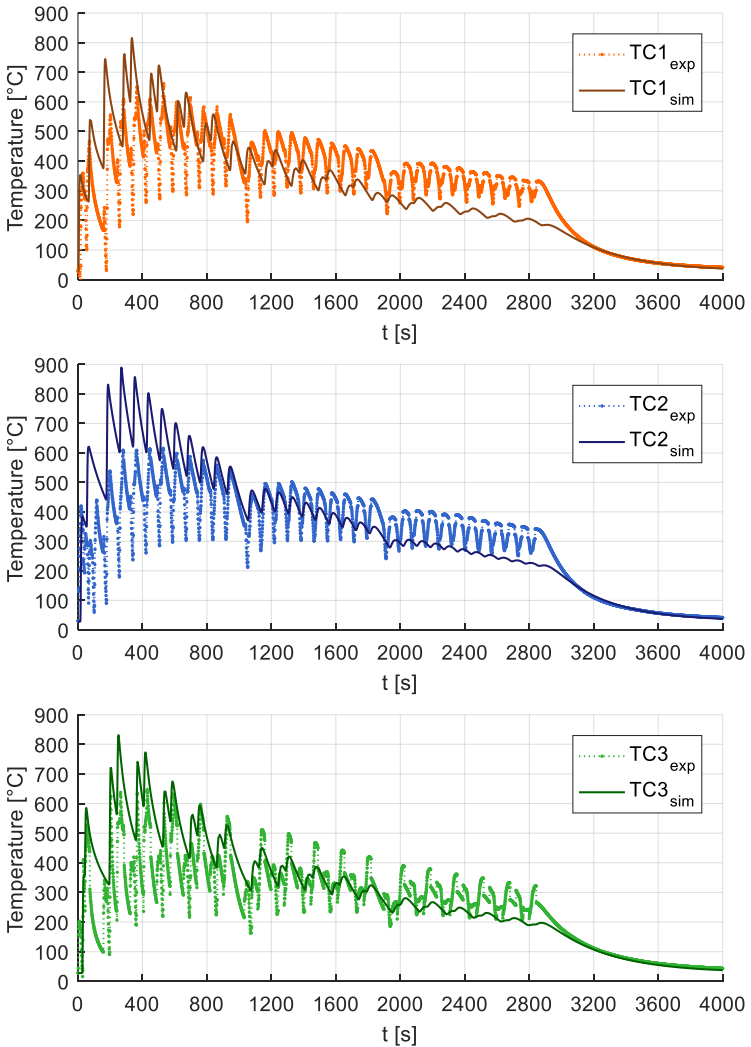


**Fig. 14** Temperature profiles obtained during single wall deposition

The overall trend of the temperature evolution is well reflected by the simulation. Referring to the calibration procedures, the peak temperatures in the first layers are overestimated. Over the building time, the thermal profiles of the experiment show a less pronounced temperature decrease than the numerical results. A figurative reason is

believed to be the pilot arc. During dwell times between layers, the torch travels to its park position with the pilot arc active, thus affecting the cooling behaviour of the deposited wall. The initially assumed free convection is locally disturbed by the hot plasma streams of the pilot. Considering the trajectory timings defined in Simufact Welding for the welding process (see Fig. 8), no energy input is defined during the pause time after the end of a trajectory. The cooling curve after the deposition process, however, is well reflected by the simulation indicating that the parameters set for the thermal boundary conditions are accurate. Further, a distinct noise in the experimental measurement signal can be noticed. This may be due to insufficient shielding of the thermocouple against the electromagnetic influence of the plasma.

### *Mechanical*

The mechanical behavior of the additively manufactured walls is investigated. The total distortion is an important evaluation index of plasma metal deposited components. Distortion has a strong impact on the dimensional precision. Fig. 15 displays measured and numerical post process displacements along the longitudinal direction after cooling and under different cases of unclamping. The course of the displacements between the data points has been modelled using spline interpolation. In the case for  $y=0$  mm at the top surface, no data points along the wall are available. Thus, the interpolation between the four remaining points, ( $x=-89.5$  mm,  $x=-82.5$  mm and  $x=82.5$  mm,  $x=89.5$  mm, respectively) serves only as an indicator for the gradient in the out-of-plane distortion between these points and cannot be compared with the other measurement lines at the top surface.

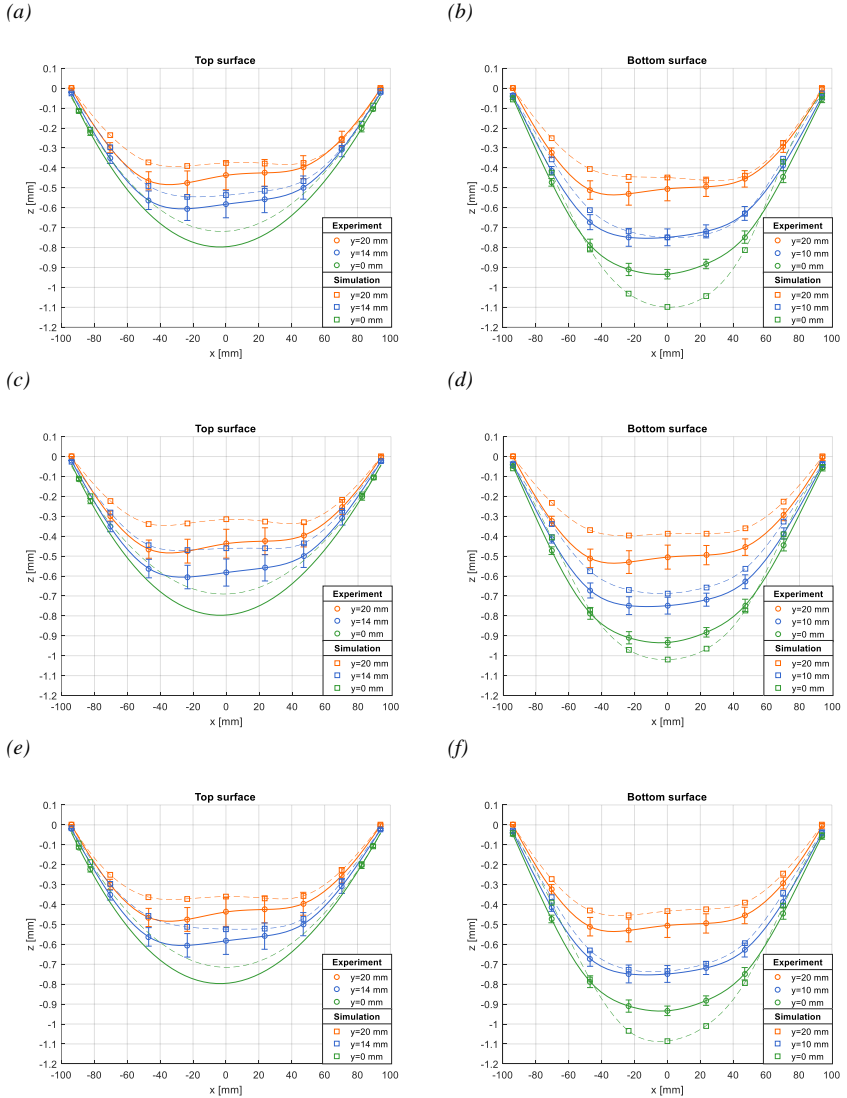


**Fig. 15** Out-of-plane distortion along the longitudinal direction: (a) and (b) clamp 1 followed by clamp 2; (c) and (d) simultaneous unclamping; (e) and (f) clamp 2 followed by clamp 1

The predicted distortions of all three unclamping cases are compared to the measured distortion. In Fig. 15, the downward bending of the baseplate in relation to the reference

plane defined in “Post-process distortion measurements” can be seen. It should be noted that, in recent studies, the authors refer to this phenomenon as upward bending, as it is a matter of reference. To stay consistent with their terminology, upward bending is further used in this paper. The upward bending can be explained as follows [5]: the deposited layer expands during heating and contracts during cooling. The contraction of the upper layer is constrained by the previously deposited layers and generates tensile residual stress, resulting in upward bending of the baseplate. Larger distortions are found at the bottom surface. Here, the baseplate bends upwards by approximately 0.9 mm at the centreline of the surface showing the maximum distortion. Comparing the scan lines at  $y=10$  mm and  $y=14$  mm, the top surface shows a less pronounced out-of-plane distortion. The scan lines at  $y=20$  mm show similar values at both surfaces. Another prominent observation from the measured data points is their asymmetrical course over the length of the baseplate. Although a bidirectional building strategy is employed, already the deposition of the first layer causes non-uniform heating and cooling of the baseplate. As a result of the non-homogenous temperature field, non-uniform thermal expansion of the heat affected zone leads to a non-homogenous plastic deformation, triggering the asymmetric behaviour of the baseplate. Although all eight demonstrators are built with the same process parameters, the CMM points are subject to a certain range of fluctuation. Deviations in the application of the clamping forces, a modified temperature control, influence of the rolling direction of the baseplates, the geometry of the wall - all these factors impact the final distortion of each component.

A graphical evaluation of Fig. 15 reveals a qualitative agreement of the modelling results with the measurements, despite representing noticeable smaller deflections. The only exception is the longitudinal distortion along the centreline of the baseplate at  $y=0$  mm of the bottom surface. Here, the numerical results overpredict the distortion. The deviations between experimental and numerical values are strongly linked to the heat input and the mechanical and thermal boundary conditions. Referring to the temperature history plot in Fig. 14, the temperature profiles obtained from the simulation decrease at a higher rate over the building time resulting in faster cooling than the experimentally measured profiles. This in turn leads to the material being stiffer, yielding smaller displacements. In the simulation, it is also assumed that the backing plate is rigid and does not allow any penetration of the baseplate. In reality, of course, the aluminium backing plate has a lower stiffness than the titanium baseplate and tends to deform locally elastically and plastically due to mechanical clamping forces exerted on the Ti-6Al-4V baseplate. All these factors are linked to the evolution of the final distortion of the PMD single wall structure. In each of the cases in Fig. 15, the numerical results display a similar accumulation of distortion after cooling and unclamping. The case of simultaneous unclamping follows the course of the CMM points for the top and bottom surface most precisely, but shows a high deviation in the residuals. On the contrary, Fig. 15 (a), case 1 top surface, approximates the out-of-plane distortion of the top surface best, while Fig. 15 (f), case 3 bottom surface, appears to fit the data of the bottom surface best. Error metrics from statistics are used to judge the quality of the models and verify the statements above. The mean absolute percentage error (MAPE) for each case can be calculated as

$$MAPE = \frac{100\%}{n} \sum_{i=1}^n \left| \frac{x_i^{exp} - x_i^{sim}}{x_i^{exp}} \right| \quad (1)$$

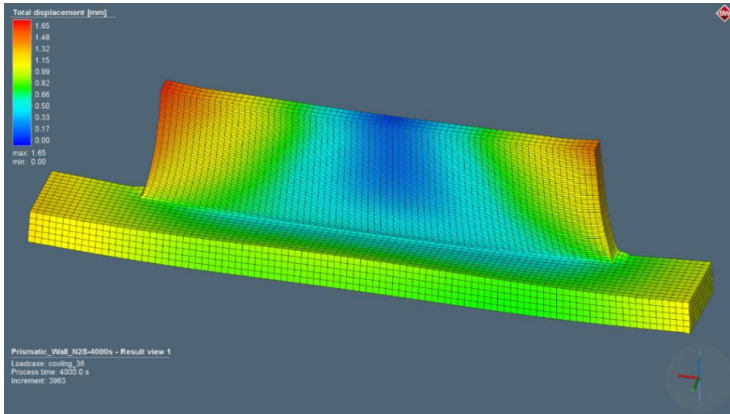
where  $n$  is the total number of data points,  $i$  the current data point,  $x^{exp}$  is the experimental value and  $x^{sim}$  is the simulated value. Table 7 shows the mean absolute percentage error for the top and bottom surface for all three unclamping cases.

**Table 7** MAPE for the unclamping cases

Case	Description	MAPE top surface [%]	MAPE bottom surface [%]
1	Clamp 1 followed by clamp 2	12.60	12.57
2	Simultaneous unclamping	15.33	15.23
3	Clamp 2 followed by clamp 1	11.96	11.16

A good correlation is achieved for each case fitting the top and bottom surface in equal measure. Thus, each unclamping strategy is, within numerical and experimental errors, suitable to predict the out-of-plane distortion of the PMD single wall structure. The largest errors are found for symmetric unclamping, while case 3 (clamp 2 follows clamp 1) shows the lowest errors for both, the top and bottom surface. The most prominent observation from these numbers, though, appears to be that the prediction of the out-of-plane distortion of the bottom surface is more accurate than the prediction of the top surface, i.e., the MAPE value of the bottom surface is smaller than the MAPE value of the top surface. Contrary to the expectation that Fig. 15 (a) matches the top surface and Fig. 15 (f) matches the bottom surface best, the unclamping strategy of case 3 fits according to the MAPE values the measured distortion most accurately. It becomes evident that different unclamping strategies affect the final distortion of the PMD walls. Fig. 16 (a) and (b) illustrate the predicted total displacement of the wall after case 3 cooling and unclamping. The distortion of the model is scaled by a factor of 4 so that the deformation becomes evident and to emphasise the deformation of the baseplate.

(a)



(b)

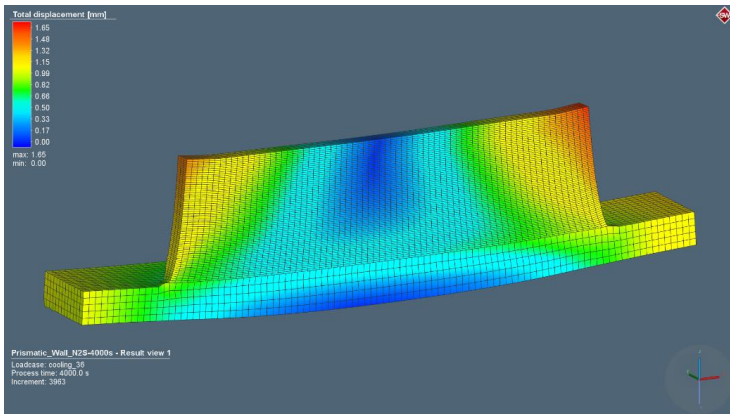
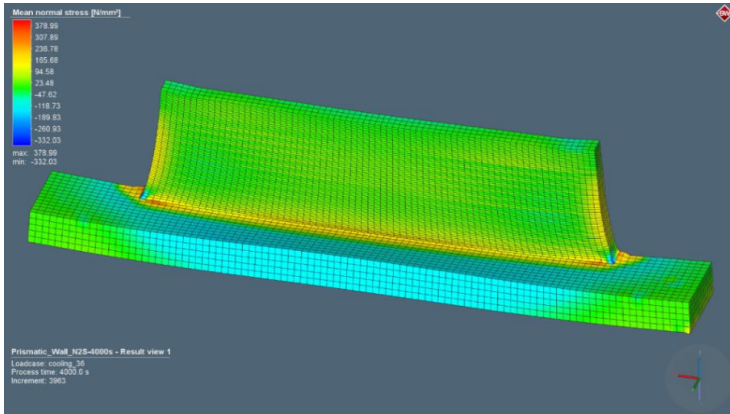


**Fig. 16** Total displacement of the PMD wall after case 3 cooling and unclamping: (a) Overview; (b) Symmetry plane

After unclamping and cooling, the component bends upwards and shows significant out-of-plane distortion. The deposition of liquid metal on a solid baseplate and its constrained shrinkage during cooling causes elastic and plastic deformations. In the central area of the wall, distortion is restricted due to the wall itself functioning as a stiffening structure. At the bottom, distortion is restricted by the backing plate. The deposited wall is pulling the baseplate upwards causing a significant residual stress state. The mean normal stress, which is the average of the three principal stresses, for case 3 cooling and unclamping is shown in Fig. 17. The mean normal stress of the model is scaled by a factor of 4.

(a)



(b)

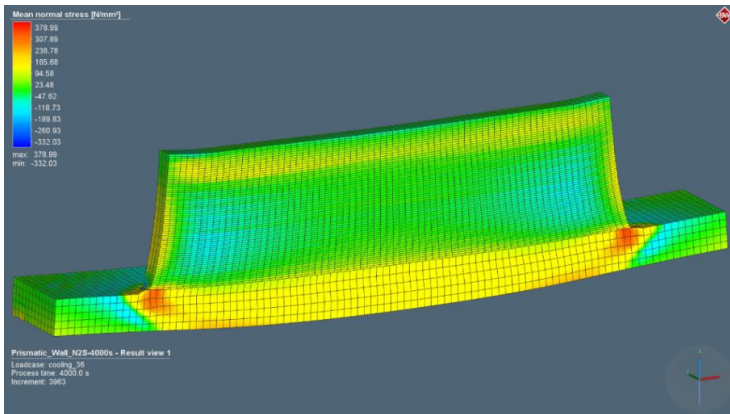


**Fig. 17** Mean normal stress of the PMD wall after case 3 cooling and unclamping: (a) Overview; (b) Symmetry plane

In Simufact Welding 8.0, the residual stress distribution can be analysed. Most areas of the component are subjected to tensile residual stresses. Compressive stresses occur in the baseplate in an area surrounding the deposited wall and in the mid-outer regions of the wall. Another interesting observation is the stress concentration at the bonding area of the wall to the baseplate. Here, tensile residual stresses reach a maximum making this critical point susceptible to cracking and delamination. Such stress concentrations can be identified by the simulation and incorporated into strategies to avoid tearing or delamination of the deposited material. Due to thermal effects inherent to plasma metal deposition, in-process and post-process distortion and residual stresses are unavoidable.

Dimensional and shape changes can be used to identify the effects of resulting residual stresses. The residual stress distribution along the centreline of the additive manufactured wall before and after releasing the mechanical boundary conditions can be seen in Fig. 18.

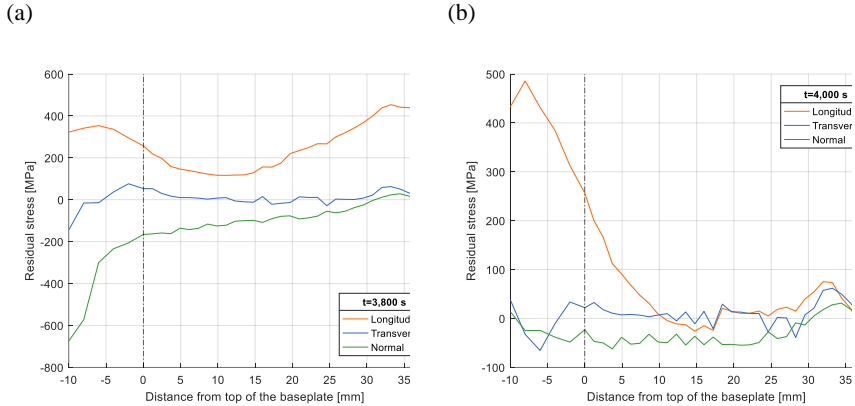


**Fig. 18** Predicted residual stress along the centreline of the wall in longitudinal (x), transverse (y), and normal (z) direction while: (a) clamps are on; (b) clamps are off

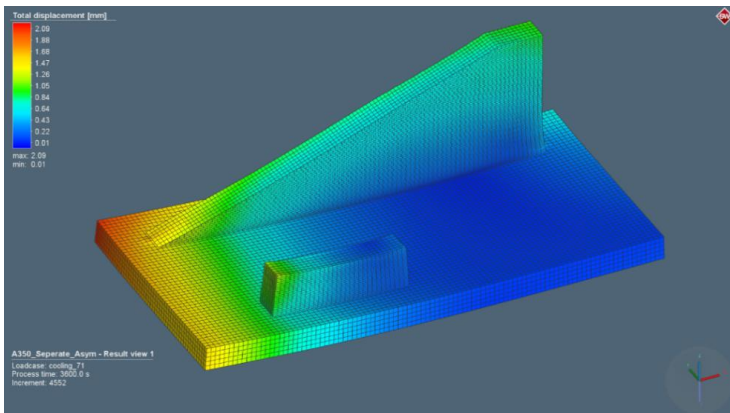
When the specimen is clamped, the longitudinal stress predicted across the wall shows first a local peak in the baseplate and then starts to decrease until a wall height of around 15 mm is reached. The stress in the first layers of the deposit is relatively uniform. Towards the final build height, the stress is increasing, reaching its highest value in the deposited wall. The transverse stress is ranging from -140 MPa to 75 MPa and is significantly lower than the longitudinal stresses. Normal stress shows a high accumulation of compressive stress in the baseplate and is steadily increasing over the build height of the wall. Upon releasing the clamps, stress relaxation occurs and inherent plastic strains cause the specimen to bend upwards. Distortion changes the stress field by reducing the tensile stresses in the top of the wall and by increasing tensile stresses in the bottom of the baseplate. The interesting aspect of the longitudinal stresses in Fig. 15 (b) occurs towards the extremities of the wall. For example, the stress at the top of the wall has a much lower value than at the bottom of the baseplate due to the distortion of the component. This distortion also causes the stress at the bottom of the plate to become highly tensile. There is a reduction of the tensile longitudinal stresses from the baseplate with an increased number of layers. Within a wall height of 10 mm to 30 mm, longitudinal and transverse stresses are almost zero, reaching a peak between 30 mm and 35 mm and are becoming compressive at the top of the wall. Interestingly, there are no significant jumps in the stress profiles at the baseplate-wall interface, as several studies reported [4], [5], [7], [17]. The difference is found to be in the clamping strategy. In this work, the baseplate has been clamped only at its four corners allowing the material to distort in the central area during the process. In Refs. [4], [5], [7], [17], a more thorough clamping restricting the movement of the baseplate is used. Investigations showed that uniform residual stresses are produced along the wall during the process being balanced

by compressive stresses in the baseplate with a non-continuous transition at the interface. Unclamping causes a redistribution of the stresses. Tensile stresses drop linearly towards the top of the wall. Colegrove et al. [5] proposed an analytical model to estimate the residual stress in the longitudinal direction. One assumption of this model is that there is no deflection of the component during deposition. Hönnige et al. [18] used the analytical model for estimating distortion and residual stress with reasonably good accuracy. It should be noted that the stress profiles in Fig. 18 are determined numerically and need, of course, experimental validation. However, the numerically obtained stress profiles are in good correlation with works conducted by Martina et al. [7] and Hoye et al. [17] showing a similar distribution of stress within an additively manufactured wall structure.

#### AEROSPACE BRACKET MODEL

Manufacturing of complex structures for industrial applications requires innovative software solutions that enable precise, reliable and reproducible predictions of distortion and residuals stress fields. Simple geometries, such as single wall structures, can be used to validate the numerical models and raise confidence in structural welding simulations to simulate more complex parts. Based on this considerations, computer-aided calculations are used to determine the optimal building strategy for the plasma deposition of a Ti-6Al-4V aerospace bracket. Two building strategies have been identified prior to the process, which are analysed virtually. The mechanical performance of both strategies after cooling and unclamping is examined. The total distortion is presented in Fig. 19 scaled by a factor of 4.

(a)



(b)

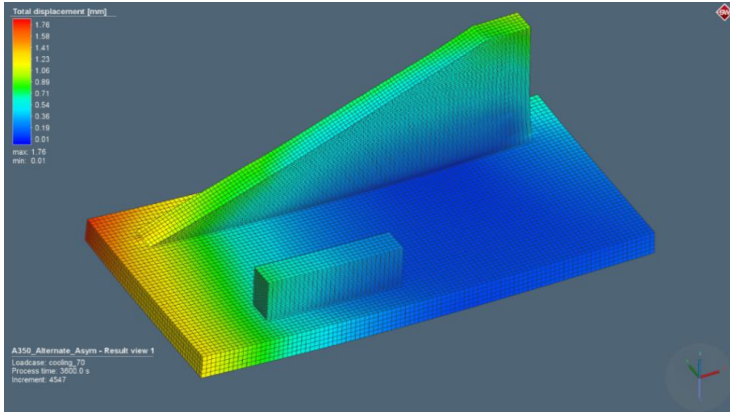


**Fig. 19** Total displacement of the aerospace bracket after cooling and unclamping: (a) Strategy 1; (b) Strategy 2

Both building strategies yield similar results regarding the total distortion. Strategy 1, however, shows larger values of distortion in the region where the inclined wall is rising. In this corner, there is no mechanical restraint and the inclined wall is pulling the baseplate upwards. Due to a more homogenous heat distribution of strategy 2, the component is subject to less distortion. Considering the manufacturing of a component on the industrial scale, more attention should be paid to the clamping strategy. To reduce the overall distortion of the bracket, a different clamping strategy would be required. However, due to the dimensions of the baseplate and the design of the plasma torch, the chosen clamping strategy guaranteed accessibility of the torch reaching every start and stop point without crashing.

Numerical simulations are a powerful technique to analyse the thermal and mechanical evolution of components and their properties during the additive manufacturing process. Assessing the results of the numerical simulations, strategy 2 is employed for the additive manufacturing of the Ti-6Al-4V bracket. Less distortion and a more homogenous heat distribution are the driving factors. Fig. 20 shows the bracket in the as-built condition and after final machining.

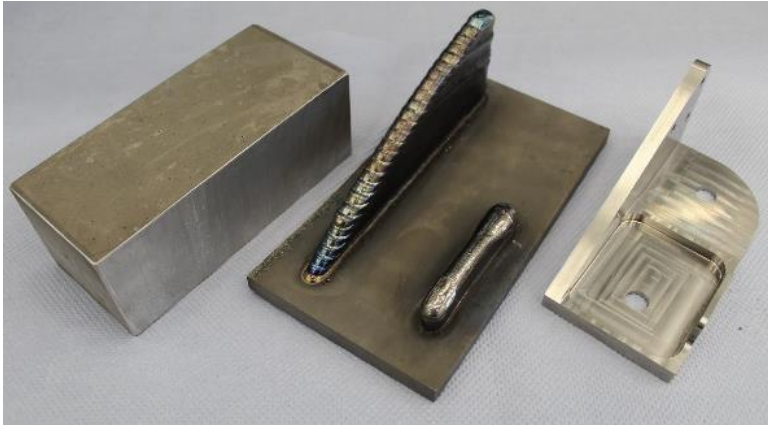


**Fig. 20** Aerospace bracket manufacturing

The walls show a homogeneous macrostructure without the occurrence of defects. It can be deduced that PMD can be used to produce large-volume homogeneous parts and components. The advantage for a production by means of additive manufacturing is reflected in the material savings, reduced mechanical post-processing and resulting cost savings. In comparison to conventional production methods, the production by means of generative methods allows material savings up to approximately 80 %.

## DISCUSSION

Structural welding simulations allow the prediction of geometrical deviations and accumulated residual stresses as well as their optimisation before conducting experiments. Due to the length of the multi-layer welds, calculation times for fully transient thermo-mechanical simulations are relatively long, the calculation stability suffers from a high number of bodies in contact elements in the model and the modelling effort is high, since the geometries need to be sliced and positioned layer-wise. Depending on the complexity of the models, the simulation times can vary from a few minutes to several days [15], [19]. The comparison of computational times used for the models is presented in Table 8. The simulations have been performed on an eight core 3.30 GHz i7-5820K processor with 32 GB installed RAM. All models have been calculated by using parallelisation, i.e., the calculation of one simulation is done in parallel using several CPU cores. Simufact supports two parallelisation options, namely domain decomposition method (DDM) and shared memory parallelisation (SMP) [20]. DDM subdivides the model into several sub-models that are connected with each other, whereas SMP allows one solver to use multiple cores.

**Table 8** Computational time comparison between different models

Model	Adaptive mesh refinement	Parallelisation	Elements [-]	Computational time [h]
Single wall	no	yes	21,820	~ 24
Aerospace bracket	no	yes	61,612	~ 100

When comparing the single wall model and the aerospace bracket model in Table 8, it becomes obvious that, with increasing size and complexity of the models, the computational times increase gradually. Besides the model size, adaptive mesh refinement increases the computational costs by adding elements to the model. However, there are various ways to reduce computational times including adaptive mesh refinement and un-refinement, the use of symmetry in the models, parallel computing, reduced number of contact bodies and reasonable mesh sizes [15], [19], [21]. Efforts of software tool developers to implement dedicated direct energy deposition (DED) modules in the field of additive manufacturing help to fully exploit the potential of DED and make the calculation of complex models on an industrial scale economical [22].

## CONCLUSION

Plasma metal deposition of large-scale Ti-6Al-4V multi-layer structures is investigated experimentally and numerically. A finite element simulation using Simufact Welding 8.0 is set-up to predict the mechanical behaviour of multi-layer components. Experiments are carried out in order to provide data for verifying the calculated temperature profiles and the out-of-plane distortion. Moreover, an airplane bracket is analysed to identify the optimal building strategy and to verify the simulation process for the industrial purpose. According to the results of this study, the following conclusions are drawn:

1. Based on experimental results, the Goldak double ellipsoid heat source model is verified to suit the experimental determined conditions. As an important feature for the application of structural welding simulations, more accurate temperature measurements for the heat source calibration are necessary. Improved temperature measurements can be addressed by using shielded thermocouples, different attachment techniques, higher frequency of data logging and the recording of the weld pool shape.
2. In the simulations, the thermal and mechanical boundary conditions are assumed to be constant throughout the deposition process. In fact, these parameters are not only temperature-dependent but also a function of the build height and geometry.
3. The results obtained from Simufact Welding 8.0 reproduce the distortion and temperature distribution of the experiment well. Discrepancies between simulation and experiment can occur due to inaccuracies in the calibration of the heat source, thermal and mechanical boundary conditions. Also, the level of detail in the modelling of the bead and wall geometry should be considered as influencing quantity. The weld bead profile for the deposition of the wall is modelled as a rectangle.

4. The virtual process development of the aerospace bracket emphasizes the potential of numerical simulations as digital twin to reduce the number of costly experimental trials.

## APPENDICES

The following appendices are intended to roughly present how the mechanical boundary conditions for the thermo-mechanical simulation in Simufact Welding are determined.

### MECHANICAL BOUNDARY CONDITIONS

#### *Clamp stiffness*

A linear elastic analysis using Abaqus CAE 6.14 is performed to estimate the spring stiffness of the clamp. The clamp consists of two parts, a steel step block and a steel step clamp. The clamp is loaded with an arbitrary constant force of 2,500 N acting on the negative of the surface that actually presses on the baseplate of the experimental setup described in “Materials and setup”. The model is constrained by fixing all degrees of freedom of the bottom surface of the step block. The step block (master) and step clamp (slave) are connected using a surface-to-surface tie constraint. Isotropic material behaviour has been specified. A drawing of the model can be seen in Fig. 21 (a). The calculated deflection is set in relation with the force applied (Fig. 21 (b)). The slope of the linear curve yields the translational spring stiffness of the clamp.

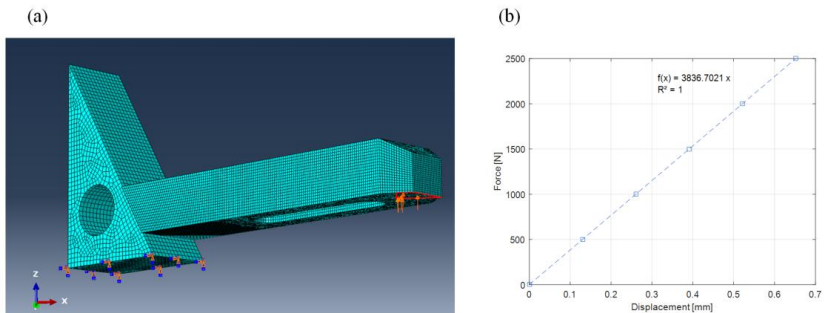


**Fig. 21** (a) Meshed CAD model of the clamp assembly; (b) Force-Displacement relation of the clamp

To impose a mechanical boundary condition, the real clamping system is simplified, whereby the clamp is replaced by a spring with a corresponding spring stiffness. The spring stiffness is set to a constant value of 3,837 N/mm.

*Contact force*

To estimate the contact pressure of the clamp on the baseplate, another analysis using Abaqus CAE 6.14 is performed. The model consists of six parts, an aluminum backing plate, a titanium baseplate, a steel stud, a steel hexagonal flange nut, a steel step block and a steel step clamp. As outlined in “Materials and setup”, the baseplates are fixed to the backing plate of the welding chamber by using clamps placed at specified positions. The steel bolts are pre-tensioned with a torque of 80 Nm. In Abaqus, the pretension is adjusted over the length, which is determined as the following: firstly, the flange nut is tightened manually until it makes contact with the clamp and, secondly, a torque wrench is used to apply a torque of 80 Nm, whereas the number of turns of the nut is counted. After about 5/8 turns, the required torque is reached. The thread pitch, which is 1.75 mm in the case of a M12 metric thread, multiplied by the number of turns is used as a satisfactory approximation to calculate the preload length of the screw. The stud is hence pre-tensioned with a length of 1.09 mm. The model is constrained by fixing all degrees of freedom of the bottom surface of the backing plate and symmetry boundary conditions on the cut surfaces. A drawing of the model can be seen in Fig. 22.

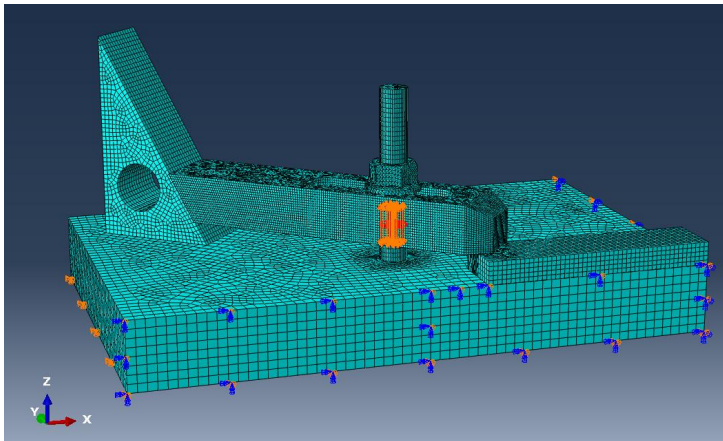


**Fig. 22** Meshed CAD model of the contact force assembly

To reduce computational costs and time, firstly, isotropic material behaviour is assumed, and secondly, friction is only considered in the contact area of the clamp with the baseplate. All other interactions are modelled using a tie constraint. After the finite element model is solved, the average contact pressure at the baseplate of the surface in contact with the step clamp is determined. The average contact pressure is multiplied by the area of the surface to get the initial force applied on the baseplate. Since no static coefficient of friction for dry conditions is found for the material pairing steel-titanium, the contact behaviour is defined in a first step as frictionless. Then a value of 0.20 is

applied, which is a typical value for steel/steel dry contact [23]. At last, the friction coefficient is set to 0.36, which corresponds to a Ti-6Al-4V/Ti-6Al-4V contact pair [24].

**Table 9** Contact force estimation

Friction-coefficient [-]	Mean contact pressure [MPa]	Contact surface area [mm <sup>2</sup> ]	Mean contact force [kN]
<i>frictionless</i>	435.7	159.5	69.5
$\mu = 0.20$	424.0	159.5	67.6
$\mu = 0.36$	413.6	159.5	66.0

Table 9 shows the difference between frictionless and frictional contact. Since the baseplates have been machined prior to the PMD process and, therefore, have a good surface quality, the friction coefficient of 0.20 is used to calculate the contact force. Ultimately, the clamping movement can be controlled by “Stiffness & Force” with a constant stiffness of 3,837 N/mm and a constant contact force of 67,6 kN.

## References

- [1] T. WOHLERS, R. I. CAMPBELL, O. DIEGEL, J. KOWEN, N. MOSTOW and I. FIDAN: *Wohlers report 2022: 3D printing and additive manufacturing: global state of the industry*, Fort Collins, Colo: Wohlers Associates, 2022.
- [2] F. MARTINA, J. MEHNEN, S. W. WILLIAMS, P. COLEGROVE and F. WANG: ‘Investigation of the benefits of plasma deposition for the additive layer manufacture of Ti-6Al-4V’, *J. Mater. Process. Technol.*, vol. 212, no. 6, pp. 1377-1386, Jun. 2012, doi: 10.1016/j.jmatprotec.2012.02.002.
- [3] MARTIN BIELIK ET AL.: ‘Plasma Metal Deposition in aerospace applications - Enabling a cost-efficient technology for high tech industries’, Vienna, Austria, 2020.
- [4] J. DING ET AL.: ‘Thermo-mechanical analysis of Wire and Arc Additive Layer Manufacturing process on large multi-layer parts’, *Comput. Mater. Sci.*, Jul. 2011, doi: 10.1016/j.commatsci.2011.06.023.
- [5] P. A. COLEGROVE ET AL.: ‘Microstructure and residual stress improvement in wire and arc additively manufactured parts through high-pressure rolling’, *J. Mater. Process. Technol.*, vol. 213, no. 10, pp. 1782-1791, Oct. 2013, doi: 10.1016/j.jmatprotec.2013.04.012.
- [6] N. HOYE, H. J. LI, D. CUIURI and A. M. PARADOWSKA: ‘Measurement of Residual Stresses in Titanium Aerospace Components Formed via Additive Manufacturing’, *Mater. Sci. Forum*, vol. 777, pp. 124-129, Feb. 2014, doi: 10.4028/www.scientific.net/MSF.777.124.
- [7] F. MARTINA ET AL.: ‘Residual stress of as-deposited and rolled wire+arc additive manufacturing Ti-6Al-4V components’, *Mater. Sci. Technol.*, vol. 32, no. 14, pp. 1439-1448, Sep. 2016, doi: 10.1080/02670836.2016.1142704.
- [8] H. E. COULES: ‘Contemporary approaches to reducing weld induced residual stress’, *Mater. Sci. Technol.*, vol. 29, no. 1, pp. 4-18, Jan. 2013, doi: 10.1179/1743284712Y.0000000106.
- [9] J. GOLDAK, A. CHAKRAVARTI and M. BIBBY: ‘A new finite element model for welding heat sources’, *Metall. Trans. B*, vol. 15, no. 2, pp. 299-305, Jun. 1984, doi: 10.1007/BF02667333.
- [10] ‘Simufact Welding 2021’, <https://www.simufact.com/what-s-new-in-SW-v2021.html> (accessed Jul. 17, 2022).
- [11] ‘Simufact Infosheet Heat Source’.
- [12] M. MEGAHED, H.-W. MINDT, N. N’DRI, H. DUAN and O. DESMAISON: ‘Metal additive-manufacturing process and residual stress modeling’, *Integrating Mater. Manuf. Innov.*, vol. 5, no. 1, pp. 61-93, Dec. 2016, doi: 10.1186/s40192-016-0047-2.

- [13] M. CHIUMENTI, M. CERVERA, A. SALMI, C. AGELET DE SARACIBAR, N. DIALAMI and K. MATSUI: 'Finite element modeling of multi-pass welding and shaped metal deposition processes', *Comput. Methods Appl. Mech. Eng.*, vol. 199, no. 37-40, pp. 2343-2359, Aug. 2010, doi: 10.1016/j.cma.2010.02.018.
- [14] P. MICHALERIS: 'Modeling metal deposition in heat transfer analyses of additive manufacturing processes', *Finite Elem. Anal. Des.*, vol. 86, pp. 51-60, Sep. 2014, doi: 10.1016/j.finel.2014.04.003.
- [15] R. MARTUKANITZ ET AL.: 'Toward an integrated computational system for describing the additive manufacturing process for metallic materials', *Addit. Manuf.*, vol. 1-4, pp. 52-63, Oct. 2014, doi: 10.1016/j.addma.2014.09.002.
- [16] B. WU, Z. PAN, D. DING, D. CUIURI and H. LI: 'Effects of heat accumulation on microstructure and mechanical properties of Ti6Al4V alloy deposited by wire arc additive manufacturing', *Addit. Manuf.*, vol. 23, pp. 151-160, Oct. 2018, doi: 10.1016/j.addma.2018.08.004.
- [17] N. HOYE, H. J. LI, D. CUIURI and A. M. PARADOWSKA: 'Measurement of Residual Stresses in Titanium Aerospace Components Formed via Additive Manufacturing', *Mater. Sci. Forum*, vol. 777, pp. 124-129, Feb. 2014, doi: 10.4028/www.scientific.net/MSF.777.124.
- [18] 'Analytical Model for Distortion Prediction in Wire + Arc Additive Manufacturing', Oct. 2018, pp. 277-282. doi: 10.21741/9781945291890-44.
- [19] J. DING ET AL.: 'Thermo-mechanical analysis of Wire and Arc Additive Layer Manufacturing process on large multi-layer parts', *Comput. Mater. Sci.*, Jul. 2011, doi: 10.1016/j.commatsci.2011.06.023.
- [20] 'Simufact Infosheet Parallelisierung'.
- [21] P. HELBIG: 'Kalibrierung von Ersatzwärmequellen für die numerische Simulation von Laserschweißprozessen', Universität Kassel, 2018.
- [22] Simufact Engineering GmbH, 'Simufact Welding', *Simufact Welding*, Jan. 08, 2020, <https://www.simufact.com/simufactwelding-welding-simulation.html> (accessed Jan. 08, 2020).
- [23] A. SCHWEIZER: 'Schweizer-FN', *Formelsammlung und Berechnungsprogramme Anlagenbau*, May 01, 2020, <https://www.schweizer-fn.de/stoff/reibwerte/reibwerte.php> (accessed Jan. 05, 2020).
- [24] 'Coefficient of friction', May 01, 2020, [http://www-eng.lbl.gov/~ajdemell/coefficients\\_of\\_friction.html](http://www-eng.lbl.gov/~ajdemell/coefficients_of_friction.html) (accessed Jan. 05, 2020).



# **VI Microstructural Modelling in Weld Metal and Heat Affected Zone**



# EXTRACTION OF PROCESS-STRUCTURE-PROPERTY LINKAGE USING DEEP LEARNING METHODS

J. INOUE\*, S. NOGUCHI\*\*

*\*Institute of Industrial Science, The University of Tokyo, Chiba, Japan*

*\*\*Dept. of Advanced Interdisciplinary Studies, The University of Tokyo, Tokyo, Japan*

DOI 10.3217/978-3-85125-968-1-21

## ABSTRACT

The establishment of the process–structure–property linkage is essential for designing new materials with desired properties. Based on the concept, the discovery of new materials has been accelerated in the field of functional and bio- materials by combining quantum and molecular modeling tools with efficient machine learning methods. However, in the case of structural materials, even though the development of Integrated Computational Materials Engineering (ICME), it is still difficult to efficiently design new materials because of the uncertainties within models and experimental data. In the present paper, our recent development of a general methodology for extracting the linkage between hierarchical microstructure and process conditions as well as properties will be reviewed. In the proposed method, the uncertainties will be captured in the form of probability density functions using deep learning methods.

Since microstructures of typical structural materials are composed of finite kinds of dissimilar phases developing competitively with totally different physical processes, they are supposed to have different geometrical features while maintaining spatial orders. The framework, thus, has two functional components: one is for extracting geometrical features of material microstructures necessary to decompose each different microstructures, and the other is for clarifying spatial orders among the extracted characteristic components. The method was applied for generating virtual steel microstructures obtained after a certain continuous cooling process and those for desired mechanical properties. The obtained results show that the proposed methodology not only generates realistic microstructural images comparable to real experimental images but also clarifies a part of microstructures critically affecting the target property. The proposed approach has been developed to help designing the optimum welding parameters as well as structural materials with an improved weldability.

Keywords: PSPP linkage, uncertainty, deep generative models, virtual microstructure, hotspot

## INTRODUCTION

Since the performance of structural materials is highly dependent on their microstructures, the materials design approach has mainly focused on optimizing microstructure to satisfy product-level performance requirements. In addition, microstructures of structural materials are usually composed of various phases developed with different kinetic processes to each other. Accordingly designing structural materials with targeted performance requires a combined strategy of bottom-up modeling and simulation

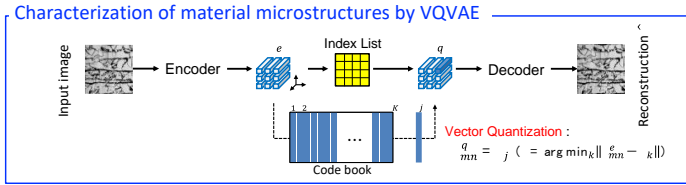
approaches which take into account the development of various levels of hierarchical material microstructures as well as their effects on the properties [1]. Especially in the case of welding process, since materials are subject to variety of temperature histories in heat affected zone (HAZ), it is expected to develop a method which can efficiently predict the microstructures and their properties in HAZ. Considering these facts, computational materials science and multiscale mechanics modeling play key roles in designing structural materials, which has brought much attention to the development of Integrated Computational Materials Engineering (ICME) in the materials community [2]. On the other hand, computational materials science and microstructural optimization based on numerical models encounter many uncertainties, such as stochasticity of processes, incomplete understanding of underlying physics, lack of complete data to quantify material microstructure, and ambiguity even in the selection of mathematical descriptors representing the hierarchical microstructures [3]. These uncertainties sometimes prevent us to apply the simple materials informatics approach, in which attention is focused mainly on data mining and providing convenient and powerful tools for designing or selecting new materials, and hence brought us difficulty in inverting process–structure and structure–property relations.

To take into account these uncertainties, the authors have developed a data-driven approach composed of two different kinds of convolution neural networks [4,5]. One is for extracting descriptors representing the hierarchical microstructure and the other for understanding the correlation between a spatial arrangement of the extracted descriptors and corresponding process parameters or mechanical properties. The present paper is a brief review of our results obtained for the several problems of extracting process–structure [4] and structure–property [5] linkages.

## METHODOLOGY

### EXTRACTION OF MICROSTRUCTURAL FEATURES AND THEIR ARRANGEMENTS

Metallurgists implicitly share the feeling that material microstructures are composed of finite kinds of dissimilar phases or small-scale microstructures. In addition, since individual small-scale microstructures develop competitively with completely different formation kinetics, they are supposed to have different geometrical features while maintaining certain spatial orders depending on process conditions such as cooling rate and holding temperature. Following this understanding, we demonstrated that a convolutional neural network (CNN) provides an efficient route to extract a finite number of geometrical features representing each small-scale microstructure and successfully provide an unsupervised segmentation for steel microstructures [6]. The concept was further implemented into a variational autoencoder to enable the automatic generation of virtual microstructures of steel [4]. In this framework, we adopted a vector quantized variational autoencoder (VQVAE) [7] to extract a certain number of characteristic geometrical features from micrographs of steel as well as to reveal their spatial arrangement in the microstructure.



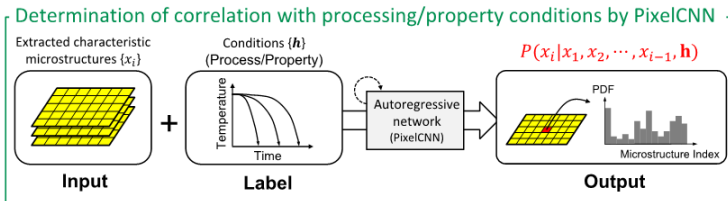
**Fig. 1** Characterization of material microstructures by VQVAE

Fig.1 shows the schematic of the architecture of VQVAE. As mentioned above, VQVAE is used for the extraction of a finite number of geometrical features representing each small-scale microstructure in an unsupervised way. It is composed of a convolutional encoder and a convolutional decoder. The encoder maps input microstructure images into the corresponding spatial arrangement of characteristic microstructures (index list), and the decoder maps the extracted features back to the original microstructure images. For example, as candidates of the characteristic microstructures of steel alloys, ferrite and martensite phases or their grain boundaries can be considered. As a result, we can extract the index lists of characteristic small-scale microstructures constructing the input microstructure images. A more detailed discussion of the strategy for capturing the qualitatively different characteristic microstructures can be found in [4].

EXTRACTION OF P-S/S-P LINKAGE

The spatial arrangement of microstructures has a strong correlation with process conditions, such as cooling rate and holding temperature, and mechanical properties. A pixel convolutional neural network (PixelCNN) [8,9] was applied to reveal spatial orders of small-scale microstructures as a function of process parameters/mechanical properties.

Fig. 2 shows the schematic of the architecture of PixelCNN. PixelCNN is used for the determination of spatial correlation among extracted characteristic microstructures which is dependent on processing parameters and/or material properties  $\mathbf{h}$ . PixelCNN is an autoregressive model for building the joint distribution of each component over a spatial arrangement (index list)  $\mathbf{x} = \{x_1, x_2, \dots, x_n\}$  as the following product of conditional distributions:



**Fig. 2** Determination of spatial orders of small-scale microstructures as a function of process paramters/mechanical properties by PixelCNN

$$P(\mathbf{x}|\mathbf{h}) = P(x_1|\mathbf{h}) \prod_{i=2}^n P(x_i|x_2, \dots, x_{i-1}, \mathbf{h}), \quad (1)$$

where  $\mathbf{x}$  represents the two-dimensional arrangement of extracted characteristic structures  $x_i$ , and  $\mathbf{h}$  is the given condition. Since each  $x_i$  corresponds to some small-scale characteristic microstructure, Eq. (1) can be understood to represent a certain stochastic spatial interaction among them. This enables us to capture stochastic spatial correlation in the target material structures. This is one of the important advantages of our framework. Owing to this definition of spatial correlation, the uncertainties behind the generation of material microstructures can be considered.

## APPLICATION OF PROPOSED APPROACH

### AUTOGENERATION OF STEEL MICROSTRUCTURE

Using the trained network, microstructures can be generated for given conditions such as processing parameters and/or material properties. First, we obtain the probability distribution of spatial arrangement of characteristic microstructures by giving desired conditions into the trained PixelCNN. Then, a two-dimensional spatial arrangement of microstructures sampled from the distribution can be converted into a corresponding micrograph by the trained decoder. As a result, we can construct a stochastic mapping from desired conditions into material microstructures. The detailed procedure of the autogeneration of material microstructures was given in our previous paper [4].

### CONTINUOUS COOLING MICROSTRUCTURE

As an example of the applications of the proposed approach, we considered the problem of autogeneration of microstructure of low-carbon-steels obtained after a certain continuous cooling process [4]. An Fe-0.15C-1.5Mn (wt.%) low-carbon steel samples were austenitized at 1000 °C and cooled at 1.0, 3.0, 10.0, and 30.0 °C/s to room temperature. To create a training dataset, square patches (128 × 128 pixel) are cropped from the original microstructure images (1024 × 786 pixel). In total, 52 800 square images were cropped from 160 original images.

We trained VQVAE and PixelCNN presented in Figs. 1 and 2 using the training dataset. In this application, the cooling rate was given as the condition  $\mathbf{h}$  to PixelCNN. As a result of training, we can obtain a stochastic mapping from the cooling rate to the corresponding microstructures. Fig. 3 shows the generated microstructures corresponding to the given cooling rates by the proposed methodology along with the sampled training images in the dataset for each cooling rate.

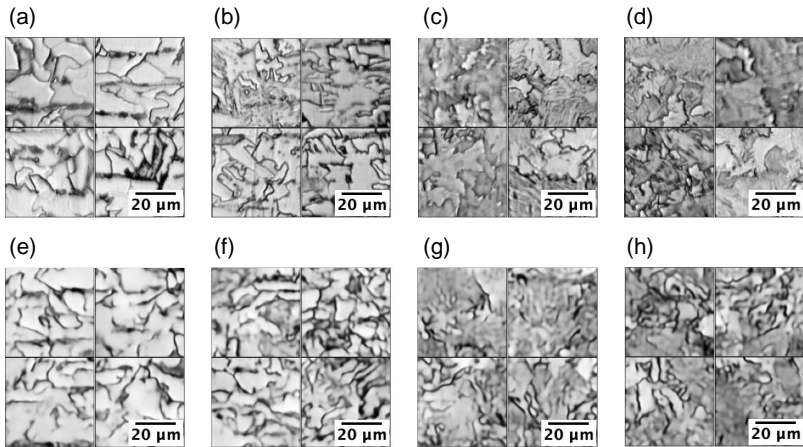


**Fig. 3** Original microstructures images and generated microstructures images corresponding to the given cooling rates. Parts (a)-(b) are original microstructures for each of the four cooling rates, respectively. Parts (e)-(h) are generated microstructures for each of the four cooling rates, respectively. Each panel has four microstructure images.

These results indicate that the proposed method can produce qualitatively realistic microstructure images for each cooling rate in the sense that the generated microstructures have similar features to those observed in training microstructure images in terms of the basic topology of microstructures and a similar trend relative to the change in the cooling rate. It should be emphasized that the introduced method can generate new microstructures in the sense that the generated microstructure images are not exactly the same as the images in the training microstructure dataset. In addition, it should be noted that this method can generate an ensemble of microstructures illustrating the distribution of material microstructures for any given parameters. In this way, the uncertainty of microstructure resulting from the stochastic nature of their formation kinetics can be naturally treated, and hence help to understand the process–structure linkage.

To validate the generated microstructures quantitatively, we consider two traditional descriptors of microstructure morphology: the volume fraction and the average grain size. We calculated the ferrite volume fraction for 1000 training and 1000 generated images for each of the four cooling rates. Fig. 4 shows the box plot of the calculated ferrite volume fraction for the training images and the generated images corresponding to each cooling rate. In terms of mean values, the ferrite volume fractions of the generated images for all cooling rates are in satisfactory good agreement with those of the training images. Also, the volume fraction of ferrite in the generated images in Fig. 4 clearly shows a similar trend of variances to the observed microstructures; as the cooling rate increases, the variance of the volume fraction of ferrite also increases.

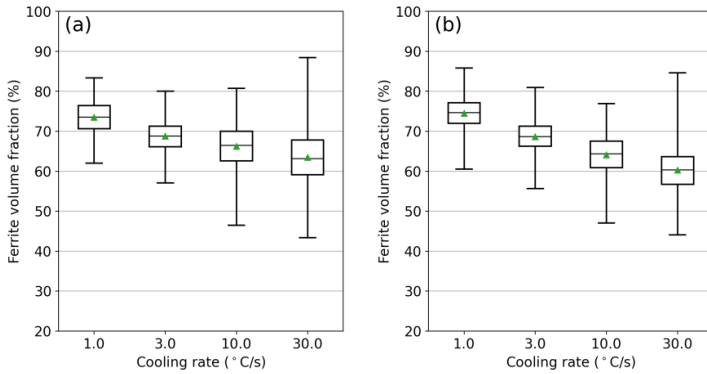


**Fig. 4** Box plots of the ferrite volume fraction in (a) the microstructure patches cropped from the original images, and (b) the microstructure patches generated by the proposed methodology. The black lines and green triangles in the boxes denote median and mean values of sets of images for each cooling rates, respectively.

Next, we consider the average grain size in a micrograph. Fig. 5 shows the box plots of the local average grain sizes and their mean values as the overall averages for each patch cropped from original microstructures and the generated images. The local average grain sizes are calculated for 1000 training and 1000 generated images for each of the four cooling rates. The trend of the predicted average grain size is in good agreement with the trend of the grain size calculated using the original microstructure images. This result demonstrated that the proposed approach can also capture the trend of the traditional microstructural characteristic including their spatial variation from the given datasets.

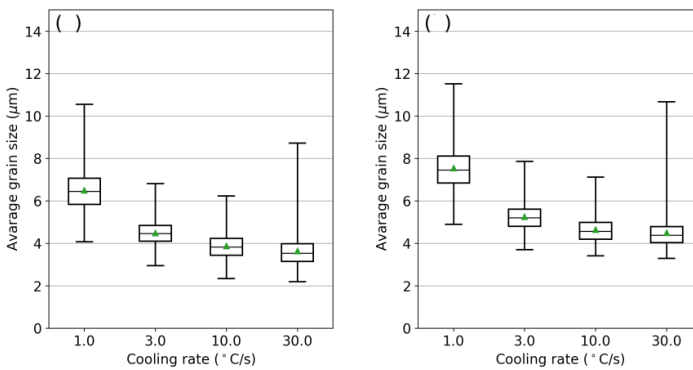


**Fig. 5** Box plots of the average grain sizes (a) in each patch cropped from the original images, and (b) in each generated microstructure patch by the proposed methodology. The

black lines and green triangles in the boxes denote median and mean values of sets of images for each cooling rates, respectively.

#### MECHANICAL PROPERTIES

As a second example, we applied the proposed methodology to the problem of clarifying a hotspot critically affecting the target property [5]. The sample problem is the structure optimization of artificial dual-phase steels composed of the soft phase (ferrite) and hard phase (martensite). The prepared dual-phase microstructures can be divided into four major categories: laminated microstructures, microstructures composed of rectangle- and ellipse-shaped martensite/ferrite grains, and random microstructures. The size of microstructure images is also  $128 \times 128$  pixel and the total number of prepared microstructures is 3824. As an example of a target material property, the fracture strain was selected since fracture behavior is strongly related to the geometry and distribution of the constituent phases. The fracture strain is the elongation of materials at rupture estimated using the Gurson–Tvergaard–Needleman (GTN) model [10]. Using this dataset, we investigate whether the machine learning framework can identify a part of material microstructures that strongly affects a target property in a similar way that human experts can predict based on their experiences.

To identify a critical part of microstructures, we consider calculating a gradient of material microstructures with respect to the fracture strain based on the mapping obtained by our methodology in the same way as shown in the previous section. This assumes that human experts unconsciously consider the *sensitivity* of material microstructures to a slight change in target property. If the machine learning framework correctly captures the physical correlation between the geometry of the material microstructures and the fracture strain, the gradient calculated based on the correlation is expected to correspond to the areas that highly affect the determination of the fracture strain even without giving the physical mechanism itself.

Fig. 6 shows the comparison of the parts of microstructures critically affecting the fracture strain obtained by the physical model and our machine learning framework. Figs. 6 (a) and (b) illustrate the crucial parts of the microstructures composed of relatively long and narrow rectangle-shaped martensite grains. We can see an acceptable agreement between the results of the physical and machine learning methods in terms of the overall distribution of crucial areas which are shown in red in the colormaps. Figs. 6 (c) and (d) show the results for the microstructures composed of similarly shaped martensite grains. In Fig. 6 (c), the rectangle-shaped martensite grains are irregularly arranged, and some martensite grains are close to each other, whereas, in Fig. 6 (d), circular martensite grains are almost regularly arranged. In both Figs. 6 (c) and (d), the machine learning framework identifies the crucial parts that are predicted by the physical model. As mentioned above, the hotspots are in the regions where martensite grains are close to each other.

For incompletely laminated structures such as that shown in Fig. 6 (a) the martensite layers are suggested to expand to achieve a higher fracture strain. Similarly, we can see in Fig. 6 (c) that it is suggested to fill a small gap between martensite grains. Together with the fact that eliminating tiny holes that could cause hotspots and reaching *completely* laminated structures markedly improve their fracture strains [5,11], these results imply

that the framework recognizes the potential of laminated structures to achieve a higher fracture strain in a similar way that human researchers reach an intuition on complete laminate structures as a result of the consideration of reducing the occurrence of hotspots.

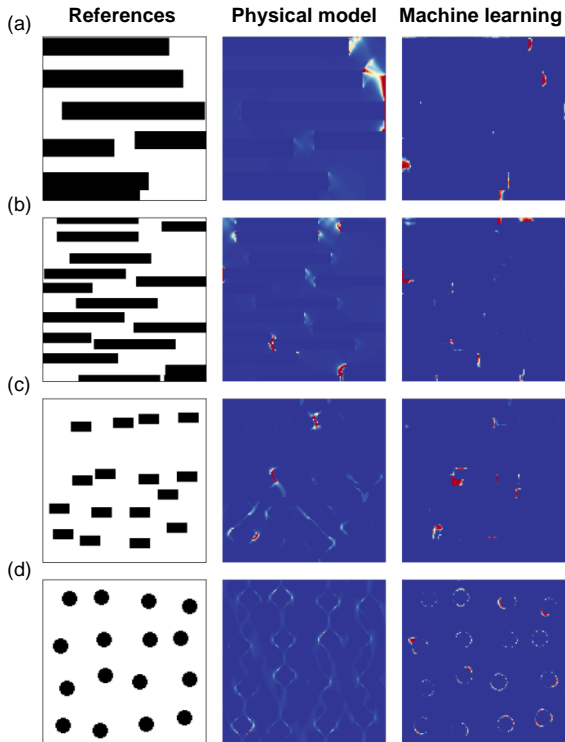


**Fig. 6** Comparison of derivative of microstructures with respect to the fracture strain obtained using deep learning framework with the distributions of void volume fractions calculated on the basis of physical model. The left, middle, and right column in (a)-(d) correspond to the reference microstructures, the void distributions by the physical model, and the derivative by the deep learning framework, respectively.

From the above results, we can conclude that our framework can identify the areas that critically affect a target property without human prior knowledge.

## CONCLUSION

In the present paper, our recent development of a general methodology for extracting the linkage between hierarchical microstructure and process conditions as well as

properties was reviewed. In the proposed method, the uncertainties are captured in the form of probability density functions using deep learning methods. The method was applied for generating virtual steel microstructures obtained after a certain continuous cooling process and those for desired mechanical properties. The obtained results show that the proposed methodology not only captures the stochastic nature of the real microstructure but also helps to clarify a part of microstructures critically affecting the target property

## ACKNOWLEDGMENTS

This work was supported by Council for Science, Technology and Innovation(CSTI), Cross-ministerial Strategic Innovation Promotion Program (SIP), “Materials Integration” for Revolutionary Design System of Structural Materials(Funding agency: JST).

## References

- [1] G. B. OLSON: ‘Computational design of hierarchically structured materials’, *Science*, 277, 1237-42, 1997.
- [2] T. M. POLLOCK, J. E. ALLISON, D. G. BACKMAN, M. C. BOYCE, M. GERSH, E. A. HOLM ET AL.: ‘Integrated computational materials engineering: A transformational discipline for improved competitiveness and national security’, National Materials Advisory Board, NAE, *National Academies Press*, 2008, Report Number: ISBN-10: 0-309-11999-5.
- [3] J. H. PANCHAL, S. R. KALIDINDI, D. L. MCDOWELL: ‘Key computational modeling issues in Integrated Computational Materials Engineering’, *Computer-Aided Design*, 45, 4-25, 2013.
- [4] S. NOGUCHI, J. INOUE: ‘Stochastic characterization and reconstruction of material microstructures for establishment of process-structure-property linkage using the deep generative model’, *Physical Review E*, 104, 025302, 2021.
- [5] S. NOGUCHI, H. WANG, J. INOUE: ‘Identification of microstructures critically affecting material properties using machine learning framework based on metallurgists’ thinking process’, *Scientific Reports*, <http://doi.org/10.1038/s41598-022-17614-0>.
- [6] H. KIM, J. INOUE, T. KASUYA: ‘Unsupervised microstructure segmentation by mimicking metallurgists’ approach to pattern recognition’, *Scientific Reports*, 10, 17835, 2020.
- [7] A. VAN OORD, O. VINYALS, K. KAVUKCUOGLU: ‘Neural discrete representation learning’, In: *Neural Information Processing System Conference*, 2017.
- [8] A. VAN OORD, N. KALCHBRENNER, K. KAVUKCUOGLU: ‘Pixel recurrent neural networks’, In: *International Conference on Machine Learning*, 2016.
- [9] A. VAN OORD, N. KALCHBRENNER, L. ESPEHOLT, O. VINYALS, A. GRAEVS: ‘Conditional image generation with pixelcnn decoders’, In: *Neural Information Processing System Conference*, 2016.
- [10] V. TVERGAARD, A. NEEDLEMAN: ‘Analysis of the cup-cone fracture in a round tensile bar’, *Acta Materialia*, 32, 157-169, 1984.
- [11] T. KOSEKI, J. INOUE, S. NAMBU: ‘Development of multilayer steels for improved combinations of high strength and high ductility’, *Materials Transactions*, 55, 227-237, 2014.



# MICROSTRUCTURE EVOLUTION SUBROUTINE FOR FINITE ELEMENT ANALYSIS

Y. V. SHAN\*, B. VIERNSTEIN\*, E. KOZESCHNIK\*

*\*Institute of Materials Science and Technology, TU Wien, 1060 Vienna, Austria, 0000-0002-1254-1117*

*DOI 10.3217/978-3-85125-968-1-22*

## ABSTRACT

Existing Finite Element Method software can be used in a broad field of material characterization, such as heat conduction, plasticity, electric conductivity or fluid mechanics. However, in terms of microstructure, there is a lack of sophisticated packages to thoroughly model the evolution of these parameters. In the present work, a simple but extensive subroutine is presented, to express the kinetics of precipitation and grain growth on the one hand, and the evolution of structural defects, such as dislocation density and vacancy concentration, on the other hand, in dependence of temperature and deformation rate. As a result, further technologically important material properties, such as yield strength, can be derived with the knowledge of aforementioned parameters. The basic functionality of the subroutine is outlined and the handling of the state parameters, which are used during calculation, are explicated.

Keywords: microstructure evolution, strengthening

## INTRODUCTION

In the field of manufacturing, it is crucial to understand residual stress and distortions that may occur during production. This helps in optimizing both, component design and processing parameters. The complete manufacturing process, starting from solidification, must be considered to simulate stress evolution that depends on temperature and strain rate. An accurate material model is necessary to link flow stress to plastic strain, and various models have been developed over the years [1-5]. Nowadays, empirical models or data table methods are standard and integrated into most Finite Element (FE) software tools such as ANSYS or ABAQUS.

The present work is based on the "simple MicroStructure Evolution" (sMSE) model, which has been introduced by Viernstein et al. [6], in which the treatment of the yield strength and precipitates is thoroughly described. The current work can be seen as a supplement for the aforementioned work. Instead of focusing on strengthening mechanisms, the structure of the subroutine is rolled up from a microstructural point of view. The focus will be on lattice defects, namely point defects (vacancies), line defects (dislocations), planar defects (grain boundaries) and bulk defects (precipitates). A short

overview is also given of all defect evolution equations with particular emphasis on their interdependence. A brief overview on the usage of the subroutine is presented as well.

## MICROSTRUCTURE EVOLUTION

### VACANCIES

The evolution of the vacancy concentration,  $X_{Va}$ , is described using the FSAK framework introduced by Fischer et al. [7]. Vacancies can form and annihilate at dislocation jogs

$$\Delta X_{Va,d} = -\frac{X_{Va}}{X_{Va,eq}} \frac{D_m}{f} 2\pi\rho X_{j,eq} \log\left(\frac{X_{Va}}{X_{Va,eq}}\right), \quad (1)$$

and grain boundaries

$$\Delta X_{Va,gb} = -\frac{X_{Va}}{X_{Va,eq}} \frac{D_m}{f} 15\pi \frac{1}{R^2} \log\left(\frac{X_{Va}}{X_{Va,eq}}\right), \quad (2)$$

where  $X_{Va,eq}$  is the equilibrium vacancy concentration,  $D_m$  the effective matrix diffusion coefficient,  $f$  a geometrical correlation factor (0.7815 for fcc and 0.7272 for bcc),  $\rho$  the dislocation density,  $X_{j,eq}$  the jog fraction at equilibrium (estimated to be around 0.02) and  $R$  the grain radius.

Excess vacancies form during quenching and can accelerate the effective matrix diffusion of elements,  $D_{eff}$ , by several orders of magnitude until their annihilation

$$D_{eff} = D_m \frac{X_{Va}}{X_{Va,eq}}. \quad (3)$$

The vacancy concentration has no direct influence on the evaluation of stresses. However, it has a severe influence on all long-range diffusion processes, especially precipitation kinetics.

### DISLOCATIONS

The evolution of the dislocation density  $\rho$  is described by a simple modified Kocks and Mecking model [8]

$$\Delta\rho = \frac{M}{bA} \sqrt{\rho} \dot{\epsilon} - 2BM \frac{d_{crit}}{b} \rho \dot{\epsilon} - 2CD_d \frac{Gb^3}{k_B T} (\rho^2 - \rho_{eq}^2), \quad (4)$$

where  $M$  is the Taylor factor,  $\dot{\epsilon}$  the strain rate,  $b$  the Burger's vector,  $d_{crit}$  the critical annihilation distance between dislocations,  $D_d$  the diffusion coefficient along dislocations,  $G$  the shear modulus,  $k_B$  the Boltzmann constant,  $\rho_{eq}$  the equilibrium dislocation density and  $A$ ,  $B$  and  $C$  material parameters. These material parameters can be either defined as user input or calculated with the initial hardening rate  $\theta$  and the saturation stress  $\sigma$  according to the model introduced by Kreyca et al. [9].

The dislocation density contribution to the stress is evaluated by the Taylor equation [10]

$$\sigma_d = \alpha M b G \sqrt{\rho}, \quad (5)$$

with  $\alpha$  being the dislocation strengthening coefficient. Furthermore, dislocations act as sources and sinks for vacancies, as mentioned above, or can be seen as possible nucleation sites for precipitates.

#### GRAIN BOUNDARIES

Grain boundaries are described by the average grain radius  $R$  and their evolution by the formula for ideal grain growth [11]

$$\Delta R = 2k_D M \frac{\gamma}{R}, \quad (6)$$

where  $k_D$  is the proportionality factor,  $M$  the mobility of the grain boundary and  $\gamma$  the grain boundary energy. Their contribution to the stress is described by the Hall-Petch equation for fine grain hardening [12,13]

$$\sigma_{FG} = \frac{K}{\sqrt{2R}}, \quad (7)$$

where  $K$  is the Hall-Petch coefficient.

The evolution of the grain radius is, like the dislocation density, not dependent on other defect types (in the current version of the subroutine, pinning of grain boundaries by precipitates is not yet considered). However, they influence the generation and annihilation of vacancies and can act as potential nucleation sites for precipitates.

#### PRECIPITATES

The kinetics of precipitation and their influence on stress is described in detail in the original work of Viernstein et al. [6]. Here, a short summary of the key aspects and an emphasis on the interdependence with the other defect types is presented. The nucleation rate of precipitates,  $J$ , is given by classical nucleation theory [14]

$$J = N_0 Z \beta e^{-\frac{G^*}{k_B T}}, \quad (8)$$

where  $N_0$  is the number of available nucleation sites,  $Z$  the Zeldovich factor,  $\beta$  the atomic attachment rate and  $G^*$  the critical nucleation energy.  $N_0$  is calculated depending on the type of nucleation site

$$N_{0,d} = P_d \frac{\rho}{b}, \quad (9)$$

$$N_{0,gb} = P_{gb} \frac{A n}{b^2}, \quad (10)$$

where  $P_d$  and  $P_{gb}$  are the efficiencies of dislocation and, respectively, grain boundary nucleation sites,  $\rho$  the dislocation density,  $b$  the Burger's vector,  $A$  the area of one grain

and  $n$  the number of grains per unit volume. The atomic attachment rate is proportional to the effective diffusion coefficient in the matrix and, therefore, influenced by the vacancy concentration. As a result, a higher supersaturation of vacancies leads to a faster precipitate nucleation process.

The growth of precipitates is described by the original SFFK growth by Svoboda et al. [15]

$$\Delta r = \frac{d}{k_B T} \frac{1}{r} D_{\text{eff}}, \quad (11)$$

where  $d$  is the driving force. Similar to the nucleation process, the growth is also directly affected by the vacancies.

### SUBROUTINE

The subroutine is written in C code and consists of a single function ‘myuserfunc\_’ taking 9 arguments, which are described in Table 1. During the FE simulation, all relevant variables are saved in the state variable vector (see Table 2 for the structure), which consists of 222 lines. The subroutine covers 4 modes of execution, which can be set by the call mode. The first call mode (1) initializes the material parameters in the state variable vector based on the default settings and should be run once before the FE calculation. An initialization from external is also possible with call mode (2). The main call mode (3) is used for the iteration process during the FE simulation. The subroutine evaluates the evolution of the current state variables (lines 123 to 170 in the state vector) for the given timestep, temperature, and strain rate and saves it without overwriting the current state variables (lines 171-218). The first state variable is the time and is always compared to the calculated time from the last iteration. If the current time (line 123) is set to the calculated time (line 171), the last iteration process is counted as accepted and the calculated state variables will be transferred into the lines of the current ones. The last call mode (4) is reserved for the final call and writes the results of the evaluated stress and its derivatives into the output variables.

**Table 1** Arguments for SMSE subroutine

argument	C type	I/O	description
piCallMode	int*	input	call mode of subroutine (1-4)
pdTimeIncrement	double*	input	time increment for current iteration
pdTemp	double*	input	temperature
pdTempIncrement	double*	input	temperature increment for current iteration
pdStrainRate	double*	input	strain rate
vStateVec	double[222]	input/output	state variable vector
pdSigma	double*	output	evaluated stress
pdJacStrain	double*	output	derivative of evaluated stress according to temperature
pdJacStrain	double*	output	derivative of evaluated stress according to strain rate

**Table 2** Structure of the state variable vector ‘vStateVec’

index	variables	I/O	description
0-38	material parameter	input	basic material properties
39-66	material parameter	input	dislocation evolution
67-71	material parameter	input	solid solution strengthening
72-82	material parameter	input	cross core diffusion
83-118	material parameter	input	precipitate evolution
119-122	material parameter	input	vacancy evolution
123-170	state variable	input	state variables at beginning of current time step
171-218	state variable	output	calculated state variables for time step
219-221	numerical parameter	input	switches for numerical methods

## SUMMARY

A compendium of formulas describing the evolution of lattice defects, such as vacancies (point defects), dislocations (line defects), grain boundaries (planar defects) as well as precipitates (bulk defects) during thermo mechanical treatments is presented. While the dislocation density evolution is mainly dependent on the strain rate, grain growth follows from material properties. The vacancy evolution follows from the dislocation density and grain size. Precipitation kinetics is finally derived by the former parameters. The focus is laid on efficient processing for computationally demanding calculations without losing the interdependence of microstructural properties and their influence on the mechanical properties of the material.

## ACKNOWLEDGEMENTS

The authors would like to thank the ministry of ‘Climate Action, Environment, Energy, Mobility, Innovation and Technology’ (BMK), the ministry of ‘Digital and Economic Affairs’ (BMDW), the Austrian Funding Agency (FFG), as well as the four federal funding agencies Amt der Oberösterreichischen Landesregierung; Steirische Wirtschaftsförderungsgesellschaft m.b.H.; Amt der Niederösterreichischen Landesregierung; Wirtschaftsagentur Wien. Ein Fonds der Stadt Wien for funding project ‘We3D’ in the framework of the 8th COMET call.

## References

- [1] P. LUDWIK: ‘Über den Einfluss der Deformationsgeschwindigkeit bei bleibenden Deformationen mit besonderer Berücksichtigung der Nachwirkungserscheinungen’, *Phys. Zeitschrift*, Nr. 12, pp. 411-417, 1909.
- [2] E. VOCE: ‘A Practical Strain Hardening Function’, *Metallurgia*, pp. 219-226, 1955.
- [3] G.R. JOHNSON, W.H. COOK: ‘A Constitutive Model and Data for Metals Subjected to Large Strains, High Strain Rates and High Temperatures’, *Proc. Seventh Int. Symp. Ballist.*, pp. 541-547, 1983.

- [4] F.J. ZERILLI, R.W. ARMSTRONG: 'Dislocation-Mechanics-Based Constitutive Relations for Material Dynamics Calculations', *J. Appl. Phys.*, Vol. 61, pp. 1816-1825, 1987.
- [5] S. HUANG, A.S. KHAN, S. HUANG, A.S. KHAN: 'Modelling the Mechanical Behavior of 1100-0 Aluminum at Different Strain Rates by the Bodner-Partom Model', *Int. J. Plast.*, Vol. 8, pp. 501-507, 1992.
- [6] B. VIERNSTEIN, T. WOJCIK, E. KOZESCHNIK: 'State Parameter-Based Yield Strength Model for Integration in Finite Element User-Material Routines', *Metals*, Vol. 12, No. 1207, pp. 1-16, 2022.
- [7] F.D. FISCHER, J. SVOBODA, F. APPEL, E. KOZESCHNIK: 'Modeling of Excess Vacancy Annihilation at Different Types of Sinks', *Acta Mat.*, Vol. 59, pp. 3463-3472, 2011.
- [8] P. SHERSTNEV, P. LANG, E. KOZESCHNIK: 'Treatment of Simultaneous Deformation and Solid-State Precipitation in Thermo-Kinetic Calculations', *ECCOMAS 2012 – Eur. Congr. Comput. Methods Appl. Sci. Eng. E-b. Full Pap.*, No. Ecomas, pp. 5331-5338, 2012.
- [9] J. KREYCA, E. KOZESCHNIK: 'State Parameter-Based Constitutive Modelling of Stress Strain Curves in Al-Mg Solid Solutions', *Int. J. Plast.*, Vol. 103, pp. 67-80, 2018.
- [10] G.I. TAYLOR: 'The Mechanism of Plastic Deformation of Crystals Part I - Theoretical', *Proc. R. Soc. A Math. Phys. Eng. Sci.*, Vol. 145, pp. 362-387, 1934.
- [11] G. GOTTSSTEIN: *Materialwissenschaft und Werkstofftechnik Physikalische Grundlagen*, Berlin, pp. 361ff, 2014.
- [12] E.O. HALL: 'The Deformation and Ageing of Mild Steel: III Discussion of Results', *Proc. Phys. Soc. Lond.*, Vol. 64, No. 9, pp. 747-753, 1951.
- [13] N.J. PETCH: 'The Cleavage Strength of Polycrystals', *J. Iron Steel Inst. London*, Vol. 173, pp. 25-28, 1953.
- [14] K.C. RUSSELL: 'Nucleation in Solids: The Induction and Steady State Effects', *Adv. Colloid Interface Sci.*, Vol. 13, pp. 205-318, 1980.
- [15] J. SVOBODA, F.D. FISCHER, P. FRATZL, E. KOZESCHNIK: 'Modelling of Kinetics in Multi-Component Multi-Phase Systems with Spherical Precipitates I: Theory', *Mater. Sci. Eng. A*, Vol. 385, pp. 166-174, 2004.

# STRESS-STRAIN PROPERTIES OF HSS STEEL WELDED JOINT HETEROGENEOUS STRUCTURE: EXPERIMENTAL AND NUMERICAL EVALUATION

D. TOMERLIN\*<sup>1</sup>, D. KOZAK\*\*\*, N. GUBELJAK\*\*\*,  
M. MAGIĆ KUKULJ\*

*\*DOK-ING Ltd., HR-10000, Zagreb, Croatia*

*\*\*Mechanical Engineering Faculty, University of Slavonski Brod, HR-35000, Slavonski Brod, Croatia*

*\*\*\*Faculty of Mechanical Engineering, University of Maribor, SI-2000, Maribor, Slovenia*

*<sup>1</sup>corresponding author*

DOI 10.3217/978-3-85125-968-1-23

## ABSTRACT

Welded joints show significant heterogeneity as they are composed of base metal, heat affected zone and weld metal. Heat Affected Zone (HAZ) is further divided into characteristic segments. All the listed zones of the welded joints have certain microstructural differences and consequent differences in mechanical properties. Mechanical experimental examination and determination of stress-strain characteristics of such heterogeneous welded joints structure, especially in certain segments of the HAZ is very difficult. The classical approach to stress-strain testing using standard tensile specimens have only limited applicability, as even the subsize tensile specimens are difficult to position within the narrow HAZ segments. Difficulties in such experimental measurements and the possibility of testing the welded joints in full scope are the motivation for use of alternative experimental methods. The paper considers double-V butt joint made of High Strength Steel (HSS), welded with filler metal having approximately the same mechanical properties as base metal. Experimental work is focused on stress-strain properties determination with Mini tensile Specimens (MTS) used to determine the properties along the transverse weld line. The aim of the paper is the development of an appropriate computer model based on sufficient experimental data, describing the complete welded joint and its specific zones. The evolution of such model is done, starting with a simple model and refining it to a complex, fully segmented welded joint model. This final welded joint model is implemented into ASTM E8 large size specimen, oriented transverse to the welded joint, and covering all specific zones of the welded joint. Material behaviour is simulated using the ductile damage initiation criterion. Tensile test simulation results show good correlation between experimental data and numerical evaluation. Simulated tensile specimen fracture location matches the HAZ segment with decreased strength values, most prone to failure. The paper demonstrates the possibility of experimental determination of stress-strain mechanical properties throughout the heterogeneous welded joint regions, using the MTS specimens. These results can then be used to create a fully segmented welded joint model for tensile testing, or some similar applications.

Keywords: Stress-strain, welded joint heterogeneity, high strength steel, experimental methods, numerical analysis

## INTRODUCTION

In scope of fusion welded joint, several characteristic zones can be observed: base metal (BM), weld metal (WM) and heat affected zone (HAZ). HAZ refers to part of the base metal which has not undergone the melting process during the fusion welding, rather it was heated to an elevated temperature below the melting point, and subsequently cooled. Width of HAZ strongly depends on chosen welding process, welding parameters, heat input, welded joint geometry, number of passes etc. [1, 2]. The HAZ can be further divided into several characteristic segments with different microstructures and mechanical properties. In the past studies, significant research of fusion weld characteristic zones is already done [3-5]. When choosing the filler material in relation to base metal, the discrepancy between WM and BM mechanical properties is described by "weld strength mis-match" [6, 7].

In scope of overall welded joint, HAZ is most failure prone zone during service life. Because of this it is of great importance to control the overall welding process parameters in order to maintain HAZ width and its mechanical properties within tolerable limit. Heterogeneity is indicative throughout the welded joint, and can be observed in the microstructural and mechanical properties variations.

Experimental investigations of high strength steel welded joints properties, as well as correlated numerical simulations, have previously been conducted by various researchers [8-12]. Investigations presented in scope of this paper are aimed to give deeper insights into mechanical properties of heterogeneous welded joint made from high strength steel, with emphasis on stress-strain behaviour.

The challenge of finding the suitable experimental method for determination of stress-strain characteristics of heterogeneous welded joints structure, is addressed by the authors. General issues relate to the selection of suitable experimental specimens that are able to describe mechanical properties of welded joint and certain segments of the HAZ [13-16]. Since such specimens must be of subsize dimensions, the problems of their manufacture also occur consequently. Some of the experimental methods that can be applied are:

- ASTM E8 tensile subsize specimens for determination of welded joint properties on general scale.
- Mini Tensile Specimens (MTS) for determination of stress-strain properties along the transverse weld line [6].
- Profilometry-based Indentation Plastometry (PIP) method for detailed stress-strain measurement on small surface area using the special indenter equipment [17-19].

In scope of this paper, MTS specimen method is used to determine the stress-strain behaviour of heterogeneous welded joint structure. The test coupon of 40mm thick rolled plates is welded using double-V butt joint. Transverse section cut is done, and complete subsection volume for MTS specimens extracted. Shown in Fig. 1.

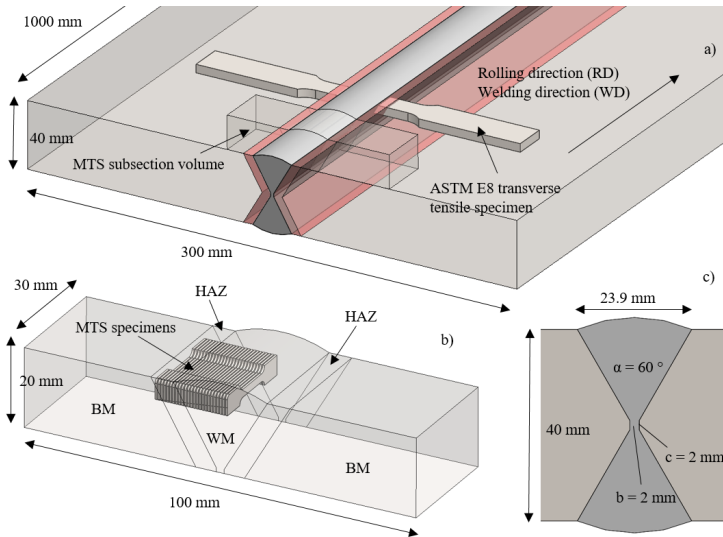


**Fig. 1** Experimental methods for determination of stress-strain characteristics of heterogeneous welded joint structure: (a) welded test coupon, (b) MTS subsection volume with specimens and (c) X joint preparation and dimensions

Detailed characterization of mechanical properties throughout the heterogeneous welded joint is extremely important for the development of a realistic welded joint model and the implementation of numerical analysis. Several welded joint models are created, starting with a simple model and refining it to a complex, fully segmented welded joint model. Modelling of such a complex joint, and simulating its material behaviour, is made possible by using the MTS method experimentally collected material data.

Validation of segmented welded joint model is done based on the uniaxial tensile test, using the ASTM E8 large size flat specimen, oriented transverse to the welded joint, and covering all the specific zones, Fig.1. Ductile damage initiation criterion, integrated into ABAQUS software, is used to simulate response during the tensile test. Numerical simulation is giving the accurate insight into stress-strain behavior, while predicting the specimen damage evolution and final fracture location. Good correlation between experimental stress-strain and simulation results can be observed [20-25].

MATERIALS AND EXPERIMENTAL METHODS

MATERIALS AND WELDED JOINT

The paper considers double-V butt joint (X joint) made of High Strength Steel (HSS), welded with filler metal having the mechanical properties selected according to base metal. The HSS base metal (BM) is S690QL1 fine-grained steel for structural applications, manufactured by quenching and tempering (QT) process, with declared yield strength  $R_{p0.2} \geq 690$  MPa. Weld metal (WM) inside the joint is Mn3Ni1CrMo (ER110S-G) and is deposited using the gas metal arc welding (GMAW) process with 1.2mm diameter filler wire. WM declared yield strength is  $R_{p0.2} \approx 800$  MPa.

Weld strength mismatch is determined using the equation:

$$M = \frac{\sigma_{YW}}{\sigma_{YB}} \tag{1}$$

where  $\sigma_{YW}$  and  $\sigma_{YB}$  represent the yield strength of the weld metal (WM) and the yield strength of the base metal (BM), respectively. In this welded joint, mismatch factor  $M = 1.16$  which indicates the slightly over-matching (OM) weld metal [6, 7].

The BM plates used in X welded joint are of 40 mm thickness. The joint is welded using multiple passes as shown in Fig. 2. Process parameters are given in Table 1.

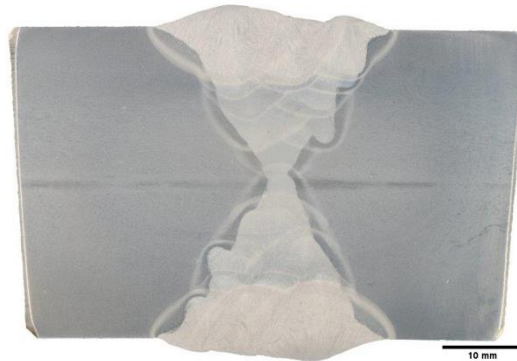


**Fig. 2** X welded joint

**Table 1** Welding process parameters

Pass no.	Location	$I$ [A]	$U$ [V]	$v_w$ [cm/min]	$\eta$	$Q$ [kJ/mm]
1-3	root	195	26	28.5	0.8	0.85
4-22	fill + cover	280	29	45	0.8	0.87

MTS TESTING

The tensile properties along the transverse welded joint line are obtained using the set of Mini Tensile Specimens (MTS) [6]. These are basically flat sheet specimens, with specific dimensions  $L = 24$  mm,  $A = 9$  mm,  $B = 6$  mm,  $C = 5$  mm, and thickness  $T = 0.5$  mm, geometry is shown in Fig. 4. MTS are positioned in filler pass zone (MTS R1-24 and R25 at centerline) of X welded joint. Set is placed in transverse direction including BM, HAZ, and WM up to joint centerline, as shown in Fig. 1 and Fig. 3. MTS are manufactured using the Electrical Discharge Wire Cutting (EDWC) technology, with the wire diameter 0.25 mm, which also dictates the lateral distance between the test specimens.

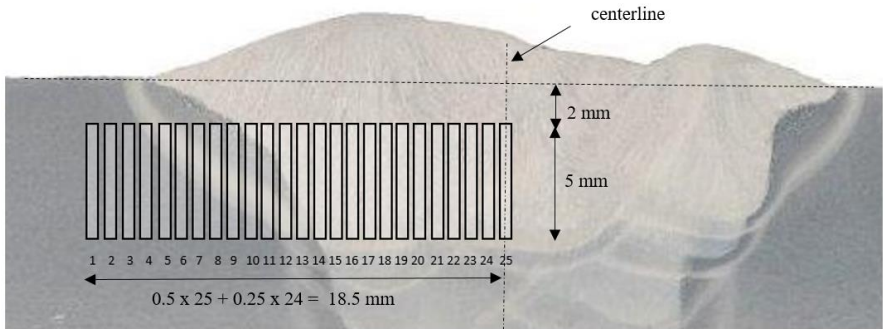


**Fig. 3** MTS specimens positioning along the welded joint

Using MTS specimens experimental testing method, it is possible to gain deeper insight into tensile properties of welded joint characteristic zones, as well as specific HAZ segments. Observing the specific locations from which the individual MTS specimens were extracted, a rough division can be made along the welded joint transverse line, according to characteristic zones:

- MTS R1 - MTS R5 (BM)
- MTS R6 - MTS R13 (HAZ)
- MTS R14 - MTS R25 (WM)

Engineering stress-strain curves obtained from MTS tensile tests are given in Fig. 4. It can be observed that the strength values are following an increasing trend from BM to WM. In HAZ zone, there is the continuity interruption, with peak values in locations MTS R11 - R13.

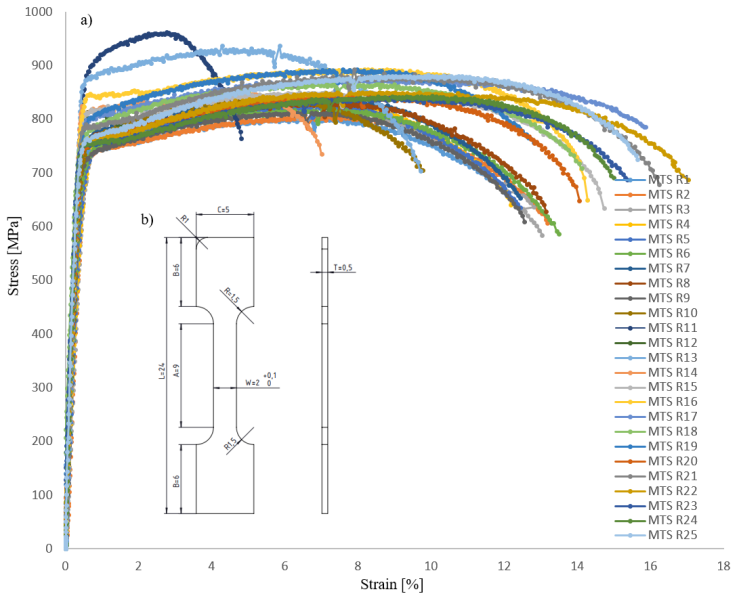


**Fig. 4** MTS specimens tensile testing: (a) engineering stress-strain curves and (b) MTS specimen dimensions

Local mechanical properties, along the transverse welded joint line, are shown in Fig.5.

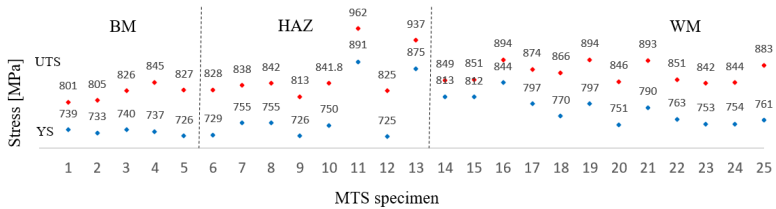


**Fig. 5** Tensile properties along the transverse welded joint line

NUMERICAL MODELLING

DUCTILE DAMAGE

In order to describe the behaviour of elasto-plastic metallic materials, taking into account progressive damage material degradation up to failure, ductile damage model is used. The ductile damage initiation criterion is model for predicting the onset of damage due to nucleation, growth, and coalescence of voids. The typical tensile test stress-strain curve, with progressive damage degradation is shown in Fig. 6. Initial curve partition (0a) is linear-elastic part. Past the yield stress  $\sigma_0$ , in curve partition (ab), the material undergoes stable plastic deformation with strain hardening effect. The point  $b$  is the initiation threshold of plastic instability, with damage parameter  $D = 0$ . In the failure partition (bd) stiffness degradation and damage evolution is present. At point  $d$  damage parameter  $D = 1$ , and crack initiates as an indication of failure. [20].

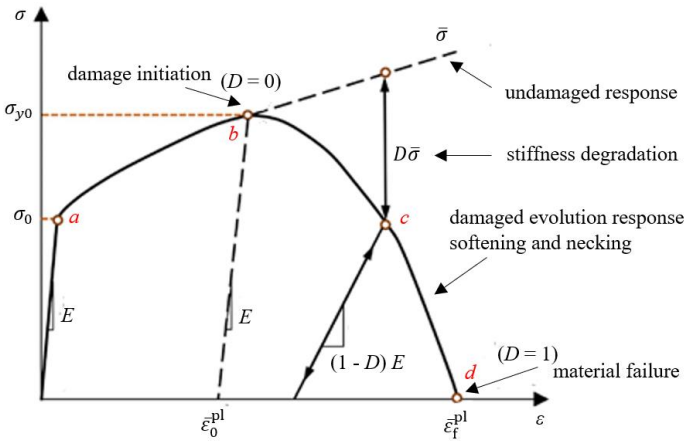


**Fig. 6** Stress-strain curve with progressive damage degradation

The damage parameter  $D$ , governing the failure model, is defined by the equation:

$$D = \sum \frac{\bar{\varepsilon}^{pl}}{\bar{\varepsilon}_f^{pl}} \leq 1 \tag{2}$$

where  $\bar{\varepsilon}^{pl}$  is equivalent plastic strain, and  $\bar{\varepsilon}_f^{pl}$  is plastic strain at failure. Damage parameter  $D$  is changing from 0 (non-damaged) to 1 (material failure). At arbitrary time increment in the analysis, the damaged stress state is given by the scalar damage equation:

$$\sigma_D = (1 - D)\bar{\sigma} \tag{3}$$

where  $\bar{\sigma}$  is the effective (undamaged) stress calculated in the current increment. For the ductile damage initiation, the model assumes that the equivalent plastic strain at the damage onset  $\bar{\epsilon}_D^{pl}$  is function of stress triaxiality  $\eta$  and equivalent plastic strain rate  $\dot{\epsilon}^{pl}$ :

$$\bar{\epsilon}_D^{pl}(\eta, \dot{\epsilon}^{pl}) \tag{4}$$

Damage evolution defines the post damage-initiation material behavior. The equivalent plastic displacement  $\bar{u}^{pl}$ , after damage initiation, is defined according to equation:

$$\dot{\bar{u}}^{pl} = L \dot{\bar{\epsilon}}^{pl} \tag{5}$$

where  $L$  is the characteristic mesh element length. Parameter  $\bar{u}_f^{pl}$  relates to elongation of the element from damage initiation to failure. Severely damaged elements, reaching the maximum degradation limit, are deleted from the model thus achieving the specimen geometry separation. Assuming the constant stress triaxiality and strain rate, material damage behavior is strongly dependant on damage initiation fracture strain  $\bar{\epsilon}_D^{pl}$  parameter and damage evolution displacement at failure  $\bar{u}_f^{pl}$  parameter [20-25]. The comparison of several Ductile Damage Models (DDM) is shown in Fig. 7, with parameters given in Table 2.

**Table 2** Ductile Damage Models parameters

Model	$L$ [mm]	$\bar{\epsilon}_D^{pl}$	$\bar{u}_f^{pl}$ [mm]
DDM 1	0.5	0.08	0.005
DDM 2	0.5	0.08	0.1
DDM 3	0.5	0.20	0.005
DDM 4	0.5	0.20	0.1

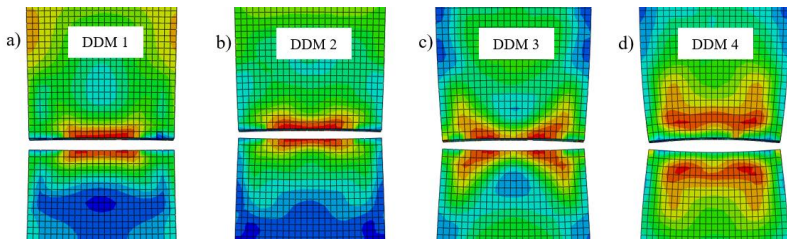


**Fig. 7** Fracture surfaces of tensile specimens: (a) DDM 1, (b) DDM 2, (c) DDM 3 and (d) DDM 4

It can be observed that increase in fracture strain value leads to fracture ductility with more prominent necking effect, and increased concavity of the fracture surface. Displacement at failure affects the element elongation from damage initiation to failure.

WELDED JOINT - MODEL EVOLUTION

The purpose of welded joint model is to describe the overall weld behaviour in scope of numerical simulations application. Due to the existence of heterogeneity, localization of mechanical properties is extremely important for the development of a realistic welded joint model. The authors have investigated several Welded Joint Models (WJM) gradually upgrading them according to the degree of complexity, shown in Fig. 8.

WJM 1 is basic model that includes BM + WM + BM zones. Construction of this model requires material properties only on general scale that can be obtained using the standard size specimens located in BM and All-Weld Metal (AWM). Depending on the mismatch of material properties, fracture will occur either in BM or WM.

WJM 2 is an upgraded model that includes BM + HAZ + WM + HAZ + BM zones. General material properties of HAZ zone need to be determined, and ASTM E8 tensile subsize specimens are suitable for this purpose, Fig. 1. Considering the mechanical properties, and material mismatch, failure will occur in the weakest zone.

WJM 3 is the final, most complex, fully segmented model that includes BM + HAZ + WM + HAZ + BM zones (24 + 1 + 24 = 49 segments). Using the MTS method, material properties are determined for specific segments, and corresponding model is constructed. Failure can be precisely located in most damage prone segment. This model is an improvement against the earlier status, giving more accurate predictions.

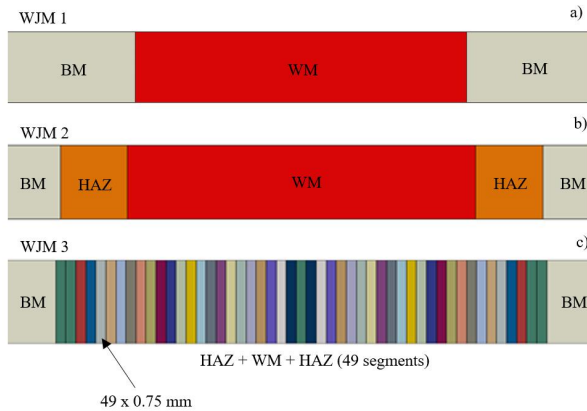


**Fig. 8** Welded Joint Models (WDM) evolution: (a) WJM 1 basic, (b) WJM 2 upgraded and (c) WJM 3 segmented model

## RESULTS AND DISCUSSION

## TENSILE TESTING SIMULATION

Finite element analysis of all tensile tests in scope of this work is done using the ABAQUS/Explicit. ASTM E8 tensile large size flat sheet specimens positioned in transverse direction to welded joint is modelled. Their dimensions are  $L = 200$  mm,  $A = 57$  mm,  $B = 62.6$  mm,  $C = 20$  mm,  $W = 12.5$  mm, and thickness  $T = 5$  mm. Specimens are meshed using the hexahedral C3D8 element. Fine mesh is used in the whole reduced section volume ( $A \times W \times T$ ), with characteristic element length of  $L = 0.5$  mm. Selected mesh element size is in accordance with previous study done by Yan et al. indicating that 0.5 mm element could not affect the accuracy of fracture simulation [22]. Bottom grip section of specimen is fully clamped, while top grip section is subjected to displacement, simulating the tensile loading conditions, Fig. 9.

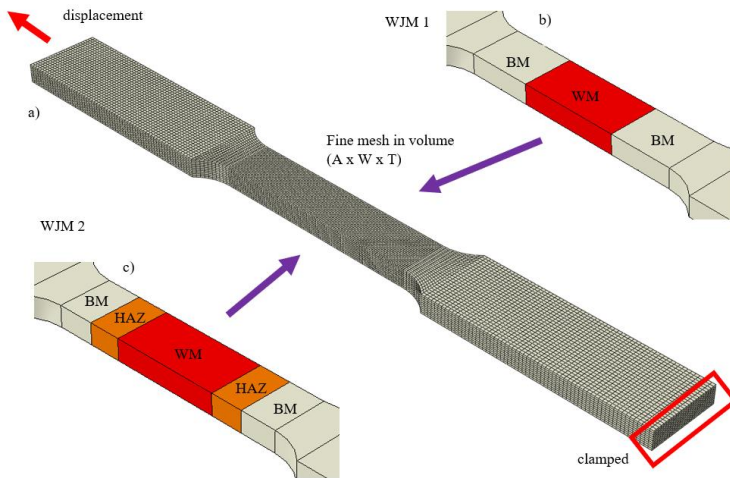


**Fig. 9** Tensile flat sheet specimen ASTM E8 (a) FE model, (b) WJM 1 and (c) WJM 2 model

Initial considerations and simulations address models WJM 1 and WJM 2 based on the material properties on general scale, with fundamental welded joint heterogeneity taken into consideration. Simulations were carried out with the purpose of determining the location of tensile specimen breakage due to the various combinations of welded joint material properties mismatch. Material properties can be either under-matched (UM) or over-matched (OM), while matched properties are not considered here and thus simulated. Based on the results of ASTM E8 tensile subsize specimens testing for determination of welded joint properties on general scale, four steel materials are

identified and implemented into models. Their strength and damage parameters are given in Table 3.

**Table 3** Strength and damage properties from ASTM E8 tensile testing on general scale

Material	$R_{p0.2}$ [MPa]	$R_m$ [MPa]	$\bar{\epsilon}_D^{pl}$	$\bar{u}_f^{pl}$ [mm]
Steel 1	760	810	0.2	0.05
Steel 2	780	835	0.09	0.005
Steel 3	785	840	0.12	0.02
Steel 4	800	860	0.18	0.01

The comparison of several WJM 1 and WJM 2 models with strength mismatch and damage variations is shown in Fig. 10, with material variations and mismatch factors  $M$  given in Table 4.

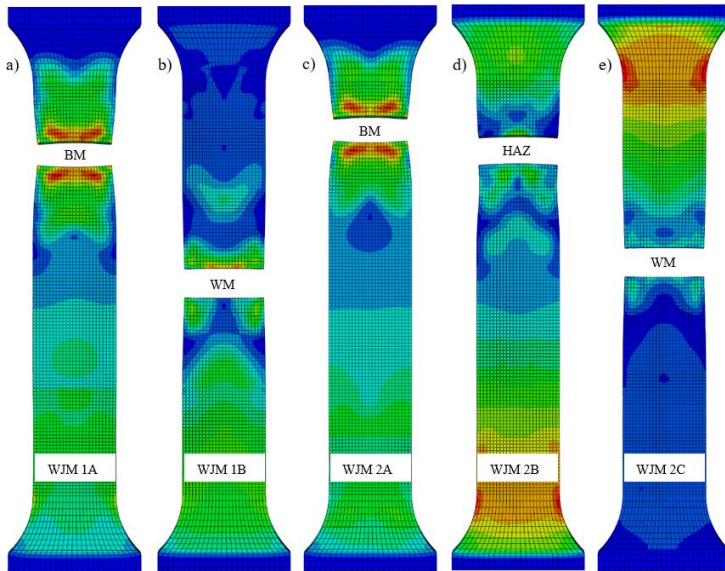


**Fig. 10** Fracture locations for WJM 1 and WJM 2 models, based on material properties mismatch

**Table 4** Mismatch material variations for WJM 1 and WJM 2 models

Model	BM	WM	HAZ	M
WJM 1 A	Steel 1	Steel 4	-	1.053 (OM)
WJM 1 B	Steel 4	Steel 2	-	0.975 (UM)
WJM 2 A	Steel 1	Steel 4	Steel 2	1.053 (OM)
WJM 2 B	Steel 2	Steel 4	Steel 1	1.026 (OM)
WJM 2 C	Steel 4	Steel 2	Steel 3	0.975 (UM)

It can be observed that fracture of all simulated samples occurs in the material region with the lowest strength, corresponding to Steel 1 or 2 material. Using the WJM 1 and WJM 2 models, with known strength data of individual zones of the material, even at a general level, predictions of the critical locations where breakage will occur can be simulated. Damage parameters define the fracture geometry and evolution, as depicted by DDM models.

After performing analyzes of simple models WJM 1 and WJM 2, the fully segmented welded joint model WJM 3, which describes the welded joint heterogeneity in detail, is integrated into tensile specimen model. Same tensile specimen geometry per ASTM E8 as well as numerical modeling preparation and conditions are applied. Purpose of this model is to accurately represent the real damage response, therefore previously determined material properties from MTS testing are used. Elastic modulus is experimentally determined for each of the 25 material segments, while Poisson’s ratio of 0.3 is used. Tensile specimen with WJM 3 is shown in Fig. 11.

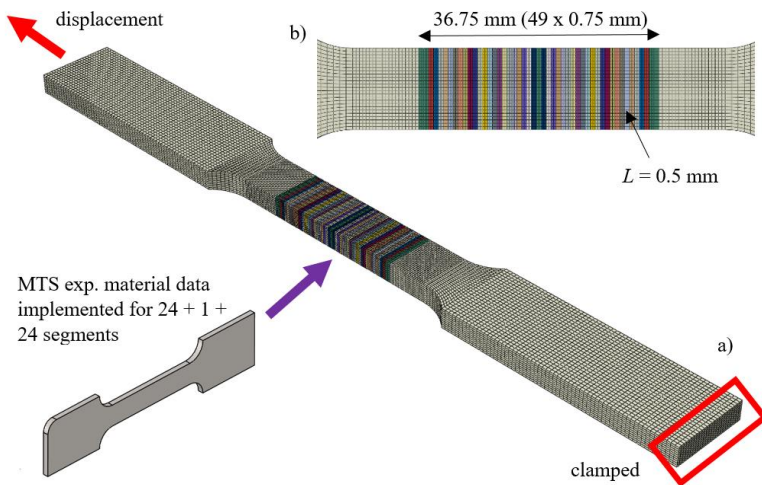


**Fig. 11** Tensile specimen WJM 3 (a) FE model and (b) fully segmented welded joint model

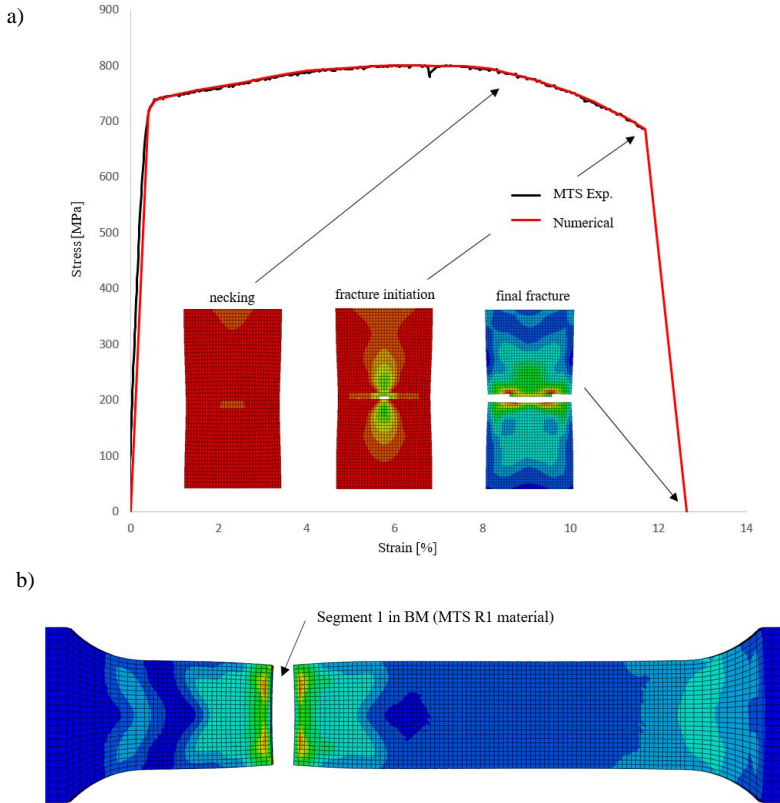


**Fig. 12** Tensile testing FE analysis using WJM 3 model (a) stress-strain diagram and (b) specimen fracture location

WJM 3 tensile specimen failed in segment with lowest UTS value, corresponding to MTS R1 located in the BM zone. This is in an agreement with slightly over-matching WM, and local strength variations in BM. Stress-strain curve from FE analysis is compared with experimental curve for MTS R1 specimen. Good correlation can be observed, Fig. 12. Ductile damage parameters for MTS R1 specimen material are given in Table 5. It can be concluded that this damage model has the most similarities with DDM2 model, resulting in similar necking behavior and fracture surface appearance, Table 2 and Fig. 7.

Observing the numerically simulated damage behaviour of tensile specimen, initiation of ductile fracture is located at the central position of the necking region, which is generally expected during the experimental tensile testing. Tensile specimen behaviour is simulated and the corresponding steps are shown in Fig. 12.

**Table 5** Ductile Damage parameters for transverse tensile testing of WJM 3 model

Model	L [mm]	$\bar{\epsilon}_p^{pl}$	$\bar{u}_f^{pl}$ [mm]
MTS R1	0.5	0.065	0.068

## CONCLUSION

The paper addresses the heterogeneity of welded joint made of HSS steel, using experimental methods and proposing a model for application in computer simulations. The primary conclusions are as follows:

- Detailed characterization of mechanical properties throughout the heterogeneous welded joint is extremely important for the development of a realistic welded joint model. Material properties in narrow segments can be determined using the MTS experimental method.
- Simple WJM 1 and WJM 2 models enable predictions of the critical locations in scope of welded joint where breakage will occur.
- Evolution of welded joint models is done in order to build a model suitable for describing the heterogeneity of the welded joint. Finally, WJM 3 fully segmented model is proposed.
- Tensile testing FEM damage simulation shows the ability of welded joint model to replicate the experimental response. Model is able to predict the exact fracture location.
- Segmented welded joint model has potential for similar applications where it is necessary to describe the heterogeneity of the welded joint.

## ACKNOWLEDGEMENTS

This work has been supported by Slovenian research agency ARRS for part of the research supported by Program P2-0137 "Numerical and Experimental Analysis of Nonlinear Mechanical Systems" and DOK-ING Ltd., Zagreb, Croatia, providing the research material, and funding the test specimens preparation and associated works.

## References

- [1] K. E. EASTERLING: *Introduction to the Physical Metallurgy of Welding*, Second Edition, London, Butterworth-Heinemann, 1992.
- [2] S. KOU: *Welding Metallurgy*, Second Edition, John Wiley and Sons, Hoboken, New Jersey, 2003.
- [3] E.F. NIPPES: 'The weld heat-affected zone', *Weld J*, 38 (1), pp. 1-17, 1959.
- [4] W.F. SAVAGE, E.F. NIPPES, E.S. SZEKERES: 'A Study of Weld Interface Phenomena in a Low Alloy Steel', *Weld J*, 55 (9), pp. 260-268, 1976.
- [5] O.M. AKSELSEN, G. RØRVIK., M.I. ONSØIEN, Ø. GRONG: 'Assessment and Predictions of HAZ Tensile Properties of High-Strength Steels', *Weld J*, 68 (9), pp. 356-362, 1989.

- [6] L. STARČEVIĆ, N. GUBELJAK, J. PREDAN: ‘The Numerical Modelling Approach with a Random Distribution of Mechanical Properties for a Mismatched Weld’, *Materials*, 14, 5896, <https://doi.org/10.3390/ma14195896>.
- [7] P. KONJATIC, M. KATINIĆ, D. KOZAK, N. GUBELJAK: ‘Yield Load Solutions for SE(B) Fracture Toughness Specimen with I-Shaped Heterogeneous Weld’, *Materials*, 15, 214, <https://doi.org/10.3390/ma15010214>.
- [8] D. TOMERLIN, D. KOZAK, N. GUBELJAK, D. DAMJANOVIĆ: ‘Numerička analiza distorzija i zaostalih napreznja pri zavarivanju kutnih spojeva S690QL limova’, *10. Susret HDM*, 01. i 02. listopada, Slavonski Brod, 2020.
- [9] H. ISMAR, Z. BURZIC, N.J. KAPOR, T. KOKELJ: ‘Experimental Investigation of High-Strength Structural Steel Welds’, *Journal of Mechanical Engineering*, 58, 6, pp. 422-428, 2012, DOI:10.5545/sv-jme.2011.281
- [10] E. CADONI, D. FORNI: ‘Strain-rate effects on S690QL high strength steel under tensile loading’, *Journal of Constructional Steel Research*, volume 175, 106348, 2020, <https://doi.org/10.1016/j.jcsr.2020.106348>.
- [11] M. GÁSPÁR, D. FORNI: ‘Effect of Welding Heat Input on Simulated HAZ Areas in S960QL High Strength Steel’, *Metals*, 9, 1226, 2019, <https://doi.org/10.3390/met9111226>.
- [12] M-M. RAN, F-F. SUN, G-Q. LI, A. KANVINDE, Y-B. WANG, R.Y. XIAO: ‘Experimental study on the behavior of mismatched butt welded joints of high strength steel’, *Journal of Constructional Steel Research*, 153, pp. 196-208, 2019, <https://doi.org/10.1016/j.jcsr.2018.10.003>.
- [13] C. RODRÍGUEZ, J.G. CABEZAS, E. CÁRDENAS, F.J. BELZUNCE, C. BETEGÓN: ‘Mechanical Properties Characterization of Heat-Affected Zone Using the Small Punch Test: Use of the small punch test for the mechanical characterization of small areas such as the different zones that characterize the HAZ showed promise’, *Welding Journal*, 88, 2009.
- [14] J. GIGAX, A. TORREZ, Q. MCCULLOCH, H. KIM, S. MALOY, N. LI: ‘Sizing up mechanical testing: Comparison of microscale and mesoscale mechanical testing techniques on a FeCrAl welded tube’, *Journal of Materials Research*, 35(20), 2817-2830, 2020, doi:10.1557/jmr.2020.195
- [15] P.A. STATHERS, A.K. HELLIER, R.P. HARRISON, M.I. RIPLEY, J. NORRISH: ‘Hardness-tensile property relationships for HAZ in 6061-T651 aluminum’, *Faculty of Engineering and Information Sciences*, Papers: Part A. 2846, 2014, <https://ro.uow.edu.au/eispapers/2846>.
- [16] L. ZHANG, W. HARRISON, M.A. YAR, S.G.R. BROWN, N.P. LAVERY: ‘The development of miniature tensile specimens with non-standard aspect and slimmness ratios for rapid alloy prototyping processes’, *Journal of Materials Research and Technology*, Volume 15, pp. 1830-1843, 2021, <https://doi.org/10.1016/j.jmrt.2021.09.029>.
- [17] T.W. CLYNE, J.E. CAMPBELL, M. BURLEY, J. DEAN: ‘Profilometry-Based Inverse Finite Element Method Indentation Plastometry’, *Advanced Engineering Materials*, vol. 23, 9, 2100437, 2021, <https://doi.org/10.1002/adem.202100437>.
- [18] W. GU, J. CAMPBELL, Y. TANG, H. SAFAIE ET AL.: ‘Indentation Plastometry of Welds’, *Advanced Engineering Materials*, 2101645, 2022, <https://doi.org/10.1002/adem.202101645>
- [19] J.E. CAMPBELL, M. GAISER-PORTER, W. GU, S. OOI ET AL.: ‘Indentation Plastometry of Very Hard Metals’, *Advanced Engineering Materials*, 2101398, 2022, <https://doi.org/10.1002/adem.202101398>
- [20] ABAQUS: *Abaqus/Explicit User's Manuals*, Version 6.11, Dassault Systèmes Simulia Corp. Providence, RI, USA, 2011.
- [21] Y. CHO, C. LEE, J.-J. YEE, D.-K. KIM: ‘Modeling of Ductile Fracture for SS275 Structural Steel Sheets’, *Appl. Sci.*, 11, 5392, 2021, <https://doi.org/10.3390/app11125392>.
- [22] S. YAN, X. ZHAO, A. WU: ‘Ductile Fracture Simulation of Constructional Steels Based on Yield to-Fracture Stress–Strain Relationship and Micromechanism-Based Fracture Criterion’,

*Journal of Structural Engineering*, Vol 144, Issue 3, 2018, [https://doi.org/10.1061/\(ASCE\)ST.1943.541X.0001970](https://doi.org/10.1061/(ASCE)ST.1943.541X.0001970).

- [23] F. SHEN, S. MÜNSTERMANN, J. LIAN: 'Investigation on the ductile fracture of high-strength pipeline steels using a partial anisotropic damage mechanics model', *Engineering Fracture Mechanics*, Vol 227, 2020, <https://doi.org/10.1016/j.engfracmech.2020.106900>.
- [24] V.N. VAN DO: 'The Behavior of Ductile Damage Model on Steel Structure Failure', *Procedia Engineering*, Vol 142, 26-33, 2016, <https://doi.org/10.1016/j.proeng.2016.02.009>.
- [25] C. LI, D.E, N. YI: 'Analysis on fracture initiation and fracture angle in ductile sheet metal under uniaxial tension by experiments and finite element simulations', *Journal of Materials Research*, 31(24), 3991-3999, 2016, doi:10.1557/jmr.2016.412.

# **VII Cracking Phenomena and Hydrogen Effects**



# ANALYSIS OF SOLIDIFICATION CRACKING CONSIDERING MECHANICAL AND METALLURGICAL FACTORS

S. MAEDA\*, T. KATO\*, K. IKUSHIMA\*, M. SHIBAHARA\*

*\*Graduate School of Engineering, Osaka Metropolitan University, Osaka, Japan*

DOI 10.3217/978-3-85125-968-1-24

## ABSTRACT

The introduction of tack welding by large-heat-input welding instead of using an out-of-plane constraint has been considered for butt welding automation. However, the occurrence of solidification cracking in welding is a major issue in large-heat-input welding. Solidification cracking is a welding defect that can significantly reduce the strength of weld joints and structures; therefore, it is important to predict its occurrence for its prevention. Solidification cracking is a phenomenon caused by the interaction of mechanical and metallurgical factors and it is known to have a tendency to occur where columnar crystals collide. In the present study, we proposed a numerical analysis method to evaluate the occurrence of solidification cracking in welding using the thermal elastic-plastic analysis using finite element method (FEM) while considering mechanical and metallurgical factors. As a mechanical factor, a cracking evaluation index using the increment of plastic strain that occurs in the solidification brittle temperature range (BTR) during the cooling process is proposed. As a metallurgical factor, the solidification shrinkage strain and the strength of the solid-liquid coexistence region that changes with the solid fraction are modelled. In addition, we proposed a simplified method for predicting the direction of columnar crystal growth using temperature gradients in the BTR. The proposed method was applied to butt welding, and the effect of welding conditions on solidification crack generation was investigated. It was found that the direction of columnar crystal growth predicted by the simplified method using temperature gradient in the BTR was in good agreement with the experimental results. In addition, the crack generation positions obtained with an evaluation index using the plastic strain increment in the BTR were in good agreement with the cracking positions observed in experiments. The influence of the solidification shrinkage strain on solidification crack generation was examined in terms of the relation between the collision angle of columnar crystals and the restraining state around the melting part. Based on these results, it can be concluded that the effects of mechanical and metallurgical factors on solidification cracking in welding can be analysed using the proposed method.

Keywords: Solidification cracking in welding, Thermal elastic-plastic FEM, Plastic strain increment in the BTR, Solid fraction, Solidification shrinkage, Crystal growth direction.

## INTRODUCTION

In recent years, the Japanese shipbuilding industry has been attempting to automate welding due to the difficulty in securing welding workers [1]. This is partly due to the increase in welding operations as vessels have become larger in order to reduce transportation costs. In automated welding, as shown in Fig. 1, the out-of-plane constraint

is required to be changed to in-plane tack welding from the viewpoint of operability. In this case, it is necessary to re-melt the in-plane tack welding from the viewpoint of weld quality, and welding with a large heat input is required. However, there is concern about the occurrence of weld solidification cracking during large-heat-input welding [2]. Weld solidification cracking is a welding defect that occurs when large tensile strain is applied in the temperature range just below the melting point of the weld metal as it solidifies and can significantly reduce the integrity of the weld part [3-5]. Therefore, non-destructive testing is performed after welding on welds where cracking is likely to occur, and if cracking is confirmed, then repair welding is performed, which is one of the reasons for the increase in manufacturing costs. Thus, it is important to establish an analytical method that can predict the occurrence of weld solidification cracking and study the effects of various factors.

In the present study, a solidification cracking analysis method that can take into account metallurgical solidification phenomena and mechanical strain behaviour in the molten part is proposed. As a metallurgical factor, the relationship between the brittle temperature range (BTR) and the solid fraction determined from the metal composition and the solidification shrinkage strain calculated from the solid fraction are considered in the evaluation of BTR plastic strain by the thermal elastic-plastic analysis using finite element method (FEM). A simple method for predicting the direction of columnar crystal growth, which affects the location of solidification cracking, is also proposed using the temperature gradient. And proposed method is used to evaluate the collision angle at which columnar crystals collide with each other.

Then, the developed method is applied to large-heat-input butt welding in order to demonstrate the validity of the proposed method through comparison with experimental results. In addition, the effects of welding deformation as a mechanical factor and solidification shrinkage strain as a metallurgical factor on the solidification cracking are also discussed.

Through the above studies, we show the utility of the plastic strain increment in the BTR for the evaluation of solidification cracking initiation and clarify that the crack initiation location can be predicted by considering both mechanical and metallurgical factors.

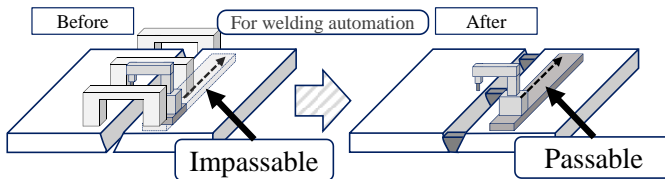


**Fig. 1** Transition of constraint states for butt welding automation

HOT CRACKING ANALYSIS METHOD

The occurrence of weld solidification cracking is affected by phenomena associated with both the solidification of the molten metal and the welding deformation of the entire member due to locally large heat input.

In the present study, we propose a solidification cracking analysis method that can take into account the effects of metallurgical and mechanical factors using thermal elastic-plastic analysis using FEM, which is used to analyse weld deformation and residual stresses. Specifically, the shrinkage associated with the solidification in the BTR and the strength of the molten metal are considered in thermal elastic-plastic analysis using FEM while reproducing the progress of solidification based on the relationship between the solid fraction and temperature in the BTR. An evaluation index for solidification cracking using the plastic strain in the BTR is also proposed. In addition, we propose a simple method for predicting the direction of columnar crystal growth, which has a significant influence on the occurrence of solidification cracking in heat conduction FEM. Since the solidification cracking analysis requires the detailed elements in the weld part, an efficient simulation was achieved using a large-scale thermal elastic-plastic analysis method referred to as the idealized explicit finite element method (IEFEM) [6].

This section describes the details of the analysis method for solidification cracking proposed by authors.

MATERIAL CONSTANTS FOR HOT CRACKING ANALYSIS

In thermal elastic-plastic analysis using FEM, the temperature and mechanical fields from the heating process to the cooling process by welding are sequentially analysed based on the temperature dependency of the material properties. Fig. 2 shows the temperature dependent material properties of Japanese Industrial Standards G 3106 SM490A [7]. In the present study, in addition to setting the material properties used in general welding mechanics analysis, a method for setting material properties in the BTR was proposed for the analysis of solidification cracking.

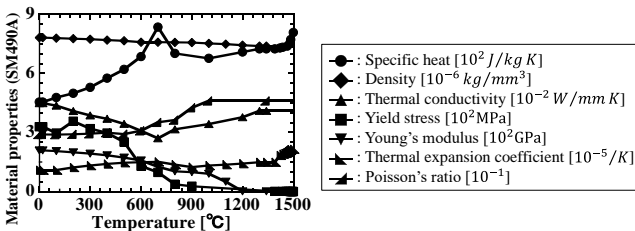


Fig. 2 Temperature dependent material properties of Japanese Industrial Standards G 3106 SM490A [7]

*Relationship between temperature and solid fraction*

In solidification cracking analysis, it is necessary to consider the progress of solidification of the molten metal. In the present study, the progress of solidification was represented by determining the solid fraction of each element from the temperature obtained by the heat conduction FEM. Table 1 shows the chemical composition of JIS G 3106 SM490A [7].

In the present study, the three elements shown in Table 2 were used in a simplified calculation model of micro-segregation proposed by Clyne et al [8]. The derived relationship between the temperature and the solid fraction is shown in Fig. 3. The figure shows that the BTR is 110°C, from 1390°C to 1500°C.

**Table 1** Chemical composition of JIS G 3106 SM490A [7]

Composition	C	Si	Mn	P	S
(wt%)	0.16	0.24	1.51	0.012	0.005

**Table 2** Thermophysical data [8]

Element		k	D	$\alpha$	$m_i$	$C_0$
C	$\delta$	0.200	6.4e-3	64	90	0.160
	$\gamma$	0.360	6.4e-4	6.4	70	
P	$\delta$	0.130	4.0e-5	0.4	50	0.012
	$\gamma$	0.060	2.5e-6	0.025	50	
S	$\delta$	0.060	1.6e-4	1.6	20	0.005
	$\gamma$	0.015	3.9e-5	0.39	20	

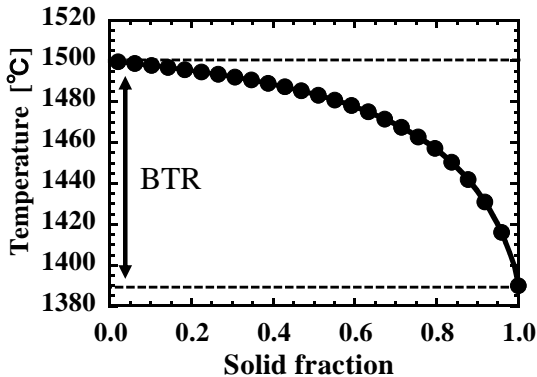


**Fig. 3** Relationship between temperature and solid fraction in BTR

*Solidification shrinkage strain*

During solidification of a molten metal, the liquid phase is pulled toward the solid phase due to the solidification shrinkage strain  $\varepsilon_{sh}$  caused by the density difference between the liquid and solid metals. Specifically, in carbon steel, it is known that there is a density difference of approximately 3.0% [9,10] and its influence cannot be ignored compared to the critical strain for crack initiation [11]. This causes a solidification shrinkage strain of approximately 1.0 % in one direction.

The increment of the solidification shrinkage strain  $\Delta\varepsilon_{sh}$  when the solid fraction  $f_s$  changes in the BTR can be expressed as follows:

$$\Delta\varepsilon_{sh} = \Delta f_s^c \left( \frac{\rho_s}{\rho_l} - 1 \right) \quad (1)$$

where  $\rho_s$  is the density of solid,  $\rho_l$  is the density of liquid, and  $(\rho_s / \rho_l - 1)$  on the right-hand side is the solidification shrinkage coefficient [12,13].

In the present study,  $(\rho_s / \rho_l - 1)$  is defined as 0.03, and, based on the relationship between temperature and solid fraction shown in Fig. 3, solidification shrinkage is considered as thermal strain by introducing the increment of solidification shrinkage strain into the thermal expansion coefficient, as shown in Fig. 2.

*Strength of molten metal*

When considering shrinkage around molten metal, it is important to reproduce the difference in strength between solid and liquid metals. For example, rather than the solid phase which has higher strength, the liquid phase which has lower strength, is tensile due to solidification shrinkage.

It has been confirmed through high-temperature tensile tests that molten metals can retain a stress of approximately 1.0 MPa near the solidus temperature due to partial crystal bonding caused by solidification [14]. Therefore, the yield stress at 1390°C, which is the solidus temperature, was set to 1.0 MPa in the present study. In the temperature range above the liquidus temperature, the strength of the molten metal is considered to be approximately zero. It is thought that the strength of the molten metal can be reproduced by making the yield stress very small above the liquidus temperature in the thermal elastic-plastic analysis using FEM. However, if the yield stress is set to be too small, the analysis becomes unstable. In the present study, therefore, a value of 0.1 MPa, which is sufficiently smaller than 1.0 MPa, was used. In the BTR, the yield stress is assumed to be proportional to the solid phase ratio, as shown in Fig. 4.

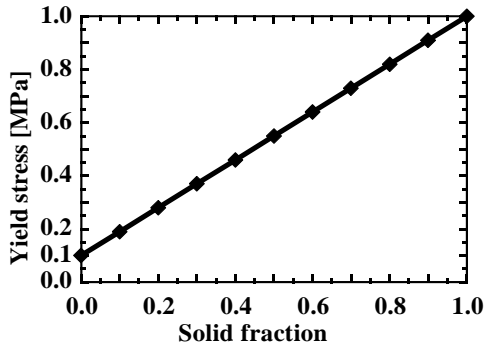


Fig. 4 Relationship between Yield stress in BTR and solid fraction

HOT CRACKING EVALUATION INDEX

Solidification cracking is evaluated by the displacement and strain acting on the weld metal in the BTR, and cracking occurs when these values exceed the critical ductility curve, as shown in Fig. 5 [15]. In other words, the amount of strain generated in the BTR is important to evaluate the occurrence of solidification cracking.

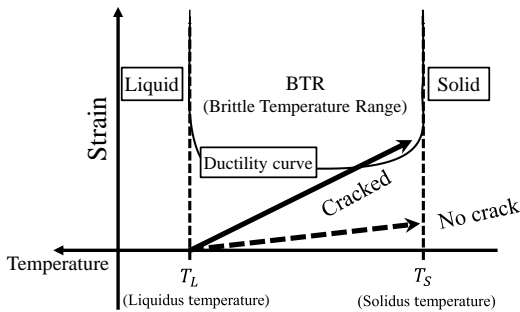


Fig. 5 Schematic illustration of initiation of solidification cracking

Strain in the thermal elastic-plastic analysis using FEM is defined as the strain used in ordinary elastic-plastic analysis and the thermal strain. In addition to these strains, it is necessary to consider the solidification shrinkage strain associated with the solidification of the molten metal in solidification cracking analysis, as described above. In other words, the total strain increment is the sum of the elastic strain increment  $\Delta\epsilon^e$ , the plastic strain increment  $\Delta\epsilon^p$ , the thermal strain increment  $\Delta\epsilon^T$  and the solidification shrinkage strain increment  $\Delta\epsilon^{sh}$ , as shown in the following equation:

$$\Delta \varepsilon = \Delta \varepsilon^e + \Delta \varepsilon^p + \Delta \varepsilon^T + \Delta \varepsilon^{sh} \quad (2)$$

On the other hand, solidification shrinkage is a phenomenon in which liquid metal shrinks during solidification. Therefore, the solidification shrinkage strain increment  $\Delta \varepsilon_{sh}$  shown in Equation (2) is a negative strain that represents shrinkage in the BTR and contributes to solidification cracking. Accordingly, it is necessary to use an index that can evaluate the effect of the solidification shrinkage strain increment on solidification cracking.

In the present study, the plastic strain increment in the BTR  $\Delta \varepsilon_{BTR}^p$  shown in Fig. 6 is considered as an evaluation index of solidification cracking. As shown in the figure, this represents the difference in plastic strain when the liquidus and solidus temperatures are reached during the cooling process. Note that the weld part can be evaluated as tensile due to the negative strain increment caused by solidification shrinkage strain. In the present study, the plastic strain increment in the BTR was calculated by the thermal elastic-plastic analysis using FEM as follows:

$$\Delta \varepsilon_{BTR,i}^p = \sum_{I=n_0}^{n_{t_1}} {}^{(I)} \Delta \varepsilon_{ii}^p (i = x, y, z) \quad (3)$$

where  $t_0$  is the solidification start time,  $t_1$  is the solidification completion time,  $n_{t_0}$  is the solidification start time step,  $n_{t_1}$  is the solidification completion time step, and  ${}^{(I)} \Delta \varepsilon_{ii}^p$  is the plastic strain increment in direction  $i$  at time step  $I$ .

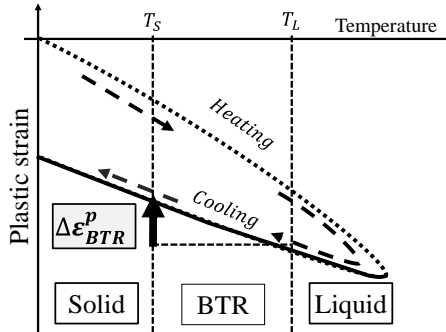


**Fig. 6** Schematic illustration of plastic strain increment in BTR during cooling

Solidification cracking is classified into cracking at the position at which the dendrite tips collide and cracking that occurs between neighbouring dendrites. Both types of cracking are considered to be caused by strain perpendicular to the liquid film. In the present study, the plastic strain increment in the BTR during the cooling process was used to evaluate the solidification cracking at the position at which the dendrite tips collide.

SIMPLIFIED PREDICTION OF COLUMNAR CRYSTAL GROWTH DIRECTION

The solidification morphology of molten metal during welding is determined by the temperature gradient and cooling rate and is generally columnar solidification consisting of cells or dendrites [16].

In the research field of metallurgy, the influence of the direction of crystal growth of the molten metal on solidification cracking has been studied. The relationship between the collision angle of columnar crystals and crack initiation has been evaluated based on grain boundary energy [17,18], and it has been reported that solidification cracking is more likely to occur when the collision angle is large [19,20]. In the present study, the direction of solidification growth of columnar crystals and the collision angle between columnar crystals are calculated simply as shown in Fig. 7 using a simplified prediction method for the direction of columnar crystal growth based on the heat conduction analysis using FEM. The direction of growth of columnar crystals in the molten pool is assumed to be the direction of the maximum temperature gradient when each element reaches the BTR in the cooling process, which is defined as the temperature gradient vector in the BTR  $G_{BTR}$ :

$$G_{BTR} = \sum_{\alpha=1}^m \left( \frac{\partial N^{\alpha}}{\partial x} \mathbf{i} + \frac{\partial N^{\alpha}}{\partial y} \mathbf{j} + \frac{\partial N^{\alpha}}{\partial z} \mathbf{k} \right) T^{\alpha} \quad (4)$$

where  $N^{\alpha}$  is the shape function in the FEM,  $m$  is the number of nodes per element,  $i, j$  and  $k$  are basis vectors in the directions, and  $T^{\alpha}$  is the temperature of each node when each element reaches the BTR in the cooling process.

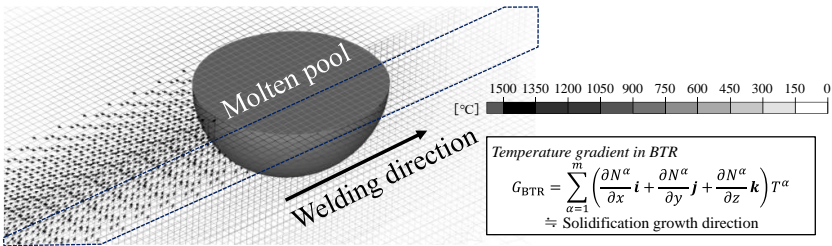


**Fig. 7** Temperature gradient vector in BTR for columnar crystal growth direction

By using the temperature gradient vector in the BTR  $G_{BTR}$ , the direction of columnar crystal growth can be easily predicted. Furthermore, the position of cracking generation is evaluated using the collision angle of the columnar crystals. It has been reported that the collision angle of columnar crystals has a significant effect on crack initiation [19,20]. Moreover, it is known that solidification cracking is likely to occur where columnar crystals collide and a liquid film which remains over a wide area.

In the present study, the solidification form that is prone to cracking is investigated in the relationship between the temperature gradient vector in the BTR  $G_{BTR}$  and the plastic strain increment in the BTR  $\Delta\varepsilon_{BTR}^p$  generated in the weld zone.

IDEALIZED EXPLICIT FEM

Analysis of solidification cracking requires detailed temperature and strain distribution histories in the weld zone. As such, it is necessary to place fine elements around the melting zone. The IEFEM is an analytical method based on the dynamic explicit FEM that can perform large-scale thermal elastic-plastic analysis at high speed and with little memory [6]. This section provides an overview of the analysis method.

In the IEFEM, the following steps are followed, as shown in Fig. 8.

- (1) In the welding transient state, load and temperature increments are applied and the state is maintained.
- (2) Calculate the displacement until static equilibrium is reached based on Equation (5) of the dynamic explicit FEM.
- (3) When a static equilibrium state is obtained, return to step (1) to calculate the next load step.

$$\left( \frac{1}{\Delta t^2} [M] + \frac{1}{2\Delta t} [C] \right) \{U\}_{t+\Delta t} = \{F\}_t - \sum_{e=1}^{N_e} \int_{V^e} [B]^T \{\sigma\} dV \tag{5}$$

$$+ \frac{2}{\Delta t^2} [M] \{U\}_t - \left( \frac{1}{\Delta t^2} [M] - \frac{1}{2\Delta t} [C] \right) \{U\}_{t-\Delta t}$$

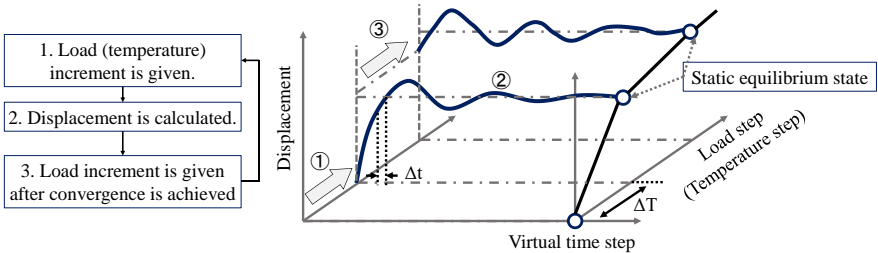


Fig. 8 Schematic illustration of Idealized Explicit FEM (IEFEM)

where  $[M]$ ,  $[C]$ ,  $[B]$ , and  $\{\sigma\}$  are the mass matrix, damping matrix, displacement-strain relation matrix and stress vector, respectively.  $\{U\}_{t+\Delta t}$ ,  $\{U\}_t$ ,  $\{U\}_{t-\Delta t}$  and  $\{F\}_t$  are the displacement vectors at times  $t+\Delta t$ ,  $t$  and  $t-\Delta t$  and the load vector at time  $t$ . Moreover,  $N_e$  is the number of elements in the analysis model, and  $V_e$  is the volume of the elements. By making the mass matrix  $[M]$  and the damping matrix  $[C]$  nodal-intensive diagonal matrix,

the matrices operations in Equation (5) are no longer simultaneous equations and can be analysed with less memory.

Since the effects of the inertia and damping terms become negligible once the static equilibrium state is obtained by the above calculation procedure, in the process of obtaining the static equilibrium state in the calculation procedure of steps (1) and (2), the mass matrix  $[M]$  and the damping matrix  $[C]$  can be adjusted to reduce the time steps required to reach static equilibrium.

By using the above calculation procedure, the IEFEM can be analysed based on the dynamic explicit FEM while considering convergence to a static equilibrium state. The accuracy of the analysis is equivalent to that of the static implicit FEM, while achieving high speed and reduced memory requirements.

## APPLICATION OF PROPOSED METHOD TO LARGE-HEAT-INPUT BUTT WELDING

### ANALYSIS MODEL AND CONDITIONS

In order to investigate the validity of the solidification cracking analysis method presented in the previous section, the proposed method was applied to large-heat-input butt welding. A JIS G 3106 SM490A steel plate was used as the test specimen. Downward single-sided welding was performed using GMAW. A JIS Z 3313 T49J 0 T5-1 C A-U flux-core wire was used, and a groove filler was sprayed in the groove to stabilize the molten pool. As shown in Fig. 9, the process of joining two steel plates of 600 mm in length, 150 mm in width and 25 mm in thickness by butt welding was studied.

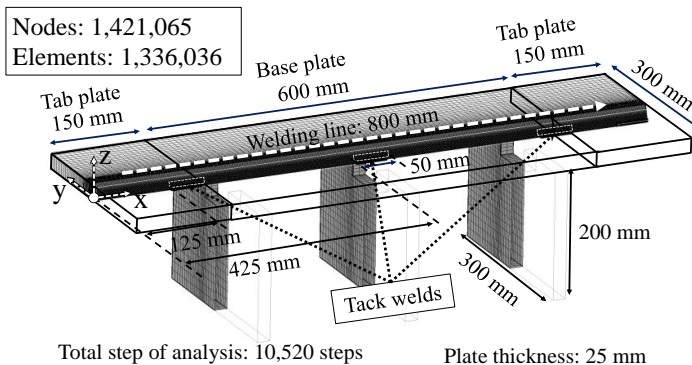


**Fig. 9** Shape and size of test plates of butt welding

Tab plates of 150 mm in length, 150 mm in half-width and 25 mm in thickness were attached to the start and end of the base plates. Tack welds of 50 mm in length and 5 mm

in thickness were installed at  $x = 125$  mm, 425 mm and 725 mm, and constraint plates were attached on the opposite side of the welding at  $x = 200$  mm, 440 mm and 680 mm, as shown in Fig. 9 (b). The constraint plate has a U-shape with a width of 300 mm, a height of 200 mm and a thickness of 20 mm. The weld start position is  $x = 50$  mm and the weld end position is  $x = 850$  mm, i.e., the weld length is 800 mm. The 800 mm welding line is divided into 800 elements in the direction of the weld line and unequal elements in the direction of the plate width. The weld part is a V-groove with a  $35^\circ$  groove angle and a root gap of 5 mm. The model shape of the weld metal is based on the experimental cross-sectional macro photograph. The number of nodes and elements are 1,122,416 and 1,059,664, respectively. The current, voltage, welding speed and thermal efficiency were set to 520 A, 43 V, 250 mm/min, and 0.6, respectively, meaning that the heat input is 3,219.8 J/mm. To show the validity of the proposed method, a comparison was made with experimental results under the same conditions. At the start of the heat conduction analysis using FEM, the element corresponding to the weld metal was disabled, and the element was activated when the torch reached the weld during welding. At the beginning of the heat conduction analysis using FEM, the element corresponding to the weld metal was disabled, and the element was activated when the torch reached the weld during welding. The room temperature was set at  $20^\circ\text{C}$ .

#### INVESTIGATION OF PENETRATION SHAPE AND COLLISION ANGLE OF COLUMNAR CRYSTALS

In this section, we investigate the validity of a simple method for predicting the direction of columnar crystal growth. This method is a simplified prediction that assumes the direction of macroscopic epitaxial growth and does not assume the morphology of the base metal, anisotropy in the direction of preferential growth or crystal size. Fig. 10 (a) shows a cross-sectional macro photograph and Fig. 10 (b) shows the penetration shape and the distribution of the temperature gradient vector in the BTR obtained from the heat conduction analysis using FEM. Based on these figures, it can be confirmed that the penetration shape obtained by proposed analysis is in good agreement with the experimental results.

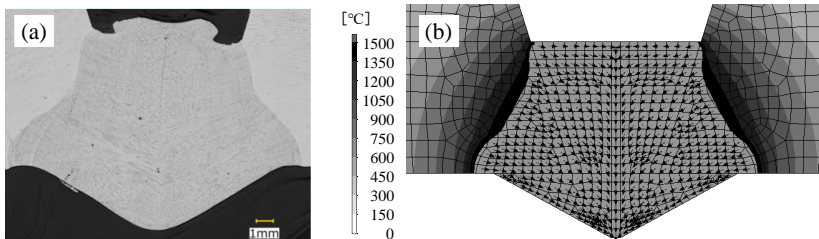


**Fig. 10** Penetration shape and direction of columnar crystal growth: (a) Experimental result, (b) Analysis result

The collision angles were calculated at each of the 14 points at which the vertical line passing through the centre of the welding line. The collision angles obtained from experiments and from the temperature gradient vector in the BTR are compared, as shown in Fig. 11.

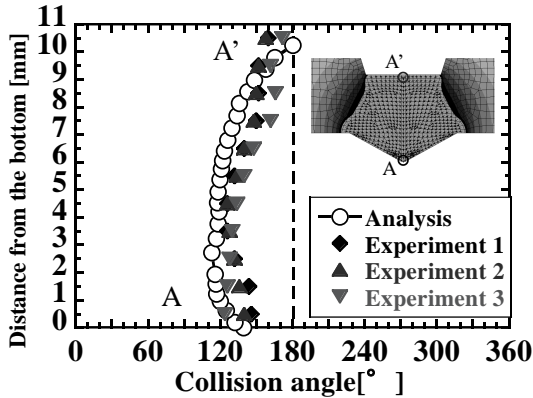


**Fig. 11** Collision angle as determined by analysis and experimental results along A-A'

The experimental results were derived from cross-sectional macro photographs obtained from three different cross sections of the same test. The figure shows that the experimental results are highly repeatable with little variation. It can also be seen that the collision angles are close to 180 degrees in the entire plate thickness direction, especially at the upper part, where columnar crystals collide. It can also be found that the distribution trends of the collision angles in the experimental result and analysis results are in good agreement. These results suggest that the temperature gradient vector in the BTR can be used to predict the growth direction and collision angle of columnar crystals with a certain degree of accuracy.

#### EVALUATION OF SOLIDIFICATION CRACKING INITIATION

In this section, the analysis of the proposed method considering solidification shrinkage strain is performed and compared with the experimental results for the cracking position. Fig. 12 (a) show the distribution of the BTR plastic strain increment in the transverse section at  $x = 425$  mm. Fig. 12 (b) shows the experimental cross-sectional macro photographs at  $x = 425$  mm.

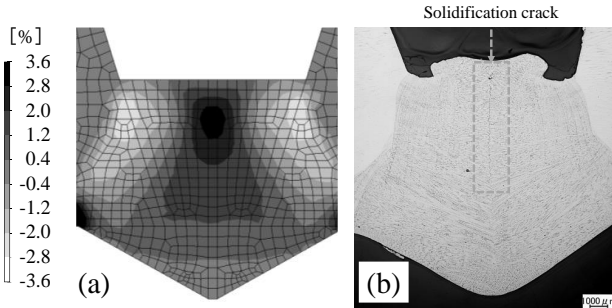


**Fig. 12** Distribution of plastic strain increment in BTR and cracking position on transverse cross section at  $x = 425$  mm: (a) Analysis result, (b) Experimental result

In this figure, large tensile plastic strain increment in the BTR of approximately 3.0% is observed at the upper part. As shown in Fig. 12 (b), the experimental results show that cracking occurs at the upper part, and the cracking position is in good agreement with the position of the large tensile plastic strain increment in the BTR obtained by using the proposed method.

Fig. 13 (a) shows the distribution of the plastic strain increment in the BTR in the longitudinal section along the welding line, and Fig. 13 (b) shows the cracking position in the experiment. In Fig. 13 (a), a large plastic strain increment in the BTR can be observed over a wide area behind the tack weld position at the middle and end of the welding line. In addition, from Figs. 13 (a) and 13 (b), it is shown that cracking occurs at the same locations as those with a large plastic strain increment in the BTR. From these figures, it is found that the proposed method can evaluate solidification cracking initiation in the longitudinal direction as well.

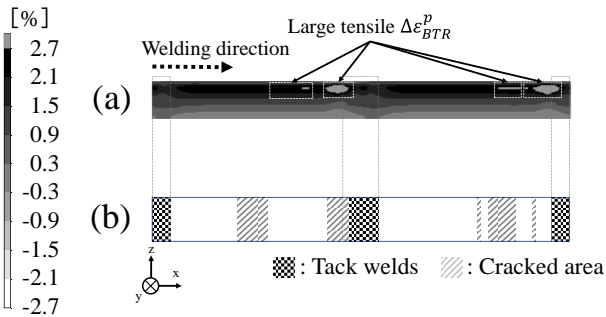


**Fig. 13** Distribution of plastic strain increment in BTR and experimentally obtained cracking position: (a) Analysis result, (b) Experimental result

In the above results, it was shown that the proposed method can predict the crack position in both the thickness direction and the longitudinal direction in the solidification cracking evaluation.

EFFECT OF SOLIDIFICATION MORPHOLOGY ON CRACK INITIATION

In this section, the effect of solidification shrinkage strain on the distribution of plastic strain increment in the BTR is examined. As described above, in the transverse section at  $x = 425$  mm, the crystals collided in the upper part, which is a cracking-prone solidification condition.

Analyses were conducted using the conventional method without considering solidification shrinkage strain and the proposed method with solidification shrinkage strain. Fig. 14 shows the distribution of the plastic strain increment in the BTR along line A-A' of the cross section at  $x = 425$  mm for the comparison of the influence without or with solidification shrinkage strain.

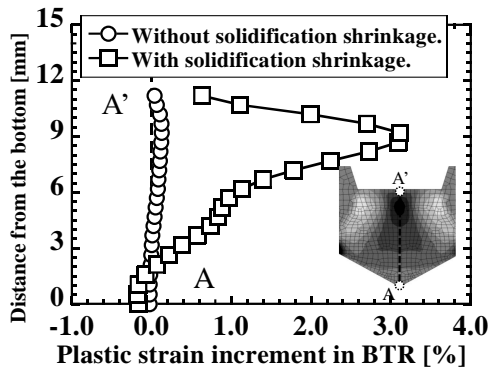


**Fig. 14** Influence of solidification shrinkage on plastic strain increment in BTR along A-A'

Fig. 14 shows that the effect of solidification shrinkage strain is not uniform throughout the weld metal, but rather varies depending on the cooling conditions at each position. With the conventional method that does not consider solidification shrinkage strain, it can be confirmed that a tensile plastic strain increment in the BTR of less than 0.2% is distributed throughout the entire plate thickness direction. With the proposed method, which takes into account the solidification shrinkage strain, a large tensile plastic strain increment in the BTR of approximately 3.0% can be confirmed at the upper part. In other words, a large plastic strain increment in the BTR was generated due to the large influence of solidification shrinkage strain at upper part.

Fig. 15 shows the temperature distributions on lines X-X' and Y-Y' in the figure at the start of solidification. Line X-X' is located at the upper part where the crystals collide, and

line Y-Y' is located at the backside where a small plastic strain increment in the BTR is generated.

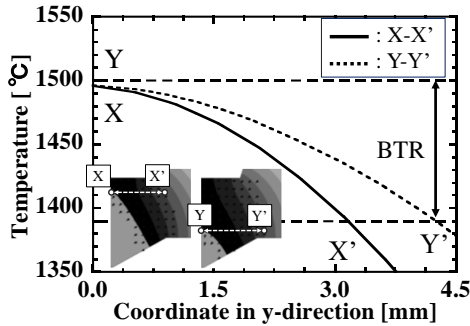


**Fig. 15** Temperature distribution in transverse cross section at the start of solidification at  $x = 425$  mm

Fig. 15 shows that the temperature gradient in the width direction is large on line X-X' at the upper part, i.e., the distance from the region of the solid phase where stiffness is recovered to the BTR is small. On line Y-Y' of the backside of the weld metal where the collision angle is smaller, the temperature gradient in the width direction is small, i.e., the distance from the region of the solid phase to the BTR is large. In other words, when solidification shrinkage occurs at the upper part of the weld metal, there is greater restraint from the region of solid phase. This is considered to cause cracking susceptibility, due to the greater effect of solidification shrinkage strain.

The above suggests that solidification cracking is likely to occur at the position at which columnar crystals collide, because the effect of solidification shrinkage strain becomes large due to the large surrounding restraints.

### CONCLUSIONS

In the present study, a new evaluation method for solidification cracking initiation based on the thermal elastic-plastic analysis using FEM considering mechanical and metallurgical factors is proposed. As metallurgical factors, the direction of solidification growth was simply predicted using the temperature gradient vector in the BTR, and the cracking position was evaluated based on the collision angle of columnar crystals. Analysis was also conducted considering solidification shrinkage strain based on the relationship between temperature and solid fraction in the BTR. From a mechanical point of view, the strain generated in the weld zone was evaluated using the plastic strain increment in the BTR. Furthermore, the proposed method was applied to large-heat-input butt welding.

The results showed the validity of a simple evaluation method for the direction of columnar crystal growth using the temperature gradient vector in the BTR and a

solidification cracking evaluation method using the plastic strain increment in the BTR. This indicates that the proposed method can be used to predict the cracking position.

In addition, it was found that the position at which the collision angle is close to 180° and the crystals collide provides greater restraint against solidification shrinkage, suggesting that the tensile strain at the weld is large, i.e., such solidification morphology is prone to solidification cracking.

#### References

- [1] Y. OKUMOTO: 'Applications of Welding and Joining Technology (Shipbuilding)', *Journal of the Japan Welding Society*, Vol. 79, No. 6, pp. 593-598, 2010.
- [2] K. HOSOI and N. HARA: 'Cracking of Welded Joint', *Journal of the Japan Welding Society*, Vol. 78, No. 6, pp. 555-561, 2009.
- [3] T. SENDA, F. MATSUDA, G. TAKANO, K. WATANABE, T. KOBAYASHI and T. MATSUZAKA: 'Study on Solidification Crack Susceptibility for Weld Metals with Trans-Varestraint Test (1)', *Journal of the Japan Welding Society*, Vol. 41, No. 6, pp. 709-723, 1972.
- [4] N. N. PROKHOROV: 'The Technical Strength of Metals while Crystallising during Welding', *Welding Production*, Vol. 9, No. 4, pp. 1-8, 1962.
- [5] W. S. PELLINI: 'Strain Theory of Hot Tearing', *Foundry*, Vol. 80, pp. 125-199, 1952.
- [6] K. IKUSHIMA and M. SHIBAHARA: 'Development of Analytical Method for Welding mechanics Using Idealized Explicit FEM', *Transaction of JWRI*, Vol. 39, No. 2, pp. 384-386, 2010.
- [7] *Project of Integrity Assessment of Flawed Components with Structural Discontinuity (IAF) Material Properties Data Book at High Temperature for dissimilar metal welding in Reactor Pressure Vessel*, Japan Nuclear Energy Safety Organization, pp. 120-128, 2013.
- [8] T. W. CLYNE, M. WOLF and W. KURZ: 'The Effect of Melt Composition on Solidification Cracking of Steel with Particular Reference to Continuous Casting', *Metallurgical and Materials Transaction B*, Vol. 13, pp. 259-266, 1982.
- [9] P. J. WRAY: 'Predicted Volume Change Behaviour Accompanying the Solidification of Binary Alloys', *Metallurgical and Materials Transaction B*, Vol. 7, pp. 639-646, 1976.
- [10] N. CONOGLIO and C. E. CROSS: 'Towards Establishment of Weldability Testing Standards for Solidification Cracking', *Cracking Phenomena in Welds IV*, pp. 37-66, 2016.
- [11] *Mechanical Engineering Handbook B-2-5 and 7*, Japan Society of Mechanical Engineers, 1984.
- [12] M. RAPPAZ, J. M. DREZET and M. GREMAUD: 'A New Hot-Tearing Criterion'. *Metall Mat Trans. A*, Vol. 30, No. 2, pp. 449-455, 1999.
- [13] YOKOYAMA T, UESHIMA Y, MIZUKAMI H, KAKIMI and M. KATO: 'Effect of Cr, P and Ti on Density and Solidification Shrinkage of Iron', *Tetsu-to-Hagane*, Vol. 83, No. 9, pp. 557-562, 1997.
- [14] H. MIZUKAMI, S. HIRAKI, M. KAWAMOTO and T. WATANABE: 'Tensile Strength of Carbon Steel during and after Solidification', *Tetsu-to-Hagane*, Vol. 84, No. 11, pp. 763-769, 1998.
- [15] F. MATSUDA: 'Hot Cracking in Welded Joints of Steels', *Sanyo Technical Report*, Vol. 5, No. 1, pp. 8-19, 1998.
- [16] M. GAUMANN and W. KURZ: 'Why is it so difficult to produce an equiaxed microstructure during welding?', *Presented at the Mathematical Modelling of Weld Phenomena Conference*, Vol. 4, pp. 125-136, 1997.
- [17] P. RONG, N. WANG, L. WANG, R.N. YANG and W. J. YAO: 'The influence of grain boundary angle on the hot cracking of single crystal superalloy DD6', *Journal of Alloys and Compounds*, Vol. 671, No. 15, pp.181-186, 2016.

- [18] N. WANG, S. MOKADEM, M. RAPPAZ and W. KURZ: 'Solidification cracking of superalloy single- and bi-crystals', *Acta Materialia*, Vol. 52, No. 11, pp. 3173-3182, 2004.
- [19] J. MELLENTHIN, A. KARMA and M. PLAPP: 'Phase-field crystal study of grain-boundary premelting', *Physical Review B*, Vol. 78, paper no. 184110, 2008.
- [20] S. OSHITA, N. YURIOKA, N. MORI and T. KIMURA: 'Prevention of Solidification Cracking in Very Low Carbon Steel Welds', *WJ Research Supplements*, pp. 129s-136s, 1983.



# NUMERICAL STUDY OF THE TEKKEN WELDING TEST

A. A. M. PAGET\*\*\*, V. ROBIN\*\*\*\*\*, J. DRAUP\*\*\*,  
S. HENDILI\*\*, R. UFARTÉ\*\*, T. KHAN\*\*\*\*\*, J. DELMAS\*\*,  
M. C. SMITH\*

\*The University of Manchester (MaSC), M13 9PL, Manchester, United-Kingdom  
\*\*EDF R&D (PRISME), 78401, Chatou, France  
\*\*\*EDF Energy R&D UK Center (MaSC), M13 9PL, Manchester, United-Kingdom  
\*\*\*\*EDF Direction Technique, 69007, Lyon, France

Corresponding Author ORCID: 0000-0002-3090-2414

DOI 10.3217/978-3-85125-968-1-25

## ABSTRACT

To improve the assessment methods of the cold cracking risk, the usage of the Tekken welding test is proposed. The test load is generated by the residual stresses, whose magnitude is controlled by the size of the Tekken mock-up. In order to conduct a subsequent test benchmarking campaign, the optimum dimensions providing a suitable, realistic load are sought. A 2D computational model is developed to answer this question. A range of thicknesses from 15 mm to 150 mm is investigated. An enrichment by experimental data allows predictions with a great level of confidence. For the welding parameters and metals selected, it is found that the level evolution of the self-restraint conditions reaches a stabilization above a thickness of 50 mm. Moreover, the non-negligible effect of the solid-solid phase transformation induced material property changes is highlighted.

Keywords: cold cracking, residual stresses, Tekken test, metallic microstructure, nuclear industry

## INTRODUCTION

### GENERAL BACKGROUND

As one of the world's major electricity operators and with 73 operating reactors on several continents, the *EDF group* faces some technical challenges in maintaining and modernizing its fleet of nuclear power plants. The research presented here is motivated by the need to qualify innovative repair methods and accredit them with the local regulatory bodies. More precisely, we are focusing on repair methods using nickel-based alloys for ferritic steel components of the nuclear steam supply system, the core element of a pressurized water reactor.

Part of the technical solution explored here is focused on cladding using multi-pass welding, optimized with bead tempering principles [1]–[6] in place of additional

conventional heatings to tackle their difficulties of execution. Indeed, these additional heating steps are generally applied [7] for such massive parts to meet a high level of quality and safety of the welding bead deposition during the manufacturing processes [8], as well as for repair operations only if the component can be accessible or disassembled and manipulated. However, in contrast with the oil & gas industry, most of the elements constituting a nuclear reactor cannot be easily accessible or removed, because of reduced space, structural embedment, and radioactivity (often from the component itself).

Therefore, to address the necessity to increase the expertise on these innovative methods prior to their deployment in the nuclear industry, several experimental and numerical analyses are being conducted. Among others, the base metal resistance to cold cracking [8] must be assessed in the weld configuration proposed for these new methods (this is also known as *hydrogen assisted cold cracking*, *delayed cracking*, or *under-bead cracking* [9]). To conduct this assessment, strong couplings between experiments and modelling are of great interest to inform and/or validate each other. Within this research project [10], one of the objectives is to establish a comparative benchmark between a conventional welding quality test and another, potentially more realistic test, respectively the implant and Tekken tests [5], [11]–[15]. Both are allowed by the standard *ISO 17642* for characterizing the risk of cold cracking. This comparison allows the following to be assessed:

- First, the performance of the Tekken test in comparison with the implant test. The latter is historically used in France for welding process qualification of potentially susceptible components.
- Second, the accuracy of further computational models able to quantify the margins against cold cracking.

All the modelling presented here was undertaken using the platform *Salome\_Meca* [16]. The finite element solver used was *Code\_Aster* [17]. Both are open-source software and code developed by *EDF* with other partners.

#### TEKKEN TEST: LITERATURE REVIEW

The Tekken test was conceived and developed by the *Technical Research Institute of the Japanese National Railways* [11]. This is a self-restraint test made from a plane-slotted specimen, as shown in Fig. 1. High stress state is achieved by the slot/slit and groove characteristics and the mock-up thickness [14], [18], [19]. It was principally designed for quantitatively assessing base metal weldability in a configuration representative of the intended application thanks to its massiveness and intrinsic architecture. The Tekken test focuses mainly on assessing the risk of cold cracking. It can be also used for other defect types within the base and/or the weld metal. It requires good repeatability in the case of non-cracking to confirm this result. The Tekken specimen has been studied by a number of researchers who have provided relevant conclusions on the slot/slit types, shapes, and locations within this monolithic mock-up [20]–[23]. However, it is still difficult to estimate or even to find in the literature accurate details of the stress state surrounding the weld of a Tekken test.

METHOD APPROACH

Based on previous research, it was decided to conduct this research project [10] with centered y-slit Tekken and circular V-notched implant designs.

In parallel, prior to manufacture the Tekken specimens, it was decided to conduct a series of computational studies to optimize the specimen thickness. The local stress level increase with thickness, at the expense of higher material consumption. It was decided to aim at maximum load in order to generate the highest risk of cold cracking.

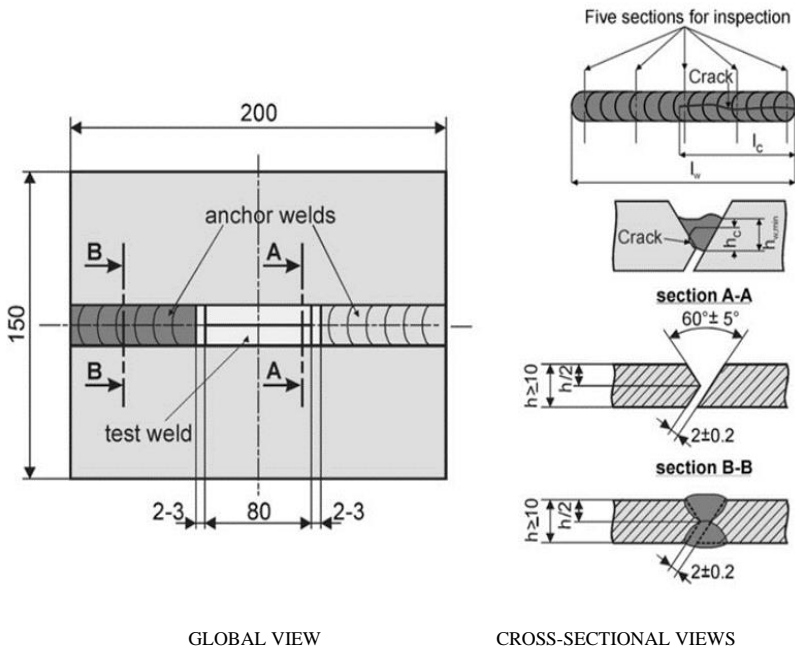


**Fig. 1** Illustration of a Tekken test mock-up ; before & after the weld bead deposition [11]

A 2D thermo-metallo-mechanical finite element model was constructed to compare the evolution of local stress level depending on the mock-up thickness. The 2D idealization ensures a good ratio between the calculation duration and sufficient accuracy of the results. The model represents a mid-length transverse cross-section of a Tekken mock-up, as shown in Fig. 2. This ignores the perturbations at the welding start and stop regions at the bead extremities. Models were generated and run for a full range of different mock-up thickness (15 mm to 150 mm), allowing rapid identification of the stress state level for each Tekken size, for the base and filler metals selected and for welding parameters previously defined by parallel experiments.

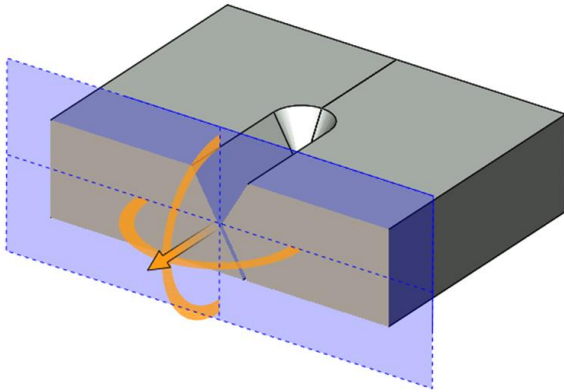


**Fig. 2** Illustration of the modelled 2D slice position within the Tekken test mock-up

#### MATERIAL DATA

The base metal employed is from a *18MND5* material batch whose chemical composition diverges slightly from specification, allowing it to be treated – *only for research purposes* – as a *16MND5*, commonly used for manufacturing reactor pressure vessels. It is equivalent to similar specifications such as *SA-508 Grade 3 Class 1* or *SFVV3* [24], [25]. The filler metal utilized is nickel-based alloy *52M*, which has been selected previously for the proposed repair procedure. A potential application is repairs to the nickel-based alloy *182* welds which join the vessel to the bottom-mounted instrumentation nozzles. The exact metal chemical compositions are given in Table 1, as well as additional details.

The thermal, metallurgical and mechanical properties used in the simulations have been principally identified by several previous studies carried out by *EDF* with different partners [26]. These have been supplemented with updated values from recent studies. In order to reliably reproduce the actual mechanical properties of this metal batch after quenching-tempering-rolling operations, the initial distribution of micro-constituents was assumed to be a mixture made of 61 % ferrite and 39 % bainite (which may not reflect the real microstructure composition).

In addition, some major features considered in all the simulations presented in this study can be highlighted. For the base metal:

- Metallo-dependent elasto-visco-plastic model, including the effects of the solid-solid phase transformation induced plasticity and of the strain-hardening recovery
- Grain growth modelling during the austenitization steps (driving parameter for the micro-constituent fraction predictions)

Concerning the filler metal:

- Chaboche elasto-visco-plastic model (parameters recently calibrated within parallel studies [27], [28])

**Table 1** Chemical composition analysis of the employed metal batches (values from the material certificates provided by the suppliers *Creusot-Loire Industries* and *Special Metals Corporation*)

Base Metal											
considered designation	C	Si	Mn	Ni	Cr	Mo	P	S	Cu	V	Al
16MND5 rolled quenched tempered	0,181	0,216	1,53	0,625	0,202	0,479	0,0063	0,0029	0,111	≤ 0,005	0,022
Filler Metal											
commercial designation	C	Si	Mn	Ni	Cr	Mo	P	S	Cu	Co	Al
Inconel 52M (coiled wire)	0,017	0,12	0,72	59,36	30,05	0,01	0,004	0,001	0,03	0,006	0,11
	Nb + Ta	Fe	Al + Ti	Ti	B	Zr	other				
	0,83	8,49	0,34	0,23	0,001	≤ 0,01	≤ 0,50				

In order to refine the microstructure prediction abilities used for the particular chemical composition of this steel batch, a specific continuous cooling transformation diagram was calculated using a tool recently developed at the *Modelling and Simulation Center (EDF & The University of Manchester)*, based on Li's model [29]–[32]. However, a preliminary estimation of the austenitization temperature and prior austenite grain size range that could be typically encountered in the gas tungsten arc-welding process was necessary. Considering the observations of [29], a range from 3 μm to 130 μm was adopted. Hence, the average value (66 μm) and the commonly considered temperature of welding molten pools (1 450 °C [33], [34]) were utilized to run this continuous cooling transformation diagram calculation. It was directly returned under a table format readable by the *Code\_Aster* solver. An overview of this continuous cooling transformation diagram is given in Fig. 3. During simulation, the feature enabling this solver to adapt its interpretation of the continuous cooling transformation diagram as function of the calculated grain size was activated.

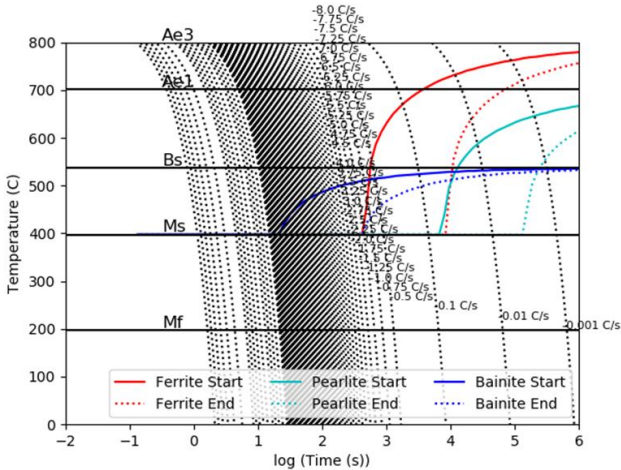


**Fig. 3** Representation of the continuous cooling transformation diagram calculated for the base metal (each dotted line represents a cooling rate step)

## SIMULATION: FIRST CALIBRATION & QUALIFICATION

### DILATOMETRY

Different thermal cycles have been explored using dilatometry testing in parallel studies [27], [28], [35]. In a few words, a dilatometry machine measures the material expansion as a function of the temperature. It allows investigation at the same time of both conventional thermal expansion behavior and solid-solid phase transformation. The experimental data produced on the base metal have been used as reference to assess the reliability of the numerical continuous cooling transformation data set utilized in the welding simulation. Testing has been performed both on the used *16MND5* material lot, and also on the *SA-508 Grade 3 Class 1* steel. The 2D axisymmetric modelling of the dilatometry test specimen (half-rod) comprised an imposed heating temperature (reproducing the induction heating), a heat exchange (reproducing the convective loss and gas cooling), and the radiation loss. The nodes of one half-rod end were considered as embedded along the longitudinal direction, and the nodes of the half-rod axis of symmetry as fixed along the transverse direction. The displacement was therefore followed using the nodes on the other half-rod end. The mesh was built of 125 linear quadratic elements about  $400 \mu\text{m} \times 400 \mu\text{m}$ .

A few examples of the predicted temperature-strain cycles compared with the experiments are presented in Fig. 4 & 5. Agreement is generally good, confirming the suitability of the calculated continuous cooling behavior.

## Mathematical Modelling of Weld Phenomena 13

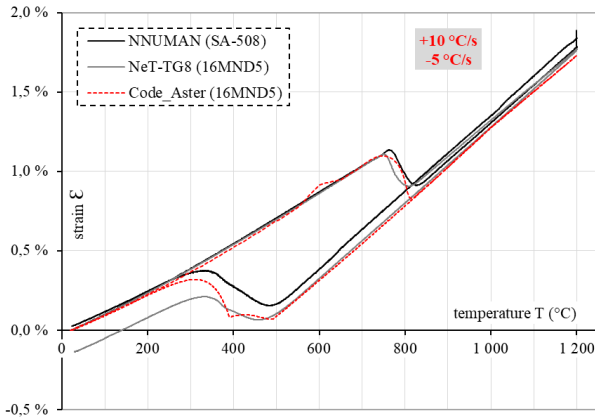


**Fig. 4** Comparison between the simulated *16MND5* behavior and the experimental observations for this modelled steel (*NeT-TG8* project [27], [28]) as well as for the *SA-508* (*NNUMAN* project [35], [36])

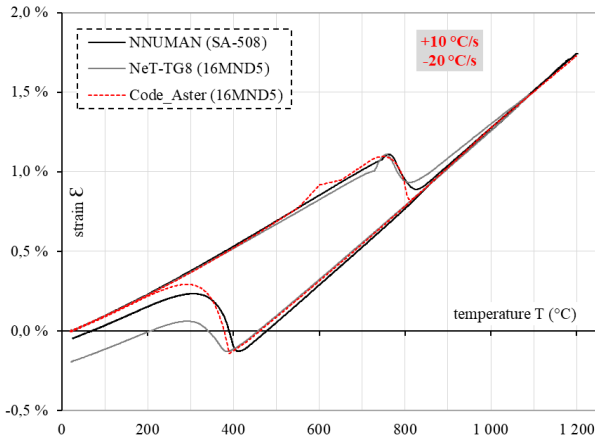


**Fig. 5** Comparison between the simulated *16MND5* behavior and the experimental observations for this modelled steel (*NeT-TG8* project [27], [28]) as well as for the *SA-508* (*NNUMAN* project [35], [36])

## TEKKEN MODELLING

## MESHING STRATEGY

As presented above in Fig. 2, only slices representing the mid-length transverse cross-section of the Tekken mock-ups were modelled in 2D. The meshes were built of linear quadratic elements (4 977 for the 30 mm specimen). Particular attention was paid to the element refinement and quality in the critical areas surrounding the weld bead. The element size adopted in these locations is about  $250\ \mu\text{m}$ , and it is gradually increased in the remote areas that were expected to be relatively unaffected. The weld bead thickness was estimated of 4,5 mm.

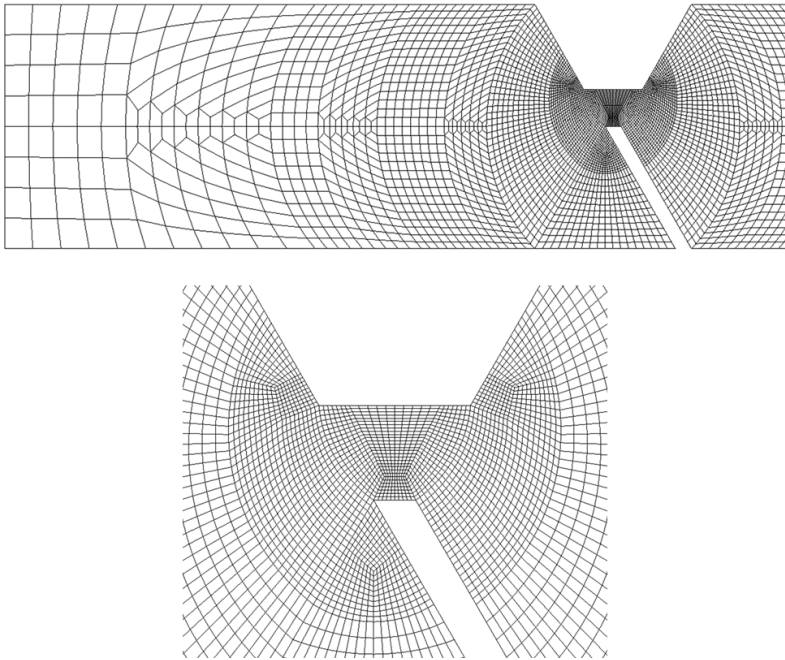


**Fig. 6** Illustrations of the mesh generated for a mock-up thickness of 30 mm

The sketching and meshing operations were fully executed using *Python* command script instructions for *Salome\_Meca*. To aid computation, the slices were sub-divided into different zones constituting the global geometry and then concatenated. Some illustrations of the mesh modelling the 30 mm thick mock-up are given in Fig. 6.

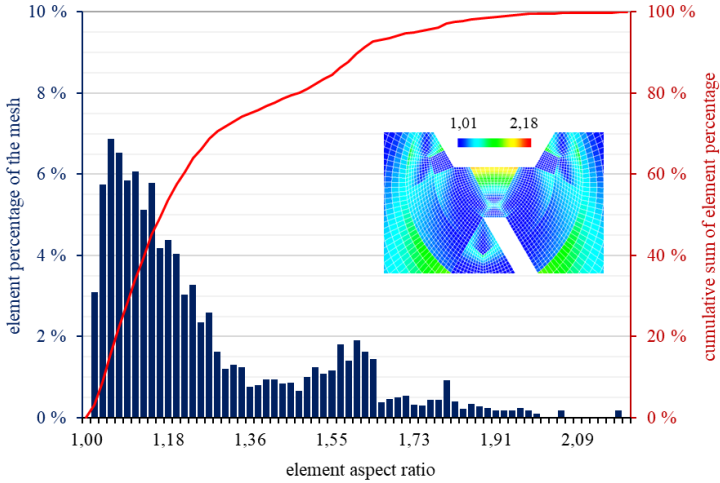
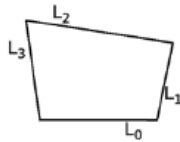


**Fig. 7** Results of the mesh element quality control, the criterion being based on the shape ratio of the quadrangles (size: 30 mm thick)

The global element quality assessment has shown that 82 % of the elements have an aspect ratio inferior at 1,5 , which is considered acceptable for this study (refer to Fig. 7). In particular, elements within the heat-affected zone and fusion zone all have relatively good aspect ratios despite of the geometry singularities. The method utilized for calculating this ratio is given with Equations (1)-(2)-(3) [16]. Note that a perfect square would have a ratio equal to 1,0.

$$q = \frac{L_{max}(L_0+L_1+L_2+L_3)}{4A} \quad A = \frac{1}{2} \|\vec{L}_0 \times \vec{L}_1\| + \frac{1}{2} \|\vec{L}_3 \times \vec{L}_2\| \quad (1) (2)$$



$$L_{max} = \max(L_0, L_1, L_2, L_3) \quad (3)$$

AUTOMATION OF COHERENT MESHING’S

Considering the wide range of Tekken mock-up thicknesses to investigate, a sampling of representative thicknesses was selected: every 5 mm from 15 mm to 50 mm thick, then every 10 mm from 50 mm to 100 mm, and a final thickness of 150 mm. This resulted in a total of 14 Tekken tests to simulate.

The meshing command script was coded to automatically adjust the element sizes when necessary to ensure suitable junctions at the refinement zone frontiers. The element size of the critical area mentioned previously was however imposed. In addition, the biggest element size (at the mock-up edges) was set at 3 mm for mock-ups under 25 mm thick, and then at 4 mm for other sizes.

This algorithmic automation has permitted the Tekken test meshes to be produced with constant and coherent characteristics, to minimize the risk of mesh differences confusing the results. Fig. 8 illustrates this with the extreme cases, 15 mm and 150 mm thick.

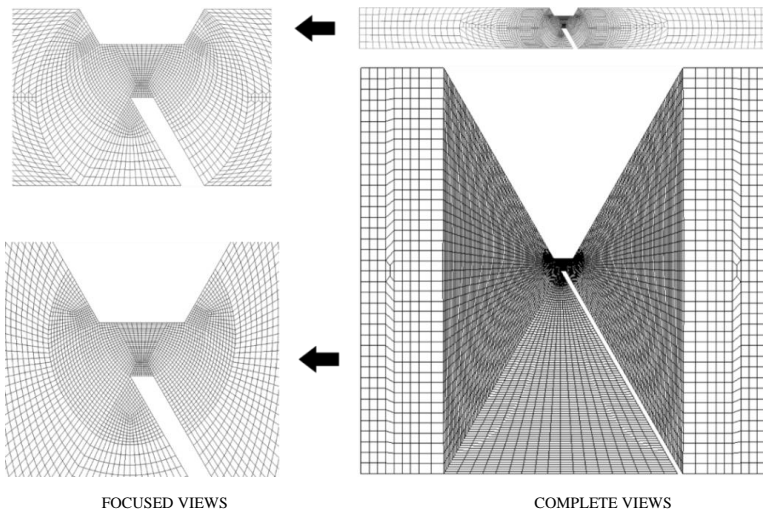


**Fig. 8** Coherence illustration from the 15 mm to the 150 mm meshes with a focus on the weld bead area

#### BOUNDARY CONDITIONS

Conventional convection exchange and radiation loss were taken into account in the thermal calculation. The value of the convection exchange with air was set at  $h = 15 \text{ W}\cdot\text{m}^{-2}\cdot\text{K}^{-1}$ , which is slightly superior to a natural convection in order to add the effect of the shielding gas flow. The emissivity coefficient was assumed at  $\mathcal{E} = 0,50$  as the average value for ground or machined steel surfaces. In the mechanical calculation the nodes of the two slice extremities were considered as fully embedded for reproducing the mock-up stiffness (refer to Fig. 9).

MODELLING OPTIMIZATION

The selected modelling type was axisymmetric about the Y-axis. This approach allows more realistic out-of-plane constraint than mathematical plane strain, and aids mechanical solution convergence in *Code\_Aster*, according to the developer team.

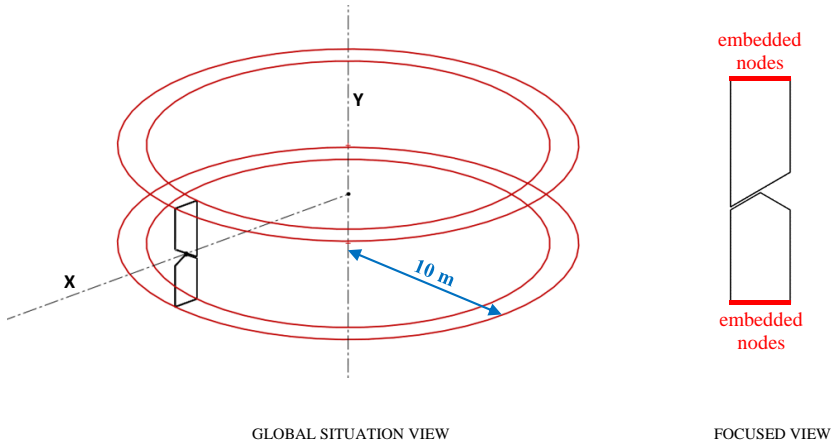


**Fig. 9** Schematic view of the mesh re-positioning (modified scale) and mechanical boundary conditions

However, the Tekken test specimens are not axisymmetric. Therefore, the modelled mock-up has been rotated by 90°, and placed at 10 meters from the Y-axis to give an effectively infinite radius and tackle the non-axisymmetry of this test device. The impact of this large radius was successfully examined by a quick comparison with one meter shorter and one meter longer radii: the results were not affected. Fig. 9 summarizes this re-positioning.

EQUIVALENT HEAT SOURCE

The heat input induced by the electric arc was reproduced through an imposed time-dependent heat flux  $H_{flux}$  on the weld metal elements. This was simply composed of two stages: a heating phase as described in Equations (4) and a cooling phase as described in Equations (5).

$$H_{flux} = \frac{Q_{max}}{Dt_1 \times t} \qquad H_{flux} = \frac{Q_{max}}{Dt_2 \times (t - (Dt_1 + Dt_2))} \qquad (4) (5)$$



**Fig. 10** The thermocouple-instrumented mock-up before assembly and after the welding run completion

For calibrating the parameters of this modelled heat source, a thermocouple-instrumented Tekken test was performed at *EDF* with the welding parameters selected for this research project [10]. These have been optimized within parallel studies [27], [28], [37] to ensure the weld bead deposition quality, as well as maximizing the hydrogen absorption (deliberate placement in unfavorable conditions [38]–[40]). These welding parameters are detailed in Table 2.

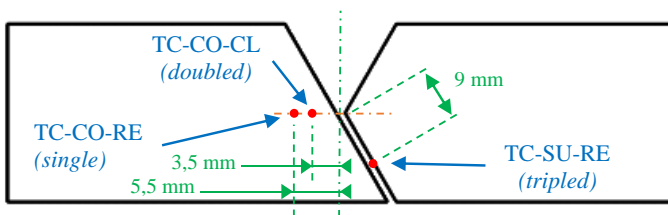


**Fig. 11** Thermocouple locations utilized for the heat source calibration with a 40 mm Tekken mock-up

Welds were deposited using a robotized tungsten inert gas welding station *Valk Welding VWPR QE Extern* (composed of a *VWPR-TIG I* welding torch and a *WGIII-E1400* robot system (*Panasonic TA-I400* model)). A 40 mm thick mock-up made from two parts was utilized (Figure 10). *K*-type thermocouples were placed at five different buried and surface locations. The device utilized for recording the temperatures is a *NI 9213 / cDAQ 9174* acquisition system supplied by *National Instruments*, coupled with the software *LabVIEW – SignalExpress*. The Tekken test device was then placed on special supports designed to minimize the heat transfer to the welding table. Some thermocouple locations were doubled or tripled to determine repeatability. For this study calibration, only three positions were selected in order to get rid of any potential perturbations caused by the heat source shape assumptions. They are detailed in Fig. 11.

**Table 2** Welding parameters selected for this research project

parameter	value
shielding gas	<i>Linde – Varigon 5</i> (5 % H <sub>2</sub> + 95 % Ar)
gas flow rate	11,0 ± 0,3 l/min
welding torch travel speed	0,12 m/min
nominal current intensity	240 ± 1 A
pulsing frequency	0 Hz (direct current)
filler wire feeding speed	3,0 m/min
contact-tip to workpiece distance	30,75 ± 0,50 mm
standoff distance	21,25 ± 0,35 mm
electrode stick out	15,00 ± 0,1 mm
electrode extension	24,50 ± 0,25 mm
arc length (from groove bottom)	6,25 ± 0,25 mm
filler metal wire-electrode distance	2,50 ± 0,25 mm
gas cup internal diameter	Ø 11,25 ± 0,10 mm
filler metal wire diameter	Ø 0,9 mm
arc polarity	electrode [ - ]
electrode	tungsten – 2 % lanthanum
electrode diameter	Ø 2,4 mm
electrode angle	30°
arc voltage control feature (A.V.C.)	enabled
voltage	15,60 ± 0,75 V
welding process type	tungsten inert gas (T.I.G.)
deposited metal section	15,9 mm <sup>2</sup>
linear energy	18,7 kJ/cm
average power	3,7 kW

Following the welding test, the three thermal cycle curves from the experiment were generated by first synchronizing the time axis, and then averaging when doubled or tripled. A wide range of heat source parameter combinations were simulated using a

design of experiment matrix. Then, the set providing the most suitable match in terms of peak temperatures and cooling rates was selected. Hence, the identified parameters used in Equations (4)-(5) was  $Q_{max} = 18,0 \text{ J}$ ,  $Dt_1 = 6,0 \text{ s}$  and  $Dt_2 = 8,6 \text{ s}$ . The heating phase has been considered as having a limited effect for this study needs. The base material heat capacity function has been also slightly adjusted. The comparison between the experimental data and the obtained simulation results with the calibrated heat source are presented in Fig. 12.

Although there is a certain degree of uncertainty about how suitable this calibration would be for other mock-up thicknesses, which still have slight meshing differences, these parameters were assumed as being constant.

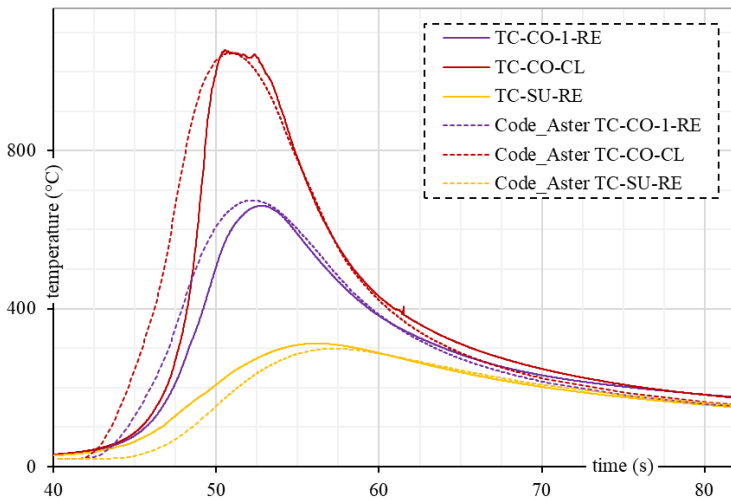


**Fig. 12** Comparison of the experimental thermocouples data with the virtual ones of the *Code\_Aster* simulation after the heat source parameter calibration using a 40 mm Tekken test mock-up

## RESULTS

Once the thermal model was calibrated, the 2D thermo-metallo-mechanical simulation was run on each mesh. According to [41], mainly a uniform normal stress is experienced by bead deposited in an oblique y-slot. Considering this, the temporal evolution of the nodal loads on the restrained faces (as shown in Fig. 9) was extracted and used to estimate the average normal stress  $\sigma_{avg}$  occurring on the weld bead cross-section. This last value was then utilized as the benchmark criterion for studying the effect of thickness. This comparison is presented in Fig. 13 at a focused time scale. Fig. 14 shows an observation over a period of 10 hours for the 15 mm, 30 mm and 50 mm specimens.

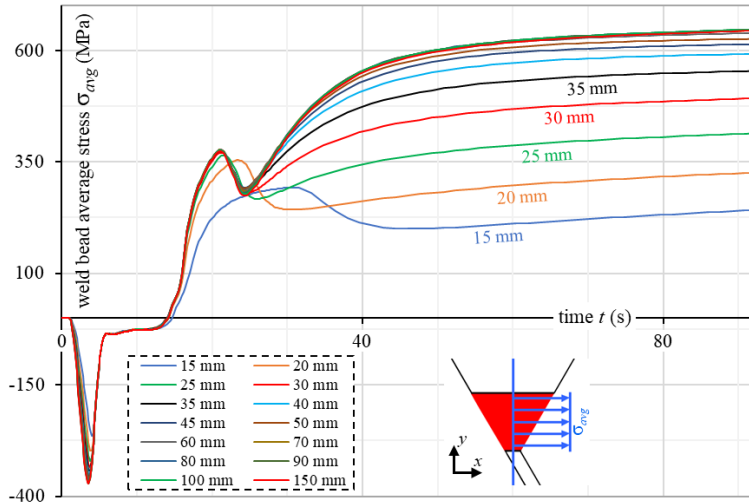


**Fig. 13** Benchmarking of the relative effect of the Tekken mock-up thickness on the average stress  $\sigma_{avg}$  experienced by the weld bead perpendicular cross-section (relative stress value)

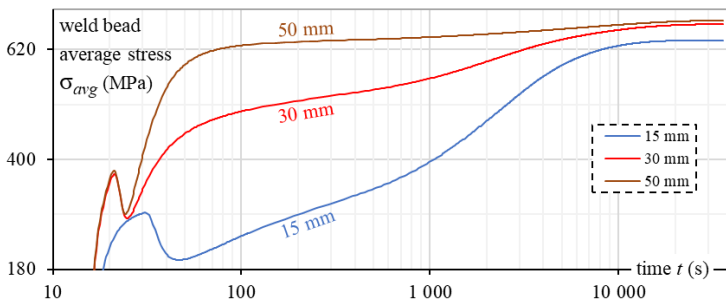


**Fig. 14** Average stress  $\sigma_{avg}$  evolution 10 hours after the weld completion for the 15 mm, 30 mm and 50 mm Tekken specimens (relative stress value)

## DISCUSSION

The results show a compressive stress state during the filler metal deposition and the beginning of the cooling. This is in line with the experimental observations by indirect measurement conducted by [21] using similar y-slit crack test specimens. However, this must be treated with caution : the simulation approach considers the weld metal elements already in place before their simulated deposition (no “inactive element method”), without a deactivation or mitigating feature for their thermo-mechanical characteristics (no “quiet element method”). Considering that the weld metal is molten at this stage, the magnitude of this first part of the mechanical results cannot be considered as entirely correct. Only the results after complete metal solidification can be exploited here. According to the experimental and computational results produced, it can be estimated that the weld metal is fully solidified approximately five seconds after the passage of the welding torch. At that stage, the stress state is more or less equal to zero.

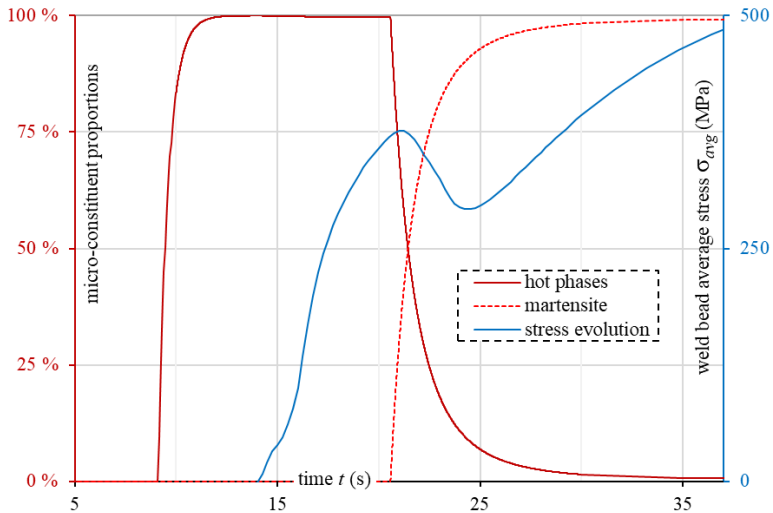


**Fig. 15** Focus on the thermocouple *TC-CO-CL* location (Tekken 40 mm) : correlation between the drop in the stress increase during the metallurgical changes

Following this, rapid growth of the tensile stress is observed, until a sudden drop. The divergences for the smallest thicknesses start at the end of this first stress increase. The drop observed results from metallurgical changes (solid-solid phase transformations), principally from “hot” to “cold” micro-constituents, as seen previously with the dilatometry testing. This aspect has been studied in detail by [42], who measured a similar drop in magnitude during their welding test. This is mainly caused by the atomic re-arrangement occurring within the unit cells during solid-solid transformations, as well as differences in the thermo-mechanical properties of the different micro-constituents. This

correlation is shown in Figure 15 with a 40 mm Tekken mock-up by focusing on the local changes surrounding the closest thermocouple to the fusion boundary (*TC-CO-CL*).

After solid-solid phase transformations are complete, the tensile stress increase resumes. The increasing rate is rather moderated in the thinnest specimen thicknesses due to their lower mass, which reduces the cooling rate. From this point onwards, there is a net effect of the thickness. The maximum achievable self-restraint condition is reached above a thickness of 50 mm. It can take more than 10 hours to experience the final residual stress level. Moreover, it was found that this stabilization phenomenon is insensitive to variations of the material and equivalent heat source parameters made during the model calibration steps, which raised confidence in these findings.

### CONCLUSION

A numerical study enriched by experimental analyses was conducted to develop understanding of the Tekken welding test. The finite element model was used to investigate the effect of mock-up thickness on the self-restraint conditions. The thickness is often considered as the major parameter for driving the stress state self-generated in this test device [14], [18], [19], [43].

Nevertheless, there was a lack of precise information on this impact. This study has permitted to propose a qualitative estimation through a first approach in 2D. A complete benchmarking of the different thicknesses was established, focusing on the level of the average normal stress experienced by the weld bead. The following are the main findings:

- Although the standard Tekken design allows thicknesses up to 150 mm, the residual stress saturates above a thickness of 50 mm using these materials and welding parameters.
- Moreover, this saturation stress is rapidly reached at such thicknesses because of fast heat dissipation into the material remote from the weld. This demonstrates that the mechanical loading peaks quickly after weld completion when the hydrogen level is at its peak, which is thereby the moment when the risk of cold cracking occurrence is the highest.

Thanks to this study and the established benchmarking, it has been possible to conclude that for the remainder of this research project [10], a thickness approaching 50 mm would provide the best compromise for quickly maximising the stress state using this metal combination with these specific welding parameters.

## RECOMENDATIONS

Finally, this study has also permitted to identify several elements that would require further development :

- Quantitively speaking, the convergence to a maximum stress state of about 650 MPa may seem plausible (relative value). Nevertheless, this would require additional verifications before any conclusion on the absolute values of the residual stress experienced. For instance, an extensive experimental small-scale testing under different temperature intervals and for several microstructure types of this base metal would be of interest to finely adjust its material properties and calibrate the model.
- Improvements of the meshing strategy are now possible using the weld macrography realised at the end of this project. This would allow modelling of the actual weld bead shape, the y-slot dimensions, fusion boundaries, and heat-affected zone limits.
- The equivalent heat source could also be improved by modelling its shape accurately and refining its parameters using the experimentally measured isotherm boundaries.
- The calculation duration could be optimised by applying simpler material behaviour models to regions outside the heat-affected zone.
- Prior austenite grain size is an important variable, as the prediction of the micro-constituent proportions within the heat-affected zone is highly dependent on this parameter. This only had an impact in the smallest thicknesses, since heat dissipation there was insufficient to lead to fully martensitic heat-affected zones. However, a lack of experimental data and model development makes optimisation of this part of the solver difficult.
- Finally, a transposition to a 3D model would be of interest to validate a part of the assumptions made for these 2D simulations.

## ACKNOWLEDGEMENTS

We warmly thank the researchers and technicians who were involved in the dilatometry test projects (*NeT-TG8* and *NNUMAN* programs [27], [28], [35], [36]) for having kindly shared their experimental results.

We also very appreciated the help and the quality of the work undertaken by the staff from all the different entities across England and France, from the specimen manufacture to their analyses, as well as for the computational model developments.

Bibliographic References

- [1] P. BRZIAK, M. ŁOMOZIK, R. MIZUNO and F. MATSUDA: 'Repair Welding of SQV2A Pressure Vessel Steel by Temper Bead Techniques Without Post Welding Heat Treatment', *Archives of Metallurgy and Materials*, vol. 56, no. 2, Jan. 2011, Document identifier = DOI: 10.2478/v10172-011-0024-x.
- [2] V. ROBIN and P. GILLES: 'Prevention des risques d'apparition de défaut par la simulation numérique des procédés de fabrication', in *10ème colloque national en calcul des structures*, Giens, France, 2011, Document URL: <https://hal.archives-ouvertes.fr/hal-00592704> (consulted on 03/10/2019).
- [3] A. S. ALORAIEF, A. AL-MAZROUEE, J. W. H. PRICE and T. SHEHATA: 'Weld repair practices without post weld heat treatment for ferritic alloys and their consequences on residual stresses: A review', *International Journal of Pressure Vessels and Piping*, vol. 87, no. 4, pp. 127-133, Apr. 2010, Document identifier = DOI: 10.1016/j.ijpvp.2010.02.001.
- [4] A. S. ALORAIEF, R. N. IBRAHIM and J. GHOJEL: 'Eliminating post-weld heat treatment in repair welding by temper bead technique: role bead sequence in metallurgical changes', *Journal of Materials Processing Technology*, vol. 153-154, pp. 392-400, Nov. 2004, Document identifier = DOI: 10.1016/j.jmatprotec.2004.04.383.
- [5] M. CONSONNI: 'A review of the machine GTAW ambient temperature temper bead repair technique for nuclear power plant components', *Members Technical Literature Review - TWI Ltd (The Welding Institute)*, 2013, Document identifier = TWI ref.: 22952.
- [6] J.-M. CARPREAU, S. FABRICE, C. GILLES and D. BASTIEN: 'Soudage Temperbead appliqué aux matériaux nucléaires', presented at the *Journées Nationales du Soudage 8 - Matériaux*, EDF R&D Chatou, 2010.
- [7] G. K. PADHY, V. RAMASUBBU, N. MURUGESAN, C. REMASH and S. K. ALBERT: 'Effect of preheat and post-heating on diffusible hydrogen content of welds', *Science and Technology of Welding and Joining*, vol. 17, no. 5, pp. 408-413, Jul. 2012, Document identifier = DOI: 10.1179/1362171812Y.0000000023.
- [8] J.-M. CARPREAU: 'Fissuration et soudage', presented at the *EDF (Électricité De France), 8ème Colloque Modélisation et simulation Numérique du soudage*, 2010.
- [9] G. K. PADHY and Y. KOMIZO: 'Diffusible hydrogen in steel weldments: a status review', *Transactions of JWRI (Joining and Welding Research Institute of Osaka University)*, vol. 42, no. 1, pp. 39-62, Jun. 2013, Document identifier = ISSN: 03874508.
- [10] A. A. M. PAGET: *Exploration of the cold cracking risks and limits for welding repair applications of low-alloy ferritic steel nuclear components*, PhD thesis, University of Manchester, Manchester, 2023.
- [11] T. KANNENGIESSER and T. BOELLINGHAUS: 'Cold cracking tests – an overview of present technologies and applications', *Weld World*, vol. 57, no. 1, pp. 3-37, Feb. 2013, Document identifier = DOI: 10.1007/s40194-012-0001-7.
- [12] S. DEBIEZ and P. GERARD: 'Pratique et signification de l'essai de fissuration à froid sur implant', *Soudage et Techniques Connexes*, 1980.
- [13] S. DEBIEZ: 'Détermination des conditions de soudage des aciers faiblement alliés pour prévenir le risque de fissuration à froid', *Soudage et Techniques Connexes*, vol. 38, no. 5, pp. 188-205, 1984.
- [14] H. GRANJON: 'Informations sur les essais de fissuration', *Soudage et Techniques Connexes*, pp. 7-8, 1963.
- [15] A. TALEBI HANZAEI, S. P. H. MARASHI and E. RANJBARNODEH: 'The effect of hydrogen content and welding conditions on the hydrogen induced cracking of the API X70 steel weld', *International Journal of Hydrogen Energy*, vol. 43, no. 19, pp. 9399-9407, May 2018, Document identifier = DOI: 10.1016/j.ijhydene.2018.03.216.

- [16] SALOME\_MECA: *EDF (Électricité de France) & CEA (Commissariat à l'Énergie Atomique et aux Énergies Alternatives)*, Document URL: [www.salome-platform.org](http://www.salome-platform.org).
- [17] CODE\_ASTER: *EDF (Électricité de France)*, Document URL: [www.code-aster.org](http://www.code-aster.org).
- [18] R. KURJI and N. CONIGLIO: 'Towards Establishment of Weldability Test Standards for Hydrogen Assisted Cold Cracking', *International Journal of Advanced Manufacturing Technology*, vol. 77, pp. 1581-1597, 2015, Document identifier = DOI: 10.1007/s00170-014-6555-3.
- [19] W. CAMPBELL: 'Experiences with HAZ cold cracking tests on a C-Mn structural steel', *Welding Journal*, vol. 55, no. 5, 1976.
- [20] K. SATOH and T. TERASAKI: 'Effect of joint geometry on stress concentration factor at the root of weld', *Journal of the JWS (Japan Welding Society)*, vol. 48, no. 5, pp. 298-303, 1979, Document identifier = DOI: 10.2207/qjzws1943.48.298.
- [21] F. MATSUDA, H. NAKAGAWA, K. SHINOZAKI and H. KIHARA: 'Evaluation of transformation expansion and its beneficial effect on cold crack susceptibility using Y-slit crack test instrument with strain gauge', *Transactions of JWRI (Joining and Welding Research Institute of Osaka University)*, vol. 13, no. 1, pp. 47-55, Jul. 1984, Document identifier = DOI: 10.18910/6144.
- [22] R. D. STOUT, R. VASUDEVAN and A. W. PENSE: 'A field weldability test for pipeline steels', *Welding Journal - Welding Research Supplement*, vol. 55, no. 4, pp. 89s-94s, Apr. 1976, Document URL: [http://files.aws.org/wj/supplement/WJ\\_1976\\_04\\_s89.pdf](http://files.aws.org/wj/supplement/WJ_1976_04_s89.pdf).
- [23] R. VASUDEVAN, R. D. STOUT and A. W. PENSE: 'A field weldability test for pipeline steels – part II', *Welding Journal - Welding Research Supplement*, vol. 59, no. 3, pp. 76s-84s, Mar. 1980, Document URL: [http://files.aws.org/wj/supplement/WJ\\_1980\\_03\\_s76.pdf](http://files.aws.org/wj/supplement/WJ_1980_03_s76.pdf).
- [24] L. M. DAVIES: 'A comparison of Western and Eastern nuclear reactor pressure vessel steels', *International Journal of Pressure Vessels and Piping*, vol. 76, no. 3, pp. 163-208, Mar. 1999, Document identifier = DOI: 10.1016/S0308-0161(97)00075-6.
- [25] M. YU, Y. J. CHAO and Z. LUO: 'An assessment of mechanical properties of A508-3 steel used in chinese nuclear reactor pressure vessels', *J. Pressure Vessel Technol.*, vol. 137, no. 3, pp. 031402-031402-7, Jun. 2015, Document identifier = DOI: 10.1115/1.4029434.
- [26] V. CANO and J. ANGLES: 'Recueil bibliographique de caractéristiques thermiques, métallurgiques et mécaniques de l'acier 16MND5', *EDF (Électricité De France)*, EDF R&D Clamart, EDF internal publication H-T64-2008-03224-FR, Mar. 2010.
- [27] X. S. QINGRONG: 'NeT TG8 - dissimilar metal welding between 18MnD5 and alloy 52 - final technical report', *EDF - UoM – MaSC*, University of Manchester, Post-Doctoral technical report, Jun. 2019.
- [28] V. ROBIN ET AL.: 'Net Project Task Group 8 – an international benchmark on residual stress assessment for welding repair', presented at the *PVP2022 - ASME 2022 Pressure Vessels and Piping Conference*, Las Vegas, Nevada, 2022, vol. Volume 4B: Materials and Fabrication, Document identifier = DOI: 10.1115/PVP2022-85083.
- [29] Y. L. SUN ET AL.: 'Effects of dilution on alloy content and microstructure in multi-pass steel welds', *Journal of Materials Processing Technology*, vol. 265, pp. 71-86, Mar. 2019, Document identifier = DOI: 10.1016/j.jmatprotec.2018.09.037.
- [30] M. V. LI, D. V. NIEBUHR, L. L. MEEKISHO and D. G. ATTERIDGE: 'A computational model for the prediction of steel hardenability', *Metall Mater Trans B*, vol. 29, no. 3, pp. 661-672, Jun. 1998, Document identifier = DOI: 10.1007/s11663-998-0101-3.
- [31] C. J. HAMELIN ET AL.: 'Validation of a numerical model used to predict phase distribution and residual stress in ferritic steel weldments', *Acta Materialia*, vol. 75, pp. 1-19, Aug. 2014, Document identifier = DOI: 10.1016/j.actamat.2014.04.045.
- [32] J. DRAUP: 'Python based Continuous-Cooling-Transformation (CCT) digitizer tool', *EDF Energy R&D (UK Center - MaSC)*, University of Manchester, EDF internal publication UKC-R-2018-0xx (provisional), Dec. 2019.

- [33] J. ANGLES: 'Modélisation et Simulation de la Fissuration à Froid: Etude numérique d'une maquette pour la préparation d'essais', *EDF (Électricité De France)*, EDF R&D A.M.A., EDF internal publication H-T59-2011-02090-FR, 2011.
- [34] M. SOKOLOV, A. SALMINEN, E. I. KHLUSOVA, M. M. PRONIN, M. GOLUBEVA and M. KUZNETSOV: 'Testing of new materials and computer aided optimization of laser beam welding of high-strength steels', *Physics Procedia*, vol. 78, pp. 255-264, Jan. 2015, Document identifier = DOI: 10.1016/j.phpro.2015.11.036.
- [35] M. C. SMITH, A. N. VASILEIOU, D. W. RATHOD, J. FRANCIS, N. M. IRVINE and Y. SUN: 'A review of welding research within the new nuclear manufacturing (NNUMAN) programme', presented at the *PVP2017 - ASME 2017 Pressure Vessels and Piping Conference*, Waikoloa, Hawaii, 2017, vol. Volume 6B: Materials and Fabrication, Document identifier = DOI: 10.1115/PVP2017-66180.
- [36] G. OBASI ET AL.: 'Measurement and prediction of phase transformation kinetics in a nuclear steel during rapid thermal cycles', *Metall and Mat Trans A*, vol. 50, no. 4, pp. 1715-1731, Apr. 2019, Document identifier = DOI: 10.1007/s11661-018-05102-y.
- [37] A. FERRARI: 'Dosages d'hydrogène réalisés avec le procédé TIG automatique et l'emploi d'un fil Inconel 52M sur substrat en acier faiblement allié 18MnNiMo5', *IS groupe (Institut de Soudure)*, IS technical report 4325-5G465Y-V1, Feb. 2021, Document identifier = IS ref.: 4325-5G465Y-V1.
- [38] A. OUDRISS ET AL.: 'Consequence of the diffusive hydrogen contents on tensile properties of martensitic steel during the desorption at room temperature', *Materials Science and Engineering: A*, vol. 598, pp. 420-428, Mar. 2014, Document identifier = DOI: 10.1016/j.msea.2014.01.039.
- [39] V. ROBIN: 'Chapter 1 - Industrial challenges where computational welding mechanics becomes an engineering tool', in *Thermomechanical industrial processes*, J.-M. Bergheau, Ed. *ISTE Ltd & John Wiley & Sons*, 2013, pp. 1-74, Document identifier = ISBN: 978-1-84821-358-6.
- [40] V. ROBIN, F. GOMMEZ, C. PRIMAULT and J. DEVAUX: 'Implant test modeling for risk of cold cracking assessment during welding operations', presented at the *PVP2012 - ASME 2012 Pressure Vessels and Piping Conference*, Toronto, 2012, pp. 557-565, Document identifier = DOI: 10.1115/PVP2012-78376.
- [41] N. YURIOKA and H. SUZUKI: 'Hydrogen assisted cracking in C-Mn and low alloy steel weldments', *International Materials Reviews*, vol. 35, no. 1, pp. 217-249, Jan. 1990, Document identifier = DOI: 10.1179/imr.1990.35.1.217.
- [42] F. MATSUDA, H. NAKAGAWA, K. SHINOZAKI, Y. NISHIO and H. KIHARA: 'Effect of transformation expansion on restraint stress of weldment in relation to cold cracking of high strength steels', *Transactions of JWRI (Joining and Welding Research Institute of Osaka University)*, vol. 11, no. 2, pp. 57-65, Dec. 1982, Document identifier = DOI: 10.18910/9554.
- [43] A. L. WINGROVE: *An appraisal of the Tekken test*, PhD thesis, University of Wollongong, Wollongong, 1986, Document URL: <https://ro.uow.edu.au/cgi/viewcontent.cgi?referer=https://scholar.google.com/&httpsredir=1&article=2606&context=theses> (consulted on 05/10/2021).



# **VIII Modelling Tools and Computer Programs**



# ASSESSMENT OF FATIGUE BEHAVIOUR OF UHSS STEEL BUTT-WELDED JOINTS BY MEANS OF A FRACTURE MECHANICS METHODOLOGY

C. STEIMBREGER\*, N. GUBELJAK\*\*, T. VUHERER\*\*,  
N. ENZINGER\*\*\*, W. ERNST\*\*\*\*, M. D. CHAPETTI\*

*\*Laboratory of Experimental Mechanics (LABMEX), INTEMA (Institute for Material Science and Technology), CONICET -  
University of Mar del Plata, J.B. Justo 4302 (B7608FDQ), Mar del Plata, Argentina*

*\*\*University of Maribor, Faculty of Mechanical Engineering, Smetanova 17 (2000), Maribor, Slovenia*

*\*\*\*Graz University of Technology, Institute for Materials Science and Welding, Kopernikusg. 24 (8010), Graz, Austria*

*\*\*\*\*voestalpine Stahl GmbH, Linz, Austria*

DOI 10.3217/978-3-85125-968-1-26

## ABSTRACT

Advances in steel manufacturing technologies made possible the use of high-strength steel (HSS) and ultra-high strength steel (UHSS) in bridges, cranes, offshore structures, oil pipelines and automotive parts. Welding procedures had to be developed to join these materials successfully, but this is still a major issue in mechanical design of HSS elements. Particularly in welding codes and design documents, fatigue resistance of as-welded joints is normally considered to be independent of the base material (BM) static strength. However, cyclic loaded as-welded components with high quality or post-weld treated joints have shown improved performance when using HSS and UHSS as the base material.

The present work aims to apply a fracture mechanics methodology to the analysis of fatigue behaviour of welded joints. The approach requires estimating the driving force available for subcritical crack growth at the location of maximum stress concentration. In this regard, stress intensity factor proved to be a sensible parameter that can account for loading scheme and local weld geometry. It can be determined by numerical modelling, which demands a change from continuum mechanics stress analysis to one that estimates fracture mechanics parameters, considering the existence of defects and cracks. Then, the total driving force applied to the crack can be compared to its threshold for propagation, resulting in the effective driving force for crack growth.

Particularly, the effect of welding process on the fatigue behaviour of ultra-high strength steel butt-welded joints was studied. Sheets of steel S960MC and S960QL were joined with different welding techniques: Gas Metal Arc Welding (GMAW), Laser Hybrid Welding (LHW) and Electron Beam Welding (EBW). To validate the model, fatigue tests were performed with stress ratio  $R = 0.1$ , under four points bending loading. Joints manufactured with GMAW exhibited the highest fatigue strength of the three configurations. Compared to the fatigue limit of the BM, a decrease in fatigue strength around 60% was observed in welds jointed with LHW and EBW, although the latter showed longer fatigue lives for higher nominal stresses.

Proposed methodology allows to assess the effect of microstructure, defect size, hardness, and joint geometry resulting from each welding technique. Results conservatively describes the fatigue behaviour of each weld configuration and highlights the relative influence of all factors considered in the assessment. Although the validated results request further studies to improve understanding of the acting

## Mathematical Modelling of Weld Phenomena 13

mechanism, they also show the potential of welded HSS and UHSS joints compared to the standard design approaches.

Keywords: Welding process; Welded joints; Ultra-high strength steel; Fracture mechanics approach

### NOMENCLATURE

$a$	crack length
$a_f$	final crack length
$a_i$	initial size of defect/initial crack length
$(area)^{1/2}$	square root area parameter
$C, m$	environmental sensitive material constants
$d$	microstructural dimension (e.g., grain size)
$da/dN$	crack propagation rate
HV	Vickers hardness
$k$	material constant that accounts for development of $\Delta K_C$
$N_f$	cycles to failure in S-N curves
$P$	applied load in the four points bending test
$R$	stress ratio (minimum stress/maximum stress)
$s, L$	half the minor and major span in four points bending scheme
$t$	plate thickness
$Y$	geometrical factor
$\alpha$	material exponent for $R$ correction
$\beta$	weld reinforcement angle
$\Delta K$	applied stress intensity factor range
$\Delta K_C$	“extrinsic” component of $\Delta K_{th}$
$\Delta K_{dR}$	microstructural crack propagation threshold
$\Delta K_{th}$	fatigue crack propagation threshold
$\Delta K_{thR}$	fatigue crack propagation threshold for long cracks
$\Delta\sigma$	nominal applied stress range
$\Delta\sigma_{eR}$	plain fatigue limit (material endurance, dependent on $R$ )
$\Delta\sigma_{th}$	threshold stress range for crack propagation
$\sigma_{UTS}$	ultimate tensile strength
$\sigma_{ys}$	static yield strength

### INTRODUCTION TO THIS DOCUMENT

Among construction materials, high-strength low-alloyed (HSLA) structural steel is particularly attractive due to its satisfactory weldability and high ductility. Immediate applications include structures where the volume of material needed to bear design loads is high, and therefore the weight of metal is comparable to external loads (for example, cranes, long-span beams, and drill string components, among others). At the present time, strength up to 1300 MPa can be found in the market, but this development has not been accompanied accordingly in design codes, as it is usually the case. The former exclusion of HSS and UHSS from documents devoted to welded constructions was due to safety

issues related mainly to the lack of experimental data on these materials in the welded condition, and the uncertainty in their mechanical behaviour. Extensive discussions and well-proved results are needed to achieve a fully developed standard or code dealing with new materials, which justifies this late upgrade in legal documents. This highlights the need for a deep understanding of mechanical response of HSS and UHSS weldments to different loading conditions.

There are currently several methods available to determine fatigue resistance of welded joints, which make use of different stress definitions (nominal stress, structural stress, notch-stress, or hot-spot stress) or, alternatively, employ local strain measurements [1-4]. However, an important aspect in welded joints is that crack initiation period is greatly reduced or suppressed, due to the usual existence of weld flaws and local stress concentrators. Early works on this matter revealed initial crack-like defect depths of about 20-400  $\mu\text{m}$  [5, 6], depending on the welding conditions. In IIW recommendations [1] initial crack lengths in the range of 50 to 150  $\mu\text{m}$  are suggested for fracture mechanics applications. Radaj et al. [4] recommended an initial crack size above  $a_i = 100 \mu\text{m}$  for life prediction of welded structures. A review by Grover [7] pointed out that even high-quality welds contain flaws up to a depth of about 100  $\mu\text{m}$ . Such defect sizes fall clearly within the short crack regime. This prompted Chapetti et al. to propose in the 2003 annual meeting of the International Institute of Welding [8] (see also reference [9]) a fracture mechanics methodology that employs the resistance curve concept, including the short crack regime, to estimate the fatigue behaviour of welded joints. After this, various studies were performed in order to assess the influence of different mechanical, geometrical and microstructural parameters on the fatigue resistance of welded joints [10-13]. Recently proposed IBESS model [14-16], is also a fracture mechanics methodology, based on the same resistances curve concept that considers the short crack regime. Principal differences arise from methodological aspects and simplification hypothesis, which are out of the scope of the present study. Other assessment techniques can be found in literature (see, for instance, [17] and [18]), but they do not consider the short crack regime and differ in the basic assumptions.

In the present study, a fracture mechanics methodology is described and applied to different butt-welded joints to predict their fatigue behaviour. Three welding processes were considered to join UHSS plates. Fatigue tests were carried out to determine the strength of the welds under constant amplitude loading. Microstructures, hardness, and size of weld defects were measured and used as data input in the assessment.

## MATERIALS AND WELDING TECHNIQUES

Materials employed in the present study are structural high-strength low-alloyed steels, designated as S960MC and S960QL in EN 10149-2 [19] and EN 10025-6 [20], respectively. The former is a microalloyed, thermomechanical-processed steel with fine-grained microstructure, consisting principally of martensite and tempered martensite [21, 22]. The second is a hot-rolled, quenched, and tempered steel, with similar microstructure. Steels are supplied in 8 mm thick sheets. Chemical composition is exhibited in Table 1.

**Table 1** Chemical composition of steel products, in wt %

Chemical elements	C	Si	Mn	P	$\Sigma$ (Cr, Ni, Mo)	$\Sigma$ (V, Nb, Ti)	CEV [23]	CET [23]	P <sub>CM</sub> [24]
S960MC	0.09	0.12	1.69	0.007	1.63	0.14	0.66	0.34	0.27
S960QL	0.17	0.22	1.23	0.007	0.857	0.05	0.54	0.36	0.3

Butt-welded joints were manufactured with gas metal arc welding (GMAW), laser-hybrid welding (LHW) and electron-beam welding (EBW), with a 2.5 m long weld seam. Weld direction was parallel to the rolling direction. The filler material was BÖHLER alform 960 IG [25], and BÖHLER EMK 8 [26] for GMAW and LHW, respectively. Chemical composition and standard designation of the wires are listed in Table 2. Welding parameters were defined by trial and error [27] with the aim at producing sound and representative welds for each welding process.

**Table 2** Chemical composition of steel products, in wt %

Chemical elements	C	Si	Mn	Ni	Cr	Mo	CEV [23]	CET [23]	P <sub>CM</sub> [24]
G4Si1*		0.1	1.0	1.7	-	-	0.38	0.27	0.22
G89 5 Mn4Ni2.5CrMo**	0.12	0.8	1.9	2.35	0.45	0.55	0.79	0.45	0.34

\*BÖHLER EMK 8

\*\*BÖHLER alform 960-IG

## FRACTURE MECHANICS APPROACH

A fracture mechanics methodology was employed for the fatigue assessment of welded components to analyse different variables of the damaging process. Description of this method and hypothesis needed for its application were thoroughly presented in previous publications from the authors [9-11]. Weld toe geometry, joint design and the presence of undercuts were already studied, and their effect on fatigue strength of weldments could successfully be analysed. This approach is based on the resistance curve concept that compares the total driving force applied to a crack with its threshold for crack propagation. The difference is the energy needed for crack growth, known as the effective driving force.

The applied driving force can be determined as a function of loading configuration (simple traction, bending, or torsion), sample geometry and crack length. To do this, the applied stress intensity factor range,  $\Delta K$ , has proven to be a proper parameter. Likewise, crack propagation threshold,  $\Delta K_{th}$ , can be employed to describe crack growth resistance. Both quantities depend on crack size and include the short crack regime. This is particularly useful in the present assessment because of the use of high-strength steels and good quality welds. Relationship between  $\Delta K$  and  $\Delta K_{th}$  can be expressed as a modified Paris Law according to Eq. (1).

$$da/dN = C (\Delta K - \Delta K_{th})^m \quad (1)$$

where  $C$  and  $m$  are material constants that depend on the environment. It is important to mention, that in the case of fatigue limit determination, the value adopted by these

constants in Eq. (1) is irrelevant, since for  $da/dN$  approaching to zero, the critical stress range is just defined by  $\Delta K = \Delta K_{th}$ . For higher level of stress, where  $\Delta K > \Delta K_{th}$ , Eq. (2) must be solved.

$$N_f = \int_{a_i}^{a_f} \frac{da}{c (\Delta K - \Delta K_{th})^m} \tag{2}$$

where  $N_f$  is the number of cycles needed to grow a crack from initial crack length,  $a_i$ , to final crack size,  $a_f$ . Both situations described previously can be visualised in Fig. 1a and 1b, for the fatigue strength and the fatigue resistance for finite life estimation, respectively. In the former case, there is a value of  $\Delta\sigma$  for which both curves touch at a single point. This is the critical stress or fatigue limit of the configuration, and the contact point between the two curves is the non-propagating crack length. In the second case, the shaded area represents the energy available for fatigue crack growth.

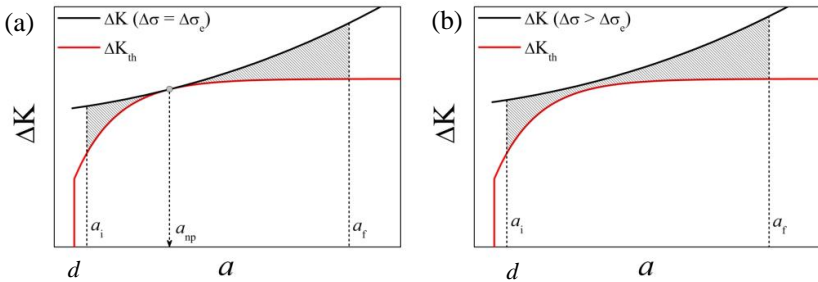


**Fig. 1** Graphical method to estimate fatigue resistance of a welded joint for (a) infinite fatigue life (fatigue limit) and (b) finite fatigue life, considering an initial crack length,  $a_i$

To determine the crack propagation threshold, it was suggested [28] that location  $d$  of the strongest microstructural barrier defines a microstructural threshold for short crack propagation. This parameter can be expressed as follows:

$$\Delta K_{dR} = Y \Delta\sigma_{eR} (\pi d)^{1/2} \tag{3}$$

where  $Y$  is a geometrical factor and  $\Delta\sigma_{eR}$  is the plain fatigue limit, defined as the lowest nominal stress range for crack propagation in a smooth sample. It depends on the stress ratio  $R$ , and therefore the microstructural fatigue threshold is also affected by  $R$ . The value of microstructural barrier  $d$  can be estimated with the ferrite grain size and bainite or martensite lath length [28, 29].

Long crack behaviour is characterised by a constant threshold, represented by  $\Delta K_{thR}$ , for a given stress ratio  $R$ . Difference between this mechanical threshold and microstructural fatigue threshold  $\Delta K_{dR}$ , is constant and depends on the stress ratio  $R$ . However, a transition exists from the short crack behaviour, characterised by  $\Delta K_{dR}$ , to the long crack regime, where  $\Delta K_{thR}$  domains crack growth. Chapetti proposed [28] that the development of the extrinsic component  $\Delta K_C$  can be calculated with Eq. (4).

$$\Delta K_C = (\Delta K_{thR} - \Delta K_{dR}) \{1 - \exp[-k(a - d)]\} \tag{4}$$

where  $k$  is a material constant that characterises the transition zone for each stress ratio, and  $a$  is the crack length in mm, measured from the free surface.

In summary, the shape of the threshold curve is given by Eq. (5), and it describes the resistance of a material to fatigue crack propagation.

$$\Delta K_{th} = \Delta K_{dR} + \Delta K_C = Y \Delta \sigma_{th} (\pi a)^{1/2} \quad (5)$$

Replacing Eq. (4) into (5) gives the full form of the threshold curve, as expressed by Eq. (6):

$$\Delta K_{th} = \Delta K_{dR} + (\Delta K_{thR} - \Delta K_{dR}) \{1 - \exp[-k(a - d)]\} \quad (6)$$

which is valid for  $a \geq d$ .

The expression for  $k$  is given in Eq. (7). It defines a threshold for fatigue crack propagation that correlates well with experimental data [28].

$$k = \Delta K_{dR} / [4d (\Delta K_{thR} - \Delta K_{dR})] \quad (7)$$

#### ESTIMATION OF THE APPLIED $\Delta K$ . FINITE ELEMENT MODEL

Crack propagation can be quantified by means of a Fracture Mechanics Approach that is extensively described in previous works from the authors [10-13, 28]. In order to apply these methodologies, stress intensity factor range as a function of crack length must be known. With this objective, different finite element (FE) models were conducted, considering representative real weld profiles resulting from each welding procedure. 8 mm plates made of S960MC and S960QL steels were used as the base material and three different welding processes were employed (LHW, EBW and GMAW). Each process gives quite different weld profiles, which results in different crack growth behaviour. These geometries were obtained from cross sections of relevant weld beads, as can be seen in Figs. 2a, 2b and 2c for LHW, EBW and GMAW, respectively. Corresponding weld reinforcement heights and reinforcement angles were 1.08, 0.2 and 0.97 mm, and 144, 150 and 160°, respectively. Average weld toe radius at the crack initiation site was 0.4 mm for LHW and 1.4 mm for GMAW specimens. Because of the presence of undercuts, and crack nucleation from flaw root, toe radius was not determined for EBW samples.

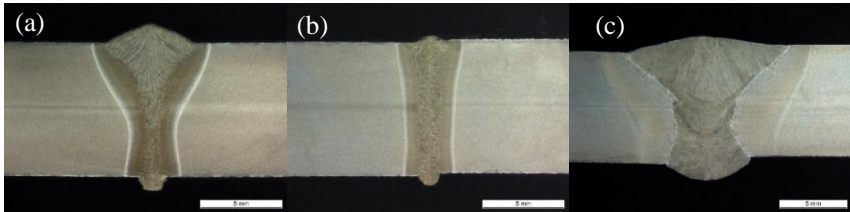


**Fig. 2** Weld profile for FEM. (a) LHW (LM). (b) EBW (EM). (c) GMAW (MM)

FE model is depicted in Fig. 3. It consists in a simplified 2D symmetric weld, with a crack,  $a$ , growing from the weld toe. Four points bending scheme was considered for stress analysis. Minor and major span are represented by  $s$  and  $L$ , respectively,  $t$  is the plate thickness and  $P$  is the applied load. All these variables define the maximum nominal stress on the surface that is used in S-N curves. Stress intensity factors and real crack path were obtained following software procedure for fracture mechanics simulations [30]. Cracks were introduced as “seam cracks” growing from the weld toe and the maximum energy release criterion was used to determine the crack propagation direction. Concentric circular partitions were done at the crack tip, and the area defined by the first circle was the crack front, which will later be computed as the first contour integral. Mesh at the crack front was constructed with 6-node quadratic plane strain triangles, which use a modified second-order interpolation. The software converts the elements in the crack front to collapsed quadrilateral elements. To improve accuracy, a square root singularity is recommended to be assigned to the crack tip, which constrains the collapsed nodes to move together. 8-node biquadratic plane strain quadrilateral elements were assigned to the rest of the mesh. It must be mentioned that residual stresses and linear or angular misalignment were not considered in this work. Figs. 4a to 4c illustrate examples of mesh configuration and Von Mises (VM) stress distribution close to the crack for LHW, EBW and GMAW, respectively. In all cases, crack length was assumed equal to 0.2 mm and nominal stress equal to the fatigue strength of each weld detail. Note that stresses above 960 MPa are only reached in a very small region around the crack tip.

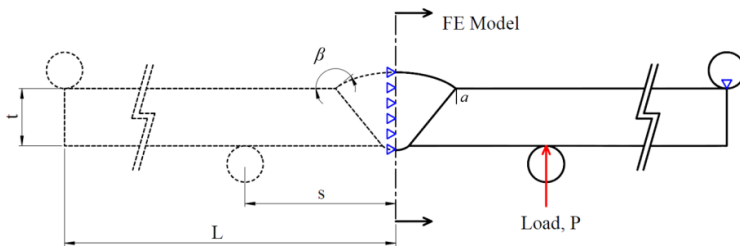


**Fig. 3** Geometry, load configuration and boundary conditions of the finite element model.  $t$  is the plate thickness,  $a$  is the crack length,  $\beta$  is the reinforcement angle,  $s$  is half the minor span,  $L$  is half the major span and  $P$  is the applied load

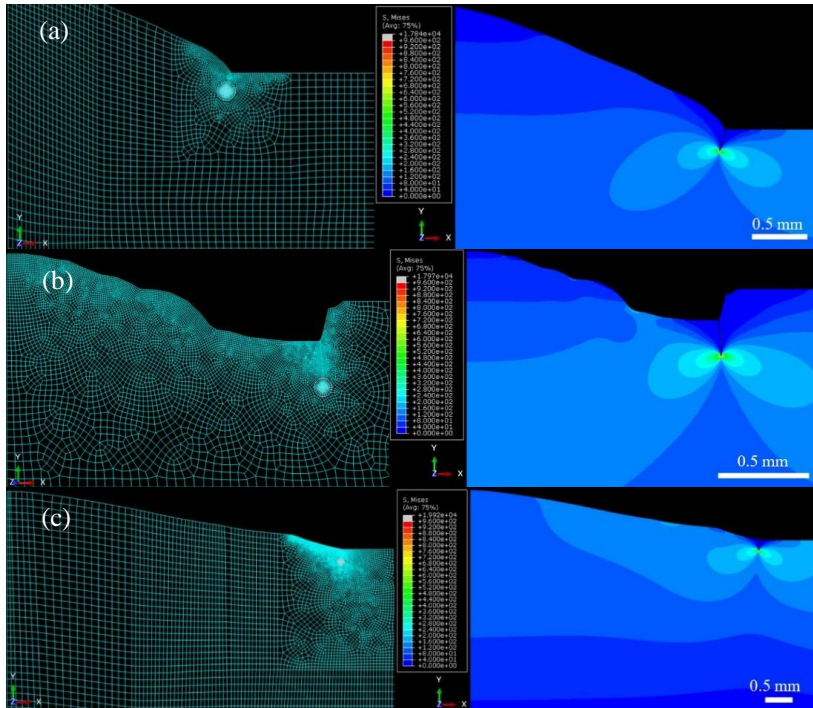


**Fig. 4** 2D FE mesh and VM stress distribution for  $a = 0.2$  mm and a nominal stress range of 169 MPa. (a) LHW,  $\Delta\sigma_{e0.1} = 175$  MPa. (b) EBW,  $\Delta\sigma_{e0.1} = 189$  MPa. (c) GMAW,  $\Delta\sigma_{e0.1} = 204$  MPa

Stress intensity factor depends on weld geometry, crack length and applied remote stress. Having defined the weld detail and load in the bending test, their values can be obtained for different crack lengths by means of the finite element analysis described previously. This procedure was repeated for different crack lengths ranging from  $50 \mu\text{m}$  to 4 mm, following the path that maximise energy release rate [30]. Step size was varied from  $25 \mu\text{m}$  to  $100 \mu\text{m}$  in the first millimetre, to obtain an accurate profile in the short crack range. For larger crack lengths, 0.5 mm was selected. Fig. 5 presents values of  $\Delta K$  for different crack lengths. These curves can be plotted together with threshold curve to determine fatigue limit for each case, as it was explained in Fig. 1.

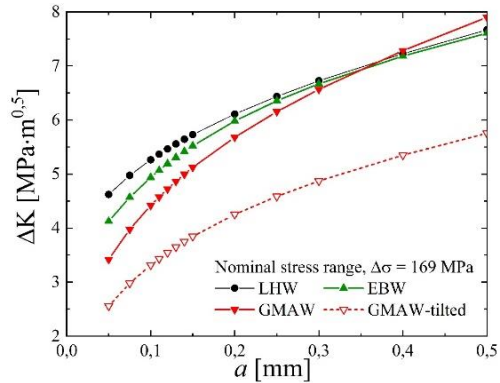


**Fig. 5** Stress intensity factor as a function of crack length. Nominal stress range 169 MPa

To explain crack behaviour observed experimentally in some GMAW specimens, where the crack grew following the fusion line, a model was considered using this tilted crack path. Fig. 6a illustrates a side view of a cracked sample, and Figure 6b presents a cross section showing similar tilted profile in early crack growth. FE results for this crack path are shown in Figure 6c, in terms of VM stress. Values of  $\Delta K$  vs.  $a$  are also displayed in Fig. 5 (GMAW-tilted).

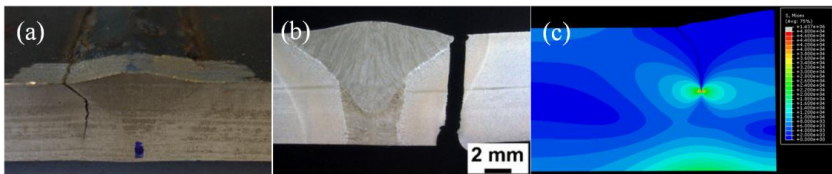


**Fig. 6** (a) Fatigue crack path at the side of the sample. (b) Cross section showing early crack growth following the fusion line. (c) FE results in terms of VM stress. Nominal stress range: 169 MPa

### THRESHOLD CURVE DETERMINATION

Threshold curve can be determined by means of several parameters and mechanical properties, defined for the microstructure developed in the crack initiation zone, preferably. In the following, each variable is considered and discussed separately.

*Strongest microstructural barrier,  $d$*

In the 80's and 90's microstructure and grain boundaries and their relation with plain fatigue limit were deeply studied [29, 31-37]. It was found that the fatigue limit of plain and blunt-notched specimens in steels is defined by the ability of the strongest microstructural barrier,  $d$ , to arrest a small crack. For engineer applications,  $d$  can be related to a microstructural characteristic dimension, such as ferrite grain size and bainite or martensite lath length [28, 29, 32]. In the present work, microstructure was analysed in the crack initiation zone, and an average local grain size was determined. Since all cracks nucleated preferably in the CG-HAZ, variation of grain size was not significant. Therefore,  $d = 30 \mu\text{m}$  will be assumed for all welds.

Intrinsic fatigue threshold in the resistance curve is also affected by  $d$  according to Eq. (3). It additionally modifies the development of the extrinsic component as shown in Eq. (7). Bigger grain sizes lead to higher values of  $\Delta K_{dR}$ , and a retarded development of the plateau in the threshold curve. The overall effect on the fatigue strength of the weld will be determined together with the applied driving force for crack propagation.

Due to the fact that cracks usually form with a semi-circular shape, the geometrical factor  $Y$  in Eq. (3) can be assumed to be 0.65 [38, 39].

*Intrinsic fatigue threshold,  $\Delta K_{dR}$*

In the present methodology, the plain fatigue limit refers to the resistance of material to fatigue cracking in conventional fatigue testing.  $\Delta\sigma_{eR}$  is 550 MPa at  $R = 0.1$  for test performed in steel S960MC under traction loading mode. Fatigue limit for bending may be different [13, 40-42]. This must be considered a first approach, since cracks may nucleate in a microstructure different from that of the BM. There are two options to take this into account in assessment. First, an empirical correlation can be used to determine  $\Delta\sigma_{eR}$  as a function of hardness or tensile strength, considering proportionality with fatigue strength [43]. In the former case, relationship can be written as presented in Eq. (8), which should later be used in Eq. (3) to obtain  $\Delta K_{dR}$ .

$$\Delta\sigma_{eR} (BM) / \Delta\sigma_{eR} (HAZ) = HV (BM) / HV (HAZ) \quad (8)$$

Second,  $\Delta K_{dR}$  can be estimated using the Murakami-Endo model, expressed as shown in Eq. (9).

$$\Delta K_{dR} = 0.0033 (HV + 120)(\sqrt{area})^{1/3} \left[ \frac{1-R}{2} \right]^\alpha \quad (9)$$

where  $\alpha = 0.266 + HV \cdot 10^{-4}$  and  $\sqrt{area}$  refers to the square root of defect/crack area projected normal to the maximum principal stress, according to Murakami's proposal [43]. Eq. (9) can be expressed in terms of the average grain size,  $d$ , as follows [44]:

$$\Delta K_{dR} = 0.00356 (HV + 120)d^{1/3} \left[ \frac{1-R}{2} \right]^\alpha \quad (10)$$

with  $\Delta K_{dR}$  in  $\text{MPa}\cdot\text{m}^{1/2}$ , for  $d$  in  $\mu\text{m}$  and HV in  $\text{kgf}/\text{mm}^2$ .

Steel S960MC and S960QL have an average hardness of 320 and 350 HV<sub>0.5</sub>, respectively. Depending on the welding process and filler materials different hardness

values are achieved in the HAZ. Measured values were in accordance with results from microstructures simulated by Gleeble. These outcomes are displayed in Table 3. Additionally, last column presents values of microstructural fatigue threshold,  $\Delta K_{dR}$ , as estimated with Eqs. (3) and (8), and (10), using Gleeble hardness and  $d = 30 \mu\text{m}$  for all welds. Fatigue strength of S960QL had to be estimated using fatigue strength of S960MC and Eq. (8).

**Table 3** Mechanical properties and important parameters for the model.  $R = 0.1$ .

Base Material	Welding Process	$d$ [ $\mu\text{m}$ ]	HV <sub>10</sub> (Gleeble)	$\Delta\sigma_{eR}$ [MPa]	$\Delta K_{dR}$ [MPa $\sqrt{\text{m}}$ ]	
		HAZ	1200°C	BM	Eqs. (3) and (8)	Eq. (10)
S960MC	LHW	30	350	550	3.80	4.09
	EBW		370		4.01	4.26
	GMAW		330		3.58	3.92
S960QL	LHW	30	420	600	4.55	4.67
	EBW		420		4.55	4.67
	GMAW		390		4.23	4.42

*Long crack propagation threshold,  $\Delta K_{thR}$*

Although long crack propagation threshold was determined experimentally, reproducible values were only obtained for BM, giving  $7.38 \pm 0.22$  and  $8.5$  MPa $\sqrt{\text{m}}$  for S960MC and QL, respectively. It is expected a lower threshold for harder microstructures, as it was found in several investigations [45, 46]. Particularly, Eq. (11) expresses the relationship between long crack propagation threshold and ultimate tensile strength [46]. Additionally, the latter can be estimated with hardness measurements according to Eq. (12). Outcomes are presented in Table 4. In this sense, it can be seen in Figs. 4 and 6 that cracks grew preferably throughout the HAZ, thus justifying the use of a smaller  $\Delta K_{thR}$  than that of the BM.

$$\Delta K_{th0.1} = -0.0021 \sigma_{UTS} + 8.4 \tag{11}$$

$$\sigma_{UTS} = 3.26 HV \tag{12}$$

It must be highlighted that the higher the  $\Delta K_{thR}$ , the wider the range of crack length covering the development of the extrinsic threshold.

**Table 4** Mechanical properties and important parameters for the model.  $R = 0.1$ . Values of  $C$  for  $\Delta K$  in  $\text{MPa}\cdot\text{m}^{0.5}$  and  $da/dN$  in  $\text{m}/\text{cycle}$ .

Zone	$\sigma_{ys}$ [MPa]		$\sigma_{UTS}$ [MPa]	$\Delta K_{thr}$ [MPa $\sqrt{\text{m}}$ ]		$C$ [mm/cycle]	$m$
	BM	BM	BM	HAZ		BM	BM
S960MC	988	1014	7.38	LHW	6.0 (350 HV)	1.64E-7 – 1.73E-6	2.08 ± 0.34
				EBW	5.87 (370 HV)		
				GMAW	6.14 (330 HV)		
S960QL	963	1043	8.5	LHW	5.52 (420 HV)	5.5E-7	2
				EBW	5.52 (420 HV)		
				GMAW	5.73 (390 HV)		

### *Paris equation constants, $C$ and $m$*

Like  $\Delta K_{thr}$ ,  $C$  and  $m$  can be obtained from experimental tests. Results are also displayed in Table 4 for base metals. Although some tests were performed for microstructures different from the base material, more outcomes are needed to assess experimental scatter, which can be large in this kind of test. In this regard, it is important to mention that a statistical determination of  $C$  and  $m$  can be done, and it may lead to better estimations of the finite life regime. The fracture mechanics model can consider these variations based on Eq. (1). For the present assessment, the lower experimental value of  $C$  was considered (1.64E-7) and the average value of  $m = 2.08$  will be used (for  $\Delta K$  in  $\text{MPa}\cdot\text{m}^{0.5}$  and  $da/dN$  in  $\text{mm}/\text{cycle}$ ), which are similar to those obtained by Lukács for a welded joint made of steel S960MC [47].

### *Initial crack length, $a_i$*

IIW recommendations [1] define an initial crack length for fracture mechanics assessment of welded joints between 50 and 150  $\mu\text{m}$ . Based on the work from Signes [5] and Watkinson [6], BS 7910 recommends values from 100 to 250  $\mu\text{m}$ . In the present work, an initial crack length of 100  $\mu\text{m}$  can be assumed for LHW and EBW, according to fracture surface inspection. In contrast, GMAW resulted in better quality toe profiles. Therefore, a slightly lower crack length of 50  $\mu\text{m}$  can be considered. Both values fall within the typical ranges from literature.

## FATIGUE STRENGTH DETERMINATION

Having calculated  $\Delta K$  vs.  $a$  for a predefined  $\Delta\sigma$  and a propagation threshold curve,  $\Delta K_{th}$ , fatigue strength can be determined by solving Eq. (2) for every stress level (above fatigue endurance).  $a_f$  was defined as  $t/2$  [1, 4] for the present analysis, where  $t = 8$  mm. Results can be appreciated in Figs. 7a and 7b, for S960MC and S960QL, respectively. Since Murakami's modified equation in Eq. (10) is well-known and widespread, fatigue estimations were calculated using the value of  $\Delta K_{dR}$  resulting from this expression.

Fatigue strength did not show significant differences when modifying the BM. LHW specimens resulted in 175 MPa and 176 MPa for S960MC and S960QL, respectively. EBW presented higher resistance to fatigue cracking, with a fatigue strength of 189 and 188 MPa for S960MC and S960QL, respectively. Finally, stronger welds were obtained with GMAW process, giving 222 and 246 MPa for respective steels and smaller initial crack size  $a_i = 50 \mu\text{m}$ .

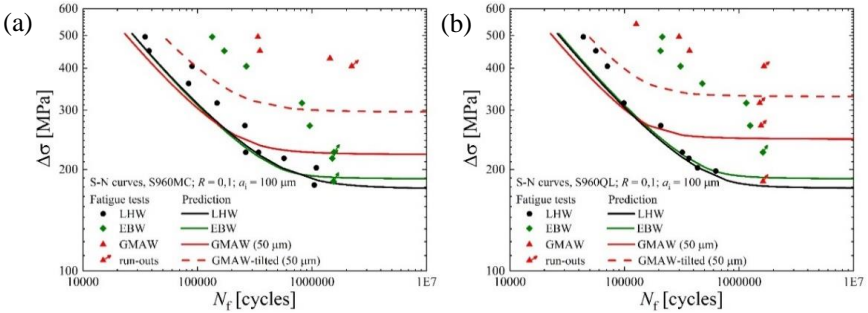


**Fig. 7** S-N curves with fatigue strength predictions for (a) S960MC and (b) S960QL

## DISCUSSIONS

In the present work two base materials (S960MC and S960QL) were welded with three different welding processes (LHW, EBW and GMAW). Sound welds were obtained with proper selection of welding parameters, and fatigue tests were carried out considering four points bending configuration. S-N curves for weld toe failure are shown in Fig. 7 and reproduced in Fig. 8 for all combinations of welding procedure and base metal. No relevant differences between S960MC and S960QL welds were found. However, a notable reduction in fatigue strength around 60% could be observed in LHW joints compared to BM S960MC. EBW unions showed slightly higher fatigue resistance than their counterpart, and longer fatigue lives for higher nominal stresses. Joints manufactured with GMAW presented the highest fatigue strength, with a ca. 20% decrease compared to standard specimens made of S960MC. Moreover, slope is similar to that of the base material. These results confirm the detrimental effect of fusion welding processes on fatigue performance. However, differences between the three welding methods were not expected to be large, since they are all butt-welds tested under the same loading configuration. IIW recommendations [1] set a maximum fatigue strength of FAT 90 for a butt joint with reinforcement, at 2 million cycles with 95% probability of survival in the as welded conditions. If a thickness effect [1] is considered for the 8 mm thick plate, a higher strength of FAT 113 is obtained. This curve is presented in Fig. 8 with a slope  $m = 3$ , laying below all experimental points. LHW results suit well to this FAT value, but it is conservative for EBW and GMAW joints. In these cases, fatigue resistance is even higher than recommendation of FAT 140 for a transversely loaded butt-weld ground flush

to plate, corrected by thickness effect ( $FAT\ 112 \cdot (25/8)^{0.2} = FAT\ 140$ ). Best FAT curves for EBW and GMAW are displayed, showing that a FAT 200 with a slope of 3.5 and a FAT 300 with a slope of 5 are respectively suitable. These high fatigue strengths and changes in slopes were also observed in high-performing welds [40, 47-49] and post weld treated joints [17, 50-52].

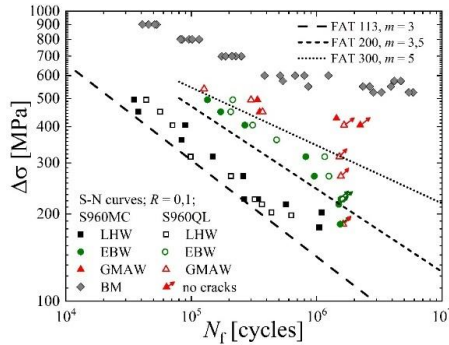


**Fig. 8** Nominal stress range vs. cycles to failure, with standard FAT curves from IIW [4]

To analyse these variations in fatigue behaviour, a fracture mechanics methodology was applied to cracks growing from weld toes. Thorough experimental measurements were made to obtain input data for the model, although some parameters had to be estimated using hardness results. This approach is different from other fatigue life estimation techniques, like the hot-spot or the notch stress approach [3], because it considers an initial crack size, disregarding the crack initiation stage. This allows to predict fatigue strengths if the short crack behaviour is included [29, 32, 33-37].

Relevant weld profiles were simulated in a finite element model, to obtain stress intensity factors for cracks growing from the weld toe. Fatigue threshold was determined using a microstructural dimension,  $d$ , of  $30\ \mu\text{m}$  and a long crack propagation threshold defined by local hardness measurements. Fatigue strengths were calculated for  $a_i = 100\ \mu\text{m}$  in LHW and EBW samples, and for  $a_i = 50\ \mu\text{m}$  in GMAW specimens. This is justified because the latter resulted in high quality welds, with smooth weld profile and no remarkable flaws at the initiation site. Results agreed with fatigue tests, giving the highest strength for GMAW batch, although prediction was still very conservative. In the finite life regime, predictions were also conservative for EBW and GMAW specimens, but slightly unconservative for LHW. As it was mentioned previously, fracture mechanics methodology can consider variations of  $C$  that may results from experimental testing. More accurate determinations of constants in Eq. (1) might definitely lead to better predictions in the finite life region. Furthermore, a statistical analysis of each variable that serves as input data for the model is feasible. This will give confident bands for predicted S-N curves.

In the case of GMAW specimens, a tilted crack path was observed during early propagation, as depicted in Fig. 16. From an energetic point of view, this is not the most

critical situation, and therefore it is expected a reduction in the stress intensity factor along the new crack path. It can be thought that some metallurgical factors (for instance, fusion line and CG-HAZ) are contributing to early crack growth, deviating crack path from what it would be, according to stress configuration. When considering the deviated initiation, a higher less-conservative fatigue strength was obtained, although predictions could not precisely reproduce the experimental endurance observed in GMAW samples. Further studies are needed to better predict these specimens' behaviour.

In summary, conservative predictions of fatigue strength were obtained for all welding processes. Results highlight the ability of fracture mechanics methodologies to safely predict the fatigue behaviour of welded components. Several contributing factors were considered, and their effects could be quantified. This is very attractive from a design point of view, but also, for developing less conservative but safe standards and construction codes. Additionally, enhanced fatigue strength observed in high quality welds and post-weld treated joints made of high strength and ultra-high strength steels, can be assessed. In the former case, fewer defects reduce initial crack length, which is translated into a higher strength as it was the case for GMAW samples. Although this could not completely explain the superior fatigue strength of GMAW specimens, it demonstrates the ability of the fracture mechanics approaches to reproduce variation in endurances when relevant parameters are changed. On the other hand, TIG-dressing not only re-shape weld profile, but also introduce residual stresses [53]. In this regard, much effort is needed to adequately include residual stresses in the analysis, which is subject of a future publication from the authors.

### CONCLUSIONS

The development of fracture mechanics methodologies that include short crack behaviour made it possible to estimate fatigue lives and fatigue limits of welded joints. The suppression or reduction of the crack initiation stage allows to consider solely crack propagation in the assessment of each weld detail, with reasonable accuracy. Additionally, the resistance curve concept is employed to relate the driving force for crack propagation with material's resistance. Determination of the latter is the main difference between models currently available for this kind of assessment. In this work, Chapetti's model was used to calculate the threshold curve. This method demands experimental measurement of some mechanical parameters, such as grain size, hardness, and plain fatigue limit, at the crack initiation region. For welds, this can be the WM, the HAZ or the BM.

In the present study, three different welding processes were used to join 8 mm thick plates made of steels S960MC and S960QL. Dog-bone samples were machined from the main plate in all configurations to obtain S-N curves under four points bending scheme. Weld geometry, microstructure, hardness, and weld defects were evaluated close to the weld toe, where all samples failed. Experimental outcomes were used in the fracture mechanics methodology, which was applied to all combinations of welding processes and base materials. Results conservatively describe the fatigue behaviour of each configuration and highlight the relative influence of all factors considered in the assessment. Weld profile cannot solely explain the differences between S-N curves

because there is also an influence of weld defects (undercuts and underfills) on early crack propagation, particularly for LHW and EBW. GMAW samples resulted in the highest fatigue resistance, which reflects the benefits that can be experienced when using HSS or UHSS as BMs. In this regard, welds made with GMAW showed high quality profile, which can be translated into a smaller initial crack length in the fracture mechanics approach that enhances the fatigue strength. This, however, cannot reproduce by itself the superior endurance observed in GMAW specimens. Additionally, some metallurgical effects may have contributed to early crack propagation, giving a tilted crack with a lower stress intensity factor along crack path.

Although residual stresses were not considered in this work, the methodology is able to describe their effect on fatigue behaviour, which is subject of a future work from the authors. Finally, it must be pointed out that accuracy of estimations is better, the better the determination of relevant parameters. In this sense, statistical studies can be performed to obtain ranges of fatigue endurances and fatigue lives for different weld configurations.

#### ACKNOWLEDGEMENTS

Authors wish to express their gratitude to the funding provided by Agencia Nacional de Promoción Científica Tecnológica, Argentina (PICT 2017 Nro.0982). Support was also provided by the K-Project Network of Excellence for Metal JOINing which is fostered in the frame of COMET - Competence Centers for Excellent Technologies by BMWFW, BMVIT, FFG, Land Oberösterreich, Land Steiermark, Land Tirol and SFG. The programme COMET is handled by FFG. Additionally, the authors would like to acknowledge the Slovenian Research Agency (ARRS) for financial support of the Research Program P2-0137 “Numerical and experimental analysis of mechanical systems”.

#### References

- [1] A. F. HOBACHER: *Recommendations for Fatigue Design of Welded Joints and Components*, 2<sup>nd</sup> ed., Springer International Publishing, 2016.
- [2] British Standard, BS 7608-2014: *Guide to fatigue design and assessment of steel products*, BSI Standards Limited, 2014.
- [3] D. RADAJ: *Design and analysis of fatigue resistant welded structures*, Abington Publishing, 1990.
- [4] D. RADAJ, C. M. SONSINO and W. FRICKE: *Fatigue assessment of welded joints by local approaches*, 2nd edition, Woodhead publishing limited, Cambridge, England, 2006.
- [5] E. G. SIGNES: ‘Factors affecting the fatigue strength of welded high strength’, *Brit. J.*, 14, 108-116, 1967.
- [6] F. WATKINSON, P. H. BODGER, J. D. HARRISON: ‘The fatigue strength of welded joints in high strength steel and methods for its improvement’, *Int conference on fatigue welded structures*, The WI, 97, 1970.
- [7] J. L. GROVER: ‘Initial flaw size estimating procedures for fatigue crack growth calculations’, *Int conference on fatigue of welded construction*, Brighton, vol. 275, 1987.
- [8] M. D. CHAPETTI, J. BELMONTE, T. TAGAWA, T. MIYATA: ‘On the influence of short crack behaviour on fatigue strength of welded joints’, *IIW X-1545-03 XIII-1971-03*, 2003.

- [9] M. D. CHAPETTI, J. BELMONTE, T. TAGAWA and T. MIYATA: 'Integrated fracture mechanics approach to analyse fatigue behaviour of welded joints', *Sci tech weld join*, 9(5), 430-438, 2004.
- [10] M. D. CHAPETTI and L. F. JAUREGUIZAHAR: 'Fatigue behavior prediction of welded joints by using an integrated fracture mechanics approach', *International Journal of Fatigue*, 43, 43-53, 2012.
- [11] C. STEIMBREGER and M. D. CHAPETTI: 'Fatigue strength assessment of butt-welded joints with undercuts', *International Journal of Fatigue*, 105, 296-304, 2017.
- [12] C. STEIMBREGER, N. GUBELJAK, N. ENZINGER, W. ERNST and M. D. CHAPETTI: 'Influence of static strength on the fatigue resistance of welds', *In MATEC Web of Conf* (Vol. 165, p. 13010), EDP Sciences, 2018.
- [13] C. STEIMBREGER and M. D. CHAPETTI: 'Fracture mechanics based prediction of undercut tolerances in industry', *Engineering Fracture Mechanics*, 211, 32-46, 2019.
- [14] M. MADIA, U. ZERBST, H. T. BEIER and B. SCHORK: 'The IBESS model—Elements, realisation and validation', *Engineering Fracture Mechanics*, 198, 171-208, 2018.
- [15] U. ZERBST, M. MADIA, B. SCHORK, J. HENSEL, P. KUCHARCZYK, D. TCHOFFO NGOULA, ET AL.: *Fatigue and fracture of weldments. The IBESS approach for the determination of the fatigue life and strength of Weldments by fracture mechanics analysis*, Switzerland, Springer, 2019c.
- [16] U. ZERBST and J. HENSEL: 'Application of fracture mechanics to weld fatigue', *International Journal of Fatigue*, 139, 105801, 2020.
- [17] R. RANJAN, S. WALBRIDGE: '2D fracture mechanics analysis of HFMI treatment effects on the fatigue behaviour of structural steel welds', *Welding in the World*, 65(9), 1805-1819, 2021.
- [18] R. GOYAL and G. GLINKA: 'Fracture mechanics-based estimation of fatigue lives of welded joints', *Welding in the World*, 57(5), 625-634, 2013.
- [19] DIN EN 10149-2: *Hot rolled flat products made of high yield strength steels for cold forming - Part 2: Technical delivery conditions for thermomechanically rolled steels*, Deutsches Institut fuer Normung E.V., 2013.
- [20] DIN EN 10025-6: *Hot rolled products of structural steels - Part 6: Technical delivery conditions for flat products of high yield strength structural steels in the quenched and tempered condition*, Deutsches Institut fuer Normung E.V., 2020.
- [21] C. SCHNEIDER, W. ERNST, R. SCHNITZER, H. STAUFER, R. VALLANT and N. ENZINGER: 'Welding of S960MC with undermatching filler material', *Welding in the World*, 62(4), 801-809, 2018.
- [22] M. PRANGER: *Vergleich der Mikrostruktur ausgewählter hochfester Schweißungen*, Diplomarbeit, K-Projektes Network of Excellence for Metal JOINing (JOIN), Montanuniversität Leoben, 2017.
- [23] DIN EN 1011-2:2001-05: *Welding - Recommendation for welding of metallic materials - Part 2: Arc welding of ferritic steels*, Deutsches Institut fuer Normung E.V., 2001.
- [24] AWS D1.1/D1.1M:2015: *Structural Welding Code – Steel*, American Welding Society, 23rd ed. USA, 2015.
- [25] BÖHLER alform 960 IG datasheet.
- [26] BÖHLER EMK 8 datasheet.
- [27] C. SCHNEIDER: *Influence of high energy density fusion welding techniques on welding of structural steel S960*, PhD Thesis, TU Graz, 2020.
- [28] M. D. CHAPETTI: 'Fatigue propagation threshold of short cracks under constant amplitude loading', *International Journal of Fatigue*, 25(12), 1319-1326, 2003.
- [29] K. J. MILLER: 'The two thresholds of fatigue behaviour', *Fatigue & Fracture of Engineering Materials & Structures*, 16(9), 931-939, 1993.
- [30] Dassault Systèmes, Simulia: *Abaqus 6.13 User manual*, Providence, RI, USA, 2013.

- [31] D. TAYLOR and J. F. KNOTT: 'Fatigue crack propagation behaviour of short cracks; the effect of microstructure', *Fatigue & Fracture of Engineering Materials & Structures*, 4(2), 147-155, 1981.
- [32] J. LANKFORD: 'The influence of microstructure on the growth of small fatigue cracks', *Fatigue & Fracture of Engineering Materials & Structures*, 8(2), 161-175, 1985.
- [33] M. D. CHAPETTI, T. KITANO, T. TAGAWA and T. MIYATA: 'Fatigue limit of blunt-notched components', *Fatigue & fracture of engineering materials & structures*, 21(12), 1525-1536, 1998.
- [34] K. TANAKA and Y. AKINIWA: 'Resistance-curve method for predicting propagation threshold of short fatigue cracks at notches', *Engineering Fracture Mechanics*, 30(6), 863-876, 1988.
- [35] A. J. MCEVILY and K. MINAKAWA: 'On crack closure and the notch size effect in fatigue', *Engineering fracture mechanics*, 28(5-6), 519-527, 1987.
- [36] M. H. EL HADDAD, T. H. TOPPER and K. N. SMITH: 'Prediction of non propagating cracks', *Engineering fracture mechanics*, 11(3), 573-584, 1979.
- [37] J. R. YATES and M. W. BROWN: 'Prediction of the length of non-propagating fatigue cracks', *Fatigue & Fracture of Engineering Materials & Structures*, 10(3), 187-201, 1987.
- [38] T. R. GURNEY: *Fatigue of welded structures*, 2nd ed., London: Cambridge UP, 1979.
- [39] S. J. MADDOX: *Fatigue strength of welded structures*, 2nd ed., Abington, Cambridge, 1991.
- [40] R. J. M. PUIPERS: *Fatigue strength of welded connections made of very high strength cast and rolled steels*, PhD Thesis, TU Delft, 2011.
- [41] A. ESIN: 'A method for correlating different types of fatigue curve', *International Journal of Fatigue*, 2(4), 153-158, 1980.
- [42] H. ÖZDEŞ, M. TIRYAKIOĞLU and P. D. EASON: 'On estimating axial high cycle fatigue behavior by rotating beam fatigue testing: Application to A356 aluminum alloy castings', *Materials Science and Engineering: A*, 697, 95-100, 2017.
- [43] MURAKAMI: *Metal Fatigue-Effects of small defects and non-metallic inclusions*, Elsevier, 2002.
- [44] M. D. CHAPETTI: 'Fracture mechanics for fatigue design of metallic components and small defect assessment', *International Journal of Fatigue*, 154, 106550, 2022.
- [45] D. TAYLOR: *Fatigue thresholds*, London: Butterworth & Co., 1989.
- [46] M. D. CHAPETTI: 'A simple model to predict the very high cycle fatigue resistance of steels', *International Journal of Fatigue*, 33(7), 833-841, 2011.
- [47] J. LUKÁCS: 'Fatigue crack propagation limit curves for high strength steels based on two-stage relationship', *Engineering Failure Analysis*, 103, 431-442, 2019.
- [48] H. REMES, P. GALLO, J. JELOVICA, J. ROMANOFF and P. LEHTO: 'Fatigue strength modelling of high-performing welded joints', *International Journal of Fatigue*, 135, 105555, 2020.
- [49] I. LILLEMÄE, H. REMES, S. LIINALAMPI and A. ITÄVUO: 'Influence of weld quality on the fatigue strength of thin normal and high strength steel butt joints', *Welding in the World*, 60(4), 731-740, 2016.
- [50] A. AHOLA, A. MUIKKU, M. BRAUN and T. BJÖRK: 'Fatigue strength assessment of ground fillet-welded joints using 4R method', *International journal of fatigue*, 142, 105916, 2021.
- [51] M. LEITNER and M. STOSCHKA: 'Effect of load stress ratio on nominal and effective notch fatigue strength assessment of HFMI-treated high-strength steel cover plates', *International Journal of Fatigue*, 139, 105784, 2020.
- [52] R. RANJAN, S. WALBRIDGE: '2D fracture mechanics analysis of HFMI treatment effects on the fatigue behaviour of structural steel welds', *Welding in the World*, 65(9), 1805-1819, 2021.
- [53] H. METTÄNEN, T. NYKÄNEN, T. SKRIKO, A. AHOLA and T. BJÖRK: 'Fatigue strength assessment of TIG-dressed ultra-high-strength steel fillet weld joints using the 4R method', *International Journal of Fatigue*, 139, 105745, 2020.

# EFFICIENT NUMERICAL ANALYSIS OF DIRECTED ENERGY DEPOSITION PROCESSES

B. A. M. ELSNER\*, I. NEUBAUER\*\*, L. RABERGER\*\*\*

*\*Simufact Engineering GmbH, 21079 Hamburg, Germany, Orcid Id: 0000-0003-4244-1886*

*\*\*Simufact Engineering GmbH, 21079 Hamburg, Germany*

*\*\*\*Fronius International GmbH, 4600 Thalheim bei Wels, Austria*

*DOI 10.3217/978-3-85125-968-1-27*

## ABSTRACT

Directed energy deposition (DED) presents a versatile method in the field of Additive Manufacturing that allows to create complex structures by continuously welding new filler material to the underlying structure. The technology is developing quickly and DED structures with several kilometres of weld length are already engineering reality. Although numerical analysis has proven a valuable tool for the evaluation and understanding of different welding processes, typical transient simulations cannot handle such long weld tracks as time needs to be discretized in increments short enough to track the movement of the weld source in steps not larger than its own dimension. In this contribution, we present an Advanced Thermal Cycle (ATC) that allows to reduce the number of computational steps while still capturing the heat source's movement, local temperature differences, and maintaining the correct energy balance. The approach is validated by comparing the simulated thermal profile with the thermal history measured both for the substrate and the deposited weld filler of a demonstrator part.

Keywords: additive manufacturing, directed energy deposition, welding simulation, finite element method, thermal history

## INTRODUCTION

Directed energy deposition (DED) refers to a family of Additive Manufacturing (AM) methods in which a metal filler material is continuously molten by a focused energy source and deposited onto the underlying substrate to create new features or entire components [1]. Filler materials include powder or wire feedstock, while energy sources may encompass virtually all welding technologies ranging from laser or electron beam to arc and plasma welding. In contrast to powder bed fusion (PBF) processes, DED is not limited to a single build direction or the restricting dimensions of a build tank while offering much higher deposition rates. Due to this vast potential, DED technology is evolving rapidly, and successful builds of sophisticated large-scale components have already been reported [2], [3], [4].

Despite these successes, DED still holds many challenges related to the complex thermal history that the deposited material experiences during many subsequent heating

and cooling cycles. As local characteristics of the final part – such as microstructure, phase transformations, or residual stresses – strongly depend on local temperature gradients [5], a thorough understanding of the DED part's thermal history is crucial for an optimized choice of process parameters and tool path planning. Numerical process simulation offers the unique opportunity to evaluate the thermal history of a DED build without the need for elaborate experimental set-ups or the use of expensive machinery, material, or operating staff. It gives access to results which are difficult to measure during the real process and allows to compare different process variants before the first real component is manufactured.

Transient, thermo-mechanical computational weld mechanics (CWM) approaches have already been demonstrated to be capable of capturing both the local thermal history as well as the distortions arising during the DED process [6], [7]. Such models offer a detailed representation of the weld source movement and its heat input into the deposited material and are thus well-suited to evaluate local temperature gradients with a high resolution. However, the computational cost of such DED simulations strongly depends on the applied discretization in space and time and therefore increases dramatically with the total length of the deposited weld bead. This issue is illustrated by the sample component presented in [6]. In this case, the transient, thermo-mechanical simulation required 100.9 h for depositing the 17.4 m of weld bead while the real build time only amounted to 74 min.

The spatial discretization is determined by the number of elements and nodes required to adequately mesh the DED deposit. In order to retain a detailed representation of material deposition, the element size ideally does not exceed the thickness of a single layer of deposited filler material. Thus, a longer weld bead quickly leads to a dramatic increase of the element count within the model. The issue of spatial resolution can be addressed via specific meshing techniques such as the mesh zoning approach presented in [8]. However, this topic will not be treated by the present contribution.

This contribution focuses on the discretization of process time. The models presented in [6] and [7] rely on a detailed time-stepping scheme that moves the weld source along the weld path in small time increments that are chosen such that there is a certain degree of overlap between the individual positions of the weld source. With weld source dimensions in the order of millimetres and total weld bead length in the order of metres to kilometres, the number of required time steps clearly becomes a limiting factor to the accessible model size. Similar restrictions apply to the simulation of PBF processes for which voxel approaches are applied to combine the heating of several powder layers into only a few computational increments [9]. Similar approaches have been followed in the context of DED by selectively heating entire layers [10] or pre-selected model sections [11]. While these approaches allow a significant speed-up of the simulation, they require the manual partitioning of the model into meaningful sections for heat input. The issue of manual model preparation is avoided by the elongated heat source model proposed in [12]. This approach performed well on the presented model of a simple wall, but its applicability may be limited for curved features that cannot be resolved by an elongated straight heat source.

This contribution presents the approach of an Advanced Thermal Cycle (ATC) that allows a simplification of the process by combining the heat input of an arbitrary number of smaller time steps whilst maintaining locally resolved the physical energy balance of

the process, similar to the technique proposed for powder bed fusion (PBF) in [13]. In the following sections, the model is introduced and for increasing simplifications of the model the quality of the resulting temperature distribution is benchmarked against an experimental reference.

### METHODS

#### EXPERIMENTAL PROCEDURE

A thick-walled part was manufactured from G3Si1 wire filler material onto a S235JR steel substrate with the dimensions of 200 mm x 140 mm x 24 mm (length x width x height) using the Fronius CMT (Cold Metal Transfer) process.

The sample geometry consists of three subparts, as can be seen in Fig. 1(a). Subparts A and B are composed of 15 layers whilst subpart C only contains 14 layers; in total, 44 layers have been applied to form the part. Subpart C is missing one layer, due to an error in the tool path creation process.

The part was modelled in a CAD software and processed in the CAM software Mastercam (for slicing and tool path generation). It was then imported into Robotmaster; a software for robot-offline programming. The tool path for the first layer was applied to the substrate by the CMT-Marking process - as seen in Fig. 1(b). This allows visualization of the weld path before producing the part.

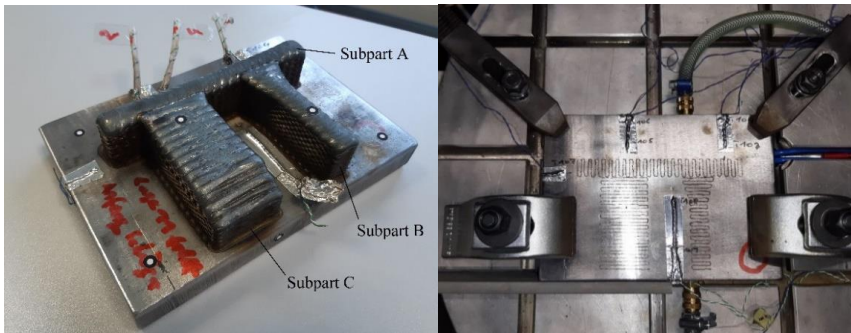


**Fig. 1** (a) Welded part after cleaning. (b) Clamped substrate with weld path applied by CMT-Marking process and temperature sensors

The substrate was clamped on four different spots onto the horizontal table with a cooling plate positioned in between, as can be seen in Fig. 2(a). The cooling plate was designed such that the coolant, which flowed at a volume flow rate of approximately 6 l/min, could directly conduct the heat from the substrate. The design of the cooling plate can be seen in Fig. 2(b).

The part was produced using a Fronius TPS 600i PULSE in combination with a Fronius MTB 500i torch and ABB IRB 2600 robot. Shielding gas with a composition of 90% Argon and 10% CO<sub>2</sub> was used with a volume flow rate of 20 l/min.



**Fig. 2** (a) Clamped welded part (b) Cooling plate

The mean temperature of the environment was 26.1°C. The feed flow and return flow temperature of the coolant has been measured and can be seen in Fig. 3. The feed flow temperature was relatively constant over time, whereas the return flow temperature fluctuates – highlighting the influence of the individual weld seams.

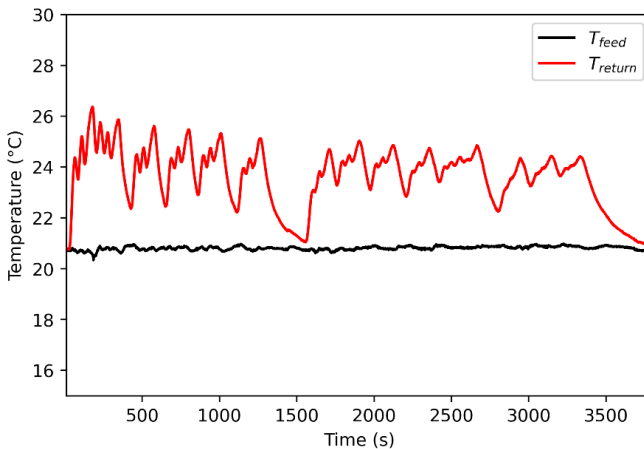


**Fig. 3** Feed and return flow temperature of the coolant

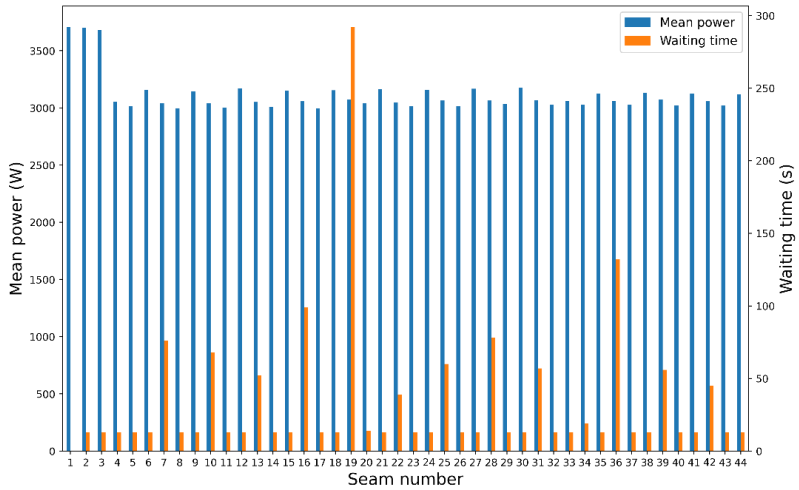


**Fig. 4** Mean power per weld seam and waiting time before each weld seam

The mean values of power for each weld seam and the waiting times before each weld seam are displayed in Fig. 4. It should be noted that the set values of power for each weld seam were chosen from experience. Such that, the power was increased for the first layer to ensure sufficient bonding to the substrate and reduced to a relatively constant mean value for weld seams 4-44 (layers 2 to 14 respectively 15).

Temperature data was gathered by application of Type K thermocouples with a diameter of 0.2 mm to the substrate on seven different positions (Fig. 8). After application, the thermocouples were covered by aluminium foil tape. Additionally, Type K thermocouples with a diameter of 1.3 mm were applied manually into the weld pool during the welding process. However, useable data was only collected from three of these thermocouples, as the others were damaged by the arc during application. Due to this manual work the waiting times before each layer deposition varied as can be seen in Fig. 4.

The total build time, including waiting times between the seams as well as the time for cooling to room temperature at the end, was about 3800 s. The total welded filler material is 1.5 kg.

#### SIMULATION MODEL

All of the here-presented simulations are performed within the framework of the finite element (FE) model provided by the commercial welding simulation software Simufact Welding 2021.1. A fully transient, thermal DED simulation is set up as reference for the

simplifications introduced via the proposed Advanced Thermal Cycle (ATC) approach and to validate the model against the experimental measurements.

Fig. 5 illustrates the DED model. The deposit geometry is represented by 28352 eight-noded, isoparametric, three-dimensional hexahedral elements with trilinear interpolation which are defined to match the layer thickness of 2 mm. It is positioned on top of the baseplate which is cooled from below by the cooling system acting as a temperature sink at 22.2°C representing the mean temperature of the coolant (see Fig. 3). Heat loss to the 26.1°C environment is considered with a constant convective heat transfer coefficient of 20 W/(m<sup>2</sup>K) and constant emission coefficient of 0.6.

Both the baseplate and deposit are approximated with the same S235 material data from the Simufact Welding database. A linear decrease of density is assumed between 20°C and 1300°C. The relevant thermal properties are shown in Table 1 as well as in Fig. 6. The weld source is modelled as a double-ellipsoidal Goldak source defined by the constant parameters listed in Table 2. For each weld seam, the experimentally recorded mean power is applied as illustrated in Fig. 4. A tolerance of 20 K is set for thermal convergence.

The deposition of material during the DED process is controlled by the element-birth routine described in [6] which controls activation and heating of elements touched by the moving weld source. In order to fully capture the transient movement of the weld source, a fixed time increment of 84 ms is chosen, resulting in a total of 21628 increments calculated for welding. The total simulation, including additional 421 increments for cooling cycles, required a total computational time of about 44 hours on a 64GB RAM Windows machine with Intel® Xeon® W-2145 CPU @ 3.70 GHz processor.

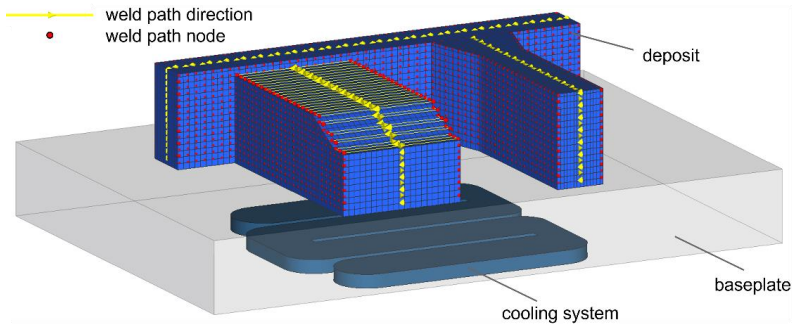


**Fig. 5** Model set up in Simufact Welding

**Table 1** S235 material data used for the DED simulations

Density (20°C)	Density (1300°C)	Solidus	Liquidus	Latent heat for melting
7852.2 kg/m <sup>3</sup>	7397.4kg/m <sup>3</sup>	1466.9°C	1517.1°C	256400.0 J/kg

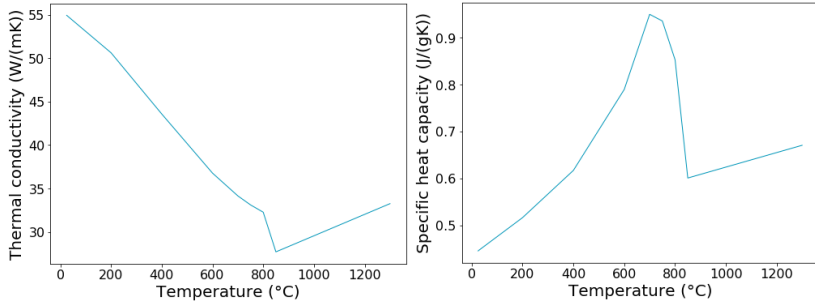


**Fig. 6** Temperature-dependent thermal conductivity and specific heat capacity used for the DED simulations

**Table 2** Layer-independent welding parameters

Velocity	Front length	Rear length	Width	Depth	Efficiency
20.0 mm/s	2.0 mm	4.0 mm	1.5 mm	3.5 mm	0.8

This fully transient model was simplified via an Advanced Thermal Cycle (ATC) that was implemented into the SF Marc solver utilized by Simufact Welding. Instead of calculating individual increments for all time steps, the ATC allows to combine an arbitrary number of time steps into segments which will then be treated in a combined fashion. The ATC is controlled by two parameters: the ATC-factor  $N$  and the ATC time step  $\theta$ .

The combination of time steps is controlled by the ATC-factor  $N$  which defines how many time steps are grouped together. With  $n$  being the total number of time steps required for transient treatment of a given weld bead, meaningful values for the ATC-factor encompass integer values in the range 2 to  $n$ . Accordingly, the total number of segments defined by the ATC-factor is the integer value of  $n/N$ .

For each segment, the solver internally processes  $N$  virtual time steps in which the weld source is moved along the weld path and the resulting fluxes are collected without applying them to the model yet. Once these virtual time steps are completed, two increments are calculated: In the first one, the accumulated heat fluxes are applied during the ATC time step  $\theta$ . With  $\theta$  being the time the weld source requires to travel the complete segment, the duration of the second computed increment is set to  $\theta - \theta$ . During this second increment, no heat fluxes are applied, and the segment is allowed to cool. Once both increments are completed, the next segment is considered in a similar fashion. In Fig. 7, this procedure is schematically shown for a weld path that requires 50 increments to complete in a transient analysis. In each of these increments, a constant heat flux of relative magnitude 1 is applied. Given an ATC factor  $N = 10$  and ATC time step  $\theta$

= 2 s, the total number of increments required for welding reduces to 10 and the relative heat flux  $f_{rel}$  in every second increment is computed from  $f_{rel} = \frac{\theta}{\theta'}$ , thus increased to 1.25. Note that the total amount of heat entering the model per segment is identical for both the transient and ATC variants.

The ATC time step  $\theta$  is a free parameter that needs to be adjusted to calibrate the peak temperature reached in the model. If the value of  $\theta$  is increased, the peak temperature decreases as a greater amount of heat can be lost to the environment or conducted into the surrounding material during heating. Likewise, the peak temperature increases as the value of  $\theta$  decreased. There are two major advantages of this simplified approach: Unlike conventional thermal cycle approaches [14], [15], the ATC maintains the physical energy balance, globally and locally. At the same time, the total number of computed increments is reduced by the factor  $2/N$ , resulting in a considerable potential to reduce the required computational time.

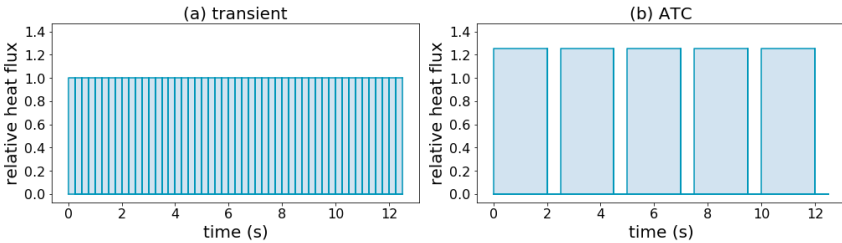


**Fig. 7** Schematic illustration of the relative heat flux during a transient analysis with 50 increments and its simplification with ATC factor  $N=10$  and ATC time step  $\theta = 2$  s. The time required to complete each segment is  $\theta = 2.5$ s.

## RESULTS AND DISCUSSION

### VALIDATION OF THE REFERENCE MODEL

In order to validate the transient reference model, temperatures were recorded for 10 positions on the baseplate and deposit as shown in Fig. 8. Although the model was set up according to the experimental process parameters, a slight timing offset was found between the experimental and numerical data sets increasing towards the end of the process. This effect is attributed to limited precision in the available velocity data of the welding robot which adds up to the observed offset of temperature peaks. To ease comparison between experimental and numerical data, the numerical time is scaled with a factor of 1.01. With this correction, Fig. 9 highlights the good agreement between numerical and experimentally measured temperature data.

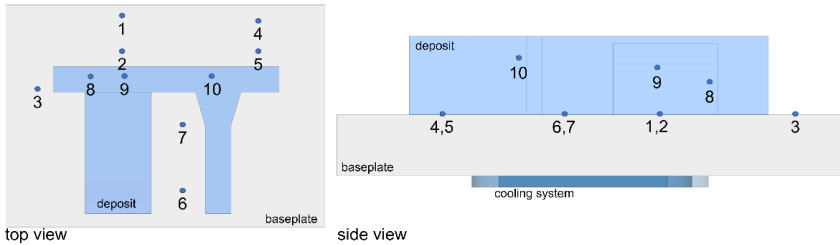


**Fig. 8** Positions of temperature measurement

Temperature differences between numerical and experimental data are shown in Fig. 10, with the corresponding values for mean and standard deviation listed in Table 3. The best agreement between numerical results and experimental data is found at measurement positions 1 and 4, situated on the baseplate at some distance to the deposit. In these positions, the mean and the standard deviation of the temperature difference are smaller than 10 °C, indicating excellent agreement between model and reality. Positions 2, 3, and 5 are also located on the baseplate, but closer to the deposit. In these positions, the mean temperature difference is still below 10 °C, but with slightly increased standard deviations up to 23 °C. Also positions 6 and 7 are located on the baseplate, enclosed by the deposit in three directions. Contrary to points 1 to 5, in these positions, the numerical prediction slightly underestimates the measured temperatures, highlighted by the mean temperature difference of -18 °C at position 7.

**Table 3** Mean,  $\mu$ , and standard deviation,  $\sigma$ , of temperature differences (simulation – experiment) for the 10 measurement positions shown in Fig. 8.

Position	1	2	3	4	5	6	7	8	9	10
$\mu$ (°C)	5.5	0.4	4.7	9.6	7.8	-7.3	-18.0	-7.0	-35.0	-40.1
$\sigma$ (°C)	8.5	22.9	13.1	8.4	20.3	15.6	22.1	169.8	197.3	137.8

This effect is probably caused by the restriction of the physical effects included in the model. While conduction, convection, and emission are included, the interaction of the deposit walls enclosing positions 6 and 7 or local variation in the surrounding temperature are not considered. Yet, it is noted that for all measurement points on the baseplate the mean difference to the experimental data lies below or very close to the thermal convergence tolerance of 20 K that is applied in the model.

For measurement positions on the deposit (positions 8-10), a more pronounced offset to the experimental data is observed with a widely spread distribution of the temperature differences. While on average, the simulation underestimates the experimental reference, the predicted peak temperatures lie well above the experimentally recorded values. Besides the unknown error introduced by the behavior of the thermocouples under extreme conditions, this issue is closely connected to the discretization of the model.

## Mathematical Modelling of Weld Phenomena 13

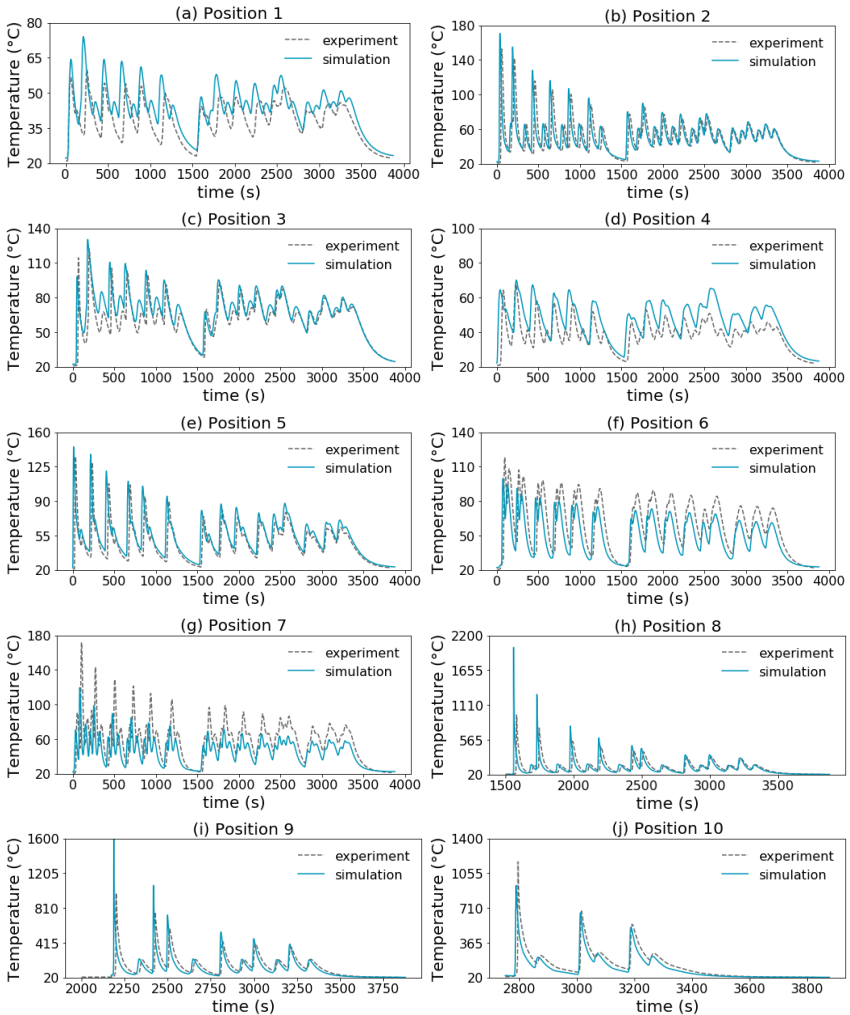


**Fig. 9** Experimental and numerical temperature data for the 10 measurement positions shown in Fig. 8

With only one linear element per deposited layer, the temperature difference between the upper and lower edges of the newly deposited element subject to heating has been observed to amount to as much as  $800^{\circ}\text{C}$ . Although this makes it difficult to accurately predict peak temperatures within the model, this localized effect is smoothed out with increasing distance to the weld source.

Despite the scaling of the numerical process time, a slight offset in timing remains between simulation and experiment. In combination with steep temperature gradients, this also contributes to the large standard deviation observed for measurement positions 8 to 10.

Considering the influences discussed above, the numerical analysis reproduces accurately the measured temperature profile, both in the baseplate as well as in the deposit. Thus, the applied model is qualified to serve as a reference for further model simplifications.

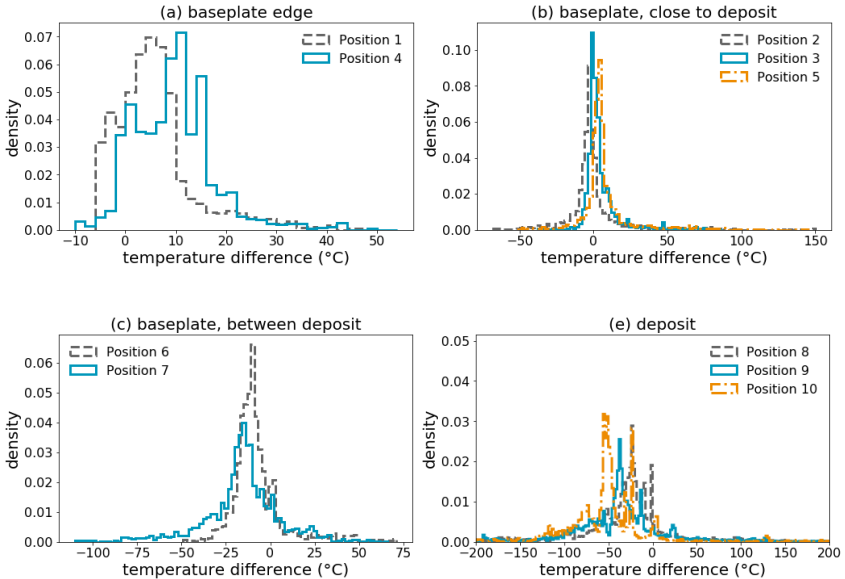


**Fig. 10** Distribution of temperature differences (simulation – experiment) for the 10 measurement positions shown in Fig. 8

SIMPLIFIED WELDING MODELS

The performance of the Advanced Thermal Cycle (ATC) described above was tested with reference to the fully transient thermal analysis. Both the influence of the ATC factor as well as the ATC time step were probed. The ATC factor was increased up to the point where entire weld seams are combined into a single segment. This was reached for a value of  $N = 688$ . For  $N = 100$ , the bottom layers are split into 15 segments each. In this case, each layer requires a maximum of 30 welding increments to complete while still maintaining a basic representation of the process direction. Fig. 11 exemplarily illustrates the temperature profile for the 6 increments required to complete the second weld bead of the second layer.

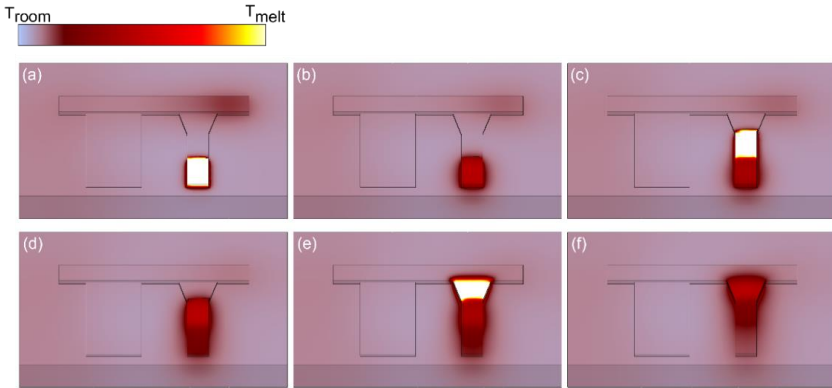


**Fig. 11** Temperature profile of the sample while completing the second weld bead of the second layer with ATC factor  $N = 100$  and ATC time step  $\theta = 0.8$  s.

Table 4 lists the total number of calculated increments for the transient reference and all tested variations of the ATC factor  $N$  and ATC time step  $\theta = 0.8$ . Table 4, together with the computational times and relative time saving illustrated in Fig. 12, emphasizes the ATC’s potential to reduce the computational cost of the simulation. Already with the moderate ATC factor  $N = 10$ , the time saving with regard to the transient reference amounts to more than 80%. As the ATC factor is increased, the required computational time is further reduced. With increasing ATC factor, the computational time required for the cooling sequences between layers (421 increments for all variants) starts to dominate the total computational time of the simulation. Accordingly, the time saving asymptotically approaches its maximum value that is associated with the ATC combining entire weld beads into one segment each ( $N = 688$ ). In this particular case, the most simplified variant with  $N = 688$  could be completed in about 46 minutes, while the variant with  $N = 100$  required about 1 hour and 20 minutes.

**Table 4** Number of calculated increments for the transient reference and different ATC factors  $N$ .

	Transient	$N = 10$	$N = 20$	$N = 50$	$N = 100$	$N = 688$
<b>Nr. of increments</b>	22049	4761	2597	1275	847	509

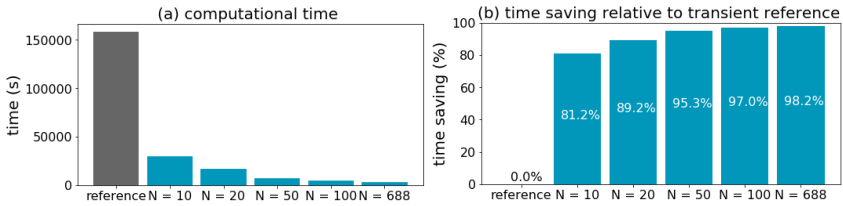


**Fig. 12** Computational time and relative time saving for the transient reference and all tested ATC variations with ATC time step  $\theta = 0.8$

With the time saving potential of the ATC established, it is necessary to check how it performs regarding the result quality. Fig. 13 shows exemplarily the thermal profile at positions 6 and 9 recorded for different ATC factors and ATC time step  $\theta = 0.8$ . The graphs highlight that the global temperature history is virtually not affected by the simplifications introduced by the ATC with factors up to  $N = 100$ . Fig. 13 (a) and (c) illustrate that even for  $N = 100$ , no significant differences are visible when the entire process is considered. Only a close-up of individual temperature peaks (Fig. 13 (b) and (c)) reveals the effect of the ATC and the impact of further simplification with  $N = 688$ .

Especially the close-up of position 9 (Fig. 13 (d)) illustrates how the time stepping is affected. Depending on the relative positions of the measurement point and the boundaries of the heated segments, the temperature peak is shifted on the time axis or smaller sub-peaks are introduced. Once the heating phase is completed, the heat spreads into the deposit and it is allowed to cool. This part of the curve is much less affected by the localized influence of the weld source and the temperatures measured for the simplified simulations merge again with the transient reference.

Position 6 is not located on the deposit, but on the baseplate. Accordingly, the timing of the temperature peaks is not as much affected by the ATC as for position 9. The close-up of position 6 (Fig. 13 (b)) merely reveals a slight decrease of the recorded peak temperatures as the ATC factor is increased.

Fig. 14 exemplarily illustrates the influence of the ATC time step  $\theta$  on the first temperature peaks recorded for constant ATC factor  $N = 20$  at positions 8 and 9, respectively. As  $\theta$  defines the length of the first increment calculated for each segment, a smaller  $\theta$  slightly shifts the temperature peak on the time axis. Due to the shorter time available for heating, a smaller ATC time step leaves less opportunity for heat losses due to conduction, convection, or radiation. Consequently, the peak temperature increases as  $\theta$  is decreased as it is observed in Fig. 14. This makes the ATC time step  $\theta$  a free parameter that needs to be calibrated to achieve the required peak temperatures. In case of the present model, the best fit was found for  $\theta = 0.8$  s.

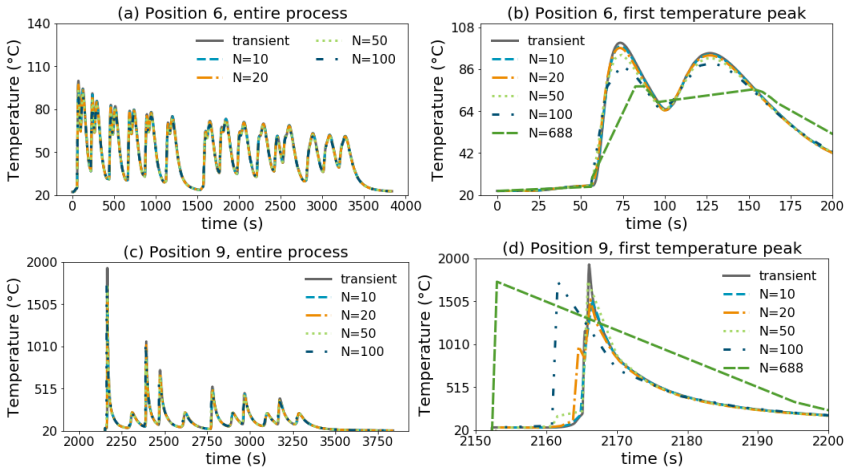


**Fig. 13** Temperatures measured at positions 6 and 9 recorded for different ATC factors and ATC time step  $\theta = 0.8$ . (a) and (c) show the entire process time, (b) and (d) a close-up of the first temperature peak, respectively

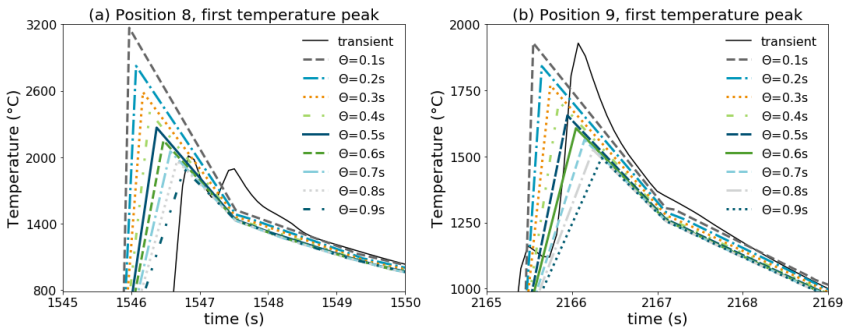


**Fig. 14** Variation of the ATC time step  $\theta$  for constant ATC factor  $N = 20$

### CONCLUSIONS

The present contribution shows how a transient DED simulation can be simplified by introducing an Advanced Thermal Cycle (ATC). To test the approach, a transient thermal model was validated by comparison to experimentally measured temperature data recorded both on the baseplate as well as on the deposit itself, and excellent agreement between numerical and experimental data was found. The ATC allows to combine multiple transient time steps into segments for which the heat input is treated in a joint

fashion. It is controlled by two parameters, namely the ATC factor and the ATC time step. The influence of both parameters was evaluated, showing very good agreement between the transient reference and the simplified models. With only a minor loss of result accuracy and resolution in time, the required computational time required for welding could be reduced by more than 97% so that the simulation can be completed within the same time as the real DED built. These results qualify the ATC as a valuable tool for the simulation of large DED processes which cannot be handled via transient simulation otherwise and as a feasible method to evaluate thermal profiles which are difficult to measure experimentally.

### References

- [1] ASTM INTERNATIONAL: ‘ASTM Standard F2792-12a: Standard Terminology for Additive Manufacturing Technologies’, 2012, doi: 10.1520/F2792-12A.
- [2] P. R. GRADL and C. S. PROTZ: ‘Technology advancements for channel wall nozzle manufacturing in liquid rocket engines’, *Acta Astronautica*, vol. 174, pp. 148-158, Sep. 2020, doi: 10.1016/j.actaastro.2020.04.067.
- [3] B. BLAKEY-MILNER et al.: ‘Metal additive manufacturing in aerospace: A review’, *Materials & Design*, vol. 209, p. 110008, Nov. 2021, doi: 10.1016/j.matdes.2021.110008.
- [4] ‘NASA looks to large-scale DED Additive Manufacturing for future rocket engines’, *Metal Additive Manufacturing*, Sep. 18, 2020, <https://www.metal-am.com/nasa-looks-to-large-scale-ded-additive-manufacturing-for-future-rocket-engines/>, accessed Mar. 29, 2022.
- [5] S. M. THOMPSON, L. BIAN, N. SHAMSAEI and A. YADOLLAHI: ‘An Overview of Direct Laser Deposition for Additive Manufacturing; Part I: Transport Phenomena, Modeling and Diagnostics’, *Additive Manufacturing*, vol. 8, p. 36, 2015.
- [6] M. BIEGLER, B. A. M. ELSNER, B. GRAF and M. RETHMEIER: ‘Geometric distortion-compensation via transient numerical simulation for directed energy deposition additive manufacturing’, *Science and Technology of Welding and Joining*, vol. 0, no. 0, pp. 1-8, Mar. 2020, doi: 10.1080/13621718.2020.1743927.
- [7] M. BIEGLER, P. KHAZAN, M. GATZEN and M. RETHMEIER: ‘Improvement of numerical simulation model setup and calculation time in additive manufacturing-laser-metal-deposition components with an advanced modelling strategy’, in *Mathematical Modelling of Weld Phenomena 12*, Seggau, 2018, pp. 979-990. doi: 10.3217/978-3-85125-615-4.
- [8] F. MONTEVECCHI, FILIPPO, G. VENTURINI, N. GROSSI and A. SCIPPA: ‘Finite Element mesh coarsening for effective distortion prediction in Wire Arc Additive Manufacturing’, *Additive Manufacturing*, vol. 18, p. 145, 2017.
- [9] E. BOOS et al.: ‘Topology Optimized Unit Cells For Laser Powder Bed Fusion’, in *Industrial perspectives in Additive Technologies*, pp. 30-39, Vienna, 2021.
- [10] G. TURICHIN, E. ZEMLYAKOV, K. BABKIN, S. IVANOV and A. VILDANOV: ‘Analysis of distortion during laser metal deposition of large parts’, *Procedia CIRP*, vol. 74, pp. 154-157, Jan. 2018, doi: 10.1016/j.procir.2018.08.068.
- [11] S. MARIMUTHU et al.: ‘Finite element modelling of substrate thermal distortion in direct laser additive manufacture of an aero-engine component’, *Proceedings of the Institution of Mechanical Engineers, Part C: Journal of Mechanical Engineering Science*, vol. 227, no. 9, pp. 1987-1999, Sep. 2013, doi: 10.1177/0954406212470363.
- [12] V. NAIN, T. ENGEL, M. CARIN, D. BOISSELER and L. SEGUY: ‘Development of an Elongated Ellipsoid Heat Source Model to Reduce Computation Time for Directed Energy Deposition Process’, *Frontiers in Materials*, vol. 8, p. 512, 2021, doi: 10.3389/fmats.2021.747389.

- [13] Y. YANG, M. ALLEN, T. LONDON and V. OANCEA: 'Residual Strain Predictions for a Powder Bed Fusion Inconel 625 Single Cantilever Part', *Integr Mater Manuf Innov*, vol. 8, no. 3, pp. 294-304, Sep. 2019, doi: 10.1007/s40192-019-00144-5.
- [14] Z. BOUMERZOUG, E. RAOUACHE and F. DELAUNOIS: 'Thermal cycle simulation of welding process in low carbon steel', *Materials Science and Engineering: A*, vol. 530, pp. 191-195, Dec. 2011, doi: 10.1016/j.msea.2011.09.073.
- [15] T. KIK: 'Computational Techniques in Numerical Simulations of Arc and Laser Welding Processes', *Materials*, vol. 13, no. 3, Art. no. 3, Jan. 2020, doi: 10.3390/ma13030608.

# PROGNOSIS OF SEAM GEOMETRY DURING LASER BEAM WELDING

C. SCHWARZ\*<sup>1</sup>, M. PUSCHMANN\*, R. MAUERMANN\*

*\*Fraunhofer Institute for Machine Tools and Forming Technology; Chemnitz / Dresden; Germany*

*<sup>1</sup>Corresponding author*

DOI 10.3217/978-3-85125-968-1-28

## ABSTRACT

Data evaluation is of great importance for quality assurance and control loops. Components and process parameters involved in the production process can be networked and evaluated using all relevant information and controlled in real time. Thermal joining processes are complex; so is laser beam welding (LBW). The numerical description of the processes provides good approximations for partial aspects. However, experiments are still the basis for determining optimal process parameters. This is time-consuming and cost-intensive.

For the evaluation of experimental data there are some AI approaches; e.g. response surface method, Taguchi method, KNN models, Kriging models, principal component analysis (PCA). Systematic backup, analysis and visualization of welding and quality data using database systems and analysis algorithms is not currently taking place on a wide scale. Expert knowledge is a mandatory prerequisite for the preparation, execution and evaluation of LBW processes. Therefore, the potentials of the process are often not fully exploited. The consequences are e.g. long commissioning times, low flexibility for new tasks and missing objective knowledge management.

In the lecture a tool based on PCA will be presented. The interdependencies between process parameters and the welding result in the form of the 2D weld geometry are mapped in a statistical model. The system is learned from experimental data sets. The weld geometry can contain further characteristic values; e.g. weld penetration depth, weld width or load-bearing weld cross-section. These characteristic values can be linked to the quality of the welded joint. The two-dimensional weld formation and all contained spatially resolved result variables can be represented; e.g. width of heat affected zones and grain size distribution. This requires the analysis of multivariate data; e.g. micrographs with a pixel number of several million, as dependent result variables with all nonlinear dependencies. To realize the spatial resolution of the result variables, the full pixel resolution is used for image analysis. From the formed statistical model, the seam geometry with all properties can be predicted ad hoc within the learned data space for arbitrary parameter combinations, or local target variables can be specified and an optimization algorithm searches for the best possible parameter combination from many model queries. Using an LBW task as an example, the evaluation principle and the GUI are shown. Key points are the permanent accumulation of knowledge, usable control strategies, quality proofs and thus time and cost savings.

Keywords: Seamprognosis; measurement data; principal component analysis; spatially resolved result variables

## INTRODUCTION

Individual operations or several operations in a process chain always have influencing variables; some can be easily influenced (controlled variables) and some are difficult to influence. In the complex operation of laser welding LBW, controllable influencing variables are e.g. feed rate, focus position and power; difficult to influence is usually the task, i.e. the materials to be welded. At present, theoretical control of the LBW-process is not sufficient to dispense with experiments. Therefore, the welding parameters are mainly determined experimentally (Fig. 1).

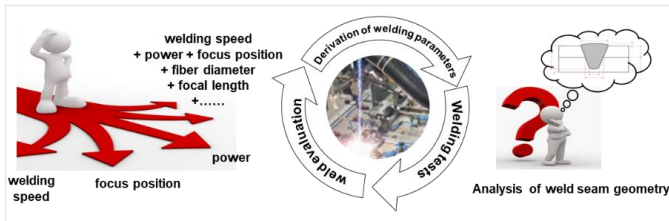


**Fig. 1** Iterative approach to experience-based welding parameter determination

There is not always sufficient time available for test series. Technological decisions often have to be made on the basis of subjective empirical values. Potentials of the processes are not exploited to the full extent. For manufacturing companies, problems arise during preparation due to long commissioning times and during processing due to non-optimal parameters.

This situation is exacerbated by the increasing individualization of production. The development is characterized by the increase of small series, one-off productions or changing component derivatives within a series production. Rapid adaptation of technology parameters to new production tasks is required. This flexibility demanded by customers poses great challenges for plant manufacturers as well as for the supply industry and contract manufacturers.

Therefore, the following objectives are pursued:

- Predict welding parameters for desired seam geometries without time-, material- and energy-intensive welding tests; that leads to fast, efficient, accurate planning processes
- improvement of quality through optimal parameter selection
- fast commissioning of welding systems even for batch size 1; making uneconomical orders profitable
- Process stabilization in automatic control loops
- make welding knowledge independent of people; constantly expand know-how.

The analysis of complex data makes sense only if a large number of setting parameters are required and the user therefore has difficulty in keeping track of the interdependencies between input variables and welding results.

STATE OF THE ART

Data evaluation is of great importance for quality assurance and control loops. Components and process parameters involved in the production process can be networked and evaluated using all relevant information and controlled in real time.

Transforming the experiential knowledge of experts into usable algorithms has been the subject of research for years. For the evaluation of experimental data there are some AI approaches [1]; e.g. Response Surface Method [2], Taguchi method [3], Neuronal Network models [4], Kriging models [5], Principal Component Analysis (PCA) [6].

As parameter studies carried out on various manufacturing processes, PCA makes it possible to analyze multivariate data with a high number of input and dependent result variables - up to the range of millions [7]. Thus, complex nonlinear dependencies can be spatially resolved and mapped with good accuracy by statistical methods.

COUPLED PROCESS ANALYSIS

Coupled Process Analysis (CPA) is discussed in [8-10].

A number of 12 tests were performed to realise a prediction in this data space from experimental data with the CPA-Tool. In Fig. 2 the processing cycle of CPA is shown beginning with a Design Of Experiments (DOE).

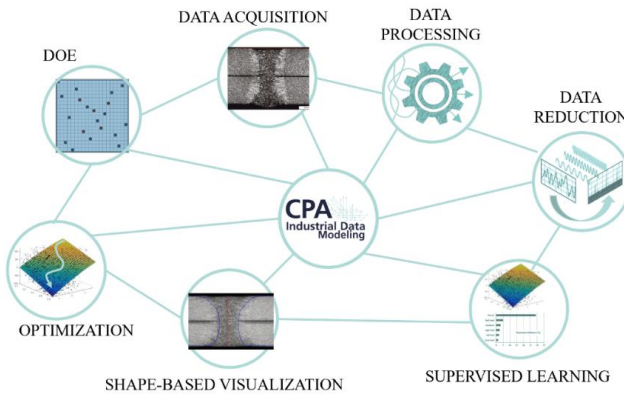


Fig. 2 CPA - processing cycle

There are indications that the acquisition of complex experimental data represents reality better and more efficiently than the attempt of numerical description. But, also targeted experiments to determine material properties [11] or serial measurements to describe processes are costly. This data acquisition incl. the preparation of the data for automatic machine readability are often 90% and more of the expenses for a successful AI project. Therefore, minimizing the experiments by maximizing the use of the data is an important criterion.

For the realized LBW task, the input variables with the selected data space are shown in Table 1; the fixed boundary conditions are shown in Table 2. As DOE a Latin Hypercube Sampling was used to determine the variable parameters for the 12 weld tests; see Table 3.

**Table 1** Data space of the input variables

Input variable	min	max
welding speed [m/min]	1,5	5
Power [kW]	2	5
Focus position (mm)	-4	5

**Table 2** Fixed boundary conditions

description	Value (const.)
Laser source	Disk laser Trumpf „TruDisk 10002“
Fiber diameter	0,4 mm
Welding optic	Trumpf MSO (focal length 200 mm)
Base material	Steel (DC04) / thickness 1,0 mm / uncoated
Weld configuration	lap joint in flat position

**Table 3** Variable laser parameters

Test	Test Speed [m/min]	Power [kW]	Focus Position [mm]
1	2,83	2,83	2
2	3,17	2	3
3	4,5	3,13	1
4	1,5	4,62	-2
5	1,83	5	-4
6	4,17	3,37	0
7	5	3,37	0
8	1	2,62	5
9	2,5	4,12	-3
10	2,17	2,88	-1
11	3,83	2,38	5
12	3,5	4,38	4

Data acquisition is carried out on the prepared 12 cross sections in high pixel resolution. An example for a narrow seam, see Fig. 3, welded at higher speed and lower power. For a wide seam see Fig. 4, welded at lower speed and higher power.

The images were taken in a high resolution with millions of pixels; each with a gray value between 1 and 256. Suitable algorithms for image preprocessing and feature extraction are available open-source [12] as well as commercially. For supervised learning classifiers up to complex neural networks, a wide range of methods exists [13].

In addition to the gray values, color and texture features can also be recorded in order to make statements about the microstructure; e.g. about the grain size distribution.

Data processing means make the data machine readable. The LBW-micrographs will be formatted to the same size, i.e. to an identical number of pixels.

Classically, the relationship to the input variables could be mapped in an extra metamodel for each pixel. This does not make sense with current computing technology. So data reduction based on PCA is used.

Supervised learning on the basis of Python-based engines determines the best mathematical approximations for various relationships. Automatic model building takes place in the reduced data space. Often simple polynomial approaches are sufficient for the description. In the case of the LBW task, 5 modes with maximum quadratic terms resulted. Based on the created analytical model, input variables with only minimal influence can be sorted out in a sensitivity analysis. In the present case with only three input variables, no parameter was sorted out.

A dynamic shape-based visualization for arbitrary parameter combinations is performed. This GUI of the relationships can be automated by analytically calculating a large number of variants for a desired target variable in an optimization run and determining the parameter combination that best satisfies the target variable.

The whole cycle can be repeated if the model quality does not meet the set requirements. In this case, a new DOE is created with a serial Latin Hypercube Sampling, whereby only new values for the variables are specified.

## LASERTOOL

In [14] the LBW-example was published for the first time. In the following the evaluation principle and the GUI are shown.

The 2D virtual micrograph is represented by different gray values, the fusion line - the boundary between laser weld seam and heat affected zone - by two blue lines. The data for the blue lines were determined manually in the 12 micrographs and then approximated. See Fig. 3 and 4 to compare the real micrograph with the image from the virtual model.

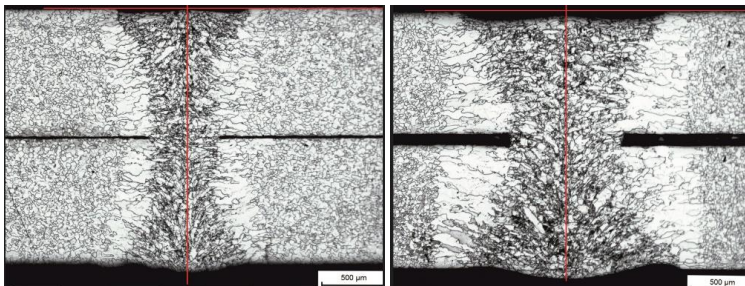


**Fig. 3** Cross sections from experiment; Test 7 left; Test 12 right

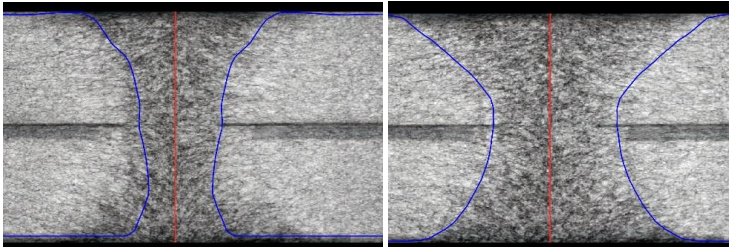


**Fig. 4** Shape-based visualization with grey values and blue fusion line from metamodel; Test 7 left; 12 right

Fig. 6 shows the Graphic User Interface.

The two target variables – grey values and blue lines - are each represented by a separate metamodel.

Model-based generation of a 2D virtual micrograph with the geometry of the heat-affected zone and the fusion area of the laser weld seam for various parameter combinations is possible in real time – see Fig. 5 and 6 for process chain and GUI.

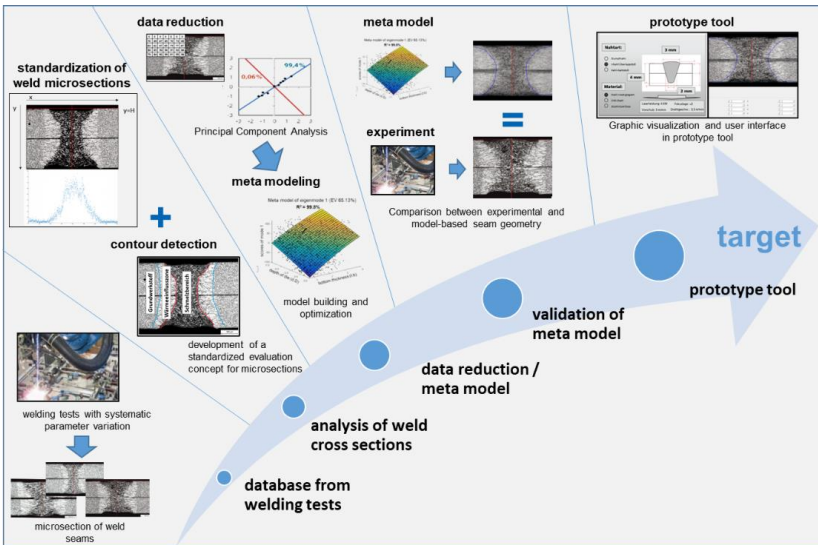


**Fig. 5** Shape-based visualization with grey values and blue fusion line from metamodel; Test 7 left; 12 right

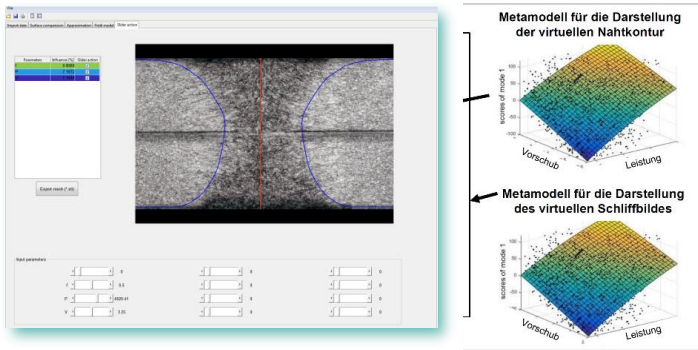


**Fig. 6** GUI Virtual, shape-based visualization

## OUTLOOK

Many other influence parameters have an impact on the process; e.g. process gas or laser parameters (e.g. laser beam wavelength, fibre diameter, spot diameter, power distribution in the beam ...). These variables multiply the solution space and the effort. Especially the material combination can hardly be parameterised.

Further characteristic values can also be evaluated for the target variables; e.g. weld penetration depth, load-bearing weld cross section or grain size distribution. These characteristic values can be linked to the quality of the welded joint.

Based on the described approach, the goals stated in the introduction can be achieved.

## CONCLUSION

For the field meta modelling approach based on the sensitivity analysis of variances it will be necessary to automate the pre- and post-processing of experiments and data analytics.

In the presented example "LBW", a prediction of the seam geometry becomes possible on the basis of micrographs using the variance-based sensitivity analysis with field metamodeling. This makes it possible to find suitable parameters for welding processes.

Often the data acquisition can be the biggest cost driver. What is sought is the analytical model that achieves the best process description at the lowest cost for measurement. Such an analytical model is then used as a basis for the automatic control of processes based on the developed software workflow via suitable control variables; e.g. laser parameters.

## References

- [1] J. E. R. DHAS and S. J. H. DHAS: 'A Review on Optimization of Welding Process', *Procedia Engineering*, 38 (2012), S. 544-554; 2012.

- [2] G. PADMANABAN and V. BALASUBRAMANIAN: 'Optimization of laser beam welding process parameters to attain maximum tensile strength in AZ31B magnesium alloy', *Optics & Laser Technology*, 42 8, S. 1253-1260; 2010.
- [3] E. M. ANAWA and A. G. OLABI: 'Using Taguchi method to optimize welding pool of dissimilar laser-welded components', *Optics & Laser Technology*, 40 2, S. 379-388; 2008.
- [4] J. MIRAPEIX, P. B. GARCÍA-ALLENDE, A. COBO, O. M. CONDE and J. M. LÓPEZ-HIGUERA: 'Real-time arc-welding defect detection and classification with principal component analysis and artificial neural networks', *NDT & E International*, 40, 4, S. 315-323; 2007.
- [5] Y. YANG, Z. GAO and L. CAO: 'Identifying optimal process parameters in deep penetration laser welding by adopting Hierarchical-Kriging model', *Infrared Physics & Technology*, 92, S. 443-453; 2018.
- [6] S. DATTA, G. NANDI, A. BANDYOPADHYAY and P. KUMAR PAL: 'Application of PCA-based hybrid Taguchi method for correlated multicriteria optimization of sub-merged arc weld. A case study', *The International Journal of Advanced Manufacturing Technology*, 45 3-4, S. 276-286; 2009.
- [7] CH. SCHWARZ, S. KRIECHENBAUER, R. MAUERMANN, W.G. DROSSEL: *Field meta modelling for process design in complex sheet metal forming*; 41<sup>st</sup> International Deep Drawing Research Group Conference, Lorient-France, 2022.
- [8] CH. SCHWARZ, P. ACKERT, T. FALK, M. PUSCHMANN, R. MAUERMANN, W.G. DROSSEL: 'Model-based joining process design for the body shop process chain', International Conference on Advanced Joining Processes, *Proceedings Engineering Mechanics*, [https://doi.org/10.1007/978-3-030-95463-5\\_2](https://doi.org/10.1007/978-3-030-95463-5_2), AJP 2022.
- [9] CH. SCHWARZ, P. LINK; ST. IHLENFELDT, W.G. DROSSEL: 'Application of Fourier-related data reduction methods in sheet metal forming', *Procedia CIRP*, Volume 99, Pages 260-265, ISSN 2212-8271, Naples-Italy, 2021.
- [10] CH. SCHWARZ, P. ACKERT, R. MAUERMANN: 'Principal component analysis and singular value decomposition used for a numerical sensitivity analysis of a complex drawn part', *Int J Adv Manuf Technol*; 94: 5-8. p. 2255-2265. DOI: 10.1007/s00170-017-0980-z.; 2018.
- [11] D. MOHR: *Creating Big-Data on Sheet Metal Plasticity and Failure*, 41<sup>st</sup> International Deep Drawing Research Group Conference, Lorient-France, 2022.
- [12] OPENCV: *Open Computer Vision Library*, <http://opencv.org>, retrieved: 31.07.2018.
- [13] R. O. DUDA, P. E. HART and D. G. STORK: *Pattern Classification*. s.l.: Wiley-Inter-science 2012.
- [14] CH. SCHWARZ, P. ACKERT, T. FALK, M. PUSCHMANN, R. MAUERMANN, W.G. DROSSEL: 'Model-based joining process design for the body shop process chain', International Conference on Advanced Joining Processes, *Proceedings Engineering Mechanics*, [https://doi.org/10.1007/978-3-030-95463-5\\_2](https://doi.org/10.1007/978-3-030-95463-5_2), AJP 2022.

# **IX Solid State and Friction Stir Welding**



# NUMERICAL ANALYSIS OF ULTRASONIC VIBRATION ENHANCED FRICTION STIR WELDING OF DISSIMILAR AL/MG ALLOYS

C. L. YANG<sup>\*,\*\*</sup>, C. S. WU<sup>\*</sup>, M. BACHMANN<sup>\*\*</sup>,  
M. RETHMEIER<sup>\*\*\*,\*\*,\*\*\*\*</sup>

*\*Institute of Materials Joining, Shandong University, Jinan 250061, China*

*\*\*Welding Technology, Bundesanstalt für Materialforschung u. -prüfung (BAM), Unter den Eichen 87, 12205 Berlin, Germany*

*\*\*\*Institute of Machine Tools & Factory Management, Technische Universität Berlin, Pascalstraße 8-9, 10587 Berlin, Germany*

*\*\*\*\*Joining and Coating Technology, Fraunhofer Institute for Production Systems and Design Technology, Pascalstraße 8-9, 10587 Berlin, Germany*

DOI 10.3217/978-3-85125-968-1-29

## ABSTRACT

The ultrasonic vibration enhanced friction stir welding (UVEFSW) process has unique advantages in joining dissimilar Al/Mg alloys. While there are complex coupling mechanisms of multi-fields in the process, it is of great significance to model this process, to reveal the influence mechanism of ultrasonic vibration on the formation of Al/Mg joints.

In this study, the acoustic-plastic constitutive equation was established by considering the influence of both ultrasonic softening and residual hardening on the flow stress at different temperatures and strain rates. And the ultrasonic induced friction reduction (UiFR) effect on friction coefficient in different relative directions at the FSW tool-workpiece interface was quantitatively calculated and analyzed.

The Al/Mg UVEFSW process model was developed by introducing the above acoustic effects into the model of Al/Mg friction stir welding (FSW). The ultrasonic energy is stronger on the aluminum alloy side. In the stirred zone, there is the pattern distribution of ultrasonic sound pressure and energy. The heat generation at the tool-workpiece contact interface and viscous dissipation were reduced after applying ultrasonic vibration. Due to the UiFR effect, the projections of friction coefficient and heat flux distributions at the tool-workpiece interface present a "deformed" butterfly shape. The calculated results show that ultrasonic vibration enhanced the material flow and promoted the mixing of dissimilar materials.

Keywords: Friction stir welding; Ultrasonic vibration; Al/Mg alloys; Numerical simulation

## INTRODUCTION

With the development of the economy and society, the demand for energy conservation and emission reduction has increased, and light materials such as aluminum and magnesium alloys are widely used in automobile, aerospace, and high-speed train industries [1]. This inevitably faces welding of dissimilar Al/Mg alloys, and the joining of aluminum alloy and magnesium alloy can make full use of their advantages and make up

for each other's shortcomings. However, due to the great differences in crystal structure and physical properties between the two materials, the high-quality joining of Al/Mg dissimilar alloys faces special challenges [2]. Although friction stir welding (FSW) has some prominent advantages in the joining of Al/Mg alloys [2-5], there is still growing demand for further improvement in the microstructures and mechanical properties of dissimilar joints.

Recently, ultrasonic vibration has been used to improve the FSW process of dissimilar material FSW. Sachin et al. [6] applied ultrasonic vibration to the tool along the welding direction. Strass et al. [7-10] exerted the ultrasonic vibration to one side of the workpiece through rollers. Ji et al. [11-13] conducted the static shoulder FSW with the ultrasound applied to the back of the workpieces. Lv et al. [14] used the ultrasonic vibration enhanced FSW (UVEFSW) for joining Al/Mg alloys, and the ultrasonic vibration was applied to the top surface of the workpieces in front of the tool. All the above experimental studies show that ultrasonic vibration can improve weld quality and decrease welding loads.

However, there are complex coupling mechanisms of multi-fields in the Al/Mg dissimilar UVEFSW process, and the influence of ultrasonic vibration on the "heat generation/temperature profile-stress/strain-material flow-material mixing" behaviors is more complex. Therefore, it is of great significance to model the UVEFSW process of dissimilar Al/Mg alloys and conduct the coupled numerical analysis of multi-physical fields, to reveal the influence mechanism of ultrasonic vibration on the formation of dissimilar Al/Mg joints and realize the effective utilization of ultrasonic energy field in friction stir welding of dissimilar Al/Mg alloys.

For dissimilar FSW of Al/Mg alloys without ultrasonic assistance, Singh et al. [15] established a heat transfer model of 6061 Al/AZ31 Mg, and Lim et al. [16] developed a finite element model based on the coupled Euler-Lagrange method for Al 6061-T6 and AZ61 Mg to predict the temperature and strain. The authors' group has established computational fluid dynamics (CFD) model of Al-Mg considering local turbulence [17]. On the other hand, for the UVEFSW of a single material (Al alloy), Shi et al. established a CFD model which considered the acoustic softening effect [18], on this basis, the acoustic softening & residual hardening effects [19] and the ultrasonic induced friction reduction (UiFR) effect were considered [20] separately. However, the ultrasonic field induces all these influences simultaneously during the UVEFSW process of Al/Mg alloys, which should be considered in a single comprehensive model.

In this study, a multi-physical coupling model including the acoustic plasticity (softening & residual hardening effects) and UiFR effect was developed and experimentally validated for UVEFSW of dissimilar Al/Mg alloys. The ultrasonic effects on the friction coefficient, heat generation, temperature, and material flow fields were analyzed quantitatively.

## EXPERIMENT

In the Al-Mg UVEFSW process, as shown in Fig. 1, ultrasonic vibration is transmitted to the top of the workpiece in front of the FSW tool directly through the sonotrode at a certain angle. FSW was performed on dissimilar AZ31B-H24 Mg and 6061-T4 Al alloys.

The Mg alloy sheet was on the advancing side (AS), and the Al alloy sheet was on the retreating side (RS). The sheet size was 200 mm (length)  $\times$  60 mm (width)  $\times$  3 mm (thickness). The FSW tool constituted a concave shoulder (diameter 12 mm) and a frustum-shaped right-hand threaded pin (tip diameter 4.2 mm, root diameter 3.2 mm, and length ground from 3 mm to 2.7 mm), and its material was tool steel. The tool was rotated anticlockwise with a tilt angle of  $2.5^\circ$ . The tool rotation speed, welding speed, and shoulder plunge depth were 800 rpm, 50 mm/min, and 0.15 mm respectively. The tool offset was 0.3 mm to the Mg sheet (AS). The frequency of the ultrasonic vibration is 20 kHz, the amplitude is 40  $\mu\text{m}$ , and the effective power is 220 W. The radius of the sonotrode tip is 4.0 mm, the center of the tip is 20 mm away from the axis of the FSW tool, and the angle between the axis of the sonotrode with the welding direction is  $40^\circ$ , the pressing force on the sonotrode is 300 N.

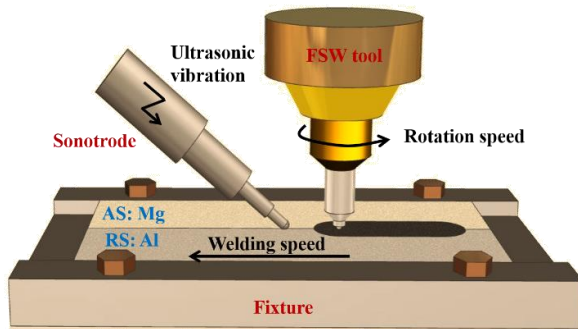


**Fig. 1** Schematic of Al-Mg UVeFSW

After welding, metallographic samples at the horizontal section around the keyhole for FSW and UVeFSW were prepared.

#### AL/MG UVEFSW CFD MODEL

The Al/Mg dissimilar UVeFSW model is a combination of the UVeFSW model with acoustic softening and hardening effects [19], the UVeFSW model considering the UiFR effect [20], and the Al/Mg dissimilar FSW model [17]. The geometric model of the Al/Mg UVeFSW process is shown in Fig. 2.

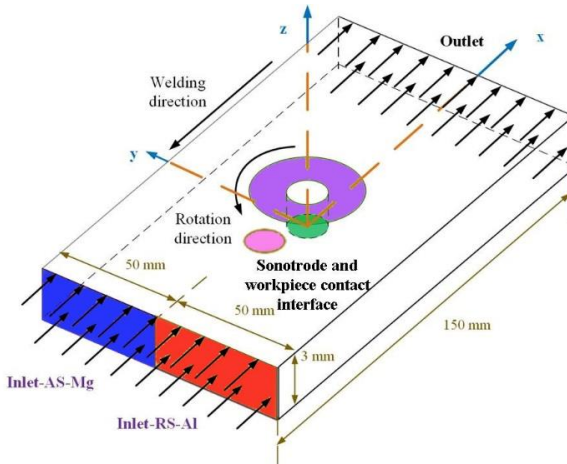


**Fig. 2** The geometry model in UVeFSW of Al/Mg alloys

There are three kinds of acoustic effects considered during the welding process model: the preheat effect, the acoustic-plastic effect (acoustic softening and residual hardening effects) as well as the ultrasonic induced friction reduction (UiFR) effect.

#### THE PREHEAT EFFECT

When the ultrasound is applied, not only frictional heat is generated on the sonotrode-workpiece interface, but also the heat due to plastic deformation exists.

According to the frictional law, the heat generated ( $Q_F$ ) at the interface between the ultra-sonic horn and the workpiece is as follows [21],

$$Q_F = \frac{4\xi_0 f_w \cos \varpi \mu_{\text{tool}} F_N}{A_{\text{tool}}} \quad (1)$$

where  $\xi_0$  is the amplitude of the ultrasonic vibration,  $f_w$  is the frequency of the ultrasonic vibration,  $\varpi$  is the angle between the sonotrode and the workpiece surface (horizontal plane),  $F_N$  is the axial pressure due to the clamping force acting on the sonotrode,  $\mu_{\text{tool}}$  is the friction coefficient at the sonotrode-workpiece contact interface, and  $A_{\text{tool}}$  is the area of sonotrode-workpiece contact interface.

The heat ( $Q_W$ ) generated by plastic deformation at the contact surface between the ultrasonic horn and the workpiece can be expressed by the following equation,

$$Q_w = \sqrt{\left(\frac{\sigma_y}{2}\right)^2 - \left(\frac{F_N/A_{\text{tool}}}{2}\right)^2} 4\xi_0 f_w \cos \varpi \quad (2)$$

where  $\sigma_y$  is the temperature-dependent yield stress.

The total heat generation at the sonotrode-workpiece contact interface is written as,

$$Q_{s-w} = Q_F + Q_W \quad (3)$$

#### THE ACOUSTIC PLASTIC EFFECT

In the upsetting process of metal samples, when ultrasonic is applied at a certain moment, the stress decreases, which indicates that the deformation resistance of the material decreases due to ultrasonic action, which is called the acoustic softening effect. If the ultrasonic action time is long enough, the stress will increase when the ultrasonic application is stopped, which is called the acoustic residual hardening effect [22].

In the process of applying ultrasound, the dislocations in the material absorb acoustic energy, so that they are easier to be activated and leave their pinned equilibrium positions, and the amplitude of dislocation oscillation increases until they exceed the normal distance from the equilibrium positions. As the dislocation absorbs additional acoustic energy, the shear stress required for metal plastic deformation is significantly reduced, which is called the acoustic softening effect.

When there is a superposition of acoustic stress and internal stress caused by lattice defects, dislocations are forced to move in the preferred direction, thus changing the internal structure. In other words, the material properties will change permanently, and the ultrasound enhances the proliferation and redistribution of dislocations, which will lead to the acoustic hardening effect.

During the process of ultrasonic application, the activated dislocations are much larger than the proliferated dislocations, and finally, show a softening effect. However, when the application of ultrasound is stopped, the activation disappears, but the dislocation proliferation caused by the application of ultrasound is permanent, so it shows the hardening effect.

Although we calculate the situation in the process of ultrasonic application, there is a difference between the final softening shown and the actual softening effect, so it is necessary to comprehensively consider the acoustic softening and hardening effects to describe the acoustic plastic effect.

In the process of metal plastic deformation, dislocations proliferate and annihilate simultaneously. The strength of dislocation proliferation and annihilation determines the increase or decrease of the dislocation density. The change of the dislocation density, in turn, determines the increase or decrease of the strength of the materials [23]. We describe the acoustic softening effect by considering the influence of ultrasonic vibration on the activation process of dislocation, and reflect the acoustic residual hardening effect by expressing the influence of ultrasound on the proliferation process of dislocation. Finally, we can use Eq. (4) to express the acoustic plastic effect of ultrasound.

What's more, for the Mg alloy AZ31B, Dong et al [24] found that the stress gradually de-creases with the increase of strain when strain is over 0.2, which is due to the softening caused by recrystallization. When the softening reaches a certain level, the stress-strain curve tends to be a straight line. On the other hand, the parameters of the constitutive equation taken by Yu et al. [25] in modeling the FSW of the magnesium alloy were all measured near the peak of the stress-strain curve (corresponding to the strain 0.2). According to the experimental results of Liu et al. [26], the strain around the tool in the FSW process can reach 35 or even higher. Therefore, the constitutive equation is modified by multiplying a softening coefficient to avoid the calculation result caused by excessive stress from being inconsistent with the experimental ones.

$$\sigma_{s,am}^r = \frac{\xi_{am}}{\alpha} \ln \left\{ \left( \frac{\bar{\varepsilon}}{A} \exp\left(\frac{Q_s}{RT}\right) \right)^{1/n} + \left[ 1 + \left( \frac{\bar{\varepsilon}}{A} \exp\left(\frac{Q_s}{RT}\right) \right)^{2/n} \right]^{1/2} \right\} \quad (4)$$

where  $\sigma_{s,am}^r$  is the flow stress,  $\xi_{am}$  is the softening coefficient when recrystallization is considered,  $\bar{\varepsilon}$  is the strain rate,  $R$  is the gas constant,  $T$  is the temperature,  $\alpha$ ,  $A$ ,  $n$  are the material constants,  $Q_s$  is the activation energy with the acoustic plastic effects, and can be expressed as follow,

$$Q_s = Q - \frac{\beta R \Delta F}{k_B} \left( \frac{E}{\tau_0 + \mu_m a b \sqrt{\rho}} \right)^m \quad (5)$$

where  $Q$  is the activation energy without the ultrasound affected,  $\beta$  and  $m$  are experimentally determined parameters in the model of the change in the dimensionless stress ratio caused by the acoustic softening effect,  $\Delta F$  is the change of Helmholtz free energy,  $k_B$  is Boltzmann constant,  $E$  is the sound energy density,  $\tau_0$  is the lattice resistance,  $\mu_m$  is the shear elastic modulus,  $a$  is a parameter close to 1/3,  $b$  is the length of the Burgers vector and  $\rho$  is the dislocation density. Based on the Kocks-Mecking (KM) [i,ii] dislocation model as well as the acoustic hardening effect,  $\sqrt{\rho}$  is then expressed by the following,

$$\sqrt{\rho} = \left[ k_1 (1 + \eta_{k_1}) - \exp\left(\frac{-k_2 \varepsilon M}{2}\right) \right] / k_2 \quad (6)$$

where  $k_1$  is the dislocation storage coefficient, and  $k_2$  is the dislocation dynamic recovery coefficient  $\varepsilon$  is the strain. In this study,  $\varepsilon$  takes a value of 30 [26]. The acoustic residual hardening effect is introduced into the constitutive equation model via the parameter  $\eta_{k_1}$ , which is the dimensionless parameter that defines the rate of change of  $k_1$  under the action of ultrasound.  $M$  is the Taylor factor.

Using the Logistic function to describe the S-shaped saturation phenomenon of dislocation density [29-31]

$$\eta_s = KP_0 / [P_0 + (K - P_0) \exp(-r_a t_v)] \quad (7)$$

where  $P_0$  and  $K$  are the initial and saturation values,  $t_v$  is the duration time of the ultrasound exertion, and  $r_a$  is the growth rate of dislocation density which is mainly affected by the intensity of the ultrasonic energy field. In this study,  $r_a$  is considered to be proportional to the vibration amplitude ( $\xi_0$ ), and the ratio is  $\varphi$ , that is  $r_a = \varphi \xi_0$ . The duration time of the ultrasound exertion ( $t_v$ ) equals to the time during which the material flows through the FSW tool shoulder (about the time when the material undergoes the combined action area of the plastic deformation and the ultrasonic vibration).

And then the viscosity  $\mu_s$  is expressed as [32],

$$\mu_s = \frac{\sigma_{s,am}^r}{3\dot{\epsilon}} \quad (8)$$

And then the viscosity was used for the momentum equation and the viscous dissipation source in the energy equation.

#### THE ULTRASONIC INDUCED FRICTION REDUCTION EFFECT

The friction coefficient between the FSW tool/workpiece is a prerequisite for determining the heat generation and velocity boundary. When ultrasonic vibration is applied in UVEFSW, the ultrasonic induced friction reduction (UiFR), i.e., the friction reduction effect due to ultrasonic vibration, must be taken into account.

The relative direction between the vibration direction and the relative sliding direction is different, and the reasons for the reduction of friction caused by ultrasound are different. Referring to the contact plane and the sliding direction, the ultrasonic vibration can be exerted in three orthogonal directions: ① In-plane parallel, i.e., longitudinal, ② In-plane perpendicular, i.e., transverse, and ③ Out-of-plane perpendicular, i.e., normal, as shown in Fig. 3.

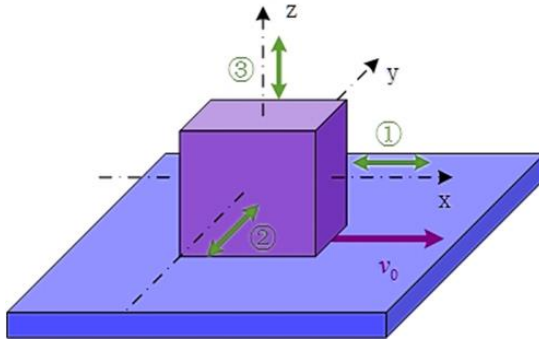


**Fig. 3** Ultrasonic vibration application direction in contact friction

The ultrasonic induced friction reduction (UiFR) caused by in-plane vibration is generally interpreted as the ultrasonic reversal effect [33,34]. It implies that when the vibration occurs, the normal force and the instantaneous friction coefficient remain the same, but the direction of the friction force is changed or reversed within a vibration cycle, resulting in a decrease in the average coefficient of friction during one vibration cycle. Storck et al. proposed an ultrasonic reversal effect model based on the Coulomb friction law [34,35]. For a slider that slides at the speed  $v_0$ , the friction coefficient without ultrasonic vibration is written as  $\mu_0$ . When the ultrasonic vibration is applied along the longitudinal direction (direction ①), the amplitude of the vibration velocity is expressed by  $\hat{v}$ . Then, the ratio between the average friction coefficient  $\mu_L$  with UiFR and the friction coefficient without UiFR in the longitudinal direction can be written as [34,35]:

$$\frac{\mu_L}{\mu_0} = \begin{cases} 1 & \zeta_L \geq 1 \\ \frac{2}{\pi} \sin^{-1}(\zeta_L) & -1 < \zeta_L < 1 \\ -1 & \zeta_L \leq -1 \end{cases} \quad (9)$$

where  $\zeta_L = v_0/\hat{v}$ . The subscript  $L$  denotes the longitudinal direction of vibration. Only if  $\zeta_L = v_0/\hat{v} < 1$ , i.e.,  $\hat{v} > v_0$ , the motion direction of the slider is reversed, and the ultrasonic vibration can decrease the friction coefficient. The larger is  $\hat{v}$ , the more obvious the ultrasonic induced friction reduction (UiFR) is. In the UVeFSW system, the vibration amplitude at the sonotrode end is 40  $\mu\text{m}$  (idle condition), and the amplitude of the vibration velocity is estimated to be 3.2 m/s. Here the amplitude of the vibration velocity ( $\hat{v}$ ) under the idle condition is at the workpiece location with the maximum sound pressure, and the values of  $\hat{v}$  at other workpiece locations are determined according to the sound pressure distribution.

When the ultrasonic vibration is applied in the transverse direction (direction ②), the

ratio of the average friction coefficient  $\mu_T$  with UiFR to the coefficient of friction without UiFR in the transverse direction is written as [34,35],

$$\frac{\mu_T}{\mu_0} = \frac{2 \operatorname{sgn}(\zeta_T)}{\pi \sqrt{1 + \frac{1}{\zeta_L^2}}} K\left(\frac{1}{1 + \zeta_L^2}\right) \quad (10)$$

where  $K(s)$  is the first type of complete elliptic integral, which can be obtained by integrating the eight-node Gauss-Legendre quadrature formula.

When ultrasonic vibration is exerted in the normal direction (direction ③ in Fig. 3), the normal force of the friction pair changes periodically, which leads to the periodic change of the real interface contact area. Then, in friction metal forming under normal ultrasonic vibration, the ratio of the contact friction coefficient  $\mu_N$  to the contact friction coefficient  $\mu_0$  without ultrasonic action in the normal direction is expressed as [36],

$$\frac{\mu_N}{\mu_0} = \frac{\tau - \alpha_N \xi}{\tau} \frac{H}{E^*} \cdot \sqrt{\frac{\pi R_N}{s_D}} = \left(1 - \frac{\alpha_N \xi}{\tau}\right) \cdot \frac{\sqrt{\pi}}{\psi} \quad (11)$$

where  $\tau$  is the shear strength without ultrasonic vibration, respectively,  $\alpha_N$  is the relevant parameter related to the acoustic softening effect,  $\xi_0$  is the vibration amplitude,  $H$  is the hardness of the softer material,  $E^*$  is the Hertz elastic modulus,  $R_N$  is the radius of curvature of the micro-convex peaks at the contact surface, and  $s_D$  is the standard deviation of the height of the micro-convex peaks at the contact surface, and  $\psi = (E^*/H) \cdot \sqrt{s_D/R_N}$  is the plasticity index proposed by Greenwood and Williamson [36].

In UVeFSW, the ultrasonic vibration is in all three directions on the workpiece. For a point at the horizontal plane (between the shoulder/pin bottom and the workpiece), where the amplitude of vibration is  $\xi_0$  and the velocity amplitude of the vibration is  $\hat{v}$ , we have,

$$\text{Longitudinal: } \zeta_L = \omega r / (\hat{v} \cos \varpi \sin \theta) \quad (12)$$

$$\text{Transversal: } \zeta_T = \omega r / (\hat{v} \cos \varpi \cos \theta) \quad (13)$$

where  $\omega$  is the rotation speed,  $r$  is the length between the elemental and the tool axis,  $\theta$  is the angle between the welding direction and the  $r$  radius vector direction.

When  $\zeta_L$  and  $\zeta_T$  are calculated from Eqs. (12) and (13),  $\frac{\mu_L}{\mu_0}$  and  $\frac{\mu_T}{\mu_0}$  is determined by

Eqs. (8) and (9). And  $\frac{\mu_N}{\mu_0}$  is determined by the following equation,

$$\frac{\mu_n}{\mu_0} = \left( 1 - \frac{\alpha_N \xi \sin \varpi}{\tau} \right) \cdot \frac{\sqrt{\pi}}{\psi} \quad (14)$$

For a point at the contact interface between the pin side and the workpiece, where the amplitude of vibration is  $\xi$  and the velocity amplitude of the vibration is  $\hat{v}$ , we have

$$\text{Longitudinal: } \zeta_L = \omega r / (\hat{v} \cos \varpi \sin \theta) \quad (15)$$

$$\text{Transvers: } \zeta_T = \omega r / (\hat{v} \sin \varpi) \quad (16)$$

Then,  $\frac{\mu_L}{\mu_0}$  and  $\frac{\mu_T}{\mu_0}$  is determined by Eqs. (15) and (16). And  $\frac{\mu_N}{\mu_0}$  is determined by the following equation,

$$\frac{\mu_N}{\mu_0} = \left( 1 - \frac{\alpha_N \xi \cos \varpi \cos \theta}{\tau} \right) \cdot \frac{\sqrt{\pi}}{\psi} \quad (17)$$

Taking into account the friction reduction effect from all three directions, the final friction coefficient after considering the ultrasonic friction reduction effect is the product of  $\mu_L$ ,  $\mu_T$ ,  $\mu_N$ , and  $\mu_0$ ,

$$\mu_f = \frac{\mu_L}{\mu_0} \cdot \frac{\mu_T}{\mu_0} \cdot \frac{\mu_N}{\mu_0} \cdot \mu_0 = \frac{\mu_L \cdot \mu_T \cdot \mu_N}{\mu_0^2} \quad (18)$$

And then,  $\mu_f$  is used as the friction coefficient in the UVEFSW instead of  $\mu_0$  to calculate the velocity boundary and heat generation at the FSW tool-workpiece interface.

While for the other details for the UVEFSW CFD model, the control equations [17], boundary conditions [17,20], heat generation [17,20] of the FSW part, and the ultrasonic sound field [18] involved in the multi-field coupling model of Al-Mg dissimilar UVEFSW can refer to [17-20]. All the above were solved by employing the Ansys Fluent software. The volume fraction of each material was determined by the Volume of Fluid (VOF) method, and the physical parameters at each grid were weighted by the volume fractions of two materials inside the control element [17].

## RESULTS AND DISCUSSION

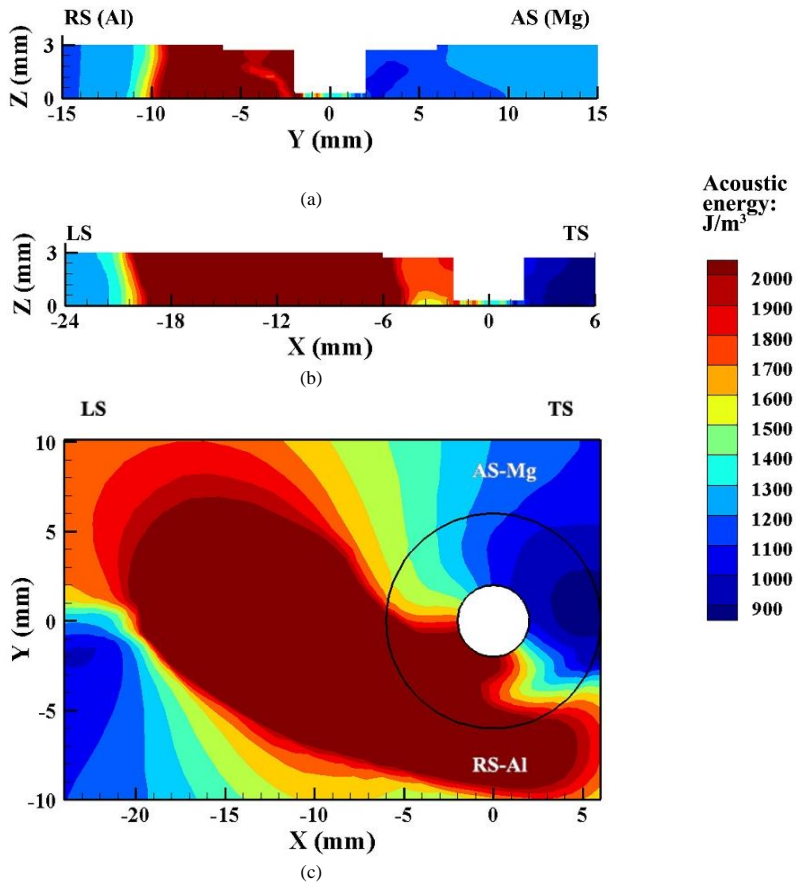
### ULTRASONIC FIELD OF AL/MG DISSIMILAR ALLOYS UVEFSW

Fig. 4 shows the acoustic energy distribution after the sound pressure field is stabilized in Al/Mg UVEFSW. From (a) to (c) are the acoustic energy distribution at  $x = 0$  mm transverse cross-section,  $y = 0$  mm longitudinal cross-section, and  $z = 1.5$  mm horizontal

section, respectively. The AS, RS, LS, and TS in the figures are abbreviations of the advancing side, retreating side, leading side, and trailing side, respectively. Owing to the material flow and the different physical parameters between the two materials, the acoustic energy is distributed asymmetrically about the x-axis and y-axis.

The sonotrode was placed in front of the FSW tool and tilted forward, which conducts ultrasonic energy to the workpiece in front of the FSW tool, as shown in Fig. 4(b), the distribution law obtained from the longitudinal cross-section is similar to that of Al alloy UVeFSW [18]. While in the transverse cross-section (Fig. 4a), it is different from the Al alloy UVeFSW: (1) the acoustic energy is higher on the aluminum alloy (RS) than the Mg side (AS) due to the significantly different properties of aluminum alloy and magnesium alloy; (2) the acoustic energy distribution is no longer monotonically changes from one side to another but presents a pattern in the nugget zone, due to the complex material mixing in the weld nugget zone. While in the horizontal plane (Fig. 4c), on the one hand, the area with higher acoustic energy tends to extend to the tool pin as shown in the Al alloy UVeFSW [14], on the other hand, the high acoustic energy area tends to rotate around the FSW tool due to the influence of material distribution.

It is obvious that the sound energy field is distributed asymmetrically rather than symmetrically, because there are differences in physical parameters and plastic deformation between the two materials. The transmission of ultrasonic sound to the aluminum alloy side is more obvious, and the propagation of ultrasound in magnesium alloy is a little difficult. The density of magnesium alloy is smaller than that of aluminum alloy, and the sound speed in magnesium alloy is also smaller than that of aluminum alloy, resulting in a larger attenuation coefficient in magnesium alloy. The sound pressure on the magnesium alloy side is generally lower than that on the aluminum alloy side. According to the calculation process of the sound field, this is due to the low incoming sound pressure and large attenuation coefficient on the magnesium alloy side.



**Fig. 4** The calculated acoustic energy density field at the (a) transverse cross-section, (b) longitudinal cross-section and (c)  $z = 1.5$  mm horizontal plane

#### THE INFLUENCE OF ULTRASONIC VIBRATION ON FRICTION COEFFICIENT

Considering the UiFR effect, the friction coefficient distribution on the tool-workpiece interface in the Al/Mg dissimilar alloys UVeFSW model will be more complicated. Fig. 5 compares the distribution of the friction coefficient on the tool-workpiece contact interface with and without the UiFR effect.

Without UiFR, the friction coefficient gradually decreases with the increase of the distance away from the tool axis, because the slip ratio model and friction coefficient model proposed by Arora et al. [37] based on the rolling process, and a slight difference between AS and RS due to the dissimilar materials are placed on each side, as shown in Fig. 5(a).

After considering the UiFR effect, the friction coefficient near the tool axis is small and increases gradually with the increase of radial distance, which is similar to the case of 6061 UVeFSW [20]. Because the UiFR in the longitudinal direction plays a leading role [20], and according to Eq. (9), the smaller the ratio of material relative sliding speed to ultrasonic vibration speed is, the greater the UiFR effect will be. Based on that the amplitude of ultrasonic velocity is not much different at all parts of the FSW tool-workpiece contact interface, the closer the material is to the axis of the FSW tool, the smaller the relative sliding speed will be, and the smaller the ratio will be, the greater the UiFR effect will be.

However, in the case of Al-Mg UVeFSW, the UiFR effect is asymmetric due to the asymmetrical ultrasonic field, and finally, the friction coefficient presents a complex "deformed" butterfly shape, as shown in Fig. 5(b).

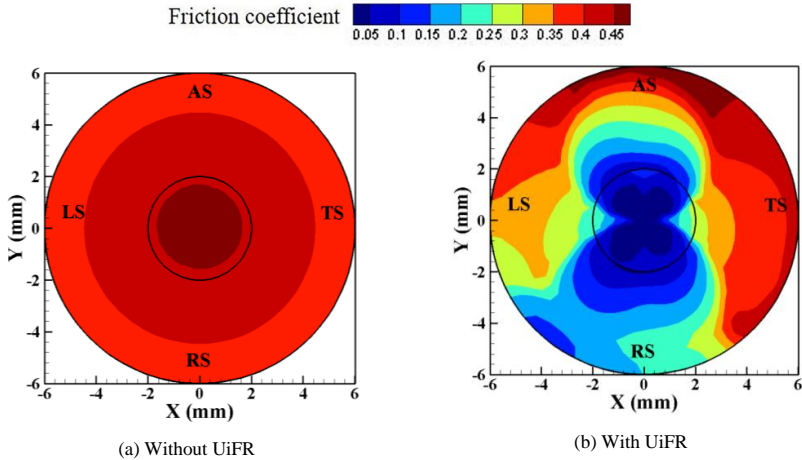


**Fig. 5** The distribution of friction coefficient on the tool-workpiece contact interfaces (vertical view)

THE EFFECT OF ULTRASONIC VIBRATION ON HEAT GENERATION AND TEMPERATURE

The heat generation of each part in FSW and UVeFSW models is compared in Table 1. It can be seen that after applying ultrasound, the sonotrode preheats the workpiece. Although the preheat effect will increase the temperature, the temperature around the

FSW tool will decrease due to the UiFR effect, and the viscous dissipation of the plastic deformation zone decreases with the viscosity.

**Table 1** Comparison of the heat generation (W) of the contact interface in FSW/UVeFSW

	Shoulder	Shoulder side	Pin side	Pin bottom	Sonotrode	Viscous dissipation
FSW	315.069	67.159	45.465	22.119	0	94.64
UVeFSW	201.689	51.338	10.963	5.721	137.04	79.691

The friction coefficient distribution with the UiFR effect is very complex, making the heat flux distribution on the tool-workpiece interface becomes complex. The heat flux distribution of FSW/UVeFSW projected on the  $z = 0$  mm horizontal plane is shown in Fig. 6. After applying ultrasonic, the distribution of friction coefficient is a "distorted" butterfly due to the UiFR effect, and the distribution of heat flux is distorted similarly as friction coefficient, but the deformation of the butterfly of heat flux is weakened by plastic heat generation. What's more, the heat flux is higher on AS than that on the RS after the ultrasonic application, because the degree of UiFR effect is different between the AS and RS.

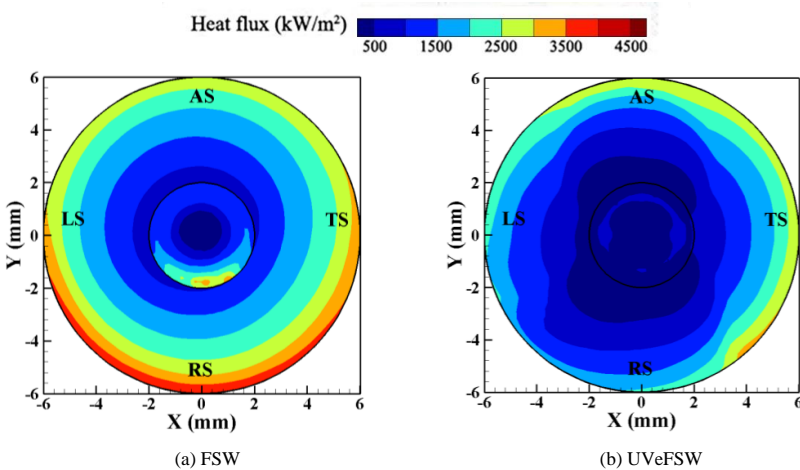


**Fig. 6** The heat flux on the tool-workpiece contact interfaces in FSW/UVeFSW (vertical view).

Fig. 7 shows the temperature distribution on the top surface (including the shoulder). There is a small area in the sonotrode-workpiece interface where the temperature is higher due to the preheat of ultrasound.

For the tool-workpiece interface and its surroundings, after ultrasonic application, the highest temperature area around the tool pin disappears while the area of the sub-high temperature increases due to the coupling of the preheat and UiFR effects.

According to Fig. 5 and Fig. 6, the UiFR effect reduces the heat generation on the FSW tool-workpiece contact interface, so that the temperature of the part close to the contact interface will drop and the highest temperature area around the tool pin disappears.

However, due to the acoustic plastic effect of ultrasound, the softening effect of ultrasound is dominant in the area with a low strain rate, that is, the outer ring below the shoulder, and the flow stress will drop [20]. So that more areas will participate in the plastic deformation, resulting in viscous dissipation in more areas, so the sub-high temperature range will increase.

In addition, due to the preheating effect and the applied ultrasound to the leading side (LS), the high-temperature area shifts from the magnesium alloy (AS) to the area between AS and LS.

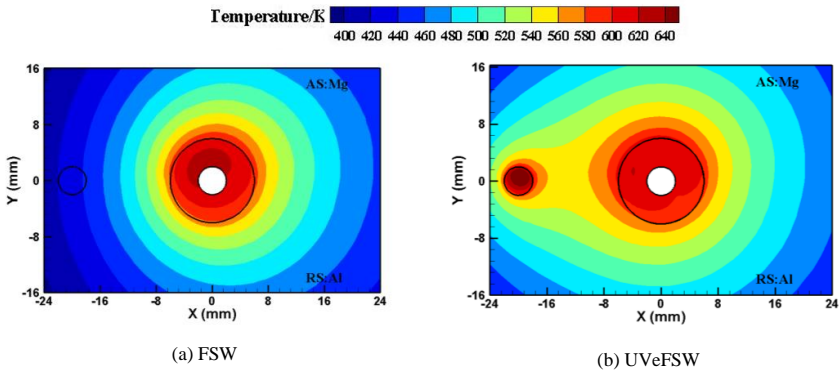


**Fig. 7** The calculated temperature on the top surface of the workpiece (including the contact surface of the shoulder)

THE EFFECT OF ULTRASONIC VIBRATION ON MATERIAL FLOW AND MIXING

Figs. 8 and 9 compare the macrograph of FSW and UVeFSW at different horizontal cross-sections with the corresponding calculation results, the right column is the experimental results, and the left column is the simulation results. In the simulation results, the boundary of the mixing zone is highlighted by the white dotted line.

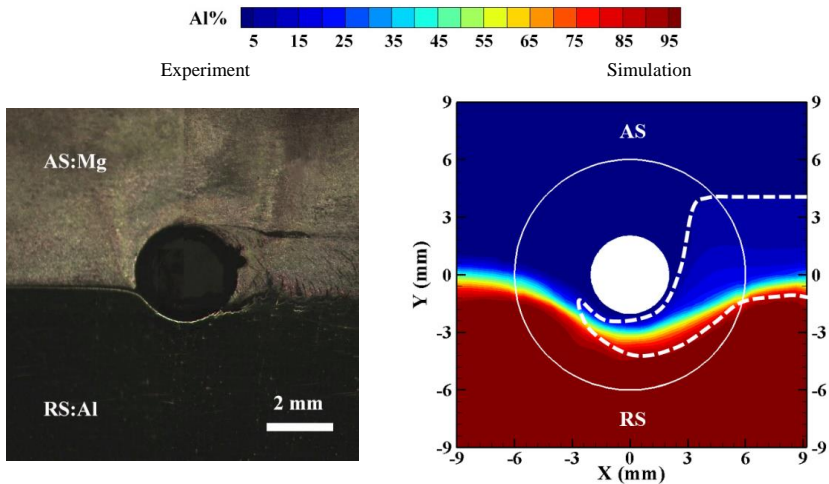
After applying ultrasound, the width of the mixing zone becomes wider at the mid-depth plane (Fig. 8) and the plane of the pin bottom (Fig. 9), both in the experimental and calculated results, due to the acoustic plastic effect (soften and harden effects). The aluminum alloy goes deeper into AS (Fig. 8) also due to the acoustic plastic effect.

When we only studied the acoustic-plastic effect of ultrasound in FSW [20], we found that for the low level of the strain rate, the flow stress obtained by the constitutive equation considering ultrasonic hardening and softening is lower than that obtained by the constitutive equation only considering acoustic softening. When the strain rate is large enough, the flow stress calculated by the former is larger than that by the latter. The

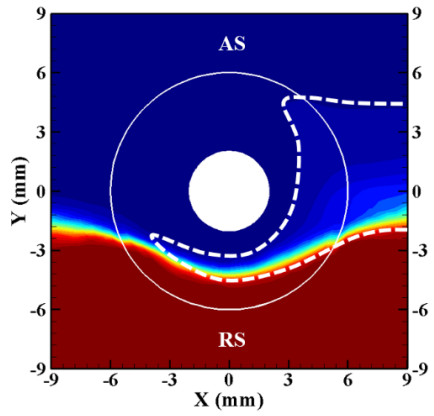
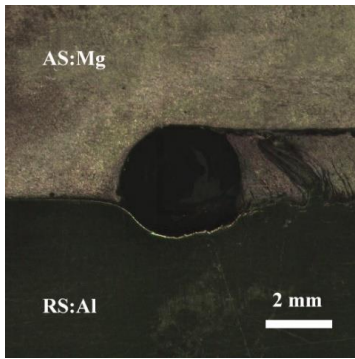
acoustic softening and hardening effects dominate the conditions of high and low strain rates, respectively.

In the inner annular region near the pin side surface, the flow stress calculated by the constitutive equation considering ultrasonic hardening and softening is higher than that obtained by the constitutive equation only considering acoustic softening. But near the outer annular region, the flow stress by the former is lower than that by the latter.

It is easy to understand that at locations where the flow stress is reduced, the fluidity is improved, and it is easier to get rid of the rotating motion that follows the tool and to restore its horizontal flow in reverse to the welding direction. This means that if the flow stress in the region where the material flows through is reduced, the streamlines are not shifted to the rear AS.

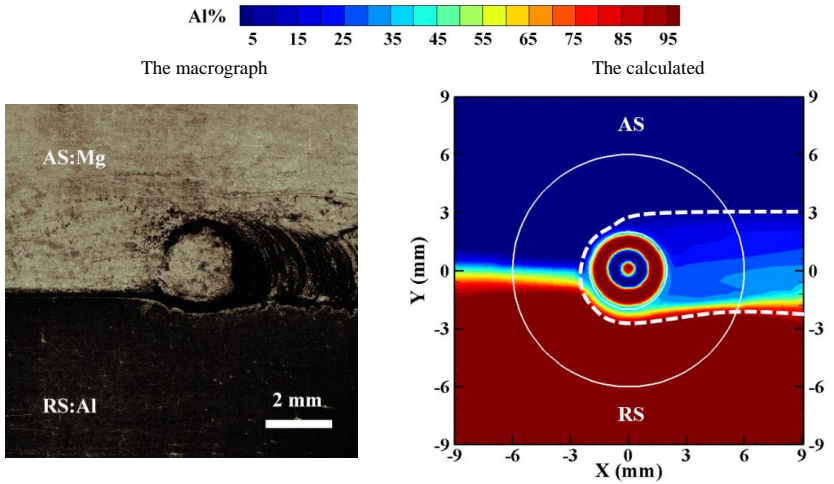


(a) FSW

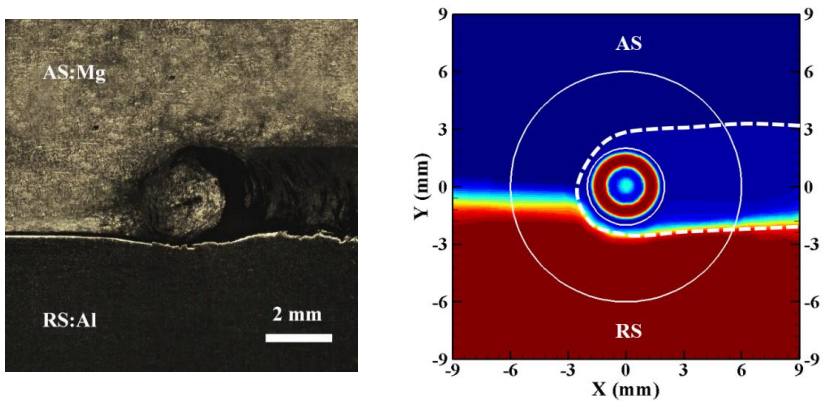


(b) UVeFSW

**Fig. 8** The material distribution at mid-depth horizontal cross-sections



(a) FSW



(b) UVeFSW

**Fig. 9** The material distribution at the plane of pin bottom horizontal cross-sections

Considering the combined effect of hardening and softening of ultrasound, the flow stress in the outer region below the shoulder is reduced, and the material on the RS that flows through there is not offset toward the rear AS. However, at the inner region around the tool, the flow stress is not decreased, thus, the streamlines on the AS after bypassing the tool offset toward the rear AS. As the strain rate is gradually reduced from the inside to the outside of the regions covered by the FSW tool, the flow stress distribution of the inner and outer rings below the shoulder is different, which causes the flow lines flowing through different positions to be more biased toward the AS, while others are biased toward the RS. That means the combination of the two effects (acoustic softening and residual hardening) will lead to the widening of the mixed zone.

However, at the bottom of the tool pin or near the pin bottom surface, the strain rate is slightly higher. If only acoustic plasticity is considered, the softening of the material will be minimal at the inner ring below the shoulder, and the mixing will hardly be intensified. Therefore, it is difficult to explain this phenomenon just with the acoustic plastic effect. At the same time, the UiFR effect will also reduce the velocity boundary inputted as well as the material flow around the pin bottom. Therefore, the preheating effect is the main reason explaining the mixing intensification of the material around the pin bottom.

Additionally, at the plane of the pin bottom which did not show the acoustic hardening effect, the materials mixing just below the pin bottom is intensified, and the characteristics of ring-shaped aluminum outside and magnesium inside are weakened (Fig. 9), which is a consequence of the thermal effects.

## CONCLUSIONS

In the Al/Mg UVeFSW model, the acoustic energy is stronger on the aluminum alloy side, the distribution of acoustic energy presents a pattern in the nugget zone, and the area

with high acoustic energy tends to extend to the tool pin and rotating around the FSW tool. Considering the ultrasonic vibration, the friction coefficient decreases. The distribution of the friction coefficient presents a "deformed" butterfly shape. With ultrasound, the heat generations at the tool-workpiece interface and the viscous dissipation are reduced. The heat flux at the tool-workpieces interface shows a less "deformed" butterfly-like than the friction coefficient. Comparing the material distributions with and without ultrasound at horizontal planes, the mechanism that ultrasonic vibration is beneficial to the mixing of dissimilar materials is clarified.

### ACKNOWLEDGMENTS

The financial support from the National Natural Science Foundation of China (Grant No. 52035005) and the Humboldt Research Fellowship Programme for Postdoctoral Researchers are acknowledged.

### References

- [1] R. DHINGRA and S. DAS: 'Life cycle energy and environmental evaluation of downsized vs. lightweight material automotive engines', *J Clean Prod*, Vol. 85, pp. 347-358, 2014.
- [2] B. L. FU, G. L. QIN, F. LI, X. M. MENG, J. Z. ZHANG and C. S. WU: 'Friction stir welding process of dissimilar metals of 6061-T6 aluminum alloy to AZ31B magnesium alloy', *J Mater Process Tech*, Vol. 218, pp. 38-47, 2015.
- [3] L. H. SHAH, N. H. OTHMAN and A. GERLICH: 'Review of research progress on aluminum-magnesium dissimilar friction stir welding', *Sci Technol Weld Joi*, Vol. 23, pp. 256-270, 2018.
- [4] L. E. MURR: 'A review of FSW research on dissimilar metal and alloy systems', *J Mater Eng Perform*, Vol. 19, pp. 1071-1089, 2010.
- [5] A. ESMAEILI, C. SBARUFATTI and A. M. S. HAMOUDA: 'Characteristics of intermetallic compounds in dissimilar friction stir welding: a review', *Metallography Microstructure and Analysis*, Vol. 8, pp. 445-461, 2019.
- [6] S. KUMAR, C. S. WU and S. GAO: 'Process parametric dependency of axial downward force and macro-and microstructural morphologies in ultrasonically assisted friction stir welding of Al/Mg alloys', *Metall Mater Trans A*, Vol. 51, pp. 2863-2881, 2020.
- [7] M. THOMÁ, G. WAGNER, B. STRAB, C. CONRAD, B. WOLTER, S. BENFER and W. FÜRBETH: 'Realization of ultrasound enhanced friction stir welded Al/Mg and Al/Steel-joints: process and robustness, mechanical and corrosion properties', *Minerals Metals & Materials Series, Friction Stir Welding and Processing IX, Part V*, pp. 179-194, 2017.
- [8] B. STRASS, G. WAGNER, C. CONRAD, B. WOLTER, S. BENFER and W. FÜRBETH: 'Realization of Al/Mg-Hybrid-Joints by ultrasound supported friction stir welding-mechanical properties, microstructure and corrosion behavior', *Minerals Metals & Materials Series*, Vol. 966, pp. 521-535, 2017.
- [9] M. THOMÁ, G. WAGNER, B. STRAB, C. CONRAD, B. WOLTER, S. BENFER and W. FÜRBETH: 'Recent developments for ultrasonic-assisted friction stir welding: joining, testing, corrosion-an overview', *IOP Conf Ser Mater Sci Eng*, Vol. 118, No. 1, pp. 012014, 2016.
- [10] S. BENFER, B. STRASS, G. WAGNER and W. FÜRBETH: 'Manufacturing and corrosion properties of ultrasound supported friction stir welded Al/Mg-hybrid joints', *Surf Interface Anal*, Vol. 48, No. 8, pp. 850-859, 2016.

- [11] S. D. JI, X. C. MENG, Z. L. LIU, R. F. HUANG and Z. W. LI: 'Dissimilar friction stir welding of 6061 aluminum alloy and AZ31 magnesium alloy assisted with ultrasonic', *Mater Lett*, Vol. 201, pp. 173-176, 2017.
- [12] X. C. MENG, Y. Y. JIN, S. D. JI and D. J. YAN: 'Improving friction stir weldability of Al/Mg alloys via ultrasonically diminishing pin adhesion', *J Mater Sci Technol*, Vol. 34, pp. 1817-1822, 2018.
- [13] Z.L. LIU, X. C. MENG, S. D. JI, Z. W. LI and L. WANG: 'Improving tensile properties of Al/Mg joint by smashing intermetallic compounds via ultrasonic-assisted stationary shoulder friction stir welding', *J Manuf Process*, Vol. 31, pp. 552-559, 2018.
- [14] X. Q. LV, C. S. WU, C. L. YANG and G. K. PADHY: 'Weld microstructure and mechanical properties in ultrasonic enhanced friction stir welding of Al alloy to Mg alloy', *J Mater Process Tech*, Vol. 254, pp. 145-157, 2018.
- [15] A. K. SINGH, P. SAHLOT, M. PALIWAL and A. ARORA: 'Heat transfer modeling of dissimilar FSW of Al 6061/AZ31 using experimentally measured thermo-physical properties', *Int J Adv Manuf Tech*, Vol. 105, pp. 771-783, 2019.
- [16] J. Y. LIM and J. H. LEE: 'Development of a coupled Eulerian-Lagrangian finite element model for dissimilar friction stir welding', *Journal of the Korea Academia-Industrial cooperation Society*, Vol. 20, pp. 7-13, 2019.
- [17] C. L. YANG, C. S. WU and X. Q. LV: 'Numerical analysis of mass transfer and material mixing in friction stir welding of aluminum/magnesium alloys', *J Manuf Process*, Vol. 32, pp. 380-394, 2018.
- [18] L. SHI, C. S. WU, S. GAO and G. K. PADHY: 'Numerical simulation of ultrasonic field and its acoustoplastic influence on friction stir welding', *Mater Design*, Vol. 104, pp. 102-115, 2016.
- [19] C. L. YANG and C. S. WU: 'Constitutive equation with residual hardening effect for modeling the ultrasonic vibration enhanced friction stir welding process', *Sci Technol Weld Joi*, Vol. 24, pp. 695-705, 2019.
- [20] C. L. YANG, C. S. WU and L. SHI: 'Analysis of friction reduction effect due to ultrasonic vibration exerted in friction stir welding', *J Manuf Process*, Vol. 35, pp. 118-126, 2018.
- [21] S. ELANGOVAN, S. SEMEER and K. PRAKASAN: 'Temperature and stress distribution in ultrasonic metal welding-an FEA-based study', *J Mater Process Tech*, Vol. 209, No.3, pp. 1143-1150, 2009.
- [22] B. LANGENECKER: 'Effects of ultrasound on deformation characteristics of metals', *IEEE Transactions on Sonics and Ultrasonics*, Vol. 13, pp. 1-8, 1966.
- [23] A. S. KRAUSZ and K. KRAUSZ: 'Unified constitutive laws of plastic deformation', *San Diego: Academic Press*, 1996.
- [24] Y. Y. DONG, C. S. ZHANG, X. LU, C. X. WANG and G. Q. ZHAO: 'Constitutive equations and flow behavior of an as-extruded AZ31 magnesium alloy under large strain condition', *J Mater Eng Perform*, Vol. 25, pp. 2267-2281, 2016.
- [25] Z. Z. YU, W. ZHANG, H. CHOO and Z. L. FENG: 'Transient heat and material flow modeling of friction stir processing of magnesium alloy using threaded tool', *Metall Mater Trans*, Vol. 43A, No. 2, pp. 724-737, 2016.
- [26] X. C. LIU, C. S. WU and K. P. GIRISH: 'Characterization of plastic deformation and material flow in ultrasonic vibration enhanced friction stir welding', *Scripta Mater*, Vol. 102, pp. 95-98, 2015.
- [27] H. MECKING and U. F. KOCKS: 'Kinetics of flow and strain-hardening', *Acta Metall*, Vol. 29, No. 11, pp. 1865-1875, 1981.
- [28] U. F. KOCKS: 'Laws for work-hardening and low-temperature creep', *J Eng Mater-T*, Vol. 98, No. 1, pp. 76-85, 1976.
- [29] J. H. M. THORNLEY, J. J. SHEPHERD and J. FRANCE: 'An open-ended logistic-based growth function: Analytical solutions and the power-law logistic mode', *Ecological Modelling*, Vol. 204, pp. 531-534, 2007.

- [30] A. TSOULARIS and J. WALLACE: 'Analysis of logistic growth models', *Mathematical Biosciences*, Vol. 179, pp. 21-55, 2002.
- [31] B. GALLAGHER: 'Peak oil analyzed with a logistic function and idealized Hubbert curve', *Energy Policy*, Vol. 39, No. 2, pp. 790-802, 2011.
- [32] H. H. CHO, S. T. HONG, J. H. ROH, H. S. CHOI, S. H. KANG, R. J. STEEL and H. N. HAN: 'Three dimensional numerical and experimental investigation on friction stir welding processes of ferritic stainless steel', *Acta Mater*, Vol. 61, pp. 2649-2661, 2013.
- [33] P. GUTOWSKI and M. LEUS: 'The effect of longitudinal tangential vibrations on friction and driving forces in sliding motion', *Tribol Int*, Vol. 55, pp. 108-118, 2012.
- [34] H. STORCK, W. LITTMANN, J. WALLASCHEK and M. MRACEK: 'The effect of friction reduction in presence of ultrasonic vibrations and its relevance to traveling wave ultrasonic motors', *Ultrasonics*, Vol. 40, pp. 379-383, 2002.
- [35] W. LITTMANN, H. STORCK and J. WALLASCHEK: 'Sliding friction in the presence of ultrasonic oscillations: superposition of longitudinal oscillations', *Arch Appl Mech*, Vol. 71, No. 8, pp. 549-554, 2001.
- [36] J. A. GREENWOOD and J. B. P. WILLIAMSON: 'Contact of nominally flat surfaces', *Proceedings of the ROYAL Society of London Series A-Mathematical and Physical Sciences* Vol. 295, No. 1442, pp. 300-319, 1996.
- [37] A. ARORA, A. DE, T. DEBROY: 'Toward optimum friction stir welding tool shoulder diameter', *Scripta Mater*, Vol. 64, pp. 9-12, 2011.



# A PROCESS MODELLING APPROACH TO THE DEVELOPMENT OF LAP WELDING PROCEDURES

M. LEWIS\*, S. SMITH\*\*

*\*FTS Engineering Answers Ltd, SG18 8EH, United Kingdom*

*\*\*Transforming Stress Limited, SG8 5AB, UK*

*DOI 10.3217/978-3-85125-968-1-30*

## ABSTRACT

Process modelling (PM) is used in many industries to make considerable contributions to the development of safe and efficient engineering designs. The authors have experience of applying PM to a wide range of industries and applications; they are currently investigating the application of commercial CFD software to Friction Stir Welding (FSW). PM augments results generated by laboratory testing by providing full field and full duration predictions of important parameters such as material state. Analyses of engineering processes are increasingly conducted with commercial software, which attracts a significant license fee, but license fees may not be the only barrier to the utilisation of PM in engineering design. PM can be very complex and the requirements for an understanding of many advanced material behaviours may deter their use. It might fairly be expected that there could be a considerable investment needed before a desirable return is achieved. FSW has been the fastest growing joining technology over the last two decades and it now being used in many industries, including aerospace, automotive and shipping. The process has advantages over the more traditional techniques for joining metallic materials. Results show that FSW joints have a superior fatigue resistance when compared to fusion joining, and the lower process temperature means that thinner sheet fabrications are less likely to suffer heat-related distortion. FSW procedure development is needed for each application to show that the proposed welding procedure for any application will robustly produce defect-free welds of suitable quality. The current paper extends a FSW PM technique which assumes that accuracy mostly depends upon the conditions that exist near the FSW tool plus some straightforward mechanics and thermodynamics remote from the tool. The technique can be used for a wide range of materials using properties that are generally available and easily understood by a process engineer. Comparisons are made here against test data of a series of lap welds for a range of conditions. Of particular interest is the effect of two different tool pin designs on the corresponding welds. The test data showed that welding parameters (rotation rate and welding speed) and tool pin design strongly affect the characteristics of the typical defect features (hooking and cold lap defects). The comparisons showed that the tool pin design including thread must be captured explicitly in the model, and that the relative position of the tool as it rotates must also be modelled. This results in quantitatively accurate predictions of torque and qualitatively realistic results for hooking and cold lap defects. The approach is based upon the use of general purpose CFD software combined with a set of easy to access materials data.

Keywords: (Process Modelling, CFD, Lap Welding, Hooking, Cold Lap Defects)

## INTRODUCTION

Friction Stir Welding (FSW) tends to be a solid-state welding process because the input power would drop considerably if the material around the tool became molten. A schematic of this behaviour is shown in Fig. 1.

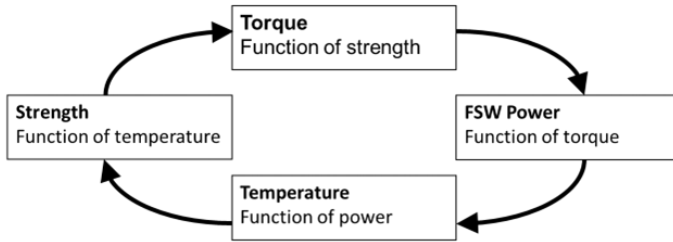


**Fig. 1** Simple relationship between the main characteristics that determine the conditions that are generated during Friction Stir Welding

The current Process Modelling (PM) assumes that the material behaviour in the heavily straining region is dominated by an exponentially weakening trend of material strength as the material temperature approaches its melting point. A simple relationship between material strength at pseudo-static strain rates and temperature,  $T$  is assumed as described in reference [1]. A simple strain rate sensitivity was added to augment the pseudo-static strength behaviour.

Work with this model has previously analysed butt welds. The current paper presents its use on lap welds where hooking and cold laps can reduce weld strengths [2, 3].

## MODEL DESCRIPTION

The current work was undertaken using the Computational Fluid Dynamics (CFD) code STAR-CCM+ [4] which provides user friendly and simple to learn facilities for the development of a FSW model. The CFD model approach is quite straight forward and has been outlined previously in [1].

Two regions are created representing the tool and the upper and lower work pieces. The travel of the tool is captured by “moving” the work piece, i.e. the upstream boundary condition is a fixed inlet velocity boundary condition and the work pieces move past the tool. The outlet boundary condition is a fixed pressure boundary condition. The Volume of Fluid method is used to separate the upper and lower work pieces, and to measure the mixing of the work pieces following welding. The tool is rotated at the given rotation rate, and the interface between the tool and the work piece experiences the shear stress associated with that. A predominantly hexahedral mesh consisting of approximately 18 million cells is used for all simulations.

All simulations are steady state, which implies an infinite weld. Subsequently, the far field temperature boundary conditions are adjusted to account for the short test section seen in the tests.

The derivation of viscosity is provided in [1]. It was assumed that the correct room temperature strength parameter was the Ultimate Tensile Strength, which was chosen to be 550MPa. The melting temperature assumed was 710°C [5].

The heat generation was assumed to be by adiabatic shearing alone. Many models of FSW adopt advanced friction characteristics that would be both expensive and laborious to develop on a bespoke basis for general analyses of FSW. The current work assumed that friction was caused by the shearing of the workpiece material in the small crevices that represent the surface of the tool, so, even at a microscopic level friction is really the adiabatic shearing of material.

### ALDANONDO TESTS

Z shaped extrusions of aluminium alloy AA2099-T83 with a thickness of 2 mm (UTS about 560MPa [6]) and sheets of aluminium alloy AA2060-T8E30 with a thickness of 2.5 mm (UTS about 540MPa [7]) were used as base materials in this work. Both alloys were in a T8 hardened temper condition.

FSW joints were performed in overlap configuration where the alloy AA2099-T83 was used as a stringer and placed on top of the alloy AA2060-T8E30 which was used as a skin. An example of this lap joint is shown in Fig. 2a. 120mm long joints were performed for each welding condition investigated.

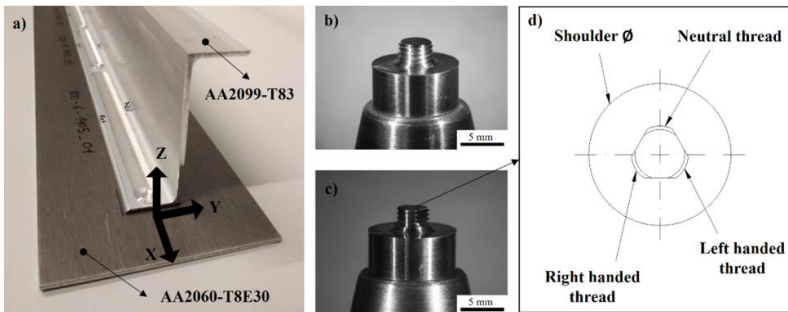


**Fig. 2** a) Friction stir welding (FSW) lap joint between AA2099-T83 extrusion and AA2060-T8E30 sheet and FSW tools used to produce them; (b) conventional threaded tool; (c) 3 flats + mixed thread tool; and (d) sketch showing details of the top view of the 3 flats + mixed thread tool. Reproduced from [3]

Two types of FSW tools were employed to produce lap joints. Both FSW tools had a plane shoulder of 10 mm in diameter and a probe 4 mm in diameter and 2.5 mm in length. The difference between the tools was the probe design. One probe had a conventional right-handed thread cylindrical probe (Fig. 2b) while the other tool had a probe with 3

flats and 3 types of threads in the 3 cylindrical sections (Fig. 2c,d). The flats were used to divide the probe in three different threaded sections. All threads were produced with the same pitch and depth dimensions, but each had different thread orientations. One section had a right handed thread, another one a left handed thread and the other thread was neutral (no inclination). The main purpose of this probe design was to avoid any preferential vertical plasticized material flow to reduce the hook formation, while promoting sufficient flow at the faying surface to break the oxide layers and produce a mixing between the parts to be welded. All the welds were performed with a tool tilt angle of 1.5°.

Combinations of two rotational speeds and two welding speeds were investigated. The rotational speeds investigated were 800 rpm and 1200 rpm, and the welding speeds investigated were 150 mm/min and 250 mm/min.

### FRICITION STIR WELDING PROCESS MODELLING OVERVIEW

The modelling approach developed using the CFD code is outlined in Lewis [1] with a few minor adjustments. Previously, it was noted that the torque was under-predicted, and subsequent analysis showed this was due to the simplified representation of the tool thread; so the tool thread has to be captured explicitly. Here the two Aldanondo tool types are investigated: a standard threaded tool and a mixed threaded tool (see Fig. 3).

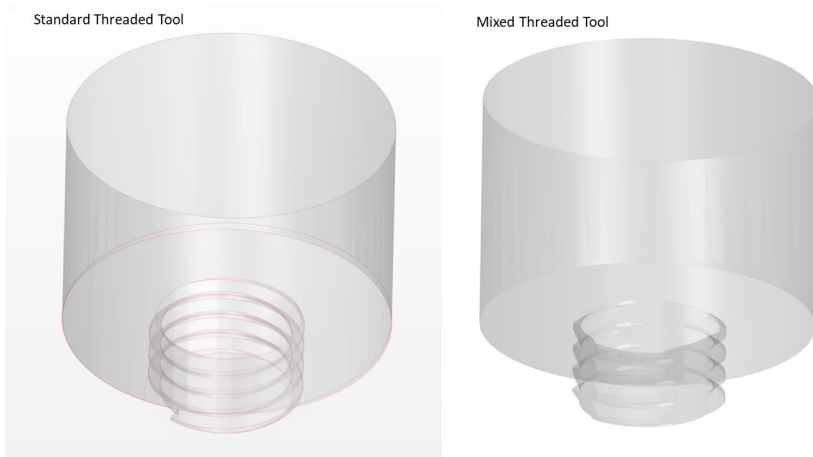


**Fig. 3** Standard threaded tool and mixed threaded tool used in this study

The tool rotation can be captured explicitly using a transient analysis, but this is computationally expensive. Instead, the simulations are steady state and the tool rotation is captured using a rotating reference frame such that the shear stress of the movement is experienced by the material close to the tool. To study the effect of keeping the tool in

one orientation, separate simulations were carried out with the tool at four different angles of rotation (see Fig. 4).

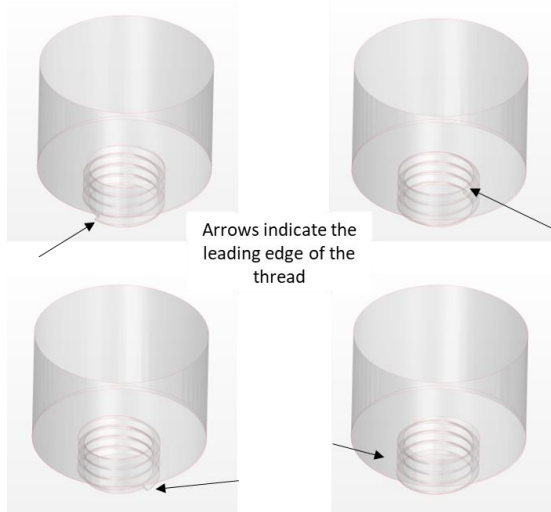


**Fig. 4** Four orientations of the tool used in steady state analyses to accommodate the behaviour of real tool rotation

Each of these steady state simulations with different tool pin leading edge rotations produce slightly different results. This is clearly demonstrated in Fig. 5 for the conventional threaded tool at a rotational rate of 1200rpm and welding speed of 250mm/min. The contour plots show a transverse section post welding where the colours show the mixing of the top (white) and bottom (black) plates. Hooking is shown at 0° and 90° and a cold lap defect is shown at 270°.

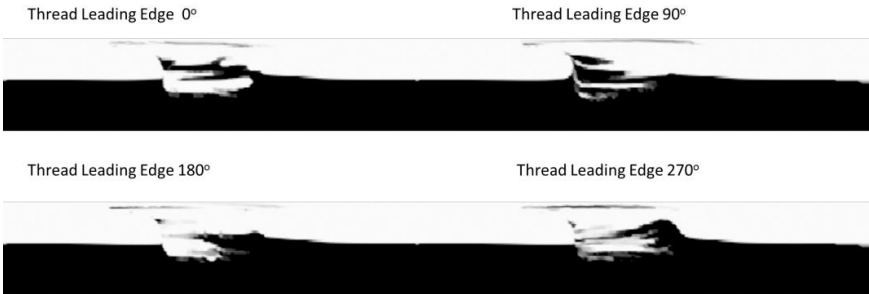


**Fig. 5** A series of contour plots with the tool pin in a different rotational position, each contour plot is of a transverse section post welding; colours show the mixing of the top and bottom plates; for the conventional threaded tool at 1200rpm and 250mm/min

The results from each of these four simulations have then been averaged to get an overall behaviour. Fig. 6 shows the average behaviour via a contour plot of a transverse section post welding where the colours show the mixing of the top and bottom plates for conventional threaded tool at a rotational rate of 1200rpm and welding speed of 250mm/min.



**Fig. 6** Contour plot of a transverse section post welding; colours show the mixing of the top and bottom plates; for the conventional threaded tool at 1200rpm and 250mm/min

Fig. 7 shows the Aldanondo [3] cross section for a weld made with the conditions used to create the CFD result shown in Fig. 6. The hooking and cold lap defects that are clear from the measurements can be inferred from the CFD simulation results.

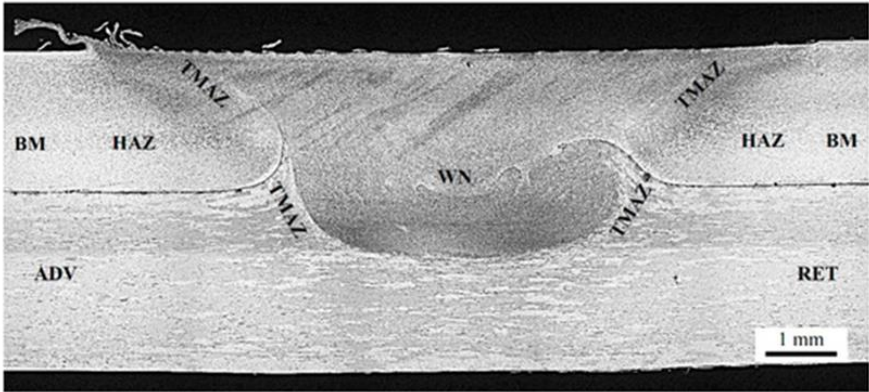


**Fig. 7** Cross-section and microstructural zones of a FSW lap joint produced using a conventional threaded tool at 1200 rpm and 250 mm/min (Reproduced from [3])

Fig. 8 shows contour plots from the CFD which show the mixing of the weld for the conventionally threaded tool at a range of rotational rates and welding speeds. Fig.9 shows transverse macro sections from the equivalent welds from [3]. Comparing these two figures it can be seen that the hooking and cold lap defects, clear from the actual welds, can be inferred from the edge of the mixing zone in the CFD results.



**Fig. 8** Contour plot of a transverse section post welding; the grey scale shows the mixing of the top and bottom plates; for the conventional threaded tool

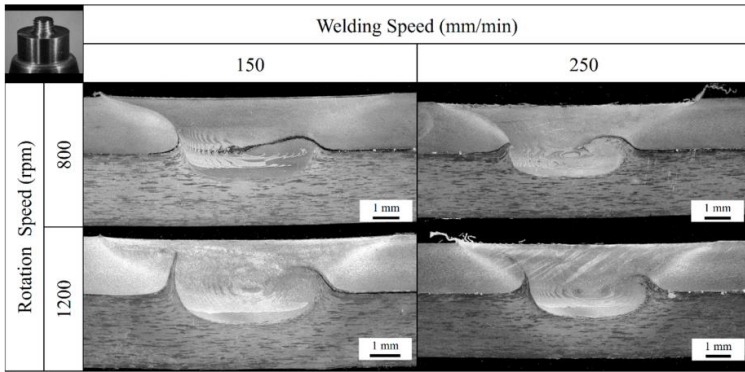


**Fig. 9** Cross-section and microstructural zones of a friction stir welding (FSW) lap joint produced using a conventional threaded tool (Reproduced from [3])

Fig. 10 shows contour plots from the CFD which show the mixing of the weld for the mixed threaded tool at a range of rotational rates and welding speeds. Fig. 11 shows transverse macro sections from the equivalent welds from [3]. Comparing these two figures it can be seen that the reduction in the cold lap defects seen in the test sections for the mixed threaded tool is reproduced in the CFD simulations.

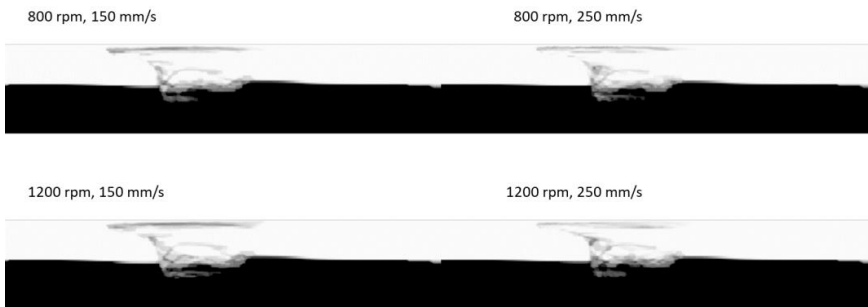


**Fig. 10** Contour plot of a transverse section post welding; grey scale shows the mixing of the top and bottom plates; for the mixed threaded tool

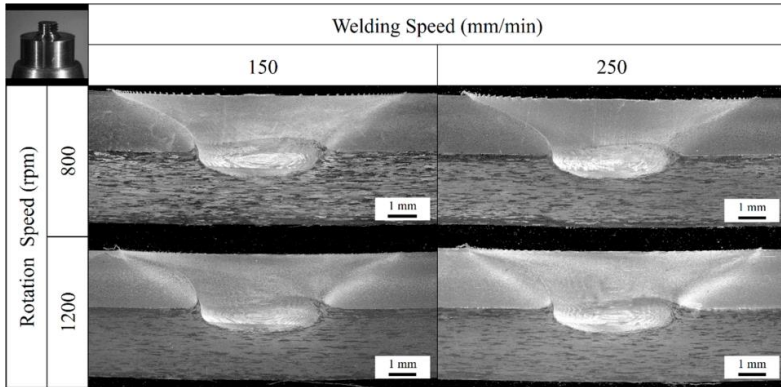


**Fig. 11** Cross-section and microstructural zones of a friction stir welding (FSW) lap joint produced using a mixed threaded tool (Reproduced from [3])

Fig. 12 shows comparisons of measured and predicted torques for the mixed threaded tool; the trends are captured quantitatively as are the individual values of torque.

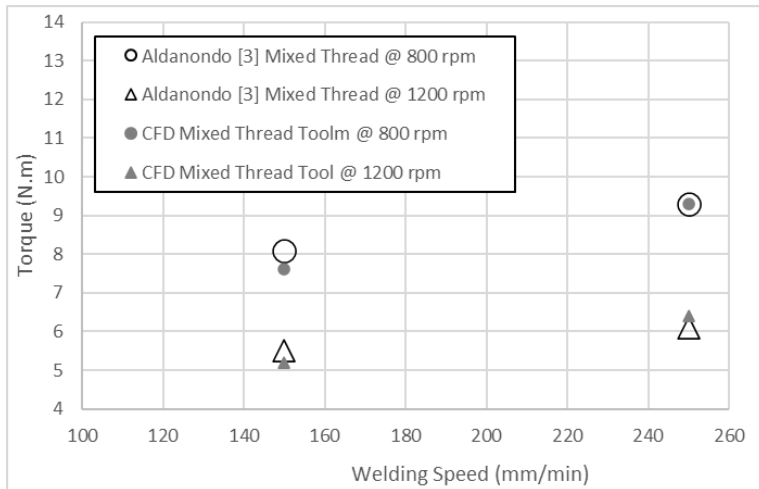


**Fig. 12** Torque predictions and measurements for the Mixed Thread tool

## DISCUSSION AND CONCLUSIONS

The comparisons showed that the tool pin design including thread must be captured explicitly in the model. However, the simulations are steady state and the relative position of the tool as it rotates influences the results. A series of simulations for a range of tool angular orientations has been modelled and then the results averaged. The method produces quantitatively accurate predictions for torque and qualitatively realistic results for hooking and cold lap defects. The approach is based upon the use of general purpose CFD software combined with a set of easy to access materials data.

PM can be applied to lap welds and is now available for use by welding engineers to provide a detailed understanding of FSWs based upon an extension the CAD/CAM tools that they are currently familiar with.

## References

- [1] M. LEWIS and S. SMITH: 'The Development of FSW Process Modelling for Use by Process Engineers', in: Y. Hovanski, Y. Sato, P. Upadhyay, A. A. Naumov, N. Kumar (eds), Friction Stir Welding and Processing XI, *The Minerals, Metals & Materials Series*, Springer, Cham, 2021.
- [2] R. N. SHUBHAVARDHAN and M. M. RAHMAN: 'Effect of FSW Parameters on Hook formation, Microstructure and Fracture Strength of Al, Mg alloys', *International Journal of Engineering Development and Research*, Vol. 5, Issue 2, 1730-1736, 2017.
- [3] E. ALDANONDO, J. VIVAS, P. ÁLVAREZ and I. HURTADO: 'Effect of Tool Geometry and Welding Parameters on Friction Stir Welded Lap Joint Formation with AA2099-T83 and AA2060-T8E30 Aluminium Alloys', *Metals*, 10, 872, 2020.
- [4] SIEMENS: 'Engineer innovation with CFD - focused multiphysics simulation', <https://www.plm.automation.siemens.com/global/en/products/simcenter/star-ccm.html>.
- [5] T DORIN, A VAHID, J LAMB: 'Fundamentals of Aluminium Metallurgy', *Chapter 11 - Aluminium Lithium Alloys*, Woodhead Publishing 2018.
- [6] ALCOA: *ALLOY 2099-T83 AND 2099-T8E67 EXTRUSIONS*, <https://www.spacematdb.com/spacemat/manudatasheets/Alloy2099TechSheet.pdf>.
- [7] A KARANIKA, N VOURDAS, A MAKRIKOSTAS, R MARINI, T PLAGIANAKOS, S KALOGEROPOULOS: 'Development of a new environmentally friendly anticorrosive surface treatments for new Al-Li protection with the frame of Clean Sky2', *Structural Integrity Procedia*, 10, 66-72, 2018.

# **X Special Joining Processes**



# IMPACT OF ACTIVATION IN PROJECTION WELDING WITH CAPACITOR DISCHARGE USING MULTIPHYSICS SIMULATION AND A PROCESS-INTEGRATED TRANSITION RESISTANCE MEASUREMENT

J. KOAL\*, M. BAUMGARTEN\*\*, J. ZSCHETZSCHE\*,  
U. FÜSSEL\*

*\*Technische Universität Dresden, Institute of Manufacturing Science and Engineering, Chair of Joining Technology and Assembly, Dresden, Germany, ORCID: 0000-0003-0763-552X*

*\*\*Technische Universität Dresden, Institute of Manufacturing Science and Engineering, Chair of Joining Technology and Assembly, Dresden, Germany, ORCID: 0000-0001-8486-1235*

*DOI 10.3217/978-3-85125-968-1-31*

## ABSTRACT

Capacitor discharge welding (CDW) is defined by a pulsed current profile. It is usually used for projection welding and is characterized by very high power density and very short welding time. The process can be classified into four phases: Contacting, Activating, Material Connection and Holding Pressure. High-speed images show the formation of metal vapor during the activation phase. This removes impurities and oxide layers from the contact zone and activates the surfaces. The material connection is achieved by pressing the activated surfaces together. The purpose of the investigation is to describe the impact of activation on the formation of the material connection.

A capacitor discharge welding system at the Technische Universität Dresden has the unique feature of interrupting the current flow at a given time. That allows different current profiles with the same rate of current increase. This unique feature permits the experimental investigation of activation and their impact on the formation of the material connection. To achieve this, projection components with different interruption times were welded. The transition voltages were measured before, while and after welding at each contact area. The mechanical strength of the welded joints was measured and a metallographic investigation was performed. To evaluate the impact of the activation in time and location, the experimental results were combined with simulative investigations. The evaluation of temperature and current density distributions enables the physical description of the activation. An iteratively coupled electrical-thermal and mechanical-thermal FEM-model was used. The experimental measured process variables force and current were used as boundary conditions for the simulation. A contact theory was implemented. In addition, the model considers temperature-dependent material characteristics and a remeshing procedure to model high projection deformations. The validation of the simulation was done by comparing measured and simulated transition voltages at the contact areas.

Keywords: Capacitor Discharge Welding, Projection Welding, Numerical Simulation, Contact Resistance, Transition Resistance, Activation

Symbol	Description	Unit
$C$	Capacity	F
$E_{el}$	Electrical energy	J
$I$	Current	A
$j$	Current density	A/m <sup>2</sup>
$\kappa$	Numerical parameter	-
$\rho$	Specific electric resistance	$\Omega \cdot m$
$\rho_1$	Specific electric resistance of material 1	$\Omega \cdot m$
$\rho_2$	Specific electric resistance of material 2	$\Omega \cdot m$
$\rho_{film}$	Specific electric resistance of surface	$\Omega \cdot m$
$\dot{q}$	Heat flux density	W/m <sup>2</sup>
$Q$	Amount of heat	J
$\dot{Q}$	Heat flux	W
$\dot{Q}_W$	Heat flux caused by the resistance heating	W
$\dot{Q}_R$	Heat flux caused by the contact resistance heating	W
$R$	Resistance	$\Omega$
$R_K$	Contact resistance	$\Omega$
$\sigma_s$	Yield strength of the soft material	N/mm <sup>2</sup>
$\sigma_K$	Contact pressure	N/mm <sup>2</sup>
$t$	Time	s
$T$	Temperature	T
$U_C$	Charging voltage	V
$\xi$	Numerical parameter	-

## INTRODUCTION

Capacitor discharge welding (CDW or CD-Welding) is a stable, efficient, cost-effective and easy-to-use joining process. It is mostly used for projection welding. For example, finished components with diameters up to 200 mm can be welded in a few milliseconds [1]. The Chair of Joining Technology and Assembly at the Technische Universität Dresden has developed a new process understanding in recent years [2-4]. The process is classified into four phases transitioning into each other (contacting, activating, material connection, holding pressure). When activating, the power density in the joining zone is so high that metal vaporization appears. This results in the activation of the surfaces. The joint is established without a welding nugget. The joint is established just by pressing the activated surfaces together. Plastic deformation of the projection activates further surface areas by displacing the surface layer. Activation by metal vaporization has been verified by high-speed imaging [2, 3]. It has not been possible yet to determine the impact of activation, because the joint is formed under electrical, thermal and mechanical stress, hidden and nearly immediately within a very short time (5 to 15 ms). Only by numerical process simulation, it is possible to investigate the hidden short-time process in a location- and time-dependent way. The finite element method allows electrical, thermal and mechanical evaluation, local resolution of the stress, time resolution of the stress and sensitive analysis with boundary conditions that cannot be adjusted experimentally. Therefore, a numerical simulation model has been developed to provide a more holistic representation of the CD projection welding process. The joining process includes the following complexities that make model development difficult:

- Very high temperature gradients

- Strong temperature-dependent deformation of the projection
- Emergence of different phases (melt, metal vaporization)

The high temperature-dependent projection deformations produce a high distortion of the mesh. This results in convergence problems. To avoid this, the simulation model must be remeshed at the time of strong distortion [5-7]. By experimental investigations on a new machine technology for CD welding, it is possible to measure transition resistances before and after welding in a process-integrated way for the first time. The current flow can also be interrupted. This means that for the first time, different current intensities can be investigated at the same rates of current rise. In addition to the simulimative analysis, this also enables an experimental estimation of the influence of activation. Capacitor Discharge projection Welding

PROCESS FUNDAMENTALS

CD welding is mostly used for projection welding and is a conductive resistance welding process. Before starting the welding process, one or more capacitor banks are charged. This causes an electrical energy  $E_{el}$  to be stored in the capacitor as a function of the charging voltage  $U_C$  and the capacity  $C$  (see equation 1) [8].

$$E_{el} = \frac{1}{2} C * U_C^2 \tag{1}$$

Discharging the electrical energy  $E_{el}$  starts the welding process. The current flow is transferred to the joining point. This results in the transformed and unregulated welding current as shown in Fig. 1. The peak current  $I_p$  is reached in a few milliseconds. This time is called the current rise time  $t_p$ . The welding time  $t_h$  is reached when the peak current  $I_p$  drops by 50%. The current flow time  $t_l$  is reached when the current drops to 95% . [1]

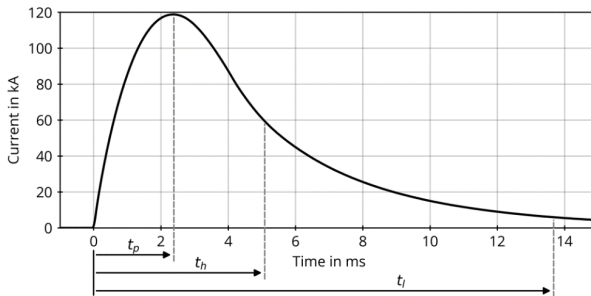


**Fig. 1** Characteristic current curve of a capacitor discharge projection welding

This clearly illustrates the differences to mid-frequency (MFDC) spot welding. This means that very high current intensities are obtained in very short current rise times [1, 9]. The projection geometry in the joining zone focuses the current flow and therefore increases the electric current density  $j$ . Based on Joule's heat law, the amount of heat  $Q$  is

generated in an electrical wire as a function of the square of the current and the ohmic resistance  $R$  (see equation 2). A differential observation based on equation 3 allows the local description of the heating by the heat flux density  $\dot{q}$ . This depends on the specific electric resistance  $\rho$  of the material and the current density  $j$ . The differential description is useful, for example, for using the finite element method (FEM). Equation 3 shows that a high current density in the joining zone results in a high heat flux density. The high power density in the joining zone is the critical parameter for the heating of the short-time projection welding process. That's why the heat flux  $\dot{Q}_W$  caused by the resistance heating in the projection and component is much smaller than the heat flux  $\dot{Q}_R$  caused by the contact resistance heating in the joining zone at the beginning of the process (see equation 4). As a result, no weld lenses are obtained in CD projection welding (see Fig. 2). [10]

$$Q = I^2 \cdot R \cdot t \tag{2}$$

$$\dot{q} = \frac{\dot{Q}}{V} = \rho \cdot j^2 \tag{3}$$

$$\dot{Q}_R = \iint j^2 \cdot R_c \cdot dA \gg \dot{Q}_W = \iiint I^2 \cdot R \cdot dV \tag{4}$$

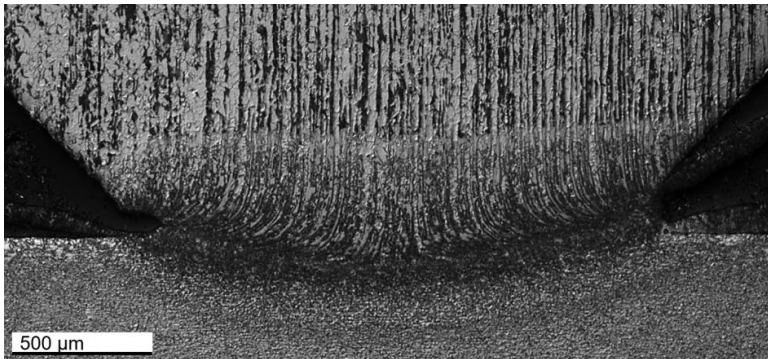


**Fig. 2** Missing of a joint without nugget lens in the joining zone during CD projection welding

#### SURFACE ACTIVATION

Investigations using high-speed imaging have shown that metal vaporization occurs due to the high power density in the joining zone [10]. CD projection welding is always associated with the appearance of weld spatter. Objective criteria for evaluating weld spatter were defined in [10]. This makes it possible to classify the weld spatter into four classes (classes 0 to 3). These classes are shown in Fig. 3. No sparks or weld spatter can be detected in class 0. Only a glow in the contact area may be visible. There is hardly any weld spatter visible in Class 1. These glow after a very short time. In Class 2, weld spatter

is clearly visible. The direction of travel of the weld spatter is towards the ground. They do not reach the ground. Strong weld spatter can be seen in Class 3, which flies down to the ground and can also continue to glow there.

In [2-4] a new process understanding with four characteristic phases has been defined: Contacting, Activating, Material Connection and Holding Pressure. When contacting the electrodes moves onto the components. The electrode force is increasing up to the predefined welding force. Plastic deformation begins in the contact area of the projection. When activating, the current flow starts with high current density gradients. This results in very high power densities in the contact area. This eliminates the foreign and oxide layers on the surfaces. With this begins the activation of the contact surface. To build the material connection, the activated contact areas are pressed together. The current and the current density decreases. The heat conduction of the projection starts. Further softening and plastic deformation of the projection occurs. With a further decrease of the current density, the last phase begins: Holding Pressure. The electrodes continue to follow-up. Further plastic deformation of the projection continues. This increases the contact area. Finally, the follow-up of the electrodes ends. The heat conduction continues and the joining zone is cooling down.

Following the characterization of the process phases, an activation of the surface by metal vaporization is necessary for the formation of the material connection. This means that a joint cannot be formed without activation. A capacitor discharge welding system at Technische Universität Dresden has the unique property of interrupting the current flow at a specific point of time. This allows different current profiles at the same rate of current rise. This unique feature allows the experimental investigation of activations and their effects on the formation of the material connection.

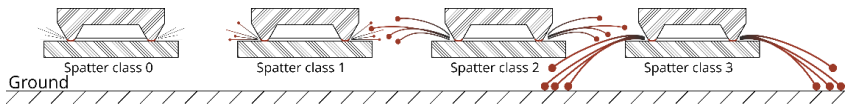


**Fig. 3** Classification of welding spatters in capacitor discharge welding [9]

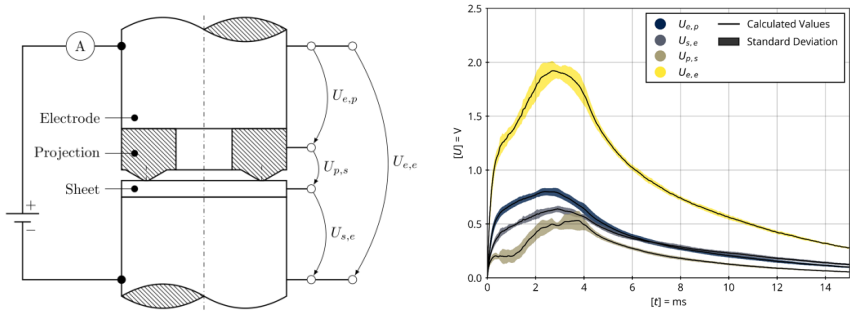
### NUMERICAL SIMULATION

In addition to the experimental investigation of surface activation, the finite element method can also be used. The FEM allows an electrical, thermal and mechanical evaluation, local resolution of the stress, temporal resolution of the stress and sensitive analyses with boundary conditions that cannot be set experimentally. An iteratively coupled simulation model for CD projection welding was developed at the Technische Universität Dresden with *ANSYS MECHANICAL APDL*. The iterative simulation process is described in detail in [11]. Input data are the current and the force as a function of time by experimental measurement data. The mechanical environment is solved for a small time step  $\Delta t$ . Then the contact pressure  $\sigma_K$  is determined in all contact areas. Using the contact pressure  $\sigma_K$  and the room temperature  $T_R$  at the beginning, it is possible to calculate the contact resistance  $R_C$  by equation 5 [12]. This temperature and contact

pressure dependant contact theory according to SONG is validated for projection welding of steel alloys. The yield strength  $\sigma_s$  of the soft material, the specific electric resistances  $\rho_{1,2}$  and a specific film resistance  $\rho_{\text{film}}$  are considered. Two numerical parameters are also considered. According to Song, the numerical parameters  $\xi$  and  $\kappa$  describes the surface condition.

$$R_K(T, \sigma_K) = 3\xi \cdot \left(\frac{\sigma_s(T)}{\sigma_K^\kappa}\right) \cdot \left(\frac{\rho_1(T) + \rho_2(T)}{2} + \rho_{\text{film}}\right) \quad (5)$$

The developed numerical process simulation is adapted to experimental measurement data. For this, the transition voltages  $U_{e,p}$ ,  $U_{p,s}$  and  $U_{s,e}$  of the single contact zones are measured during the process. When evaluating the transition voltages, they are corrected by subtracting the induced voltage of the CD welding machine [13]. The measurement setup is shown in Fig. 4a. The numerical parameters are time varied in the numerical process simulation so that the voltage curve matches the reality (Fig. 4b). [11]



a) Experimental Setup

b) Voltage curve of all contact zone

**Fig. 4** Experimental Setup to measure the dynamic transition resistance for adjusting the numerical parameters for all contact zones

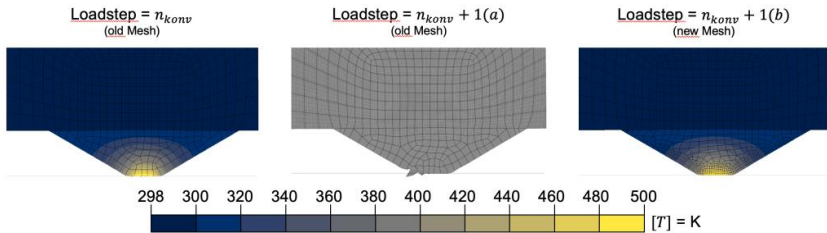


**Fig. 5** Illustration of the remeshing process within a structure simulation. A deformation of the projection is calculated for the given temperature distribution. From left to right: last converged load step ( $n_{\text{konv}}$ ), convergence problems in the following load step ( $n_{\text{konv}} + 1$  (a)), converged solution after remeshing ( $n_{\text{konv}} + 1$  (b))

With the progress of the simulation time, strong temperature-dependent plastic deformation appears. These result in such strong mesh distortions that convergence problems occur. Therefore, a remeshing is necessary [5-7]. Fig. 5 shows a situation where mesh distortion becomes too big. The initial situation for the remeshing process is a converged solution  $n_{\text{konv}}$ . The next load step  $n_{\text{konv}} + 1(a)$  results in convergence problems because of strong mesh distortion. A remeshing will result in the solution of the load step  $n_{\text{konv}} + 1(b)$ .

Since the distortion of the mesh with the high temperature-dependent deformation occurs in the mechanical environment, remeshing starts there. Proprietary simulation applications usually provide remeshing for structural analysis to calculate large deformations [14]. In the thermo-electric environment, these tools usually cannot be used. Therefore, the challenge is to remesh the thermo-electric environment as well and implement it into the iteratively coupled simulation process. Both indirectly coupled simulation environments require the same mesh. To do this, the last converged load step in the structural simulation is loaded. The global node coordinates (physical coordinates) are exported. The remeshing is then performed in the region of greatest distortion. Based on the new mesh geometry, the thermo-electric simulation must be continued. For this, the temperature distribution on the old mesh must be transferred to the new mesh generated in the mechanical domain. To do this, all the associated elements of new coordinates are defined in the old mesh. Then the natural node coordinates (element coordinates from -1 to 1) of the new physical coordinates in the old elements are determined. With the determined natural node coordinates, the temperature and electric voltage can be interpolated using to the element solution of the old mesh and the shape functions. At the end, interpolated solutions are available for all nodes in the new mesh, which can be applied as initial conditions. As a last step, a converged solution on the new mesh must be generated in order to continue the thermal electric simulation.

## EXPERIMENTAL AND NUMERICAL PROCEDURE AND RESULTS

### EXPERIMENTAL INVESTIGATION

The resistance welding task consists of a sheet and a ring projection with a projection diameter  $d_R = 15$  mm, radial contact area  $A_R = 1$  mm and a projection angle  $\alpha_R = 45^\circ$  (see Fig. 6a). The sheet thickness of the component is  $t_s = 3$  mm. The ring projection and the sheet are made of S355MC. The resistance welding electrodes are made of CuCr1Zr. The investigations are performed on a portal system „*KKP 18-MCS/gKE*“ of the company Kapkon GmbH. The system has an electric servo motor with an electrode force of up to 30kN. It is possible to weld both MFDC and CD. This enables investigation of the electrical influence on the welded joint without affecting the mechanics. Four capacitor banks are available for capacitor discharge. Peak currents of up to 210kA in 2.1ms can be realized. A unique feature is the process-integrated transition resistance measurement during CD welding. During the transition resistance measurement, the CD circuit is disconnected so that the measurement current flows solely through the welding task. Additionally, current flows in the welding process can be interrupted using a pulsed

capacitor discharge. This results in different current profiles depending on the interruption time  $t_1$ . Fig. 6b shows this behavior. The capacitor bank was charged with a voltage  $U_C = 1000\text{ V}$ . This capacitor bank has a capacity of  $21320\text{ }\mu\text{F}$ . This charging voltage  $U_C$  allows the activation to be investigated, since no welding connection is established at an interruption time  $t_1 = 0.4\text{ ms}$  and the upper limit of the welding range has been established at an interruption time  $t_1 = 30\text{ ms}$ . The interruption time  $t_1 = 30\text{ ms}$  is equivalent to no interruption, because after  $30\text{ ms}$  the capacitor banks are already completely discharged. The upper limit is defined by the appearance of class 2 to 3 weld spatter and by imperfections in the cross section. A total of 11 interruption times  $t_1$  were investigated. Each interruption time was repeated 7 times. A static press-out test was performed for each experiment. A total of 76 experiments were evaluated, as one false measurement was removed.

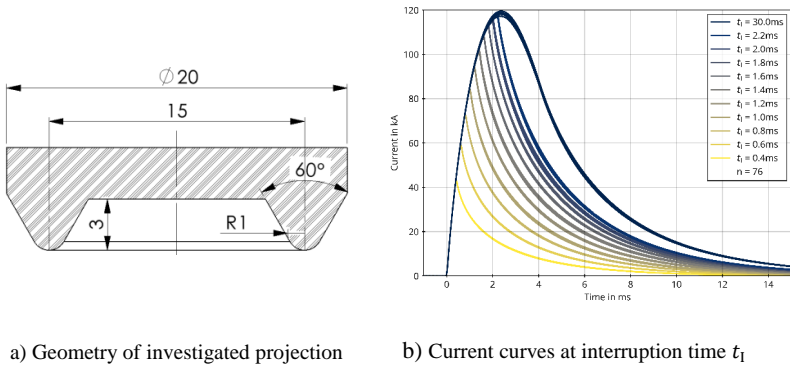
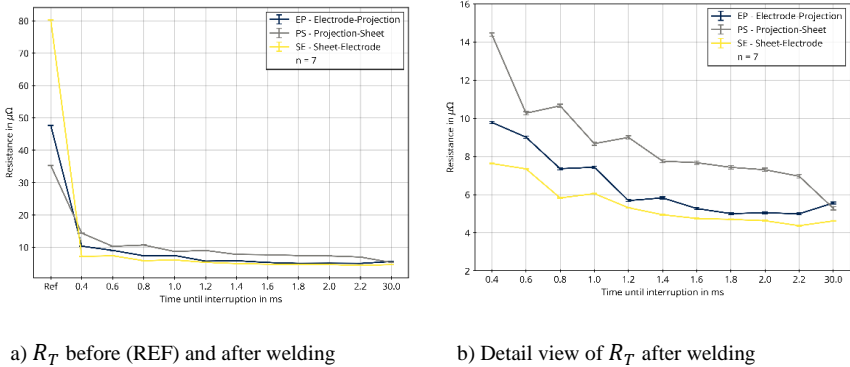


**Fig. 6** Geometry of the ring projection and current curves as a function of the interruption time  $t_1$

The results of the transition resistance measurement before and after welding are shown in Fig. 7a. An instantaneous drop of all transition resistances  $R_T$  can be observed at an interruption time of  $t_1 = 0.4\text{ ms}$ . The drop in the transition resistances  $R_T$  changes the order of the single transition resistances  $R_{EP}, R_{PS}, R_{SE}$ . The transition resistance  $R_{EP}$  in the welding zone now represents the largest value of  $14.35\text{ }\mu\Omega \pm 0.03\text{ }\mu\Omega$  for  $t_1 = 0.4\text{ ms}$ . The transition resistance before welding was  $R_{PS} 35.27\text{ }\mu\Omega \pm 0.16\text{ }\mu\Omega$ . At an interruption time of  $t_1 = 0.4\text{ ms}$  no material connection is established, even though the resistances drop significantly. Only at an interruption time of  $t_1 = 0.8\text{ ms}$  and bigger it is possible to establish a material connection. The transition resistances have fallen further to  $R_{PS} 10.66\text{ }\mu\Omega \pm 0.02\text{ }\mu\Omega$ . But that does not mean high press-out forces  $F_Z = 6.87\text{ kN} \pm 1.06\text{ kN}$  (see Fig. 8) can be reached. Fig. 7b shows a detailed evaluation of the transition resistances after welding. Especially in the joining zone, the transition resistance  $R_{EP}$  decreases strongly with an increase of the interruption time from  $t_1 = 0.4\text{ ms}$  to  $t_1 = 0.6\text{ ms}$  ( $-4.08\text{ }\mu\Omega \pm 28.4\%$ ). As the process continues, the transition resistances continue to decrease. From an interruption time  $t_1 = 1.4\text{ ms}$  a value of approx.  $7.3\text{ }\mu\Omega$  until  $7.8\text{ }\mu\Omega$  is reached for the joining zone. From this time on, the destructive force  $F_Z$  of the press-out

test also stops increasing and varies between 23kN until 30kN (see Fig. 8). A connection is completely established at an interruption time of  $t_1 = 1.4$ ms and more. The further energy up to  $t_1 = 30$ ms does not provide a significant increase of the press-out force. Only from  $t_1 = 30$ ms a lower standard deviation is evident. But in this range, a spatter class 3 is always detected or bonding defects are present in the microsection.



a)  $R_T$  before (REF) and after welding

b) Detail view of  $R_T$  after welding

**Fig. 7** Transition resistances  $R_T$  before and after welding. Before welding is the reference (REF)

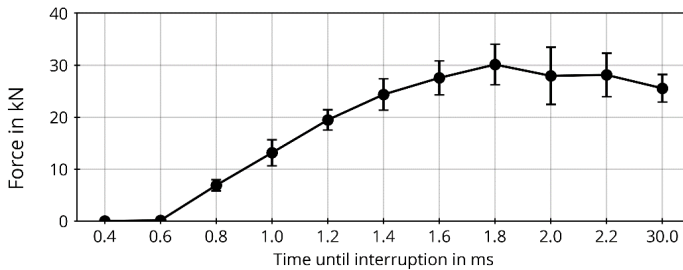


**Fig. 8** Press-out force  $F_Z$  of the ring projections as a function of the interruption time  $t_1$

### NUMERICAL INVESTIGATION

The numerical process simulation is based on the modeling method according to [11]. This considers the continuous adjustment of the contact resistance as a function of temperature and contact pressure, a nonlinear adaptive remeshing according to [7], the input parameters as time-dependent measurement data and the temperature-dependent material data for S355MC and CuCrZr. The material data used are in the appendix. In

Table 1 are the temperature-dependent thermomechanical properties of S355MC. In Table 2 are the temperature-dependent thermomechanical properties of CuCr1Zr. Table 4 and Table 5 show the corresponding temperature-dependent flow-stress curves for S355MC. In [15] the flow-stress curves for CuCr1Zr are shown.

The experimental investigations have shown that a significant collapse of the transition resistances already begins at  $t_1 = 0.4$  ms. Fig. 9a shows the temperature distribution for the time  $t = 0.4$  ms. The heating is the highest at the edges of the projection cross-section. The temperature is about 80 K over the value in the middle of the cross section. Fig. 9b shows the temperature distribution for  $t = 0.8$  ms. A connection might be established at this time. The heating continues to increase at the edge of the projection cross-section, since the contact resistance heating continues to dominate over the conductive heating (see equation 4). The temperature difference is now about 220 K. No strong projection deformations are noticeable at both time points. The current density is at its highest in the regions of the highest temperature increases. The maximum current density at  $t = 0.4$  ms is  $j = 6.17 \cdot 10^9$  A/m<sup>2</sup> and at  $t = 0.8$  ms it is  $9.07 \cdot 10^9$  A/m<sup>2</sup>. This results in a maximum power density of 0.585 MW/cm<sup>2</sup> at  $t = 0.4$  ms and 1.501 MW/cm<sup>2</sup> at  $t = 0.8$  ms.

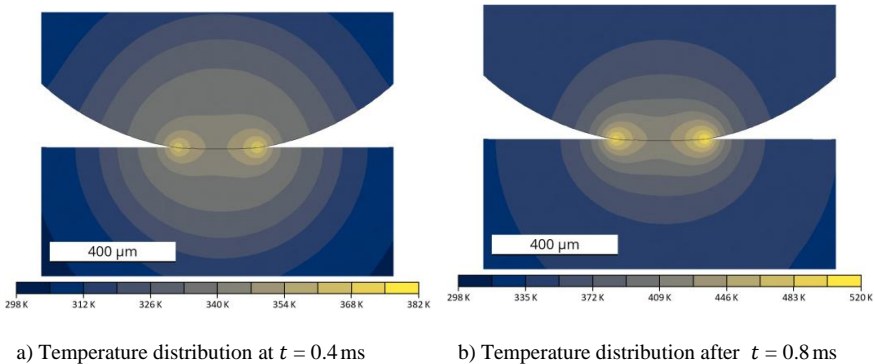


**Fig. 9** Temperature distribution of the numerical process simulation in the projection cross-section in the joining zone after different interruption times  $t_1$

Fig. 10 shows the distribution of the current density  $j$  at the time of maximum current ( $I_w = 117$  kA,  $t_w = 2.4$  ms). This results in a maximum power density of 32.56 MW/cm<sup>2</sup>. The deformation of the projection starts to increase further at this time. Contact resistance heating continues to be highest in the outer zone of the projection ( $T_{max} = 2100$  K).

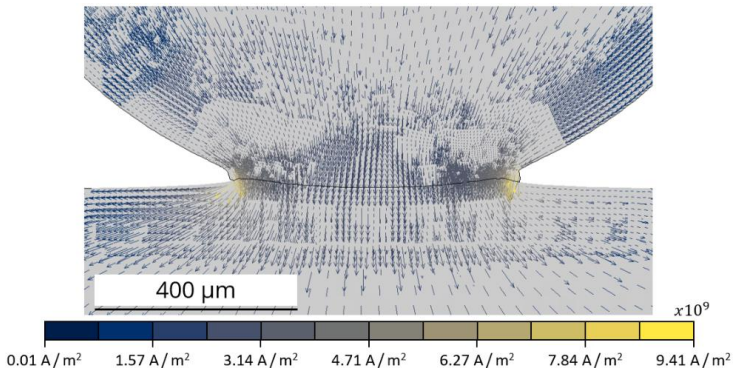


**Fig. 10** Current density distribution at the time of maximum current ( $t = 2.37\text{ms}$ )

## DISCUSSION

The decrease of the transition resistance in the contact zone points to a surface activation even at very low current maxima. With a small increase of the interruption time to  $t_1 = 0.6\text{ms}$  no connection could be established. It can be concluded that activation is not completed yet. With a further increase of to  $t_1 = 0.8\text{ms}$  a connection with low press-out forces can be reached. This shows that the surface activation at this point is enough to establish a connection. The remaining energy at this interruption time is not high enough to optimize the connection. As interruption times continue to increase, the connection quality becomes better. These investigations are consistent also with the observations from high-speed imaging [3, 10].

The numerical process simulation shows the heating in the outer area of the projection. This is the reason why the activation is clearly visible on the high-speed images. The heating proceeds from the outside to the inside. Investigations in laser keyhole welding with steel alloys indicate this. In laser keyhole welding a metal vapor-filled keyhole is formed, when high power densities are achieved. The required power densities depends on the material, the traveling speed and the depth of the keyhole. Recent investigations show that these vary between 1 and 5  $\text{MW}/\text{cm}^2$  [16-18]. The evaluation of the power density confirms the hypothesis of surface activation by metal vapor. These values are not reached with interruption times of  $t_1 = 0.4\text{ms}$ . The connection is also not established at these interruption times. However, the necessary power densities are reached at  $t_1 = 0.8\text{ms}$  and the formation of a welded connection can also be discovered for the first time. The power density in the joining zone increases with a further increase in the current intensity. The experiments also show this, because the splash class increases up to class 3. This defines the upper limit the welding range. The use of a multi-pulse technology is useful to further increase the connection quality. One pulse can be initiated to activate the surfaces. The connection is then established with a following second pulse.

The combination of experiment and simulation confirms the hypothesis of surface activation by metal vaporization. The formation of the connection by pressing activated

surfaces onto each other is to be analyzed in further investigations. Additionally, the activation of the surface is to be investigated as a function of different surface properties. Finally, further investigations with multi-pulse discharges are intended.

### CONCLUSIONS

The experimental investigations show an immediate drop in the transition resistances of all contact zones after just  $t_1 = 0.4$  ms. First connections could only be established after  $t_1 = 0.8$  ms. The connection quality did not increase further after approximately  $t_1 = 1.4$  ms. From the experimental investigations it can be concluded that activation does not occur sufficiently at the lowest interruption times. The temperature distribution and current density distribution were investigated in numerical simulations to describe this physically. It was determined that the heating occurs in the outer region of the projection and moves inward. The current density is also the highest there because of the concentration of heating in the outer region. Power density of  $0.585 \text{ MW/cm}^2$  was observed for the interruption time  $t_1 = 0.4$  ms. This is close to the power densities necessary for deep-hole welding. Metal vaporization is well known to occur there. Power densities of  $1.501 \text{ MW/cm}^2$  are determined from an interruption time of  $t_1 = 0.8$  ms onwards. The occurrence of metal vaporization during CD projection welding for steel alloys can be demonstrated by combining experimental and simulative investigations. This also confirms the observations from high-speed imaging.

### APPENDICES

**Table 1** Thermophysical properties of S355MC

$T / \text{K}$	$\rho_D / \text{kg} \cdot \text{m}^{-3}$	$E / \text{GPa}$	$\mu / 1$	$\alpha / \text{K}^{-1} \cdot 10^{-5}$	$\lambda / \text{W} \cdot \text{m}^{-1} \cdot \text{K}^{-1}$	$h_V / \text{MJ} \cdot \text{m}^{-3}$	$\rho / \mu\Omega \cdot \text{mm}^2 \cdot \text{m}^{-1}$
298	7807	208	0.290	Reference	37.368	1	0.251
333	7797	207	0.291	3.185	38.113	10	0.272
373	7785	205	0.293	3.216	38.787	103	0.297
403	7775	204	0.294	3.239	39.163	216	0.317
433	7766	202	0.295	3.263	39.426	332	0.337
473	7753	199	0.297	3.296	39.601	491	0.366
503	7743	197	0.298	3.320	39.602	613	0.389
533	7733	195	0.299	3.345	39.497	737	0.413
573	7720	191	0.301	3.379	39.200	908	0.448
603	7710	189	0.302	3.405	38.871	1040	0.475
633	7700	186	0.303	3.432	38.458	1175	0.504
673	7686	181	0.304	3.468	37.799	1360	0.546
703	7675	178	0.306	3.495	37.236	1504	0.580
733	7664	175	0.307	3.523	36.627	1652	0.615
773	7650	170	0.308	3.561	35.768	1856	0.665
803	7639	166	0.309	3.590	35.102	2016	0.704

## Mathematical Modelling of Weld Phenomena 13

833	7628	162	0.311	3.619	34.433	2181	0.745
873	7612	156	0.312	3.659	33.550	2413	0.802
533	7733	195	0.299	3.345	39.497	737	0.413
573	7720	191	0.301	3.379	39.200	908	0.448
603	7710	189	0.302	3.405	38.871	1040	0.475
633	7700	186	0.303	3.432	38.458	1175	0.504
673	7686	181	0.304	3.468	37.799	1360	0.546
703	7675	178	0.306	3.495	37.236	1504	0.580
733	7664	175	0.307	3.523	36.627	1652	0.615
773	7650	170	0.308	3.561	35.768	1856	0.665
803	7639	166	0.309	3.590	35.102	2016	0.704
833	7628	162	0.311	3.619	34.433	2181	0.745
873	7612	156	0.312	3.659	33.550	2413	0.802
903	7602	152	0.314	3.691	32.478	2645	0.860
933	7593	147	0.316	3.725	31.742	2849	0.906
973	7581	141	0.318	3.774	30.823	3136	0.967
1003	7574	-	-	3.813	30.146	3368	1.011
1033	7577	-	-	3.868	29.055	3620	1.057
1073	7597	125	0.334	3.969	27.325	3956	1.103
1103	7605	-	-	4.039	26.694	4162	1.116
1133	7589	-	-	4.072	27.035	4291	1.126
1173	7566	-	-	4.116	27.512	4415	1.138
1203	7548	-	-	4.150	27.869	4546	1.147
1233	7531	-	-	4.184	28.227	4678	1.156
1273	7508	105	0.351	4.232	28.703	4855	1.167
1303	7491	-	-	4.269	29.060	4987	1.176
1343	7469	-	-	4.320	29.535	5165	1.187
1373	7451	-	-	4.360	29.891	5300	1.195
1403	7434	-	-	4.401	30.246	5435	1.202
1433	7417	-	-	4.443	30.601	5571	1.210
1473	7394	84	0.363	4.501	31.076	5751	1.220
1503	7378	84	0.363	4.546	31.434	5885	1.227
1533	7362	84	0.363	4.593	31.791	6019	1.234
1573	7341	84	0.363	4.658	32.269	6198	1.243
1603	7325	84	0.363	4.708	32.627	6333	1.250
1633	7309	84	0.363	4.761	32.984	6469	1.256
1673	7287	84	0.363	4.833	33.461	6651	1.264
1703	7271	84	0.363	4.889	33.819	6788	1.271
1733	7250	84	0.363	4.937	34.144	6946	1.291
1738	7192	84	0.363	4.824	33.917	7203	1.369
1743	7165	84	0.363	4.777	33.843	7350	1.409
1748	7153	84	0.363	4.764	33.851	7427	1.406
1753	7139	84	0.363	4.745	33.844	7518	1.403
1758	7121	84	0.363	4.718	33.819	7627	1.399
1763	7099	84	0.363	4.679	33.767	7760	1.394
1768	7071	84	0.363	4.625	33.679	7930	1.388

## Mathematical Modelling of Weld Phenomena 13

1773	7034	84	0.363	4.548	33.538	8149	1.380
1778	6983	84	0.363	4.436	33.318	8445	1.371
1803	6924	84	0.363	4.357	33.519	8789	1.367
1833	6900	84	0.363	4.382	34.067	8929	1.372
1873	6868	84	0.363	4.416	34.798	9114	1.379
1973	6785	84	0.363	4.500	36.626	9566	1.396
2073	6700	84	0.363	4.585	38.454	10000	1.414
2173	6613	84	0.363	-	40.282	10420	1.431
2273	6525	84	0.363	4.754	42.109	10820	1.448
2373	6435	84	0.363	-	43.937	11200	1.465
2473	6344	84	0.363	-	45.765	11570	1.482
2573	6251	84	0.363	-	47.593	11920	1.499
2673	6158	84	0.363	-	49.420	12250	1.516
2773	6065	84	0.363	5.176	51.248	12560	1.532
2873	5971	84	0.363	-	53.076	12860	1.549
2973	5877	84	0.363	-	54.904	13150	1.566
3073	5782	84	0.363	-	56.732	13420	1.583
3173	5688	84	0.363	-	58.559	13670	1.600
3273	5594	84	0.363	-	60.387	13900	1.616

**Table 2** Thermophysical properties of CuCr1Zr

$T / K$	$\rho_D / \text{kg}\cdot\text{m}^{-3}$	$E / \text{GPa}$	$\mu / 1$	$\alpha / \text{K}^{-1}\cdot 10^{-5}$	$\lambda / \text{W}\cdot\text{m}^{-1}\cdot\text{K}^{-1}$	$h_V / \text{MJ}\cdot\text{m}^{-3}$	$\rho / \mu\Omega^2\cdot\text{mm}^2\cdot\text{m}^{-1}$
298	8882	87.8	0.326	Reference	326	0	0.021
473	8803	81.0	0.298	1.650	305	623	0.033
573	8755	-	-	1.720	291	968	0.039
673	-	77.9	0.279	-	-	-	-
773	8656	-	-	1.800	281	1660	0.054
873	-	69.6	0.230	-	-	-	-
973	8549	-	-	1.890	275	2820	0.070
1073	-	65.1	0.238	-	-	-	-
1173	8425	60.6	0.212	2.020	268	3680	0.098

**Table 3** Flow-stress curve of S355MC for 298 K until 673 K

$\epsilon / 1$	$\sigma_F / \text{MPa}$							
	298K	323K	373K	423K	473K	523K	573K	673K
0.00	277.2	252.6	217.5	193.8	177.0	164.7	155.4	142.8
0.02	422.3	393.1	350.3	320.5	298.4	281.3	267.4	245.7
0.04	466.8	435.6	389.6	357.4	333.4	314.6	299.2	274.6
0.06	495.6	463.0	415.0	381.3	356.1	336.2	319.8	293.4
0.08	517.2	483.7	434.2	399.3	373.2	352.5	335.3	307.5
0.10	534.7	500.4	449.7	413.9	387.0	365.7	347.9	319.0
0.15	568.2	532.4	479.4	441.9	413.6	391.0	372.1	340.9
0.20	593.3	556.4	501.8	463.0	433.6	410.1	390.4	357.4
0.25	613.6	575.8	519.8	480.0	449.8	425.6	405.1	370.8
0.30	630.7	592.2	535.1	494.4	463.5	438.6	417.6	382.1
0.35	645.5	606.4	548.3	507.0	475.4	450.0	428.5	392.0
0.40	658.6	619.0	560.1	518.1	486.0	460.1	438.1	400.7
0.50	681.2	640.6	580.3	537.2	504.2	477.5	454.7	415.7
0.60	700.2	658.9	597.3	553.3	519.6	492.2	468.7	428.5

0.70	716.7	674.7	612.1	567.3	532.9	504.9	480.9	439.5
0.80	731.3	688.7	625.3	579.8	544.8	516.3	491.7	449.3
0.90	744.5	701.4	637.1	591.0	555.5	526.5	501.5	458.1
1.00	756.4	712.8	647.9	601.2	565.2	535.8	510.4	466.2
2.00	840.1	793.3	723.4	672.9	633.7	601.3	573.0	522.7

**Table 4** Flow-stress curve of S355MC from 773K until 1673K

$\epsilon / 1$	$\sigma_F / \text{MPa}$						
	773K	873K	973K	1073K	1273K	1473K	1673K
0.00	135.5	135.4	131.9	0.0	58.4	42.3	34.8
0.02	228.7	214.3	200.9	0.0	101.2	72.5	41.4
0.04	254.9	237.4	221.8	0.0	116.2	83.1	41.4
0.06	271.7	252.3	235.2	0.0	126.1	83.1	41.4
0.08	284.4	263.4	245.3	0.0	133.7	83.1	41.4
0.10	294.7	272.4	253.4	0.0	139.9	83.1	41.4
0.15	314.3	289.7	269.0	0.0	151.9	83.1	41.4
0.20	329.1	302.6	280.7	0.0	161.1	83.1	41.4
0.25	341.0	313.0	290.1	0.0	167.5	83.1	41.4
0.30	351.1	321.8	298.1	0.0	167.5	83.1	41.4
0.35	359.9	329.4	305.0	0.0	167.5	83.1	41.4
0.40	367.7	336.1	311.1	0.0	167.5	83.1	41.4
0.50	381.0	347.7	321.6	0.0	167.5	83.1	41.4
0.60	392.3	357.5	330.4	0.0	167.5	83.1	41.4
0.70	402.1	366.0	338.1	0.0	167.5	83.1	41.4
0.80	410.8	373.5	344.9	0.0	167.5	83.1	41.4
0.90	418.7	380.2	346.3	0.0	167.5	83.1	41.4
1.00	425.8	386.4	346.3	0.0	167.5	83.1	41.4
2.00	475.8	429.4	346.3	0.0	167.5	83.1	41.4

## References

- [1] DEUTSCHER VERBAND FÜR SCHWEIßEN UND VERWANDTE VERFAHREN E.V.: *Kondensatorentladungsschweißen – Grundlagen, Verfahren und Technik*, DVS Merkblatt 2911, Düsseldorf, 2016.
- [2] U. FÜSSEL, M.-M. KETZEL, J. ZSCHETZSCHE: 'Erwärmungsverhalten der Kontaktzone beim Kondensatorentladungsschweißen unter Berücksichtigung der dynamischen Stromänderung und des Nachsetzverhaltens der Elektroden', *Abschlussbericht IGF- Nr. 18.987 BR/DVS-Nr. 04.069*, Technische Universität Dresden, Dresden, 2018.
- [3] J. ZSCHETZSCHE, M.-M. KETZEL, U. FÜSSEL, H.-J. RUSCH, N. STOCKS: 'Process Monitoring at Capacitor Discharge Welding', *ASNT Research Symposium 2019, Proceedings*, 2019.
- [4] N. STOCKS: *Erhöhung der Verschleißbeständigkeit durch partielle Integration von Hartmetallinserts mithilfe der KE-Mehrpulstechnik*, Ph.D Thesis, Technische Universität Dresden, Institute of Manufacturing Science and Engineering, Dresden, 2021.
- [5] M. WEHLE: *Basics of Process Physics and Joint Formation in Resistance Projection Welding Processes*, Ph.D Thesis, University of Stuttgart, Institute of Materials Science, Stuttgart, 2020.
- [6] F. X. LONG: *Development of a Remeshing Method for the Finite-Element Simulation of a Capacitor Discharge Press Fit Welding Process*, Bachelor Thesis, Karlsruhe Institute of Technology, Karlsruhe, 2018.
- [7] J. KOAL, M. BAUMGARTEN, J. ZSCHETZSCHE, U. FÜSSEL: *Numerische Simulation großer Deformationen beim Buckelschweißen durch Kondensatorentladung*, DVS Congress 2021, Essen, 2021.

- [8] H. BUMILLER, M. BURGMAIER, W. EICHLER, B. FEUSTEL, T. KÄPPEL, W. KLEE, J. MANDERLA, O. REICHMANN, J. SCHWARZ, K. TKOTZ, U. WINTER, K. ZIEGLER: *Electrical Engineering Textbook*, Europa Lehrmittel, ISBN: 3808532408, 2016.
- [9] U. DILTHEY: *Schweißtechnische Fertigungsverfahren*, 1. Springer-Verlag GmbH, ISBN: 9783540331544, 2006.
- [10] M.-M. KETZEL, M. HERTEL, J. ZSCHETZSCHE, U. FÜSSEL: ‘Heat development of the contact area during capacitor discharge welding’, *Welding in the World*, Vol. 63, No. 5, pp. 1195-1203, 2019.
- [11] J. KOAL, M. BAUMGARTEN, S. HEILMANN, J. ZSCHETZSCHE, U. FÜSSEL: ‘Performing an Indirect Coupled Numerical Simulation for Capacitor Discharge Welding of Aluminium Components’, *Processes*, Vol. 8, No. 11: 1330, 2020.
- [12] Q. SONG: *Testing and Modeling of Contact Problems in Resistance Welding*, Ph.D Thesis, Technical University of Denmark, Kongens Lyngby, Denmark, 2003.
- [13] M.-M. KETZEL, J. ZSCHETZSCHE, U. FÜSSEL: ‘Elimination of voltage measuring errors as a consequence of high variable currents in resistance welding’, *Welding and Cutting*, Vol. 16, No. 3, pp. 164-168, 2017.
- [14] ANSYS INC.: *Documentation Mechanical APDL – Chapter 4: Rezoning*, 2022.
- [15] J. WANG, H. P. WANG, F. LU, B. E. CARLSON and D. R. SIGLER: ‘Analysis of Al-steel resistance spot welding process by developing a fully coupled multi-physics simulation model’, *International Journal of Heat and Mass Transfer*, Vol. 89, pp. 1061-1072, 2015.
- [16] V. SEMAK, A. MATSUNAWA: ‘The role of recoil pressure in energy balance during laser materials processing’, *Journal of Physics D: Applied Physics*, Vol. 30, No. 18, pp. 2541-2552, 1997.
- [17] X. CHEN, H.-X. WANG: ‘A calculation model for the evaporation recoil pressure in laser material processing’, *Journal of Physics D: Applied Physics*, Vol. 34, No. 17, pp. 2637-2642, 2001.
- [18] J. Y. LEE, S. H. KO, D. F. FARSON, C. D. YOO: ‘Mechanism of keyhole formation and stability in stationary laser welding’, *Journal of Physics D: Applied Physics*, Vol. 35, No. 13, pp. 1570-1576, 2002.

# SIMULATION MODEL FOR LASER HARDENING OF SMALL-DIAMETER HOLES

A. EVDOKIMOV\*, F. JASIEWICZ\*\*, N. DOYNOV\*,  
R. OSSENBRINK\*, V. MICHAILOV\*

*\*Department of Joining and Welding Technology, Brandenburg University of Technology Cottbus - Senftenberg, 03046  
Cottbus, Germany*

*\*\*Berlin Industrial Group Technology Services GmbH, Schwarze-Pumpe-Weg 16, 12681 Berlin, Germany*

DOI 10.3217/978-3-85125-968-1-32

## ABSTRACT

The Gaussian laser beam can be transformed into a ring-shaped beam profile. The laser hardening can be performed by directing the obtained ring spot to the inner surface of the small-diameter holes. In this case, the laser irradiation falls inclined to the material surface. In this study, a simulation model was developed, which allows for the computation of temperature distribution during the laser hardening of the holes. The heat source model was developed to describe the intensity distribution on the inner surface of the holes as a function of the inclination, distance to the laser focal plane, and parameters of the laser beam. The intensity distribution changes during the hardening of complex holes (varied diameters along the hole). The developed simulation model accounts for the changes in the laser inclination, the distance to the focal plane, and the circumference of the irradiated area inside the hole during the processing. The simulations were performed using the open-source software FEniCSx. The developed model was validated by comparing the computed and experimentally measured temperature cycles.

Keywords: Heat source model, Laser hardening, Optimization

## INTRODUCTION

Axicon lenses allow the transformation of the Gaussian laser beam into a ring-shaped beam. By directing the obtained ring spot to the inner surface of the holes the hardening can be performed. A significant advantage is that no optic elements must be inserted into the hole. It enables the hardening of small-diameter holes. However, this technique implies high incidence angles between the laser beam and the material surface. Fig. 1 schematically shows the process.

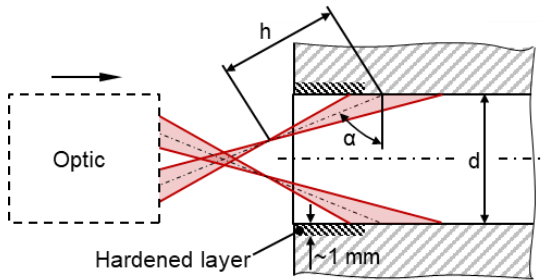


**Fig. 1** Scheme of the hardening process

Such inclination leads to a crucial change in the size of the laser spot on the surface [1]. The higher the incidence angle ( $\alpha$ ), the larger the irradiated area and the lower the laser intensity. Moreover, processing outside of the beam focal plane ( $h \neq 0$ ), besides further increase in the spot area, results in asymmetric intensity distribution [2,3]. Furthermore, the circumference of the irradiated area changes with the diameter of the hole, affecting the local intensity distribution. Geometric singularities such as sharp edges concentrate the heat flow, leading to local overheating and melting. To maintain the required temperature to achieve the uniform hardness distribution along the hole and to avoid melting, the laser power needs to be dynamically adapted during the processing. It can be normally handled by the control loops [4]. However, the integration of such loops is challenging due to the limited optical accessibility inside the hole. Alternatively, processing parameters can be optimized in advance using simulation techniques. The current study aims to develop a simulation model to enable prompt parameter optimization for the laser hardening of complex holes.

## EXPERIMENTAL SETUP

Laser hardening of holes made of C45 steel was performed without shielding gas. The chemical composition of the alloy can be found in Table 1. First, the hardening of simple holes with constant diameter ( $d = 10$  mm) was performed. The temperature cycles were measured using Ni/CrNi type K thermocouples. These trials served to validate the FE model. Subsequently, to demonstrate the applicability of the developed simulation model, the complex holes were hardened. The complex holes exhibit two diameters along the length ( $d_{max} = 13$  mm and  $d_{min} = 7$  mm).

**Table 1:** Chemical composition of C45 steel (wt. %) [5]

C	Si	Mn	Mo	Cr	Ni	P	S
0,42-0,5	<0,40	0,5-0,8	<0,1	<0,4	0,4	<0,045	<0,045

SIMULATION MODEL

Numerical simulation of the considered laser hardening technique primarily requires a heat source model, which properly defines the laser intensity distribution on the inner surface of the holes as a function of the processing parameters, hole geometry, and parameters of the applied laser beam. The influence of the beam inclination on the intensity distribution was extensively discussed in work [1]. In the current study, we adapted the suggested approach to the laser hardening of holes. Fig. 2 shows the irradiation area inside the hole. The laser energy is evenly absorbed along the entire circumference. As mentioned earlier the location of the highest intensity point does not match the geometrical center of the irradiated area if the material surface is outside the laser focal plane ( $h \neq 0$  in Fig. 1).

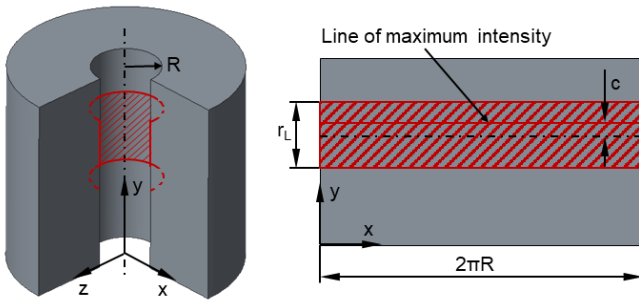


Fig. 2 Energy absorption inside holes

The geometrical parameters of the irradiated area can be calculated using the equations suggested in [1].

$$r_L = \sqrt{\frac{w_0^2 + \theta^2 h^2}{\cos^2 \alpha - \theta^2 \sin^2 \alpha} + \frac{(\theta^2 h \sin \alpha)^2}{(\cos^2 \alpha - \theta^2 \sin^2 \alpha)^2}} \quad (1)$$

$$c = \frac{\theta^2 h \sin \alpha}{\cos^2 \alpha - \theta^2 \sin^2 \alpha} \quad (2)$$

where  $\alpha$  is the beam incidence angle,  $h$  is the distance to the focal plane,  $\theta$  is the divergence half-angle of the beam and  $w_0$  is the beam waist. The asymmetric intensity distribution was captured using the same principle as in the well-known double ellipsoidal model [6]. One half of the source is based on one ellipsoid and the other half on another ellipsoid. The surface heat source model for the two-dimensional axisymmetric FE model (Fig. 3) is then

$$q(x, y) = (2 - f_2) \cdot \frac{\sqrt{2} \cdot P \cdot \eta}{\sqrt{\pi} \cdot r_{L1} \cdot 2\pi R} \cdot \exp \left[ -2 \cdot \left( \frac{y^2}{r_{L1}^2} \right) \right] + f_2 \cdot \frac{\sqrt{2} \cdot P \cdot \eta}{\sqrt{\pi} \cdot r_{L2} \cdot 2\pi R} \cdot \exp \left[ -2 \cdot \left( \frac{y^2}{r_{L2}^2} \right) \right] \quad (3)$$

where the radius of the first  $r_{L1}$  and second  $r_{L2}$  ellipsoids are

$$r_{L1} = r_L - c \tag{4}$$

$$r_{L2} = r_L + c \tag{5}$$

and the coefficient  $f_2$  is

$$f_2 = \frac{2}{1 + \frac{r_{L1}}{r_{L2}}} \tag{6}$$

The heat efficiency coefficient depends on many parameters such as wavelength, polarization, surface roughness, surface contamination, formation of the oxide layer and therefore cannot be normally calculated precisely and should be determined experimentally. The heat efficiency coefficient was found to be 0.75 for the current research. The open-source software GMSH was used for meshing. The meshing strategy is shown in Fig. 3. All boundaries experience heat exchange with the ambient. The contact with the clamping device was neglected. Mesh convergence analysis was done to ensure mesh-independent computational results. The FE computations were performed using the open-source FEniCSx software. The FEniCSx implementation was successfully verified by comparing the results with the ones obtained using Ansys. Regarding the mathematical formulation required for FEniCSx please refer to work [1].

Additional subroutines have been added to calculate the hole radius, incidence angle, and distance to the focal point at any time step during simulations. The optimization algorithm to determine the required laser power is shown in Fig. 4. The peak temperature on the inner surface is assessed after each simulation step and compared to the target temperature,  $T_R$ . Based on this comparison the laser power is set for the next step.

The hardness model was established using physical simulations. The Gleeble-samples were heated up to various peak temperatures and cooled down at different rates. The hardness of the achieved microstructures was measured. In the simulation model, the hardness is calculated directly as a function of the temperature cycle. In detail, this approach is described in [7–9].

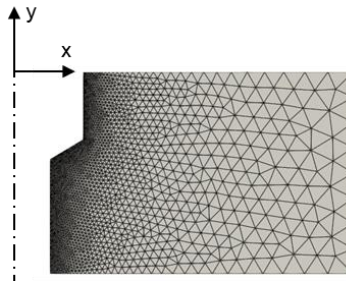


Fig. 3 Axisymmetric two-dimensional FE model (complex hole)

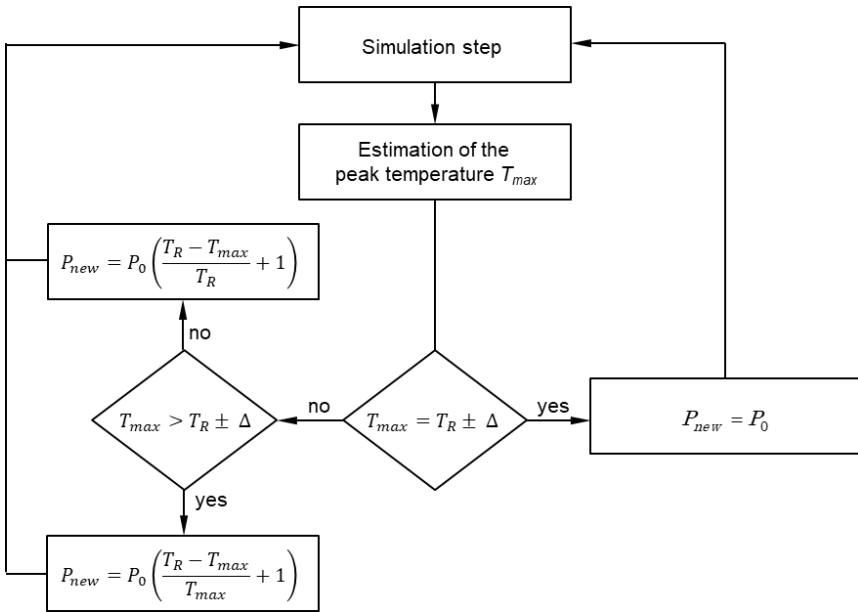
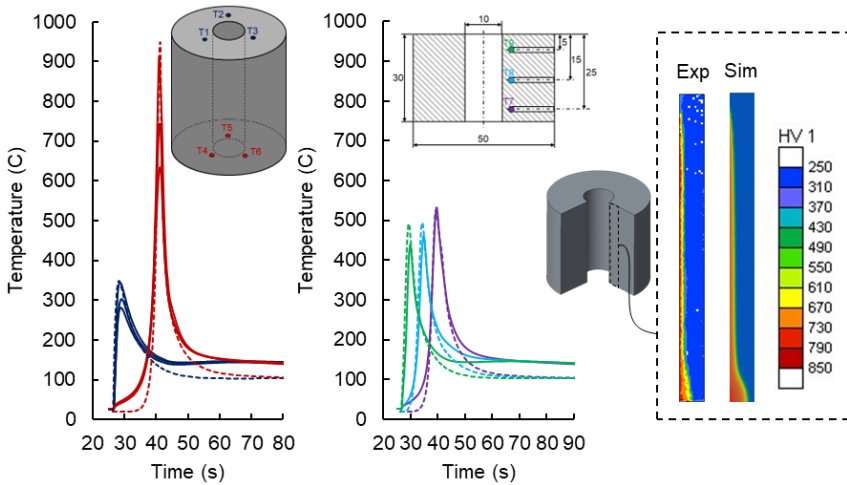


Fig. 4 Optimization algorithm

## RESULTS AND DISCUSSION

The developed FE model allows computation of full temperature history during laser hardening of the holes. Fig. 5 shows computed temperature cycles (dashed lines) and hardness versus measured ones for the simple hole.



**Fig. 5** Validation of the simulation model

As can be seen, the computed maximum temperatures, heating, and cooling rates as well as the hardness distribution are in good agreement with the measurements, thus validating the model. This validated model was used to compute the laser power for the hardening of the complex hole. The scanning speed was set to 2 mm/s. Fig. 6 shows the expected (computed) and real (measured) hardness profiles in the complex hole. The simulation showed that the hardening of the area next to the transition is challenging. The same area could not be hardened during the experimental trials in good agreement with the simulation. Since the irradiated area becomes large due to the beam inclination, melting of the sharp edges and hardening of the surfaces close to those edges cannot be controlled separately. The power is reduced to avoid the edge melting and at the same time, the temperature becomes insufficient to harden the material close to the edges. The developed simulation model makes it possible to identify the limits of the process and to show in advance whether the hole can be uniformly hardened. For the holes, which are suitable for this hardening technique, the model can be used to determine the optimal processing parameters.

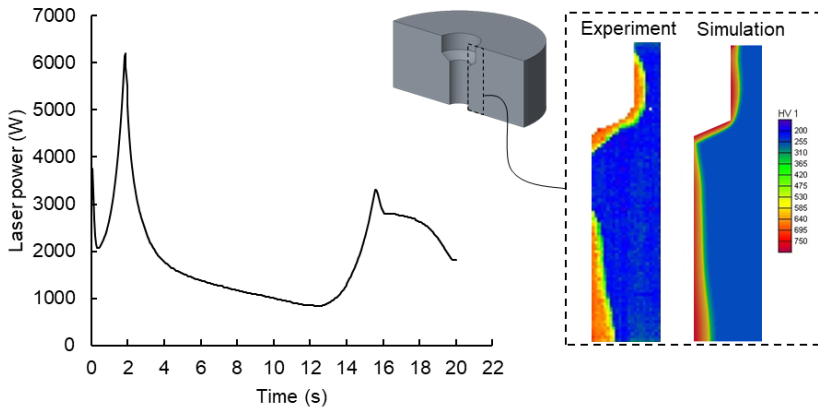


**Fig. 6** Computed optimal laser power for hardening of the complex hole (left). The computed versus measured hardness profile (right)

## CONCLUSIONS

The study presented a numerical model for laser hardening of holes. The heat source model calculates the intensity distribution on the inner surface as a function of beam parameters (beam waist, divergence half-angle), processing parameters (laser power, incidence angle, distance to the focal plane), and the circumference of the hole. The implementation was done using open-source FE code. The simulation allows optimization of the processing parameters, making the new hardening technique more attractive to the industry.

## APPENDICES AND ACKNOWLEDGEMENTS

This work was supported by BTU Graduate Research School (Conference Travel Grant); German Federal Ministry for Economic Affairs and Climate Action [grant no. ZF4259517US9].

## References

- [1] A. EVDOKIMOV, F. JASIEWICZ, N. DOYNOV, R. OSSENBRINK, V. MICHAILOV: ‘Simulation of surface heat treatment with inclined laser beam’, *J Manuf Process*, 2022, 81:107-14, <https://doi.org/10.1016/j.jmapro.2022.06.051>.
- [2] T. RUDLAFF: *Arbeiten zur Optimierung des Umwandlungshärtens mit Laserstrahlen*, n.d.

- [3] H. DANIELEWSKI, M. LOREK, W. ZOWCZAK: ‘Influence of a beam inclination on the results of laser welding’, Proceedings Volume 10974, *Laser Technology 2018: Progress and Applications of Lasers*, 109740T, 2018, <https://doi.org/10.1117/12.2516676>.
- [4] S. MARTÍNEZ, A. LAMIKIZ, E. UKAR, I. TABERNEO, I. ARRIZUBIETA: ‘Control loop tuning by thermal simulation applied to the laser transformation hardening with scanning optics process’, *Appl Therm Eng*, 2016, 98:49-60. <https://doi.org/10.1016/j.applthermaleng.2015.12.037>.
- [5] O. DREIBATI: *Physical welding simulation of the cold crack susceptibility*, Shaker Verlag, 2014.
- [6] J. GOLDAK, A. CHAKRAVARTI, M. BIBBY: ‘A new finite element model for welding heat sources’, *Metall Trans B*, 1984, 15:299-305, <https://doi.org/10.1007/BF02667333>.
- [7] A. Evdokimov: Numerical welding simulation of dissimilar Steel-Aluminum overlap joints, 2020.
- [8] R. OSSENBRINK: *Thermomechanische Schweißsimulation unter Berücksichtigung von Gefügewandlungen*, Aachen, Shaker Verlag, 2009.
- [9] A. Deflorio: *Distortion Simulation of Cylindrical Body Shape during Laser Beam Welding*, Aachen, Shaker Verlag, 2008.

# Author Index

## A

Abhuri Venkata, K. 341  
Alphonso, W. E. 21  
Alrumayh, A. A. 283  
Antonissen, J. 57  
Artinov, A. 101, 143, 161, 237  
Azuke, J. E. 189

## B

Bachmann, M. 101, 143, 161, 237,  
517  
Baumard, A. 127  
Baumgarten, M. 551  
Bayat, M. 7, 21  
Ben Hamouda, H. 57  
Benardos, P.G. 221  
Bergmann, J. P. 305  
Bielik, M. 361  
Bokelmann, T. 255  
Brosse, A. 127  
Bruyere, V. 127

## C

Cadiou, S. 127  
Chapetti, M. D. 473  
Chen, S. 71

## D

Delmas, J. 449

Dilger, K. 319  
Doynov, N. 567  
Draup, J. 449  
Drexler, H. 39

## E

Easton, M. 39  
Elsner, B. A. M. 491  
Emadmostoufi, S. 255  
Enzinger, N. 189, 473  
Ernst, W. 473  
Evdokimov, A. 567

## F

Felice, I. O. 57  
Fischer, M. 305  
Füssel, U. 551

## G

Gao, H. 205  
Girresser, T. 331  
Goldak, J. 331  
Gubeljak, N. 413, 473  
Gumenyuk, A. 143

## H

Hattel, J. H. 7, 21  
Haunreiter, F. 39  
Hendili, S. 449  
Hermsdorf, J. 255

Hildebrand, J. 305  
Hovden, S. 39

## I

Ikushima, K. 431  
Inoue, J. 397

## J

Jasiewicz, F. 567

## K

Kasprowicz, M. 341  
Kato, T. 431  
Khan, T. 449  
Kising, P. 161  
Kitzmantel, M. 361  
Koal, J. 551  
Kozak, D. 413  
Kozeschnik, E. 361, 407  
Kronsteiner, J. 39  
Kruska, J. 255

## L

Lammers, M. 255  
Lewis, M. 539  
Loose, T. 331

## M

Maeda, S. 431  
Magić Kukulj, M. 413  
Mauermann, R. 507  
Mendez, P. F. 71  
Meng, X. 101, 143, 161, 237

Michailov, V. 567  
Mokrov, O. 255  
Molotnikov, A. 39  
Muránsky, O. 221

## N

Neubauer, E. 361  
Neubauer, I. 361, 491  
Nied, H. F. 283  
Nitschke-Pagel, T. 319  
Noguchi, S. 397  
Núñez Sánchez, V. 71

## O

O'Toole, P. 39  
Oliveira, J. P. 57  
Ossenbrink, R. 567

## P

Paget, A. A. M. 449  
Poletti, M. C. 189  
Puschmann, M. 507  
Putra, S. N. 237

## R

Raberger, L. 491  
Rasche, S. 305  
Reisgen, U. 255  
Rethmeier, M. 101, 143, 161, 237,  
517  
Rissaki, D.K. 221  
Robin, V. 449

## S

Schob, B. 341  
Schwarz, Ch. 507  
Shan, Y. V. 407  
Sharma, R. 255  
Shibahara, M. 431  
Smith, M. C. 221, 449  
Smith, S. 539  
Steimbregger, C. 473  
Sun, J. 319  
Szalowski, B. 189

## T

Tomerlin, D. 413

## U

Ufarté, R. 449  
Üstündağ, Ö. 143

## V

Vallant, R. 189  
Vasileiou, A.N. 221  
vd Aa, E. 205  
vd Veldt, T. 205  
Viernstein, B. 407  
Vosniakos, G.-C. 221  
Vuherer, T. 473

## W

Wang, P. 189  
Wu, C. S. 517

## Y

Yan, Z. 71  
Yang, C. L. 517  
Yang, F. 237

## Z

Zschetzsche, J. 551  
Zwart, R. 205

